Design, Synthesis and Biological Evaluation of Novel P62zz Ligands with Therapeutic Potentials

by

Shifan Ma

Bachelor of Science, China Pharmaceutical University, 2012

Master of Science, University of Pittsburgh, 2015

Submitted to the Graduate Faculty of

School of Pharmacy in partial fulfillment

of the requirements for the degree of
Doctor of Philosophy

University of Pittsburgh

2021

UNIVERSITY OF PITTSBURGH

SCHOOL OF PHARMACY

This dissertation was presented

by

Shifan Ma

It was defended on

March 22, 2021

and approved by

Robert B Gibbs, PhD

Paul Edward Floreancig, PhD

Lee Apostle McDermott, PhD

Junmei Wang, PhD

Terence Francis McGuire, PhD

Dissertation Advisor: Xiang-Qun (Sean) Xie, PhD

Design, Synthesis and Biological Evaluation of Novel P62 Ligands with Therapeutic

Potentials

Shifan Ma, MS

University of Pittsburgh, 2021

p62 is a multifunctional protein containing multiple protein interaction domains, which participate in a wide array of signaling pathways. Among them, p62 is closely involved in autophagy and the ubiquitin-proteasome system (UPS) via its PB1, LIR, and ubiquitin-bounding domain (UBA) motifs. Our lab discovered the first small molecule ligand **XRK3** as our lead that interacts with p62 through its ZZ domain. Our previous studies found that **XRK3** showed an inhibitory potency on myeloma cell growth and reduced tumor size, and it recovered bone formation in myeloma models. To increase the efficacy and improve the pharmacokinetic profile of **XRK3**, we performed chemical modification on **XRK3** and screened the anti-proliferative effects on three multiple myeloma cell lines. We identified compound **6.28**, which has a higher *in vitro* anti-proliferative effect ($IC_{50} < 500nM$). Compound **6.28** also has good *in vitro* druggable properties and increases autophagosome number without inducing autophagy flux. The mechanism underlying this anti-tumor effect can be illustrated by signaling studies that show procaspase-8 accumulation, which causes procaspase-8 self-activation and activation of apoptosis signaling that results in cell death.

In addition, we found that a majority of our compounds can enhance autophagosome formation as represented by LC3B conversion. If our compounds activate autophagy flux and increase the clearance of misfolded and aggregated proteins in the brain by the autophagic process, they might be helpful in reducing help reduce the neurotoxic proteins that cause some degenerative

disorders. This hypothesis is consistent with a previous study by Dr. Kwon, who found that**XRK3** can increase the mutant huntingtin clearance by autophagy. Therefore, we measured the neuroprotective effects of our compounds in differentiated SH-SY5Y cells against hydrogen peroxide, which is associated with oxidative stress and neurotoxicity. We discovered a compound capable of inducing autophagic flux and reducing tau and α-synuclein levels with demonstrated neuroprotective effect. This compound **5.8** may have therapeutic relevance towards the treatment of neurodegenerative diseases.

Keywords: p62/SQSTM1, p62-ZZ ligands, multiple myeloma, neurodegenerative diseases, autophagy, oxidative stress.

Table of Contents

LIST OF TABLES

LIST OF FIGURES

Preface

I am heartily thankful to my advisor, Dr. Xiang-Qun Xie, whose encouragement, guidance, and support from the initial to the final stages enabled me to have a deeper understanding of the project. Dr. Xiang-Qun Xie has been my inspiration as I overcame all the obstacles to complete this research.

I would like to thank Dr. Terence Francis McGuire, who shared his extensive biology studies experience to support me when conducting and analyzing the bioassays' results.

I also appreciate the kind help from Dr. Jaden Jungho Jun and Dr. Peng Yang. They taught me some valuable tips, approaches, and knowledge about chemical synthesis and purification. Their valuable suggestions about compound design and synthesis helped me promote this study's chemical modification.

I want to thank Dr. Lirong Wang, who helped construct several disease-based chemogenomic databases applied in this study.

I appreciate the instruction from Dr. Zhiwei Feng to do the manual docking and homology modeling construction. He made this work more complete.

I also appreciate the kind help and great suggestions from my committee members: Dr. Robert B Gibbs, Dr. Lee Apostle McDermott, Dr. Junmei Wang, and Dr. Paul Edward Floreancig.

I would like to show my great appreciation for Dr. Liyong Zhang, Dr. Shoucheng Jin, Min Li, and Dr. Tong Qin, who taught me to do some bioassays. Min Li tested the anti-proliferative efficacy of some of my compounds on the U266 cell line. Dr. Jin measured the anti-multiple myeloma (MM) activity of compound 6.28 using different cell lines and shared some knowledge

about the underlying signaling pathways related to p62. Dr. Zhang taught me how to do immunoblotting, confocal immunofluorescence microscope, and immunostaining. Dr. Qin taught me how to do the radio-labeled ligand competitive binding assay using CB2 proteins and how to set up the initial protocols for some of the bioassays currently running in our lab. Dr. McGuire taught me about cell culture and the protocol for MTT assays.

I would like to appreciate the great work from Liping Wang, who synthesized the first generations of this p62-ZZ ligand and provided guidelines for our chemical modifications.

I want to show my gratitude to all the members of Dr. Xiang-Qun Xie's group for their help over the years.

I want to thank my parents and friends, who support me all the time.

Finally, I offer my regards and blessings to all of those who supported me in any aspect during the completion of the project.

Sincerely,

Shifan Ma

March 202

1.0 Introduction

1.1 p62 and Its Multiple Domains

Sequestosome 1/p62, initially identified in 1996 by Joung et al., functions as an intracellular signal modulator in multiple signaling pathways. As shown in **Figure 1**, p62 is a multifunctional protein that consists of some protein-interaction domains. The structure includes an N-terminal Phox-BEM1 (PB1) domain, a ZZ-type zinc finger (ZZ) domain, a nuclear localization signal (NLS), a TNF receptor-associated factor 6 (TRAF6) binding domain (TBS), a nucleus export system (NES), an LC3-interacting region (1), a Keap1-interacting region (KIR), and a C-terminalubiquitin bounding domain (UBA) (2).
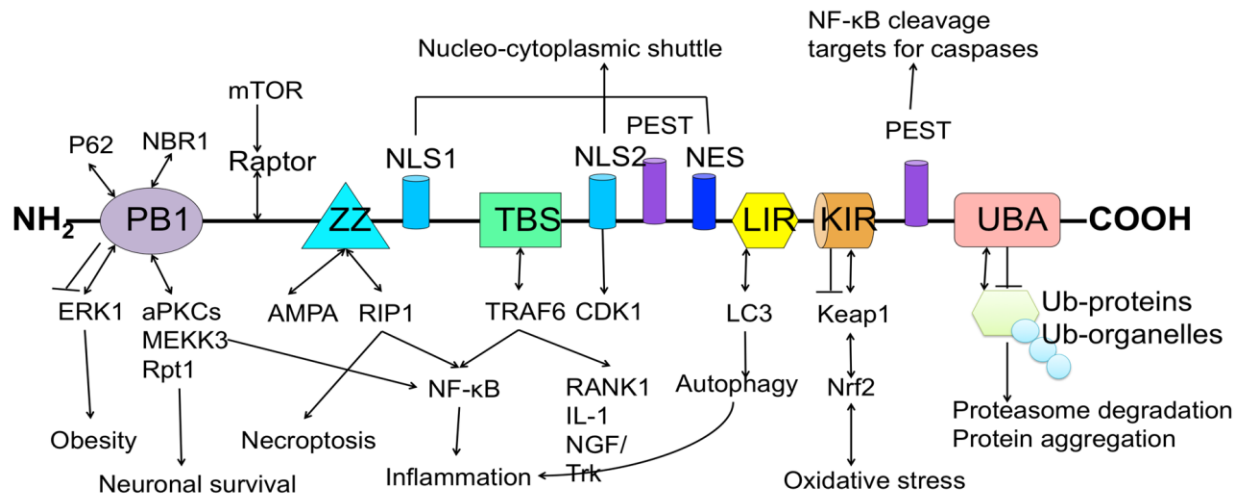
Figure 1. The Structure of p62 and Its Multiple Protein-Interaction Domains

Among its multiple motifs, p62 has an N-terminal PB1 domain. This protein-protein interaction module presents in many other signaling molecules, such as atypical protein kinases Cs (αPKCs) and mitogen-activated protein kinase kinase kinase 3 (MEKK3). Both these proteins and p62 can bind to each other and themselves through their PB1 domains. (3, 4) First, p62 interacts with itself and aggregates via the PB1 domain, facilitating its homo-oligomerization and cellular function (5). Additionally, heter-oligomerization can also occur with p62 and other PB1 domain-containing proteins, including αPKCs, mitogen-activated protein kinase 3 (ERK1), and MEKK3, all of which play critical roles in different signaling pathways that modulate adipogenesis, angiogenesis, neuron survival, cardiovascular pathogenesis, as well as osteoclastogenesis (6). The interaction between p62 and aPKC is associated with the activation of the nuclear factor kappa-B (NF-κB), which is downstream of cell stimulation by interleukin 1 (IL-1), receptor activator of NF-κB ligand (RANKL)(7), and nerve growth factor (NGF). It has also been reported that the interaction between p62 and ERK1 promotes adipogenesis (8).

Next, the ZZ-type zinc finger domain in p62 interacts with the receptor-interacting protein (RIP) to modulate the NF-κB pathway, inflammation, and necroptosis (9, 10). Also, p62 possesses a newly identified region located between the ZZ and TBS that interacts with the mammalian target of rapamycin (mTOR) regulator raptor (11), making p62 an integral component for the mTORC1 complex. P62 is necessary for mTORC1 activation in response to the uptake of amino acids and the subsequent mTORC1 recruitment to lysosomes (11). Xie lab and their collaborators have discovered P62 ZZ domain-specific inhibitors and identified them as potential treatments for multiple Myeloma and Huntington's disease (1, 12-15). These inhibitors have demonstrated an impact on modulating autophagy and proteolysis. (16-18)

Moreover, p62 interacts with TRAF6, a lysine 63 E3 ubiquitin ligase, via its central TB

domain (19-21). The interaction between p62 and TRAF6 induces p62-TRAF6 aggregation, which leads to the activation of NF-κB (20-22). Impaired osteoclastogenesis was observed iin TRAF6 and p62 knockout mice, suggesting that increased NF-κB signaling promotes cell survival pathways and osteoclast formation (20, 22, 23).

Furthermore, the LIR domain and C-terminal UBA domain enable p62 to function as an adaptor between autophagy and ubiquitinated proteins. P62 binds to ubiquitinated proteins via its UBA and then traffics the protein complex to the autophagosome membrane through interaction with microtubule-associated protein light chain 3 (LC3)-II. Additionally, p62 has a KIR domain that directly binds to Keap1 and interferes with the Keap1-Nrf2 axis, activating the Nrf2 mediated reactive oxygen species (ROS) elimination.

Furthermore, scientists have discovered two nuclear localization systems and one nuclear export system in the structure of the p62 protein. They are involved in the nucleo-cytoplasmic shuttling for p62 and other scaffold proteins. P62 contains two proline (P), glutamic acid (E), serine (S), and threonine (T) rich regions, which serve as proteolytic signals for rapid degradation (24).

1.2. SQSTM1/p62: A Signaling Hub for Many Pathways

P62 protein is a multifunctional scaffold protein for different signaling pathways (20, 25). The PB1 domain interacts with aPKC to regulate downstream targets. The downstream signaling cascades will be elevated or suppressed based on the up- or down-regulation of p62 protein expression level. The aPKC can activate the NF-κB signaling, promoting neuron survival and triggers inflammation (22, 26). The p62 PB1 domain also binds to MEKK3, thus activating NF-κB signaling (27). Knocking out p62 would reduce the aPKC activity, thus increasing mitogen-

activated protein kinase (MAPK), protein kinase B (AKT), and c-Jun N-terminal kinase (JNK) signaling (3) and leading to Aβ pathology and inflammation in neurodegenerative disease. The Glycogen synthase kinase (GSK3β) activity was also enhanced in the p62 knock-out mice, leading to tau hyperphosphorylation (28, 29). Usually, p62 will suppress ERK activity, knocking out p62 activated ERK signaling, leading to insulin resistance, impaired plasma glucose levels, and obesity (30, 31)
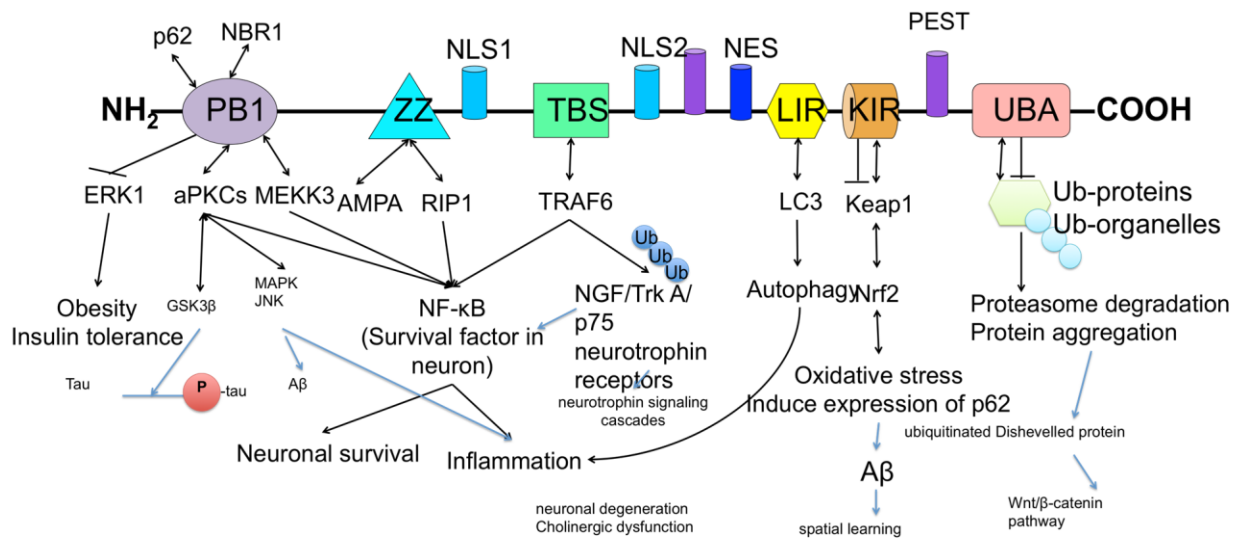
Figure 2. p62 as A Signaling Hub

As shown in **Figure 2**, p62 has another important domain: the TRAF6 binding site interacts with TRAF6 to regulate different signaling pathways that play a role in neurodegenerative diseases (20). In 2001, Sanz et al. reported that p62 interacts selectively with TRAF6, thereby activating the NF-κB activation in response to IL-1 (32). NGF interacts with p75 and Tropomyosin receptor kinase A (TrkA), leading to NF-κB activation (33). In 2001, Wooten and his colleagues showed that p62 binds to TrkA but not p75, whereas TRAF6 binds to p75 but not TrkA. They demonstrated an interaction between p62 and TRAF6 could act as a bridge to link p75 and TrkA signaling and a high-affinity binding site for NGF. They also suggested that p62 serves as a scaffold protein for

the activation of NF-κB signaling by NGF, which mediates neuron survival and differentiation responses (33). Geetha and his coworkers found that NGF stimulated TrkA polyubiquitination, a reduced level of which was observed in p75 knock-out mice. Both mutations in ubiquitin (K63R) and an absence of TRAF6 will abolish the polyubiquitination (23). Moreover, blocking the TBS domain in p62 and mutating the K485 in Trk A with arginine will also eliminate the polyubiquitination of TrkA, and the following NGF activated NF-κB signaling (23). In 2005, Wooten showed that p62 facilitated the polyubiquitination of TRAF6 (34). This polyubiquitination will be inhibited or blocked by mutation or deletion of either the PB1, or UBA, or TBS domain in p62. NGF stimulates the TRAF5 polyubiquitination and p62-TRAF6-PKC complex formation, which are suppressed by the blocker of p62-TRAF6 interaction (34). C Zheng et al. reported that in PC12 cells, Aß impaired the Trk A phosphorylation, ubiquitination, complex formation with TRAF6-P62-P75 (35). They also observed similar impairment on Trk A tyrosine phosphorylation, ubiquitination, and downstream signaling in AD patient brain samples compared with the control. A possible explanation is the nitrotyrosylation of TrkA increased in the AD hippocampus, which might, in turn, reduce the TrkA that undergoes ubiquitination and phosphorylation (35, 36). Additionally, they reported a reduced production of matrix metalloproteinase-7 (MMP-7) in AD hippocampus samples, which cleaves proNGF, resulting in an accumulation of proNGF and an attenuated level of active NGF (35). The accumulated proNGF will activate the p75 (not with TrkA), thereby inducing apoptosis and neuron death. Further analysis showed that Aß and AD lessened the ubiquitination and phosphorylation of Trk A and Trk A regulated downstream signaling, such as NF-κB, p38-MAPK, phosphatidylinositol-3-kinase (PI3K)-AKT pathways (20, 35, 36). Furthermore, studies showed that deregulation of TrkA/p75 induced neurotrophin signaling caused by lack of p62 or p75 have been linked to cholinergic dysfunction in AD (37).

The Keap1 interaction region is another crucial signaling domain in p62. Keap1 is an adaptor for Cullin-3 ubiquitin ligase that senses oxidative stress and binds to nuclear factor erythroid 2–related factor 2 (Nrf2). Nrf2, an essential leucine zipper protein, is responsible for a series of antioxidant proteins and detoxifies enzymes, which protect cells against oxidative damage triggered by injury and inflammation (38). Keap1 binds to KIR at the same binding site for Keap1-Nrf2 interaction, thus inhibiting the interaction between Keap1 and Nrf2, leading to the stabilization of Nrf2 and transcriptional hyperactivation of the Nrf2 target gene (38, 39). Given that p62 is closely involved in selective autophagy, the p62-Keap1-Nrf2 axis is also linked to selective autophagy by some post-translational modifications like phosphorylation and ubiquitination (40). Moreover, since p62 is degraded through autophagy, the lack or deficiency of autophagy in hepatocellular carcinoma cells or liver disease patients will result in the p62 accumulation, thereby evoking persistent activation of Nrf2 (41, 42).

On the other hand, Nrf2 stimulates the p62 protein expression, producing a positive feedback loop between Nrf activation and p62 protein expression. These studies showed that p62 served as a bridge to link the selective autophagy and ubiquitination system to the oxidative stress response system and redox regulation (43). Maintenance of homeostasis of p62 protein levels is crucial for neuron health. Kanninen showed that the AD symptoms in transgenic AD mice were improved by elevated Nrf2 expression (44-46) (**Figure 2**).

In addition to the signaling pathways mentioned above, p62 protein interacts with other proteins and regulates different signaling pathways influential to brain function. For instance, p62 has a ZZ(7) domain, which interacts with RIP to regulate NF-κB signaling and inflammation pathways in conjunction with atypical PKC(47, 48). Additionally, p62 binds to ubiquitinated Dishevelled protein. It mediates its autophagic clearance so that p62 can inhibit the Wnt signaling,

24

which is known to play a role in AD pathogenesis by controlling neuron development and maintaining the brain's synaptic function (49). Moreover, scientists reported that p62 could induce the intracellular aggregation and autophagic clearance of cyclic adenosine monophosphate (cAMP) phosphodiesterase-4A4 (PDE4A4), thereby augmenting the cAMP signaling. The reduced p62 protein expression will attenuate the cAMP signaling, which plays a vital role in the mediation of memory and synaptic plasticity. (50-53)

1.3. Autophagosome Formation and Autophagic Flux
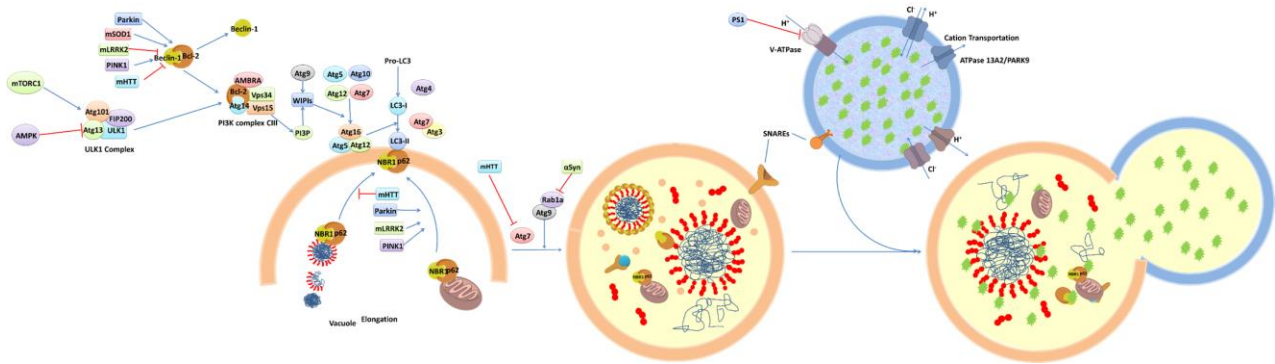
Figure 3. Key Components of the Autophagy Process.

Regulation of the autophagy process is associated with many neurodegenerative diseases. Abnormal interactions of mutant superoxide dismutase 1 (mSOD1), Leucine-rich repeat kinase 2 (LRRK2), Parkin, PTEN-induced kinase 1 (PINK1), and mutant Huntington (mHTT) with Beclin 1 could alter the initiation steps of autophagy. PINK and Parkin play a vital role in eliminating damaged mitochondria, and mutations in these proteins, as seen in Parkinson's disease (PD), could interfere with the overall mitophagy, the selective degradation of mitochondria by autophagy. mHTT expression leads to altered cargo recognition and autophagy failure. α-Synuclein (α-syn) can interfere with autophagy through interaction with Rab1a. Presenilin-1 (PS1) mutations cause impairment in lysosomal acidification and autophagy impairment. In PD, modifications in ATP13A2 could alter the function of lysosomes.

As indicated in **Figure 3**, autophagosome formation can be induced by inhibition of the mTORC1 complex and activation of AMP-activated protein kinase (AMPK). The increased autophagosome formation will lead to the phosphorylation of autophagy, activating kinase 1 (ULK1), thus phosphorylating all the components in the ULK1autophagy-related proteins 1(Atg1) complex, including Atg 13, Atg 101, ULK1, and ULK2 (54). The phosphorylated ULK1 can also phosphorylate AMBRA in the PI3K class III complex, composed of vacuolar protein sorting (Vps)34, Vps15, Atg14, and B-cell lymphoma 2 (BCL-2)-interacting protein (Beclin-1), enabling the complex to relocate from the cytoskeleton to the isolation membrane in the pre-autophagosome structure. In the PI3K CIII complex I, Beclin-1 is negatively regulated by Bcl-2 and Bcl-X. They are related to ER (Endoplasmic reticulum) stress (54, 55). Then, Vps34 in PI3K CIII complex will generate PI3K, which selectively interacts with the PI3P effector's WD repeat domain phosphoinositide-interacting 1 and 2 (WIPIs), catalyzing two reactions that mediate the isolation membrane elongation (54). The first reaction is the covalent conjunction of Atg5 and Atg12 in the presence of Atg7 and Atg10, followed by the Atg5-Atg12-Atg16 complex formation (54). This complex will translocate to the membrane of early autophagosomes and promote the covalent interaction of LC3-I with phosphatidylethanolamine (PE). In the process, Atg4 helps pro-LC3 translocate from the cell membrane to the early autophagosomal membrane, thus conjugating with PE and becoming LC3-II. LC3-II can interact with p62 bodies (p62/NBR1 (neighbor of BRCA1 gene 1 protein) complex with ubiquitinated proteins and organelles) and thereby facilitate the elongation and closure of autophagosomal membrane (Shown in **Figure 3**).

Finally, the autophagosome will fuse with the lysosome, forming an autolysosome where the ubiquitinated proteins and organelle complexes are degraded. Autolysosomes move along

26

microtube tracks to merge with the lysosome. Microtube acetylation, regulated by histone deacetylase 6 (HDAC6), is essential for fusion. Autolysosome formation requires late endosome proteins, such as Rab7, several "SNAP Receptors" (SNAREs), and Lysosomal-associated membrane protein (LAMPs)(54). In the lysosomal degradation process, lysosomal acidification relies on vATPase, a proton channel on the lysosome membrane. "The electrical gradient created is counterbalanced by a parallel influx of anions mediated by chloride proton antiporters." Cations, including calcium, can efflux through distinct channels or transporters, including two-pore calcium channel protein 2 (TPC2) and TRPML (mucolipin), which may also influence pH" (54). The cargo with organelle debris and proteins will be degraded in the autolysosome (**Figure 3**)(54).

1.4. Role and Biomarker of SQSTM1 in Autophagy AND UPS

Ubiquitin-enriched misfolded protein inclusions represent an invariant characteristic for almost all neurodegenerative diseases (56). P62 serves as a protein adaptor for ubiquitinated substrates and selective autophagy (51). As shown in **Figure 4**, three domains contribute to the role of p62 to shuttle ubiquitinated proteins to autophagosome for degradation (51). Misfolded proteins aggregated and bound to chaperone and then ubiquitinated by UPS (ubiquitin-proteasome system) enzymes. The mono- or poly-ubiquitinated proteins then recruit p62 via its C-terminal ubiquitin-associated (57) domain, leading to p62-promoted protein aggregation. The UBA domain binds to both mono- and poly-ubiquitinated proteins, with a preference for the K63 ubiquitinated proteins. Tanji et al. reported that K63-linked polyubiquitin is the most stable enhancer for protein inclusions formation by increasing the protein accumulation and facilitating intracellular inclusion bodies' formation under normal conditions. Under pathological conditions, co-cultured with tau

and SOD1 mutation, K63 promotes the accumulation of tau and the formation of SOD1-contained inclusion bodies. K63-linked polyubiquitin, acts as a partner with p62 to enhance autophagic clearance of protein inclusions linked to common neurodegenerative diseases (58). P62 may regulate K63-linked polyubiquitination via interaction with K63 ubiquitinating E3 ligases (TRAF6) (36, 59, 60).
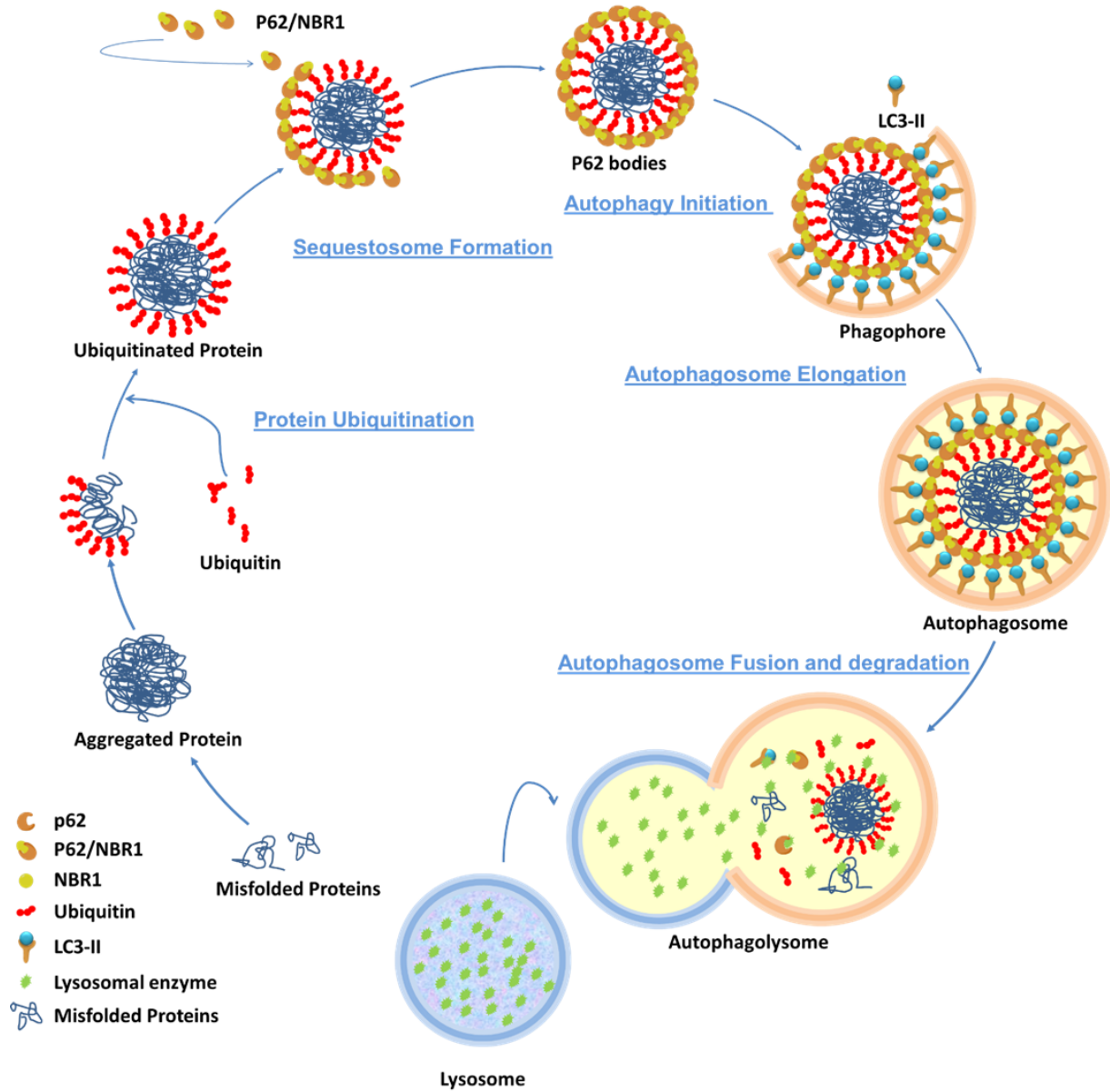
Figure 4. The Trafficking Role of p62 in Selective Macroautophagy.

As shown in **Figure 4**, ubiquitinated protein/p62 aggregates grow and become p62 bodies, which transport to a phagophore-forming location to form an autophagosome. The formation, growth, and transportation of p62 bodies cannot be achieved without the assistance of the N-terminal Phox-BEM1 (PB1) domain in p62. The construction of p62 bodies relies on p62 dimerization and further oligomerization. PB1 domain is indispensable and responsible for p62 dimerization. Any mutation or variants in PB1 domain will hamper the p62 dimerization. Both p62 homo-dimerization and heter-dimerization with NBR1, which are essential for p62 bodies' formation, are regulated by the PB1 motif. Although the underlying mechanism is still unknown, the transportation of p62 bodies to autophagosome formation location is also dependent on the p62-PB1 mediated homo-dimerization and heter-dimerization (51, 59-61).

There are several biological processes related to p62. These processes could be detected using their correlated biomarkers, such as LC3B and Beclin 1, biomarkers for macroautophagy. These autophagy biomarkers might also be used as a clinical prognostic biomarker, providing information on the likely outcome of diseases on patients and helped identify patients for the specific treatment group. For instance, LC3B is one of the best and the most commonly used autophagy marker in multiple *in vitro* assays. In addition to LC3B, Other proteins, such as LC3A, Beclin 1, ULK1, and VPS34, are also used as autophagy biomarkers to monitor autophagosome formation and autophagy flux. They might be applied as a potential clinical prognostic biomarker for many cancers as well. The Beclin 1-VPS34 complex is a central coordinator for autophagy downstream. (62) Beclin-1 is a potential prognostic biomarker with favorable outcomes for lung cancer, breast cancer, lymphoma, and gastric cancer (63). Additionally, p62 itself is a biomarker for autophagy flux. Accumulation of p62 protein measured by immunofluorescence and Western

blot is usually considered an indication of autophagy inhibition. (62) P62 is an autophagy biomarker in many human cancer specimens, such as multiple myeloma samples (13).

LC3 protein is the critical component in autophagy necessary for autophagosome elongation and closure, as displayed in **Figures 3 and 4**. LC3 protein is cleaved by Atg4 protease to expose its C terminal Gly residue and then conjugates to a phosphatidylethanolamine (PE) group to get its active form LC3-II. LC3-II links p62 and autophagosome membrane together to form autophagosome with p62 bodies. P62 interacts with LC3-II via its LIR domain (amino acid 332-343). LIR binds to a key mitophagy component, BCL2 E1B 19 kDa protein-interacting protein (NIX) (64, 65), as well as the autophagy-dependent p53-inducible nuclear protein 1 (TP53INP1)(66). The LIR domain is a short oligomer constituted of about 11 amino acids shared by ten proteins, including p62. The interaction between p62 and LC3-II anchors the p62 bodies onto the LC3-II-containing autophagosomal membrane, continuing its maturation and elongation in the autophagy process. Based on the selective interaction between LC3-II and p62, the autophagosome will only contain the ubiquitinated protein aggregates with p62/NBR1, and go through a selective autophagic degradation with lysosome fusion. Therefore, p62 and LC3-II are indispensable regulators for misfolded protein clearance through selective autophagy. Knocking down of LC3 proteins has been shown to induce the accumulation of p62/NBR1-ubiquitinated proteins in the cell plasma. Other studies have shown that ubiquitinated unfolded proteins or organelles could interact with p62/NBR1, then attach to LC3-II in the autophagosomal membrane, to trigger specific autophagic elimination (60, 67). To summarize, p62 is a cargo protein that shuttles the ubiquitinated proteins to autophagic degradation (59).

1.5. Therapeutic Significance of p62

1.5.1. p62 and Multiple Myeloma

1.5.1.1. Multiple Myeloma

Multiple Myeloma is a cancer of plasma cells in the bone marrow and is the second most common hematological malignancy after non-Hodgkin lymphoma. Plasma cells develop from B cells, a type of white blood cells in our immune systems, in response to a foreign substance that enters the body. Each plasma cell develops in response to a particular antigen and produces antibodies specific to the antigen to fight agonist disease and infection. In multiple Myeloma, the plasma cells undergo a complicated process and transform into malignant plasma cells, called myeloma cells. Myeloma cells locate in more than one spot of bone marrow produce many abnormal antibodies called M proteins. Unlike normal antibodies, M proteins did not fight disease. The cancerous myeloma cells multiply and grow too much. They accumulate in the bone marrow and occupy the space for normal healthy blood cells located in the bone marrow, such as red blood cells, healthy white blood cells, and platelets (Shown in **Figure 5**).
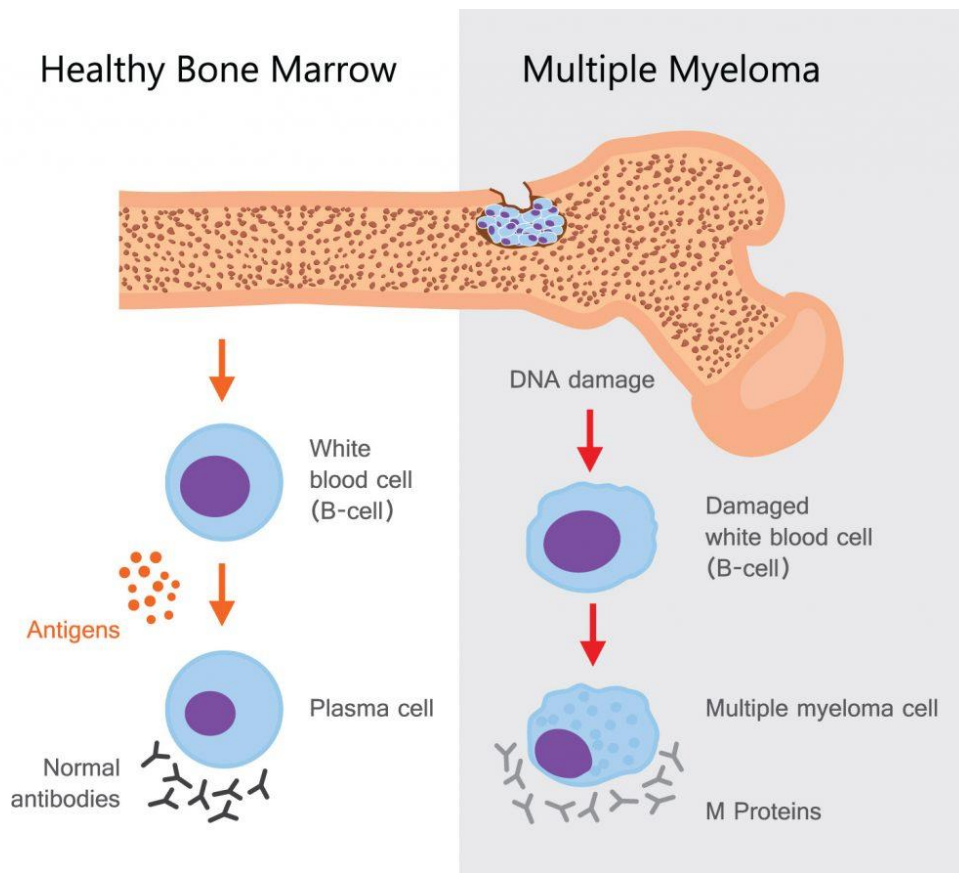
Figure 5. Basics in Multiple Myeloma

The reduced number of normal blood cells will cause anemia, excessive bleeding, and decreased ability to fight infection, common symptoms of multiple Myeloma. The accumulation of large quantities of M proteins in blood and urine can damage the kidneys and other organs. The buildup of myeloma cells in the bone can cause osteolytic lesions and pain of the bone, increasing the risk of the bone fraction.

The American Cancer Society's estimates for multiple Myeloma in the United States for 2021 are: about 34,900 new cases will be diagnosed (19,320 in men and 15,600 in women); nearly 12,830 deaths are expected to occur (6,840 in men and 5,570 in women) (68). In 2017, there were about 130,000 cases of Myeloma, translating to an age-standardized incidence rate of 2.1 per 100,000 persons. Multiple Myeloma caused 98,437 deaths globally, with an age-standardized

incidence ratio of 1.5 per 100,000 persons. In 2018, the latest year for which incidence data are available, 25,286 new Myeloma cases were reported, and 12,266 people died of Myeloma in the United States.(69)
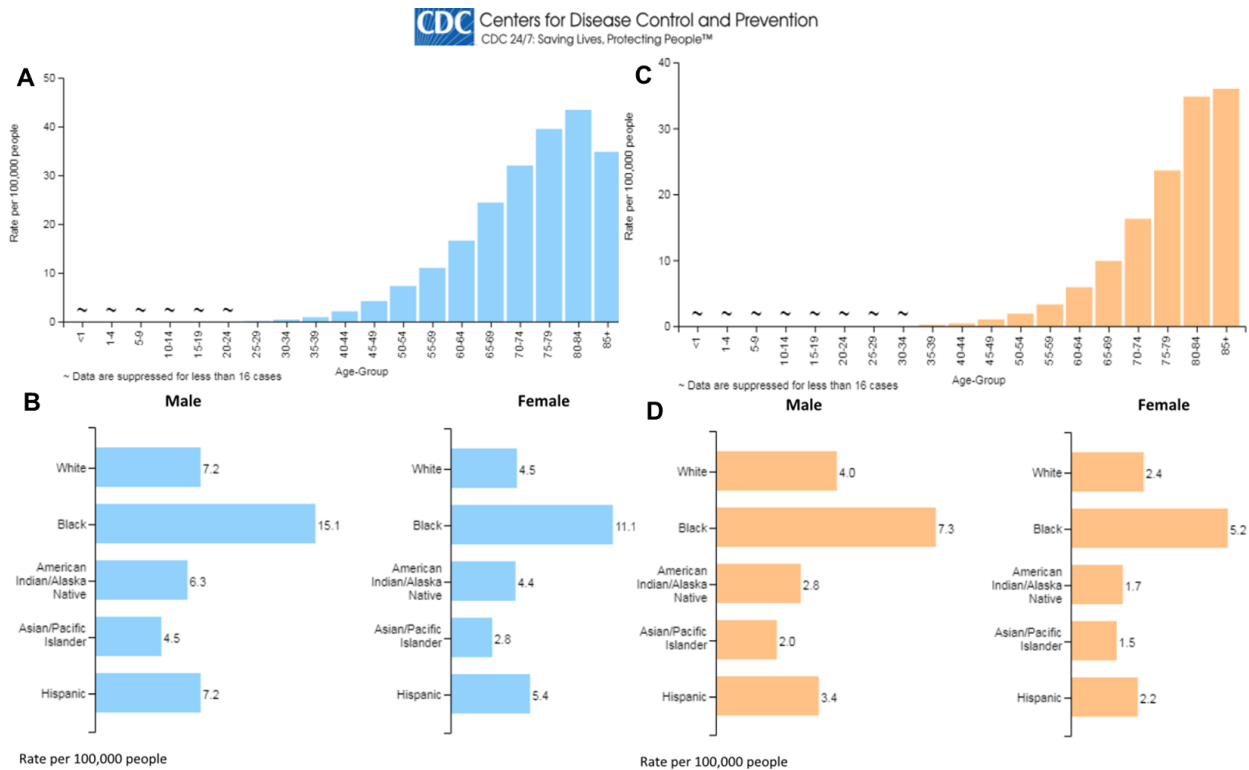
Figure 6. Epidemiology of Multiple Myeloma in the US.

A. Rate of new myeloma cases appears in different age groups. B. Rate of new myeloma cases by different races/ethnicity and sex. C. Death rate from Myeloma in various age groups. D. Death rates from Myeloma by other sex and races/ethnicity. Chart and data were collected from the Center for Disease Control and Prevention (CDC) website (69).

As illustrated in **Figure 6**, Multiple Myeloma was estimated to account for 1.8% of all new cancer cases and 10% of all hematological malignancies in the United States in 2018 from NCI

cancer statistic results. From the epidemiology result, both the incidence and death rates of multiple Myeloma are 2–3-times higher in black individuals than in white individuals but is lower in Asian and Hispanic individuals. People older than 70 have more possibility to have Myeloma, and more deaths were caused by Myeloma in elders.

The actual underlying pathological mechanism for multiple Myeloma is not known yet. However, many efforts have been made for a better understanding of the process of multiple myeloma development.

Currently available treatment for multiple Myeloma aims to improve patients' quality of life by easing their symptoms and helping them receive more nutrition to fight against the disease. Some of the drugs can slow down the spread of the disease for the patients. However, these drugs cannot cure the disease, and about 15% of patients do not benefit from the currently available MM medications. More effective drugs specific for MM are still in urgent need.

Several classes of medications can be used to treat MM, including chemotherapy, proteasome inhibitors, immunomodulators, glucocorticoids, HDAC (histone deacetylases) inhibitors, anti-CD38 (cluster of differentiation 38) monoclonal antibodies, an anti-SLAMF7 (signaling lymphocytic activation molecule family 7) antibody, a nuclear export inhibitor, bisphosphonates for bone disease, antibody-drug conjugates, and programmed death-ligand 1 (PD-L1) and PD-1 ligands (70).

All currently used drugs in the clinic for MM, their relapse, and accompanying symptoms treatments are summarized with their classification, drug name, approved year, company, brand name, adverse effects, mechanism of actions, and mechanism of potential drug resistance in **Appendix**.**Table of FDA-Approved MM Medications**

Chemotherapy is a class of medications that destroy or inhibit tumor cells' growth, including cyclophosphamide, melphalan, etoposide, melphalan flufenamide, bendamustine, cisplatin, vincristine, doxorubicin, , and pirarubicin. It is one of the major types of drugs applied for MM (70). However, due to the increasing number of agents that have been developed recently, chemotherapy has become less critical and used less frequently than before. It is often used in combination with immunomodulators and corticosteroids. On February 26, 2021, the Food and Drug Administration (FDA) granted accelerated approval to melphalan flufenamide (Pepaxto, Oncopeptides AB) in combination with dexamethasone for adult patients with relapsed or refractory MM who have received at least four prior lines of therapy and whose disease is refractory to drugs (71).

Chemotherapy can destroy cancer cells as well as normal cells. Therefore, it can cause adverse effects, including infection, nausea, vomiting, hair loss, tummy upsets, diarrhea, and constipation. In addition, long-term use of chemotherapy will lead to irreversible damage of the heart and kidney, making it hard to balance the benefits and risks of applying these drugs. Moreover, increased expression of efflux proteins, such as P-gp and ABCG2, plays a crucial role in chemotherapeutic drug resistance for MM (72). Besides, RECQ1 overexpression protects the cells from cytotoxicity due to melphalan and bortezomib treatment (72). Additionally, MAGE-A expression enhances resistance to melphalan by regulating Bcl-2 and overexpression of Bcl-xL in myeloma cells associated with a reduced response to chemotherapeutic agents (71).

Corticosteroids, such as dexamethasone and prednisone, are a classof medication frequently applied in MM treatment. Corticosteroids can help decrease nausea and vomiting caused by chemotherapeutic agents. Side effects of corticosteroids are heartburn, indigestion,

mood change, insomnia, increased appetite and weight gain. The suppression of the immune system due to steroids' long-term use will cause infections and weaken the bones. Drug resistance is a common problem that occurs with the use of corticosteroids. A truncated glucocorticoid receptor (GCR) lacking the C-terminal hormone-binding domain was found in MM cells resistant to dexamethasone (72). An elongation block was found in the GCR gene NR3C1. Additionally, FK506 binding protein 51 (FKBP5) overexpression, oncogenes FGFR3, and MYC (72) were induced by dexamethasone treatment in MM cells. (71, 73)

Immunomodulators are used in the first line to treat MM. The first one to be developed, thalidomide, caused severe birth defects when taken during pregnancy, leading to its withdrawal from the market before becoming available again. Common adverse effects of immunomodulating agents are drowsiness, fatigue, severe constipation, painful nerve damage, thrombocytopenia (low platelets), and low white blood cell counts. The most important mechanism behind immunomodulators' resistance to MM was the downregulation of cereblon, a common primary target for immunomodulating agents, a part of the E3 ubiquitin ligase complex, and a substrate receptor of CRL4 (72, 74).

Proteasome inhibitors work by inhibiting the proteasome activity that degrades the proteins, which is essential for cell division, especially in tumor cells. This drug's common adverse effects include nausea, vomiting, diarrhea, constipation, tiredness, nerve damage, fever, decreased blood counts, and reduced appetite. Long-term treatments with proteasome inhibitors is frequently observed with primary and secondary drug resistance problems (75).

Panobinostat is an HDAC inhibitor that can be used to treat patients who have already been treated with bortezomib and an immunomodulating agent. It affects gene activation. Common side effects include fever, weakness, nausea, loss of appetite, swelling in the arms or legs, lower blood

cell counts, liver damage, and cardiac arrhythmia. A majority of currently available MM medications cause drug resistance problems and come with some adverse effects. (70, 71)

All currently available drugs has adverse side effects and drug resistance problem, which makes the disease have a high replase rate. Therefore, there is always a need for new drugs treating multiple Myeloma, especially those that have different mechanism of actions from currently available agents.

The next section provides some evidence that p62 can be an important therapeutic target on multiple myelom. Thus, our p62ZZ ligands targeting a new potential therapeutic signaling pathways may work differently from previous available agents, which might help to reduce drug resistance problem when used in combination with other drugs if they can effectively treat this disease.

1.5.1.2. The Role of p62 in Cancer

P62 is overexpressed in various carcinogenesis, including colorectal, breast cancer, lung, ovarian, kidney, liver, esophageal, prostate, head and neck, gastric cancer, and Myeloma. It indicates that p62 might have an essential role in carcinogenesis. Based on previous studies, p62 is related to carcinogenesis through autophagy, Ras-induced NF-κB signaling, and Nrf2-mediated oxidative stress pathway.

First, p62 influences tumorigenesis via autophagy. Autophagy serves as a double-edged sword for cancer, depending on the context in the tumorigenesis process. No one doubts that autophagy plays a vital role in tumor formation, proliferation, metastasis, and metabolism, but the exact function of autophagy in these processes is still controversial. In the initial stage of cancer, autophagy helps to suppress tumor progress. Deregulation of autophagy and failure to remove the

damaged cargos contribute to genetic instability, genome damage, inflammation, necrosis, and tumorigenesis. Also, autophagy's hyperactivity might lead to autophagic cell death, another mechanism to suppress tumor growth (76). However, in the late stage of tumorigenesis, autophagy is extensively supported to promote tumor cell survival and facilitate cancer progression. Besides, autophagy might have its protective effect through regulation of tumor-associated inflammation, facilitation of tumor cell spreading throughout the organ, protection of tumor cells from anoikis (programmed cell death in anchorage-dependent cells when they detach from the surrounding extracellular matrix (ECM)), thus promoting tumor progression and metastasis (77, 78). Therefore, autophagy is a double-edged sword for cancer, which might play both pro- and anti-metastasis roles depending on contextual demands (79). Although overexpression of p62 occurs in most cancers, some studies also show a contradictory result. For instance, hyperactivity of autophagy and a low level of p62 was observed in recurrent pulmonary metastasis of colorectal tumor patients (80, 81).

Specific for multiple Myeloma, plasma cells have a high autophagy activity (82). Autophagy has a key role in immunoglobulin production. Multiple Myeloma is a cancer of long-lived plasma cells in the bone marrow. In multiple myeloma patients, myeloma cells multiply rapidly and synthesis a large number of abnormal immunoglobulins, resulting in a significant amount of unfolded or misfolded proteins located in the endoplasmic reticulum, which might be toxic to cells. Cells can rely on several clearance mechanisms to remove these potential poisonous proteins, including proteasome-ubiquitin system, autophagy-lysosome system, and heat shock protein chaperones. Among them, myeloma cells might be more relevant with autophagy-lysosome pathways, which could degrade protein aggregates and recycle energy to meet the demand for the rapid proliferation or synthesis of antibodies. As evidence, a high basal autophagy

level (82) and a high immunoreactivity against crucial autophagy biomarker (Beclin-1 and p62) in myeloma cells correlated with prolonged patients survival (81, 83, 84).

Ras proto-oncogene is mutated in more than 25% of cancers and is an essential activator of NF-κB that is important for cell survival. Mutation of Ras inhibited NF-κB activation and led to cell death. P62 is also a multi-domain protein that was involved in many signaling pathways. PB1 domain interacts with aPKCs. The ZZ domain binds RIP. The TBS domain binds TRAF6. The three domains link p62 to NF-κB activation, which is correlated with TNFα-induced osteoclastogenesis and Ras-induced tumorigenesis. P62 is necessary for Ras to induce IκB kinase (IKK) through polyubiquitination of TRAF6, then triggering activation of NF-κB and promoting tumor cell survival and transformation. P62 level was increased in human cancers and induced by Ras. The deficiency of p62 produces enhanced ROS levels and accounts for increased cell death and reduced tumorigenicity. (85) Additionally, another study shows p62 affects tumorigenesis through a feedforward loop, where Ras induces activation of NF-kB through p62, then NF-κB increases p62 expression transcriptionally (84, 86).

Excessive production of intracellular reactive oxygen species (ROS) often occurs in malignant transformation caused by oncogene activation or enhanced metabolism in tumor cells. Tumor cells often possess a high ROS level accompanied by low levels of anti-oxidative or anti-toxic proteins, which is harmful to cells. For multiple Myeloma, a large amount of abnormal antibody production requires more energy, further increasing oxidative stress induction (84). Keap1 is an adaptor for Cullin-3 ubiquitin ligase that senses oxidative stress and binds to nuclear factor erythroid 2–related factor 2 (Nrf2). Nrf2, a basic leucine zipper protein, is responsible for a series of antioxidant proteins and detoxifies enzymes, which protect cells against oxidative damage triggered by injury and inflammation (38). Keap1 binds to KIR at the same binding site for Keap1-

Nrf2 interaction, thus inhibiting the interaction between Keap1 and Nrf2, leading to the stabilization of Nrf2 and transcriptional hyperactivation of Nrf2 target gene (38, 39).

On the other hand, Nrf2 stimulates the p62 protein expression, producing a positive feedback loop between Nrf2 activation and p62 protein expression. Increased p62 level will activate Nrf2, which induces the antioxidant and detoxifies proteins gene expression, promoting cell survival and tumorigenesis. These studies showed that p62 could be a crucial adaptor to regulate the oxidative stress response system in tumorigenesis (43).

As discussed above, p62 is tightly involved in the autophagy process. Autophagy is one of the primary mechanisms regulating cellular homeostasis via the clearance of cytoplasmic components and organelles. Cellular homeostasis is critical for maintaining cellular level internal steady-state, which is essential for cell survival. A cellular steady-state helps to respond to environmental stresses and prevent cellular damage, thus having a cytoprotective effect of promoting cell survival. Therefore, autophagy is closed related to several disorders, such as neurodegeneration and cancer. Targeting autophagy is emerging as an attractive therapeutic strategy to treat these diseases (87). More than 100 clinical trials for autophagy modulation were ongoing. Most of them target autophagy for cancer treatment, such as autophagy inhibitors chloroquine (CQ) or hydroxychloroquine (HCQ), already showing encouraging results. (88)

However, the role of autophagy in cancer is cytotoxic or cytoprotective depends on the diverse cellular context. A deep understanding of autophagy's function in different cellular contexts is crucial for finding an appropriate autophagy modulation in cancer (87, 88). Here, we discussed the dual role of autophagy in cancer and summarized the currently available drug candidates targeting autophagy for cancer treatment in **Table 37** in **Appendix Table of Autophagy modulators**. Some of them can overcome drug resistance issue that occurs in

40

conventional chemotherapy. P62ZZ ligands have the potential to mediate autophagy, thus affecting carcinogenesis through autophagy.

1.5.1.3. The Role of p62 in Osteoclastogenesis

The interactions between the bone marrow microenvironment and myeloma cells are essential for multiple myeloma development, progression, and treatment. There are several types of cells in bone marrow microenvironment, including hematopoietic cells (T cells, B cells, neural killer cells, osteoclast, and myeloid-derived suppressor cells) and non-haematopoietic cells (bone marrow stromal cells, osteoblasts, and endothelial cells). These cells secrete different factors that could influence the proliferation and metastasis of myeloma cells and themselves could contribute to the formation or damage of bone. (89)

Bone marrow stromal cells create a favorable niche for myeloma cell proliferation and migration. The interaction between vascular cell adhesion protein 1 (VCAM1) on bone marrow stromal cell membrane and integrin on myeloma cell surface results in secretion of cytokines that favor myeloma cell proliferation and protect cells agonist apoptosis (90). BMSCs, osteoblasts, endothelial cells, and multiple myeloma cells all produce CXC-chemokine ligand 12 (CXCL12), which can bind to CXC-chemokine receptor type 4 (CXCR4) on myeloma cells to induce migration of myeloma cells to bone marrow niche (91). Moreover, factors produced in the microenvironment can be related to angiogenesis. For example, bone marrow stromal cells secrete VEGF. This well-known angiogenic factor enhances oxygen supply via increasing local abundance of blood vessels, a factor that contributes to migration and leads to worse outcome in clinic. (89) (Displayed in **Figure 7**)

Interaction with bone marrow stromal cells can mediate the level of crucial factors, such as NF-κB ligand (RANKL) and osteoprotegerin (TNFRSF11B), which contribute to bone damage. Osteoclasts have a role in bone resorption, while osteoblasts play a role in bone formation. Bone diseases are often associated with a reduced level of osteoblast and enhanced number and activity of osteoclasts. The interplay of myeloma cells with bone marrow stromal cells and osteoblasts will increase the production of RANKL and reduce osteoprotegerin levels (92). RANKL binds to a RANK receptor, an NF-κB activator, leading to enhanced differentiation of preosteoclasts into mature osteoclasts (92). Osteoprotegerin serves as a decoy receptor for the RANK receptor. A reduced level of osteoprotegerin will increase the number of active RANK receptors. CC-chemokine ligand 3 (CCL3) produced by BMSCs is also involved in the differentiation of osteoclasts (93). This is how the interplays between myeloma cells and cells in the bone marrow microenvironment to induce the imbalance between activity and the number of osteoclasts and osteoblasts, eventually resulting in bone diseases. (89) (**Figure 7**)

Additionally, other types of cells also produce a wide range of factors involved in tumor progression. Endothelial cells can play a role in multiple myeloma cell migration. Endothelial cells secrete extracellular cyclophilin A (94). Macrophages produce IL-1β (95), which act on BMSCs and induce IL-6 production, promoting myeloma cell proliferation and resistance to apoptosis (96). Monocytes and osteoclasts can produce a proliferation-inducing ligand (APRIL) and induce NF-κB activation. Myeloma cells can negatively affect T cells by the production of programmed cell

death one ligand 1 (PDL1) (96, 97). The anti-myeloma response via dendritic cells (DCs) is partially impaired due to low T cell activation capacity (89, 96). (**Figure 7**)
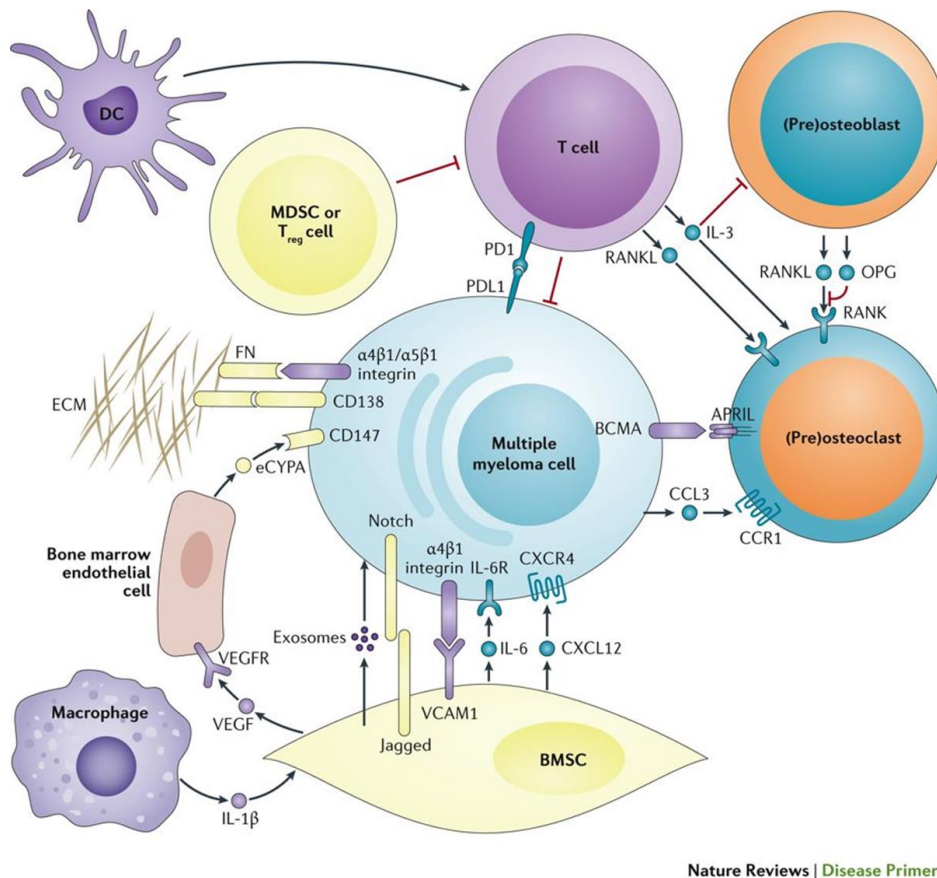
Figure 7. The Pathological Mechanism of Multiple Myeloma

As shown in **Figure 8**, p62 plays a role in osteoclastogenesis. Following the above discussion, changes in factors that cause an imbalance between osteoclasts and osteoblasts might lead to bone diseases. NF-κB activation pathway is important in osteoclastogenesis. NF-κB is a protein complex that controls DNA transcription, cytokine production, and cell survival. The activation of NF-κB is known to be central for the regulation of the synthesis and activity of inflammatory cytokines, including TNF-α and IL-1β, and also several other mediators also involved in the pathogenesis of osteoarthritis and osteoporosis (cyclooxygenase-2 (COX-2), inducible nitric oxide synthase (iNOS) and MMP-1) (98).

RANKL can activate osteoclastogenesis through both canonical and noncanonical NF-κB signaling pathways. In the canonical pathway, RANKL, IL-1, and TNFα bind to RANK, IL-1, and TNF receptors, leads to the quickly binding of TRAF6 to the TBS domain in p62. P62 activates aPKC through the PB1 domain, which induces the activation of IκB kinase (IKK). Activated IKK then phosphorylates IκBα, IκBα undergoes subsequent ubiquitination and degradation by the proteasome, which then releases an active form of NF-κB (usually a heterodimer formed by p50 and RelA). Consequently, the activated NF-κB can be translocated into the nucleus and binds to specific DNA sequences to regulate transcription and translation, eventually mediating cellular functions. In the non-canonical pathway, RANKL binds to a RANK receptor and triggers TRAF3 binding. Here, it prevents osteoclasts precursors from apoptosis and promotes osteoclastogenesis and osteoclast-mediated osteolysis. P62 also binds to RIP1 through its ZZ domain, relevant to NF-κB signaling activation and osteoclast formation. The p62 complex also binds to phosphoinositide-dependent kinase 1 (PDK1), recruiting aPKCs to TNF-α signaling complexes (Displayed in **Figure 8**). It was reported that mice with p62 deficiency exhibited impaired RANKL-induced osteoclastogenesis *in vitro* and *in vivo* (99).
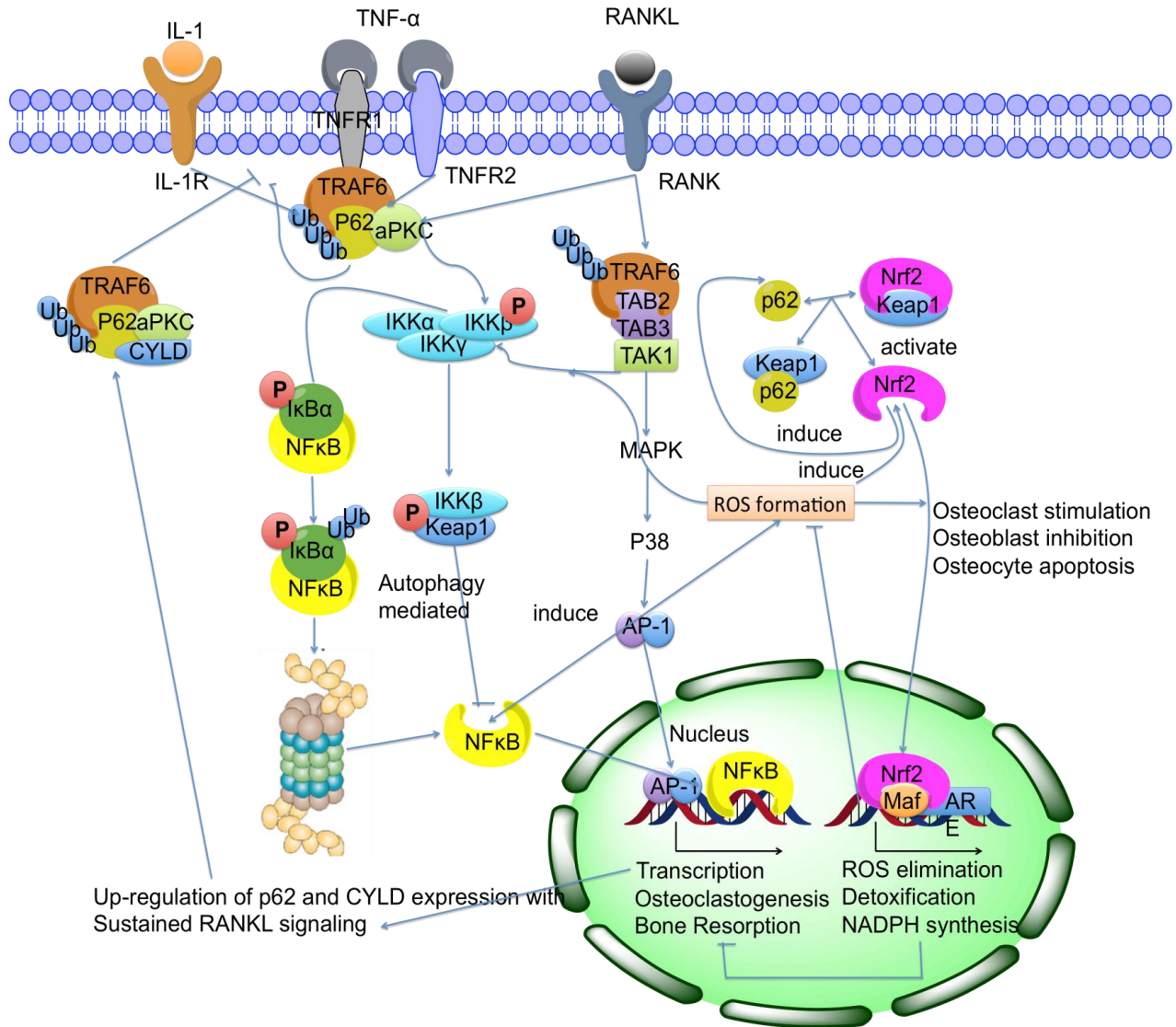
Figure 8. p62 in Osteoclast Signaling and Protein Trafficking.

The binding of RANKL to the receptor protein RANK at the plasma membrane induces a trimer's formation, triggering the recruitment of a series of adaptor proteins. TRAF6 catalyzes Lys63-linked autoubiquitination via intrinsic E3 ubiquitin ligase activity, which is regulated by the UBA domain of p62, and eventually deubiquitinated post-recruitment of CYLD to p62. In the interim, this ubiquitination permits activation of the TAB1-TAB2-TAK1 complex, activating the MAP kinases and NF-κB-inducing kinase (NIK), which leads to phosphorylation and activation of IKKβ. Activation of TRAF6 and p62 also leads to activation of the Akt/PKB pathway. Simultaneously, p62 binds aPKC through its N-terminal PB1, allowing for the phosphorylation of IKKβ by the aPKC. Once activated, IKKβ phosphorylates IκB, which is subsequently ubiquitinated, and

degraded through the proteasome system, liberating NF-κB to translocate to the nucleus and interact with transcription promoters.

1.5.2. p62 and Neurodegenerative Diseases

1.5.2.1. Neurodegenerative Disease

Neurodegenerative diseases result from the progressive loss of function and eventual death of neurons in the central and peripheral nervous systems. Common neurodegenerative conditions include Alzheimer's disease (AD), Parkinson's disease (PD), Huntington's disease (HD), Amyotrophic lateral sclerosis (ALS), Motor neuron disease, Prion Diseases, Spinocerebellar Ataxia, and Spinal Muscular Atrophy (SMA)(100). Millions of people worldwide are suffering from neurodegenerative disease, among which at least 500,000 Americans are affected by AD and even more with PD.

These disorders primarily affect neurons. Unlike other cells in the body, neurons lack regenerative capabilities: once damaged or injured, they cannot be repaired, renewed, or replaced. These conditions' onset results in inevitable progressive neuron dysfunction leading to neuron death, resulting in brain function loss with related physical and mental symptoms. Current pharmacological treatments can only reduce the symptoms associated with neurodegenerative diseases to improve the comfort and wellbeing of the patient. But current methods are unable to prevent, stop, or reverse disease progression.

Researchers work on understanding the genetic and biochemical etiological components in addition to studying the pathogenesis of common neurodegenerative diseases. Studies show these conditions are likely caused by complex interactions of several factors, including genetic,

epigenetic, pathogenic, environmental, and other unknown ones. These disorders' complexity makes it challenging to map the biochemical and physiological pathways to identify potential treatment better.

Jaekyoon Shin and his colleagues first identified the SQSTM1 gene codes for p62. As shown in **Figure 9**, p62 is a scaffold protein crucial in modulating enzyme function through several domain interactions. For example, p62 promotes autophagy degradation by directly binding to an autophagy biomarker LC3 through LIR. Combined with its ability to bind ubiquitinated proteins at the C-terminus ubiquitin-binding domain (57), p62 serves as an autophagy receptor in the clearance of unwanted protein molecules and aggregates. In addition to UBA and LIR, which play critical roles in autophagy uptake, other protein-interaction motifs, including an N-terminal PB1, a ZZ domain (7), and a TBS domain, are functional domains influential in the regulation of inflammation, oxidative stress, osteoclast genesis and apoptosis (4, 101). In the past decade, studies have shown that p62 is associated with several diseases, including Paget's disease of bone (PDB), PD, AD, HD(102), liver cancer (101), breast cancer (103), obesity, and diabetes (104).
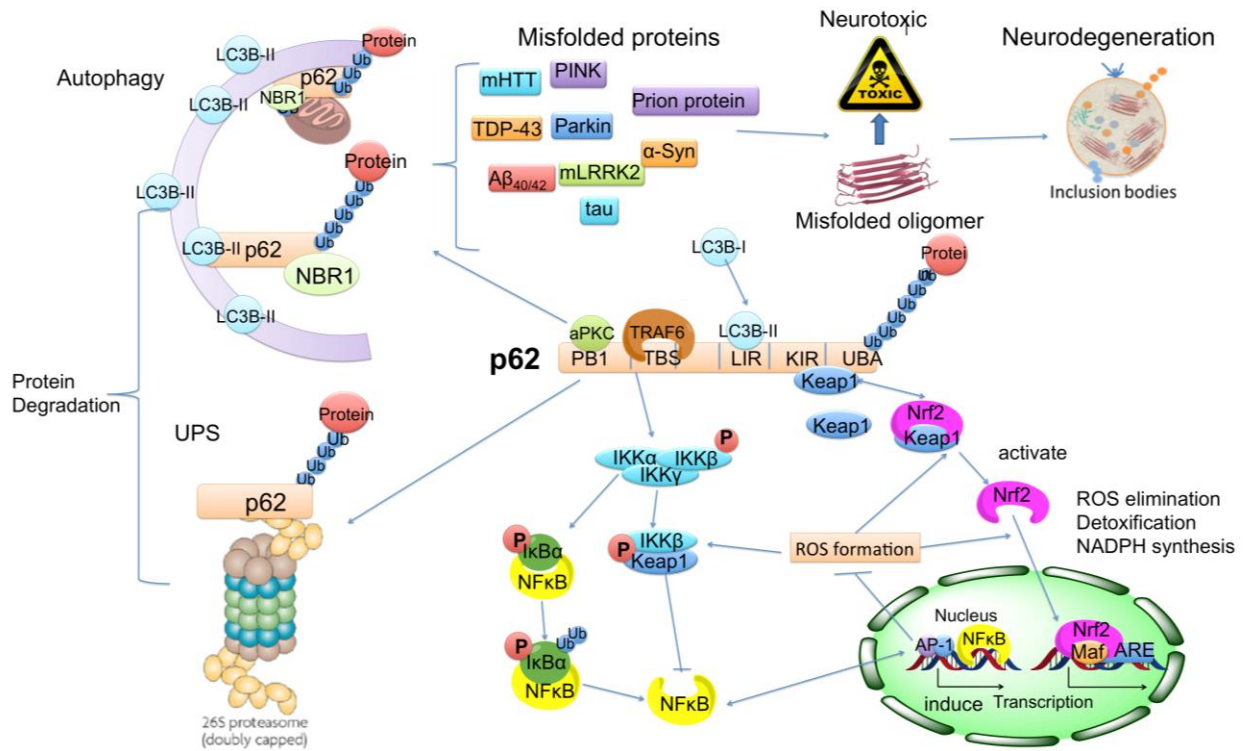
Figure 9. p62 Can Be A Signaling Hub Related to Neurodegenerative Diseases.

1) p62 is tightly involved in autophagy through its UBA, LIR, and PB1 domain. 2) p62 also participates in the ubiquitin-proteasome system (UPS), another mechanism that controls protein degradation in the cells via its UBA. 3) p62 can regulate NF-κB signaling

1.5.2.2. Neurodegenerative Disease and Misfolded Protein Aggregation.

The maintenance of protein hemostasis is essential in sustaining a viable neuronal microenvironment to support neuron health and adequate function, especially under metabolic stress (25). Protein misfolding and aggregation are hallmark signs for the most common forms of neurodegenerative diseases (56). For this reason, these conditions are often referred to as "proteinopathies". As shown in **Figure 10**, under normal conditions, malfunctioning proteins are removed by a protective mechanism. However, impairment of these mechanisms can lead to the

accumulation of misfolded peptides, disrupting protein homeostasis and causing neuronal toxicity. (105). Evidence suggests that polypeptide conformational changes can lead to instability of the misfolded intermediates due to interactions between hydrophobic regions and the surrounding aqueous solution. Consequently, the polypeptide forms β-sheets to shield the hydrophobic regions. Aggregation of the β-sheet oligomers can seriously disrupt the neuronal environment, as in the case of β-amyloid buildup into plaques associated with Alzheimer's disease. (56). The conversion of misfolded protein oligomers into insoluble fibrillary species can be directly linked to cell death (105). The most cytotoxic molecule is considered the oligomeric soluble protein, an intermediate in the amyloid fibril production. Autophagy cleared the misfolded monomers and the toxic oligomeric aggregates. Larger oligomer molecules and insoluble fibrils will form inclusion bodies that can be visualized and measured as protein amyloid cells. Thereby, one of the attractive therapeutic strategies to treat proteinopathies, including neurodegenerative diseases, is the removal of toxic oligomeric molecules (**Figure 10**). (106)
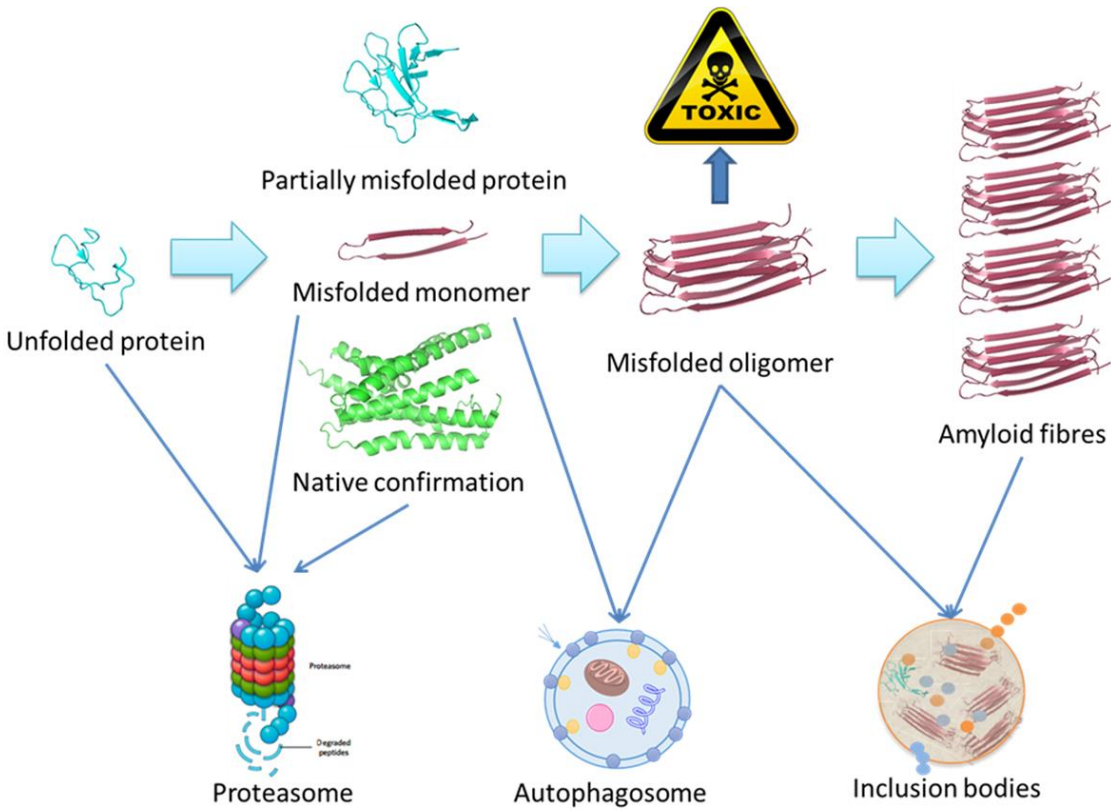
Figure 10. Schematic Representation of Misfolded Protein Degradation Processes.

The abnormal protein and protein aggregates were eliminated by different systems according to their different size. In the neurodegenerative disease context, the mutations or alterations lead to protein misfolding, followed by oligomerization, which is toxic for neurons. For instance, α-synuclein, β-amyloid peptides, and polyQ proteins are prone to misfolding and aggregation in PD, AD, and HD cellular conditions. The three types of machinery, including proteasome, autophagy, and inclusion bodies, form a quality control system to remove the misfolded proteins and aggregates from the cellular environment. Unfolded peptides and the small size misfolded monomers are degraded through ubiquitin-proteasome machinery. The larger size misfolded monomers, native formations, and misfolded toxic oligomers are cleared by macroautophagy. The three pathways all start from protein ubiquitination.
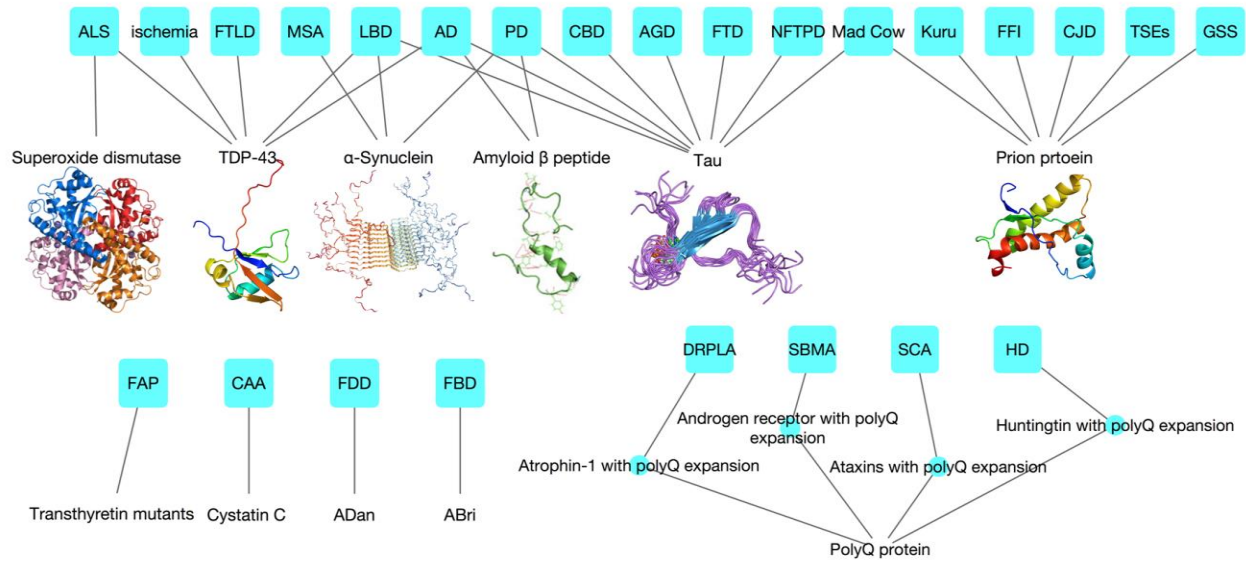
Figure 11. Misfolded and Aggregated Proteins Related to Neurodegenerative Diseases.

Abbreviation: Amoebic gill disease (AGD), Corticobasal degeneration (CBD), Neurofibrillary Tangle Predominant Dementia (NFTPD), transmissible spongiform encephalopathies (TSEs).

As shown in **Figure 11**, many neurodegenerative diseases share many of the hallmark misfolded protein aggregates, highlighting a common underlying mechanism for neuron dysfunction (25). AD is characterized by amyloid plaques comprised of Aβ and intracellular neurofibrillary tangles formed by the accumulation of phosphorylated tau protein. The mutations in β-amyloid precursor protein (APP) and presenilin 1, two proteins in Aβ metabolism signaling, are identified as disease-related gene changes. The presence of protein deposits called Lewy bodies, formed by aggregated α-synuclein and polyubiquitinated proteins is the central pathological feature of PD. Lewy bodies have also been linked to the pathological outcomes of multiple system atrophy (MSA). Poly-Q expanded huntingtin, one of the various mutations of the Poly-Q protein, is known to cause HD. (102). Other disease-associated mutations of the Poly-Q protein have been identified in other neurodegenerative diseases, including Dentatorubral-pallidoluysian atrophy (DRPLA), Spinal and Bulbar Muscle Atrophy (SBMA), and

51

Spinocerebellar Ataxia (SCA). TDP-43 was noted as the disease-causing protein for both Frontotemporal Dementia (FTLD) and ALS. Mutations in TDP-43 cause familial ALS, while cytoplasmic and nuclear inclusions of TDP-43 are found in glial cells and neurons for nearly all anatomical studies of sporadic ALS and FTLD. Prion diseases are a family of rare progressive neurodegenerative disorders characterized by the spongiform changes associated with neuronal loss and failed response to inflammation. Prion disease is caused by a "prion", which refers to a transmissible, pathogenic agent that can trigger misfolding of cellular proteins called prion proteins, most of which are located in the brain. The common types of Prion diseases affecting humans include Creutzfeldt-Jakob Disease (CJD), Variant Creutzfeldt-Jakob Disease (vCJD), Gerstmann-Straussler-Scheinker Syndrome (GSS), Fatal Familial Insomnia (107), and Kuru disease. In summary, many of the misfolded protein aggregates are associated with neurodegenerative diseases. Targeting the degradation of these misfolded or aggregated proteins might be a strategy to treat neurodegenerative disorders. Macroautophagy is the major cellular clearance mechanism of these toxic protein aggregates (61). (**Figure 11**)

1.5.2.3. Neurodegenerative Disease and Autophagy.

Autophagy plays a crucial physiological and pathological role in regulating cell growth, survival, and death, as well as macromolecule catabolic signaling, aging, inflammation, and immunity. A deficiency or over-activation of autophagy will cause neuronal dysfunction, an underlying condition for several brain pathologies (55). The process of autophagy can be divided into several sequential steps: induction, initiation/vesicle nucleation, autophagosome elongation and completion, maturation and fusion, and degradation (**Figure 4**). Genetic and pharmacological

regulations of many key players in the autophagy process are associated with neurodegeneration, indicating a strong relationship between autophagy and neurodegenerative diseases (55, 108).

1.5.2.3.1. Neurodegeneration due to abnormal gene regulation of components in autophagy.

Many studies have reported that the Beclin-1 level is closely associated with neurodegeneration. Reduced Beclin-1 level was detected in early-stage AD (100) and HD (109). Impaired Beclin-1 expression will increase Aß accumulation and mutant Huntington accumulation in AD (100) mice and HD patients (109). Upregulation of Beclin-1 expression can be used to increase the clearance of aggregated proteins and improve neuron functions, thus providing protection against neurodegeneration and prolonging the life span in AD (100, 110), HD (111, 112), PD (113), and Machado–Joseph disease, a disease characterized by polyglutamine protein accumulation (109). Interestingly, an enhanced Beclin-1 level has been reported in ALS (107), but a reduced Beclin-1 level in ALS patients has been found to increase neural protective activity against the disease (55, 114).

Several research studies have indicated that regulating the Beclin-1 through its interaction with other proteins can alter the initiation step in autophagy and modulate aggregated protein clearance in neurodegenerative disease models (55). In PD, both Parkin and PINK1 can interact with Beclin-1 to alter autophagy function (115, 116). Parkin, PINK1, and mutant LRRK2 can also regulate the elimination of damaged ubiquitinated mitochondria, affecting the mitophagy pathway (117). For ALS, the mutant SOD1 will interfere with the interaction between Beclin-1 and BCL-X, thus influencing the autophagy level (114). VPS35, a rare mutation observed in PD patients, can also contribute to autophagy dysfunction due to impaired vesicle sequestering (55, 118).

In the autophagosome elongation step, several mutations of the autophagy adaptor protein p62 have been identified in both familial and sporadic ALS patients. Gene expressions of p62 are also related to many neurodegenerative diseases, as mentioned above (119). mHTT expression leads to altered cargo recognition and autophagy failure. It is also reported that α-Synuclein can bind to Rab1a and inhibit the interaction between Rab1a and the Atg9 complex, thus hampering the trafficking of autophagy vesicles (120). The genetic inactivation of Atg5 and Atg7 in the central nervous system of mice will induce autophagy dysfunction and spontaneous neurodegeneration, causing accumulation of aggregated proteins, extensive neuron loss, and death of the mice. (121, 122). Silke Metzger et al. reported that the age of onset in HD could be modified by a polymorphism in Atg7 (123).

In the fusion and degradation step, the proteolytic ability of the lysosome depends on the luminal pH in the lysosome (55). The pH in the lysosome is regulated by ion channels on the lysosomal membrane, including v-ATPase proton channels, chloride proton antiporters, and calcium transporters, and so on. In AD, presenilin-1 can interact with v-ATPase subunit, regulating its maturation and function to control the pH level in the lysosome, thereby influencing lysosome function (124). Other studies showed restored lysosome function could alleviate AD-related symptoms and improve neural function, which is in accordance with the above findings (125). Mutations in ATPase ATP13A2 in the lysosomal membrane were observed in familial PD (126), accompanied by impaired lysosome function, altered proteolytic activity, and abnormal accumulation of autophagosome and α-Synuclein, indicating that lysosome dysfunction also influences the occurrence of PD (127).

These studies indicate a critical role of autophagy in neurodegenerative pathologies in clearing toxic protein aggregates, protecting neurons against degeneration, and prolonging neuronal survival.

1.5.2.3.2. Autophagy stimulators as therapeutic agents for neurodegenerative diseases.

Since autophagy serves as an efficient approach to selectively degrade abnormal disease-related proteins and damaged organelles in neurodegenerative diseases, several compounds were screened and identified to enhance autophagy in specific steps and have potential therapeutic efficacy to treat different neurodegenerative disorders. Here, we have summarized some of the studies with compounds that can induce autophagy, promote autophagic degradation of disease-related protein aggregates, and improve neuron function in cell and animal models (**Appendix**. **Table of Autophagy Modulators**). Some of the compounds have shown therapeutic efficacy in clinical trials. We will use the mTOR inhibitor rapamycin, an agent widely tested in preclinical models in different neurodegenerative diseases, as an example to illustrate the pharmacological effect of targeting autophagy in neurodegenerative diseases.

Inhibition of mTOR by rapamycin enhances autophagy in the early stage of AD, improving cognitive function, correlating with reduced levels of amyloid-β and tau phosphorylation as well as delayed formations of plaques and tangles (128-130). D. Rubinsztein et al. reported that rapamycin has a protective function agonist neurodegeneration in fly and mouse HD models, inducing the clearance of mHTT associated with motor activity (131, 132). Rapamycin administration also protects neurons against degeneration and death in both *in vitro* and *in vivo* HD models, accompanied by an ameliorated amount of Lewy bodies and α-synuclein in the brain

(133). Rapamycin increases autophagy in both FTLD-U (134), and SOD mutated mice models (135). The rapamycin-induced autophagy alleviated the FTLD symptoms in the mice models (134) but augmented the motor degeneration in ALS models (135). Rapamycin might exacerbate the ALS pathology via apoptosis, oxidative stress, and other mechanisms in SOD1^{G93A} mice, according to the severe mitochondrial impairment, higher Bax levels, and greater caspase-3 activation (135).

1.6. Previous Studies for p62 Small Molecular Ligands

Our group was the first to report some p62 small molecule ligands **XIE62-1004** (**XRK3**), **XIE2008,** and **XRK3F2** (As shown in **Figure 12**). These compounds are mainly applied as 1) Potential indication for neurodegenerative diseases (autophagy-related, **XIE62-1004**); 2) Potential indication for cancer treatment (multiple myeloma, **XRK3F2**); 3) Available pharmacological tools to investigate the p62 related signaling and mechanisms. Here, we summarized the previous studies related to our group's four compounds, our collaborators, and other researchers. This could help us understand our compounds' mechanism, applications, and bioactivities to guide our future studies in this project.
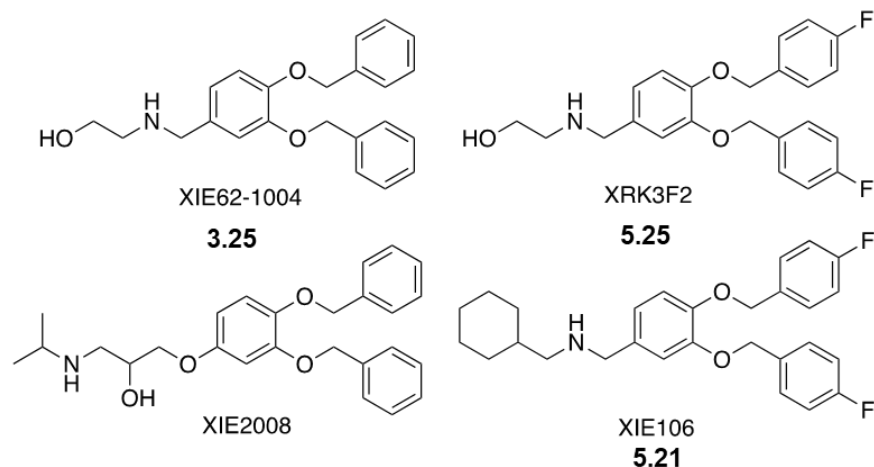
Figure 12. Chemical Structures of p62ZZ Ligands in Previous Studies.

1.6.1. Previous Studies for XIE62-1004 (XRK3) and XIE2008

Our lab constructed a homology model of full-length p62 using Modeller v9.18 based on multiple templates, and the structure of the homology model was checked by ProSA and Ramachandran plot. Virtual screening was carried out by Glide docking on an in-house chemical database pre-filtered by our established cell-based partition chemistry-space matrix calculation algorithm. A lead compound **XIE62-1004 (XRK3)** was discovered through pull-down assay with wide-type and mutated p62 for biotinylated **XIE62-1004/XIE2008** and p62. The result showed that biotinylated XIE2008 bound wildtype p62 but not mutants carrying point mutations within the ZZ domain. Moreover, pulldown assays using C-terminally or N-terminally deleted p62 mutants showed that biotinylated **XIE2008** pulled down ZZ-containing fragments but not ZZ-lacking fragments. Finally, we confirmed that biotinylated XIE2008 and XIE62-1004 could block the interaction between p62 and RIP1 through the ZZ domain by co-IP.

57

Non-reducing SDS-PAGE showed that XIE62-1004 and XIE2008 induced the aggregation of p62 (HEK293 cell lysate was incubated with p62 ligand). The oligomerization and aggregation of p62 protein with a point mutation of residue in the ZZ domain or ZZ deletion in response to **XIE62-1004** and **XIE2008** was lessened. Immunostaining of HeLa cells showed that treatment of **XIE62-1004** and **XIE2008** induced the formation of cytosolic puncta positive for p62 time- and dose-dependently. Glutathione-S-Transferase (GST)-pulldown assay coupled with ELISA showed that **XIE62-1004** increase p62 interaction with LC3. The results suggested **XIE62-1004** and **XIE2008** bind to the p62 ZZ domain and promote some conformational changes that induce p62 self-oligomerization and aggregation and increase its interaction with LC3B. P62 ligands also induce autophagosome formation. Immunostaining showed that the induction of ligand-driven p62 puncta formation coincided and colocalized with the stimulation of LC3-positive cytosolic puncta formation. Immunoblotting showed that **XIE62-1004** increase the level of LC3B and turn over from LC3B-I to LC3B-II, which was blocked by p62 knockdown. Co-treatment with various autophagy inhibitors HCQ, bafilomycin A1, MG132 with **XIE62-1004** synergistically increased the synthesis and activation of LC3, indicating the stimulation of autophagy flux. Dr. Kwon's group monitored the ratio of red fluorescence protein (RFP) vs. green fluorescence protein (GFP) signals in HeLa cells stably expressing RFP–GFP–LC3. This assay relies on the differential pH stability of RFP (red puncta, acid-resistant) and GFP (green puncta, acid-sensitive). RFP-GFP-LC3 expressed in HeLa cell generates yellow fluorescent signals (RFP+GFP) in autophagosomes (neutral condition) and red fluorescent signals (only RFP) in autolysosomes (acidic condition), which revealed the distribution of LC3B. (18, 136)

P62 ligands were shown to induce autophagic degradation of mHTT, mutated Huntington proteins. Immunoblotting showed that **XIE62-1004** and **XIE2008** decreased the level of GFP-HDQ103 aggregates, an mHTT carrying 103 glutamine repeats, in the insoluble fraction of HeLa cells stably expressing GFP-HDQ103. Immunostaining assays showed that GFP-HDQ103 puncta were colocalized with p62 and distributed to aggregates. Both the signal of GFP-HDQ103 and p62 were reduced by the treatment of XIE62-1004 or XIE2008 in HeLa cells expressing GFP-HDQ103 but not changed in MEF ATG5 (a protein that is essential for autophagy) knockout cells. (18, 136)

An article published by our collaborators, Dr. Kwon's group, provided more information about the mechanism of **XIE62-1004** acting on autophagy. It was showed that **XIE62-1004** increased LC3B-II, inducing the formation of autophagosome in MEF cells that expressed wild-type p62 but not in MEF cells with p62-ZZ mutation and p62 knockout. Co-treatment with late-stage autophagy blocker, HCQ, did not alter the LC3B level increase and conversion from LC3-I to LC3-II. These results confirmed that **XIE62-1004** induced autophagosome formation and autophagy flux through interaction with the p62 ZZ domain. (136)

To validate previous results in animals, Dr. Kwon's group injected C57BL/6 mice *i.v.* with 10 mg/kg **XIE62-1004** and sacrificed them after 1, 3, 6, or 24 h. The animals showed a time course induction of LC3-1 level and its conversion to LC3-II, associated with enhanced levels of autophagic core components such as ATG3, ATG5, and ATG7. Immunostaining assay using the brain section from the mice showed that in the control brain without treatment, the basal level p62 and LC3 puncta are not colocalized with each other. In contrast, in the brains of mice treated with **XIE62-1004**, LC3 positive cytosolic puncta are increased. This indicates **XIE62-1004** induces p62-dependent macroautophagy *in vivo*. (136)

Immunoblotting showed a lower level of ubiquitinated protein aggregates measured by FK2 (ubiquitinylated protein antibody FK2) in cells treated with **XIE62-1004** cotreated with proteasome inhibitor MG132. XIE62-1004 facilitated the formation of ubiquitin-positive and LC3 positive puncta under proteasomal and V-ATPase inhibition. The distribution and degradation of the model subtract CL1-YFP, which is spontaneously misfolded and forms cytosolic aggregates, was monitored to support that **XIE62-1004** facilitates the delivery of ubiquitinated protein to the autophagosome. Immunostaining analysis showed that CL1-YFP accumulated and colocalized with LC3+ autophagic vacuoles when autophagic flux was blocked by HCQ, which was further increased by treating **XIE62-1004**.

In addition to the above studies, **XIE62-1004** was applied as a chemical tool that can bind to p62, induce p62 self-oligomerization and macroautophagy in some studies done by other researchers. **XIE62-1004** and **XIE2008** were shown to activate p62 through facilitating disulfide bond-mediated self-oligomerization. Other molecules that can mediate p62 self-oligomerization, such as verteporfin and CORM-3, induce oligomers of p62 that are interacted covalently with each other through a disulfide bond independent mechanism and are carbonylated under oxidative stress. These crosslinked p62 oligomers have less capacity to bind ubiquitinated proteins than the disulfide bond p62 oligomers. The production of these covalently crosslinked p62 oligomers can inhibit the process of macroautophagy. Therefore, verteporfin and CORM-3 will inhibit autophagy, while **XIE62-1004** and **XIE2008** will induce autophagy through p62. (137-139) Young-Sun Lee and his colleagues found that **XIE62-1004** treatment led to LC3B lipidation and puncta formation but did not elevate BiP and HO-1 expression and the level of glutathione. This result suggested that **XIE62-1004** induces autophagy without inducing ER stress and affecting the glutathione antioxidant system. (137)

A paper recently published by Rastislav Horos in EMBL also applied our compound **XIE62-1004** as a tool compound to bind to p62 ZZ, induce p62 oligomerization and induce autophagy. This paper reported a vault RNA (vtRNA, small non-coding RNAs transcribed by RNA polymerase III) that directly binds to the p62 ZZ domain confirmed by immunoprecipitation and radioactive labeling binding assay. Overexpressing of vtRNA1-1 inhibits autophagy, and knockout of vtRNA1-1 enhances autophagy. Treating the vtRNA1-1 knockout cells with **XIE62-1004**, which also binds to the ZZ domain, can activate autophagy stronger than the corresponding control cell line. This finding further affirmed the role of vtRNA1-1 as a negative 'riboregulator' of autophagy directly via p62 and interference with p62 oligomerization. (137, 139) (138)

1.6.2. Previous Studies for XRK3F2

XRK3F2 (an analog of **XRK3** as shown in **Figure 12**) was tested by another collaborator, Dr. Roodman's group, on multiple myeloma treatment and related mechanism. The research of the p62 ZZ ligand in this direction also attained some positive preliminary results and some publications.

In the previous study, our collaborators Dr. Roodman's group identified p62 as a potential target for multiple myeloma treatment, supported by the following point. 1) Marrow stromal cells from MM patients had increased VCAM-1 and IL-6 expression levels. 2) NF-κB, p38-MAPK signaling, and PKCξ phosphorylation were rising in response to TNF-α increased to a greater extent in MM stromal cells than normal cells. 3) p62 is a common component that serves as a platform for forming these signaling complexes. 4) Knocking-down p62 in patient-derived stromal cells significantly decreased PKCξ, VCAM-1, IL-6 levels and reduced activator of NF-κB and p38-MAPK signaling as well as decreased stromal cell support of MM cell growth and osteoclast

formation. In the subsequent study, we found that XRK3F2 inhibited MM cell growth and bone marrow stromal cells (BMSC) growth enhancement of human MM cells. We discovered that **XRK3F2** specifically interacted with p62 and inhibited $TNF\alpha$ induced murine $p62^{+/-}$ osteoclast formation but not $p62^{-/-}$ osteoclast precursor. **XRK3F2** also blocked RANKL-induced osteoclast formation by a high dose. To evaluate the effect of **XRK3F2** on downstream signaling induced by $TNF\alpha$ and RANKL on osteoclast formation, we found that **XRK3F2** treatment reduced the level of c-Fos and NFATc1 and decreased the phosphorylation of $PKC\delta$ and $I_\kappa B\alpha$ induced by $TNF\alpha$. (140)

Also, **XRK3F2** blocked TNFα-induced signaling processes in MM patient BMSC and MM cells. Moreover, **XRK3F2** directly inhibits the growth of MM cell lines and primary multiple myeloma cells but does not affect BMSC viability. Furthermore, **XRK3F2** induces new cortical bone formation in MM bone disease *in vivo*. μCT and X-ray were used to evaluate bone disease at the end of the study. Marked periosteal reactions were observed on X-ray of 6 out of 17 **XRK3F2**-treated and one vehicle-treated animal, suggesting new bone formation along the tibia. However, μCT and histology analysis confirmed an increase of cortical bone in **XRK3F2** treated MM-bearing animals, determined by the ratio of new cortical bone volume to total bone volume. Interestingly, no new bone formation was detected in the non-MM-bearing leg of **XRK3F2**-treated animals, indicating a lack of effect on bone without MM. **XRK3F2** induced more cortical bone formation in animals with tumor burdens measured by IgG2b levels at the end of the study than animals with low tumor burden, suggesting that **XRK3F2** has less effect on normal bone formation than MM-related bone formation. (140)

To investigate the mechanism behind the effect of **XRK3F2** on new bone formation, we tested whether XRK3F2 influences the production of MM-derived osteoblast inhibitor, or induces osteoblast differentiation directly, or alters MM-induced suppression of osteoblast differentiation. The results showed that **XRK3F2** did not induce IL-7 and TNF-α expression (osteoblast differentiation suppressor) in 5TGM1 MM cells or induce osteoblast differentiation measured by osteoblast differentiation biomarkers Ocn and Runx2 in primary murine BMSC and MC4 cells, a mouse osteoblast precursor cell line. The expression of Runx2 was suppressed in MC4 cells by co-culturing with 5TGM1 MM cells. This suppression on the Runx2 level was blocked by treatment of **XRK3F2**. Therefore, **XRK3F2** inhibits the MM-induced osteoblast differentiation measured by Runx2 expression. (141)
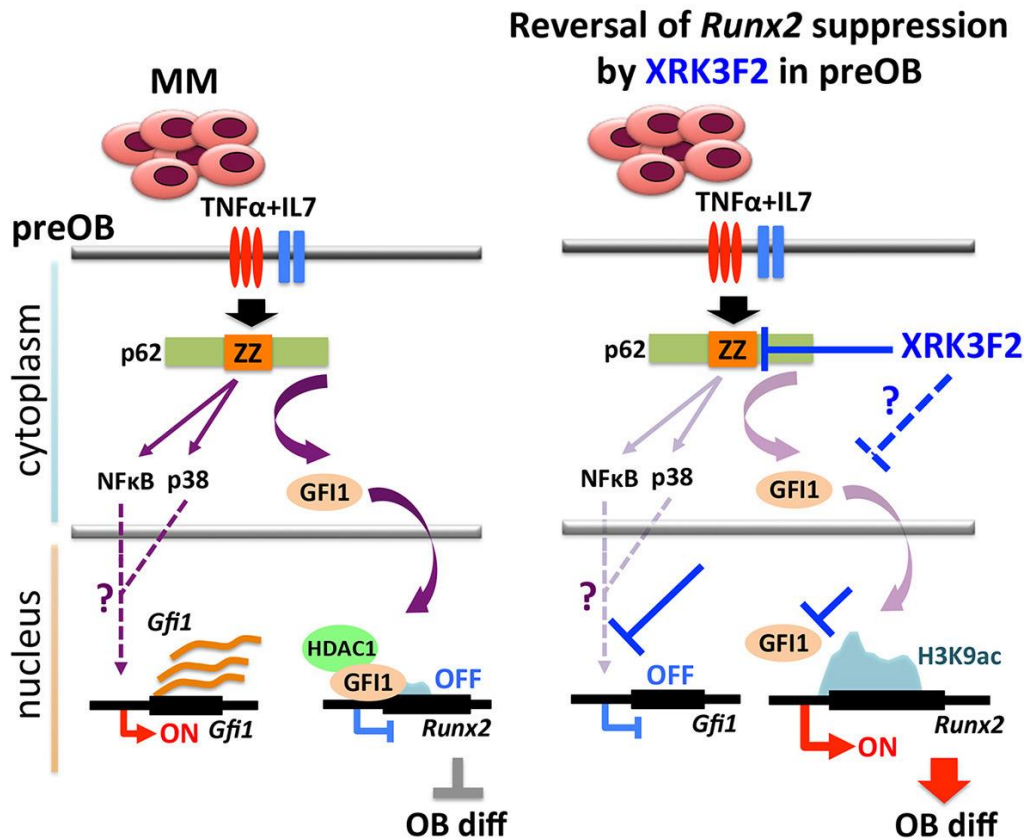
Figure 13. The Mechanism of Action of XRK3F2 to Inhibit Osteoblast Formation.
The signaling mechanism behinds XRK3F2 inhibiting the MM-induced osteoblast differentiation by Runx2 expression. The figure is from the paper published by our collaborators (141).

Some reports indicate that multiple myeloma cells induce repressive chromatin in BMSC on the Runx2 gene directly through interaction with transcriptional repressor GFI1 that recruits histone modifiers (HDAC1, histone deacetylase 1; EZH2, enhancer of zeste homolog 2), as shown in **Figure 13**. It was reported that **XRK3F2** blocked MM-induced upregulation of GFI1 and suppressed Runx2 expression in osteoclast precursors co-cultured with MM cells. It also showed that **XRK3F2** could prevent TNFα and IL-7 induced upregulation of GFI1 and repression of Runx2 in osteoblast differentiation. Chromatin immunoprecipitation (ChIP) analyses suggested that **XRK3F2** reduced TNFα and IL-7 or MM induced GFI1 occupancy at the Runx2-P1 promoter

and blocked the recruitment of HDAC1, thus maintaining H3K9ac (a transcriptionally permissive chromatin mark) on Runx2 promoter and allowing osteoblast differentiation. **XRK3F2** treatment increased H3K9ac levels on Runx2 gene promoter in MM-hBMSC (primary BMSC from MM patients) to the level observed in HD-hBMSC (primary BMSC from health donors) but did not alter HD-hBMSC. Additionally, **XRK3F2** treatment of long-term MM-hBMSC cultures after exposure to MM cells rescued MM-induced suppression of Runx2 and its downstream osteogenic differentiation and mineralization. (141)

Therefore, **XRK3F2** might be applied to treat multiple myeloma, which was demonstrated effectively to inhibit MM-induced osteoblast differentiation and myeloma cell growth/replication and increase osteoclast formation *in vitro*. Treatment of **XRK3F2** also leads to new bone formation in MM-bearing animals. The potential mechanism of the **XRK3F2** effect on p62 signaling in multiple myeloma is displayed as follows. "MM cell co-culture or TNF-α plus IL7 stimulation of preOB activate p62-ZZ domain signaling, which results in activation of downstream pathways involving NF-κB and p38 MAPK. Further, p62-ZZ domain activation increases GFI1 levels, which subsequently translocate into the nucleus, bind the Runx2 gene, and recruits the chromatin modifier HDAC1 to deacetylate and repress the Runx2-P1 promoter. Inhibition of the p62-ZZ domain by **XRK3F2** may act differently to prevent transcriptional repression of Runx2 by GFI1. First, suppressing activation of transcription factors such as NF-κB or C/EBPβ, thus preventing Gfi1 transcription. Second, by inhibiting nuclear translocation of GFI1, thereby preventing its ability to target the Runx2 promoter. (141)

In conclusion, there are three potential applications of our p62 compounds. (1) Our p62-ZZ ligand **XRK3** (also known as **XIE1004**), the first small molecule that binds with the P62 ZZ domain, can be applied as a tool compound study the related endogenous signaling and genetic perturbation or chemical perturbation induced pharmacological effects on these signaling. (2) Our p62 ligands can be applied to treat multiple myeloma, supported by three pieces of evidence. First, *in vitro* antiproliferative effects on several multiple myeloma cell lines (MM1.S, MM1.R, RPMI8226, U266, MM-hBMSC (human), MC4 (mouse), 5TGM1 MM (mouse)) and osteoblast/preOB cells. Second, *in vivo* anti-MM effects of **XRK3F2** measured by tumor size change and bone fraction/osteoporosis recovery in rats and mice. Third, signaling studies revealing the acting mechanism behinds the scene. (3) Our p62 compounds can help to treat neurodegenerative diseases. Dr. Kwon's group reported that **XIE1004 (XRK3)** could bind to p62 ZZ, induce p62 self-oligomerization, activate autophagy flux increase the clearance of misfolded mutated Huntingtin, the accumulation of which is a principal mechanism underlying the Huntington's disease. Therefore, we suppose our p62 compounds might induce autophagy flux and enhance the clearance of other misfolded and aggregated proteins in the brain that are association with pathological mechanism behinds the other neurodegenerative diseases, such as Alzheimer's disease, Parkinson's disease, ALS, FTLD, and Pick's disease.

2.0. Novel P62 Ligands to Treat Multiple Myeloma

Multiple myeloma (MM) is a plasma cell cancer that damages the bones, immune system, kidneys, and red blood cell count. Under healthy conditions, the plasma cells produce antibodies to fight infections; however, with MM, the cells release too much immunoglobulin into the blood and bones. The immunoglobulin accumulates in the body, causing organ damage, and it releases chemicals and triggers other normal blood cells to dissolve bone, leading to lytic lesions on the bone. As the disease worsens, the abnormal plasma cells will spread out of the bone marrow throughout the body and damage more organs.

Although great efforts have been made to improve the symptoms and lengthen the lifetime of MM patients, some subgroups of MM patients cannot benefit from the currently available medications and still face a high risk of death. In addition, drug resistance issues often occur during the treatment of multiple myeloma, which results in a high relapse rate of this disease. Thus, more diverse treatment is required for this disease.

P62 can be a potential therapeutic target for MM. First, p62 is overexpressed in various carcinogenesis, including colorectal, breast cancer, lung, ovarian, kidney, liver, esophageal, prostate, head and neck, gastric cancer, and myeloma (80, 81). It indicated that p62 might play an important role in carcinogenesis. Based on previous studies, p62 is related to carcinogenesis through autophagy, Ras-induced NF-κB signaling, and the Nrf2-mediated oxidative stress pathway (76-78).

P62 also plays a role in osteoclastogenesis. RANKL can activate osteoclastogenesis through canonical and noncanonical NF-κB signaling pathways. P62 activate aPKC through PB1 domain, which activated inhibitor of NF-κB kinase and then phosphorylated NF-κB inhibitor α

NF-κB inhibitor α undergoes subsequent ubiquitination and degradation by the proteasome, which then releases an active form of NF-κB. Consequently, activated NF-κB is translocated into the nucleus and binds to specific sequences of DNA to regulate transcription and translation, eventually mediating osteoclastogenesis. It was reported that mice with a p62 deficiency exhibited impaired RANKL-induced osteoclastogenesis *in vitro* and *in vivo* (99). Multiple myeloma is related to high osteoclast activity and low osteoblast activity. It was reported that p62 acts as a signaling hub for bone marrow stromal cells (BMSCs), inducing an increase of osteoclast formation and the accompanying growth and spread of disease.

Recently, we identified **XRK3F2** targeting the p62/SQSTM1 ZZ domain with a potential to inhibit MM cell growth and TNFα-induced osteoclast formation. Our study also showed that **XRK3F2** induced new bone formation and reduced the tumor size in the high MM burden area without converting non-tumor-bearing bone in 5TGM1 MM rat models. Another study reported that **XRK3F2** could reverse epigenetic-based mechanisms of MM-induced Runx2 suppression and promote osteogenic differentiation.

Our previous studies have shown the beneficial effect of our compounds targeting p62 in the treatment of MM on both *in vitro* MM cell lines and MM animal models. To improve the efficacy of our lead compound, we performed a chemical modification on our lead compound and attained more than 100 analogs (I synthesized more than 70). We developed one compound with a 10-fold anti-proliferation effect compared with the lead compound in MM cell lines and better drug-like properties, such as higher solubility, less toxicity on BJ cells, and better selectivity with more difference between the results from p62-KO cells and normal cells. In this study, we further identified that our p62 compounds kill the myeloma cells through p62-LC3-iDISC-apoptosis signaling using fluorescence microscope (FM) and immunoblotting (IB).

I this section, we described how we used computational methods to help design and decide which compounds we made at first. We explained how we did chemical modifications and how we measured efficacy and some properties of the compounds we got.

2.1. Computer-Aided Drug Design for P62ZZ Ligands

At first, we described how the computer-aided drug design methods helped us to design and prioritize the synthesis of our compounds. From the economic aspect, it's better to have some computational methods that can help us decide which compounds to synthesize at first. In this study, we applied

From our previous studies, we screened the NCI database by molecular docking using on the homology models of full-length p62 protein constructed in our lab. Based on the docking results, including scores, poses, and other properties, we tested several compounds and identified our lead compound **XRK3,** which proves interaction with p62. Using similar molecular docking methods, we built a homology model of full-length p62 and validated the structure. We then screened our designed compounds against the p62 structure to prioritize the compounds we synthesized at first. The compounds we designed are based on our chemical inventory and the chemical accessibility of the compounds. Fewer steps, less cost, and easy procedures are preferred for the design of final compounds.

We used both structure-based molecular design and ligand-based molecular design approaches to design and screen our compounds virtually. Molecular docking using a homology model of full-length p62 represents structure-based molecular design. Ligand-based molecular design, including similarity search and fragment-based drug design, was conducted using multiple myeloma medications and clinical drugs. Since not much information is available for p62 specific small molecules, we modify them based on our lead compound, **XRK3**.

2.1.1. Structure-based Molecule Design

The structure of a protein is needed for structure-based molecular design, mainly molecular docking. No available crystal, NMR, or cryo-EM structure was reported for our target full-length p62 protein. Therefore, it is necessary for us to build a homology model using templates from other crystal structures and a full-length sequence of p62 protein before molecular docking. Member in our lab did that previously, which works well to identify our lead compound, **XRK3**. I made some modifications to that model by adding zinc ions in the ZZ domain, checking disulfide bonds, and Psi/Phi dihedral bonds.

2.1.1.1 p62 Wild-Type Full-Length Homology Model

As shown in **Figure 14**, a homology model of a full-length human p62 protein was built using MODELLER-9.19 with multiple sequence alignments and structure modeling protocol by our lab member. The models were further refined by clustering, docking, and energy minimization with a harmonic constraint of 100 kJ/mol/Å2 applied for all protein atoms, using the steepest descent and conjugate gradient technique to eliminate wrong contacts between protein atoms and structural water molecules. The identification of problems in theoretical models of protein structures is a significant challenge in computational structural biology. A series of tests were applied to the refined homology model to evaluate its internal consistency and reliability and to identify potential problems in the protein models. As a result, the best and the most reliable homology structure of the p62 protein was then used in virtual screening and molecular docking studies.
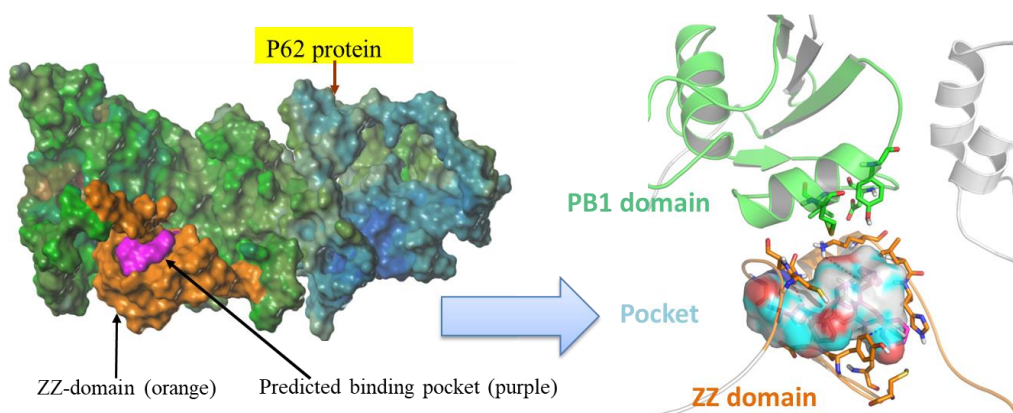
Figure 14. Homology Model of Full-Length p62 Protein and Binding Site in ZZ Domain.

Backbone conformation was investigated by the Psi/Phi Ramachandran plot using RAMPAGE. RAMPAGE generates a Ramachandran plot using data derived by the Richardsons and his colleagues. The Ramachandran diagram plots Phi versus Psi dihedral angles for each residue in an input PDB file. Favored, allowed, and disallowed regions are defined in the plot based on density-dependent smoothing for non-glycine, non-proline, glycine, proline, pre-proline, and non-pre-proline residues from high-resolution protein structures. The Ramachandran plot for the p62 structure model using RAMPAGE server revealed that among the 438 residues, 387 residues (88.4%) were in the favored region, 42 (9.6%) were in the allowed regions and 9 (2.1%) were in the disallowed region, indicating that the predicted model is acceptable (**Figure 15**). The reliable homology model of full-length p62 was used in the next section to screen compounds through docking.
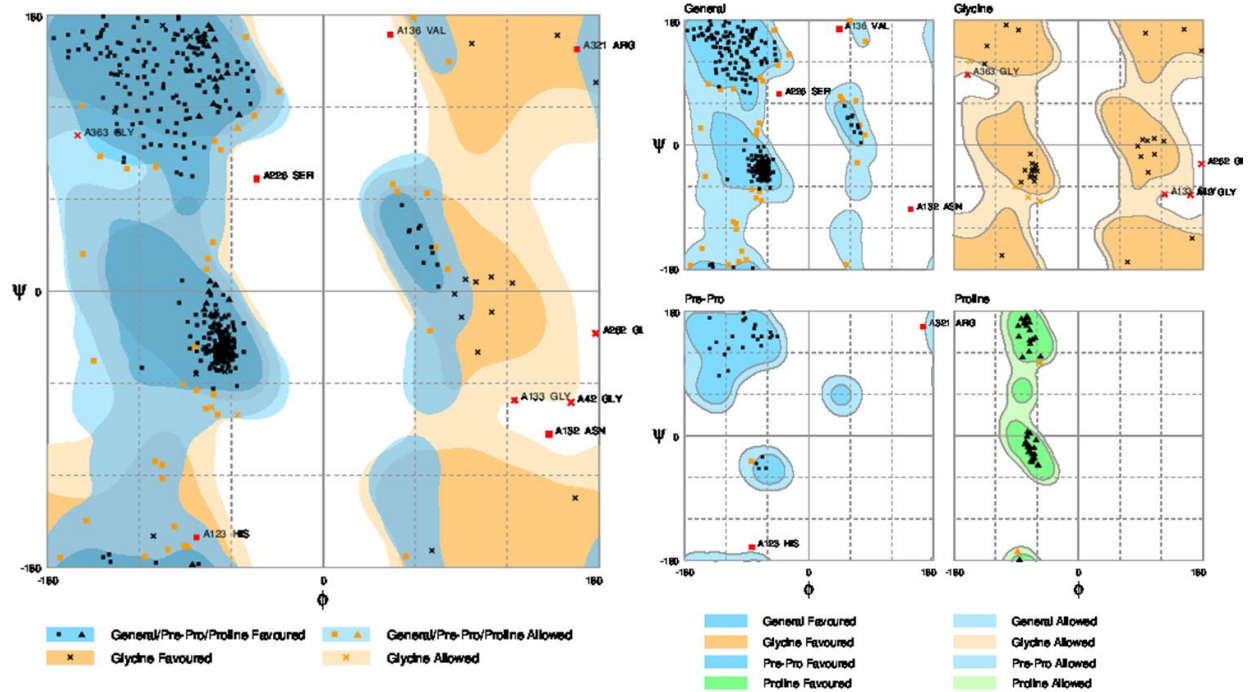
Figure 15. Ramachandran Plot of p62 Homology Model Calculated by Rampage.

2.1.2. Virtual Screening for p62-ZZ Ligands by Molecular Docking

The predicted 3D structure of the p62 protein was then used for molecular docking virtual screening studies using the reported protocols (18, 142). The binding pocket in p62ZZ was defined using the MOLCAD module in SYBYL-X 1.3. Several residues were involved in our putative binding cavity, including, Arg139, Cys142, Cys145, Asp147, Cys154, Lys157, Leu159, His160, Asp129, Asn132, Tyr148, Asp149, and Cys151. The compounds were designed using both medicinal chemical methods based on the structure and activity of the lead compound and chemical accessibility and the computational approaches, including similarity search, fragment-based drug design, and molecular docking. The compounds with a good docking pose, chemical accessibility, and draggability were selected for the following chemical synthesis and bioassay test.

A virtual screen was carried out on p62 models against NCI chemical database to filter out several compounds for bioassay tests. Among those compounds, **XRK3** was selected as our lead compound due to its interacting with the p62 protein, inducing p62 oligomerization and autophagy flux. For the first round of chemical modification, we added substitutes on the phenyl rings and tested the analogs by bioassays. We found that **XRK3** with 4-fluoride on each phenyl ring, named **XRK3F2**, had similar activity as **XRK3** by binding with p62 and inducing autophagy. Moreover, **XRK3F2** showed a lower IC_{50} value than **XRK3** in regards to inhibiting MM cell growth. Therefore, **XRK3F2** was also investigated to find indications for further modifications. In addition to changing the different substituents on the two benzoyl rings, we also considered making diverse side chains on the amino group.

Two structures have higher anti-proliferation activities on three MM cell lines than **XRK3F2** and share the same signaling activity as **XRK3**. **XIE106** is one of the two structures. We performed a series of *in vitro* and *in vivo* bioassays on this compound. This compound shows a good and specific anti-MM activity on both cell lines and rat models. Compound **6.28** was a new compound for this series. We added a guanidine group to mimic N-arginine aggregation and their effect on p62 and macroautophagy. Coincidently, compound **6.28** possessed a higher anti-cancer activity in MM cell lines compared to that of other p62 ligands that were synthesized.

As a representative of our chemical modification process for this series of p62 ligands, we selected **XRK3F2, XIE106,** and compound **6.28** to illustrate how the chemical modification would influence the interaction between p62 and p62 ligands based on the docking poses of the four analogs. As shown in **Figure 16A**, one benzoyl ring in **XRK3F2** has a π-π interaction with Tyr148 and His160, which stabilizes the compounds in the ZZ domain. The other side chain of **XRK3F2** points to the PB1 domain and forms a hydrogen bond with Asp73 and Tyr89 in the PB1 domain

and Cys151 in the ZZ domain. Meanwhile, another 4-fluorobenzoyl group approaches the other side of the pocket and forms hydrophobic interaction with Cys151, Asp149, and Tyr148. As illustrated in **Figure 16B**, compound **6.28** shares similar binding poses as **XRK3F2**; the 2-aminoethan-1-ol side chain was replaced by the amino-guanidine group, which has more hydrogen bond donors and acceptors to interact with Asp73 and Tyr89. The increased size of amino-guanidine shoves the other hand of the structure to a position that is suitable to π-π interaction with Tyr148 and His160. The fitted π-π interaction and more hydrogen bonds may increase the competition of compound **6.28** for binding with the p62 protein. With this pose in **Figure 16C**, **XIE106** has a hydrophobic interaction with residues Asp149 and Asn132 as well as a hydrogen bond with Asp149; the other side of the benzoyl ring forms π-π interaction with Tyr148 and His160.
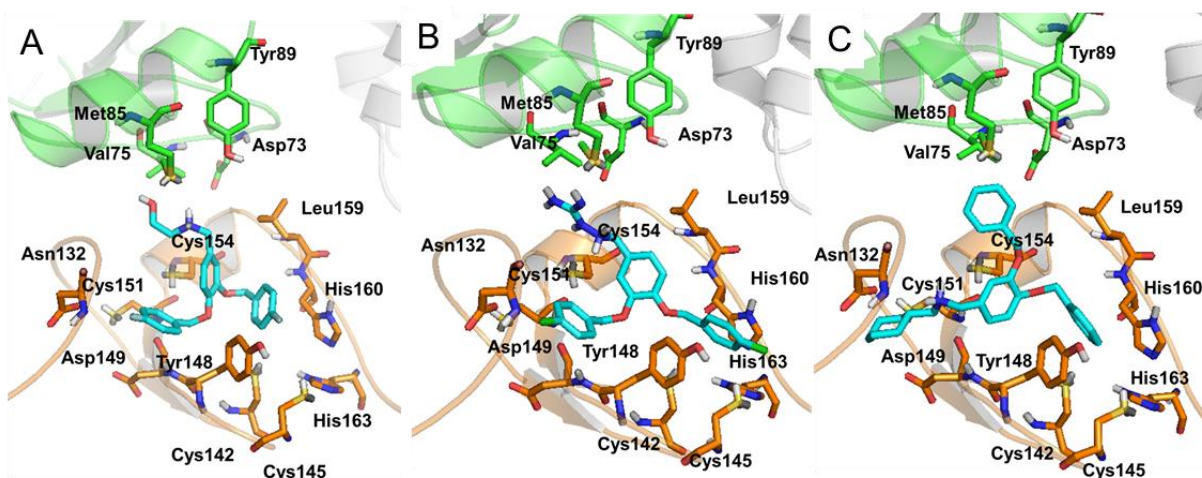
Figure 16. Docking Poses of XRK3F2, 6.28, and XIE106 in p62.

(A) The docking pose of **XRK3F2** (**5.25**) with p62. (B) The docking pose of compound **6.28** with p62. (C) The docking pose of **XIE106 (5.21)** with p62. The compounds are represented by cyan sticks. The ZZ domain is in orange, and the PB1 domain is in green.

In addition to alkyl groups linked to the amine, heterocyclic rings were also substituted for the amine to investigate the influence of diverse functional groups on interactions with the p62 protein, as shown in **Figure 17**. Compared to benzene, heterocyclic aromatic rings are more favorable to form π-π stacking with His160. In **Figures 17A and 17B**, the benzo[d][1,3]dioxole in **3.16** and the pyridine in **3.10** all have face-to-face localized stacking with both benzene in Tyr148 and imidazole in His160 as a sandwich. The other two hands in the three structures filled in the ZZ domain and extended to the PB1 domain, interconnecting with the surrounding residues. Based on the docking poses, the three compounds are assumed to have a strong binding affinity with the p62 protein.
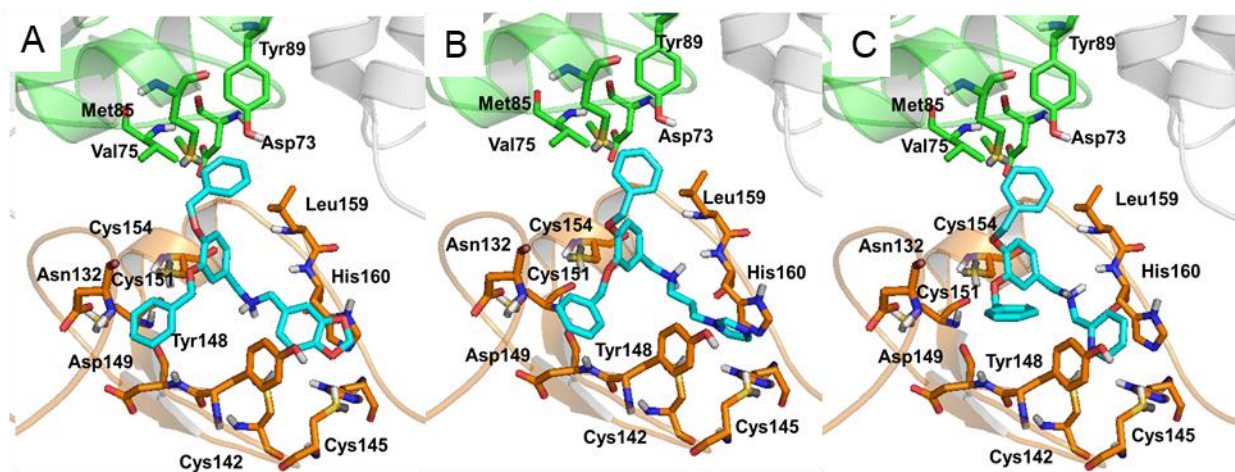
Figure 17. The Docking Poses of Compounds with Heterocyclic Rings.

(A) The docking pose of **3.16** with p62. (B) The docking pose of **3.10** with p62. (C) The docking pose of **3.9** with p62. The compounds are represented by cyan sticks. The ZZ domain is in orange, and the PB1 domain is in green.

The imidazole in compound **3.10** possesses edge-to-face stackings with benzene in Tyr148 and imidazole in His160 in **Figure 17B.** The other parts of the compounds retained interactions with residues Cys151, Cys154, and Asp149 in the ZZ domain as well as Asp37 and Tyr89 in the

PB1 domain. Moreover, the amine in these six compounds connected to the heterocyclic rings forms hydrogen bonds with His160.

This molecular docking part will help us decide the priority we synthesized compounds for the test. We can also look back to this data to find any important interactions between compounds and p62 if any 10-fold difference in activity was identified in analogs with small modifications. Some of the docking data will be mentioned in the discussion of results from the next section. The compounds we synthesized all have a good docking score and performance, which is summarized in **Table 4-11.**

2.1.2. Fragment-based Drug Design

Other than molecular docking, which is a structure-based drug design, we also try to screen compounds and predict compound activities by ligand-based drug design methods. We do not have enough ligand data targeting p62 protein. So, we propose a disease-specific fragment-based drug design approach to design compounds that may have the potential to treat multiple myeloma. I collected anti-MM drug structures to make anti-MM fragments. One thousand compounds were virtually re-synthesized from the fragment database in the hope that they might have the potential to treat MM. The resynthesized compounds were filtered using tools provided in our databases and docked into our previously established p62 homology model to find p62ZZ-specific compounds with therapeutic potential for MM treatment. Four compounds that share the same scaffold with our p62ZZ ligands were selected from the resynthesized molecules pool. They were synthesized and evaluated with anti-MM activity *in vitro.* The activities of these four compounds are discussed together with other p62ZZ compounds in the next section.

2.1.2.1. Multiple Myeloma Drugs

I collected the anti-MM drug information from DrugBank (www.drugbank.com), ClinicalTrial.gov (www.clinicaltrials.gov), NCI website (www.cancer.gov), and MetaCore (portal.genego.com). From the databases, about 200 agents were found in clinical trials, and 18 drugs are approved by the Food and Drug Administration (FDA) to treat different stages of myeloma. The drug and formulation information is listed in the **Appendix Table of Drug Candidate in MM Clinical Trials** and **Appendix Table of FDA-Approved MM Medications**

2.1.2.2. Multiple Myeloma Fragment and Resynthesized Compounds
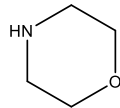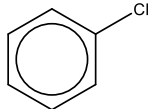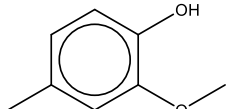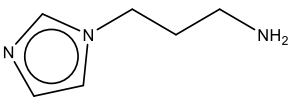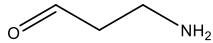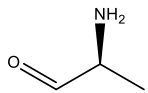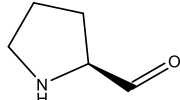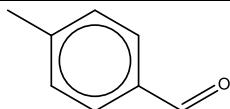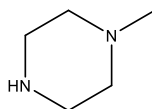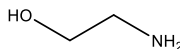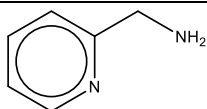
The anti-MM fragment database construction workflow is illustrated in **Figure 18,** based on MM medication data we collected. First, we combined all anti-MM medications to remove duplicated drugs according to CAS ID and molecular fingerprints and to eliminate the biologic agents (combined regime and different brand numbers of agents might cause a replication problem). A database of 109 anti-MM small molecules was established. After that, a fragment dataset was generated based on the structure of 109 anti-MM compounds using RECAP algorithms. Duplicated fragments were eliminated based on molecular fingerprint similarity. Unfavorable fragments with toxicity or nonselective covalent t interaction with proteins were filtered out by our database-implemented toxic and Pan Assay Interference Compounds (PAINS) remover. The fragments were also filtered through "rule of three," in which ClogP <3.5, $50 \leq$ molecular weight (MW) ≤ 350, polar surface area (PSA) ≤ 100 Å^2, rotatable bonds ≤ 3, hydrogen bond donors (HBD) ≤ 3, hydrogen bond acceptors (HBA) ≤ 5, and ring counts ≤ 4. After all of the filters, an anti-MM fragment database was constructed with 250 fragments and was ranked by frequency.
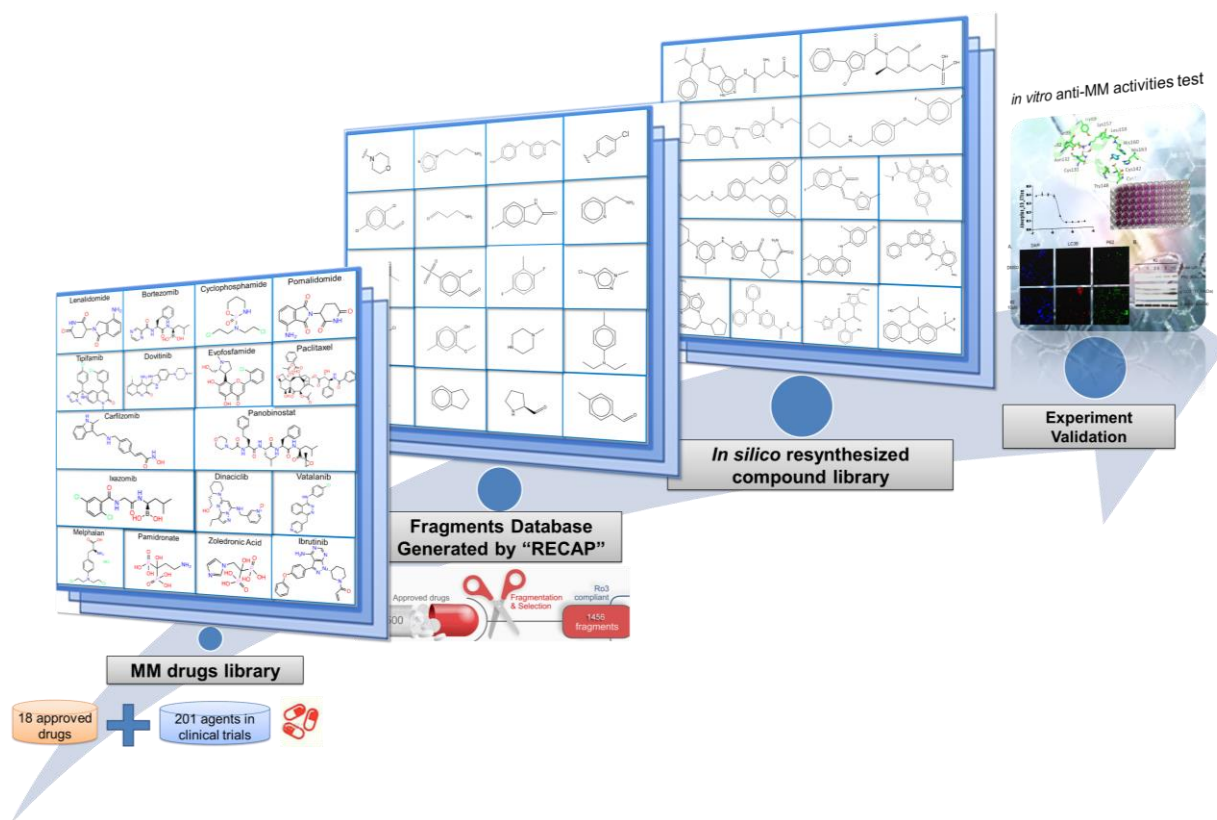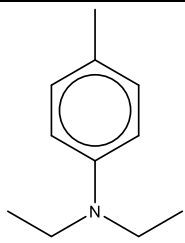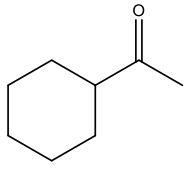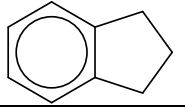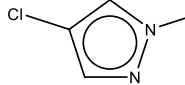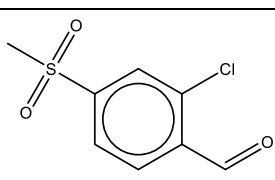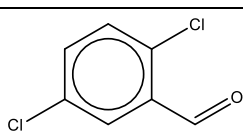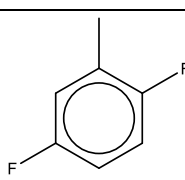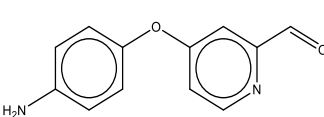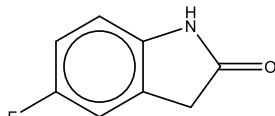
Figure 18. Workflow to Design Compounds with Anti-Multiple Myeloma Activity.

The top 20 ranked fragments were listed in **Table 1** with frequency, ClogP, MW, HBD, and HBA. 3D principal component analysis (PCA) plots for fragments before or after the filter with ClogP, MW, and ring counts (as well as HBA, HBD, and rotatable bonds) are displayed in **Figures 19A and 19C**. All of the fragments after the filter fit into the range defined by the rule of three, while before the filter, some fragments did not meet the criteria from the rule of three as outliers.

Table 1. Top-Ranked Multiple Myeloma Fragments After the Filter.

Structure	ID	Freq	ClogP	PSA	MW	HBA	HBD	RBC
	1	6	-0.39	21.26	87.07	2	1	0
	2	5	2.34	0	112.01	0	0	1
	3	4	1.71	29.46	138.07	0	1	4
	4	4	-0.4	48.72	125.1	2	2	3
	5	4	-0.47	43.09	73.05	2	1	3
	6	4	-0.47	43.09	73.05	2	1	3
	7	4	-0.06	29.1	99.07	2	1	1
	8	4	1.81	17.07	120.05	1	0	2
	9	4	-0.48	15.27	100.1	2	1	1
	10	3	0.88	46.25	61.05	2	2	3
	11	3	0.17	38.91	108.1	2	2	0

	No		ClogP	PSA	MW	HBA	HBD	RBC
(structure)	12	3	2.84	3.24	163.13	1	0	6
(structure)	13	2	2.18	17.07	126.1	0	0	2
(structure)	14	2	2.83	18.2	118.07	0	0	0
(structure)	15	2	1.07	17.82	116.01	1	0	2
(structure)	16	2	1.56	59.59	217.98	3	0	4
(structure)	17	2	2.81	17.07	173.9639	1	0	3
(structure)	18	2	2.84	0	128.04	0	0	2
(structure)	19	2	2	66	214.0	3	1	4
(structure)	20	2	1	29	151.04	2	1	1

Note: Lists of the structure of fragments with their ClogP, polar surface area (PSA), molecular weight (MW), hydrogen bond acceptor (HBA), hydrogen bond donor (HBD), and the number of rotatable bonds (RBC).

The anti-MM fragments were mixed with 100 of the most commonly used fragments and resynthesized 1,000 compounds *in silico* from fragments. The resynthesized compounds were filtered through the rule of 5 and a toxic filter to attain 758 compounds. These compounds were then docked into our previously established p62 homology model using Maestro. The result was ranked according to an overall performance based on docking score, binding free energy, and binding pose. The top-ranked re-synthetic compounds are listed in **Table 2** with their structure, ClogP, MW, HBD, HBA, and docking score. A PCA analysis was also performed for the resynthesized compounds dataset, as shown in **Figures 19B and 19D.** All of the compounds in the filtered datasets met the basic requirement of the "rule of 5". We selected compounds that are easy to synthesize. The synthesis route is shown in **Figure 23**. Afterward, several small molecules were synthesized and evaluated by bioassays for their anti-proliferation effect on MM cell lines.
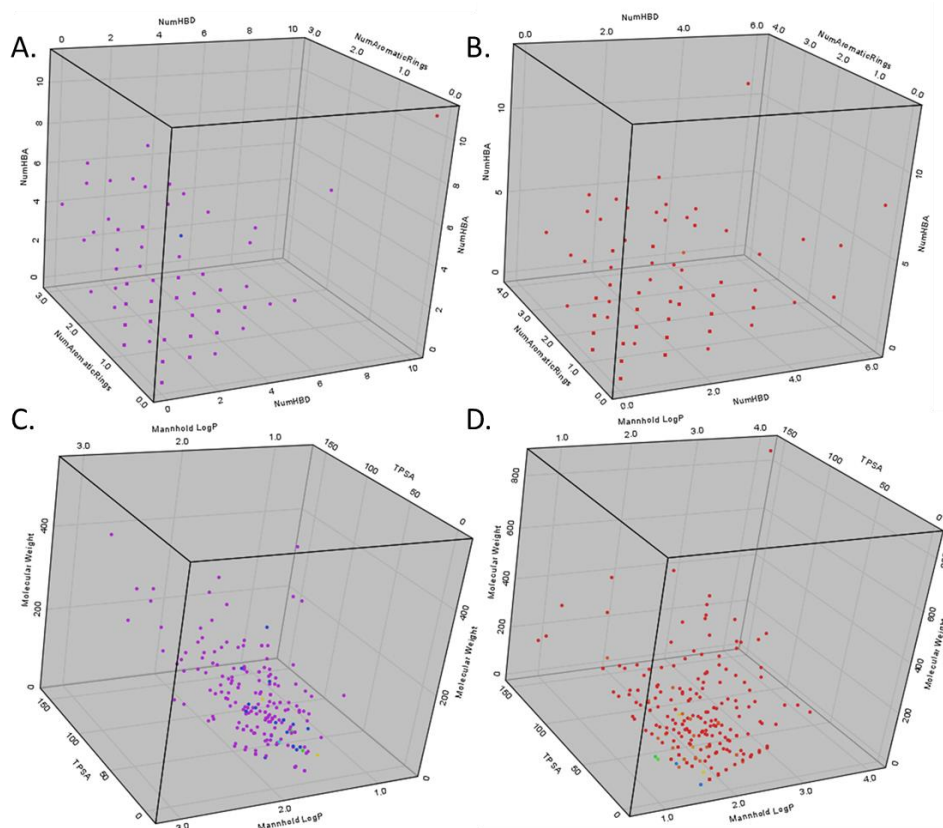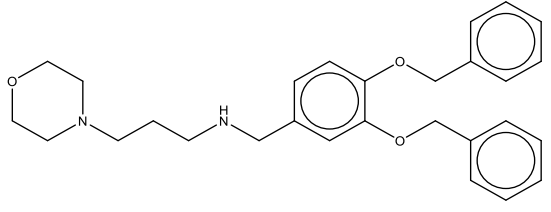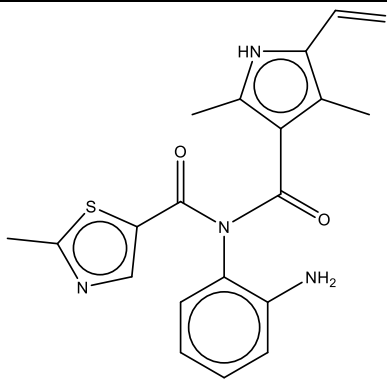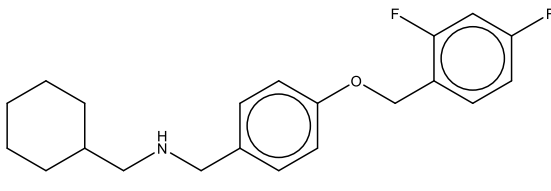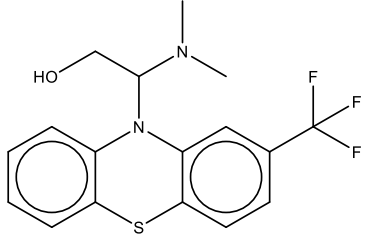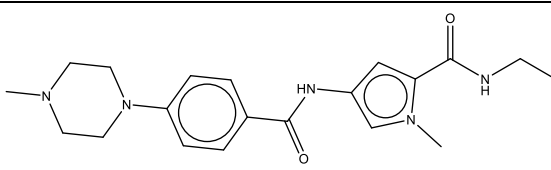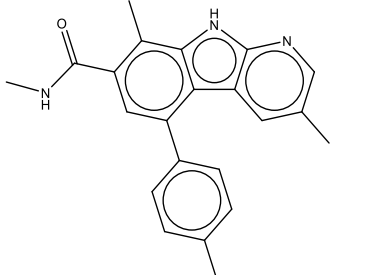
Figure 19. The Plot of Physiochemical Properties for Multiple Myeloma Fragments.
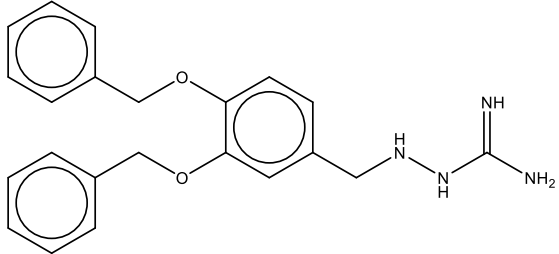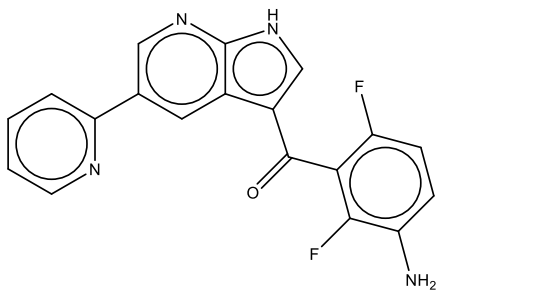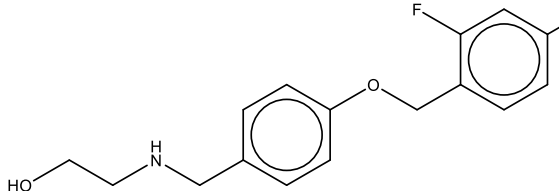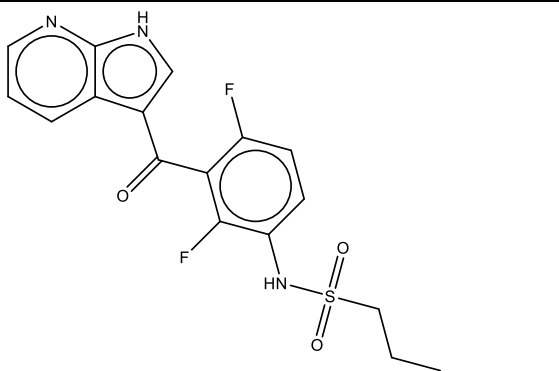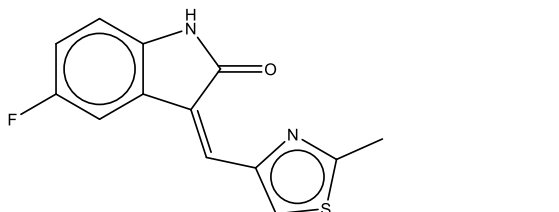
(A and B) The plot of the number of HBDs and HBAs against the aromatic ring count for the MM fragment database (A) and resynthesized compounds database based on MM fragments (B). (C and D) The plot of LogP and MW against PSA for the MM fragment database (C) and resynthesized compounds database based on MM fragments (D).
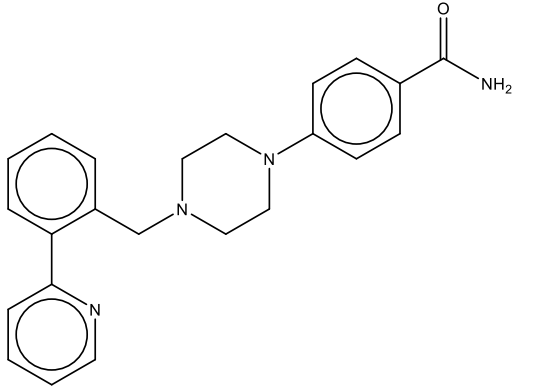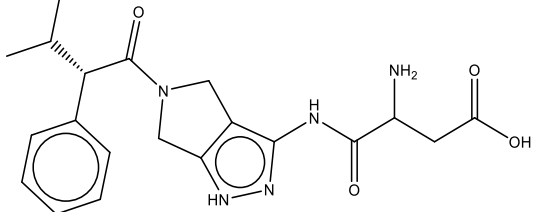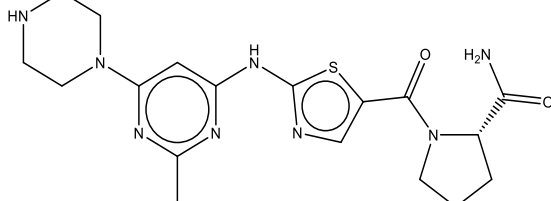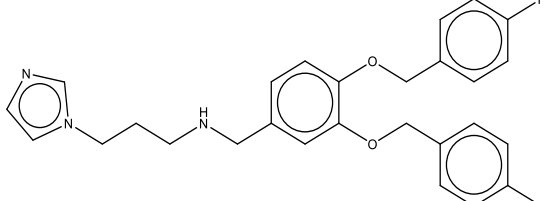
Table 2. Top-Ranked Resynthesized Compounds After filter.

Structure	SlogP	TPSA	MW	HBA	HBD	RBC
	3.69	58.12	318.15	5	1	5

	4.65	42.96	446.59	3	1	12
	4.11	120.32	380.13	5	2	4
	5.21	21.26	345.43	1	1	7
	4.18	52.01	354.10	3	1	4
	1.78	69.61	369.22	6	2	5
	4.67	57.78	343.17	3	2	2

	3.33	92.39	376.46	4	4	10
	3.71	84.66	350.10	4	2	3
	2.62	41.49	293.31	2	2	7
	3.22	100.3	379.08	5	2	6
	3.08	70.23	260.04	3	1	1

Structure						
(chemical structure)	3.17	62.46	372.19	5	1	5
(chemical structure)	1.43	141.41	399.19	8	4	7
(chemical structure)	0.48	157.61	416.17	10	3	5
(chemical structure)	5.49	48.31	463.53	2	1	12

Our study is to design compounds targeting p62 to treat multiple myeloma. Therefore, fragments and resynthesized compounds were also docked into the p62 homology model to explore the possible binding site and binding mode for reference. As shown in **Figure 20A**, a general binding pocket was defined in the p62 ZZ domain based on our previous studies. The fragments accumulated in four locations, especially locations 3 and 4, as displayed in **Figure 20.**

2.1.2.3. Docking Poses for Multiple Myeloma Fragments and Resynthesized Compounds.
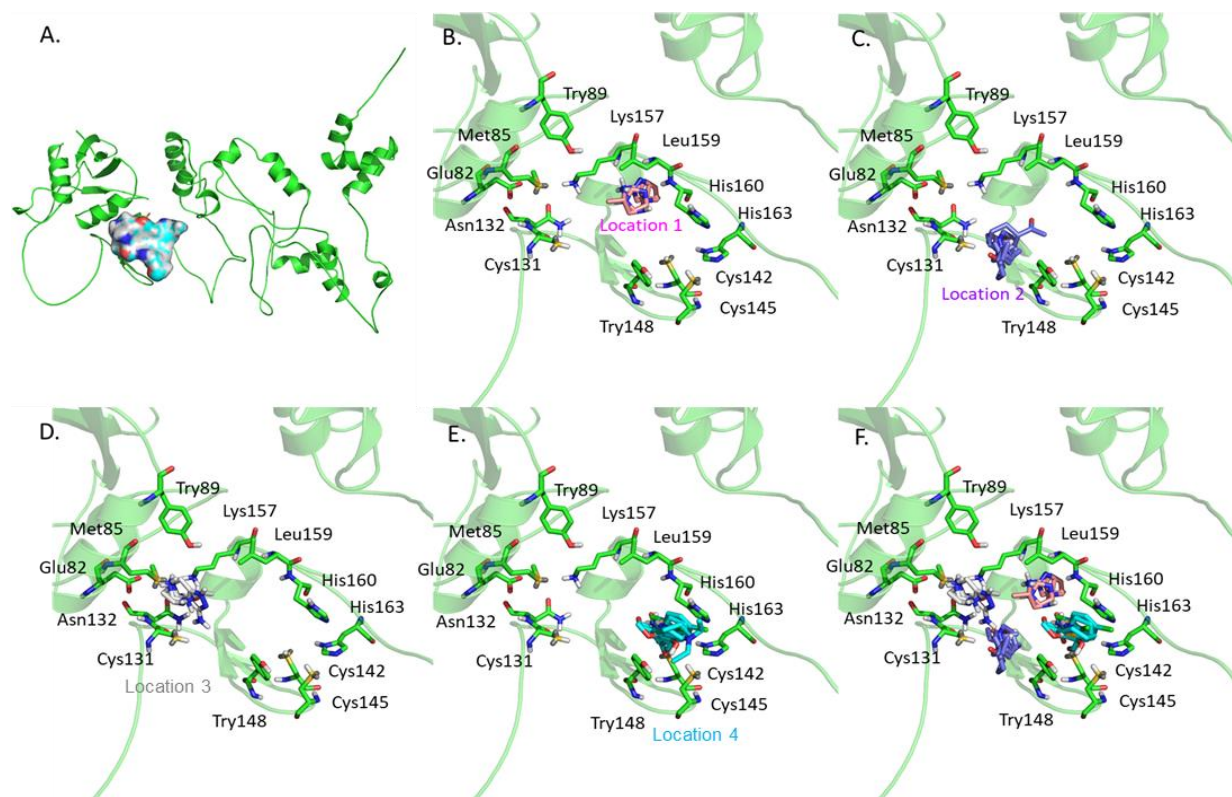
Figure 20. Binding Pocket, Docking Poses, and Locations of Fragment Clusters in P62.

(A) The full-length p62 homology model (green cartoon) and the defined binding pocket in the ZZ domain. The pocket is marked by the surface. (B) Fragments (pink sticks) clustered in location 1 surrounded by important residues in the binding pocket of p62 (green sticks). (C) Fragments (purple sticks) clustered in location 2 surrounded by important residues in the binding pocket of p62 (green sticks). (D) Fragments (white sticks) clustered in location 3 surrounded by important residues in the binding pocket of p62 (green sticks). (E) Fragments (blue sticks) clustered in location 4 surrounded by important residues in the binding pocket of p62 (green sticks). (F) All the clusters of fragments in the binding pockets are surrounded by key residues. The oxygen is highlight by red, nitrogen is in blue in the sticks, and the polar bond hydrogen is in white in all sticks.

Some fragments showed a higher docking score, low binding free energy, and a good pose. To illustrate, we aligned two or three fragments with their resynthesized compounds. We found some compounds display a binding pose that overlaps with these fragments, indicating the potential of these compounds to be p62 ZZ domain ligands with anti-MM effects. For instance, in **Figure 21,** compound **6.10** (**Figure 21A**) overlapped very well with fragment 4 in location 4 and fragment 3 (**Figure 21B**) in location 2. **Figure 21C** shows the 3-(1H-imidazol-1-yl)propan-1-amino group of compound **6.10** forms the same aromatic π-π stacking and a hydrogen bond as fragment 4 with imidazole ring in His160, benzoyl ring in Trp148 and amide in His160, indicating the addition of fragment 4 might be beneficial for p62 binding. The core scaffold in compound **6.10** also shares the same structure and similar binding mode with fragment 3. Another example is compound **3.28** (**Figure 21D**). The guanidine group from compound **3.28** and guanidine fragment aligns well and forms several hydrogen bonds with surrounding residues, including Lys157, Glu82, Asn132, and Cys131, indicating that the introduction of the guanidine group might favor interaction with p62, as shown in **Figure 20F.**
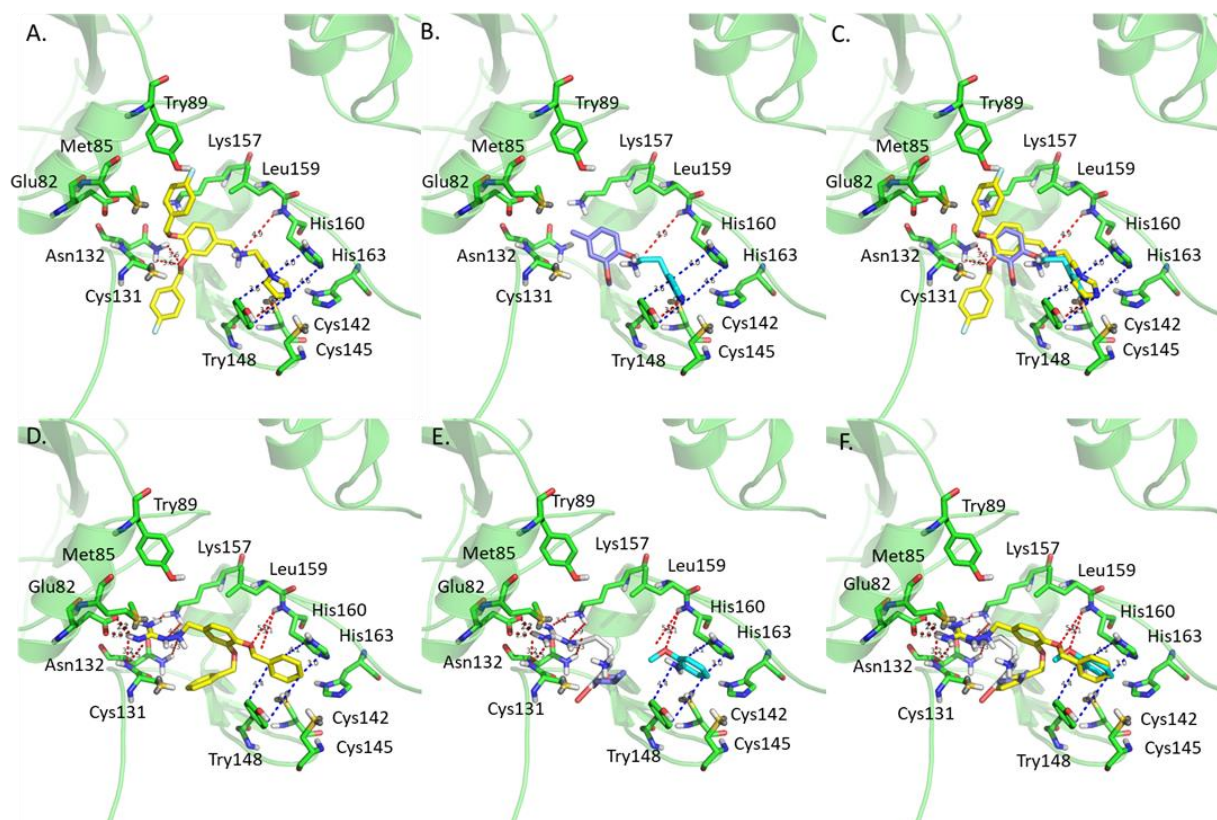
Figure 21. Binding Poses of Resynthesized Compounds 6.10 and 3.28 with p62.

(A) The binding pose of resynthesized compound **6.10** (yellow stick) in the binding site. (B) The binding poses of three fragments (white, purple, and blue sticks) that are used to synthesize the compound 6.10 virtually. (C) Overlap of the binding poses of resynthesized compound **6.10** and the three fragments that are applied to virtually synthesize the compound in the ZZ domain of the p62 protein. (D) The binding pose of resynthesized compound **3.28** (yellow stick) in the binding site. (E) The binding poses of three fragments (white, purple and blue sticks) that are used to in virtually synthesize the compound **3.28**. (F) Overlap of the binding poses of resynthesized compound **3.28** and the three fragments that are applied to virtually synthesize the compound in the ZZ domain of the p62 protein. All the clusters of fragments (white, blue and purple sticks) and resynthesized compounds (yellow stick) in the binding pockets surrounded by key residues (green stick) at the p62 protein binding site.

The π-π interaction can be formed between another hand of compound 3.28 and residues Try148 and His160. **Figure 22A-C** shows that compound **11.25** aligns well with fragment 2 and fragment 10, thus interacting with p62 through hydrogen bonds with Lys157 and π-π stacking with

Try148 and His160. **Figure 22D-F** illustrates how compounds **11.21** overlap with fragments 11 and 13, with plenty of interaction with p62. The four compounds are examples of how we choose compounds to be synthesized from the docking aspect. The fragments can be considered for chemical modification as functional groups that add to the core structure.
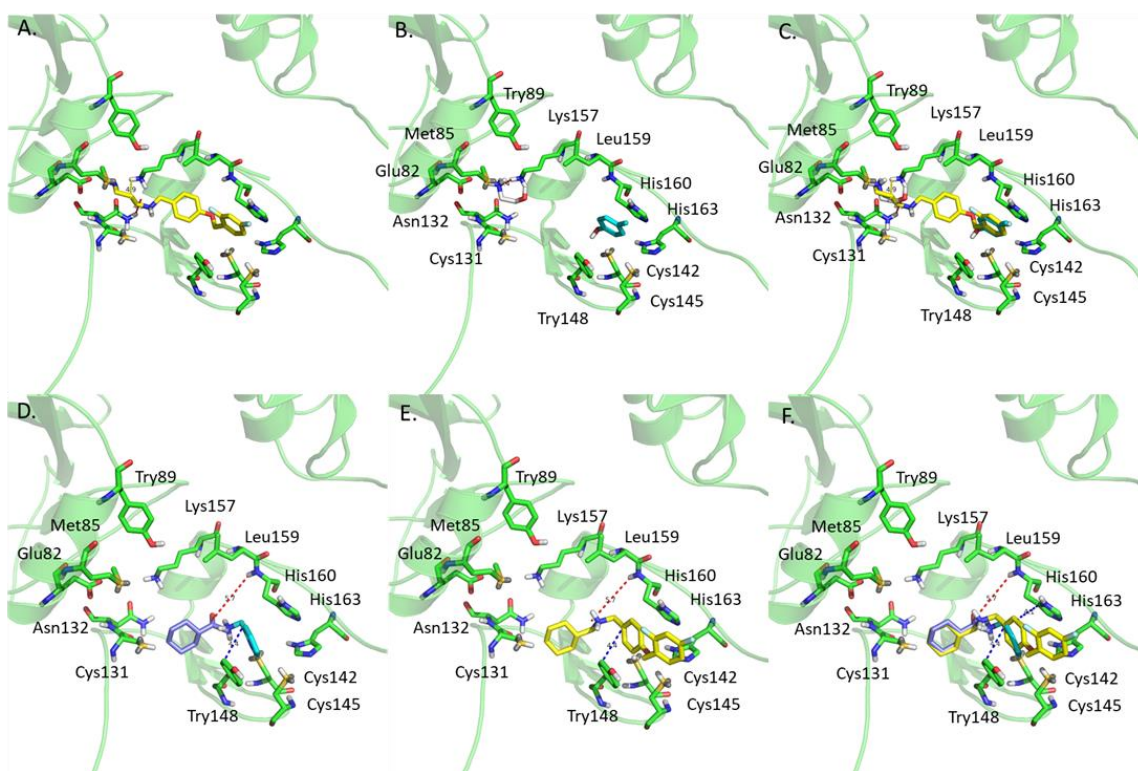
Figure 22. Binding Poses of Resynthesized Compounds 11.25 and 11.21 with p62.
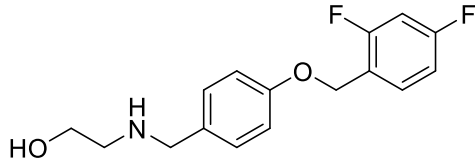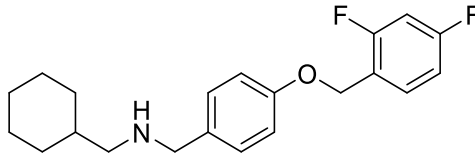
(A) The binding pose of resynthesized compound **11.25** (yellow stick) at the binding site. (B) The binding poses of three fragments (white and blue sticks) are used to synthesize the compound 11.25 virtually. (C) Overlap between the binding poses of resynthesized compound **11.25** and the three fragments that are applied to virtually synthesize the compound in the ZZ domain of the p62 protein. (D) The binding pose of resynthesized compound **11.21** (yellow stick) in the binding site. (E) The binding poses of three fragments (purple and blue sticks) are used to virtually synthesize the compound **11.21**. (F) Overlap between the binding poses of resynthesized compound **11.21** and the three fragments that are applied to virtually synthesize the compound in the ZZ domain of the p62 protein.

From that molecular docking studies for resynthesized compounds and their corresponding fragments, we selected four compounds to synthesize. After we got the four purified compounds, we measured the anti-proliferative effects on MM1.S and RPMI8226 cells by MTT assay. The results were summarized in Table 3 in the next section.
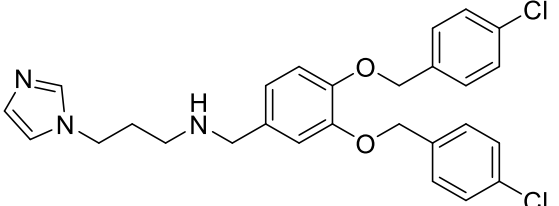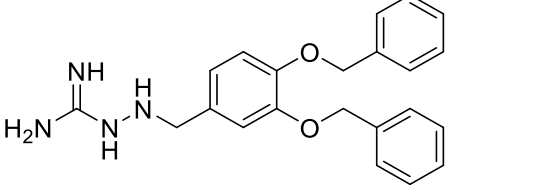
2.1.2.4. Anti-Multiple Myeloma Activities of Some Resynthesized Compounds.

The four compounds synthesized in this study are listed in **Table 3** with IC_{50} of their anti-proliferative effects on several MM cell lines. The compounds we selected all have some anti-proliferation effects on MM1.S and RPMI8226 cells, which was in line with our expectations. Among them, compound **11.25** has low anti-MM activity ($IC_{50} > 50\mu M$), while compounds **11.21, 6.10,** and **3.28** showed good anti-proliferative effects on U266 and MM1.S cell lines, which was consistent with our expectations ($1\mu M < IC_{50} < 5\mu M$). Compound **3.28** was selected for further studies, with the highest anti-MM activities ($IC_{50} = 1.07\mu M$).

Table 3. Synthesized Compounds List and their Anti-Multiple Myeloma Activities.

ID	Structure	Docking Score	$IC_{50}(\mu M)$ MM1S	$IC_{50}(\mu M)$ RPMI8226
11.25		6.76	81	68
11.21		7.12	2.8	2.59

| 6.10 | | 6.34 | 6.9 | 1.22 |
| 3.28 | | 8.73 | 3.25 | 1.07 |

In this part, we used a structure-based and ligand-based molecule design approaches to help design and prioritize compounds we can synthesize in the next step for further bioassay test. We synthesized four compounds in this section and measured their antiproliferative effects. From the fragment-based drug design part, we got a compound with an IC_{50} value of 1.07µM for future studies. In the next part, we will describe the chemical synthesis methods and strategies we applied in chemistry modification on our lead XRK3. The modified compounds we selected to synthesis all have a good molecular docking performance (a good score and reasonable pose). This section screened a large amount of *in silico* designed compounds, filtered them through ADMET properties, and provided a list of compounds pools that can be chosen for synthesis and future study development.

2.2. Chemistry Synthesis

From the above computer-aided drug design section, we screened a large number of virtual compounds. We picked up some compounds based on docking results to synthesize and test *in vitro.*

2.2.1 Introduction

Compound **XRK3** (**Figure 23**) was chosen as a lead compound due to its p62 interaction validated by pull-down assays, which can be further optimized to generate selective p62 ligands; it also showed an interesting backbone as it has three phenyl rings connected to a chiral center that is more easily modified. The lead optimization strategies that were utilized in this study added a functional group in the R^1 position, as this moiety has been shown to induce p62 binding affinity as previously discussed. In addition, the central chiral benzoyl ring was replaced by a central pyridine ring. Furthermore, three variable positions were evaluated for p62 specificity and *in vitro* anti-proliferation effects by utilizing fragments at R based on fragment size, charge, and lipophilic property (**Figure 29**).

Figure 23. Chemical Modification on p62ZZ Ligands

We designed four classes of analogs based on the structure of our lead. For the synthesis

of the first analog (**Figure 24**), commercially available 3, 4-dihydroxybenzaldehyde was reacted

with benzyl bromide in the presence of K_2CO_3 as a base in dried DMF to give bis-benzylated

benzaldehyde intermediate **A**. Then, the imine formation of **A** with an amine in heated MeOH, followed by the treatment of NaBH$_4$ for a reductive amination reaction, yielded the corresponding desired benzylamine products **B** and byproduct **C**. Fortunately, we only obtained this byproduct **7.2** from 4-CH$_3$ substituted aldehyde intermediate **7.1**. Next, the synthetic route for analog **G** is outlined in **Figure 25**. The synthesis of analogs **G** started from the commercially available 4-(2-aminoethyl)benzene-1,2-diol. To avoid unwanted benzylation on the amine nitrogen of the substrate, amine was protected by the Boc group, followed by the bis-benzylation on two hydroxyl groups to furnish the intermediate **E**. The Boc group was then removed by HCl to attain a high yield of amine·HCl intermediate **F**. A simple coupling reaction was then carried out with intermediate **F** and acyl chloride to obtain the amide analogs **G**. For the next two analogs displayed in **Figure 26**, benzylation was performed with 3,5-dihydroxybenzaldehyde and substituted benzyl bromide to give the analogs **H**, subsequently followed by reductive animation to obtain the bis-benzylated benzylamine analogs **I**. Finally, reductive amination of intermediate **J**, which was obtained from the benzylation of 4-hydroxybenzaldehyde and substituted benzyl bromide, with corresponding amines, yielded the analogs **K**. All of the desired compounds are summarized in **Tables 4-10**. These were purified by flash column chromatography and verified by NMR and LC/MS.
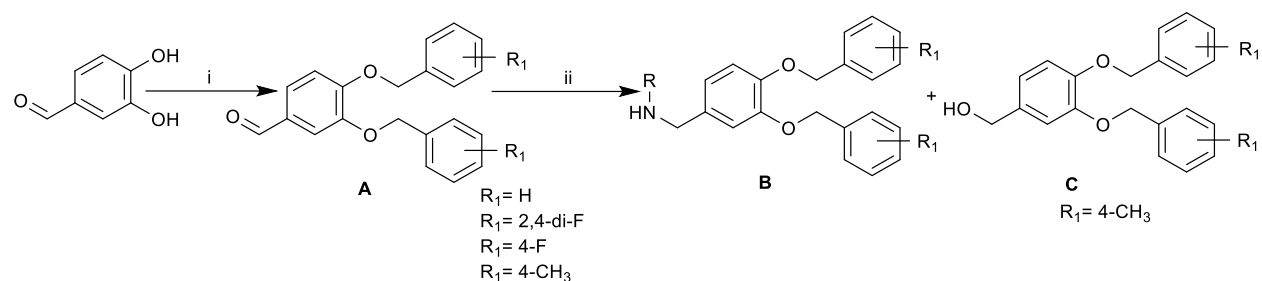
Figure 24. Synthetic Route for Analogs A, B, and C.

Reagents and conditions: (i) Benzyl bromide, K_2CO_3, DMF, 70 °C, 12 hours; (ii) step 1: RNH_2, MeOH, 12 hours, 60 °C; step 2: $NaBH_4$, MeOH, room temperature, 12 hours. (MeOH: methanol, DMF: dimethylformamide)
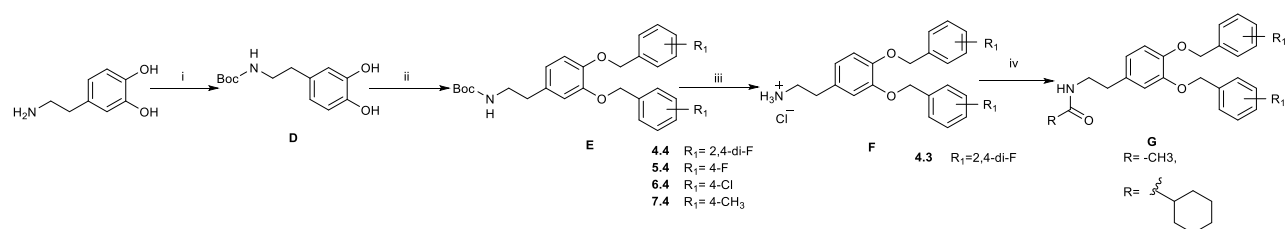
Figure 25. Synthetic Route for Analogs E, F, and G.

Reagents and conditions: (i) step 1: Di-*tert*-butyl dicarbonate, THF: water: MeOH = 2:1:1, room temperature, 6h; step 2: NaOH; (ii) Benzyl bromide, K_2CO_3, DMF, 70 °C, 12 hours; (iii) HCl,

ethanol, room temperature, 1 hour. (iv) acyl chloride, Et$_3$N, DCM, room temperature, 12 hours; (THF: tetrahydrofuran; DCM, dichloromethane)
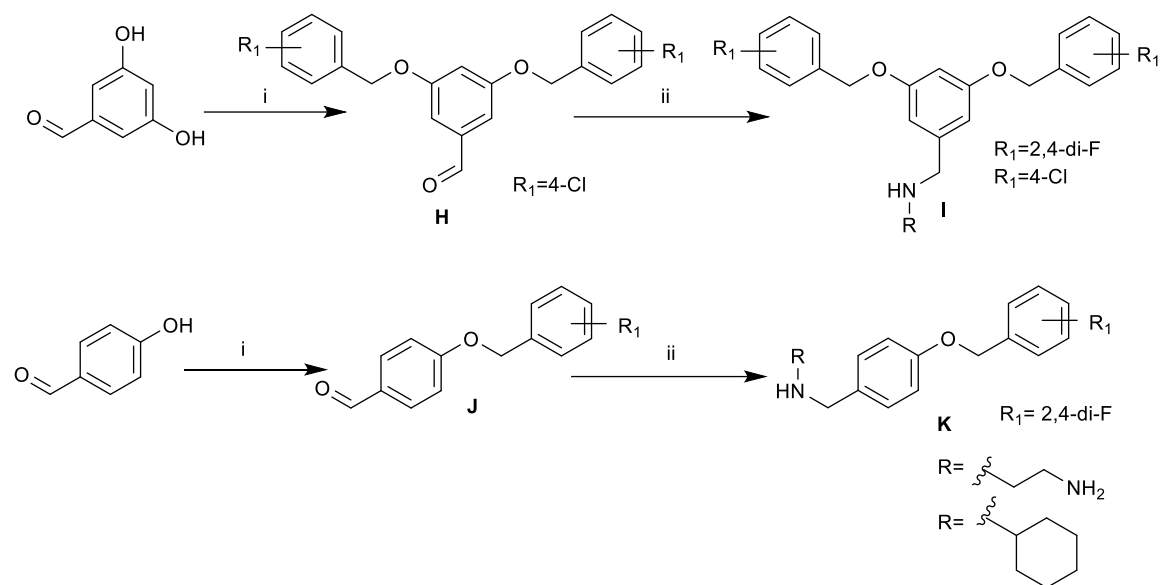
Figure 26. Synthetic Route for Analogs H, J, and K.

Reagents and conditions: (i) Benzyl bromide, K$_2$CO$_3$, DMF, 70 °C, 12 hours; (ii) step1: RNH$_2$, MeOH, 12 hours, 60 °C; step 2: NaBH$_4$, MeOH, room temperature, 12 hours.

2.2.2. Methods for chemical synthesis

2.2.2.1. Materials and Reagents

All reagents were purchased from commercial sources and used without further purification. Analytical thin-layer chromatography (TLC) was performed on SiO$_2$ plates on alumina. Visualization was accomplished by UV irradiation at 254 nm. Flash column chromatography was performed using the Biotage Isolera flash purification system with SiO2 60 (particle size 0.040−0.055 mm, 230−400 mesh). ^{1}H-NMR and ^{13}C-NMR were recorded on a Bruker 400 MHz and a Bruker 600 MHz spectrometer in Salk Hall eighth floor and BST10034.

Splitting patterns are indicated as follows: s, singlet; d, doublet; t, triplet; m, multiplet; br, broad peak. The purity of all final derivatives for biological testing was confirmed to be >95% as determined using the following conditions: a Shimadzu HPLC instrument with a Hamilton reversed-phase column (HxSil, C18, 3 μm, 2.1 mm × 50 mm (H^2)); eluent A consisting of 5% CH_3CN in H_2O; eluent B composed of 90% CH_3CN in H_2O; flow rate of 0.2 mL/min; UV detection, 254 and 214 nm.

2.2.2.2. Synthesis Procedure for 3,4-bis(benzyloxy)benzaldehyde

Method 1

3, 4-dihydroxybenzaldehyde (3.00 g, 21.7 mmol) was diluted with dry dimethylformamide (DMF, 50 mL). Benzyl bromide (7.65 g, 44.7 mmol) was added slowly, followed by anhydrous K_2CO_3 (9.60 g, 69.4 mmol). The mixture was stirred at room temperature for 2 hours. Additional K_2CO_3 (2.40 g, 17.3 mmol) was added, and the mixture was heated to 70 °C for 30 minutes and then cooled to room temperature. The mixture was partitioned between H_2O and ether (120 mL each). The organic layer was separated, and the water layer was extracted with ether (3 × 50 mL). The pooled organic layers were washed with H_2O (2 × 50 mL) and saturated aqueous NaCl (50 mL). The pale, straw-colored extracts were dried over anhydrous sodium sulfate and concentrated to yield a white cream-colored solid (6.57 g, 95%) after washing with hexanes (75 mL). The product was characterized by ^1H NMR (600MHz, CDCl3): δ 9.81 (s, 1H), 7.49-7.31 (m, 12H), 7.04 (d, J = 8.3 Hz, 1H), 5.27 (s, 2H), 5.22 (s, 2H). ^{13}C NMR (600MHz, CDCl3) δ 190.86, 154.26, 149.19, 136.56, 136.24, 130.29, 128.68, 128.60, 128.13, 128.04, 127.33, 127.08, 126.73, 113.07, 112.32, 70.96, 70.82.

2.2.2.3. General procedure for amino products

Method 2:

3,4-Bis(benzyloxy)benzaldehyde (318 mg, 1 mmol) was dissolved in dry ethanol, and ethanolamine (61mg, 1 mmol) was added. The reaction mixture was stirred for 12 hours at 60 ^{o}C. The reaction solution was cooled down to room temperature. NaBH$_4$ (57mg, 1 mmol) was added slowly in small portions, and the resulting solution was stirred for another 12 hours (143, 144). The solvent was evaporated in vacuum, and the residue was dissolved in water and extracted with ethyl acetate. The organic layers were combined and dried with Na$_2$SO$_4$, filtered, and evaporated in a vacuum. The residue was purified by a flash column to generate the desired product 2-((3,4-bis(benzyloxy)benzyl)amino)ethan-1-ol (2.0 g, 56%). ^{1}H NMR (CDCl$_3$): 7.52-7.33 (m, 10H), 7.01-6.84 (m, 3H), 5.20 (s, 2H), 5.17 (s, 2H), 3.71 (s, 2H), 3.64 (t, J = 4.8, 2H), 2.93 (s, 2H), 2.72 (t, J = 4.8, 2H).

2.2.2.4. General Procedure for Generating Aminoguanidine Blockers.

Method 3

3,4-bis((4-chlorobenzyl)oxy)benzaldehyde (3.72g, 9.6 mmol) was dissolved in dry methanol, and aminoguanidine hydrochloride salt (1.12g, 10 mmol) was added. The reaction mixture was stirred for overnight at 70 ^{o}C. The reaction solution was cooled down to room temperature. The solvent was evaporated in vacuum, and the residue was purified by a column chromatography and eluted by chloroform and methanol to generate the desired product (E)-2-(3,4-bis((4-chlorobenzyl)oxy)benzylidene)hydrazine-1-carboximidamide (1.58g, yield 37.2%).

^{1}H-NMR (300MHz, DMSO-d6): 8.006 (s, 1H), 7.715-7.710 (d, 1H), 7.523-7.448 (m, 9H), 7.310-7.305-7.283-7.277 (dd, 1H), 7.119-7.190 (d, 1H), 5.186 (s, 4H). ^{13}C NMR (300MHz, DMSO-d6) δ 155.81, 150.58, 148.74, 146.95, 136.53-136.43 (d), 132.97-132.91 (d), 130.04, 129.79, 128.93, 127.25, 123.20, 114.24, 112.15, 69.87, 69.55. LC−MS (ESI): m/z 443.5 (100%), 445.5 (M + H)$^+$.

2.2.2.5. General Procedure for Generating Amide blockers

To a solution of 2-(3,4-bis((4-chlorobenzyl)oxy)phenyl)ethan-1-aminium chloride (**6.3, 403mg, 1 mmol**) and triethylamine (TEA, 125 mg, 1.25 mmol) in anhydrous dichloromethane (DCM, 4 mL) was slowly added a solution of methyl carbamic chloride (103 mg,1.1 mmol) in anhydrous DCM (3 mL). The mixture was then refluxed for 3 days. The reaction mixture was diluted with water (5 mL) and extracted with DCM (8 mL × 3). The combined organic layers were subsequently washed with H$_2$O (10 mL× 3) and brine (10 mL × 3), dried over anhydrous Na$_2$SO$_4$, and concentrated in vacuo (145). The crude product was purified on a silica gel column (CH$_2$Cl$_2$/MeOH = 19/1, v/v) to afford N-(3,4-bis((4-chlorobenzyl)oxy)phenethyl)acetamide (white solid, **6.5, XIE5-2-73**, 270 mg, 61% yield). The chemical structured was characterized by ^{1}H-NMR (CDCl$_3$): 7.371 (m, 8H), 6.892-6.872 (m, 1H), 6.790-6.730 (m, 2H), 5.389 (s, 1H), 5.118-5.107 (d, J = 4.4 Hz, 4H), 3.846-3.471 (m, 2H), 2.759-2.742-2.725 (t, J = 6.8 Hz, 2H), 1.941 (s, 3H).

2.2.2.6. Synthesis Procedure for Boc-Protected Guanidine Amine

Method 4

Dissolve 1,3-Di-Boc-2-methylisothiourea (2.9g, 10mM) in THF (25ml), added the solution of 1,3-Di-Boc-2-methylisothiourea dropwise to a stirred solution of 1,4-diaminobutane (1.9g,

2.16ml, 26mM) in THF/H_2O (40ml, 20:1, volume/volume). After stirred for 1h in 50°C, the reaction mixture was concentrated in vacuum, and the residue was partitioned between $CHCl_3$ and 10% aqueous $NaHCO_3$. The organic layer was dried by adding Na_2SO_4 and stirring for over 1h, filter out Na_2SO_4, and evaporated the solvent. The residue was then purified by chromatography on silica gel column using $CHCl_3$ (contain 1% TEA) and Methanol system, give product 1.23g as a yellow oil (cited in JMC, 2001, vol 4-18-2955).

2.2.2.7. General Procedure for Synthesis of Removing Boc Protect Groups

Method 5

Generation hydrochloride gas by slowly adding concentrated sulfuric acid (dropwise) into sodium chloride, the additional water in the generated HCl gas was then removed by concentrated sulfuric acid and lead to the reaction mixture in a three-necked bottle by tube. The starting material (Boc-protected compounds) was dissolved in solvent (CH_2Cl_2) (not reactive to HCl) to make the reaction mixture. The hydrochloride gas was bubbled into the reaction mixture and then reacted with starting material to eliminate the protection group. The reaction mixture was stirred at room temperature with hydrochloride gas bubbled in for about 40 min. Stop the generation of HCl gas, continue stirring at r.t. for about half an hour, then evaporate the solvent, add solvent to resuspend it, and evaporate solvent several times to remove extra hydrochloride. Too much residual hydrochloride will make the product not so stable in r.t. The product was then placed under the vacuum overnight to remove the solvent. We confirmed the structures with NMR and LC-MS.

Results

This section was to synthesize new compounds and provide novel small molecules for assay test and structure-activity relationship analysis. Seventy compounds were synthesized in this

section. The structure was confirmed by proton and carbon NMR, LC-MS. The structure characterization spectrums are listed in **Appendix. B. Chemical Characterization Spectrum**s. The structure information was summarized with activity data in **Table 4-11** in the next section. After the structure and purity of the final products were confirmed, we tested the efficacy of these compounds by *in vitro* and *in vivo* bioassays. Our goal is to get some compounds that target p62 and have a potential therapeutic effect of treating multiple myeloma. If the compounds did not show any anti-proliferative activity on multiple myeloma cells, they might be less valuable for further analysis and discussion in this study.

2.3. p62ZZ Ligands Inhibit Myeloma Cell Growth

2.3.1. Introduction of the specific problem

In the above part, we described the chemistry approach we used to synthesize and design compounds. Then, we will need to measure the efficacy and other properties of these compounds. We are aiming at getting compounds to treat multiple myeloma through targeting p62 protein. Therefore, it is necessary to measure the efficacy of these compounds to inhibit myeloma cell growth by a well-acceptable and easy-to-handle *in vitro* screen assay. Their capacity to inhibit myeloma cell growth represents their potential effect of treating multiple myeloma preliminarily.

2.3.2. Methods

Here, the MTT cell viability assay was conducted to determine the anti-proliferation effects of the compounds on MM cell lines. MM1.S, MM1.R, and RPMI8226 cells were kindly provided by Dr. Deborah L. Galson (University of Pittsburgh Cancer Institute). U266 and BJ normal human fibroblasts were obtained from American Type Culture Collection (ATCC). Cell lines were maintained in an appropriate growth medium with 10% fetal bovine serum (FBS) and sub-cultured twice per week. MM1.S, RPMI8226, and U266 cell lines were authenticated by Short Tandem Repeat (STR) profiling utilizing 16 different STR loci. These studies were conducted using protocols approved by the University of Pittsburgh's IRB and Indiana University's IRB.

MM1.R, MM1.S, U266, and RPMI8226 cells were maintained at 37 °C in a humidified 5% CO_2 and 95% air atmosphere and cultured in RPMI-1640 medium (Gibco Laboratories, Grand Island, NY) containing 10% fetal bovine serum (FBS) and sub-cultured twice per week. BJ cells were cultured in Eagle's Minimum Essential Medium (EMEM, Gibco Laboratories, Grand Island, NY). The test drugs and positive control were initially dissolved in dimethylsulfoxide (DMSO), and then the solutions were diluted 1:1000 in RPMI-1640 medium. Different cells were seeded on a 96-well plate in 200 mL medium per well at a density of 3,000-15,000 cell counts per well, depending on cell type for 8 h. Then, the cells were incubated with serial concentrations of test compounds and controls for 72 hours. An MTT assay kit was utilized to determine the percentage of cell survival. MTT (3-(4,5-dimethylthiazol-2-yl)-2,5-diphenyltetrazolium bromide (Sigma, St. Louis, USA)) solution (5mg/ml, 20 μL) was added to each well, shaken at 150 rpm for 5 minutes, and then incubated for 4 hours at 37°C and 5% CO_2. The metabolism product (formazan) was dissolved in 150 μL isopropanol and shaken at 150 rpm for 5 minutes. Optical density was read at

540 nm and subtracted from the background at 720 nm. The effect of ligands on cell viability was expressed as percent cell viability, with vehicle-treated control cells set at 100%. The concentration of each drug was examined in triplicate. The concentrations of the compounds were 20, 10, 5, 2.5, 1.25, 0.625, 0.3125, 0.15625, 0.075 and 0.01 mg/mL. The data were analyzed by GraphPad Prism 7.0.

2.3.3. Results and Discussion

Cell viability was significantly altered by our p62ZZ ligands in three MM lines (MM1.S, RPMI8226, and U266). However, in the normal human cells (BJ), the cell viability was not significantly changed by the tested compounds compared to the negative control (DMSO), indicating the anti-proliferative activity in MM cell lines of our compounds was not due to their cytotoxicity, indicating favorable therapeutic indices of our p62ZZ ligands. Additionally, we measured the effect of **6.28** on cell viability on p62$^{-/-}$ cell and WT cells. We found that the knockout of p62 dramatically reduced the inhibitory effect of our compound on myeloma cells, indicating that p62 is necessary for the compounds to elicit the antiproliferative effect in these cells.

The exact IC$_{50}$ values for all the compounds are illustrated in **Tables 4-10**. To obtain more potent derivatives, we modified the lead compound **XRK3F2** by adding diverse substitutes (R$_1$) on the benzyloxy ring (**Table 4**).
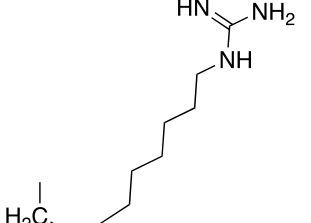
Generally, potency did not change significantly by adding chloride (**6.25**), fluoride (**4.24, XRK3,** and **XRK3F2**) into the 4-position of two benzyloxy rings compared to compound **XRK3**.

Table 4. The List of Benzyloxy Analogs with their Anti-Proliferative Activity.
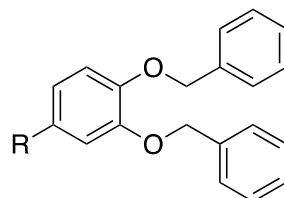
Analogs 3.1 to 3.31

ID	R-groups	MM1.R, IC$_{50}$ (µM)	RPMI8226, IC$_{50}$ (µM)	U266, IC$_{50}$ (µM)	Auto phagy	Internal ID
3.1	-CHO	> 20	> 10	15.8	=	XIE5-1-8
3.2	-CH$_2$OH	3.342	3.311	2.743	-	XIE5-1-33A
3.7		9.53	4.78	41.37	+	XIE5-2-54/55
3.8		10.57	2.27	5.28	+	XIE5-2-53
3.9		4.242	2.00	10.23	=	XIE5-2-49
3.10		4.749	1.72	2.24	=	XIE5-2-64
3.14		1.47	0.9912	4.72	+	XIE5-2-46
3.16		9.724	6.73	4.32	+	XIE5-2-51
3.25		4.4	3.7	5.9	+	XIE62PY1-9 NSC173162 XRK3
3.29		5.12	3.58	4.59	+	XIE1-4-3
3.28		3.25	1.07	6.72	+	XIEX5-2-44

3.31		10.23	9.96	21.74	=	5-1-54CT XIE5-1-64

Other than adding different substitutions at the R_1 position, replacing R with various functional groups with different sizes, lengths, hydrophobic, hydrophilic, and electronic properties was another strategy for our chemical modification. First, we introduced diverse functional groups connected to the amine in the R position as shown in **Tables 4-8**, such as guanidine (**3.28, 3.29, 3.31**), heterocyclic rings (furan, **3.8, 4.8, 5.8, 6.8**; thiophene, **3.7, 4.7, 5.7, 6.7**; pyridine, **3.9, 4.9, 5.9, 6.9, 7.9**; imidazole, **3.10, 4.10, 5.10, 6.10**), substituted aromatic rings (1,3,4-trimethoxybenzylamine **3.15, 4.15, 5.15, 6.15**; 4-(*N*,*N*-diethylamino)-benzylamine **3.13, 5.13, 6.13**; anisole **3.14, 4.14, 5.14, 6.14**), guanidine with different length linkers (C2 linker, **3.29**; C6 linker**, 3.31** to replace the 2-hydroxyethyl substitute on the amine.

The IC50 values for most of the analogs fall into the same range ($2\mu M < IC_{50} < 10\mu M$). No big difference was observed for their potency to inhibit myeloma cells in our test. Therefore, we will not go through every compound for its potency. We focus on the discussion of a few compounds that have the lowest IC_{50} values. I will also mention what kind of modification will lead to the loss of potency ($IC_{50} > 50\mu M$) or reduce potency ($IC_{50} > 10\mu M$). Sometimes, we mentioned reduced or improved potency. It is not as much as a 10-fold difference. It's just a relatively higher or lower IC50 value.

Compound **6.28** ($IC_{50} < 0.2\mu M$) possessing aminoguanidine moiety showed the highest anti-MM potency, indicating that the aminoguanidine group is favorable for anti-cancer activity on myeloma cells. Compounds **3.28, 3.29,** and **5.29** also work well in blocking myeloma cell

proliferation. Compound **3.31** (IC$_{50}$ >20µM), which has a longer carbon linker between amine and guanidine than compounds **3.28** and **3.29**, possesses a reduced potency to inhibit tumor cell growth, indicating an influence of the length of the R groups on the activity of molecules.

As compound **6.28** shows a good anti-MM activity, we compared the docking poses of compounds **6.28, 5.29, 7.30,** and **3.31** on p62, as shown in **Figure 27**. Compound **5.29** in **Figure 27A** with a two-carbon linker between amine and guanidine shares a similar pose as compound **6.28** in **Figure 26C.** The two-carbon linker was bent to the upper side of the pocket, which interacts with residues in the PB1 domain, leaving an appropriate distance for a benzoyl group to form π-π interaction with Tyr148 and His160 in the ZZ domain. Therefore, the analogs with a two-carbon linker between amine and guanidine might have comparable activity to compound **6.28**. The three-carbon linker shown in **Figure 27B** folds itself in the upper side of the pocket in the PB1 domain, thus leaving enough space for the compound to form π-π interaction with Tyr148 and His160 in the ZZ domain. The guanidine group in **Figure 27B** flips over and form hydrogen bonds with Tyr89 and Asp73.

When we further increased the length of the linker to six carbon, as seen in **Figure 27C**, there was not enough space for the linker to bend over itself; thus, the structure was pushed toward the ZZ domain side, which makes the position of benzoyl group neither parallel nor favorable to aπ-π interaction with Tyr148 and His160. Some side chain was even pushed out of the reach of the ZZ domains, losing some interactions with residues in the ZZ domain and diminishing the binding affinity and activity with p62. Thus, enlengthening the linker to six carbon or more may impair the binding of analogs to p62 and influence the downstream activities.
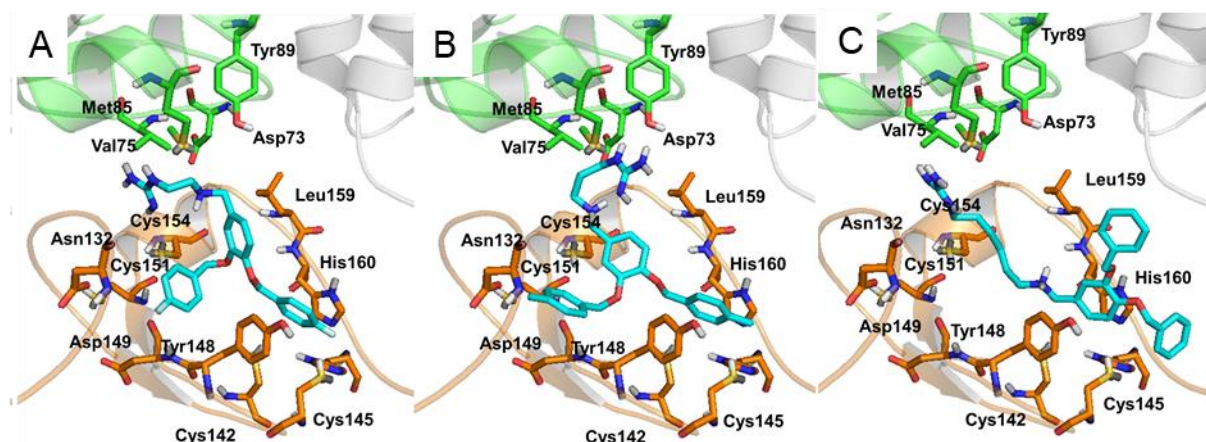
Figure 27. Docking Poses of Compounds with Guanidine.

(A) The docking pose of **5.29** with p62. (B) The docking pose of **7.30** with p62. (C) The docking pose of **3.31** with p62. The compounds are represented by cyan sticks. The ZZ domain is in orange and the PB1 domain is in green.

The employment of heterocyclic moieties was not favorable to the anti-tumor activity on MM cells. Compounds **3.7, 4.7, 5.7, 6.7** (thiophene, $IC_{50} > 10\ \mu M$), **3.8, 4.8, 5.8, 6.8** (furan), **3.9, 4.9, 5.9, 6.9, 7.9** (pyridine), **4.11, 5.11, 6.11** (3-morpholino-1-amine), and **3.10, 4.10, 5.10, 6.10** (imidazole) have similar moderate anti-proliferation effects on three MM cell lines. The RPMI8226 cell line was the most sensitive one in response to our compounds.
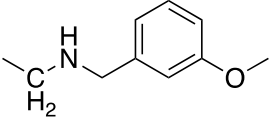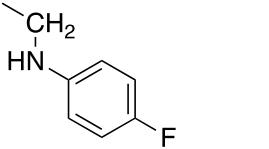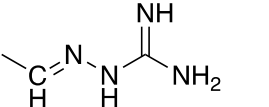
In addition to the substituted aromatic rings that linked to the amine in the R position, alkyl groups that linked to amine were also investigated. Most compounds with a long flexible chain or alky ring worked well in blocking the proliferation of myeloma cells. Certain flexible length of R groups (4-5 C-bond) favors anti-MM potency. Too short (aldehyde intermediate **3.1, 4.1, 5.1, 6.1, 7.1, 8.1, 9.1**) or too long (**3.31** and **7.31**) R groups are not favorable for high anti-proliferative potency ($IC_{50} > 10\ \mu M$).

Table 5. The List of 2,4-di-F Benzyloxy Analogs with their Anti-Proliferative Activity.
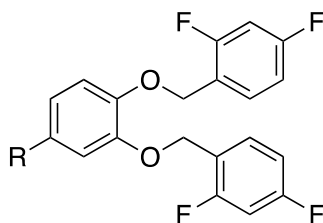
Analogs 4.1 to 4.32
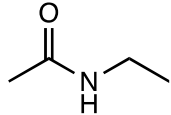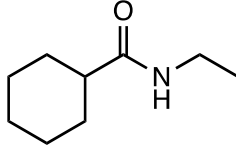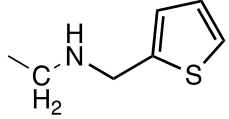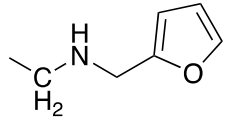
ID	R-groups	MM1R, IC$_{50}$(μM)	RPMI8226, IC$_{50}$(μM)	U266, IC$_{50}$(μM)	Autophagy	Internal ID
4.1	-CHO	> 20	> 10	> 20	=	XIE5-1-85
4.2	-CH$_2$OH	3.46	5.49	5.61	-	XIE5-2-93
4.3	-CH$_2$CH$_2$NH$_2$	3.18/11.76	1.74	5.98	-	XIE5-2-70
4.4	-CH$_2$CH$_2$NH-Boc	> 100	> 100	> 100	=	Lp1-66
4.5		0.43/> 5	0.97/> 5	0.82	-	XIE5-2-74
4.6		> 10	> 10	> 10	=	XIE5-2-79
4.7		12.83	10.3	13.51	+	XIE5-2-3
4.8		10.98	5.02	21.35	+	XIE5-2-14
4.9		9.53	3.52	20.12	=	XIE5-2-10
4.10		5.21	4.91	11.07	+	XIE5-2-13
4.11		3.06	4.20	7.44	+	XIE5-2-7
4.15		2.73	4.86	6.95	+/=	XIE5-2-11
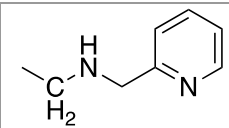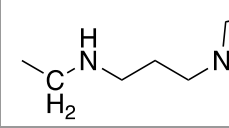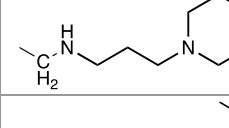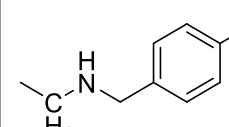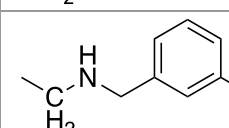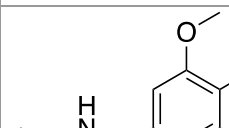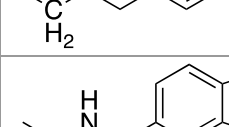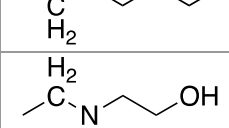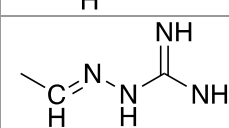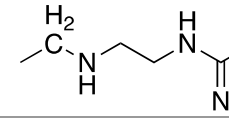
4.16		4.67	5.33	9.63	=	XIE5-2-15
4.17		8.32	2.97	9.32	-	XIE5-2-22
4.28		4.40	2.30	8.02	+	XIE5-2-40

Table 6. The List of 4-fluoride Benzyloxy Analogs with Anti-Proliferative Activity.
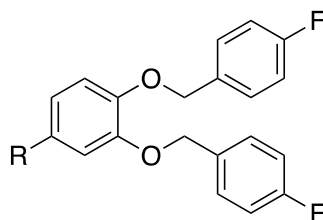
Analogs 5.1 to 5.29

ID	R-groups	MM1R, IC$_{50}$(µM)	RPMI8226, IC$_{50}$(µM)	U266, IC$_{50}$(µM)	Autop hagy	Internal ID
5.1	-CHO	> 20	> 20	> 20	=	XIE5-1-24
5.3	-CH$_2$CH$_2$NH$_2$	17.57	2.38/3.10	10.75	-	XIE5-1-68
5.4	-CH$_2$CH$_2$NH-Boc	> 100	> 100	> 100	=	Lp1-64
5.5		>10	1.20	3.51	-	XIE5-2-75
5.6		>10 (repeat)	>10	>20	=	XIE5-2-77
5.7		4.95	3.90	14.83	+	XIE5-2-16
5.8		4.43	0.68/4.74	6.98	+	XIE5-2-1

5.9		10.98	8.74	19.03	=	XIE5-2-18
5.10		2.402	1.71	6.95	+	XIE5-2-21
5.11		2.754	3.43	8.30	+	XIE5-2-17
5.13		3.34/1.51	0.66/0.82/0.74	1.25	-	XIE5-2-23
5.14		5.14	4.77	10.07	+	XIE5-2-2
5.15		3.43	4.41	6.04	+	XIE5-2-19
5.16		2.94	2.22	5.68	+	XIE5-2-20
5.25		5.30	2.50	4.00	+	XRK3F2
5.28		2.12	0.97	3.26	+	XIE5-2-43 XIE5-1-52
5.29		5.39	3.21/2.41	4.98	+	5-1-27AT XIE5-1-66

Table 7. The List of 4-Chloride Benzyloxy Analogs with their Anti-Proliferative Activity.

112
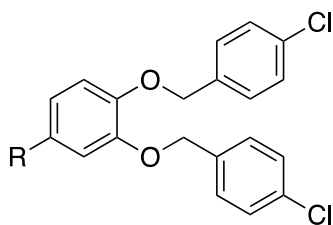
Analogs 6.1 to 6.28

ID	R-groups	MM1R, IC$_{50}$(µM)	RPMI8226, IC$_{50}$(µM)	U266, IC$_{50}$(µM)	Autophagy	Internal ID
6.1	-CHO	> 20	> 20	> 20	=	XIE5-1-84
6.3	-CH$_2$CH$_2$NH$_2$	6.00	13.00/7.00	>10		XIE5-1-71
6.4	-CH$_2$CH$_2$NH-Boc	>10	1.67/2.30	>100	-	Lp1-67
6.5		12.50/16.12	1.70	2.63	-	XIE5-2-73
6.6		2.77	1.10	5.04	=	XIE5-2-80
6.7		2.50	3.25	8.86	+	XIE5-2-33
6.8		4.67	3.25	4.78	+	XIE5-2-31
6.9		5.08	0.60	4.92	=	XIE5-2-35
6.10		6.90	1.22	6.86	+	XIE5-2-38
6.11		9.04	1.19	18.85	+	XIE5-2-39
6.13		5.26	2.96	4.91	=	XIE5-2-9
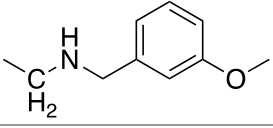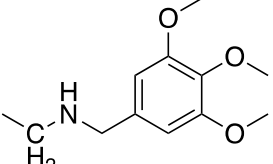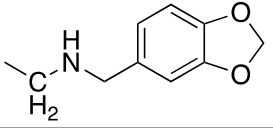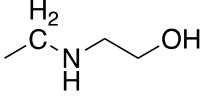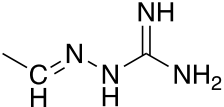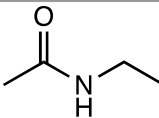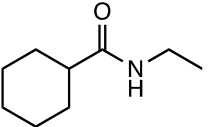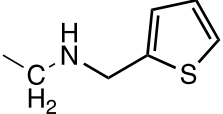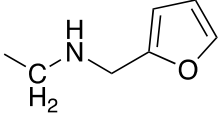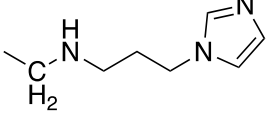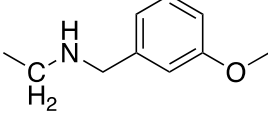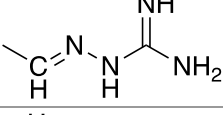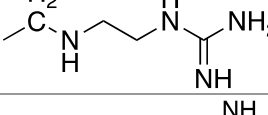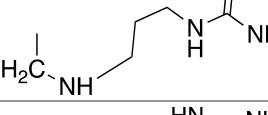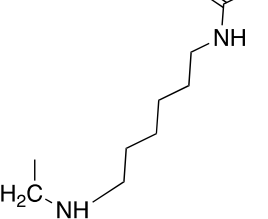
6.14		6.77	4.74	5.18	+	XIE5-2-32
6.15		4.12	4.14	3.99	+	XIE5-2-36
6.16		8.46	1.48	3.90	+	XIE5-2-37
6.25		5.12	3.72	4.35	+	PY1-32
6.28		1.19	0.17/0.47	2.10	+	XIE5-2-68-3

Table 8. The List of 4-Methyl Benzyloxy Analogs with their Anti-Proliferative Activity.
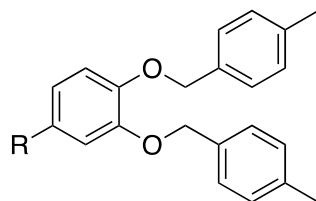
Analogs 7.1 to 7.31

ID	R-groups	MM1R, $IC_{50}(\mu M)$	RPMI8226, $IC_{50}(\mu M)$	U266, $IC_{50}(\mu M)$	Autophagy	Internal ID
7.1	-CHO	> 20	> 20	> 20	=	XIE5-1-85
7.2	-CH$_2$OH	6.20	3.50	7.30		XIE5-1-54A
7.3	-CH$_2$CH$_2$NH$_2$	25	12.42			XIE5-1-69
7.4	-CH$_2$CH$_2$NH-Boc	> 100	> 100	> 100		XIE5-1-65
7.5		2.94	3.97 /> 10	5.56		XIE5-2-76
7.6		>10 (repeat)	>10	>20		XIE5-2-78

114

7.7		6.26	2.40	7.46	+	XIE5-2-59
7.8		10.52	5.83	13.08	+	XIE5-2-59
7.10		4.75	1.72	2.24	=	XIE5-2-64
7.14		4.29	2.66	2.65	+	XIE5-2-61
7.28		5.38	3.15	9.36		XIE5-2-45
7.29		4.43	0.96	9.28		XIE5-1-26BT
7.30		13.10	6.41	10.56	+	XIE5-1-61BT
7.31		13.54	5.56/10.13	13.89	=	XIE5-1-55CT/ XIE5-1-65

Converting amine to amide is another frequently applied chemical modification strategy. The intermediate molecules **4.4, 5.4, 6.4,** and **7.4** having Boc group and compounds **4.6, 5.6, 6.6,** and **7.6** with cyclohexanecarboxamide showed a lack of anti-tumor effect on MM cells ($IC_{50} >$ 100μM). In contrast, compound **4.3** and compounds **4.5, 5.5, 6.5,** and **7.5** with acetamide showed a moderate anti-proliferation effects on MM cells ($2μM < IC_{50} < 5μM$). It suggests that a cyclic alkyl group is less advantageous for the amide group in the R position than a small and short alkyl group.

On the other hand, the substitution position on the benzoyl core ring was considered when we did the chemical modification, as shown in **Table 9**. We found that conversion from 1,3,4-substitution to 1,3,5-substitution (Analogs **8.1, 8.25, 9.1, 9.25, 9.26, to 10.34**) maintained similar anti-MM activities. The results represent that a transposition from 1,3,4-substitution to 1,3,5-substitution on the core phenyl ring of compounds makes no significant differences in the anti-MM activity.
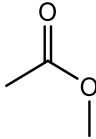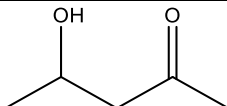
Table 9. The List of 1, 3, 5-Substituted Analogs with their Anti-Proliferative Activity.
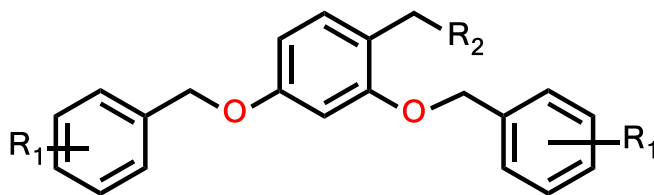
Analogs 8.1 to 8.25, 9.1 to 9.25, and 10.20 to 10.34

ID	R$_1$	R$_2$	IC$_{50}$ (µM)			Autophagy	Internal ID
			MM1R	RPMI8226	U266		
8.1	p-Cl	-CHO	>20	12.19	11.64	=	5-1-83
8.2	p-Cl	-CH$_2$OH	9.686	8.88	9.58		5-2-83
8.25	p-Cl	H$_2$C$\cdot$N(H)$\cdot$OH	2.49/9.98	0.63/0.80	10.0/4.60	+	5-2-90
9.1	p-CH$_3$	-CHO	8.15	12.20	11.74		5-1-82
9.2	p-CH$_3$	-CH$_2$OH	12.47	3.61	5.65		5-2-84
9.25	p-CH$_3$	H$_2$C$\cdot$N(H)$\cdot$OH	4.49/2.66	1.18	4.15		5-2-85
9.26	p-CH$_3$	H$_2$C$\cdot$N(H)$\cdot$NH$_2$	> 10	7.00	7.85	=	5-2-89

116
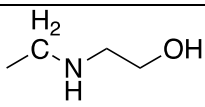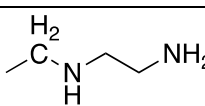
10.33	2,4-di-F		4.25	2.67		XIE5-1-52
10.34	2,4-di-F		3.42	2.15	=	XIE5-1-56

However, deletion of one substitution will lead to the loss of anti-proliferative activity (IC_{50} > 50μM) on MM cells, as shown in **Table 10**. To be specific, balancing the differences with compounds **11.25** and **11.26**.

Table 10. The List of 1,4-Disubstituted Analogs with their Anti-Proliferative Activity.
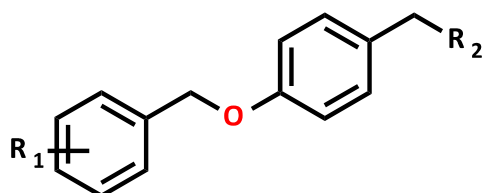
Analogs 11.20 to 11.27

ID	R$_1$	R$_2$	IC$_{50}$(μM)			Autophagy	Internal ID
			MM1.R	RPMI8226	U266		
11.25	2,4-di-F		68	81	> 100		Lp1-52
11.26	2,4-di-F		> 100	> 100	> 100	=	LP1-53

2.3.4. Conclusion

We did not do much SAR analysis based on the IC_{50} values we got from MTT assays. Most of the compounds showed some activity by a moderate IC_{50} value between 2μM to 10μM, which did not indicate a significant difference when accounting for the variance between individual experiments. Therefore, I simplified our result analysis by pointing out some functional groups that are not favorable for anti-proliferative activity on myeloma cells. We also identified some compounds with more than 20-fold higher activity.

To summarize, the compound with aminoguanidine (**6.28**) has a good potency to inhibit MM cell growth in the three MM cell lines. The side chain lengths of compounds with good activities are C4-C5 bond length, indicating that the size within this range will not significantly influence the anti-MM activity. However, too long side chains (**3.31** and **7.31**, > C8) or too short side chains (**3.1**, **4.1**, **5.1**, **6.1**, **7.1**, and **8.1**, < C2) will reduce the anti-MM activity. Compound **6.28** showed the highest anti-MM potency and was selected for our signaling studies, discussed below.

2.3. Compound 6.28 Causes MM Cell Death via Autophagy Mediated Apoptosis.

2.3.1. Compound 6.28 Inhibits the Growth of MM Cells related to the function of p62

After we got some hits that show preliminary potency to kill myeloma cells, it is important to make sure whether the compounds have their effect through the mechanism we proposed. Otherwise, the study will be more phenotype driven not mechanism-driven. The mechanism of how the compounds work is unclear, which is not favorable for potential drug development. We

proposed that the compounds targeted on p62 and have antiproliferative effects on myeloma cell lines. In order to demonstrate this, we answer the following questions.

First, do our compounds bind to p62 protein; second, how our compounds bind to p62 protein and influence its function; third, how this influence related to cell death, which signaling pathways linked our compounds' effects on p62 function and cell death; fourth, as a backup, if our compounds do not cause cell death by p62 related signaling pathways, then what kind of signaling mechanism is working behind their actions.

First, to see whether the antiproliferative effects of our compounds were related to the p62 protein. We used p62 knockout cells to see whether the knockout of p62 will influence the effect of compounds on myeloma cells

Method

As shown in **Figure 28,** according to the preliminary results from the p62 WT and knockout (p62$^{-/-}$) bone marrow stromal cells (BMSCs) transduced with various p62 domain-deletion mutants (**Figure 28A**), the p62-ZZ domain is essential for BMSC-enhanced MM growth (**Figure 28B**) and osteoclast (OCL) formation (**Figure 28C**). The design of the p62 domain-deletion construct is displayed in **Figure 28A**. These constructs and the full-length p62 were transduced into p62 knockout BMSCs. Afterward, the transduced BMSCs and WT BMSCs were co-cultured with MM1.S cells. The number of MM1.S cells was counted after the co-culture and compared in **Figure 28B.** The cell count of MM1.S co-cultured with p62$^{-/-}$ BMSCs dramatically dropped compared with cells co-cultured with WT BMSCs, indicating the key role of p62 in myeloma cell growth. The reduced cell count can be increased by the transduction of p62 constructs in BMSCs.Full-length p62 attained the highest increase rate, while p62 with ZZ domain deletion saw the smallest increase among all constructs, suggesting that the p62-ZZ domain is important for

119

myeloma cell growth. A similar experiment was performed for OCL formation; OCLs were co-cultured with the transduced and WT BMSCs. As shown in **Figure 35C,** the lack of p62 inhibits the OCL formation, which can be recovered by the addition of p62. However, adding the p62 mutant to the ZZ domain deletion results in a similar cell count as the OCL formation without any p62. This result is consistent with our hypothesis that blocking the p62-ZZ domain can reduce OCL formation and inhibit myeloma cell growth.
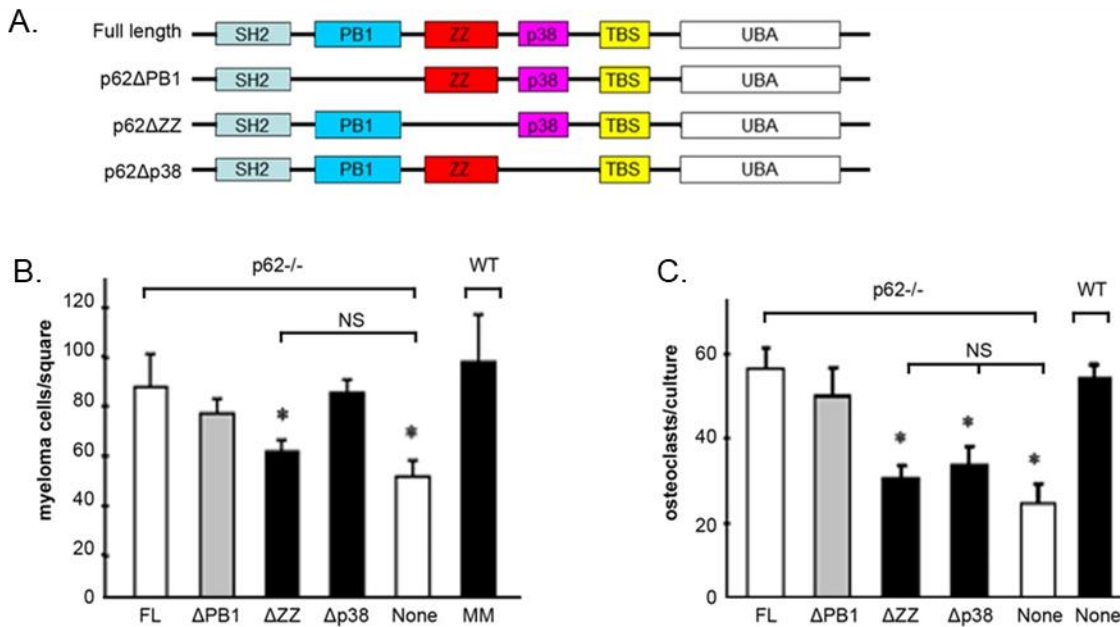
Figure 28. Deletion of P62-ZZ Inhibit Myeloma Cells Growth and Osteoclasts Formation.

(A) The design of domain deletion constructs of p62. (B) p62$^{-/-}$ BMSCs were transduced with individual p62 domain deletion mutant and subsequently co-cultured with GFP-MM1.S cells. After the co-culture, the number of MM1.S cells was counted. Data are shown as the mean $\pm$ SD (n = 5). *p < 0.01 in comparison with full-length p62 transduced BMSCs. (C) Similar to (B) except that the effects of the p62 domain deletion mutants on BMSC support of OCL formation were assessed. The results are representative of at least three independent different experiments.

To make sure our compounds' anti-proliferative effects are related to p62, we measured our compounds' effect on WT cells and p62$^{-/-}$ cells. We counted the number of MM1.S-GFP cells co-cultured with p62$^{-/-}$ bone marrow stromal cells (BMSCs) and WT BMSCs under a fluorescence microscope (FM) after the co-culture. The number of viable MM1.S-GFP cells co-cultured with p62 knockout cells was less than those co-cultured with WT BMSCs. We apply a paired t-test to analyze the difference between the two groups. We found the cell count co-cultured with WT BMSCs and the one with p62 KO BMSCs are significantly different. The effects of compound **6.28** on MM1.S-GFP cell proliferation in BMSCs from p62$^{+/-}$ and p62$^{-/-}$ mice were evaluated, as displayed in **Figure 29**. We found that compound **6.28** inhibited MM1.S-GFP cell growth dose-dependently when co-cultured with BMSC from WT mice. No inhibitory effect of compound **6.28** was observed when progenitors were co-cultured with BMSCs from p62$^{-/-}$ mice, indicating that compound **6.28** acts in a p62-dependent manner. We used multiple t-tests to investigate the difference in cell count caused by different concentrations of compound **6.28** treatment. A significantly different cell number was observed between 1µM and 2.5µM treatment groups on WT cells, indicating the effective concentration of compound **6.28** to inhibit myeloma cell growth. (**Figure 29**)
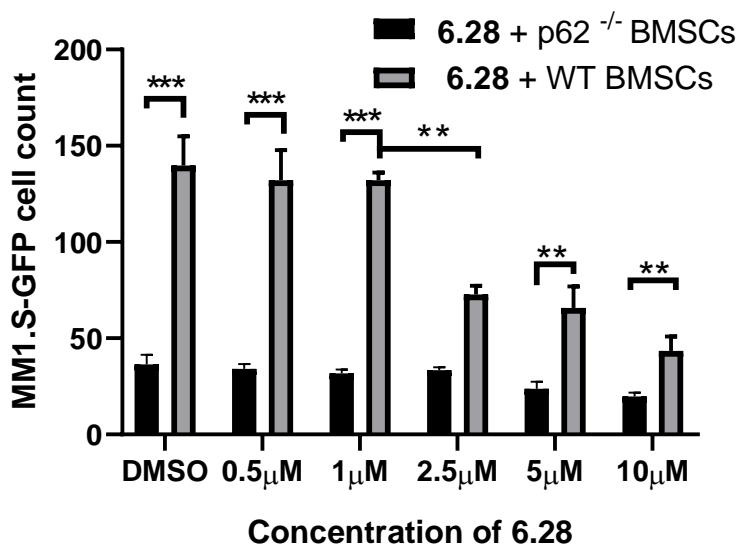
Figure 29. 6.28 Inhibits the Myeloma Cell Growth through P62-ZZ Domain.

The effect of compound **6.28** on p62 knockout cells and WT cells was meausred. MM1.S-GFP cells were co-cultured with BMSC from p62$^{+/-}$ and p62$^{-/-}$ mice, treated with increasing concentrations of compound **6.28** (0, 1, 2.5, 5, 10, 20 µM), and then stimulated with TNFα. After co-culture, the cell number of MM1.S-GFP was counted under FM. Data are shown as mean ± SD (n=3). A paired one-tail t-test was applied to analyze the results from two groups with WT BMSCs and p62 KO BMSCs. Multiple t-tests were used to analyze the cell count between groups that have different concentrations of compound **6.28** treatment. * represents p-value <0.05, ** represents p-value<0.01, *** represents p-value < 0.001

2.3.2. Compound 6.28 Induces Apoptosis Signaling in MM1.S Cells.

We chose compound **6.28**, which has a good anti-tumor activity, to investigate the molecular mechanism behind the anti-cancer effect. Our lead **XRK3F2** induced apoptosis signaling in MM cells that lead to cell death. Compound **6.28** may also induce apoptosis signaling in MM cells that cause myeloma cell death.

MM1.S cells were seeded in six-well plates (8.7×104 cells/well) overnight. Then, we treated MM1.S cells with different concentrations (0µM, 2.5µM, 5µM, 10µM, and 20 µM) for 16h, as well as with a fixed concentration (10µM) for a different duration of time (0h, 2h, 4h, 8h, and 16h). After treatment, cells were harvested, and protein extracts were prepared in radioimmunoprecipitation assay (RIPA) buffer (10 mM Tris base pH 8.8, NaCl 150 mM, EDTA 1 mM, NP-40 1%, deoxycholic acid 1%) supplemented with a mini EDTA-free protease inhibitor cocktail tablet (Roche), Phenylmethanesulfonyl Fluoride (PMSF, 1mM). Protein extracts were sonicated. Proteins extracts (25 µg) were run in 15% SDS-PAGE gels, transferred onto a nitrocellulose membrane. The membranes were blocked for 2 h at 37°C in blocking buffer (5% BSA in TBS-T solution). Then membranes were subsequently probed with anti-caspase 3 (Rabbit, 9962, Cell Signaling Technology) and anti-β-actin antibodies (mouse mAb, A5441, Sigma) overnight at 4 °C. The membrane was then washed and incubated with HRP-conjugated secondary antibody at room temperature for 2 h. Following further washings, each protein's expression was detected using an enhanced chemiluminescence detection kit (ECL, Pierce) and visualized by an Image Lab BIORAD imaging system. Immunoblotting results were quantified using ImageJ. Results are shown as mean ± SEM. Statistical significance was determined using a paired t-test. One-way ANOVA was performed to compare tumor volumes between groups.

Compound **6.28** induces caspase 8 activation dose- (**Figure 30A**) and time-dependently (**Figure 30B**), as represented by the increasing level of caspase 8 cleavages compared to procaspase 8. In addition, in agreement with caspase 8 activation, compound **6.28** enhances caspase 3 activation at a concentration as low as 5µM in the MM1.R cell line in a time and dose-dependent manner, as shown by the increased cleavage of caspase 3 at 17kDa in 5th line film in **Figure 32A**. Our results also showed that compound **6.28** induces a robust cleavage of poly (ADP-

ribose) polymerase (PARP) when starting at a concentration as low as 2.5 µM in MM1.S cells after a 16-hour treatment displayed in 96kDa of the 7th line on the left side film. The cleavage was induced in a dose-dependent (**Figure 30A**) and time-dependent manner (**Figure 30B**). In **Figure 30B**, the treatment period's extension to 16 hours did not significantly differ at PARP, caspase 8, and caspase 3 cleavage compared to the 8 h treatment. Caspase 8 and 3 activations, as well as PARP cleavage, suggest the activation of apoptosis signaling. This signaling pathway is dependent on the activation of procaspase 8, which is partially triggered by the accumulation of autophagosomes.
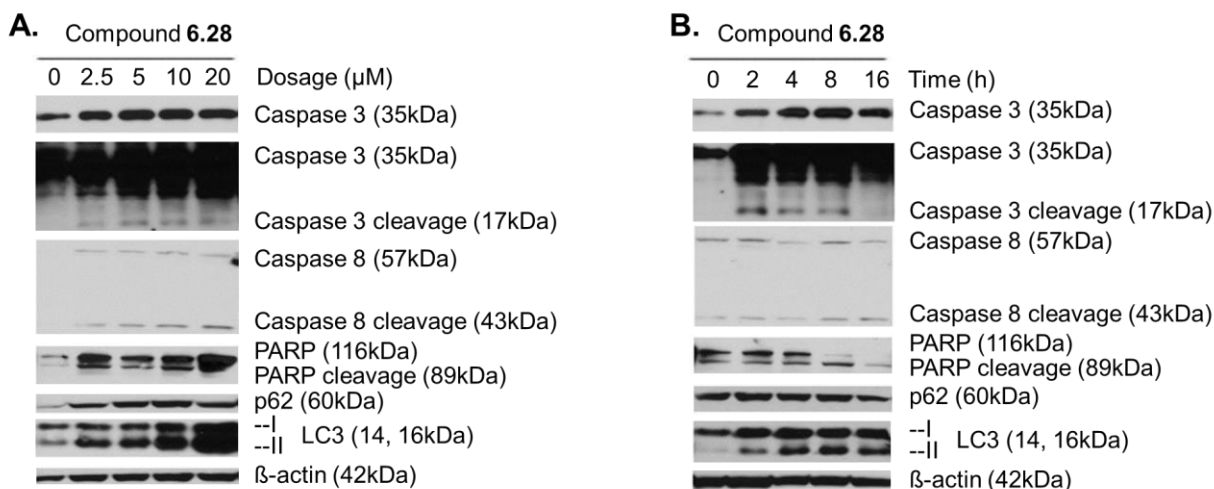
Figure 30. Compound 6.28 Induces Apoptosis Signaling Time- and Dose-Dependently.

MM1.S cells were treated with compound 6.28 at various concentrations (0µM, 2.5µM, 5µM, 10µM, and 20µM) for 16h, incubated with 10µM of compound 6.28 for different time period (0h, 2h, 4h, 8h, and 16h), as well as presented with 100nM rapamycin (positive control known as an autophagy inducer) for 16h. The immunoblotting analysis was performed on the whole-cell lysate to detect p62 level change, LC3B conversion, PARP1 cleavage, caspase 3, and caspase 8 cleavage using anti-p62, anti-LC3B, anti-PARP1, anti-caspase 3, and anti-caspase 8 antibodies. ß-actin was applied as the loading control for this assay.

124
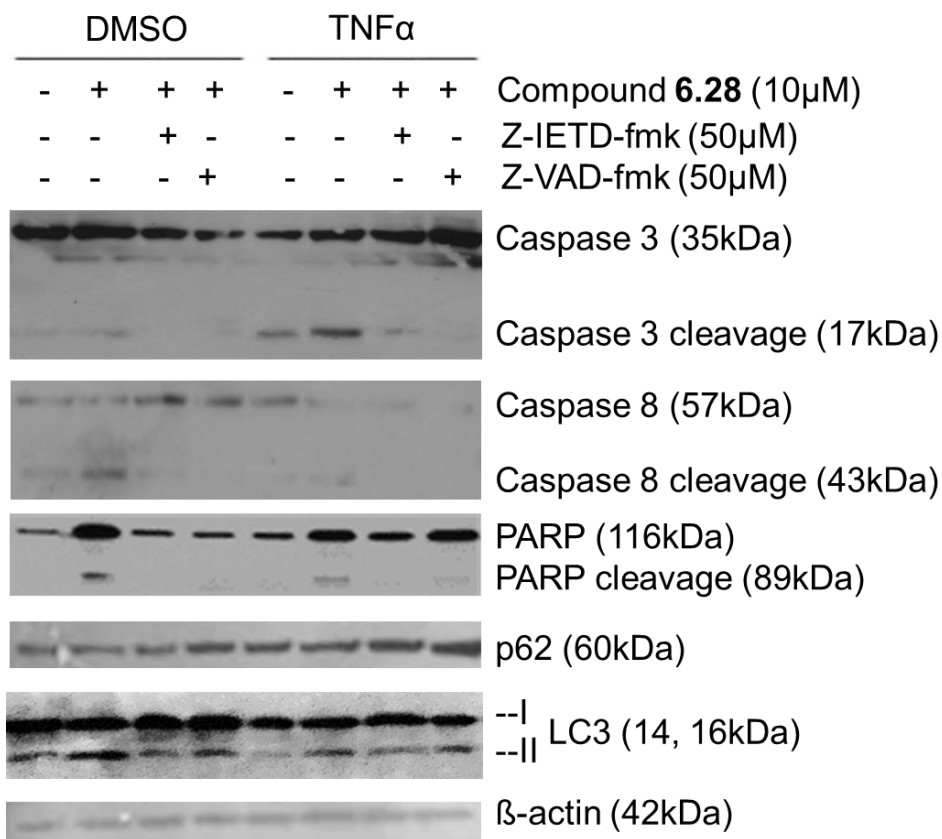
Figure 31. Compound 6.28 Induces Apoptosis that was inhibited by caspase inhibitors.

MM1.S cells were starved overnight with 2% FBS in media and treated with 10μM compound 2s and DMSO (negative control) for 16h. In the meantime, some of the cells were pretreated with 50μM Z-VAD-fmk, a Pan-caspase inhibitor, or 50μM Z-IETD-fmk, a caspase 8 inhibitor, for 3h. Half of the cells are also stimulated with 20 μM TNF-α for 10 min in comparison. Immunoblotting analysis performed on whole-cell lysates detected expression of p62, LC3B conversion, and the cleavage of PARP, caspase 3, and caspase 8. ß-actin was also detected to ensure equal sample protein loading.

To further confirm whether compound **6.28** can induce apoptosis signaling, we pretreated the MM1.S cells with caspase inhibitors, 50 μM Z-VAD-fmk (a PAN caspase inhibitor) and 50 μM Z-IETD-fmk (a caspase 8 inhibitor), then treated the cells with 10 μM of compound **6.28** for 16 h, effective dosage and treatment time demonstrated in the above experiment. The immunoblotting analysis was performed to measure the protein level change of p62, LC3B,

caspase 8, caspase 3, and PARP. As shown in **Figure 31**, we observed that cleavage of caspase 8, PARP and caspase 3 was increased by the treatment of compound **6.28**. Also, the pretreatment and co-treatment of Z-VAD-fmk and Z-IETD-fmk inhibited the induction of cleavage of caspase 8, caspase 3 and PARP caused by compound **6.28**. This result indicates that compound 2s induces apoptosis signaling and that this apoptosis is likely through the activation of caspase 8. Meanwhile, we confirmed that compound **6.28** increased the LC3B-II level, but this induction was not influenced by the pretreatment of caspase inhibitors. We also investigated the effect of TNFα induction on the apoptosis signaling and observed that TNFα increased caspase 3 cleavage. Loss of full-length caspase 8 suggested that its cleavage/activation was also increased.

	2s	2s+Z-VAD-fmk	2s+Z-IETD-fmk
IC50	1.258e-006	~ 3.782e-006	5.217e-006
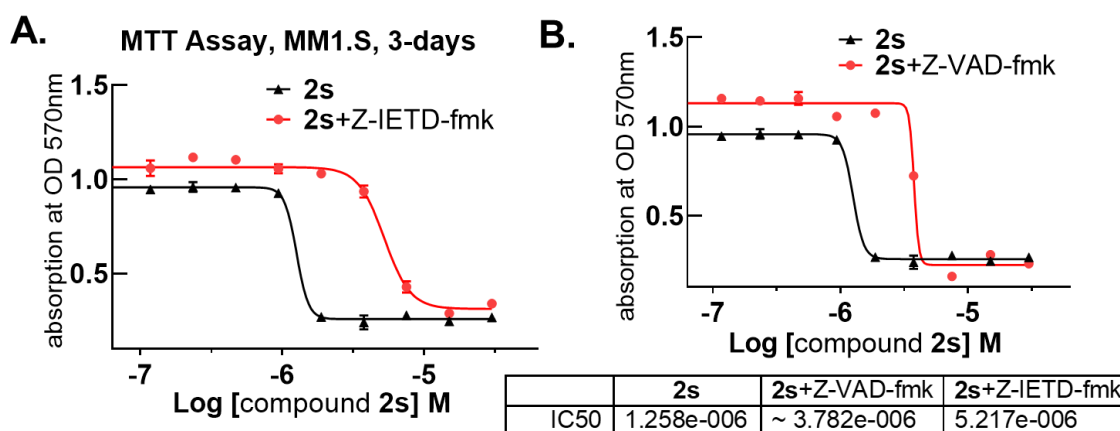
Figure 32. The cytotoxicity caused by compound 6.28 can be inhibited by caspase inhibitors.
MTT assays on MM1.S cells treated with different concentrations of compound **2s** for 72h with or without caspase inhibitors, Z-IETD-fmk and Z-VAD-fmk (both at 50 mM). Each data set was assayed in triplicate. Results are representative of two biological repeats.

As shown in **Figure 32**, we confirmed the role of caspase 8 in mediating the cytotoxic effects of compound **6.28** by measuring the viability of MM1.S cells treated with different concentrations of compound **6.28** in the presence or absence (DMSO vehicle) of caspase inhibitors. While the IC_{50} value for compound **6.28** in inhibiting myeloma cell growth was observed to be

1.258 µM, pretreatment of the cells with 50µM of Z-IETD-fmk (**Figure 34A**) or 50µM Z-VAD-fmk (**Figure 34B**) shifted the curve to the right and yielded IC_{50} values of 5.217µM and 3.782µM, respectively. The distinct inhibition of cytotoxicity by these caspase inhibitors indicates that caspase 8 plays a clear role in mediating compound **6.28-**induced myeloma cell death.

2.3.3. Compound 6.28 Increases Autophagosome Number but not Autophagy Flux.

Our compounds targets p62, and p62 is closely involved in the autophagy flux, which has a dual function on cell death and survival. In most cases, autophagy flux activation will promote cell survival in stressful conditions. Autophagy flux stimulation might not be good for cancer treatment. One lead **XRK3** activated autophagy flux in HeLa cells, which may be adverse for cancer treatment. Therefore, we want to investigate whether compound **6.28** can induce autophagy flux in myeloma cells, which may be disadvantageous to promote myeloma cell survival.

MM1.R cells were cultured in six-well plates, treated with different concentrations (0µM, 2.5µM, 5µM, and 10µM) of compound 6.28 with or without 50nM bafilomycin A1 (lysosomal inhibitor) for 16h. Cells were harvested after treatment and collected by centrifuge at 1,200 rpm for 4 min. Some of the cells were lysed in RIPA lysis buffer for IB, as we described above.

As shown in **Figure 33A**, the LC3B conversion caused by compound **6.28** treatment dose-dependently indicates that compound **6.28** increased autophagosome numbers in the cells. Although the LC3B conversion was induced by **6.28** from LC3B-I to LC3B-II, we still needed to confirm whether compound **6.28** induces autophagy flux by an LC3B turnover assay that assesses the degradation of LC3-II inside the autolysosome. As shown in **Figure 33A**, the combination treatment of compound **6.28** and lysosomal inhibitor (50nM Bafilomycin A1) did not further

increase the LC3B-II level significantly compared to the group without Bafilomycin A1 co-treatment. The quantification of the bands in immunoblotting is shown in **Figure 33B**, representing the same results. The co-treatment with lysosomal inhibitors further increased the LC3B-I level slightly but did not significantly increase the LC3B-II level.

One-way ANOVA was applied to analyze the difference in p62, LC3B-I, LC3B-II, and β-actin levels treated by the different doses of compound **6.28**. The p62, LC3B-I, and LC3B-II are influenced by various concentrations of compound 6.28 treatment significantly. The expression of β-actin is not affected. A paired t-test was used to analyze the expression level difference between the two groups treated with bafilomycin A1 and without bafilomycin A1. We confirmed that the LC3B-II level is not further increased significantly. The LC3B-I was influenced a little by the co-treatment of lysosomal inhibitor bafilomycin A. These results suggested that compound 6.28 did not induce autophagy flux.
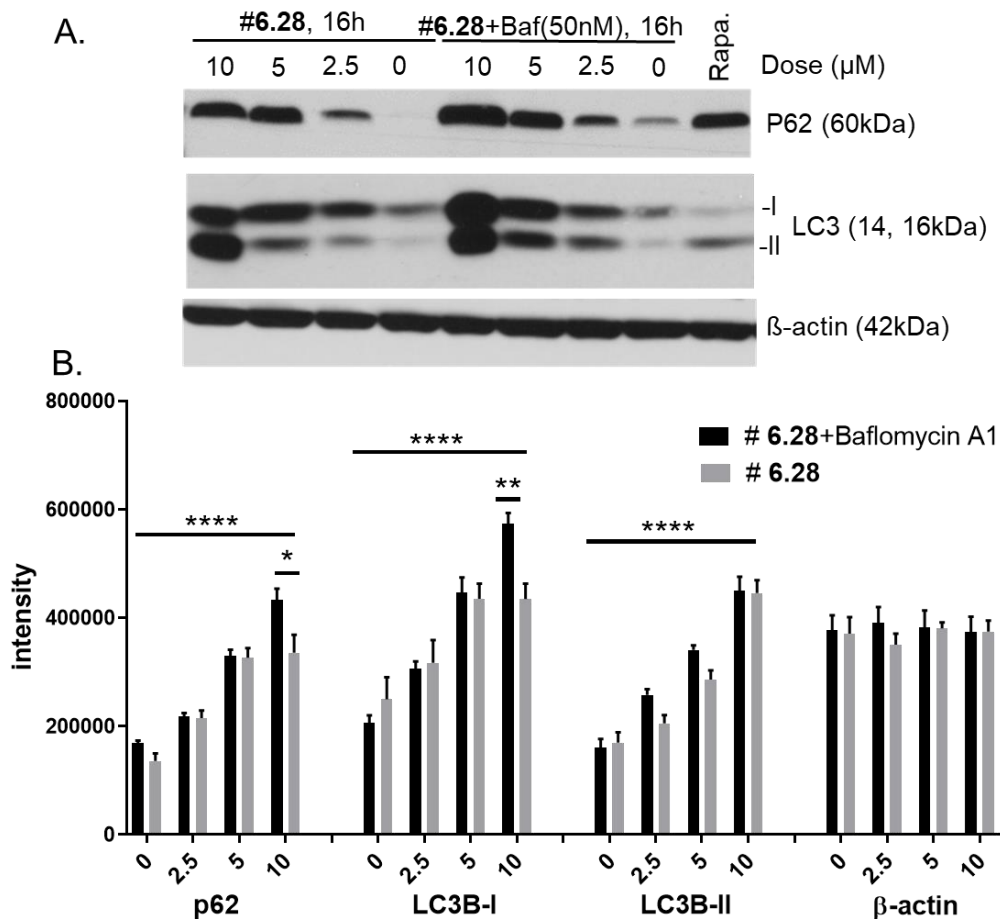
Figure 33. Compound 6.28 Induce a Weak Autophagy Flux Measured by IB.

MM1.S cells were treated with **6.28** at various concentrations (0µM, 2.5µM, 5µM, and 10µM), 50nM Bafilomycin A1 (lysosomal inhibitor) plus the same concentrations (0µM, 2.5µM, 5µM, and 10µM) of **6.28**, and 100nM rapamycin (positive control, known as autophagy inducer) for 16h. The IB was performed on the whole-cell lysate to detect p62 protein level change and LC3B conversion from LC3B-I to LC3B-II using anti-p62 and anti-LC3B monoclonal antibodies. The beta-actin was applied as the loading control for this assay. A one-way ANOVA was applied to analyze the significance of differences among the treatment groups. Multiple t-tests were performed to analyze the difference of individual dose responses between the different doses within groups. A paired t-test was applied to analyze the difference between the groups with bafilomycin A1 and without bafilomycin A1. *, $p < 0.05$; **, $p < 0.01$; ***, $p < 0.001$; ****, $p < 0.0001$.

Some of the cells after the treatment were fixed with 2% paraformaldehyde in PBS (pH=7.4) at room temperature for 15 min to observe under an immunofluorescence microscope. After washing two times with PBS, cells were collected through a centrifuge at 1,200 rpm for 3 min every time. The cells were permeabilized with 0.1% Triton X in PBS solution for 15 min. After washes with PBS three times, centrifuge at 1,300 rpm at 3min, the cells were then incubated with blocking solution (2% BSA in PBS) for 45 min and then incubated with primary antibody (made in PBS with 0.5% BSA) overnight at 4°C after one-time wash. The next day, the cells were washed three times with PBS, centrifuge at 1,300 rpm for 3 min each time to collect cells, and then incubated with secondary antibody goat anti-mouse IgG H&L (Alexa Fluor® 647, red, ab150115) and goat anti-rabbit IgG H&L (Alexa Fluor® 488, green, ab150077) for 1 h in the dark. All the procedures after that were protected from light. The cells were washed two times with PBS, centrifuge at 1,400 rpm for 3 min each time, then DAPI (1µg/ml) stained for 5 min. After three washes with PBS, the pellet of cells was resuspended by the mounting media (0.5% N-propyl gallate and 70% glycerol), then the mounting media with the cells were added to the slides dropwise. Then the coverslips were mounted on slides with mounting media and were sealed with nail polish to prevent drying and movement under a microscope. Images were taken using a fluorescence microscope.

Similar results can be observed in **Figure 34** for the immunostaining results. Compared to the DMSO treatment, both bafilomycin A1 and compound **6.28** increased the p62 puncta (green) and LC3B signal (red), and the p62-containing puncta were partially colocalized with LC3-containing autophagosomes in the cytoplasm of MM1.S cells, with no overlapping with the cell nucleus, which was stained by DAPI (blue). The combination treatment of 50 nM bafilomycin A1 and 10µM compound **6.28** did not further increase the LC3B-II levels. In conclusion, compound

6.28 increased the autophagosome level but did not significantly induce autophagy flux, as shown in **Figure 34**.
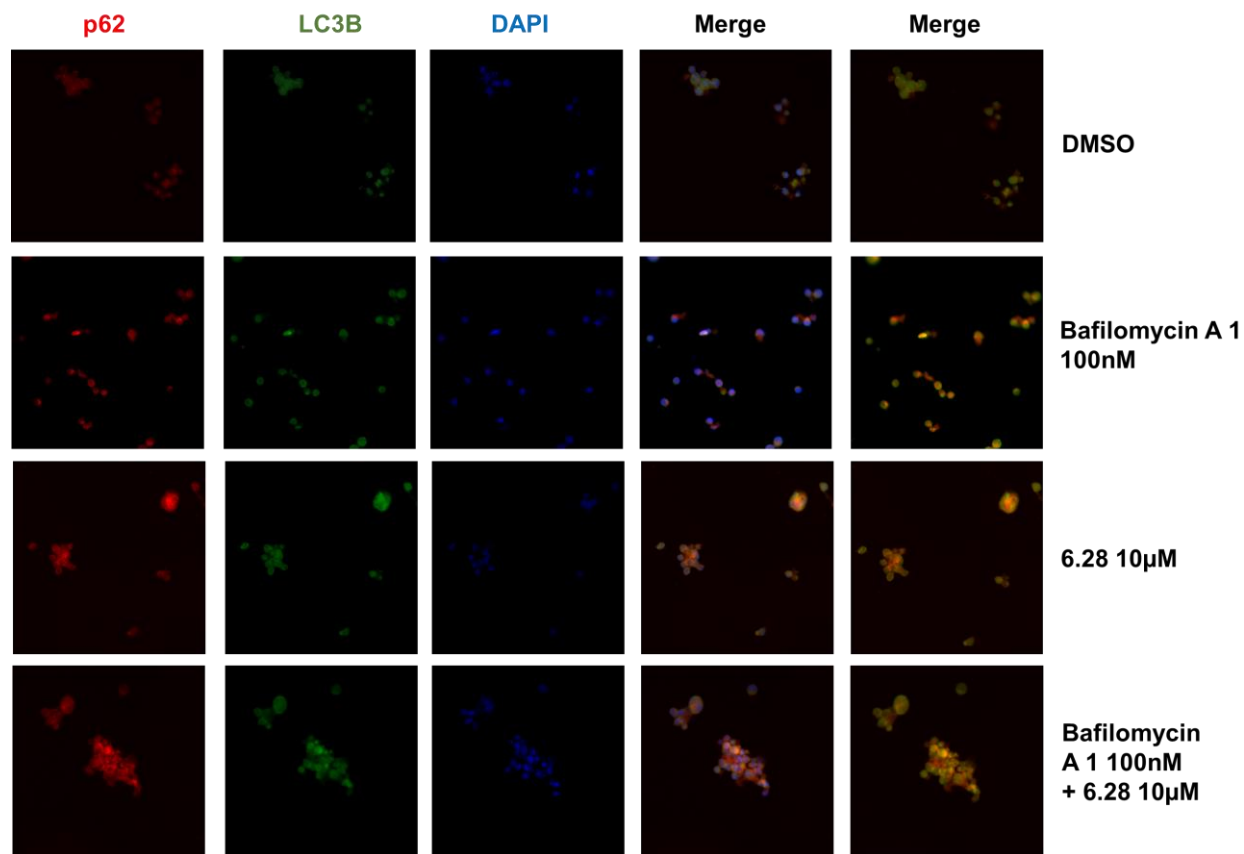
Figure 34. Compound 6.28 Induce a Weak Autophagy Flux Measured by FM.

Immunofluorescence microscopy analysis was done for p62 and LC3B colocalization. MM1.S cells were treated with DMSO, 50nM bafilomycin A1, 10µM **6.28**, 10µM **6.28** plus 50nM bafilomycin A1, as well as 10µM **6.28** plus 50nM bafilomycin A1 for 16h. The cells were then fixed with 2% paraformaldehyde in phosphate-buffered saline (PBS) and permeabilized with 0.1% Triton X in a PBS solution. After the next step of blocking, the cells were subjected to incubation with a primary anti-p62 mouse monoclonal antibody or primary anti-LC3B rabbit monoclonal antibody at 4 °C overnight. MM1.S cells were subsequently incubated with fluorescence-labeled secondary antibody goat anti-mouse IgG H&L (Alexa Fluor® 647, red, ab150115) and goat anti-rabbit IgG H&L (Alexa Fluor® 488, green, ab150077) from Abcam in the dark for 1 h. Following that, the cells were stained by DAPI (1µg/ml) for 5 min. The pellets of the cells were resuspended in mounting media and added onto slides. The slides were covered by a coverslip and sealed with

nail polishing oil to allow confocal immunofluorescence microscopy to determine the colocalization of p62-containing puncta with LC3-containing autophagosomes. This figure shows each color stain in individual plots and also merges DAPI stain (blue), anti-LC3B staining (green), anti-p62 fluorescence stain (red) together in one plot. Images were obtained in the phase of 20X magnification using the microscope.

To investigate our compounds' effect on both autophagy flux and apoptosis signaling as well as their potential overlap, we did immunofluorescence stain on p62 and LC3B, two key biomarkers in autophagy, in MM1.S cells. The cells were treated with compound 6.28 and caspase inhibitors Z-VAD-fmk and Z-IETD-fmk. The results were showed in **Figure 35** that compound **6.28** increased LC3B signaling by itself, but the level of LC3B was not changed by the addition of caspase inhibitors, indicating no significant change in autophagy flux was due to the blocking the apoptosis signaling.
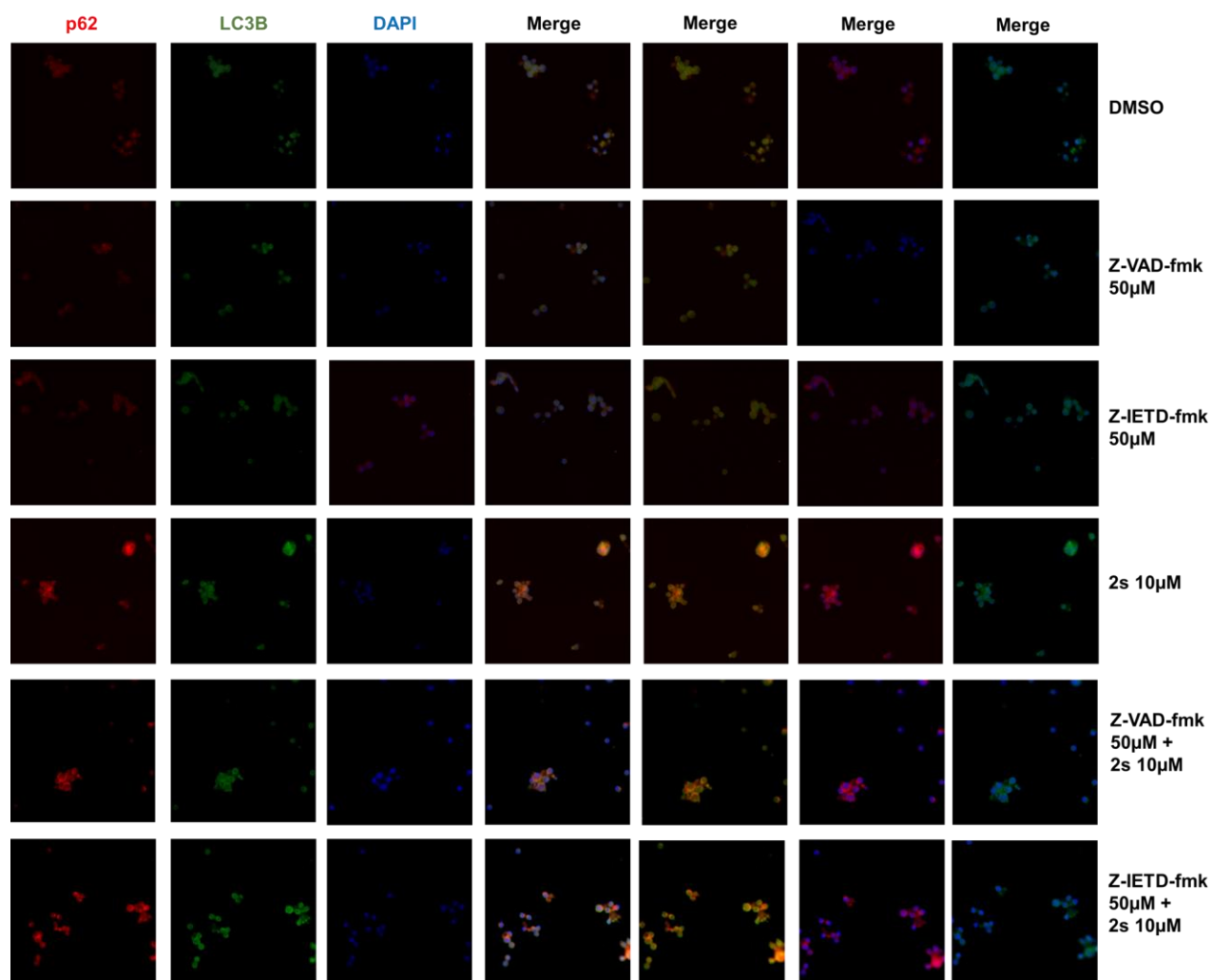
Figure 35. The effects of caspases inhibitors on autophagy signalings by FM.

Immunofluorescence microscopy analysis of p62 and LC3B colocalization. MM1.S cells were treated with DMSO, 50μM Z-VAD-fmk, 50μM Z-IETD-fmk, 10μM **6.28**, 10μM **6.28** plus 50μM Z-VAD-fmk, as well as 10μM **6.28** plus 50μM Z-IETD-fmk for 16h. The cells were then fixed with 2% paraformaldehyde in phosphate-buffered saline (PBS) and permeabilized with 0.1% Triton X in a PBS solution. After the next step of blocking, the cells were subjected to incubation with a primary anti-p62 mouse monoclonal antibody or primary anti-LC3B rabbit monoclonal antibody at 4°C overnight. MM1.S cells were subsequently incubated with fluorescence-labeled secondary antibody goat anti-mouse IgG H&L (Alexa Fluor® 647, red, ab150115) and goat anti-rabbit IgG H&L (Alexa Fluor® 488, green, ab150077) from Abcam in the dark for 1h. Following that, the cells were stained by DAPI (1μg/ml) for 5 min. The pellets of the cells were resuspended in mounting media and added onto slides. The slides were covered by a coverslip and sealed with

nail polishing oil to allow confocal immunofluorescence microscopy to determine the colocalization of p62-containing puncta with LC3-containing autophagosomes. This figure shows each color stain in individual plots and also merges DAPI stain (blue), anti-LC3B staining (green), anti-p62 fluorescence stain (red) together in one plot. Images were obtained in the phase of 20X magnification using the microscope.

2.3.4. The Signaling of Compound 6.28 to Inhibit Myeloma Cell Growth.

Macro autophagy is commonly known as a double-edged sword in cancer therapy (88). It suppresses cancer initiation by inhibiting chronic inflammation, oxidative stress, and genome instability (76). Besides, autophagy promotes cancer cell survival by maintaining cellular and organelle homeostasis by either clearing unwanted tissue debris and foreign antigens or by providing nutrients and energy essential for survival. Thus, it is challenging to clarify the role of autophagy in cancer development for potential therapeutic strategies (87).

In this study, we confirmed that compound **6.28** increases autophagosome number but has no significant inductive effect on autophagy flux. In this case, there are two possibilities. The first is that compound **6.28** induces autophagosome formation at the early stage of autophagy, but the impact on promoting the autophagic process that degrades autolysosome was impaired by a compromising mechanism that keeps autophagy at the normal level to maintain cellular homeostasis. Another assumption is that compound **6.28** could be a late-stage autophagy inhibitor, which increases the LC3B-II levels by blocking the degradation of autolysosome and causing the accumulation of LC3B and p62. Co-treatment with lysosomal inhibitors may not lead to a further increase of LC3B-II level in this case.
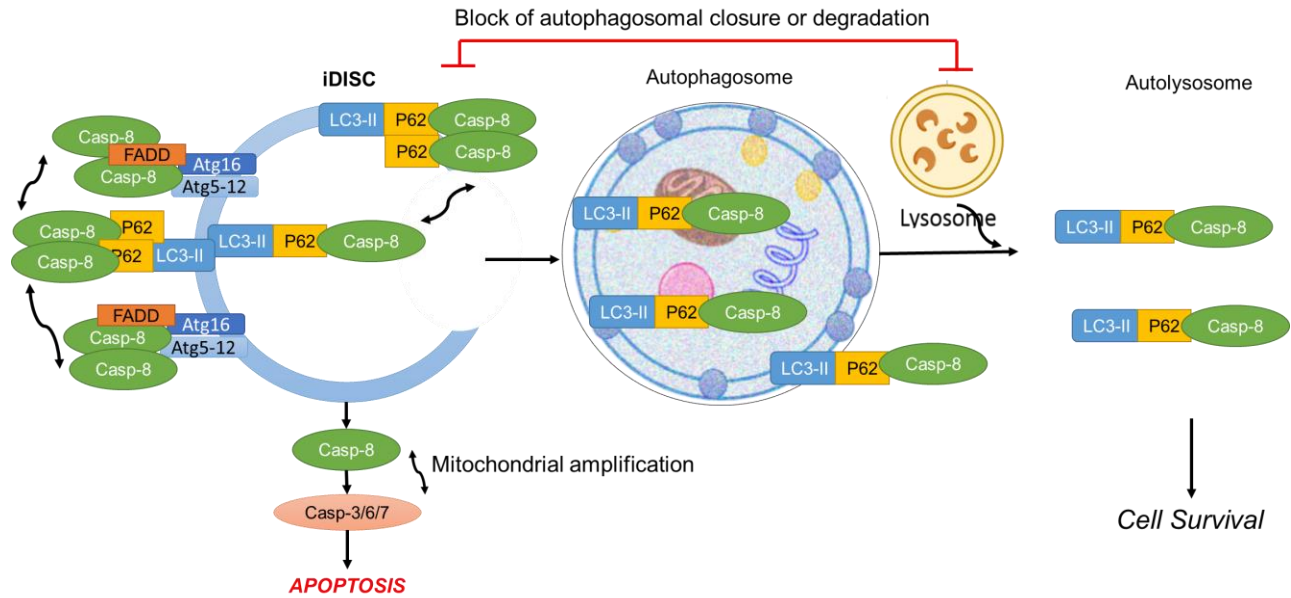
Figure 36. Induction of DISC-Mediated Autophagy-dependent Apoptosis.

As shown in **Figure 36**, autophagy and apoptosis are highly interconnected and shared some crucial regulators. The blockage of autophagosome formation and cargo recruiting might trigger the activation of caspase 8-dependent apoptosis cell death. Many efforts have been made to determine the mechanism behind the switch of autophagy from "pre-survival" to "pre-death" through the stabilization of the death-inducing signaling complex (DISC)(146)). Autophagy functions as a clearing factory for removing the excess procaspase-8 and limits the activation of caspase-8 and its downstream apoptosis pathways within an acceptable normal range. In that process, p62 binds to poly-ubiquitinated procaspase-8 and cargos procaspase-8 onto the autophagosome membrane by interaction with LC3B located on the membrane. Under normal conditions, the sealing of the autophagosome will release the p62-ubiquitinated procaspase 8-LC3B complex, one of iDISC. Autophagosome will then fuse with the lysosome to degrade the iDISC complex and prevent activation of procaspase 8. When autophagy flux was blocked by our compounds, the autolysosome degradation was impaired; ubiquitinated procaspase 8 and LC3B

accumulated on the autophagosome membrane, triggering caspase 8 oligomerization and self-activation to initiate apoptosis signaling. (103, 147)

Summary and Conclusions--Mechanisms by which Compound 6.28 Causes MM Cell Death

In sum, our compound **6.28** induces apoptosis signaling, which is commonly known as a mechanism leading to cell death. In addition, **6.28** also increases the autophagosome number but did not significantly affect autophagy flux. Collectively, there are two explanations for this result. One is that compound **6.28** increases the autophagosome formation in the cells, which might promote the localization of procaspase-8 on the autophagosome membrane. However, the treatment of compound **6.28** did not induce the autophagy flux to the degradation of autolysosome. Therefore, the excess autophagosome and the procaspase-8 might accumulate, triggering procaspase 8 self-aggregation and activation that initiate the downstream apoptosis signaling, leading to MM cell death. Another possibility is that compound **6.28** itself blocks the autophagy flux in the late stage, causing the accumulation of autophagosome and proteins inside it. The accumulation of procaspase-8 might self-activate to trigger the apoptosis signaling, resulting in myeloma cell death. The above assumption was made based on currently available data and literature reports. More evidence will be needed to prove that our compounds act through that signaling pathways to result in myeloma cell death.

2.4 Evaluation of Interaction between Compounds and p62

We designed and synthesized compounds that target p62 protein to have its functions. Thus, we need to confirm our compounds have interactions with p62 protein, and the interactions are correlated with the functions of compounds to treat multiple myeloma. We need to have some assays to confirm our compounds bind to p62 and how it links to the downstream signaling pathways. In this section, we specifically answered whether our compounds bind to p62 protein and how it relates to the autophagy flux.

2.4.1. Expression, Purification, and Refolding of p62 from *E.Coli*

Rationale: It is necessary for us to demonstrate that our compound aimed at targeting p62 has an interaction with p62 protein. And it regulated the downstream signaling pathways, which are related to p62 protein function. Here, to achieve this, first, we need to get the purified p62 protein for assay development and test. Therefore, we expressed, extracted, and purified p62 protein from E.coli to supply assay development and test p62's interaction with compounds.

Aim: Get stable large scale purified p62 protein for assay development and test

Methods for p62 protein expression: Sequestosome-1/p62(R21A) was expressed by *E. coli* BL21 (DE3) c+RIPL as inclusion bodies under numerous growth conditions tested, which varied the growth temperature and IPTG concentration. The procedure of large-scale p62 protein production from *E. Coli.* is listed in **Figure 37.** Following the procedure reported in the methods, purified refolded preparations of the p62 variant indicated a final yield of 2.5 ± 0.4 mg of p62 per liter culture (n = 4).
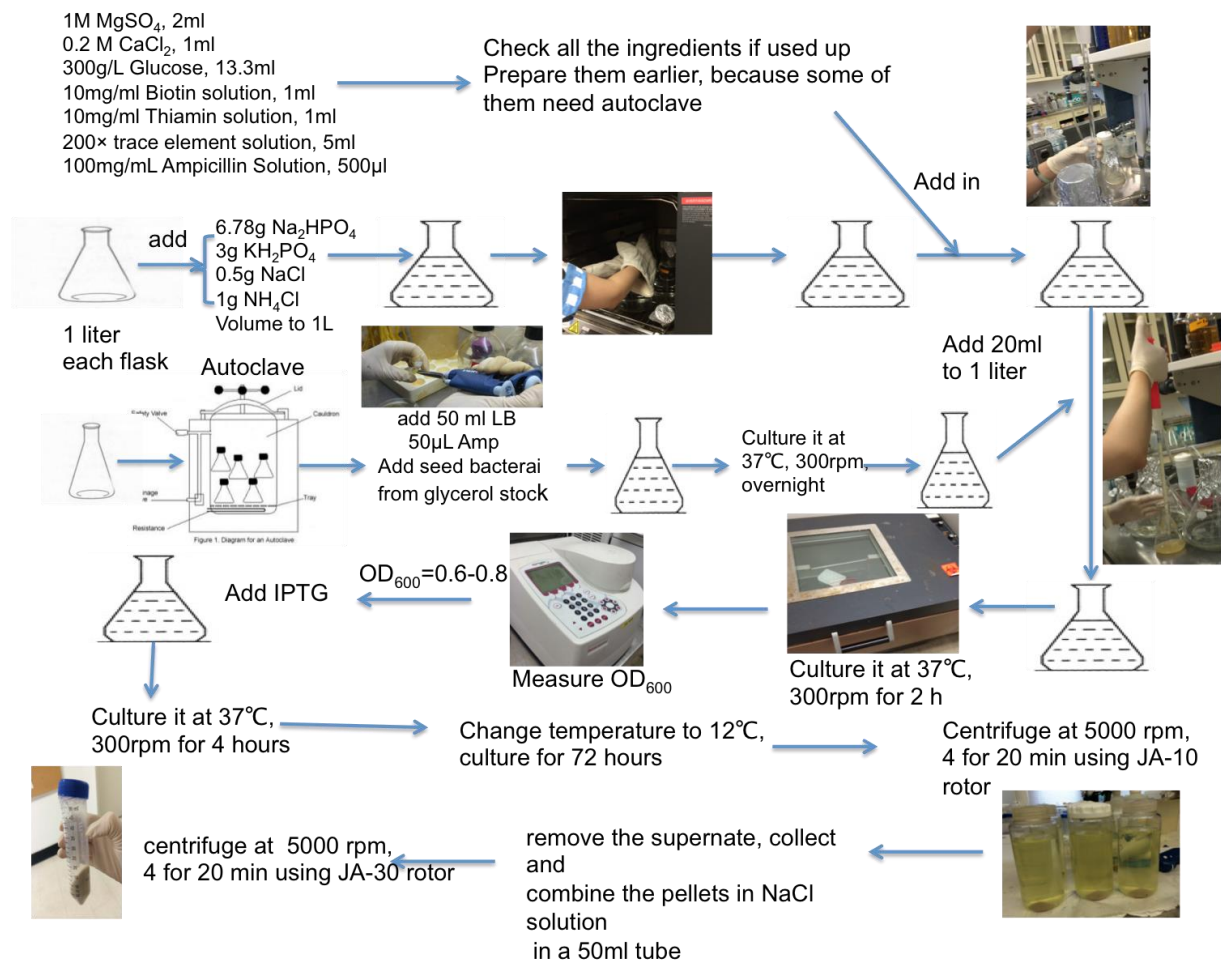
Figure 37. Large Scale Culture of p62 Protein Procedure

Methods for purification steps

Frozen bacterial pellets were allowed to thaw on ice, then resuspended in Buffer A (50 mM Tris-HCl, 0.15 M NaCl, 2 mM EDTA, 0.1% Triton X-100, pH 7.5) and sonicated for 8 on/off cycles of 30 s (output = 10 RMS watts) using a Fisher model 100 sonicator (Thermo Fisher Scientific, Waltham, MA USA). Next, PMSF (1 mM) was added to the complex mixture, which was then incubated on ice for 10 min before centrifugation (5000 rpm, 20 min, 4°C) and decanting of the supernatant. To enrich the inclusion bodies, the debris pellet was consecutively washed with

Buffers B1-B3, containing Tris-HCl (20 mM), NaCl (0.15 M) supplemented with either 0.5% Triton X-100 (B1), 2 M NaCl (B2), or 2 M Urea (B3) respectively. Pelleted IBs were solubilized in 80 ml denaturing buffer (8 M urea, 50 mM Tris-HCl, 0.3 M NaCl, 20 mM imidazole, 10 mM o-mercaptoethanol, 1 mM PMSF, pH 8.0) overnight at room temperature with gentle shaking. Membranes and debris were removed by centrifugation (20,000 rpm, 30 min, 4°C), then the supernatant was filtered by vacuum with a 0.22 µm membrane (Sartorius AG, Goettingen, Germany) and diluted with 1 volume of 0.22 µm-filtered IMAC denaturing (D) buffer (6 M urea, 50 mM Tris-HCl, 0.1 M Na_2HPO_4, 0.5 M NaCl, 20 mM imidazole, 1 mM λ-ME, pH 8.0). The material was loaded at 1 mL/min into a 5-mL IMAC HisTrap FF column, pre-equilibrated with IMAC D buffer, using an ÄKTA purifier instrument (GE Healthcare, Piscataway, NJ USA). After re-equilibration in IMAC D buffer, bound proteins were eluted using IMAC D buffer with 0.3 M imidazole. Fractions were collected and pooled, then concentrated to 2 mg/mL when appropriate using an Amicon Ultrafiltration spin cartridge (30 kDa MWCO; Millipore, Billerica, MA USA) following the manufacturer's instructions.
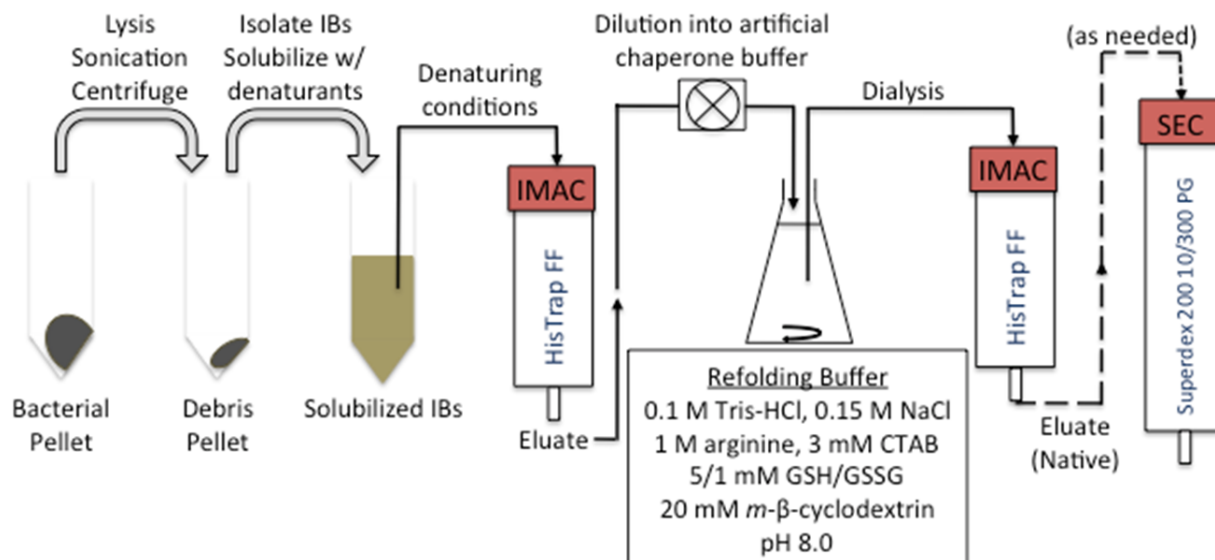
Figure 38. Experimental Procedure for Expression and Purification of P62 From *E.Coli.*

Purified denatured protein solution was diluted into refolding buffer (0.1 M Tris-HCl, 0.1 M NaCl, 1 M arginine, 5 mM GSH, 1 mM GSSG, 20 mM m-o-cyclodextrin, 3 mM CTAB, pH 8.0) in 3 pulses, with 1 h between pulses at RT. The solution was gently mixed by a magnetic stir bar (~200 RPM) after each pulse for 10 min and then allowed to incubate at RT for 48 hr. The refolding solution was dialyzed three times (twice for 4 h, then overnight at room temperature) against 1 L of IMAC native (N) binding buffer (50 mM sodium phosphate, 0.5 M NaCl, 1 mM GSH, 0.2 mM GSSG, pH 8.0) using a 6-8 kDa membrane (Fisher). The dialysate was filtered using a 0.22 µm vacuum filter prior to loading (2 mL/min) into a HisTrap FF column that was pre-equilibrated with IMAC N buffer. Recaptured protein was eluted with IMAC N buffer supplemented with 0.3 M imidazole and 10% (v/v) glycerol, then concentrated as before to the desired concentration. Protein was further purified by size exclusion using a Superdex 200 10/300 column (GE Healthcare) with IMAC buffer plus 10% (v/v) glycerol at a flow rate of 0.4 mL/min. Purified protein was dialyzed against storage buffer (50 mM sodium phosphate, 0.15 M NaCl, 1.0 mM GSH, 0.2 mM GSSG, 1 mM PMSF, 0.1 mM $ZnCl_2$, 0.02% NaN_3, 50% v/v glycerol, pH 7.5) overnight at RT using 3-mL slide-a-lyzer cassettes (Thermo Fisher). Purification steps are

summarized in the illustrative scheme shown in **Figure 38**. Immobilized metal affinity chromatography (IMAC) columns that can trap His-tagged proteins were used for protein purification. The running curves for IMAC are shown in **Figure 39**
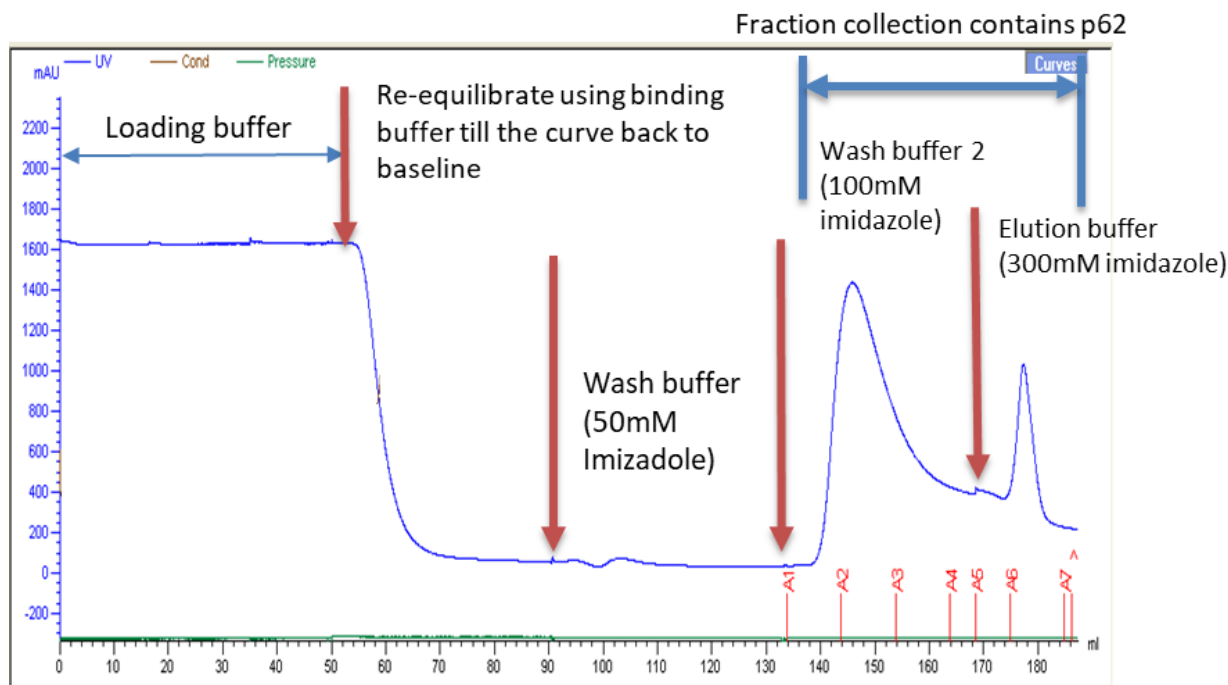
Figure 39. Immobilized Metal Affinity Chromatography Running Curves for Purification

Methods for characterization of purified p62 protein. Protein fractions were assayed for total protein using the Bio-Rad colorimetric protein assay (Bio-Rad, Hercules, CA USA) with standards prepared from bovine serum albumin solution (Thermo Fisher). Gel samples were prepared with 3x sample loading buffer and loaded into 12% polyacrylamide SDS-PAGE gels, then run at constant 120 V for about 1.5 hr using a Bio-Rad mini transblot cell apparatus. Gels were stained with Coomassie brilliant blue and imaged using a Bio-Rad Gel Doc E-Z imager. Western blots were prepared by overnight transfer at constant 0.2 amps onto a Hybond PVDF membrane (GE Healthcare). Blots were blocked with TBST buffer (20 mM Tris-HCl, 0.5 M NaCl, 0.05% tween 20) containing 5% non-fat dry milk for 1 hr at RT. After washes in TBST buffer, the

membrane was incubated with anti-p62 antibody (#P0067; Sigma-Aldrich, St. Louis, MO USA) followed by detection using HRP-linked secondary antibody and ECL developer solution (Thermo Fisher) following manufacturer's protocol.
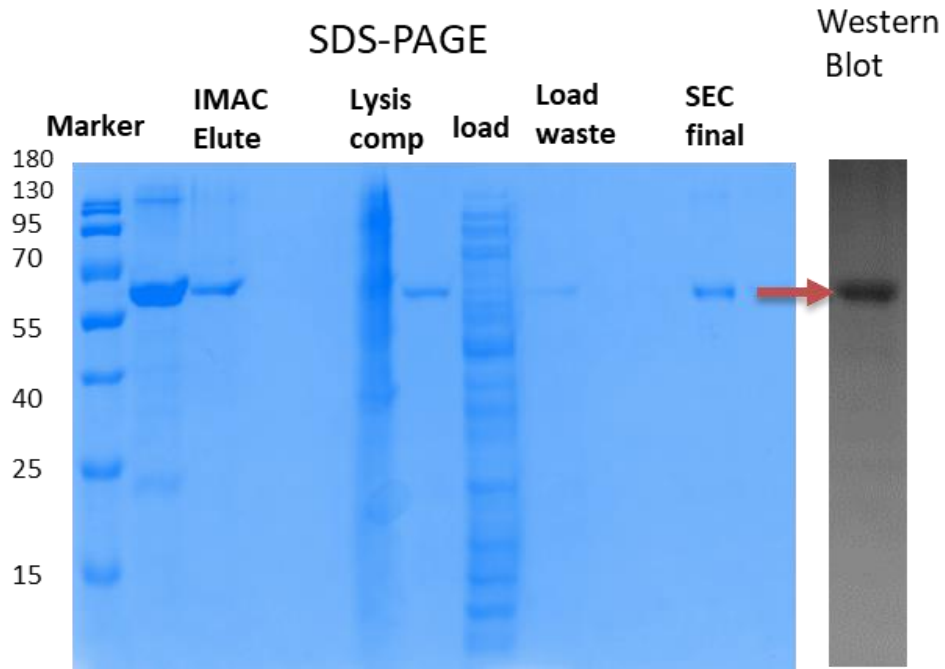
Figure 40. SDS-PAGE and IB Characterization of p62.

Results: We got large-scale purified p62 protein for assay development and test. The characterization of the corresponding p62 fraction and whole cell lysate before purification was measured by SDS-PAGE in **Figure 40**. We can find a clear, pure p62 band after both IMAC and size exclusion column purification, indicating a more than 95% purity. The identity of the resolved band as p62 is further supported by IB, in which the band is recognized by both anti-p62 antibodies (**Figure 40**).

In this section, we confirmed that we got purified p62 protein for assay development and test in the next section. We provided purified p62 for the interaction measurement study in the next section.

2.4.2. Pull-Down Assays.

To confirm whether our compounds can bind to p62 protein, we applied pull-down assays which used immobilized biotin-labeled compounds to pull down the proteins that have interactions with them. Two questions are raised for this section: 1) whether the compounds bind to p62; 2) how the compound has an effect on the signaling pathways by interacting with p62. What links the autophagy signaling and p62 function.

For example, to validate whether **Xie106** is a ligand specific to the ZZ domain, we performed *in vitro* pulldown assays in which biotinylated-**Xie106** immobilized on the streptavidin beads were mixed with cell extracts transiently expressing wild-type (WT) and mutant p62 constructs.

Plasmids expressing WT and mutant p62 constructs were transiently transfected into cells using Lipofectamine 2000. After incubation for 24 h, trypsinized cells were collected in a growth medium and centrifuged. The cell pellets were re-suspended in a hypotonic buffer (10 mM HCl, 1.5 mM $MgCl_2$, and 10 mM HEPES, pH 7.9) and incubated on ice for 30 min. The cell suspensions were subjected to five freeze-thaw cycles, followed by centrifugation at 16,000 x g at 4ºC for 20 min.

In the Xie106-biotin pulldown assay, Xie106-biotin was incubated with streptavidin agarose resin (0.5 mg peptide per ml settled resin) in 5 packed resin volumes of PBS overnight at 4ºC. The beads were centrifuged at 1,000 x g for 3 min and washed three times with an equal

volume of PBS. Soluble HEK293 extracts containing 50 µg total protein were diluted in 700 µl

binding buffer (0.05% Tween 20, 10% glycerol, 0.2 M KCl, and 20 mM HEPES, pH 7.9) and

mixed with Xie106-biotin beads (50 µl packed volume). The mixtures were incubated at 4ºC for

4 h with gentle rotation. The beads were pelleted by centrifugation at 3,000 x g for 60 sec, washed

five times with 1 ml of binding buffer at 4ºC for 20 min, resuspended in 25 µl SDS sample buffer,

and heated at 100 ºC for 15 min. SDS-PAGE and immunoblotting performed analysis.

Immunoblotting analyses of precipitated p62 proteins showed that **Xie106** was bound to full-

length p62 (**Figure 43A**). However, the deletion of the ZZ domain abolished the binding of **Xie106**

to p62 (**Figure 43A**). Next, we generated mutants for several of the residues predicted to be critical

for **Xie106** binding. We found that replacing C142/C145 or H160/H163 with alanine (Ala)

residues disrupted the binding of full-length p62 to **Xie106** (**Figure 43B**).
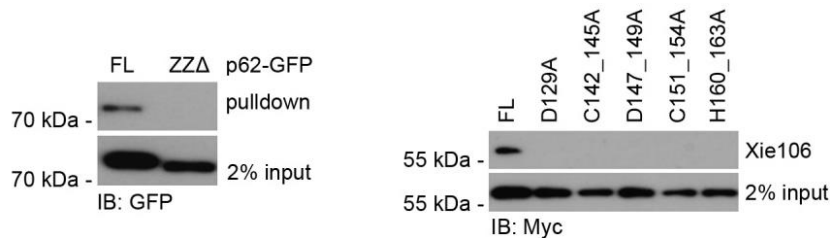
Figure 41. Pull-Down Assay of Compounds with Wide-Type and Mutated P62 Proteins.

(left) An *in vitro* pulldown assay using biotinylated Xie106 and GFP-tagged p62 (full length and

ZZ domain deletion mutant) was expressed in HEK293 cells. Total proteins (50 µg) were used in

the pulldown assay, and p62 was detected by immunoblotting with an anti-GFP antibody. (right)

An in vitro pulldown assay using biotinylated Xie106 and Myc/His-tagged p62 ZZ domain mutants

expressed in HEK293 cells. Total protein (50 µg) was used in the pulldown assay, and p62 was

detected by immunoblotting with anti-Myc antibody.

A similar inactivation was observed with the Ala mutation of three aspartic acids, Asp129 and

D147/D149 (**Figure 41B**), which are also thought to interact with an N-degron-based on the crystal

structure of the E3 ubiquitin-protein ligase UBR boxes of human UBR1 and UBR2 (148).

Moreover, **Xie106** failed to bind to p62 when Ala residues were introduced to C151/C154, which are shared by the ZZ domain of p62 and the UBR box of human UBR1 (**Figure 41B**). These results indicate that **Xie106** binds to the ZZ domain of p62 through the N-end rule interaction, which is in agreement with our previous report that p62 acts as an N-recognin that binds types 1 and 2 N-degrons through the ZZ domain and that the mutated residues are thought to be critical for N-degron binding [33].
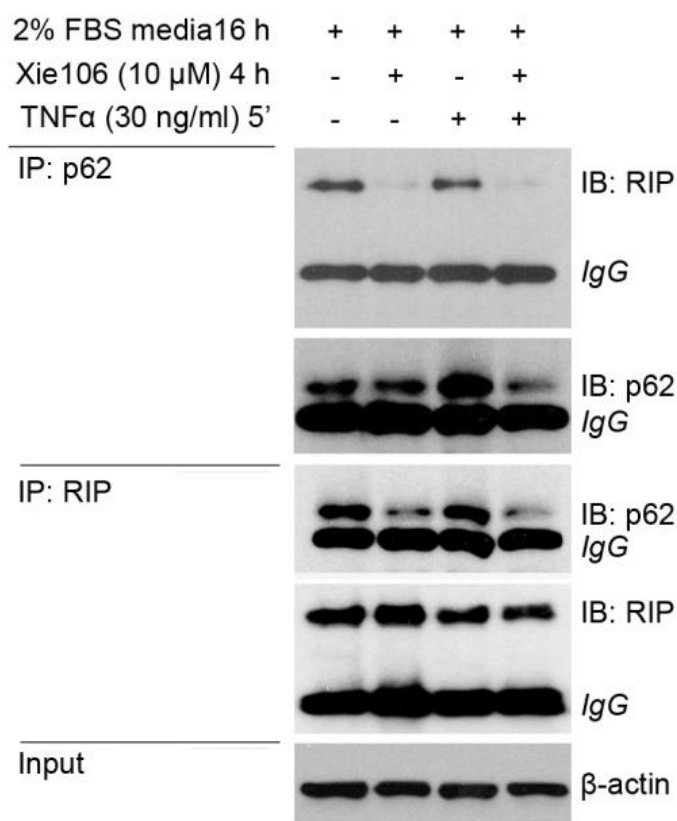
Figure 42. Co-immunoprecipitation studies for p62 and RIP1 in MM1.S Cells.

MM1. S cells were treated with 10μM **XIE106**, a compound in our series, for 4 hours. After that, MM1.S cells are induced by treatment of TNFα at 30ng/ml for 5min.

RIP1 is known to bind to p62 through its ZZ domain in response to TNFα receptor activation. In MM1.S cells, upstream signaling from oncogenic K-RAS (expressed in these cells) results in constitutive binding of RIP1 to p62 (**Figure 42**, *lane 1*). To determine whether p62ZZ ligands are

capable of disrupting the p62-RIP1 interaction, we performed co-immunoprecipitation studies with lysates prepared from MM1.S cells treated with or without 10 µM of **Xie106**. As shown in **Figure 42**, cells pre-treated with **Xie106** demonstrated a significantly reduced level of p62-RIP1 association but had little effect on p62 or RIP1 expression. These results confirm that p62ZZ ligands bind to the ZZ domain and disrupt the p62-RIP1 association. This demonstrates our compounds bind to p62 protein.

2.4.3. p62 Aggregation Evaluation

The second question is what links the autophagy signaling and p62 function. To answer this question, we measured p62 oligomerization, one of the driver steps of autophagy flux and autophagosome formation. In macroautophagy, p62 associates with its cargos (such as misfolded proteins and their aggregates) and subsequently undergoes self-polymerization, facilitating the delivery of p62-cargo complexes to autophagosomes for lysosomal degradation (149). We have previously shown that the N-terminal Arg of arginylated BiP/GRP78, an ER-residing molecular chaperone, binds to the p62-ZZ domain and induces its self-polymerization (18). To determine whether **Xie106** activates p62 self-polymerization, we performed *in vitro* p62 aggregation assays.

We made highly p62 expressed Sf9 cells that can provide more p62 proteins for assay development. Sf9 cells were transiently transfected with plasmid DNA encoding p62/SQSTM1-his using Lipofectamine 2000 following the manufacturer's instructions. After transfection for 24 h, cells were lysed with cell lysis buffer (16.7 mM 4-(2-hydroxyethyl)-1-piperazineethanesulfonic acid (HEPES), pH 7.4, 0.05 M KCl, 0.33 % Nonidet P-40, 3.33 % glycerol, protease inhibitor, and phosphatase inhibitor). Following a cycle of freeze/thaw, the cell suspension was incubated on ice

for 30 min and centrifuged at 13,000 x g for 20 min at 4 °C. Protein concentration was determined using the Bradford assay.

For the p62 oligomerization experiments, 1 μg protein was incubated with different concentrations of **XIE106** (dissolved in DMSO at 125μM, 250μM, 500μM, and 1mM) for 4 h. Samples were mixed with a non-reducing loading buffer containing 4 % lithium dodecyl sulfate (LDS), heated at 95 °C for 10 min, and resolved on 3 % stacking and 12 % separating SDS-PAGE. The monomer, oligomers, and aggregates of p62 were detected with the p62 antibody (150). We found that **Xie106** readily induced *in vitro* oligomerization/aggregation of p62 (**Figure 43a**), and this occurred in a dose-dependent manner (**Figure 43b**).

A similar assay was also done on compound **6.28**, and the results were shown in **Figure 43c**. An increase of aggregates amount was observed when the dose of the compound **6.28** increase to 1μM. A high dosage of compound **6.28** can induce p62 oligomerization and aggregation, which is an important step in the autophagy process.

147

c

6.28

0 125 250 500 1000 (μM)

Stacking gel

12% resolving gel

250kDa
75kDa
55kDa

p62 aggregates

p62 oligomer

p62 monomer (60kDa)

Non-reducing SDS-PAGE
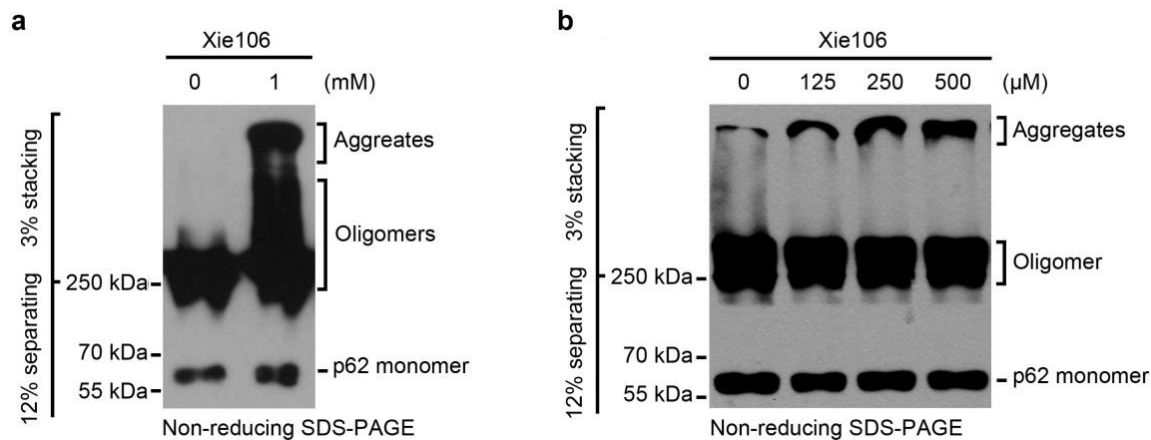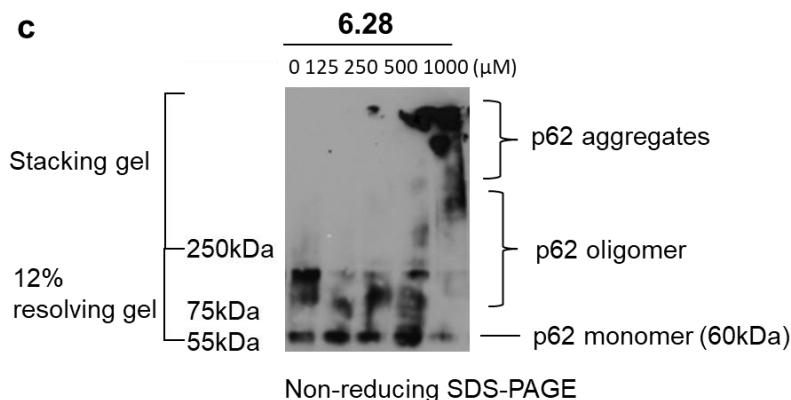
Figure 43. p62 Oligomerization and Aggregation Induced by P62 Ligands.

(a and b) An *in vitro* oligomerization assay using myc/His-tagged wild type p62. HEK293 cell lysates containing ectopically expressed myc-tagged p62 were incubated with Xie106 at the concentrations as indicated for 4 h. The various p62 forms were detected by immunoblotting analysis of anti-Myc and p62 antibodies following non-reducing SDS-PAGE. (c) Sf9 cell lysates containing highly expressed p62 were incubated with compound **6.28** at the concentrations as indicated for 4 h. The various p62 forms were detected by immunoblotting analysis of anti-p62 antibodies following non-reducing SDS-PAGE.

2.5. In vitro physicochemical properties measurement.

2.5.1. Importance of physicochemical properties

It is important to measure the physiochemical properties of some hits before stepping into the next stage of the drug candidate development. The physicochemical properties of small molecules are critical for the ADMET profiles and efficacy of the compounds. For example, the water solubility will influence the permeability of compounds to cross membranes and the absorption rate in the body. It will also influence the drug distribution in blood and tissues. Also,

148

poor solubility discovered at an early stage can be improved by formulations. Therefore, we picked up some important physicochemical properties to measure before going to the next step, water-solubility, human microsome metabolism, and chemical stability. We also did salt screening for compounds that do not have a good water solubility in order to try to make different salt forms to improve the solubility of compounds.

2.5.2. Methods to measure some physicochemical properties of small molecules.

2.5.2.1. Solubility Measurement

Water solubility testing is an important part of many scientific studies, including the early drug discovery process. Here two methods were used to test solubility. One is the standard shake-flask method by keeping adding solvent or compounds. Another one is a high throughput assay that uses a 96-well plate with a specially-developed membrane that has improved particle retention and is compatible with water/organic solutions.

Take 0.5 mg salt, try to dissolve it in 250µl Milli Q water. If the salt was dissolved, add 1 mg more salt, and see if the salt is still dissolved in the water. If the salt is not dissolved in the water, add 250µL Milli Q water and try to dissolve it. If still not dissolved, 250µL water is added each time. Stop until the salt was just dissolved; calculate the solubility by total weight of salt (mg) divided by the total volume of water (ml). When the residues were dissolved in the water, they were then lyophilized and collected. We then measured the solubility again.

The traditional shake-flask method is labor-consuming and low-throughput. Therefore, for a large-scale screen, we applied another approach. Make pH 7.4 buffer and filter to remove any particulates. It was stored at 4°C for up to one month prior to use. Using a multichannel pipette,

dispense 190 μL per well of pH 7.4 buffer into a MultiScreenHTS– PCF plate, dispense 10 μL per well of stock compound (normally at 10 mM in DMSO) from a 96-well V-bottom plate directly into the buffer in the MultiScreen solubility plate using a multichannel pipette. Cover with lid, and mix with gentle shaking at room temperature for 1.5 hours. After mixing, place the MultiScreen plate on a vacuum manifold with a grid and filter (10-12" Hg) into a clean 96-well collection plate. After filtration, use an appropriate method (UV spectroscopy, or HPLC, or LC/MS/MS) to quantify dissolved compound versus standard curves.

2.5.2.2. Human Microsome Metabolism

Add 25μl human liver microsome (20mg/ml) into conical screw top tube to yield 0.5mg/ml final concentration. Boil human liver microsome in 100 °C water bath for 10 minutes, and add 25μl boiled human liver microsome into conical screw top tube to yield 0.5mg/ml final concentration. Prepare working solution of test compounds and positive controls (200μM in DMSO). There are three positive controls in this assay: Metoprolol (moderate metabolism), Warfarin (slow metabolism), Verapamil (fast metabolism). Add 5μl working solution of test compounds and positive controls into conical screw top tube to yield 1μM final concentration. Prepare a working solution (26mM concentration) of NADPH and add 50μl working solution into a conical screw top tube to yield 1.3 mM final concentration. Prepare reaction system on ice. Add buffer into conical screw-top tubes, followed by the addition of 25μl HLM or 25μl boiled HLM, 5μl test compound or 5μl positive control to each tube according to experiment design. Then, prepare Eppendorf tubes with 200 μl acetonitrile (ACN) in them on ice. Pre-incubate all conical screw-top tubes in a 37°C water bath for 10 minutes. Start reaction by adding 50μl NADPH solution every 30s to each tube to start the reaction. Start timing right after adding NADPH to the first tube. Stop reaction at 0, 15, 30, 45, 60min time point by taking 50μl aliquot out from each

conical screw-top tube and adding into prepared ice-cold ACN-containing Eppendorf tube. Vortex it each time before taking out the aliquot. Centrifuge all eppendorf tubes at 13000g for 5 minutes. Label autosampler vials according to experiment design. Transfer 200µl of the supernatant from Eppendorf tubes to autosampler vials.

Run samples on UPLC-MS/MS. Analysis results after running. First, check if your sample is coming out at the correct retention time. Then, integrate peak area at the correct retention time to get area data. From the area under the curve, get data for 0 min and 30 min time point for each sample. Calculate $Area_{30}/Area_0$. It is the remaining percentage of test compound or positive control at 30min time point. Compare $Area_{30}/Area_0$ of test compounds with the three positive controls and find which kind of metabolism the compounds will go. Every test sample should be duplicated at least three times. All test samples and positive controls all have no NADPH groups and boiled human liver microsome groups as negative controls. The experiments must be checked and repeated if there are some problems with the negative controls. The protocols for this assay were modified from Dr. Polyac's lab

- $Area_{30}/Area_0 < 10\%$: fast metabolism

- $10\% < Area_{30}/Area_0 < 70\%$: moderate metabolism

- $Area_{30}/Area_0 > 70\%$: slow metabolism

To attain some detailed data, we can do another kind of analysis

The MS detection is performed by using a Sciex API 4000 Q trap instrument. Each compound is analyzed by reversed-phase HPLC using a Kinetex 2.6µ C18 100Å column (3.0 mm X 30 mm, Phenomenex). Mobile phase – Solvent A: water with 0.1% formic acid, solvent B: ACN with 0.1% formic acid. The amount of parent compound is determined on the basis of the peak area ratio (compound area to IS area) for each time point.

Data Analysis All calculations were carried out using Microsoft Excel. Peak areas were determined from extracted ion chromatograms. Determine the *in vitro* half-life ($t_{1/2}$) of parent compound by regression analysis of the percent parent disappearance vs. time curve. The *in vitro* half-life (*in vitro* $t_{1/2}$) is determined from the slope value:　　　*in vitro* $t_{1/2} = 0.693 / k$

Conversion of the *in vitro* $t_{1/2}$ (in min) into the *in vitro* intrinsic clearance (*in vitro* CL_{int}, in $\mu L/min/10^6$ cells) is done using the following equation (mean of duplicate determinations):

$$in\ vitro\ CL_{int} = kV/N$$

V = incubation volume (0.2 mL);

N = number of hepatocytes per well (0.1×10^6 cells).

Unbound Fraction in plasma (F_u) and Blood-to-plasma Concentration Ratio (R_B) are assumed at 1. Conversion of the Predicted hepatic intrinsic clearance (Predicted hepatic CL_{int}, in mL/min/kg) into hepatic extraction ratio (E) was done using the following equation (mean of duplicate determinations):

$$E = Predicted\ hepatic\ CL_{int}/Q$$

Scaling factors for *in vivo* intrinsic clearance prediction using different species of hepatocytes are listed below:

Species	Liver Weight (g liver/kg body weight)	Hepatocyte Concentration (10^6 cells/g liver)	Scaling Factor	Liver blood flow (Q, mL/min/kg)
Human	25.7	99	2544.3	20.7
Rat	40	117	4680.0	55.2

Control compound verapamil will be included in the assay. Any value of the compound that is not within the specified limits will be rejected, and the experiment would be repeated. The

negative control is used to exclude the misleading factor that resulted from the instability of the

chemical itself.

2.5.2.3. Salt Polymorph Screening and Characterizations for P62 Compounds.

Within the pharmaceutical industry, salt formation has become a common practice for ionizable compounds. Here, the lack of solubility of free form p62 compounds drives the decision to perform a solid form screen to get different solid forms with different properties. Changing the solid forms is changing the properties. Different screens can be performed at different points in the development process, depending on the information needed and the goal of the screen. Early development may include a small polymorph, salt, cocrystal, or amorphous dispersion screen. Polymorph screens focus on finding new forms of an API and can include unsolvated, solvated, hydrated, and even amorphous materials. Salt, cocrystal, and amorphous dispersion screens use additional materials, such as counterions, cocrystal formers, and polymers, respectively. Freebase p62ZZIs were synthesized by us, and the inorganic and organic acids were purchased from Sigma-Aldrich.

96-well plate high throughput screening will be performed by using **9.26** single solvents or binary mixtures (total 1-200 solvent systems) to select suitable counter ions from commonly used 10-12 bases and suitable solvent systems to get the crystals. Then, we will characterize the solids obtained from the screening and confirm the salt formation and scale up the crystalline salts by cooling down and solvent evaporation methods and perform characterization by ^{1}H-NMR, powder X-Ray diffractometry (XRPD), thermal gravimetric analysis (TGA), differential scanning calorimeter (DSC). This work, if completed, will provide a suitable counter ion to form an optimum salt that will overcome the solubility issue of test compounds and get salt forms of compounds with a higher bioavailability and *in vivo* efficacy.

Salt screening in 96-well plate

Make 30mg/ml p62ZZIs solution for a drug in methanol or another suitable solvent. The appropriate amount of 6 acids were dissolved and diluted to 10 ml with methanol to make a 0.1 M solution. Distribute the prepared drug solution into a 96-well plate. Each well contained 100μL of drug solution and 1 or 2 eq. prepared acid solution. Put the plate in the 37°C incubator and let the mixture evaporated to dryness. After dry, 200 μL different solvents were added to each well. Wells are covered with a film with a pinhole and evaporated under ambient conditions. Some solids with sufficient quantity will be tested by XRPD

The acid, solvent, and drug will be distributed in the plate as shown in the following table:

ID		A	B	C	D	E	F	G	H
		MeOH	EtOH	Acetone	ethyl ether	THF	EA	water	CH_2Cl_2
1	HCl								
2	H_2SO_4								
3	H_3PO_4								
4	CH_3SO_3H								
5	Citric acid								
6	Maleic acid								
7	Acetic Acid								
8	Boric Acid								
9	Carbonic Acid								
10	HF								
11	HBr								
12	Nitric Acid								

Scale-up polymorphism formation

In all cases, almost equimolar amounts of base and acid were required in a known volume of solvent, under conditions from which supersaturation could be generated either by cooling or evaporation. Thus, crystallization experiments started either from liquors prepared by mixing at room temperature, 0.1 M solutions of p62ZZ ligands and the various acids (evaporative crystallization) or from more concentrated equimolar solutions prepared at 50°C by dissolving acid and base sequentially (cooling crystallization), dissolved in room temperature and cooled down on ice is also applied

Formation of Hydrochloride by the evaporation method

Dissolve a free base p62ZZ ligand in absolute ethanol or other solvents, filter using a 22 µm filter to make a saturated solution. Drop H_2SO_4 to NaCl and produce HCl gas, control the speed of adding H_2SO_4 to make HCl bubbles at an optimum speed. Add the HCl bubbles into a saturated p62ZZ ligand solution. After an hour connection to HCl, the solution is then concentrated at 37°C under vacuum for one hour. The residue is then crystallized from the solution system and then collected by the filter without washing. The residue is then dried under vacuum for two hours for further crystallinity and thermal stability, and solubility analysis.

Formation of Mesylate by cooling down method

Freebase compound is dissolved in a solvent, CH_3SO_3H is added to the solution. The solution is cooled down to 0°C. After cooling down, the salt is precipitated in the solution, continue stirring for half an hour on ice, then filter and dried under vacuum for two hours for further crystallinity and thermal stability and solubility analysis.

Crystal polymorphism characterization

Powder X-ray Diffractometry. Powder X-ray diffraction patterns were collected using a RINT-TTR (Rigaku, Tokyo, Japan) with Cu K! radiation generated at 300 mA and 50 kV. Samples were placed on an aluminum rotation plate and rotated at 60 rpm at room temperature. Data were collected from 3 to 35 (2q) at a step size of 0.02- and scanning speed of 4-/min.

Thermal gravimetric analysis (TGA). Measurements were performed on a TA Instruments Model 2950 thermogravimetric analyzer. Samples (2–5 mg) were placed in an open platinum pan and heated at a rate of 5°Cmin.

Differential scanning calorimeter (DSC). Measurements were performed using a TA Instruments Model 2910 differential scanning calorimeter. Samples (2–5 mg) were run using crimped aluminum pans heated at a rate of 5°C/min, from -50°C to 250°C.

H^1-NMR. The sample was dissolved in d-DMSO or CDCl$_3$ with transcranial magnetic stimulation (TMS), and H1-NMR was performed using Bruker Advance (400M).

2.5.2.4. Chemical Stability Assay

Long-term stability in normal condition

Weigh out about 4mg test compounds and dissolve them in DMSO to reach a stock solution concentration of 10mM. Add stock solution into ACN to make a working solution of 1μM test compounds. Run HPLC-MS to detect the samples. Record solvent system, the retention time, and the MS peaks of the test compounds and calculate the area under the peak of the compounds. Store a small number of test compounds at 25°C, normal pressure, and humidity. After 3 months, 6 months, and 12 months, take out 4 mg compounds and dissolve them in DMSO, then dilute it in ACN to reach a concentration of 1μM for detection. Run HPLC-MS/MS for the samples, compare the retention time and MS peaks with the original one, find the UV peak for the test compounds,

and calculate the area under the peak curve. The remaining compounds' percentage is the area under the latest sample peak divided by the original test compounds' peak area.

Accelerated stability at 37 degree and 70 RH

Similar steps as above, then store a small number of test compounds at 37°C and 70RH incubator. After one week, 2 weeks, 1 month, 3 months, and 6 months, take out 4 mg compounds and dissolve them in DMSO, then dilute it in ACN to reach a concentration of 1µM for detection. We use a similar method to measure and calculate the percentage of remaining compounds by HPLC-MS.

2.5.3. Results for physicochemical properties

The physiochemical properties of some important p62 ligands (**XIE106**, **XRK3F2**, **6.28**, and **3.29**) are also measured and listed in **Table 11**, including aqueous solubility, chemical stability in normal conditions, accelerated stability, stability in aqueous solution, as well as human liver microsomal metabolism. The water solubility for the series of analogs is not high. We tested all have a solubility of less than 50µg/ml. Therefore, we tried the salt screening that converts the compound into the salt with different anions using different inorganic and organic acids. We then measured the solubility of these salts and found the one with the best solubility. Additionally, the stability of compounds in normal conditions (room temperature, normal pressure, and 35RH) and accelerated conditions (37°C and 70RH) were measured after six months. The LC-MS results showed that changes in the area under UV peak for the molecule were less than 5%, satisfying the industry requirement for drugs. Notably, the stability of **XIE106** in an aqueous buffer was not strong after a week's incubation, which means the formula of this compound in water cannot keep for a long time. Moreover, metabolism for compounds in the human liver microsome was

158

measured to estimate the half-life of compounds in the body. The half-life for **XIE106 (5.21),** **XRK3F2**, **6.28**, and **3.29** are 90 min, 120 min, 65 min, and 75 min, respectively. These compounds have a generally strong half-life that is more than one hour in human liver microsomes.

Table 11. Physicochemical Properties of Four Compounds

ID	Aqueous solubility (µg/ml)	Long-term stability, 25°C, 6 months	Accelerated stability, 37°C, 70 RH, 6 months	Stability in water, 37°C, pH=7	Metabolism in human liver microsome ($t_{1/2,}$ min)
XIE106 (5.21)	1.2	0.9%	2.3%	>5%	90
XRK3F2 (5.25)	5.1	0.8%	1.8%	>5%	120
6.28	1.5	1.3%	2.7%	1.1%	65
6.28 HCl	28.5	1.5%	3%	1.1%	67
3.29	3.5	1.1%	2%	1%	75

      XRK3F2 is our lead compound. The physicochemical properties of **XRK3** are generally druggable. One problem is it's not stable in water. Our lab previous members modified **XRK3F2** and got **XIE106** with similar good potency and a similar physicochemical profile. The solubility is a little bit lower than **XRK3F2.** Then, I modified the structure of **XRK3F2** and got compound **6.28** that is more potent to inhibit myeloma cell growth (>20-fold) than **XRK3F2**. The physicochemical properties we measured for compound **6.28** are generally good, the instability in water is improved. However, the water solubility for this compound is low. In order to improve the solubility, I made compound **6.28** in different salt forms and measured the solubility for each salt. At last, we found the hydrogen chloride salt form of compound **6.28** is stable and more soluble than the free base one. It suggested we can use HCl salt of **6.28** in our future large-scale test**.**

      To summarize, the physiochemical properties we measured for these compounds *in vitro* showed that these compounds are generally druggable and relatively stable. Further modification

might focus on improving the aqueous solubility of these analogs. This step is to make sure our compounds have good druggable properties that can move on to the next step of investigation. If some properties are not good, we can try to do some modifications to the structure or the salt form to get better compounds before going to the next stage.

2.6. Conclusions

In this section, we collectively designed and synthesized more than 70 derivatives based on the structure of the lead compound for the p62 ligand. We established bioassays to verify the actual binding of our compounds to the p62-ZZ domain and the subsequent interference in the interaction between p62 and RIP1 due to the ZZ domain blocking. Pull-down assays were applied to measure the interaction between p62 and our compounds, failure to detect an interaction between the ZZ domain mutated p62 and our compounds, which in contrast can be observed WT p62, indicating an interaction of our compounds with p62 via its ZZ domain. Co-immunoprecipitation studies have provided evidence that our compounds interfere in the interaction between p62 and RIP1 through ZZ domain blocking. We further confirmed that our compounds induce p62 oligomerization, contributing to their effects on inducing autophagosome formation and autophagy flux by IB and immunofluorescence microscope. Additionally, we also evaluated several physicochemical properties for a few of our derivatives, including thermal stability, human microsome metabolism, aqueous solubility, melting points, and long-term stability. ADME properties for some compounds were predicted based on the structures. These studies also provide information for future SAR analysis and drug development.

Nevertheless, even though we tried many times with different binding assays to quantitively measure the binding affinities for our compounds, the solid binding affinity values are still lacking. A binding affinity value is important for SAR studies and structure-based drug design. We tried several assays, including radioligand competitive binding assays, SPR, and thermal stability assays. However, all of them failed to provide solid, stable, and consistent results. I thought one of the major problems might be the instability of the p62 protein itself. As a cytosolic protein, p62 tends to oligomerize by itself in buffers; once oligomerized, the binding pocket might be blocked or changed, which makes it difficult to obtain a stable result. Another point is that p62 serves as a scaffold protein with multiple domains that could interact with many proteins and small molecules. It is possible there is more than one binding pocket in that protein, which makes it difficult to obtain a consistent binding affinity value. A third guess is that the binding assays we applied here might not be suitable for measuring small molecule interactions with p62. For example, the radioligand competitive binding assay is commonly used to detect the binding affinity of a small molecule on GPCRs. The failure in applying this assay to p62 might be due to the difference between membrane proteins and cytosolic proteins. For the accuracy of data in this dissertation, we did not include the binding assay results that were not solid enough due to high background signaling or inconsistent values. We are still trying different binding assays to figure out how to measure binding affinity to p62 quantitively. Hopefully, we can find binding affinity values for our compounds on p62 and perform further SAR studies based on those results.

In our preliminary studies, we found that our lead compound **XRK3** has an inhibitory potency on MM cell proliferation *in vitro* and myeloma tumor growth *in vivo*. The signaling study showed that **XRK3** could mediate TNF-α induced NF-κB signaling that regulates inflammation pathways through interaction with p62-ZZ. We first confirmed and emphasized that **XRK3** inhibits

myeloma cell and BMSCs growth through p62 through our observation that **XRK3** lost the inhibitory effect on p62-knockout MM cells and BMSCs. We also evaluated the mutation of the ZZ domain deletion, which led to the lack of inhibitory potency on MM cells and BMSCs. After confirming **XRK3** inhibits myeloma cell growth through p62-ZZ, we performed chemical modifications on this compound to improve the anti-MM potency and to attain better druggable properties. I designed, synthesized, and evaluated the efficacy of 87 compounds to inhibit the proliferation of three MM cell lines using MTT assays. The screening results were used for structure-activity analysis. Among them, we selected a potent compound, **6.28,** that has strong anti-proliferation ($IC_{50} < 0.5\mu M$) activity on three MM cell lines for further analysis. The partial signaling mechanism underlying this anti-tumor effect was explained by signaling studies measured by IB and a confocal immunofluorescence microscope, which showed that compound **6.28** increased autophagosome numbers, leading to the accumulation of procaspase 8 and self-activation of apoptosis signaling, which results in myeloma cell death.

3.0. The Efficiency of Novel P62 Ligands on Alzheimer's Disease

3.1. Significance and Background

3.1.1. The Morbidity and Mortality of Alzheimer's Disease

Alzheimer's disease (AD) is the most common type of dementia associated with memory loss and cognitive inability. As the size and proportion of the population older than 65 continue to increase, the number of people suffering AD or other dementias will rise over the years. In 2020, an estimated 5.8 million Americans aged 65 or older were living with AD, as shown in **Figure 44** (151). This number will continue to grow rapidly in the coming years, as the population age 65 or older will foresee a marked increase in the upcoming decades (**Figure 44**) (152). There are about 50 million AD patients worldwide and nearly 10 million new cases each year (153).
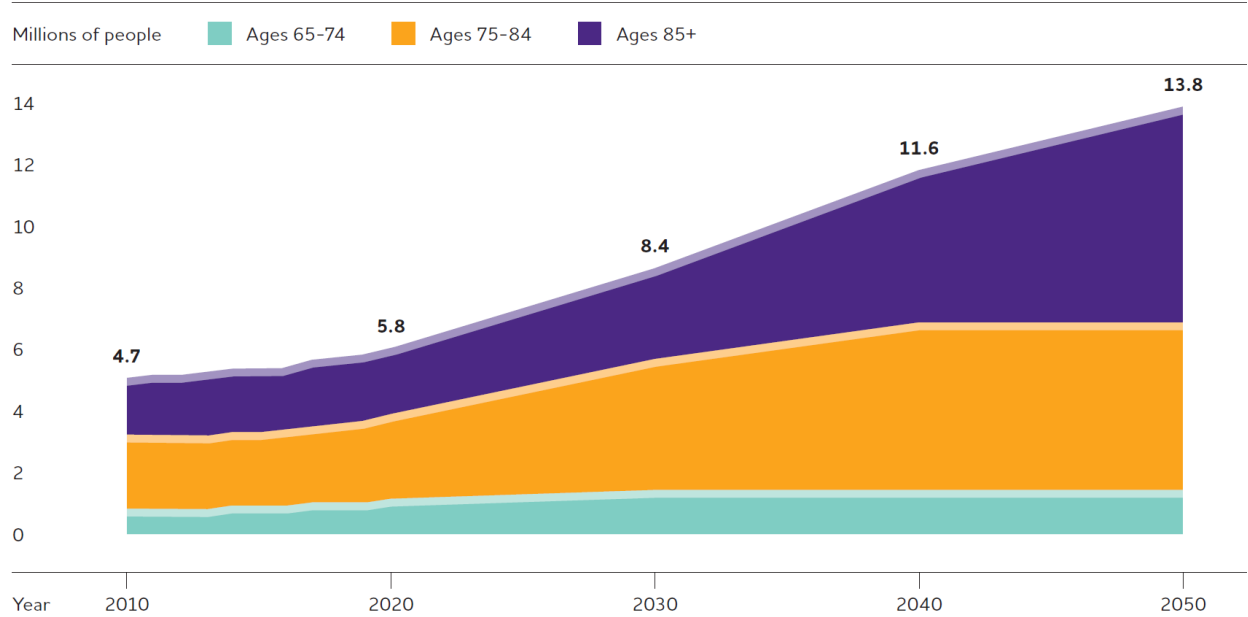
Figure 44. Projected Number of People Older than 65 in the US with Alzheimer's Disease.

The figure was adopted from Alzheimer's Facts and Figures 2020 (152), Created from data from Hebert et al. from Alzheimer's Association (154).

The prevalence of Alzheimer's dementia increases with age; 3% of people aged 65-74, 17% of people aged 75-84, as well as 32% of people aged 85 and older have Alzheimer's disease (154). A small number of people also have AD, but the prevalence in the population is uncommon to determine a certain percentage. More than 80% of Alzheimer's patients are older than 75 years, as shown in **Figure 45.**
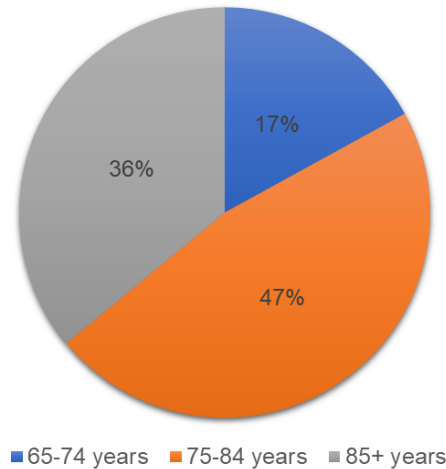
Figure 45. Number and Ages of People 65 or Older with Alzheimer's Dementia, 2020.

Modified from a figure in Alzheimer's facts and figures 2020 (152). Created from data from Hebert et al. (154). The number 5.8 million is from published prevalence estimates based on incidence data from the Chicago Health and Aging Project and population estimates from the 2010 U.S. Census.

Alzheimer's disease is officially ranked as the sixth leading cause of death and the fifth leading cause of death for seniors (older than 65). However, the actual number might be much higher, since the Center of Disease Control and Prevention (CDC) only recognizes a disease as the cause of death based on the World Health Organization description, as "the disease initiates the train of events lead directly to the death" (151, 152). Dementia often causes complications such as immobility, swallowing disorders, pneumonia, and malnutrition, which can dramatically enhance the risk of serious acute conditions that might lead to death. The cause of death for Alzheimer's patients listed in their death certifications are frequently these acute conditions rather than AD(151). Thus, the actual number of deaths caused by AD might be higher than the number listed on death certifications. (155)
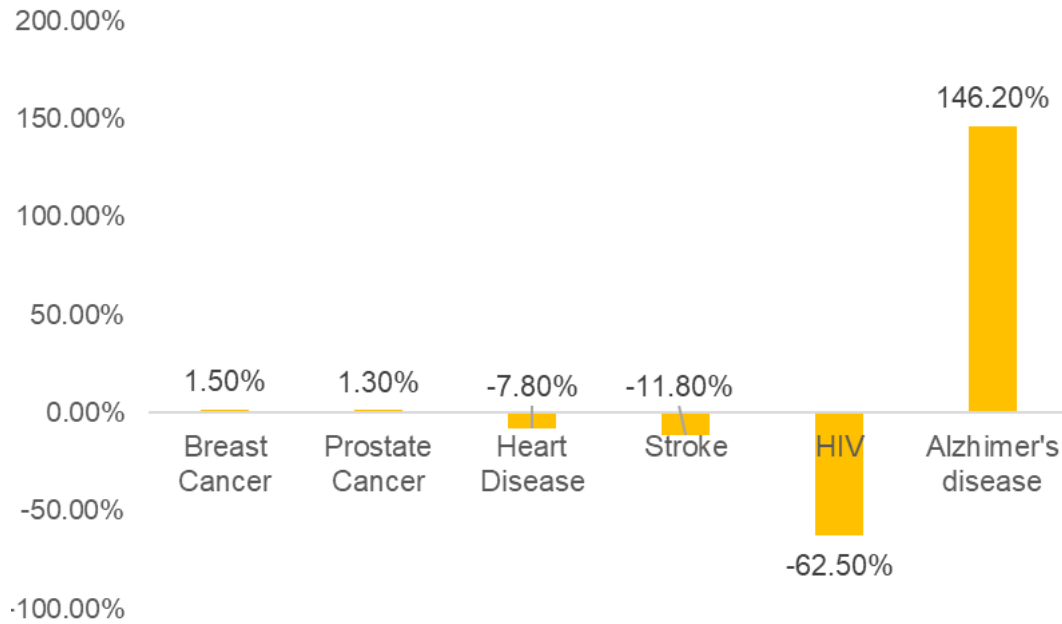
Figure 46. Percentage Changes in Causes of Death Between 2000 and 2018.

Modified from a figure from Alzheimer's Facts and Figures 2020 (152). Created from data from the National Center for Health Statistics (156).

Although the number of deaths from other leading causes has decreased significantly or stayed steady during the last two decades, the number of officially recorded deaths from AD has increased dramatically (152). As shown in **Figure 46**, the number of deaths caused by AD has more than doubled, a 246% increase from 2000 to 2018, while the number of other leading causes of deaths has decreased or remained the same, for instance, death from heart disease (the number one cause) decreased by 7.8%, death from stroke decreased by 11.8%, and death from HIV decreased by 62.5%. The death rate of AD has substantially risen over time since 2000, as illustrated in **Figure 47.**
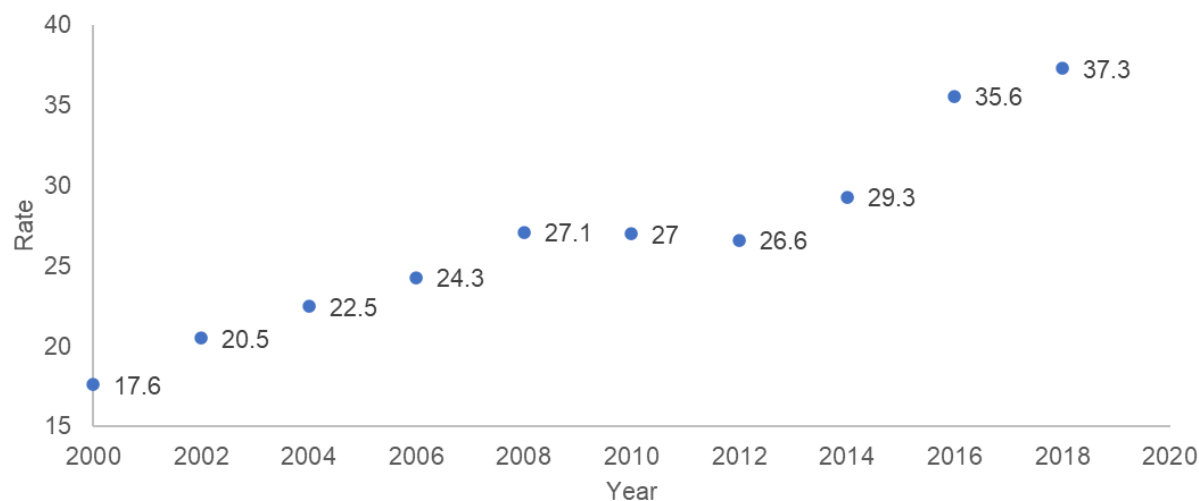
Figure 47. U.S. Annual Alzheimer's Death Rate (per 100,000 People) by Year.

Modified from a figure from Alzheimer's Facts and Figures 2020 (152). Created from data from the National Center for Health Statistics (156, 157).

Alzheimer's disease imposes a large economic burden on the patients, their families, and society. It requires substantial long-term care, which cost the US approximately $244 billion in 2019 (151, 158, 159). The statistics reported that AD is not only responsible for more deaths in the US but also contributes to increasing cases of sick and disabled Americans (152, 160, 161).

3.1.2. Currently Available Drugs for Alzheimer's Disease

The high prevalence, cost, morbidity, and mortality of AD indicate an urgent need for more efficient anti-AD therapy. However, currently available medications only contain four FDA-approved drugs and one of their combinations. Three of the approved drugs belong to the class of cholinesterase inhibitors, including donepezil, galantamine, and rivastigmine. The other one is memantine, an N-Methyl-D-aspartic acid (NMDA) receptor blocker. These drugs can temporarily slow the worst of symptoms in the initial stage and improve the quality of a patient's life. As of

167

yet, no medication can stop the disease process. The underlying pathological mechanism remains unrevealed. This situation requires worldwide efforts focusing on revealing the disease mechanism, finding a better way to treat or prevent AD. (161)

As high morbidity and mortality of Alzheimer's disease, the currently available drugs can are not enough to treat the condition. There is a high demand for a new potential treatment for Alzheimer's disease, especially those from a different mechanism. Our compounds are targeting p62, a protein closely involved in autophagy flux and oxidative stress response, which could be a potential therapeutic target for Alzheimer's disease. That's why we chose to test whether our compounds could have an effect to be beneficial in Alzheimer's disease. In the next section, we will illustrate why p62 can be a potential therapeutic target for Alzheimer's disease.

3.2. p62 as a Potential Therapeutic Target for Alzheimer's Disease.

As shown in **Figure 48**, p62 can be a therapeutic target for AD based on the mechanism that p62 is a signaling hub for several cascades related to neuron death in AD patients, including macroautophagy, UPS, NF-κB signaling pathways, ROS formation/elimination, and oxidative stress response. First, p62 is closely involved in autophagy (UBA, LIR, and the PB1 domain) and UPS (via UBA), which are two factory systems that clear the misfolded and aggregated proteins to maintain the protein hemostasis in the cell. When the two protective mechanisms are impaired, the misfolded and aggregated proteins will accumulate, leading to the disruption of protein hemostasis, neurotoxicity, and neuron death, which is known as "proteinopathies" in neurodegenerative diseases and one of the major causes for AD in the above discussion. Additionally, p62 has three protein interaction motifs, the TRAF6-interaction domain, the ZZ

domain that binds to RIP, and the PB1 domain that interacts with aPKC, which regulates an NF-κB cascade that mediates cellular response to inflammation, oxidative stress, and immunoregulation, eventually triggering cell death. NF-κB is involved in part of the pathological mechanism that regulates neuron death in AD. Moreover, the Keap1-interaction region (KIR) in p62 can interfere with the interaction between Keap1 and Nrf2, which affects the function of Keap1-Nrf2 signaling pathways that are involved in response to oxidative stress by mediating elimination of ROS, NADPH synthesis, and neuronal detoxification mechanism. These cascades are closely related to neuron death in AD models. Thus, targeting p62 might be an attractive strategy for treating AD.
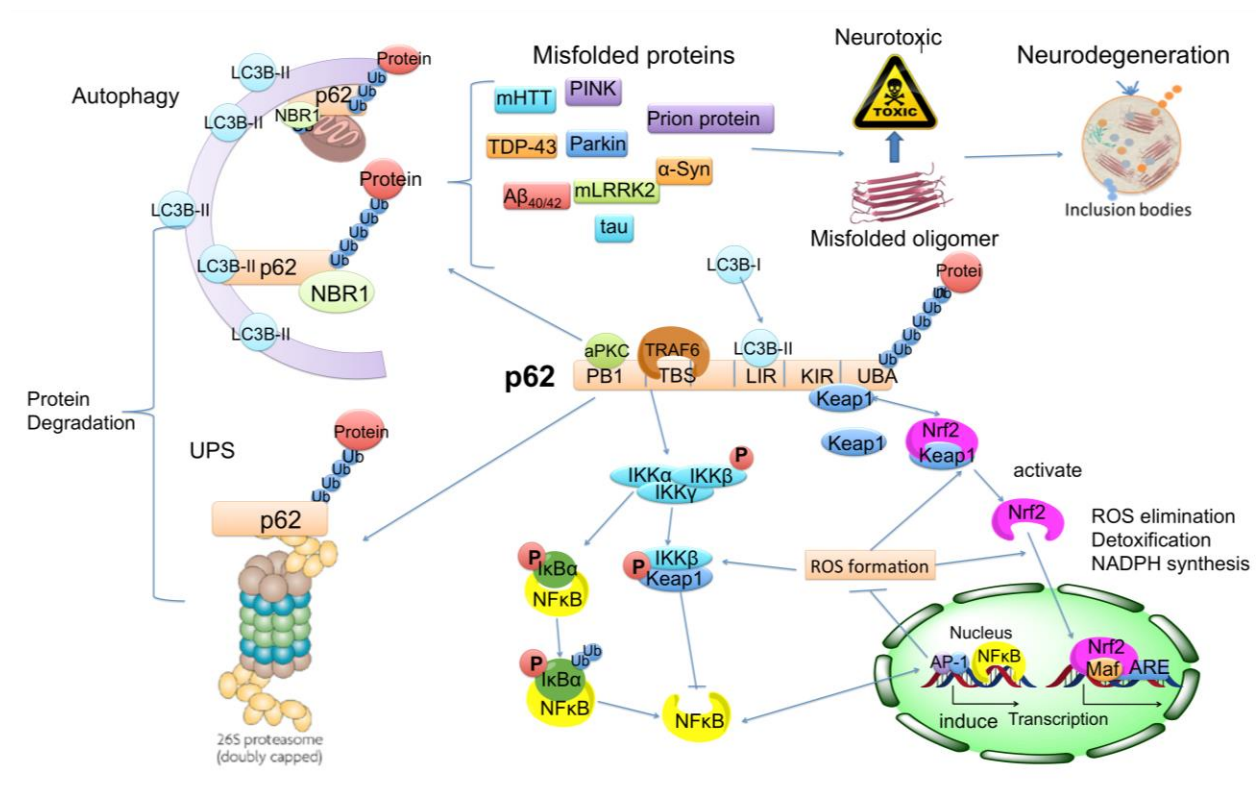
Figure 48. P62 can be Signaling Hub that is Related to Alzheimer's Disease.

p62 is closely involved in autophagy through its UBA, LIR, and PB1 domain. 2) p62 also participates in the UPS, which controls protein degradation in the cells via its UBA. 3) p62

169

regulates NF-κB signaling. 4) p62 can interfere with the Keap1-Nrf2 axes that are in response to oxidative stress to regulate ROS elimination and detoxification in neurons

Our p62-ZZ ligands are closely involved in macroautophagy and are a potential therapeutic target for neurodegeneration due to their role in autophagy to maintain protein hemostasis and as a signaling hub to regulate detoxification and oxidative stress-related pathways. In our previous study, it was shown that one of our lead compounds, **XRK3,** induces p62 self-oligomerization in cells and autophagy flux, which proceeded the autophagic clearance of misfolded and aggregated proteins in neurons, such as mHTT (mutated Huntington proteins). Fewer mHTTs and less aggregation were observed by IB in the group treated with our compounds. Our compounds are related to NF-κB and TNF-α induced signaling and regulate oxidative stress, immune response, and inflammation pathways. Therefore, we assume that our in-house compounds targeting p62 might have some neuroprotective or other therapeutic effects on neurodegenerative diseases. In this chapter, AD, the most common of neurodegenerative diseases, will be discussed as an example, but several misfolded and aggregated proteins in neurons we discussed in this chapter like tau, Aß, and α-synuclein are also related to other neurodegenerative diseases, such as Parkinson's disease, Amoebic gill disease, and Corticobasal degeneration.

According to the molecular mechanism about p62 and neurodegenerative diseases in published articles and our previous study about our lead compound XKR3, it's possible that our p62 ligands can have some neuroprotective effects in neurodegenerative disease models. However, more evidence will be needed to demonstrate our hypothesis. The first assay we did in the next section is to establish a simple *in vitro* neurodegenerative cell model to screen whether our compounds have some neuroprotective effects against neurodegeneration. If we can find some hits

in that sectsion, we can continue working on evaluation of the molecular mechanism under this neuroprotective effects.

3.3. Establish a stable in vitro cellular neuronal model for screen

As mentioned above, we need an *in vitro* cellular screen assay to measure the neuroprotective effects of our compounds. There are some specific problems we met in this part. The first is to have an how to get stable neurons for the test.

3.3.1. Rationale using differentiated SH-SY5Y cells

Commonly used *in vitro* experimental models for the neuronal disease are primary neuronal cultures from rats and mice, short-term slice cultures from human and animals, neuroblastoma cell lines from animals, including B35 (rat) cells, neuro-2A (mouse) cells, and PC12 (rat) cells, and neuroblastoma cell lines from human (SH-SY5Y). We chose to use SH-SY5Y cells to establish an *in vitro* model to screen our compounds for the following reasons. First, some neuron activities are exclusive to respective species and might be distinctive to humans; the slices and primary neuronal culture from rats, mice, and other animals might not represent or mimic some specific neuronal activity and features in humans. Thus, models that contain a human component had a higher priority.

Second, the human brain slices and neuronal culture samples are not accessible or expensive to obtain for most researchers. Our lab, which mainly works on the medicinal chemistry part of drug discovery, did not have the experience or opportunities to obtain these patients' samples. The only approach we could utilize for those brain slices and primary neuronal cultures was to test our compounds in collaboration with other labs. However, it was not convenient to completely rely on our collaborators to test all of our in-house compounds for us in the short-term human or animal slices. Even though it could be feasible, the short-term samples may have

unstable karyotypes, making their use problematic for cell signaling reproducible studies. More consistent long-term models are needed for *in vitro* screening.

Additionally, the SH-SY5Y cell line is highly p62 expressed. It is suitable for screening our compounds that are purposed to target p62 since it will be easy to observe the effects of our compounds on p62 highly expressed cells. Therefore, the human neuroblastoma cell line SH-SY5Y was selected to develop a consistent *in vitro* neuronal model for screening.

One concern is that SH-SY5Y are neuroblastoma cells with some tumor cell properties. The advantage is that the cells are easy to maintain and can keep for a long time, while the disadvantage is that the cancer-like properties make it hard for some signaling pathways to represent normal neuronal features and functions. We found a large number of reports (162, 163) using this cell line to measure neuronal properties and signaling pathways, which are discussed below in this section.

Undifferentiated cells may lack some phenotypes, for example, viral uptake, which is essential for accurate interpretation. In order to obtain a model that can best mimic neuron activity in the body, it is critical to ensure that the SH-SY5Y cells are appropriately differentiated into neurons. To attain and maintain homogenous and viable human neuronal cultures to screen compounds, we differentiated the chromosomally stable human neuroblastoma cell line, SH-SY5Y, following a method developed by Mackenzie M. Shipley (164). This method is relied on sequentially, removing serum from media to cause gradual serum-starvation and adding neurotrophic factors and extracellular matrix proteins to the media and dish. The steps following the timeline allow for the neurons to differentiate from the initial epithelial cell phenotype into an extensive network neurites phenotype, leading to a reliable, homogenous, expansive, and branched neuronal culture that can be used for *in vitro* molecules screening.

3.3.2. Methods to get stable neurons for assay development

3.3.2.1. Cell lines

SH-SY5Y (ATCC® CRL-2266™) cells were obtained from American Type Culture Collection (ATCC). Cell lines were maintained in an appropriate growth medium and sub-cultured twice per week. These studies were conducted using protocols approved by the University of Pittsburgh's IRB.

3.3.2.2. Cell Culture Media

Eagle's Minimum Essential Medium (EMEM, Gibco Laboratories, Grand Island, NY, 670086)

RPMI-1640 Medium (Gibco Laboratories, Grand Island, NY)

Gibco™ Penicillin-Streptomycin (Pen/Strep, 10,000 u/ml, 15140148)

Gibco™ Neurobasal™ Medium (Gibco Laboratories, Grand Island, NY, 21103049)

SH-SY5Y Basic Growth Media	EMEM + 15% hiFBS + Glutamine + Pen/Strep
SH-SY5Y Differentiation medium 1	EMEM+2.5% hiFBS+ Glutamine + Pen/Strep+ 10µM RA
SH-SY5Y Differentiation medium 2	EMEM+1% hiFBS+ Glutamine + Pen/Strep+ 10µM RA
SH-SY5Y Differentiation medium 3	Neurobasal + B-27 + Glutamine + Pen/Strep + 10µM RA + 20mM KCl + 50 ng/ml BDNF + 2 mM dibutyryl cyclic AMP (db-cAMP)

3.3.2.3. Differentiation of SH-SY5Y cells

174

Mackenzie M. Shipley et al. (164) reported a protocol that "describes an easy-to-follow, reproducible method to obtain homogenous and viable human neuronal cultures, by differentiating the chromosomally stable human neuroblastoma cell line, SH-SY5Y" based on a previous study (165, 166). "This protocol offers a reliable way to generate homogeneous populations of neuronal cultures that can be used for subsequent biochemical and molecular analyses, which provides researchers with a more accurate translational model of human infection and disease." (164)

Prepare all stocking solutions and conduct all procedures under strict aseptic conditions. Use heat-inactivated FBS (hiFBS) instead of FBS in all media. This procedure requires partially differentiated neurons to be re-plated and trypsinized, leaving epithelial-like cells still attached to the dish. Therefore, we incubate the cells in trypsin for a minimal amount of time to allow the lift-off of neurons but keep the other cells attached to the dish. Trituration of differentiated cells was conducted at a low speed using a pipet up and down more than five times. Split cultures when cells reached 70%-80% confluency within 10-15 passages. We split the maintenance cell cultures less than 1/5 since too low confluency will lead to cell death for SH-SY5Y cells.

Thaw the SH-SY5Y cells in a 37°C water bath for about 2 min. Add 10ml basic growth media and triturate 1-2 times, spin down at 1000 x g for 2 min. Aspirate media, resuspend pellet in 10ml basic growth media. Plate the cells in a T25 flask. Replace the media the next day to get rid of the dead cells.

According to **Figure 49**, we followed the timeline of the procedure provided by Mackenzie M. Shipley and her colleague. On Day 0, Rinse the undifferentiated cells with PBS, trypsinized for 3min, adding media (contains FBS) to quench trypsinization. Spin down at 1000 x g for 1 min, remove the supernatant and resuspend the pellet using basic growth media. Count cells using a

175

hemocytometer and dilute it to 50,000 cells/ml by media. Plate 2ml of cells per 35 mm^2 dish and incubate it in incubate at 37°C and 5% CO_2.
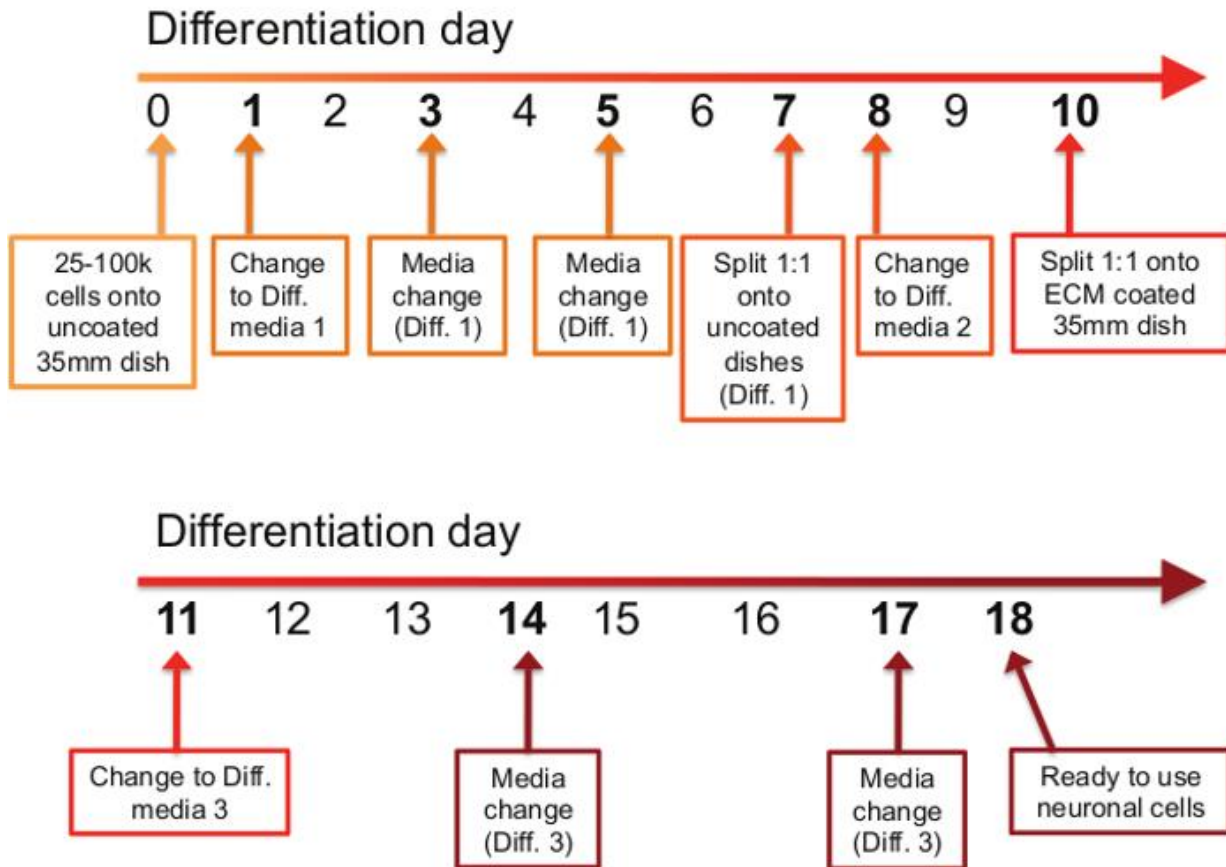
Figure 49. Timeline of Differentiation Procedure.

The figure was adopted from the report of Mackenzie M. Shipley et al. (164)

The next day (Day 1), gently aspirate the old media, add RA to warm and equilibrated differentiation media 1, immediately add 2ml media into each dish, and put it back to the incubator (37°C and 5% CO_2). Change media again using differentiated media 1 every two days (Day 3 and Day 5). On Day 7, trypsinize the cells with 200µl trypsin for 2-3min (not a too long time or too much trypsin to leave the undifferentiated cells still attached on the dish and to protect the cells) and re-plate the cells suspension with fresh differentiation media 1 in a ratio of 1:1 to 35 mm^2 dish

2ml/per dish, and incubate them in 37°C and 5% CO_2. On the next day, change media to differentiation media 2. On day 9, prepare Extracellular Matrix (ECM) coated dishes. Dilute ECM solution 1:100 into cold DMEM, dispense 2ml into each $35mm^2$ dish, place in the incubator overnight, aspirate mixture and allow it to dry in the hood for more than one hour, and store at room temperature for use.

On Day 10, transfer cells into ECM coated plates in a ratio of 1:1. Do not incubate cells with trypsin for a long time to avoid neuron damage and leave epithelial-like cells on the plates. On Day 11, change the media to differentiation media 3 with RA. Do not expose the neurons to the air for a long time. Change media every three days using differentiation media 3 with RA to maintain neuron health. Before being ready to use, cells have to be differentiated into neurons and exhibit the neuronal phenotype. Cell cultures will usually be stable after about 14 days of incubation following terminal differentiation.

3.3.3. Characterization of stable ready-to-use differentiated SH-SY5Y cells

After we follow the differentiation procedures for SH-SY5Y cells, we need to confirm whether these cells have neuron phenotypes by observing morphology change under a microscope or measuring neuronal biomarkers. We can only use stable neurons that have neuronal phenotypes to establish the *in vitro* neuroprotective screen assay.

The phenotype of neurons is checked and confirmed by microscope, immunoblotting, and immunofluorescence using neuronal biomarkers for SH-SY5Y cells, including MAP2 and ß-tubulin-III. The representative results were collected in the process of SH-SY5Y cell differentiation, as seen in **Figure 50.** The neuroblastoma cells might have different phenotypes during differentiation, and it is critical to identify healthy neurons from the others. After seven

days of treatment with retonic acid (RA) and serum deprivation (**Figure 50**, second line), the cells started to show long projections and more neuronal features. Another factor in ensuring the separation of neurons from undifferentiated cells was frequently changing the dishes and maintaining the minimum incubation time of trypsin to leave the undifferentiated epithelial cells on the original dish and only release the differentiated neurons during the course. As a control (**Figure 55**, third line), we showed when the cells did not split from the original dish after 14 days of serum deprivation, undifferentiated cells and differentiated neurons coexisted in the dishes, with former ones gradually take over the cell populations. In comparison, the SH-SY5Y cells followed the protocol for 14 days of RA treatment and serum deprivation, demonstrating longer projections that connected to neighboring cells and more neuronal phenotypes with extensions of numerous thin, branched neuritic processes.
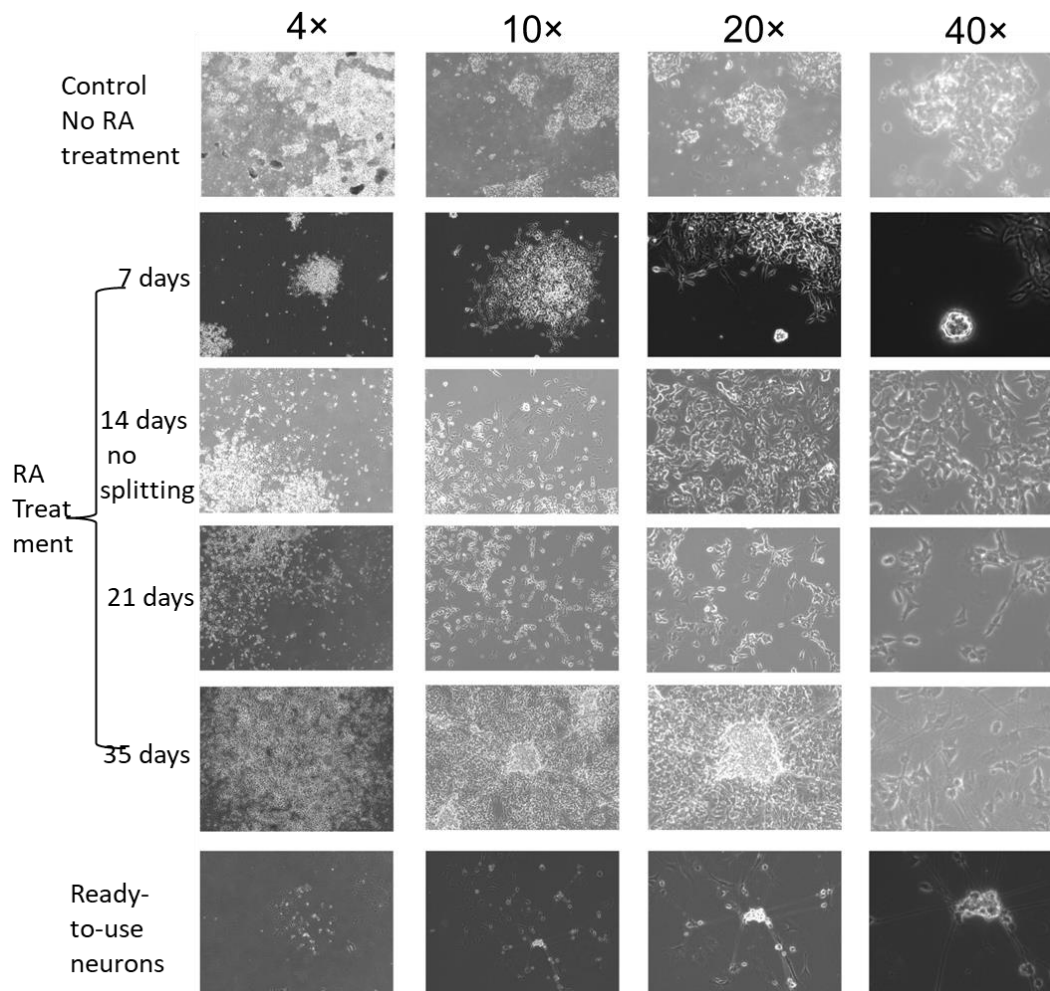
Figure 50. Morphology Changes of SH-SY5Y Cell Differentiation into Neurons.

The first line displays the undifferentiated SH-SY5Y cells. Cells with a more epithelial-like phenotype might overtake cell cultures during a long incubation long time. The second line shows the cell culture treated with RA for about 7 days before splitting to a new dish. We can observe the mixture of undifferentiated cells, partially differentiated cells, and some epithelial-like cells. Trypsinized and re-plated to a new plate can leave some epithelial-like cells on the old dish. The third line of figures shows the cell cultures that were treated with RA for 14 days without splitting into a new dish. The culture is still a mixture of epithelial-like cells and partially differentiated neurons. However, this overpopulation of epithelial-like cells due to lack of dish change or low frequency of media change might continue to overtake the cultures and outnumber the neurons. The fourth line of plots shows the cell culture in differentiation media 3 after 14 days of treatment with RA. In that stage, the cells are after two passages and culture for several other days; the

179

remaining cells are elongated and have long processes that are connected with the neighbor. Cell body cluster was also observed, and processes began to emit from the base of a large cluster. The overall survival population is neuronal and homogenous. The fifth line of figures shows the culture of cells with 32 days of treatment with RA, which is more than two weeks, followed by a second split on Day 10. This cell culture has mature neurons but too much cellular debris, which might influence the health of the neurons. The last line of cell culture figures is the cells that are ready-to-use neurons. Images were obtained in phase at 4X, 10X, 20X, and 40X magnification.

Ready-to-use neurons after 18 days of differentiation were presented in the last line of **Figure 54** with demonstrated neuronal features of extensive and elongated neurotic projections. Those differentiated neurons could not be maintained for a long time. After the maintenance of more than 2 weeks, the cellular debris accumulates in the background of the dish, stressing the neurons and making cells unhealthy or developing the epithelial-like phenotypes (**Figure 54**, fifth line). The neuronal characteristics of fully differentiated SH-SY5Y cells are demonstrated by techniques such as immunofluorescence detection of classical neuronal markers, as shown in **Figure 51**.
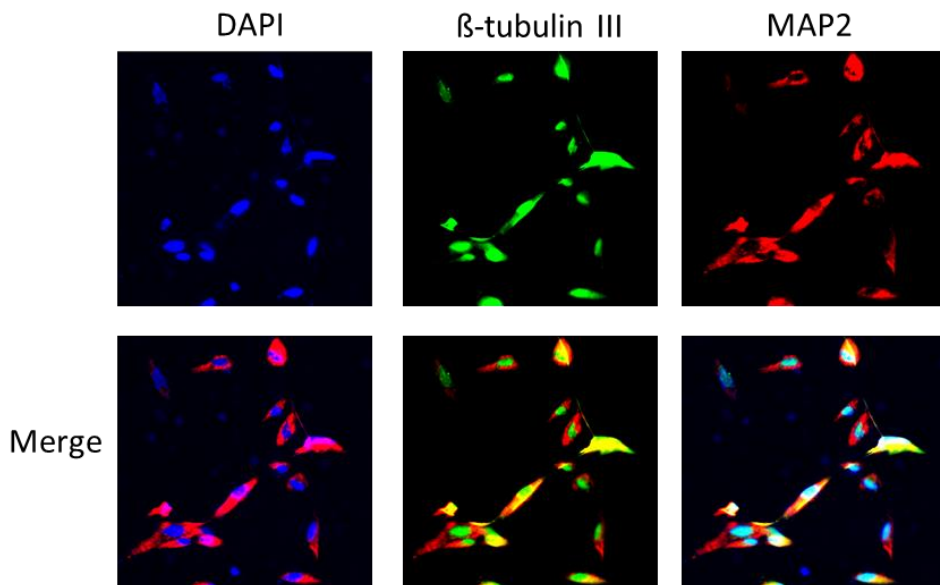
Figure 51. Neuronal Biomarkers for SH-SY5Y Cell Differentiation.

Immunofluorescence detection illuminates neuronal features of fully differentiated SH-SY5Y cells. DAPI staining shows the location of the nuclei in the cells. Anti-beta-tubulin-III (green) stains the microtubule component that is rich in some neurites and with a long process. Anti-MAP2 (red) labels microtubule-associated protein 2, which is located in the neuronal soma and proximal portion of neurites. The figures in the second line are a combination of the three stains. The first one shows that the MAP2 is mainly located in the cytoplasm of neurons with almost no overlap with DAPI stain. The second one shows the MAP2 and βbeta-tubulin-III staining overlapped with each other in the cytoplasmic cellular body. β-tubulin-III is also located in a long process and network of neurites. Images were obtained at 20X magnification using a fluorescence microscope.

3.4. Neuroprotective Effect Measured by MTT Assays on SH-SY5Y Cells.

After we got ready-to-use confirmed neurons, we need to induce a neuron injury that mimics some features of the neurodegeneration process. Then, we choose an optimum condition to get a stable neuron injury model that can be used to screen the neuroprotective effects of our compounds. There are two specific questions: 1) which method we applied to induce neuron injury that shares some similar features with neurodegeneration; 2) what is the optimum condition that stabilizes this model, which can be used to screen compounds.

3.4.1. Rationale to use hydrogen peroxide to induce neuron injury.

The rationale for testing neuroprotective effects on neurons with pretreatment of hydrogen peroxide is listed below. First, hydrogen peroxide is an uncharged, freely diffused, and stable ROS that induces oxidative stress. The pathology of AD is associated with oxidative stress. The capacity

of Aβ to produce hydrogen peroxide and to generate highly toxic ROS, indicates a potential mechanism that links oxidative stress to AD. The actions of hydrogen peroxide contain conformational and structural modifications of proteins, lipids, and DNA, all of which can be observed in the AD model's brain and may contribute to the loss of synaptic function, which is characteristic of the disease. Drugs that prevent oxidative stress, including antioxidants, modifiers of the enzymes involved in ROS generation, and agents that can remove the stimulus for ROS generation, can be considered a potential treatment for oxidative stress-related AD. Future research and development of agents that specifically target hydrogen peroxide, other ROS, and oxidative stress-related proteins may provide a potential route to AD therapy (167).

The exposure of cells to an appropriate concentration of hydrogen peroxide-induced ROS increases mitochondrial dysfunction, apoptosis signaling activation, and viability loss. Hydrogen peroxide as a ROS induces oxidative stress and apoptosis that are implicated in a variety of neurodegenerative diseases. Treatment with tomatine and naringenin significantly reduced the viability loss, apoptotic rate, and hydrogen peroxide-induced oxidative stress (162, 163).

Our p62 ligands bind to the p62-ZZ domain and induce a conformational change of p62. It might interfere with the interaction between p62 and Keap1 through the Keap1-interaction region. When p62 does not bind to Keap1, Keap1 can freely interact with the nuclear factor erythroid 2-related factor 2 (NRF2). NRF2 is an oxidative responsive mediator and a guardian of lifespan, which protects the cells from ROS stress-induced cell death. The reduced glutathione, a major small molecule antioxidant that exists in all mammalian cells, and is generated by the downstream target genes of NRF2, counterbalances the mitochondrial ROS production. It has also been reported that p62-regulated induction of macroautophagy is important for NRF2 activation and

ROS/oxidative stress elimination. The p62-Keap1-NRF2 axis is critical for the cellular protective mechanism against oxidative stress and mitochondrial dysfunction (168).

Free radical damage, oxidative stress, and mitochondrial dysfunction play a key role in the pathogenesis of various neurodegenerative disorders, including AD. The brain is sensitive to changes in redox status. Pretreatment of hydrogen peroxide-induced toxicity in the neuronal cultures leading to mitochondrial dysfunction and cell death, which represent critical pathological signaling for neurodegenerative diseases, can be used as *in vitro* models for measuring neuroprotective effects. Binding to p62 can influence the Keap1-NRF2 signaling cascade, which is a key mediator for oxidative stress and mitochondrial function in cells that regulate the elimination of ROS. p62 ligands may also affect the regulation of the NF-κB signaling pathway and selective autophagy, thereby leading to a downstream cascade related to inflammation, mitochondrial dysfunction, apoptosis, and neuron viability loss in neurodegenerative disorders. Therefore, this H_2O_2-induced neurotoxicity model is suitable for measuring the effect of p62 ligands on neuron viability.

Taken together, the present study reveals that the regulation of the p62-Keap1-NRF2 pathway through interaction with p62 and the mediation of mitochondria function and apoptosis signaling together may render our p62-ZZ ligands, protecting SH-SY5Y cells from H_2O_2-induced neurotoxicity.

3.4.2. Methods using hydrogen peroxide to establish neuron injury model

After confirmation of neuron phenotype by morphology observation under a microscope, immunoblotting, and immunofluorescence staining with neuron biomarkers MAP2 and ß-tubulin-III, the ready-to-use differentiated SH-SY5Y cells can be maintained at 37 °C in a humidified 5%

CO$_2$ and 95% air atmosphere and cultured in Differentiation Medium 3 within 2 weeks. The test drugs and positive control were initially dissolved in dimethyl sulfoxide (DMSO), and then the solutions were diluted 1:1000 in differentiation medium 3. Differentiated SH-SY5Y cells were seeded on a 96-well plate in 200 mL medium per well at a density of 1,000 cells/well for 24 h.

3.4.2.1. How to choose the optimum condition to induce irreversible neuron damage

The ready-to-use SH-SY5Y neurons were utilized to establish a model to screen compounds for neuroprotective effects against oxidative stress damage due to hydrogen peroxide pretreatment. We performed a pre-test to measure the appropriate hydrogen peroxide concentration that would cause measurable cytotoxicity but not result in irreversible damage to the neurons. The neurons were incubated with different concentration (0µM, 10µM, 50µM, 100µM, 200µM, 400µM, 500µM, 600µM, 800µM, 1600µM, and 2400µM) of hydrogen peroxide for 6h. Change the media to remove the hydrogen peroxide and incubate for another 48h. After 48h, MTT (3-(4,5-dimethylthiazol-2-yl)-2,5-diphenyltetrazolium bromide) assay kit was utilized to determine the percentage of cell survival. MTT (3-(4,5-dimethylthiazol-2-yl)-2,5-diphenyltetrazolium bromide (Sigma, St. Louis, USA)) solution (5mg/ml, 20 µL) was added to each well, shaken at 150 rpm for 5 minutes, and then incubated for 4 hours at 37°C and 5% CO$_2$. The metabolism product (formazan) was dissolved in 150 µL isopropanol and shaken at 150 rpm for 5 minutes. Optical density (OD) was read at 540 nm and subtracted from the background at 720 nm. The OD absorption was detected by Bio-Tek and analyzed by GraphPad Prism 8.0.0. The curve was generated using log$_{10}$ concentration and normalized OD value (set the OD of untreated cells as 100) to attain the IC$_{50}$ value for H$_2$O$_2$ to induce cytotoxicity in differentiated cells.

As shown in **Figure 52,** the IC$_{50}$ of hydrogen peroxide-induced cytotoxicity is between 500µM to 600µM. From 200µM, hydrogen peroxide starts to induce cytotoxicity in differentiated

SH-SY5Y cells, but in that concentration, the oxidative stress damage to the neurons can still be recovered by treatment from other reports (169-172). Therefore, we choose to pre-treat the cells with 500μM hydrogen peroxide for 6 h, which can lead to a detectable cell viability change but did not result in irreversible damage that treatments cannot retrieve. After six hours' pretreatment of 200μM H_2O_2 was then applied to induce moderate neurotoxicity in SH-SY5Y for assay development.

hydrogen peroxide-induced cytotoxicity in SH-SY5Y cells
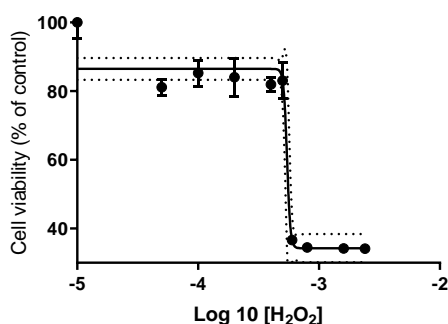
Figure 52. Hydrogen Peroxide Induced Cytotoxicity in Differentiated SH-SY5Y Cells.

The curve of the logarithmic x-axis of hydrogen peroxide concentration and normalized cell viability as y-axis using a blank control as 100%. Each concentration was tested in more than three wells, and this assay was repeated at least twice. The data were represented by mean ± SD.

We pretreated the neurons with 200μM hydrogen peroxide for 6 h to induce neuron damage which can be recovered a bit by compounds' treatment.

3.4.2.2. Methods using MTT assay to screen neuroprotective effects of compounds

Then cells were treated with different concentrations of p62 compounds, DMSO, and controls (*Cyperus rotundus rhizome* extract) for 16h, and cell viability for 72h was determined by MTT assay. MTT solution (5mg/ml, 20 μL) was added to each well, shaken at 150 rpm for 5 minutes, and then incubated for 4 hours at 37°C and 5% CO_2. The metabolism product (formazan)

185

was dissolved in 150 µL isopropanol and shaken at 150 rpm for 1 minute. Optical density was read at 570 nm and subtracted from the background at 720 nm. The effect of ligands on cell viability was expressed as percent cell viability, with vehicle-treated control cells set at 100%. The concentration of each drug was examined in triplicate. The concentrations of the compounds were 40, 20, 10, 5, 2.5, 1.25, 0.625, 0.3125, 0.15625, 0.075 and 0.01 µg/ml. Bio-Tek detects OD at 570nm. The data were analyzed by GraphPad Prism 7.0.

3.4.3. Neuroprotective Results and Discussion

Most compounds did not show a significant protective effect on neuron growth. Several compounds showed a moderate neuron protective effect on differentiated SH-SY5Y cells against hydrogen peroxide-induced cytotoxicity. As shown in **Figure 53 and Figure 54**, an example was provided for **5.7 and 5.8** to display a neuroprotective effect on hydrogen peroxide-induced neuron toxicity. Similar trends were observed in the curve, where the EC_{50} values were 3.01µM and 3.62 µM, respectively. The highest neuroprotective effect was detected when the concentration reached 20 µM. The degree of neurons restored was not as much as the positive control did. Additionally, even the positive control drug could not recover the neurons and keep them alive to a level where the neurons were not harmed by hydrogen peroxide (negative control). Using the same procedure, we calculated the EC_{50} values of the other test compounds.

Neuroprotective effect against H_2O_2 induced toxicity
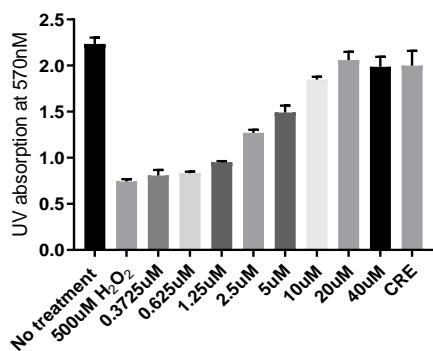
Neuroprotective effect against H_2O_2 induced toxicity
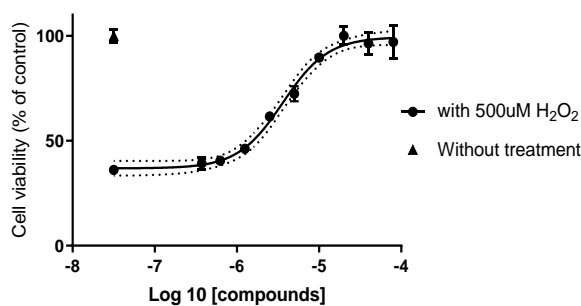
	with 500uM H_2O_2
IC50	3.624e-006

Figure 53. The EC_{50} of Neuroprotective Effect of 5.7 on H_2O_2 Induced Toxicity.
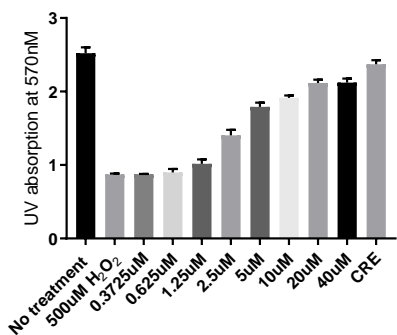
Neuroprotective effect against H_2O_2 induced toxicity

Neuroprotective effect against H_2O_2 induced toxicity
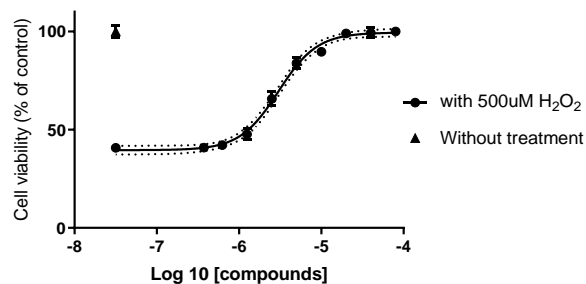
	with 500uM H_2O_2
IC50	3.014e-006

Figure 54. The EC_{50} of Neuroprotective Effect of 5.8 against H_2O_2 Induced Toxicity.

If the effect of a compound on the neurons was negligible, we represented the results as EC_{50} is larger than 50 µM. The "$EC_{50} > 50$ µM" was also applied to a condition that the test compound itself induced cytotoxicity and therefore aggravated the cytotoxicity, increasing the neuron deaths, which was detected by a reversed curve. Consequently, we used "$EC_{50} > 50$ µM" to represent all the conditions when the test compounds did not show detectable neuroprotective effects by our *in vitro* assays. Afterward, we summarized the EC_{50} values of test compounds in

Tables 12-18 and carried out a structure-activity relationship analysis based on the EC_{50} values that represented the neuroprotective effect.

The effects of compounds on autophagy were measured by observing the LC3B conversion from LC3B-I to LC3B-II and the p62 protein level change. The western blot films are summarized in **Figure 55 to Figure 56**. The results are also listed in **Tables 12-18**, where "+" indicates autophagy inducer, "-" represents autophagy inhibitor, and "=" shows that the compound does not affect autophagy.

Table 12. The List of Benzyloxy Analogs with their Neuroprotective Activities.
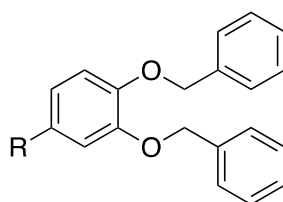
Analogs 3.2 to 3.31

ID	R-groups	SH-SY5Y, Anti-peroxide induced neuron toxicity, $EC_{50}(\mu M)$	Autophagy effect LC3 turnover	Internal ID
3.2	-CH2OH	>50	=	XIE5-1-33
3.7		7.21	+	XIE5-2-54
3.8		6.225	+	XIE5-2-53
3.9		18.8	=	XIE5-2-49
3.10		35.06	=	XIE5-2-64

188

3.14		25.94	+	XIE5-2-46
3.16		19.85	+	XIE5-2-51
3.29		>50	+	XIE1-4-3
3.28		>50	+	XIE5-2-44
3.31		>50	-	XIE5-1-54CT XIE5-1-64
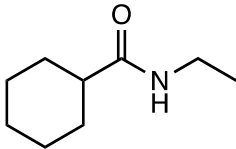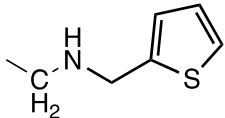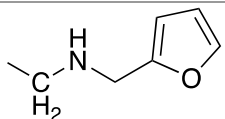
The analogs without phenyl ring substitution are listed in **Table 12.** Most analogs did not show a neuroprotective effect against hydrogen peroxide treatment. Compounds with a guanidine group (**3.28, 3.29,** and **3.31**) and a hydroxymethyl (**3.2**) showed no neuroprotection for differentiated neurons against hydrogen peroxide. The compounds with methylamino linked to heterocyclic aromatic rings, such as thiophene (**3.7**, $EC_{50} = 7.21\mu M$), furan (**3.8**, $EC_{50} = 6.23\mu M$), pyridine (**3.9**, $EC_{50} = 6.23\mu M$), and imidazole (**3.10**, $EC_{50} = 35.06\mu M$) showed a moderate neuroprotective effect in this assay. Among them, compounds with thiophene and furan showed better neuroprotective effects. When we looked at the impact of compounds on macro-autophagy, compounds **3.7** and **3.8** induced LC3B turnover dose-dependently (**Figure 55B**), indicating as autophagy inducer (marked as "+" in **Table 12**). In contrast, compounds **3.9** and **3.10** did not affect LC3B turnover, suggesting no autophagy effect (indicated as "=" in **Table 12**). We assumed that our p62 ligands might have a neuroprotective effect through autophagic clearance stimulation.
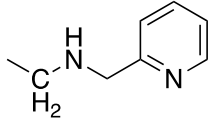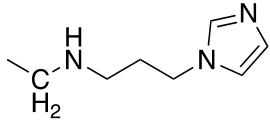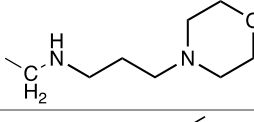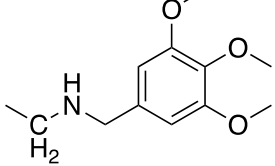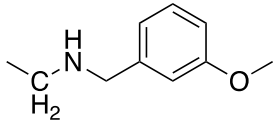
Therefore, it is reasonable that autophagy inducers had better neuroprotective effects than autophagy inhibitors or non-autophagy modulators. Besides, analogs with substituted phenyl groups also displayed trifling protection on neurons against oxidative stress, among which benzo[d][1,3]dioxole (**3.16**, EC_{50} =19.85μM) performed slightly better than anisole (**3.14**, EC_{50} =25.94μM). Overall, the p62 ligand derivatives with a heterocycle that are connected to an amine through a one-carbon linker are more likely to be a neuron protectors.

In addition to modifying the R group, we also added different substituents on two phenyl rings. The addition of 4-fluoride (**Table 13**) and 4-chloride (**Table 14**) might lead to a preferable neuroprotective effect of a compound, compared to no substitution on phenyl rings.

Table 13. The List of 2,4-Di-F Benzyloxy Analogs with Neuroprotective Effects.

Analogs 4.6 to 4.20

ID	R-groups	SH-SY5Y, Anti-peroxide induced neuron toxicity, $EC_{50}(\mu M)$	Autophagy effect LC3 turnover	Internal ID
4.6		>50	-	XIE5-2-79
4.7		13.14	+	XIE5-2-3
4.8		8.064	+	XIE5-2-14
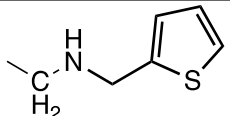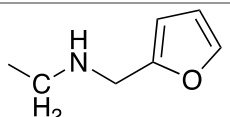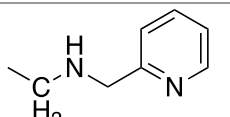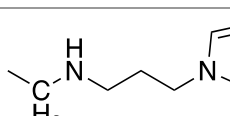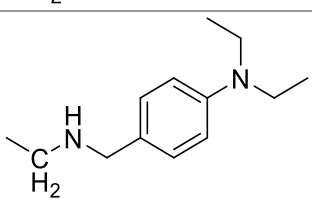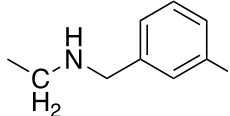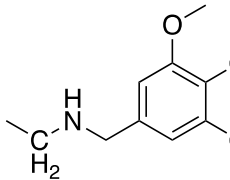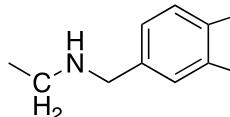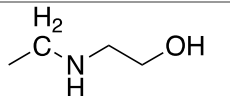
4.9		23.27	=	XIE5-2-10
4.10		14.03	+	XIE5-2-13
4.11		20.05	+	XIE5-2-7
4.15		>50	=	XIE5-2-11
4.16		14.23	=	XIE5-2-15

As shown in **Table 15**, compared to analogs in **Table 14**, the addition of 2,4-difluoride on each phenyl ring might reduce the neuroprotective effects of some compounds, including compounds with heterocyclic aromatic rings, such as thiophene (**4.7**, $EC_{50}=13.14\mu M$), furan (**4.8**, $EC_{50}=8.064\mu M$), and pyridine (**4.9**, $EC_{50}=23.27\mu M$). Compounds **4.7** and **4.8** can be identified as autophagy inducers, while analogy **4.9** did not have a significant effect on LC3B turnover. In contrast, the introduction of the addition of 2,4-difluoride may lead to an increased neuroprotective effect on some compounds, such as imidazole with a three-carbon linker (**4.10**, $EC_{50}=14.03\mu M$) and 3-methoxybenzene (**4.16**, $EC_{50}=14.23\mu M$).

Table 14. The List of 4-Fluoride Benzyloxy Analogs with their Neuroprotective Effects.
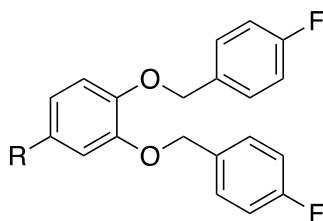
Analogs 5.7 to 5.27

ID	R-groups	SH-SY5Y, Anti-peroxide induced neuron toxicity, $EC_{50}(\mu M)$	Autophagy effect	Internal ID
5.7		3.62	+	XIE5-2-16
5.8		3.01	+	XIE5-2-1
5.9		5.618	=	XIE5-2-18
5.10		7.14	=	XIE5-2-21
5.13		>50	-	XIE5-2-22
5.14		9.21	+	XIE5-2-2
5.15		12.29	+	XIE5-2-19
5.16		7.49	+	XIE5-2-20
5.25		21.25	+	PY1-31 LP1-9B XRK3F2

As shown in **Table 14**, *4*-fluoride substitutions on phenyl rings increased the compounds' neuroprotective effects with the same R groups. For example, the analogs with heterocyclic rings, such as thiophene (**5.7**, EC_{50} = 3.62μM), furan (**5.8**, EC_{50} = 3.01μM), pyridine (**5.9**, EC_{50} = 5.62μM) and imidazole (**5.10**, EC_{50} = 7.14μM), have better EC_{50} values than compounds with the same R groups in **Table 12**. Among them, thiophene and furan performed the best to protect neurons against oxidative damage. Compound **5.9** did not influence autophagy, but **5.7** and **5.8** were indicated as macroautophagy stimulators by the LC3B conversion. For other compounds, benzo[d][1,3]dioxol-5-ylmethanamine (**5.16**, EC_{50} = 7.49μM), 1-(3-methoxyphenyl)-methanamine (**5.14**, EC_{50} = 9.21μM), and 1-(3,4,5-3-methoxybenzene)-methanamine (**5.15**, EC_{50} = 12.29μM) as R groups in compounds with *p*-fluorophenyl resulted in lower EC_{50} values compared to compounds **3.16** and **3.14**. Most of the compounds in **Table 14** that show a protective effect for neurons against oxidative damage were also identified as autophagy inducers by IB, as shown in **Figures 60** and **61**, including **5.15, 5.14** and **5.16**
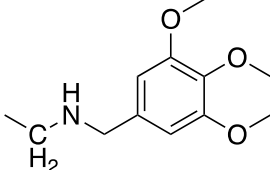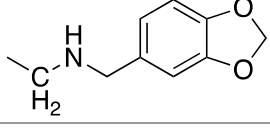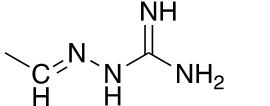
We also explored the neuroprotective effects of compounds with some other R groups since this analog in **Table 14** has the best outcome among all the analogs. The addition of 4-(aminomethyl)-*N,N*-diethylaniline group (**5.13**) led to a loss of neuroprotective effect, which may be due to the length of the compound. Moreover, the addition of an amino or hydroxyl group on the central amine did not lead to detectable neuroprotection determined by the assay. The compounds with 2-aminoethyl (**5.26**, EC_{50}=23.56μM) and 2-hydroxyethyl (**5.25**, EC_{50} = 21.25μM) groups substitutions on the amine have slight protective effects on the neurons against oxidative stress. In contrast, the compound with 3-aminopropyl substituents (**5.27**) showed no capacity for protection, which might be due to the additional carbon that increased the side chain length

Table 15. The List of 4-Chloride Benzyloxy Analogs with their Neuroprotective Effects.
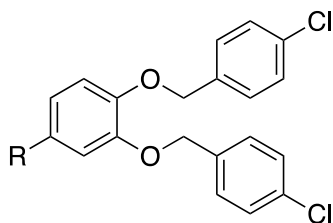
Analogs 6.6 to 6.28

ID	R-groups	SH-SY5Y, Anti-peroxide induced neuron toxicity, $EC_{50}(\mu M)$	Autophagy effect LC3 turnover	Internal ID
6.6		>50	=	XIE5-2-80
6.7		9.767	+	XIE5-2-33
6.8		6.132	+	XIE5-2-31
6.9		11.97	=	XIE5-2-35
6.10		43.05	+	XIE5-2-38
6.11		13.04	+	XIE5-2-39
6.13		>50	=	XIE5-2-9
6.14		20.33	+	XIE5-2-32

6.15	O, O, O methoxy structure; CH₂–N(H)	>50	+	XIE5-2-36
6.16	benzo[d][1,3]dioxole; CH₂–N(H)	11.23	+	XIE5-2-37
6.28	NH; C(H)=N–N(H)–C(=NH)–NH₂	>50	+	XIE5-2-68-3

Table 15 displays the analogs' activities with *p*-chlorophenyl groups, which have slightly fewer neuroprotective effects than compounds with *p*-fluorophenyl substituents in **Table 14**. First, the compounds with heterocyclic rings can still protect the neurons from oxidative damage, such as thiophene (**6.7**, $EC_{50} = 9.767\mu M$), furan (**6.8**, $EC_{50} = 6.132\mu M$), pyridine (**6.9,** $EC_{50} = 11.97\mu M$), and morpholine (**6.10**, $EC_{50} = 13.04\mu M$). Among them, compounds with furan and thiophene had the best protective effects on neurons and were identified as autophagy inducers by IB. Substance **6.9** with pyridine did not attain similar EC_{50} values as furan (**6.8**) and thiophene (**6.7**) due to the loss of activity in autophagy represented by no impact on p62 and LC3B protein levels. Second, some compounds that have substituted benzene as part of the R group showed a moderate protective effect for the neurons, for instance, analog **6.14** with a 1-(3-methoxyphenyl)-methanamine ($EC_{50} = 20.33\mu M$) and **6.16** with a benzo[d][1,3]dioxol-5-ylmethanamine ($EC_{50} = 11.23\mu M$). Some compounds with substituted benzene in R groups did not protect neurons from oxidative damage caused by the hydrogen peroxide pretreatment, such as **6.15** with a 1-(3,4,5-3-methoxybenzene)-methanamine and compound **6.13** with a 4-(aminomethyl)-*N,N*-diethylaniline. Our IB analysis showed that compounds **6.14** and **6.16** are indicated as autophagy stimulators, whereas compound **6.13** did not affect LC3B conversion.

Table 16. The List of 4-Methyl Benzyloxy Analogs with their Neuroprotective Effects.
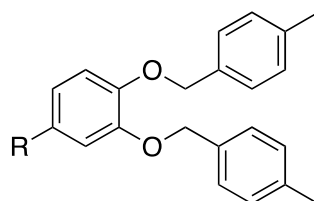
Analogs 7.7 to 7.8

ID	R-groups	SH-SY5Y, Anti-peroxide induced neuron toxicity, $EC_{50}(\mu M)$	Autophagy effect LC3 turnover	Internal ID
7.7		8.69	+	XIE5-2-59
7.8		12.29	+	XIE5-2-58
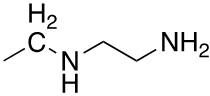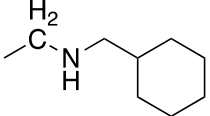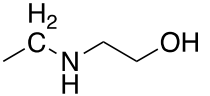
As for the p-methylphenyl derivatives listed in **Table 16**, we did not explore the neuroprotective effects for diverse R groups. Only two compounds with the R groups that possessed the most protective effects on neurons were measured. Compounds with thiophene (**7.7**, EC_{50}=8.69μM) and furan (**7.8**, EC_{50}=12.29μM) showed similar activity in **Table 12**, **Table 13**, and **Table 15**, which were lower than compounds in **Table 14**.

Table 17. The List of 1, 3, 5-Substituted Analogs with their Neuroprotective Effects.
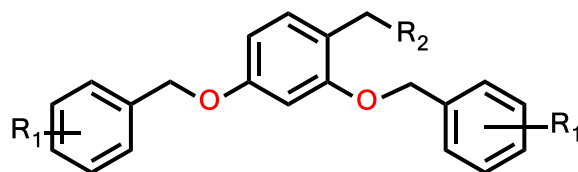
Analogs 9.26 and 10.21 to 10.27
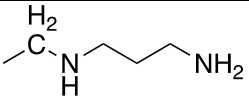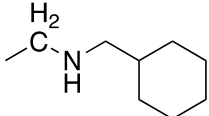
ID	R$_1$	R$_2$	SH-SY5Y, Anti-peroxide induced neuron toxicity, EC$_{50}$(μM)	Autophagy effect LC3 turnover	Internal ID
9.26	4-CH$_3$	(structure: CH_2–NH–CH$_2$CH$_2$–NH$_2$)	>50	=	XIE5-2-89
10.21	2,4-di-F	(structure: CH_2–NH–CH$_2$–cyclohexyl)	>50	+	Lp1-58
10.25	2,4-di-F	(structure: CH_2–NH–CH$_2$CH$_2$–OH)	>50	+	LP1-56

We also investigated the compounds with 1, 3, 5 substituents on the central benzene as shown in **Table 17** other than 1,3,4-substitution, involving analogs with cyclohexylmethyl (**10.21**) and 2-aminoethyl (**9.26**). They did not affect neuron growth against hydrogen peroxide.

Table 18. The List of 1,4-Disubstituted Analogs with their Neuroprotective Effects.
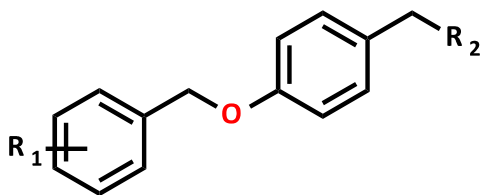
Analogs 11.21 and 11.27

ID	R$_1$	R$_2$	SH-SY5Y, Anti-peroxide induced neuron toxicity, EC$_{50}$(μM)	Autophagy effect LC3 turnover	Internal ID
11.27	2,4-di-F	$\overset{H_2}{C}$–N(H)–⟋⟍–NH$_2$	>50	-	Lp1-63
11.21	2,4-di-F	$\overset{H_2}{C}$–N(H)–CH$_2$–cyclohexyl	>50	=/-	Lp1-54

Similar tests were also performed on compounds with only two substitutions on the core benzene, as shown in **Table 18**. As we expected, compounds with cyclohexyl (**11.21**) and 3-aminopropyl (**11.27**) groups connected to the amine did not protect the SH-SY5Y differentiated neurons against oxidative injury. To summarize, almost all of our in-house p62 ligands with 2-aminoethyl, 3-aminopropyl, and cyclohexylmethyl were tested to have no neuroprotective effects, which suggested that no further cost will be recommended to put on compounds with those R groups for the treatment of neurodegeneration. Other alkyl groups are also not recommended in the development for that purpose. In contrast, it is highly suggested that derivatives with heterocyclic rings are added in R groups, improving the neuroprotective effects in almost all series of compounds. Among all the analogs we tested, compounds **5.7** (EC$_{50}$ = 3.62μM) and **5.8** (EC$_{50}$ = 3.01μM) performed the best in protecting the neurons; therefore, they are suggested for further signaling pathways studies.

In this section, we investigates whether our compound has a neuroprotective effect. First, an *in vitro* screening assay was applied to screen the neuroprotective effects of our compounds. If some compounds showed an *in vitro* neuroprotective effect, we analyzed the signaling pathways, especially the p62-related autophagic clearance of misfolded and aggregated proteins in neurons.

From the compounds that showed a positive neuroprotective effect, reasonable signaling pathways, and positive druggable physiochemical properties, we selected one or two compounds to scale up for future animal studies.

3.5. Screen of the Effects of p62ZZ Ligands on Autophagy

In addition to the neuroprotective effects of compounds, we also measured the effects of our compounds on autophagy signalings. There are three reasons for us to screen our compounds' effect on autophagy. First, our target p62 is closely involved in the macroautophagy process. Additionally, we observed that some of our compounds affected both autophagy and apoptosis in the last chapter. Moreover, we hypothesize that p62ZZ ligands can activate autophagy flux and increase the clearance of misfolded and aggregated proteins that are related to the pathogenesis of some neurodegenerative disorders. Thus, p62ZZ ligands may have a beneficial effect on treating neurodegenerative diseases.

Methods

To assess our analogs' effects on autophagy, we screened 90 compounds for their impact on autophagosome formation represented by the conversion from LC3B-I to LC3B detected by IB, as shown in **Figures 59** and **60**. Three doses for each compound were evaluated (0μM, 5μM, and 10μM). The structure-activity relationship was analyzed based on the result.

Results

Most p62 compounds can induce conversion from LC3B-I to LC3B-II, a marker for initial autophagosome formation. These compounds might be autophagy inducers or late-stage autophagy inhibitors that trigger other pathways. Some compounds did not show an obvious effect

on autophagy, and a few compounds with short functional groups (amine and alcohol) were identified as early-stage autophagy inhibitors. In most cases, the p62 protein level will not go through a significant change under the treatment of our p62ZZ ligands.

Most of our compounds can increase autophagosome formation and have a big choice to be autophagy activators. The activation of autophagic clearance is one mechanism that can degrade the misfolded and oligomerized proteins in the brain, which may be neurotoxic and a part of the pathological cause for some neurodegenerative diseases, including AD, PD, ALS, and FTLD. Therefore, these compounds that increase autophagosome count are selected for future studies in this chapter.
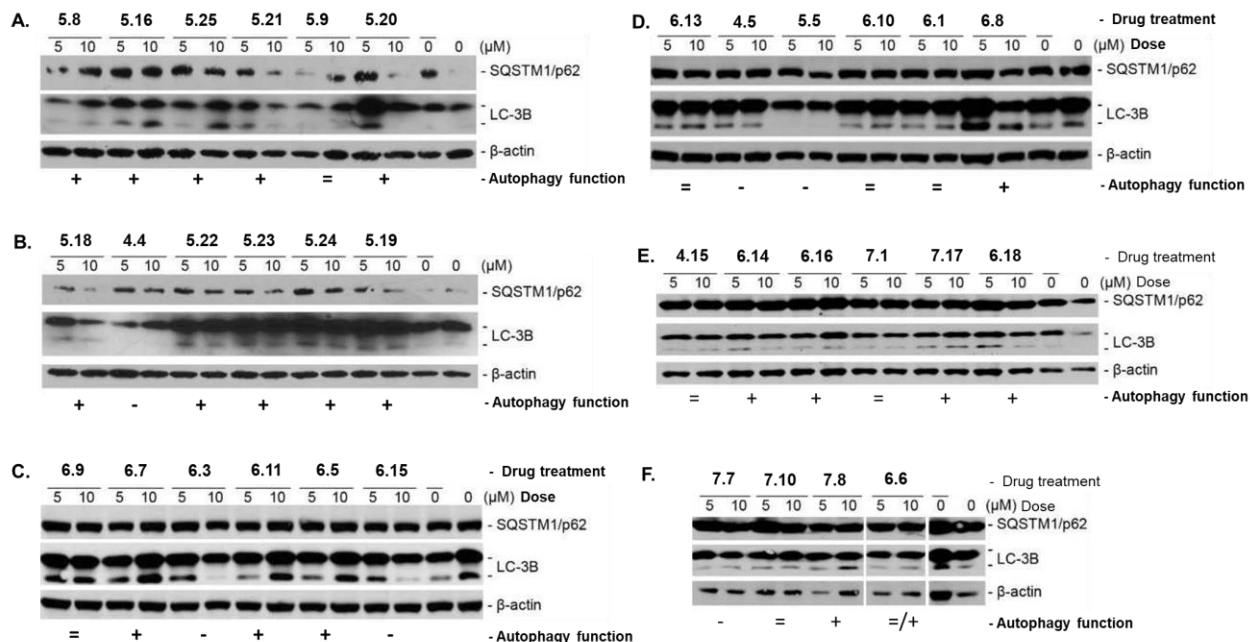
Figure 55. Profiling p62ZZ Ligands on LC3B Conversion and p62 Expression 1.

(A) Effect of analogs **5.8, 5.16, 5.25, 5.21, 5.9**, and **5.20** on autophagy. (B) Effect of analogs **5.18, 4.4, 5.22, 5.23, 5.24, and 5.19** on autophagy. (C) Effect of analogs **6.9, 6.7, 6.3, 6.11, 6.5, and 6.15** on autophagy. (D) Effect of analogs **6.13, 4.5, 5.5, 6.10, 6.1, and 6.8** on autophagy. (E) Effects of analogs **4.15, 6.14, 6.16, 7.1, 7.27,** and **6.28. (F)** Effects of analogs **7.7, 7.10, 7.8,** and **6.6.** The effects of compounds on autophagy were measured by observing LC3B conversion from LC3B-I to LC3B-II and the p62 protein level change using IB. Three concentrations of each test compound (0μM, 5μM, and 10μM) were applied to treat differentiated SH-SY5Y cells and MM1R cells for 16h. The loading control was beta-actin. Then the cell cultures were harvested for testing. The cells were treated with DMSO or without any treatment as a negative control. There are three situations in the results that represent autophagy inducer, inhibitor, or no effect on autophagy. "+" represents early-stage autophagy inducer or late-stage inhibitor in the preliminary results, which LC3B-II and p62 level increases indicate after treatment with increasing concentration of test compounds. "-" represent autophagy inhibitor, which is indicated by the lessen of p62 and LC3B level as the concentration of test compounds increases. "=" represents almost no effect on the autophagy process based on the preliminary test, which is showed by no significant changes in p62 and LC3B-I/LC3B-II level influenced by the treatment of test compounds dose-dependently.
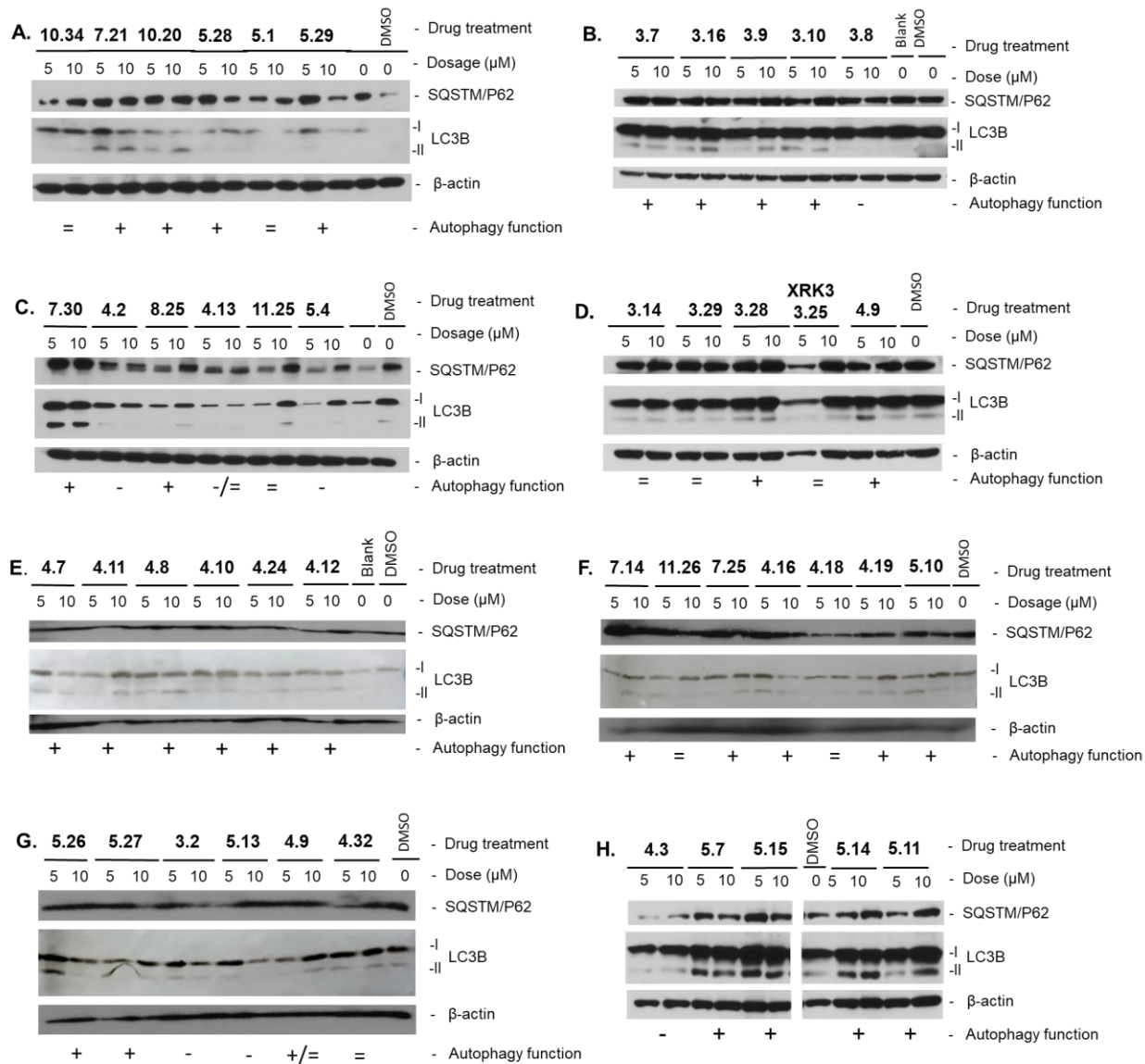
Figure 56. Profiling p62ZZ Ligands against LC3B Conversion and p62 Expression 2.

(A) Effect of compounds **10.34, 7.21, 10.20, 5.28, 5.1**, and **5.29** on autophagy. (B) Effect of compounds **3.7, 3.16, 3.9**, **3.10, 3.8**, and **5.29** on autophagy. (C) Effect of compounds **7.30, 4.2, 8.25, 4.13, 11.25,** and **5.4** on autophagy. (D) Effect of compounds **3.14, 3.29, 3.28, 3.25**, and **4.9** on autophagy. (E) Effect of analogs **4.7, 4.11, 4.8, 4.10, 4.24**, and **4.12** on autophagy. (C) The effect of analogs **4.6, 10.21, 4.21, 4.23, 5.6**, and **4.28** on autophagy. (F) Effect of analogs **7.14, 11.26, 7.25, 4.16, 4.18, 4.19,** and **5.10** on autophagy. (G) Effect of analogs **5.26, 5.27, 3.2, 5.13, 4.9, and 4.32** on autophagy. (H) The effect of analogs **4.3, 5.7, 5.15, 5.14,** and **5.11** on autophagy. Three concentrations of each test compound (0µM, 5µM, and 10µM) were applied to treat

differentiated MM1.R cells for 16h. Loading control is ß-actin. The cells were treated with DMSO as a negative control. There are three situations in the results that are represented as early-stage autophagy inducer, or late-stage inhibitor ("+"), early-stage inhibitor ("-"), or no effect ("=") on autophagy.

Discussion

Most compounds with heterocyclic rings are potential autophagy inducers represented by the LC3B-I conversion to LC3B-II. Compounds that have thiophene (**3.7, 4.7, 5.7, 6.7**, and **7.7**), furan (**3.8, 4.8, 5.8, 6.8**, and **7.8**), and morpholine (**4.11, 5.11,** and **6.11**) are potential autophagy inducers. Similarly, most compounds with imidazole are classified as potential autophagy inducers, including compounds **4.10**, **5.10,** and **6.10**. However, compounds **3.10** and **7.10** did not show a significant effect on LC3B conversion. A lack of halogen on benzyloxy might cause this result. The impact on autophagy did not influence the inhibitory activity against myeloma cells; the IC_{50} values were even lower in compounds **3.10** and **7.10** compared to molecules **4.10**, **5.10,** and **6.10.** As demonstrated above, our compounds killed the cancer cells through apoptosis signaling. The compounds that were not autophagy inducers, which in some cases promotes survival of the cells, hampering the inhibitory effects of our compounds on myeloma cell growth and proliferation, will be more potent in killing tumor cells. This assumption is consistent with our observation for compounds with imidazole. Similarly, compounds with pyridine did not affect LC3B but still possess anti-proliferative activity on MM cells.

As for compounds with substituted phenyl rings as R group, compounds with (1,3-dihydroisobenzofuran-5-yl)methanamine **(3.16, 5.16,** and **6.16),** (3,4,5-trimethoxyphenyl)methanamine (**4.15, 5.15,** and **6.15**), 4-(aminomethyl)-N,N-diethylaniline (**4.13, 5.13** and **6.13**), benzylamine (**4.12** and **5.12**), and 2-phenylethan-1-amine (**4.18, 4.19, 5.18,** and **5.19**) have the potential to be autophagy stimulators observed by the LC3B conversion. Most

compounds with (3-methoxyphenyl)methanamine were distinguished as autophagy activators, including compounds **3.14, 5.14, 6.14,** and **7.31**. Only compound **4.16** showed no significant effect on the autophagic process, which might have resulted from the additional fluoride on rings B and C. In contrast, compound **4.17** was classified as an autophagy inhibitor as the LC3B-II level was reduced by the treatment of compound **4.17**, suggesting that the length of the side chain did have an impact on the effect of compounds on the autophagic process.

We then analyzed the functions of our compounds that have alkyl groups connected to the central amine on autophagy. Most of them were identified as having the potential to be autophagy inducers, including compounds **4.21, 5.21, 7.21, and 10.21** with cyclohexylmethanamine group and compounds **4.20, 5.21, and 10.20** with cyclohexanamine. The same results were also observed in the compound **5.22** with propan-2-amine, compounds **4.24** and **5.24** that possess heptan-1-amine, as well as compounds **4.23** and **5.23** that have similar group 2-methylpropan-1-amine. Analogs of our lead compound **XRK3 (3.25)** with 2-aminoethan-1-ol, involving compounds **3.25, 4.25, 5.25, 6.25, 7.25, 10.25, 9.25, and 8.25**, were classified as potential initial-stage autophagy inducers. Compound **5.26** with ethane-1,2-diamine is likely an autophagy enhancer, whereas compound **9.26** that has the same group did not show a significant effect on autophagy, which might be caused by the transformation from 1,3,4-substitution to 1,3,5-tri-substitution on the central phenyl ring. This conversion did not influence the anti-tumor effect of compounds.

In contrast with diverse groups that linked to the central amine, which mainly led to autophagy enhancers or loss of effect on autophagy, the conversion from amine to amide afforded a different result. The compounds with amide groups either have no effect on autophagy or have an inhibitory potency on the autophagic process. For illustration, compounds **4.4, 5.4,** and **6.4** with tert-butyl carbamate and compounds **4.6, 5.6, and 6.6** with cyclohexanecarboxamide showed no

influence on the autophagic process. Compounds **4.5, 5.5, and 6.5** were all identified as early-stage autophagy inhibitors that reduce the LC3B-II level.

Other than amide, we also converted the amine to alcohol and aldehyde and evaluated their effect on autophagy. The transformation from amine to alcohol leads to early-stage autophagy blockers, as seen with compounds **3.2** and **4.2** with the methanol group. The intermediate aldehydes mainly had no impact on autophagy, including compounds **3.1, 4.1, 5.1, 6.1, 7.1,** and **8.1**. Considering the fact that they also showed a lack of anti-tumor activity against myeloma cells, the aldehyde intermediate may not have sufficient binding affinity to interact with p62 as to have their following downstream influence on other signaling pathways, such as macroautophagy. Notably, the transformation of central benzylamine to phenylethanamine also led to conversion from autophagy activators to autophagy inhibitors. Compounds **4.3, 5.2, and 6.3** that possess phenylethanamine without substitutes on amine were identified as early-stage autophagy inhibitors.

Conclusion

In sum, most of our compounds are potential early-stage autophagy activators. Furthermore, compounds with a short side chain (methanol, ethylamine, and N-ethylacetamide) in the R position are more likely to become autophagy inhibitors. Furthermore, some compounds that showed a loss of anti-MM activity were also confirmed to have no effect on autophagy. Finally, other compounds showed better anti-MM activities with no stimulating effect on autophagy compared with potential autophagy activators within the same functional group. This result may indicate that in some cases, autophagy promotes cell survival, which is not favorable for killing cancer cells.

3.6. Compound 5.8 Induces p62 Aggregation and Autophagy Flux.

The p62ZZ ligand with the best performance to protect the neurons from oxidative stress-induced damage (**5.8**, $EC_{50} = 3.01\mu M$) was selected to explore the molecular mechanism of our p62 ligand, which can have a neuroprotective effect through interaction with p62. In the above section, compound **5.8** also increases the conversion from LC3B-I to LC3B-II. To explore the molecular mechanism for compound 5.8 to protect neurons, we need to answer a few questions: 1) does compound 5.8 induce p62 oligomerization, which links the effects of compounds on p62 function to autophagy; 2) dose the compound 5.8 activate autophagy flux; 3) dose the compound 5.8 reduce the aggregation/oligomerization of amyloid-beta, alpha-synuclein, and phosphorylated tau, as we hypothesized. If compound 5.8 did show some effects as we proposed, we can do more signaling studies and propose some animal studies on this compound.

3.6.1. Compound 5.8 Induces p62 Aggregation.

Previous studies showed that p62 ligand derivatives, such as **XRK3,** can bind to the p62 protein and activate p62 oligomerization in cell lysate (149). To determine whether compound **5.8** can stimulate p62 self-oligomerization, we conducted an *in vitro* p62 oligomerization assay.

Methods

Cell extracts transiently expressing WT p62 from Sf9 cells were incubated with various concentrations of compound **5.8** or with different time courses for a fixed concentration or without treatment, followed by a non-reducing SDS-PAGE and IB. Sf9 cells were transiently transfected with plasmid DNA encoding p62/SQSTM1- his using Lipofectamine 2000 following the

manufacturer's instructions. After transfection for 24 h, cells were lysed with cell lysis buffer (16.7 mM HEPES, pH 7.4, 0.05 M KCl, 0.33 % Nonidet P-40, 3.33 % glycerol, protease inhibitor, and phosphatase inhibitor). Following a cycle of freeze/thaw, the cell suspension was incubated on ice for 30 min and centrifuged at 13,000 x g for 20 min at 4 °C. Protein concentration was determined using the Bradford assay. For the p62 oligomerization experiments, 1 µg protein was incubated with/without **5.8** (dissolved in DMSO at a final concentration of 100 mM) for 4 h. Samples were mixed with a non-reducing loading buffer containing 4 % lithium dodecyl sulfate (LDS), heated at 95 °C for 10 min, and resolved on 3 % stacking and 12 % separating SDS-PAGE. The monomer, oligomers, and aggregates of p62 were detected with the mixture of p62 and Myc antibodies, as described previously (150).

Results

As shown in **Figure 57**, compound **5.8** significantly activated *in vitro* self-polymerization of p62 in a dose- and time-dependent manner, suggesting *in vitro* self-oligomerization of p62 in cells and its targeting of autophagic vacuoles. Afterward, we tried to determine whether our compound **5.8** could induce p62 aggregation in SH-SY5Y cells. However, it is challenging to observe p62 aggregates without transiently high-expressed p62 proteins using a similar procedure. Therefore, we only performed the regular IB using a reducing loading buffer on SH-SY5Y cells for LC3B turnover and p62 expression.
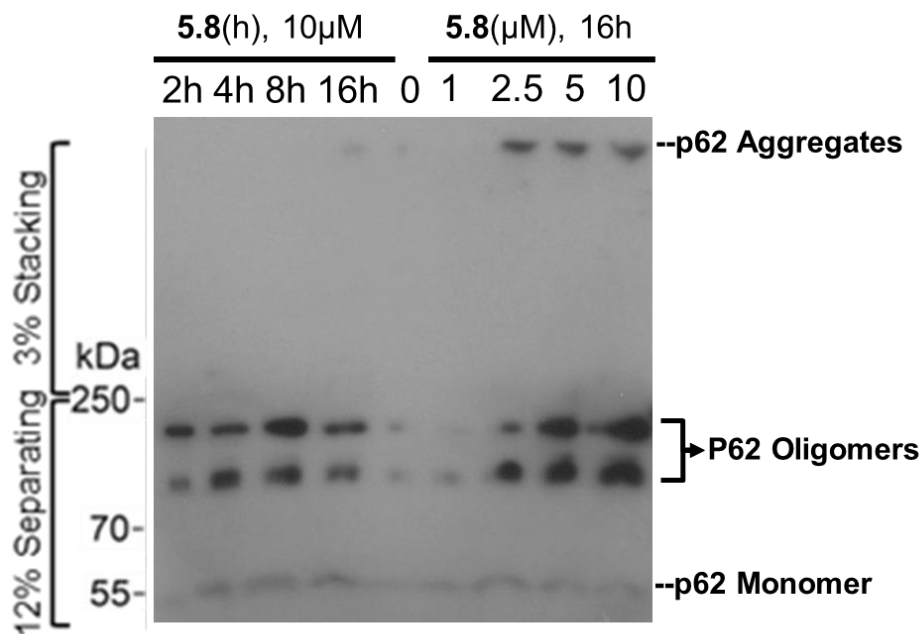
Figure 57. Compound 5.8 Induces p62 Aggregation Dose- and Time-Dependently.

An *In vitro* p62 oligomerization assay was done. Sf9 whole cell lysates containing transiently expressed p62 were incubated with compound **5.8** at various concentrations and diverse treatment duration. IB was performed to detect monomer, oligomer, and aggregate forms of p62 using p62 antibodies.

3.6.2. Compound 5.8 Induces autophagy flux.

After we confirmed that compound 5.8 activates the p62 self-oligomerization and aggregation in cell lysate, which is an important force-driven step in the autophagy process, we intended to make sure that compound 5.8 activates autophagy flux measured by IB and FM. If the compound induces autophagy flux, then it is possible that the compound can help clean the misfolded and aggregated proteins in neurons.

We confirmed compound **5.8** induced autophagosome formation and the autophagy flux using LC3B turnover assay on fully differentiated SH-SY5Y cells measured by IB (**Figure 58**)

and FM (**Figure 59**). We estimated LC3B-II degradation in autolysosomes by comparing two samples with or without lysosomal inhibitors (bafilomycin A1). As shown in **Figure 58A**, compound **5.8** increased p62 level and induced LC3B conversion from LC3B-I to LC3B-II dose-dependently. The co-treatment with 50nM bafilomycin A1 further enhanced LC3B-II levels, indicating that compound **5.8** can activate autophagosome formation and subsequent autophagy flux that leads to the autophagic clearance of misfolded and aggregated proteins in neurons. Quantitative analysis for the intensity of bands in IB was displayed in **Figure 58B**. One-way ANOVA was used to analyze the difference of protein levels induced by various concentrations of compound **5.8** treatment. We observed that compound **5.8** increases the level of p62, LC3B-I and LC3B-II significantly dose-dependently. Paired t-test was applied to analyze the difference between two samples with or without lysosome inhibitor bafilomycin A1. Significant difference and a further increase in the level of p62, LC3B-I and LC3B-II was observed, indicating the activation of autophagy flux induced by compound **5.8.**
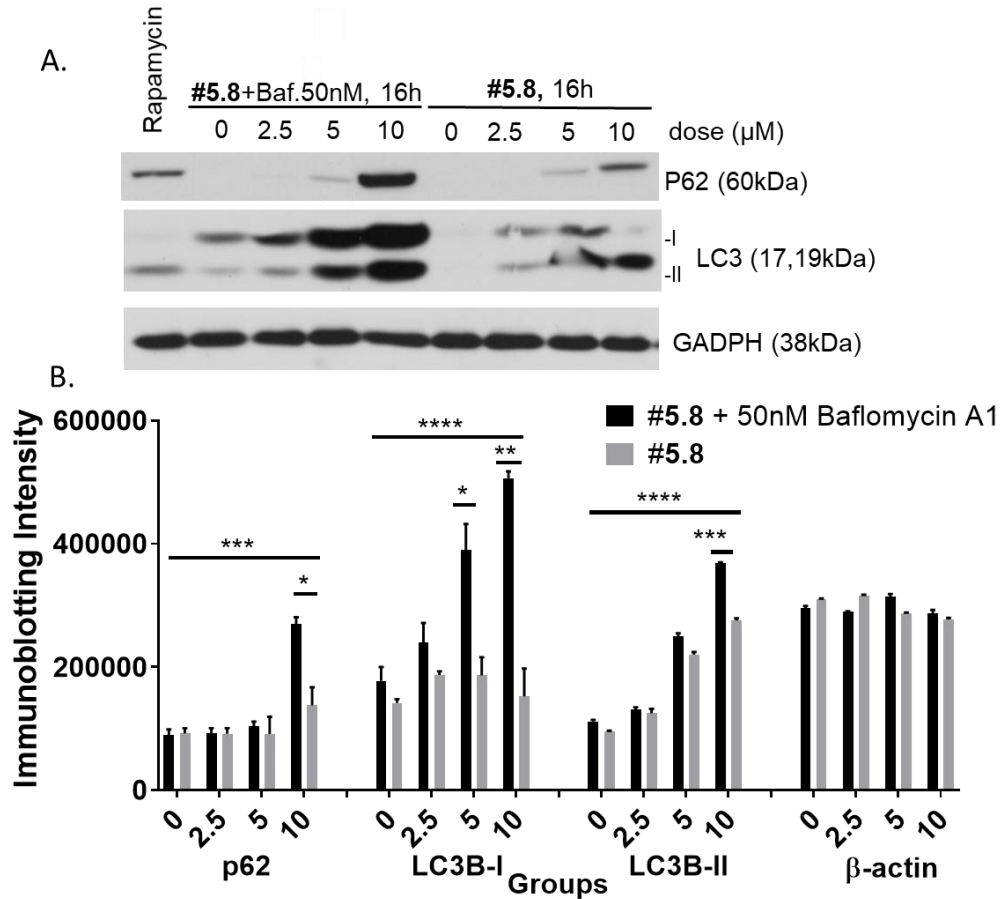
Figure 58. Compound 5.8 Induces and Autophagic Flux by IB.

Differentiated SH-SY5Y cells were treated with **5.8** at various concentrations (0µM, 2.5µM, 5µM, and 10µM) for 16h, incubated with 50nM bafilomycin A1 (lysosomal inhibitor) and a different concentration of compound **5.8** for 16h, as well as treated with 100nM rapamycin (positive control known as an autophagy inducer) for 16h. The IB was performed on a whole-cell lysate to detect p62 protein level change and LC3B turnover from LC3B-I to LC3B-II, using anti-p62 and anti-LC3B. The GADPH was applied as a loading control for neurons. One-way ANOVA was applied to analyze the significance of differences among the treatment groups. Paired t-test was used to analyze the difference of individual dose-response between the groups with and without bafilomycin A1. *, $p < 0.05$; **, $p < 0.01$; ***, $p < 0.001$; ****, $p < 0.0001$.

An immunofluorescence microscopy analysis of p62 aggregation and colocalization analysis of puncta containing p62 and LC3B showed similar results, as seen in **Figure 59**.

Differentiated SH-SY5Y cells were cultured in six-well plates with coated and sterilized coverslip in each well, treated with different concentrations of drugs with or without 50nM bafilomycin A1. Then the cells were fixed with 2% paraformaldehyde in PBS (pH=7.4) at room temperature for 15 min. After washing two times with PBS, the cells were permeabilized with 0.1% Triton X in PBS solution for 15 min. After washes with PBS three times, the cells were then incubated with blocking solution (2% BSA in PBS) for 45 min and then incubated with primary antibody (made in PBS with 0.5% BSA) overnight at 4ºC after one-time wash. The next day, the cells were washed three times with PBS and then incubated with secondary antibody for 1 h in the dark. All the procedures after that were protected from light. The cells were washed two times with PBS and then DAPI (1µg/ml) stained for 5 min. After three washes with PBS, the coverslips were mounted on slides with mounting media (0.5% N-propyl gallate and 70% glycerol). Coverslips were sealed with nail polish to prevent drying and movement under a microscope. Images were taken using a confocal fluorescence microscope.

As shown in **Figure 59**, the results demonstrated that compound **5.8** activated p62 *in vitro* by inducing its self-oligomerization, a critical step for cargo delivery in the autophagy process. SH-SY5Y cells were untreated or treated with 10µM compound **5.8** or a combination of 10µM compound **5.8** and 50nM bafilomycin A1 for 16h. Confocal immunofluorescence microscopy was utilized to determine the colocalization of p62-containing puncta with LC3-containing autophagosomes. As shown in **Figure 59**, the p62 and LC3B signals were enhanced by the treatment of compound **5.8** for 16h. When we merged the signs with DAPI, it became clear that p62 puncta (green) and LC3 (red) containing puncta are mostly colocalized, which are in different locations with DAPI (blue) spots that represent the position of the cell nucleus. p62 puncta (green) and LC3B (red) signals were colocalized in autophagosomes (yellow) in the cytoplasm. The co-

treatment with 50nM lysosome inhibitor bafilomycin A1 further increased the signals of p62 (green) and LC3B (red) containing puncta in the cytoplasm, including some axon terminal and dendrite compared to a single agent treatment, suggesting that compound **5.8** stimulated autophagosome formation and autophagy flux through the induction of p62 self-polymerization.
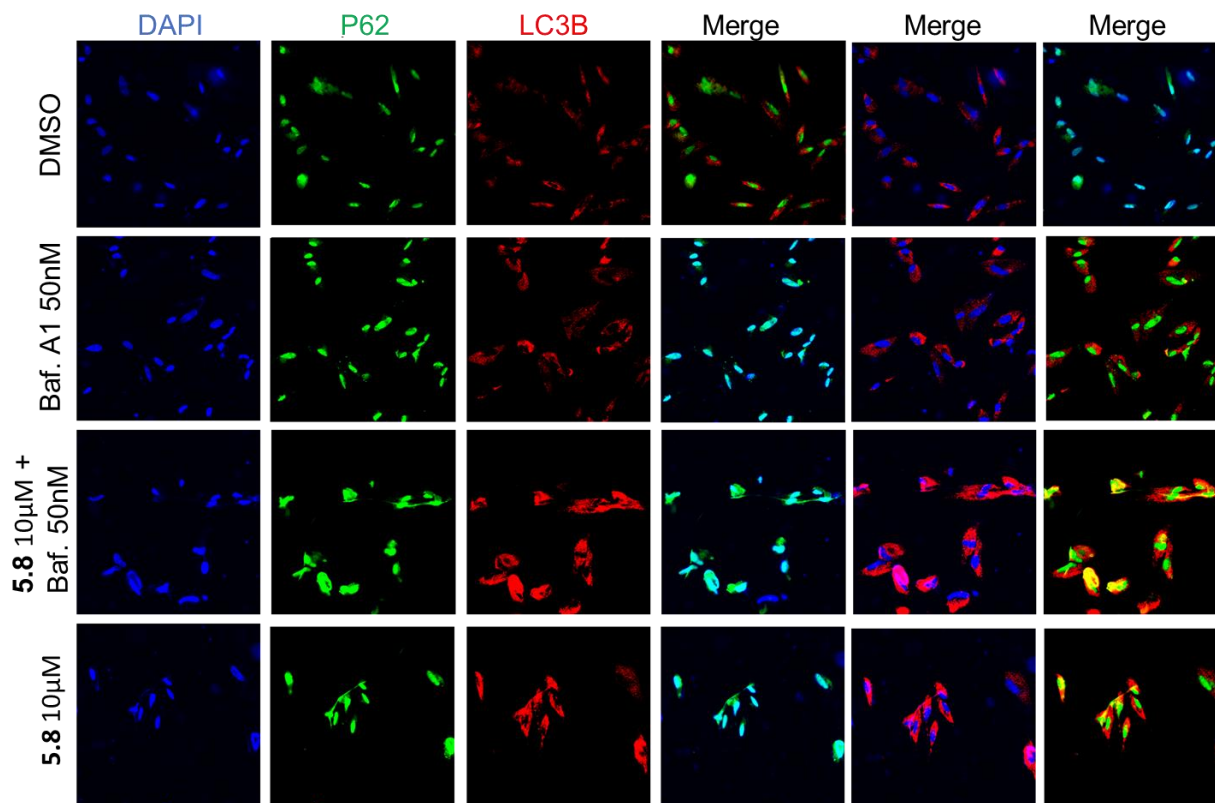
Figure 59. Compound 5.8 Induced Autophagy Flux through p62 by FM.

Confocal immunofluorescence microscopy analysis of p62 and LC3B co-localization. Ready-to-use differentiated SH-SY5Y cells were treated with 10μM **5.8**, DMSO, 50nM bafilomycin A1 as well as a mixture of 10μM **5.8** and 50nM bafilomycin A1, and then subjected to staining using an anti-p62 rabbit monoclonal antibody and anti-LC3B mouse monoclonal antibody. SH-SY5Y cells were subsequently incubated with a fluorescence-labeled secondary antibody goat anti-mouse IgG H&L (Alexa Fluor® 647, red, ab150115) and goat anti-rabbit IgG H&L (Alexa Fluor® 488, green, ab150077) from Abcam. Following that, the cells were stained by DAPI, and immunofluorescence microscopy was used to determine the colocalization of p62-containing puncta with LC3-

containing autophagosomes. This figure shows each color stain in an individual plot and merges DAPI stain, anti-LC3B stain (red), and anti-p62 fluorescence stain (green) together. Images were obtained in the phase of 20X magnification.

3.7. The Effect of Compound 5.8 on oligomerization of Aβ, p-tau and α-synuclein.

We demonstrated compound **5.8** induced autophagosome formation and subsequent autophagy flux dose and time-dependently through stimulating p62 self-aggregation by IB and FM. As for the potential therapeutic effect, we need more evidence that shows a correlation between compound **5.8** and misfolded/aggregated proteins as well as neuronal biomarkers. We assumed that compound **5.8** could induce autophagy flux and autophagic clearance of misfolded and aggregated proteins, such as p-tau, Aβ, and α-synucleins. Phosphorylated tau accumulates and forms neurofibrillary tangles (NFT), a critical biomarker for Alzheimer's disease. Unfolded α-synuclein has a propensity to form toxic soluble oligomers that aggregate into insoluble fibrils. The fibrils and amyloidal are the major components of Lewy bodies, which are linked to the pathogenesis of Parkinson's disease, Alzheimer's disease, and dementia with Lewy bodies.

As shown in **Figures 60A** and **60B**, compound **5.8** reduced the tau5 protein level and decreased α-synuclein signals while maintaining the same level of GADPH, MAP2, and β-tubulin-III as a loading control and two biomarkers for neuronal functions and features. This result suggests that compound **5.8** may induce autophagosome formation and the clearance of tau and α-synuclein and keep some neuronal typical features and functions.
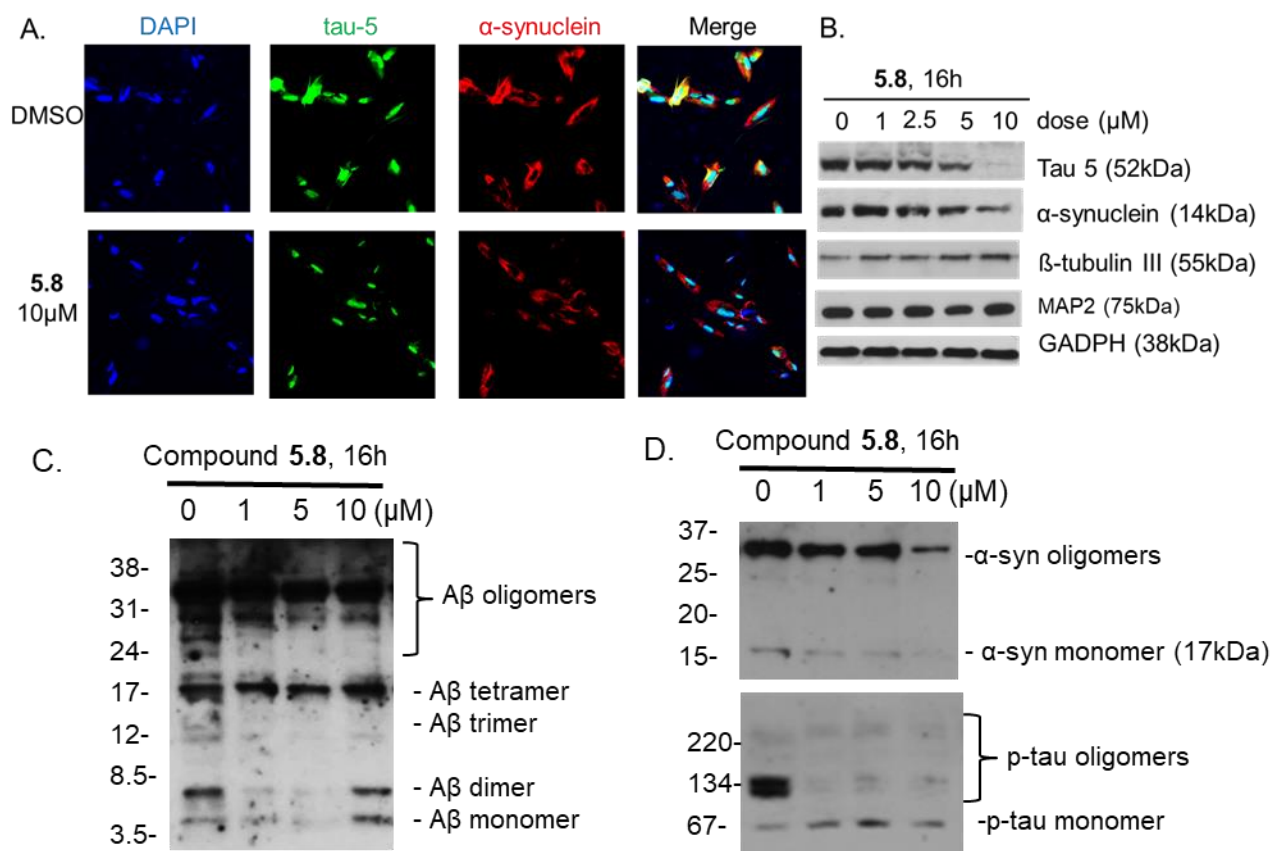
Figure 60. Effect of 5.8 reduced oligomerization of Aβ and α-synuclein by IB and FM.

(A) Immunofluorescence microscopy analysis of tau and α-synuclein colocalization. Fully differentiated SH-SY5Y cells were treated with 10µM **5.8** and DMSO and then subjected to staining using anti-Tau rabbit monoclonal antibody (TAU5, mAb, ab47579) and anti-α-synuclein mouse monoclonal antibody. SH-SY5Y cells were subsequently incubated with a fluorescence-labeled secondary antibody goat anti-mouse IgG H&L (Alexa Fluor® 647, red, ab150115) and a goat anti-rabbit IgG H&L (Alexa Fluor® 488, green, ab150077) from Abcam. Following that, the cells were stained by DAPI, and confocal immunofluorescence microscopy was used to determine the colocalization of tau-containing puncta and α-synuclein signals. This figure has one plot for each color stain and three plots that merge the DAPI stain with anti-α-synuclein staining (red), anti-tau fluorescence stain (green) with α-synuclein (red), as well as all three stains together, respectively. Images were obtained in the phase of 20X magnification. (B-D) IB. Differentiated SH-SY5Y cells were incubated with compound **5.8** at various concentrations (0µM, 1µM, 2.5µM, 5µM, and 10µM) for 16h. The IB was conducted on a whole cell lysate to detect misfolded protein tau and α-synuclein level, as well as neuronal biomarkers MAP2 and β-tubulin III level using anti-

tau, anti-α-synuclein, anti-MAP2, and anti-ß-tubulin III antibodies. The GADPH was applied as a loading control for neurons. (C/D) The oligomerization of misfolded protein Aβ, α-synuclein, and p-tau was also evaluated by IB.

An immunofluorescence microscopy analysis of misfolded proteins tau and α-synuclein showed similar results in **Figure 60A**. Alpha-synuclein polymers staining (red) did not overlap with the nucleus (blue, stained by DAPI). Tau puncta (green) overlapped with nucleus stains (blue) and α-synuclein aggregates (red), indicating that tau protein is located in both the nucleus and cytoplasm of neurons, primarily in the cytoplasm. Treatment of 10μM compound **5.8** on differentiated SH-SY5Y cells reduced the signaling and number of puncta for tau (green) and α-synuclein (red), compared to cells treated with DMSO as shown in **Figure 65A**. Simultaneously, the cell number within the view counted by nucleus numbers stained by DAPI is maintained the same or even increased. To summarize, treatment of compound **5.8** can reduce the levels of tau and α-synuclein in neurons through the activation of autophagy flux via p62 polymerization.

The oligomers of Aβ, p-tau, and α-synuclein were also measured by IB. The results were shown in **Figures 60C** and **60D.** We can see that although the general level of Aβ did not change significantly, the oligomers were slightly reduced with 10μM compound 5.8 treatment (**Figure 60C**). In addition, the oligomer for phosphorylated tau was dramatically reduced with the treatment of compound 5.8 (**Figure 60D**). Moreover, the oligomer of α-synuclein was slightly decreased by 10μM compound 5.8 treatment.

The oligomerization of the three misfolded proteins is closely related to several neurodegenerative diseases. The microtubule-associated protein, tau, is capable of self-aggregation into filamentous deposits, which are characteristic of various neurodegenerative diseases. The aggregation of tau to form NFTs is driven by phosphorylation and C-terminal truncation. A compound that hampers the aggregation of p-tau and maturation of NFTs may help

treat AD or other neurodegenerative diseases. Alpha-synuclein is also capable of self-association into toxic soluble oligomers and insoluble fibrils. The insoluble fibrils and amyloids compose Lewy bodies that are related to the pathogenesis of PD and AD. A compound that reduces the aggregation of α-synuclein may have the potential to treat PD or AD. The aggregates of Aβ in the brain were a biomarker for Alzheimer's disease. The generation, aggregation, and clearance of Aβ are correlated with the disease process. The soluble oligomer form of Aβ is neurotoxic and was identified as an important factor that caused neuron death in Alzheimer's disease patients' brains.

Therefore, our compound 5.8 that shows an effect to reduce the oligomers of misfolded protein p-tau and α-synuclein might have some beneficial effect to treat neurodegenerative disorders, such as Alzheimer's disease.

3.8. Conclusion

We investigated whether our compounds showed any neuroprotective effects by targeting p62 based on our hypothesis that p62 ligands might induce p62 polymerization and autophagy flux, which helped to clear the misfolded and aggregated proteins accumulated in neurons.

To achieve this purpose, we first established an *in vitro* cell assay to screen compounds for neuroprotective effects using fully differentiating SH-SY5Y cells pre-treated hydrogen peroxide to induce toxicity and oxidative stress. We then treated the cells with our p62-ZZ ligands for three days and measured the cell viability by an MTT assay to identify compounds with neuroprotective effects. We selected one analog to study its molecular mechanism using IB and FM from the compounds with neuroprotective effects and without cytotoxicity. More specifically, we observed that compound **5.8** increased the LC3B conversion from LC3B-I to LC3B-II, which represented an increased autophagosome count.

To further evaluate whether our compound induced autophagy flux, we compared samples with or without lysosome inhibitor treatment. We measured LC3B degradation inside autolysosome through an LC3B turnover assay using IB and FM. The results showed compound **5.8** could further increase LC3B-II level, indicating the activation of autophagy flux. Aside from the effect of compound **5.8** on p62 expression, we also detected that compound **5.8** could induce p62 oligomerization in cell lysates by IB.

Finally, we evaluated the effects of compound **5.8** on misfolded and oligomerized proteins in neurodegenerative diseases, represented by Aβ, p-tau, and α-synuclein using IB and FM. We found that compound **5.8** reduced the oligomers of Aβ, p-tau, and α-synuclein, indicating a potential of compound **5.8** for AD treatment.

4.0 Genetic Analysis of Alzheimer's Disease

4.1. Introduction

Genome-wide association scans (GWASs) allow millions of single-nucleotide polymorphisms (SNPs) to be genotyped or imputed and studied simultaneously using hypothesis-free agnostic approaches (173). Single GWAS can identify some variants associated with disease, but these variants only explain a few risk factors of diseases. As effects caused by common alleles are subtle, large sample size is needed to achieve the statistical significance to detect signals (174). Meta-analysis approaches are widely applied in genome-wide association studies to enhance the power of a single study, decrease false-positive results and reduce the limitation due to individual-level data (173). Recently, the discovery and validation of new genetic risk loci for common phenotypes were dramatically increased by the application of new technology for meta-analysis (173).

We employed a meta-analysis method to study 50 gene expression profile datasets comparing AD patients and healthy volunteers. The overall workflow for our study is illustrated in **Figure 61**. The differentially expressed genes (DEGs) were identified from each data set with a cut-off criterion and summarized as common DEGs for 50 datasets. An enrichment study for common DEGs was then explored in the Gene Oncology (GO) and Molecular Signature

Database (MsigDB). The DEGs from AD datasets were compared with DEGs induced by chemical and genetic perturbations to discover the positively and negatively associated chemical and genetic perturbations. These positively and negatively associated coding gene perturbations might be indicated as potential therapeutic targets. The negative association between the AD datasets and chemical-induced gene profile might provide some suggestions for drug reposition. When a drug induces more mRNA expression level change in a different direction compared to the influence of AD than ones in the same directions, we considered the drug is negatively associated with AD. This drug might have the potential to reverse the transcription change due to the disease progression; thus, it is possible to be a potential drug to treat the disease. We summarized the data here, and the evidence in the available clinical studies of negatively related drugs was found to have consistent results with our study.
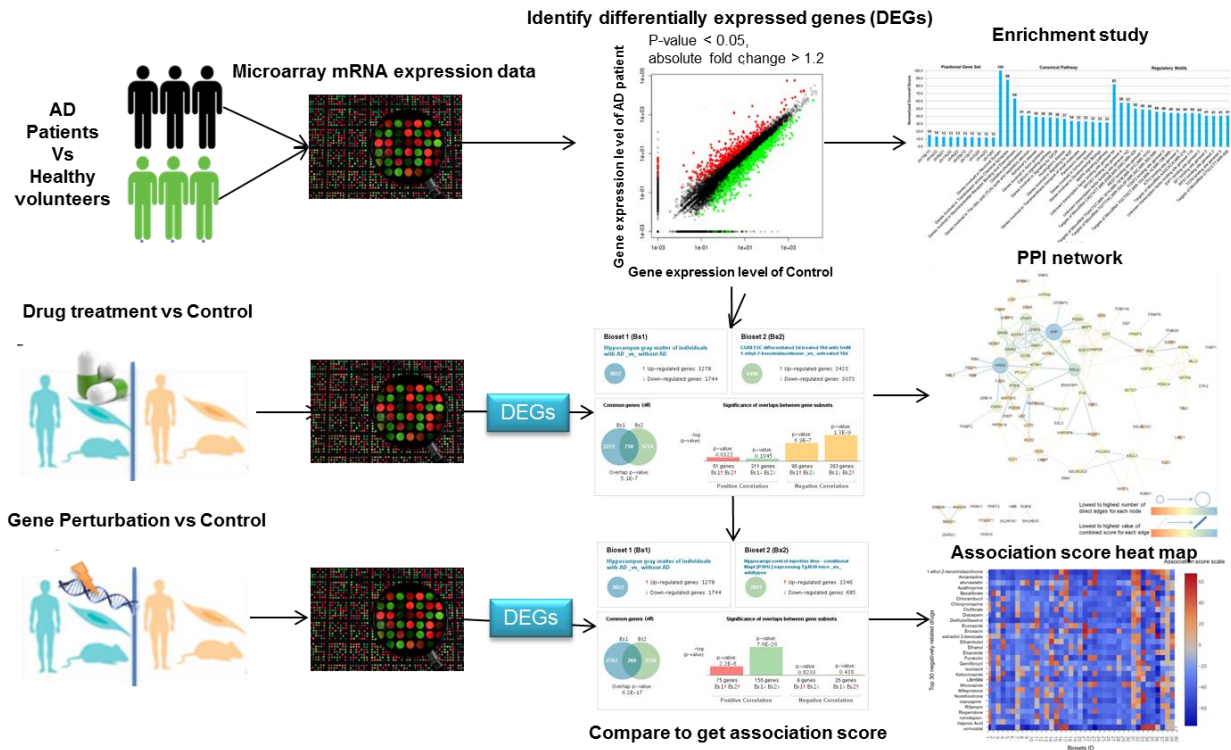
Figure 61. Workflow for this Meta-Analysis Study.

4.2. Alzheimer's Disease Datasets

We collected the AD-induced Differentially expressed genes (DEGs) from commercial software Illumina BaseSpace software (Santa Clara, CA, USA, http://www.nextbio.com) by a keyword search with "Alzheimer's disease", and refined by advanced search with experiment design "disease vs. normal", organisms "homo sapiens", and data types "RNA expression". The gene expression data in BaseSpace are mainly from Gene Expression Omnibus (GEO) (http://www.ncbi.nlm.nih.gov/geo/). **Table 19** shows the list of 40 qualified datasets that compare the RNA expression data from Alzheimer's patients with healthy donors. Their corresponding GEO ID, test sample numbers, and feature numbers are also provided. We compared the RNA expression profile in AD patients to healthy donors and obtained DEGs with p-value < 0.05 and absolute fold change > 1.2 for each bioset. The DEGs from different datasets were combined and analyzed together to afford common DEGs.

Table 19. The List of AD-Related Biosets, Features, Test Samples, and GEO IDs.

ID	Bioset Description	GEO ID	Test Samples	Feature
1	Brain RNA amplified 1x – Alzheimer patient _vs_ pooled normal donors	GSE30945	31	2133
2	Brain RNA non-amplified – Alzheimer patient _vs_ pooled normal donors	GSE30945	31	2393
3	Frontal cortex gray matter of female individuals with AD _vs_ without AD	GSE36980	79	553
4	Frontal cortex gray matter of individuals with AD _vs_ without AD	GSE36980	79	453
5	Frontal cortex gray matter of male individuals with AD _vs_ without AD	GSE36980	79	389
6	Hippocampus gray matter of female individuals with AD _vs_ without AD	GSE36980	79	2522
7	Hippocampus gray matter of individuals with AD _vs_ without AD	GSE36980	79	3052

8	Hippocampus gray matter of male individuals with AD _vs_ without AD	GSE36980	79	1824
9	Temporal lobe gray matter of female individuals with AD _vs_ without AD	GSE36980	79	1212
10	Temporal lobe gray matter of individuals with AD _vs_ without AD	GSE36980	79	1063
11	Temporal lobe gray matter of male individuals with AD _vs_ without AD	GSE36980	79	887
12	Hippocampal CA1 from incipient Alzheimer's disease patients (MMSE 20-26) _vs_ control (MMSE>25)	GSE1297	31	85
13	Hippocampal CA1 from moderate Alzheimer's disease patients (MMSE 14-19) _vs_ control (MMSE>25)	GSE1297	31	1422
14	Hippocampal CA1 from severe Alzheimer's disease patients (MMSE<14) _vs_ control (MMSE>25)	GSE1297	31	2039
15	Hippocampi from late onset Alzheimer's disease patients _vs_ healthy age-matched controls (Study: Hippocampi from late onset Alzheimer's disease (LOAD) patients)	GSE67333	8	20
16	Parietal lobe of Alzheimer's patients _vs_ healthy controls	GSE16759	16	1562
17	Temporal cortex of 8yr Microcebus murinus – AD-like (have cerebral B-amyloid plaques)_vs_healthy	GSE21779	18	1327
18	Frontal cortex synaptoneurosomes from incipient Alzheimer Disease patients _vs_ healthy controls	GSE12685	14	2058
19	CA1 hippocampal gray matter from patients with developing Alzheimer's Disease _vs_ healthy control	GSE28146	30	1714
20	CA1 hippocampal gray matter from patients with moderate Alzheimer's Disease _vs_ healthy control	GSE28146	30	2563
21	CA1 hippocampal gray matter from patients with severe Alzheimer's Disease _vs_ healthy control	GSE28146	30	3187
22	iPSC derived from fibroblasts – FAD patients with N141 mutant presenilin 2 _vs_ normal	GSE28379	4	2488
23	Hippocampus CA1 fields of late onset Alzheimer's disease patients _vs_ non-demented controls	GSE29378	63	1222
24	Hippocampus CA3 fields of late onset Alzheimer's disease patients _vs_ non-demented controls	GSE29378	63	712
25	Entorhinal cortexes from brains of post-mortem Alzheimer's disease patients _vs_ normal donors	GSE48350	253	6998
26	Hippocampuses from brains of post-mortem Alzheimer's disease patients _vs_ normal donors	GSE48350	253	7514
27	Post central gyruses from brains of post-mortem Alzheimer's disease patients _vs_ normal donors	GSE48350	253	3744

28	Superior frontal gyruses from brains of post-mortem Alzheimer's disease patients _vs_ normal donors	GSE48350	253	7561
29	Cortical tissue from Alzheimer's disease patients _vs_ normal parietal cortex	GSE15222	363	3110
30	Cortical tissue from female Alzheimer's disease patients _vs_ female normal parietal cortex	GSE15222	363	8763
31	Cortical tissue from male Alzheimer's disease patients _vs_ male normal parietal cortex	GSE15222	363	5015
32	iPSC derived from fibroblasts of subjects with familial Alzheimers _vs_ control cell lines	GSE34879	38	6177
33	iPSC derived from fibroblasts of subjects with familial Alzheimers _vs_ non-demented	GSE34879	38	1468
34	Neurons differentiated from iPSC derived from subjects with familial Alzheimers _vs_ non-demented	GSE34879	38	1411
35	Dermal fibroblasts in culture – sporadic Alzheimer's disease _vs_ healthy	GSE42492	13	697
36	Induced pluripotent stem cell-derived neurons in culture – sporadic Alzheimer's disease _vs_ healthy	GSE42492	13	5526
37	PBMCs from patients with Alzheimers disease _vs_ mild cognitive impairment	GSE18309	9	243
38	PBMCs from patients with Alzheimers disease _vs_ normal individuals	GSE18309	9	381
39	Cortical lesions of Alzheimers disease patients _vs_ cortex of healthy controls	GSE32645	12	197
40	Entorhinal cortex of Alzheimers disease patients _vs_ normal controls	GSE26927	118	318

4.3. Common Differentially Expressed Genes Identified in AD Datasets

Table 20 listed the top 30 common DEGs among the 40 AD biosets with their corresponding Gene ID, description, overall gene score, and the number of negative and positive associations in 40 datasets. The results are ranked according to the overall gene score provided by BaseSpace, which is calculated based on statistical significance and consistency of genes across the input datasets. This calculation will take a significant difference (p-value<0.05), a fold change for each related dataset, and the specificity (the number of datasets in which the gene was

222

significantly differentially expressed) into consideration. The top-ranked gene with significance was given a score of 100. All the other genes will have their score normalized according to the significant gene.

Table 20. Common Differentially Expressed Genes Shared by Alzheimer's Disease Sets

Gene	Entrez Gene ID	Gene Description	Specificity	Overall gene score	N	P
NCALD	83988	neurocalcin delta	21 out of 40	1620.593	18	3
ENSA	2029	endosulfine alpha	21 out of 40	1318.351	17	4
SCN3B	55800	sodium channel, voltage-gated, type III, beta subunit	20 out of 40	1390.593	18	2
TRIM36	55521	tripartite motif containing 36	20 out of 40	1364.084	18	2
OLFM1	10439	olfactomedin 1	19 out of 40	1168.766	15	4
AEBP1	165	AE binding protein 1	19 out of 40	1152.311	1	18
RAB6A	5870	RAB6A, member RAS oncogene family	19 out of 40	1082.909	17	2
RAP1GDS1	5910	RAP1, GTP-GDP dissociation stimulator 1	19 out of 40	1058.995	17	2
RAB15	376267	RAB15, member RAS oncogene family	19 out of 40	1052.349	18	1
ATP2A2	488	ATPase, Ca++ transporting, cardiac muscle, slow twitch 2	19 out of 40	1002.129	16	3
ATP6V1G2	534	ATPase, H+ transporting, lysosomal 13kDa, V1 subunit G2	18 out of 40	1296.968	17	1
ITGB4	3691	integrin, beta 4	18 out of 40	1255.37	2	16
ITPKB	3707	inositol-trisphosphate 3-kinase B	18 out of 40	1255.282	1	17

SLC17A7	57030	solute carrier family 17 (sodium-dependent inorganic phosphate cotransporter), member 7	18 out of 40	1146.324	17	1
AP1S1	1174	adaptor-related protein complex 1, sigma 1 subunit	18 out of 40	1138.012	16	2
HOMER1	9456	homer homolog 1 (Drosophila)	18 out of 40	1107.148	14	4
CALD1	800	caldesmon 1	18 out of 40	958.5765	4	14
RASL10A	10633	RAS-like, family 10, member A	18 out of 40	898.9544	2	16
SYNGR1	9145	synaptogyrin 1	18 out of 40	868.4472	12	6
CD44	960	CD44 molecule (Indian blood group)	17 out of 40	1357.168	3	14
CACNG3	10368	calcium channel, voltage-dependent, gamma subunit 3	17 out of 40	1290.401	16	1
AHNAK	79026	AHNAK nucleoprotein	17 out of 40	1195.087	3	14
ENC1	8507	ectodermal-neural cortex 1 (with BTB-like domain)	17 out of 40	1171.206	14	3

Note: N-negatively associated gene number; P-positively associated gene number. Overall association score calculated by BaseSpace. Gene Name highlighted in red; the genes encode proteins functions or locates in the brain and neurons. Gene Name highlighted in green; the genes encode ion channels. Gene Name highlighted by green and EntrezGene ID highlighted in red; genes encode ion channels that functions in neurons or are associated with the neuronal system.

Among the top-ranked genes, there are several genes closely related to neuron functions and synaptic activity, such as NCALD, SCN3B, OLFM1, SLC17A7, HOMER1, SYNGY1, AHNAK, and ENC1. NCALD encodes a member of the neuronal calcium sensor family of calcium-binding proteins, which plays a role in the G-protein-coupled receptor (GPCR) signal transduction. When the intracellular calcium level is enhanced, the cytosolic protein at the resting

level will interact with membranes and co-localize with the trans-Golgi network, inducing the downstream signaling. SCN3B encodes the beta subunit of one voltage-gated sodium channel that is responsible for action potential generation and propagation in neurons and muscles. OLFM1 encodes a protein with unknown functions abundant in the brain and might be necessary for neuron function. SLC17A7 encodes a sodium-dependent phosphate transporter highly expressed in the brain, which is likely related to synaptic vesicles membranes and functions in the glutamate transporter. HOMER1 encodes one of the homer families of dendrite proteins that regulate metabotropic glutamate receptor function. A protein encoded by SYNGR1 might regulate the localization of synaptophysin into synaptic-like microvesicles and therefore help microvesicle formation and maturation, thereby contributing to synaptic plasticity modulation and exocytosis regulation. AHNAK encodes a scaffold protein that may play a role in a variety of biological processes as neuroblast differentiation, blood-brain barrier formation, cell migration, and calcium channel regulation. ENC1 encodes an actin-binding protein that regulates neural crest cell differentiation and neuronal process formation. The protein encoded by CACNG3 can modulate the gating properties of the α-amino-3-hydroxy-5-methyl-4-isoxazolepropionic acid receptor (AMPAR), an ionotropic transmembrane receptor for glutamate that mediates fast synaptic transmission in the CNS through stabilization of calcium channel in inactivated states.

Pathway Names   **Normalized Overall Score**

GO Pathway

Pathway	Score
mitochondrial membrane	30.8
energy derivation by oxidation of organic compounds	31.4
envelope	32.3
regulation of neurological system process	32.7
cytoplasmic vesicle membrane	33.0
regulation of transmission of nerve impulse	33.2
cytoplasmic vesicle part	33.3
neuronal cell body	33.5
passive transmembrane transporter activity	34.5
postsynaptic membrane	35.5
cell part morphogenesis	38.9
single-organism behavior	39.0
regulation of ion transport	39.5
cell morphogenesis involved in neuron differentiation	39.5
synaptic membrane	42.6
cell junction	44.3
neuron projection development	44.5
membrane-bounded vesicle	44.8
cell projection part	45.2
cytoplasmic membrane-bounded vesicle	45.3
cytoplasmic vesicle	45.9
vesicle	45.9
neuron development	46.4
neuron differentiation	46.5
axon	46.9
cell-cell signaling	48.2
dendrite	50.5
synaptic transmission	55.1
synapse	76.3
neuron projection	87.5
transmission of nerve impulse	98.2
multicellular organismal signaling	

Broad MSigDB Regulatory Motifs

Pathway	Score
Targets of MicroRNA GTGCCTT,MIR-506	26.1
TCF8 binding site geneset 5	25.8
RFX1 binding site geneset 2	25.8
SF1 binding site geneset 2	26.0
E4F1 binding site geneset 2	27.8
Unknown transcription factor binding site geneset 119	28.2
Targets of MicroRNA AAGCACA,MIR-218	28.2
ATF3 binding site geneset 3	28.2
Targets of MicroRNA TGCTGCT,MIR-15A,MIR-16,MIR-…	28.4
FOXF2 binding site geneset 3	29.1
Targets of MicroRNA TGTTTAC,MIR-30A-5P,MIR-…	29.4
Targets of MicroRNA TGAATGT,MIR-181A,MIR-…	30.9
REST binding site geneset 1	31.2
Targets of MicroRNA CAGTATT,MIR-200B,MIR-…	32.0
Unknown transcription factor binding site geneset 142	36.6
MYOD1 binding site geneset 4	37.0
Unknown transcription factor binding site geneset 64	52.3

Broad MSigDB Canonical Pathway

Pathway	Score
MAPK signaling pathway	20.2
Genes involved in Developmental Biology	20.4
Genes involved in Immune System	20.6
Parkinson's disease	21.2
Genes involved in Transmembrane transport of small…	21.3
Genes involved in Signalling by NGF	21.6
Huntington's disease	23.3
Genes involved in Signaling by GPCR	24.0
Calcium signaling pathway	24.5
Genes involved in Axon guidance	24.7
Alzheimer's disease	24.8
Genes involved in The citric acid (TCA) cycle and…	25.9
Oxidative phosphorylation	26.1
Genes involved in Neurotransmitter Receptor Binding…	40.5
Genes involved in Transmission across Chemical…	56.2
Genes involved in Neuronal System	63.7

Broad MSigDB Positional Gene Set

Pathway	Score
chr1q42	7.6
chrxq22	7.6
chr2q32	7.6
chr12p13	7.9
chr20p12	8.0
chr8q22	8.1
chr14q32	8.2
chr6p21	8.2
chrxp22	8.6
chr19p13	9.8

0.0   20.0   40.0   60.0   80.0   100.0

Figure 62. Pathway Enrichment for Commonly Differentially Expressed Genes

The Gene Ontology (GO) Consortium's enrichment study results were shown in **Figure 62** according to a normalized score. The GO pathways related with cellular component and molecular function are identified for a close association with DEGs from AD biosets, for example, synapse, dendrite, axon, vesicle, synaptic membrane, cell projection part, postsynaptic membrane, neuronal cell body for neuron structure; transmission of nerve impulse, neuron projection, synaptic transmission, neuron differentiation and development, neuron projection development, cell morphogenesis involved in neuron differentiation, regulation of transmission of nerve impulse, and regulation of neurological system process for neuron function. In addition to the neuron-related pathways, pathways that regulate mitochondrial function and oxidative stress, as well as ion channels and transporters, are also emphasized here.

An enrichment study from the Molecular Signatures Database (MsigDB) from the Broad Institute provided a similar result. The gene sets in the MsigDB are divided into eight major collections and several sub-collections. Here, the study mainly focuses on C1, C2, and C3, which are positional gene sets, curated gene sets, and motif gene sets, respectively. Positional gene sets corresponding to each human chromosome and each cytogenetic band location that has at least one gene set. Gene sets were curated from various sources such as online pathway databases and the biomedical literature, including two sub-collections, chemical and genetic perturbations (most from literature) and canonical pathways (from online pathway databases). We mainly analyzed gene sets in canonical pathway sub-collections. C3 contains gene sets representing potential targets of regulation by transcription factors or microRNAs. The sets consist of genes grouped by short sequence motifs they share in their non-protein-coding regions. The C3 collection is divided into two sub-collections: microRNA targets and transcription factor targets.

From positional gene sets result, we can find that the 13th band in human chromosome #19 is most associated with AD DEGs. When we analyzed the result from CP, a similar result was discovered as one from the GO pathway; the neuron system function and cellular components are highly associated with the gene expression level of Alzheimer's patients. In the meanwhile, neurodegenerative diseases, such as Alzheimer's, Parkinson's, and Huntington's, are also identified here for their close association with AD, which might be due to the similar pathological signaling pathways and fundamental molecular mechanisms shared by these neurodegenerative diseases. In addition, the expression of proteins involved in some basic physiological systems regulations, such as the TCA cycle, transporters, calcium signaling, immune response, and oxidative phosphorylation, are influenced by AD progression.

As shown in **Figure 62**, regulatory motifs are harder to analyze as they do not code proteins directly; they modify protein transcription. They can be divided into two parts, transcription factors, and microRNA (one of the most important post-transcriptional regulators). MicroRNAs have lower toxic effects than other gene silencing methods, thus enhancing the expression of defensive miRNA that could be an effective therapy against neurodegeneration, including AD. In our analysis, miR-200 family perturbation has a close association with AD, which is consistent with the latest report. Scientists in Japan found miR-200 family (miR-200b, -200c, and -429) might have defensive effects that reduce the secretion of Aβ and prevent Aβ-induced cognition function impair via insulin signaling in Alzheimer's models (175). MiR-181 family (a, b, c, and d), miR-30 family (a, b, c, d, and e), miR-15a, b, -16, -195, -424, and -497 family, miR-218, and miR-506 were also identified with association to AD in our study. The miR-181 family was reported to be closely associated with AD pathology. MiR-181a was involved in hippocampus-dependent memory formation in an 8-week male C57BL/6J mice (176). MiR-181c was confirmed to be

downregulated by Aβ in primary human astrocytes cultures (177), and miR-181c expression level is negatively associated with AD progression in the cortex (178) and cerebrospinal fluid (CSF; 188, 189). However, the expression of miR-181b was significantly up-regulated in blood mononuclear cells from sporadic AD patients confirmed by qPCR, indicating a potential application of miR-181b as a predictive marker for AD (179). Another study showed an upregulation of miR-181b in the temporal cortex from schizophrenic patients that might contribute to the dysregulation of cortical gene expression (180). Downregulation of miR-15 was also found in the cortex (178) and CSF (181, 182) of AD patients. A group from Iran conducted a meta-analysis comparing differentially expressed mRNA and microRNA from AD compared to health datasets and constructed an association network by cyTargetLink with combined dates from TargetScan and MicroCosm VS. MiR-30a was identified as a network hub that regulates most genes involved in AD pathology, which is similar to our result that perturbation of miR-30 might induce many mRNA expression changes associated with AD (183). MiR-30a-5p was reported to act as a post-transcriptional regulator for brain-derived neurotrophic factor (BDNF) in the prefrontal cortex (184). The transcription factor REST silences neuronal gene expression in non-neuronal cells. REST translocates to the nucleus, occupies RE1 repressor sequences, and decreases neuronal gene expression (185). MiR-218a is highly expressed in embryonic cranial and spinal motor neurons in the developing and mature CNS of zebrafish brains (185), and its expression demonstrated an association with Huntington's disease processing (185). The enrichment of miR-218 in motor neurons makes it a useful biomarker for motor neurons degenerative diseases, such as ALS (186) and Huntington's disease (HD). MiR-506 was found to be negatively associated with the gene profile from the AD cortex (187).

4.4. Calculation of Gene Signature Correlation.

The association between different gene profiles is determined by combining a rank-based enrichment statistic, meta-analysis, and biological ontologies provided by the BaseSpace software (188-190). BaseSpace collects gene expression data from heterologous platforms and sources with different species and identifiers, and they tagged them with their corresponding ontology terms. They then translated the gene signatures from different sources into a universal NCBI GEO gene reference that relied on a standard gene dictionary and assigned them into preprocessed clusters according to a cross-organism dictionary to ensure the data are comparable. "*Rank-based enrichment statistics were applied to compute pairwise correlation scores between all signatures followed by a meta-analysis to compute individual signature-ontology concept correlation scores*" (188). All BaseSpace analyses were done utilizing the default parameters. The pairwise correlation score's magnitude reflected the similarity of the two signatures, which is measured by the extent that the genes in one signature set are enriched at the top ranks of the other signature set, and vice versa.
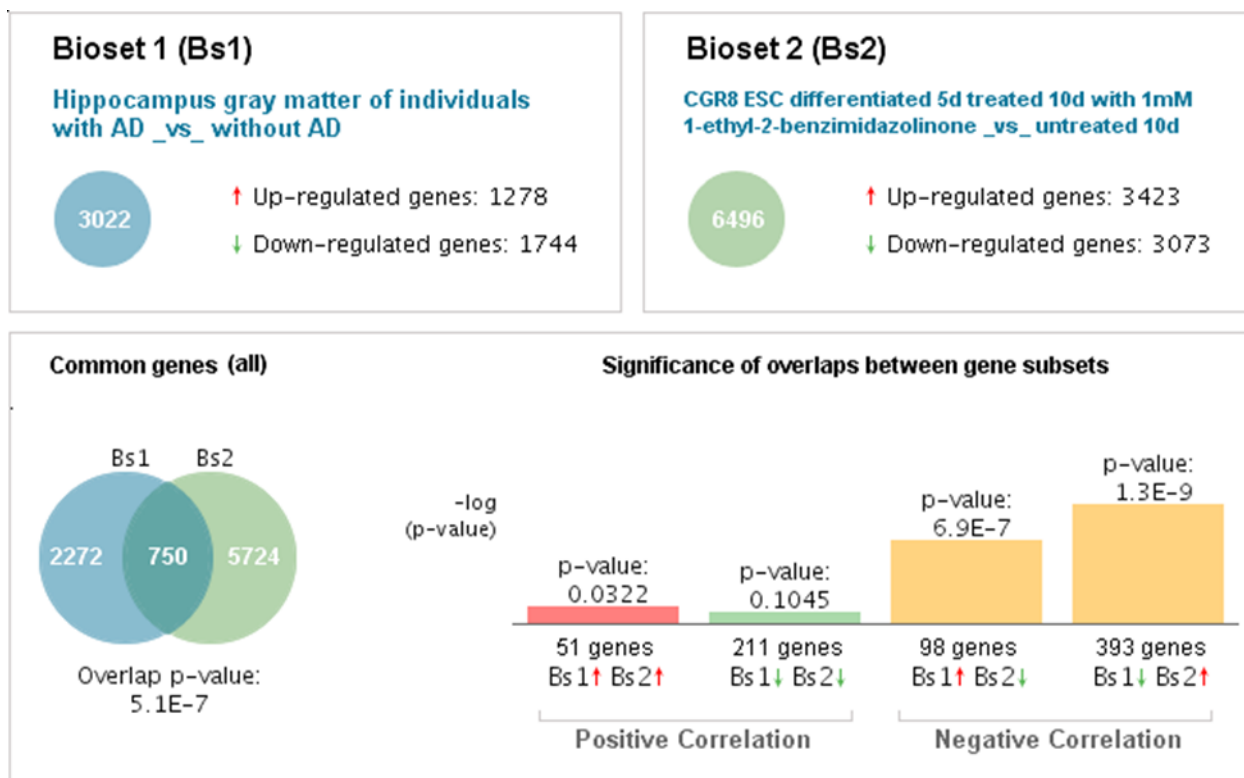
Figure 63. The Association between AD-Induced and Chemical-Induced Gene Profiles

The DEGs of each AD dataset were used as input to search against other gene expression datasets in BaseSpace to identify the highly associated gene profiles induced by chemical and genetic perturbations through Pharmaco Atlas search Knockdown Atlas search, respectively. Pharmaco Atlas contains agents-induced DEGs, while the Knockdown Atlas archives the DEGs influenced by single-gene perturbations, including gene knockdown, knockout, mutation and overexpression.

As illustrated in **Figure 63**, the association between gene signature from hippocampus gray matter of AD individuals and 1-ethyl-2-benzimidazolinone-induced gene profile in CGR8 cell line after 5-day of differentiation was calculated. Bs1 (AD individual_vs_without AD) and Bs 2 (CGR8 differentiated 5 d treated 10 d with 1 mM 1-ethyl-2-benzimidazolinone_vs_untreated 10 d) shared 750 common DEGs with an overlap p-value of $5.1E^{-7}$. The up-regulated and down-regulated genes

in bs1 and bs2 datasets were divided into four directional subsets bs1$^+$(1278 DEGs), bs1$^-$(1744 DEGs), bs2$^+$(3423 DEGs), and bs2$^-$(3073 DEGs). The correlation scores were calculated for b1$^+$b2$^+$, b1$^+$b2$^-$, b1$^-$b2$^+$, and b1$^-$b2$^-$, with p-values of 0.0322, 0.1045, 6.9E^{-7}, and 1.3E^{-9}, respectively, indicating more common DEGs in different directions. Pairwise correlation scores computed for directional subsets are positive where subsets are of the same direction and negative sign otherwise. The correlation scores of four subsets are taken together to attain a final score for b1 vs b2 (188). Here, the final correlation score for bs1 and bs2 is negative.

4.5. Enrichment Analysis for Common DEGs shared by AD datasets

A pathway enrichment study can also be done by comparing AD-induced DEGs and pathways from molecular signatures databases, such as MsigDB (191) and GO (192). The result was ranked by normalized overall biogroup score, as shown in **Figure 62**. The enrichment biogroup scores were calculated based on the overall significance and consistency of the enrichment or overlap between the sets of genes that made up a biogroup and the input query biosets. The results are normalized according to the significant top-ranked biogroup, which received a score of 100. The top 10 positional gene sets, canonical pathways, and regulatory motifs in Broad MsigDB are displayed in **Figure 62**. As AD is a progressive neurodegeneration, we found that neuronal system or disease-related pathways, such as genes involved in the neuronal system, neuron transmission, transmitters, axon and NGF signaling, AD, Huntington's, and Parkinson's disease were identified with highly significant associations in canonical pathways. In addition, some fundamental biological or physiological processes, including oxidative phosphorylation, tricarboxylic acid

(TCA) cycle, immune system, and MAPK signaling, can also be found on the highly associated list, indicating the important role of these processes in the disease condition.

4.6. Positive and Negative Correlated Genetic Perturbations.

We identified the significantly related genetic perturbations with each AD dataset through the Knockdown Atlas function in BaseSpace. As shown in **Table 21**, the connected gene perturbations from 50 datasets were used to identify and rank the highly positive and negative correlated gene perturbations, including gene knockdown, knockout, overexpression, and mutation. The positive correlation implies that most downstream gene expression level changes (DEGs) are caused by modifying a single gene that shared the same trend with AD-induced gene profile change. If a knockdown or knockout gene has a positive association with AD, then this gene's function might be impaired during the disease process. Thus, enhancing this gene's expression level or function might help to reverse the disease process. Otherwise, if a gene's overexpression will induce a similar gene signature as AD, blocking the protein encoded by this gene or affecting the regulation of transcription by this gene might help treat the disease. On the other hand, a negative association between a single gene knockdown/knockout and AD suggests that knock out this gene will lead to a majority of DEGs with different directions with DEGs induced by AD. It indicates that inhibiting the protein encoded by this gene or blocking this gene transcription might benefit the disease.

233

Table 21. The Top-Rated Associations between Gene Perturbations and AD.

Gene Knockdown			Gene Knockout			Gene Mutation			Gene Overexpression		
Gene ID	N	P	Gene ID	N	P	Gene ID	N	P	Gene ID	N	P
SETD7	15	0	FZD3	23	1	491333	24	2	MYT1L	23	3
ZNF581	15	2	LCP2	21	6	CHMP2B	22	5	POU3F2	22	3
PRRX1	14	4	ALDH1B1	19	2	LMO1	18	2	SOX5	21	1
SATB1	14	2	LAT	18	3	ADAMTS9	17	4	HOXA5	21	2
TSHZ3	14	1	LCK	18	4	MED12	17	2	ASCL1	20	2
ZIC1	14	0	REST	12	0	GNA11	16	4	NEUROG1	20	3
CNBP	13	1	CCR5	11	1	RARA	15	3	POU2F1	19	1
FOXQ1	13	1	PRMT5	10	1	PML	14	1	POU3F1	19	1
IRX6	13	1	Rela	10	2	ras	14	2	EBF3	19	2
ELL3	12	0	MKL2	9	2	SMN2	14	7	CHAT	18	1
TMED9	12	1	MLL2	9	2	TAL2	14	2	mir-124	18	1
BHLHE40	11	2	PNPLA2	9	0	HOXA	13	3	SMN2	17	3
FOXD4L6	11	1	IRAK1BP1	8	0	TLX3	12	1	MIR125A	16	2
LRPPRC	11	0	MIR181A1	8	6	FGFR1	11	5	CEMP1	14	1
PQBP1	11	2	MIR181B1	8	6	H3F3A	11	2	NEUROG2	14	1
RPL7	11	0	NTRK2	7	0	TMPRSS2	11	0	DUX4	14	2
TRIM25	11	1	PDE10A	7	2	GNAQ	10	4	MIR125B1	12	1
Chd5	10	0	BNIP3L	6	1	PDE6B	10	2	HESX1	12	5
MLXIP	10	0	BATF3	6	2	TENM1	10	1	ZNF521	12	5
BNC2	10	1	RRN3	1	26	HBB	10	26	FOXD4L1	12	6
MYT1	2	20	GNAS	1	25	TRR	1	25	Htt	4	31
MCPH1	2	17	PPT1	1	23	TYR	1	25	MAPT	0	21
ZNF282	0	16	PELP1	2	22	GRN	6	25	ENPP2	2	18
PRMT8	2	16	PEX5	0	21	GUSB	3	24	ETV2	0	16
RMST	3	15	SRRM4	1	21	Htt	4	24	LPAR1	0	16
EI24	4	14	STAR	0	20	APP	2	22	VSX2	1	15
SIX4	1	12	INSM1	1	20	FSHR	2	22	NTRK1	2	13
MIR7-1	0	11	Gm98	6	20	PSEN1	1	21	MIR22	0	12
TUT1	2	11	CHD7	5	18	TDP2	1	21	LPAR3	1	12
PHB	3	11	PCDH12	1	16	GTPBP2	1	20	MIR520G	2	12
SPINK1	3	11	PTCH1	1	16	MAPT	1	20	HOXC9	3	12
SPINT1	3	11	FUS	0	15	UNC93B1	5	20	PDGFC	0	11
GRB14	0	10	PTEN	1	15	SOD1	0	19	GATA2	1	11
PIP5K1A	0	10	RFX6	1	15	POLG	1	18	MAP2K5	1	10
PDE1C	6	10	SCML2	0	14	DST	3	18	CanA1	0	9
RBFOX3	0	9	FLCN	1	13	PRRT2	3	18	GNB1	1	8
USP27X	0	9	SMAD1	2	13	SMAD9	2	17	SP110	1	8
RPS14	1	9	HTRA2	3	13	ANKS6	0	14	NR5A1	2	8

| STUB1 | 3 | 9 | MGMT | 5 | 13 | HDAC4 | 2 | 14 | CCNB1 | 2 | 7 |
| Mir708 | 0 | 8 | Agtr1a | 0 | 12 | HRAS | 3 | 14 | FOXD4L1 | 12 | 6 |

We analyzed the top-related gene perturbations as a whole to discover the internal association. All the closely AD-correlated gene perturbations were applied using their gene ID as input on STRING to explore their functional protein association. Most of the associated genes are coding genes. The non-coding genes were excluded for protein-protein interaction analysis by STRING, including microRNAs (miR-520g, miR-22, miR-181a1, miR-181b1, miR-124, miR-125a1, and miR-125b1), transcription factors (tRNA Arginine [TRR] and GM98), and reference SNP (rs491333). We downloaded the protein-protein interaction data from STRING and mapped them in **Figure 64** using Cytoscape, which allowed us to represent proteins with the most interactions using the largest nodes and blue color and the highest interaction score by the widest edge and blue color. The combined interaction score is calculated in STRING mainly based on experimental validation and association from curated databases; other factors such as genome neighborhood, gene fusions, co-occurrence across genomes, co-expression, and co-mention in publications were also considered to make the score more accurate.
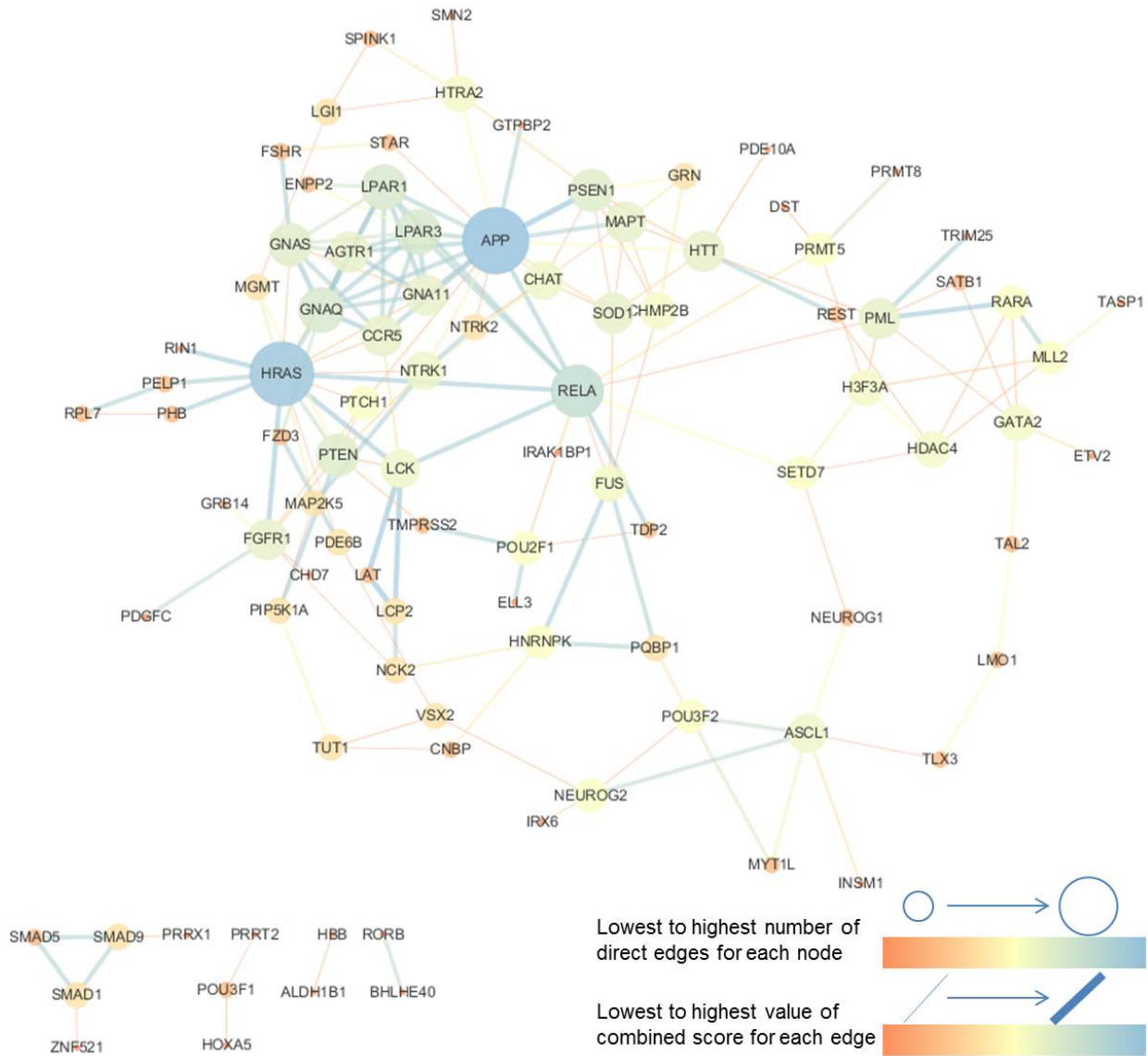
Figure 64. The AD-Associated Genetic Perturbation Encoded PPI Network.

As shown in **Figure 64**, APP, HARS, and RELA are the most frequently connected proteins in the protein association network, followed by LPAR1, LPAR3, AGTR1, PTEN, PSEN1, GNAQ, GNAS, GNA11, SOD1, HTT, MAPT, FGTR1, NTRK1, LCK, and PML. Among these, well-known AD-associated proteins APP, PTEN, PSEN1, and MAPT are identified as highly connected nodes in the protein-protein interaction (PPI) network. APP encodes the amyloid precursor protein, which is cleaved by β-secretase and ɣ-secretase to produce amyloid β, the main

component of amyloid deposit found in AD patients' brains. PSEN1 encodes presenilin protein that is responsible for modulating the APP processing through its effects on γ secretase. The inherited mutations in PSEN1 and APP are frequently found in AD patients, which increase production of a longer form of amyloid β, leading to more amyloid deposits accumulated in the brain, one of the potential pathological factors for AD. This is consistent with our analysis result. PTEN encodes phosphatase PTEN, an enzyme that antagonizes the phosphatidylinositol 3-kinase (PI3K)–AKT pathway by converting the phospholipid PIP3 to PIP2, which then increases synaptic strength of active synapses, resulting in long-term potentiation (LTP) followed by depressed postsynaptic function. Overexpression of PTEN was found to suppress the synaptic activity in mice hippocampus. Mutations in PTEN are associated with various neurological disorders, such as autism and seizures. PTEN inhibition by VO-Ohpic prevented Aβ-induced reductions in synaptic activity and LTP in hippocampal slices and improved cognitive function in an AD mouse model. In this study, the knockout of PTEN had an AD-like gene profile, which was in line with the literature reports. MAPT encodes microtubule-associated protein tau, a predominant component of neurofibrillary tangles, which is a neuropathological hallmark for AD and other neurodegenerative diseases. The formation of neurofibrillary tangles correlated well with the stage and degree of AD. Many studies have shown a strong association between tau protein and AD. Mutations in MAPT only cause FTLD, not AD. Our study suggests that mutation or overexpression of MAPT will cause a gene signature change similar to AD.

In addition to these proteins with direct connections to AD, some proteins related to other neurodegenerative diseases, such as Htt and SOD, are also found on the list. Huntington's disease is associated with an expanded polymorphic trinucleotide CAG repeat gene at the N-terminal of chromosome 4, which encodes huntingtin protein with a polyglutamine tract. The number of CAG

repeats in HD is significantly higher compared to the healthy population. Although the pathological mechanism for HD is still unclear, there is evidence that polyglutamine encoded by CAG trinucleotide repeat expansion is directly neurotoxic. Some other pieces of evidence have indicated a similar immune signature and gene expression pattern between HD and AD. SOD1 mutation is the most common cause of familial ALS, another neurodegenerative disease characterized by gradual motor neuron death. The neurodegenerative diseases share a similar disease process pattern potentially caused by the aggregated neurotoxic proteins that spread within the brain, destroy neuron functions and eventually lead to gradual neuron death. Different proteins are implicated for different proteins, tau for AD, α synuclein for Parkinson's disease, and huntingtin for HD. The discovery of positive associations for Htt and SOD1 gene mutation and overexpression induced gene signature with gene profile of AD also suggests a common underlying pathological mechanism shared by different neurodegenerative diseases. Another neuron-related gene NTRK1, encodes a high-affinity receptor for NGF, which is involved in the survival of sympathetic and nervous neurons.

Moreover, the other highly connected genes identified in the PPI network are contained in some of the basic biological processes in the body. To illustrate, LPAR1, LPAR3, GNAQ, GNAS, and GNA11 all play a part in GPCR related signaling transductions. LPAR1 and LPAR3 encode lysophosphatidic acid receptors 1 and 3, which mediate diverse cellular activities including cell migration, differentiation and proliferation via coupling with Gi/Go, G12/G13 and Gq families of heteromeric G proteins and regulating downstream signaling. LPAR1 was reported to promote Rho-dependent reorganization of actin cytoskeleton in neuronal cells and neurite retraction. GNAQ, GNAS, and GNA11 encode guanine nucleotide-binding proteins (G proteins) that function as modulators or transducers in diverse transmembrane signaling systems via GPCRs. GNAQ

plays a role in B cell selection, survival, and autoimmunity. HARS, the mutation of which is positively related to AD, is an oncogene encoding GTPase Hras involved in the activation of the Ras protein that interacts with GDP/GTPase and promotes GTPase activity. RELA, known as transcription factor 65, is a component of the RELA-NFκB heterodimeric complex, the most abundant NFκB complex in the body. NFκB is a transcription factor that directly binds with DNA and presents the endpoint of various signal transductions triggered by stimuli from diverse physiological and pathological processes, including cell growth, migration, differentiation, proliferation, inflammation, immune response, and apoptosis.

The knockout of RELA is negatively associated with AD. FGTR1 encodes FGFR 1, which is involved in the tumorigenesis process. AGTR1 encodes angiotensin II receptor 1, an important regulator for blood pressure and circulation. LCK, the knockout of which is negatively related to AD, encodes a tyrosine-protein kinase that plays an essential role in selecting and maturing developing T-cells in the thymus and the function of mature T-cells and their receptor signal transduction.

To investigate the interactions between the predicted AD targets, we use STRING software (193) developed by EMBL to plot the protein association networks. The STRING stored literature reported protein-protein interactions and also predicted potential interactions (193). We assume that AD-related protein targets can be closely connected or clustered together as they are all involved in AD signaling pathways. Modulating one protein may have a similar biological effect as modulating its closely connected proteins.

4.7. Positive & Negative Associations between AD- and Drug-Induced Gene Profiles.

The DEGs from the AD datasets were compared to chemical-induced DEGs using the implemented Pharmco function in BaseSpace. If a drug can induce a reversed gene profile as AD did, this drug might have the potential to reverse some of the disease processes and help to treat the disease. Therefore, the drugs with negative genetic associations to AD were identified and ranked according to the number of negatively associated AD biosets among the total 40 datasets. The top-rated 30 medications are listed in **Table 22**. Their association scores with each AD bioset are represented by different colors in **Figure 65**, with most negative scores in dark blue and most positive scores in red.
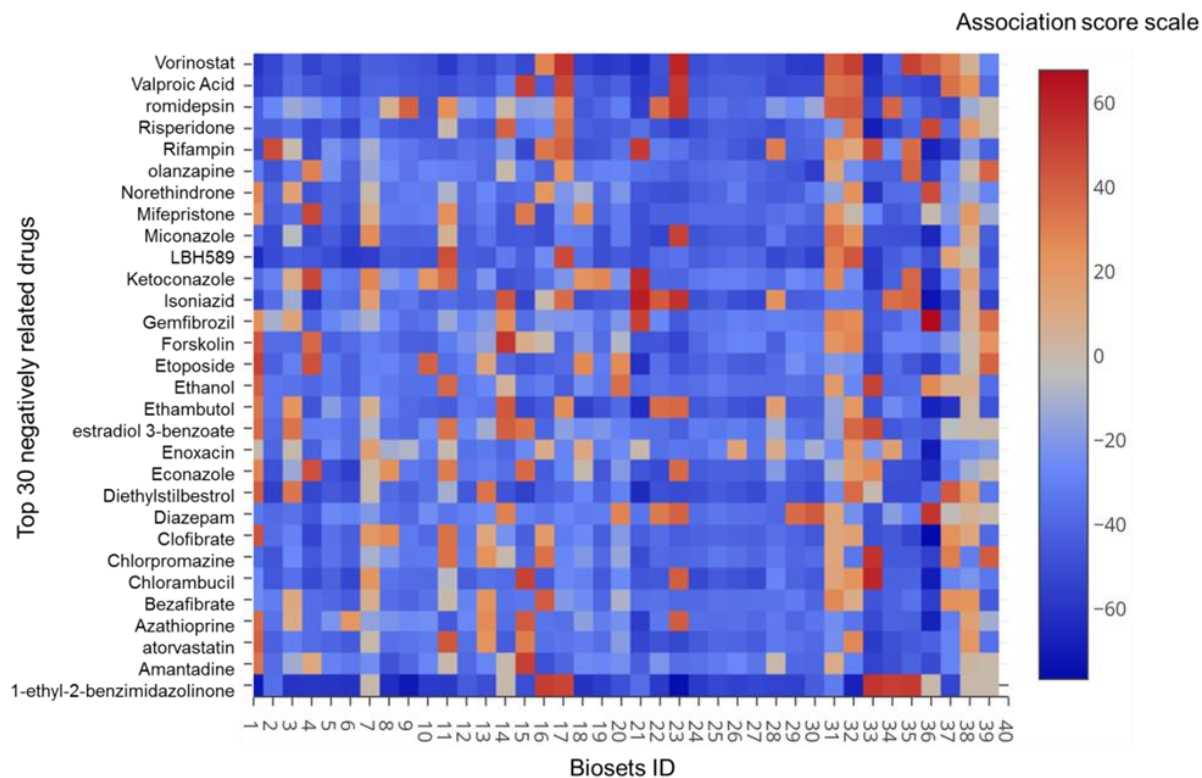
As shown in **Figure 65**, several biosets show a different mRNA expression change related to some of these drugs compared to other datasets. Looking into these biosets, we found most were derived from a specific subgroup of a patient or a specific brain region from the AD patient to compare with the control. For instance, bioset 8 is the only one with a different result compared to other biosets within its study (GSE36980). Bioset 8 only accounts for the tissue samples from the hippocampus gray matter of male individuals, suggesting different genetic characters for male AD patients in gray matter. Another example is dataset 18, which only took frontal cortex synaptoneurosomes from incipient AD patients with minimum cognition impairment into consideration to access the early-stage synaptic activity in patients' frontal cortex, which is different from other studies. The study of dataset 39 also provided a unique gene signature as it solely considers cortical lesions of AD patients and other neurodegenerative diseases. Except for these biosets, most show the same direction of correlations with the top 30 negatively related drugs.

Table 22. Associations between AD-Induced and Drug-Induced Gene Profiles.

Drug Name	Drug Classification	Negative	Positive
LBH589	Antineoplastic Agents	34	5
Norethindrone	Reproductive Control Agents	34	5
Chlorambucil	Antineoplastic Agents	33	7
Miconazole	Anti-Infective Agents	33	7
Risperidone	Central Nervous System Agents	33	7

olanzapine	Gastrointestinal Agents	32	5
atorvastatin	Lipid Regulating Agents	32	7
Chlorpromazine	Central Nervous System Agents	32	7
Azathioprine	Antirheumatic Agents	32	8
Valproic Acid	Central Nervous System Agents	32	8
Diethylstilbestrol	Unclassified Therapeutic Uses	31	7
Bezafibrate	Lipid Regulating Agents	31	8
Etoposide	Antineoplastic Agents	31	8
Gemfibrozil	Lipid Regulating Agents	31	9
Amantadine	Central Nervous System Agents	30	6
estradiol 3-benzoate	Reproductive Control Agents	30	8
Forskolin	Cardiovascular Agents	30	8
Clofibrate	Lipid Regulating Agents	30	10
Ethanol	Anti-Infective Agents	30	10
vorinostat	Antineoplastic Agents	30	10

1-ethyl-2-benzimidazolinone	Cardiovascular Agents	29	6
Enoxacin	Anti-Infective Agents	29	7
Econazole	Anti-Infective Agents	29	9
Mifepristone	Reproductive Control Agents	29	9
romidepsin	Antineoplastic Agents	29	9
Diazepam	Gastrointestinal Agents	29	10
Isoniazid	Anti-Infective Agents	29	10
Rifampin	Anti-Infective Agents	29	10
Ethambutol	Anti-Infective Agents	29	11
Ketoconazole	Anti-Infective Agents	29	11

Note: Negative-negatively associated gene number. Positive-positively associated gene number. Drug name highlighted in red; the drugs that are demonstrated associated with neuronal diseases by literature reports. Drug name highlighted in green; the drugs applied to treat cardiovascular diseases. Drug name highlighted in red, and Drug classification highlighted in green; the drugs that are currently used to treat cardiovascular diseases and additionally reported to have potential to be repurposed to treat neurodegenerative diseases.

Among the top listed drugs, some have been investigated in the clinical trials for AD treatment. We summarized these drugs with their development phases, clinical trial IDs, and

descriptions in **Table 23**. Some medicines are used to treat the accompanying symptoms of AD. Risperidone is a medication that has been evaluated for a long time and proved efficacious to treat AD patients with positive and negative psychotic and behavioral symptoms (194, 195). Olanzapine is an effective and safe treatment for anxiety symptoms caused by AD, including agitation, hallucinations, delusions, aggression, irritability, and anxiety (199; 200). Valproate is applied to delay or prevent agitation and psychosis in an AD patient; however, the phase III clinical study showed that valproate did not delay the onset of agitation and psychosis or slow cognitive or functional decline in AD patients and had significant toxicity problems (196). Growing evidence suggests that elevated cholesterol levels in mid-life are associated with an increased risk of developing AD and that statins might have a protective effect against AD and dementia (197). Atorvastatin, a cholesterol-reducing agent by inhibition of HMG-CoA reductase, has shown some clinical benefit in AD patients in a phase II study and could be a potential treatment for AD (198). Another clinical trial is currently investigating the efficacy and safety of the combined use of atorvastatin and ChEIs. Some researchers have investigated the potential of gemfibrozil, a cholesterol-reducing agent, to treat AD since gemfibrozil affects the production of two molecules that play a role in AD pathology: miR-107 and β-secretase (BACE). MiR-107 appears to reduce the production of β-secretase, which is involved in the generation of cell-damaged amyloid-beta. The decreased amount of miR-107 was reported to correlate with increased expression of BACE and the amount of Aβ in the AD process. Some studies found that gemfibrozil can augment the amount of miR-107, reduce the production of enzyme BACE, as well as ultimate Aβ. Gemfibrozil is under investigation in two phase I clinical trials. One of them is investigating the PK/PD and safety properties for the combined use of gemfibrozil and another AD medication, cerlapirdine (SAM-531), in healthy volunteers. The other trial (NCT02045056) is evaluating the safety and

effectiveness of gemfibrozil in increasing miRNA 107 levels to prevent AD in early-stage AD patients with mild cognitive deficits and healthy volunteers.

Vorinostat is a pan-HDAC inhibitor, which could rescue the synaptic number and learning impairments in HDAC2-overexpressing mice (199) and significantly increase H4K12 acetylation and restore learning-induced gene expression in aged mice (200, 201). HDAC inhibitors may ameliorate cognitive deficits and memory impairment in AD animal models by inhibition of the Aβ-induced hyperphosphorylation of tau protein and the regulation of the expression of important genes that participate in learning by modulating histone acetylation levels (201). Estradiol 3-benzoate is an estrogen derivative. Decades ago, considerable studies reported the neuroprotective and cognition-improve effects of estrogens in animal models. Some clinical trials also tested the effectiveness of estrogens used as a conjunctive treatment for AD and other neurodegeneration, but the results from clinical trials did not support estrogen use for advanced AD treatment. The use of estrogen might be effective for improving cognitive function and protecting neurons once the right time, right formulation, and right subtype of female early-stage AD patients are found (202). Mifepristone is a potent glucocorticoid and progesterone receptor antagonist. Researchers conducted a double-blind study and found mifepristone improved cognitive function compared to a placebo in nine mild to moderate AD patients for 6 weeks of treatment (203). A large-scale double-blind study is now in process to evaluate the efficacy of mifepristone in the combination treatment of AD (NCT00105105; 205).

Rifampin is a broad-spectrum antibiotic, which has shown neuroprotective activities in several neurodegenerative diseases (204). Accumulating evidence supports that rifampicin might ameliorate the free radical damage and reduce neuroinflammation, including microglial activation, anti-oligomeric effect, and apoptotic cascades, which will eventually lead to neuroprotective

245

effects (204, 205). In addition, it was recently discovered that rifampicin could stimulate the clearance of Aβ via activation of LRP1 and P-gp (204). A few clinical studies have been conducted to evaluate the neuroprotective effect of rifampicin on AD with controversial results. (206). They suggested rifampicin can effectively prevent AD with at least 450 mg daily treatment for one year (206). The inconsistent clinical results of rifampicin might be due to the different doses, treatment durations, and disease stages. Ketoconazole, an antifungal agent, might not have a direct effect on AD. Still, ketoconazole can inhibit the metabolism and clearance of ChEIs (donepezil) and prolong the effective and lasting time of other AD treatments (207).

Table 23. The List of Negative-Associated Drugs that Being Applied in Clinical Studies.

Drug	Developing Phase	Reference	Note
Risperidone	Phase ¾	NCT01119638, NCT00034762, NCT00417482, NCT00626613, NCT00249158, NCT00249145, NCT00253123, NCT00018291, NCT00015548, NCT00245206, NCT00208819, NCT00073658	treat the accompanying behaviour and pyscological symptoms with AD
Olanzapine	Phase 4	NCT00015548, NCT00208819	treat AD with agitation
Atorvastatin	Phase 2/3	NCT00024531, NCT00151502	single or combined use with ChEIs
Valproate	Phase 3	NCT00071721	treat AD
Gemfibrozil	Phase 1	NCT00966966	Safety evaluation in health to treat AD in combination
Estradiol 3-benzoate	Phase 2/3	NCT00066157	Therapeutic Potential of Estrogen in AD
Vorinostat	Phase 1	NCT03056495	Determine Tolerable Dosis of Vorinostat in Patients With Mild Alzheimer Disease

Mifepristone	Terminated in Phase 2	NCT00105105	Adjunctive Therapy in Alzheimer's Disease
Rifampin	Phase 3	NCT00439166	Effects on AD Biomarkers in CSF
Ketoconazole	Phase 1	NCT00860275, NCT00931073	The influence of Drug-Drug Interaction (DDI) w/Ketoconazole or Fluconazole

In addition to the drugs that have already been studied in clinical trials for AD, some of the other top negatively genetic-associated agents are also found in literature reports as potential AD medication. These drugs with reported connections to AD are listed in **Table 25** with their corresponding reference and description. Some of these agents share the same or similar targets with currently available AD medication. For example, amantadine has a similar structure and shares the same target with memantine (208). Miconazole is a dual inhibitor for butyrylcholinesterase (BuChE) and indoleamine 2,3-dioxygenase 1 (IDO1), two therapeutic targets for AD. A study investigated miconazole analogs as multi-target medication for AD (209). Some other drugs have similar targets and mechanisms as agents under the clinical investigation. Chlorpromazine is an antipsychotic agent targeting the dopamine 2 receptor. However, some studies reported an improved cognition function in AD patients taking antipsychotics, while other studies did not find a significant difference (210, 211). Romidepsin is one of the epigenetic drugs targeting HDAC, another potential AD treatment group under investigation. Norethindrone, a form of progesterone and a female hormone, had a controversial clinical result as estrogen and progesterone, the efficacy of which might depend on specific action time, treatment duration, stage of disease, and special female patient sub-group (212, 213).

Bezafibrate and Clofibrate are peroxisome proliferator-activated receptors (PPARs) ligands, improving behavior deficits in AD animal models. Bezafibrate improves behavior deficit and tau pathology in P301S mice (214), and clofibrate increases the locomotor activity of the animals with acute exposure in forced swim tests (215). PPARs are involved in various activities that affect the pathology process of AD. PPARα might participate in acetylcholine metabolism and excitatory amino acid neurotransmission, and oxidative stress defense (216). PPARγ agonists ameliorate the inflammatory status of the AD by reducing proinflammatory molecules, immune response, and mitochondrial function. PPARγ also plays a role in the production and metabolism of Aβ (216). The other two agents were reported to be associated to AD with different mechanisms. Forskolin, a well-known tool for raising the cAMP level in biochemistry assays measuring the GPCR ligand function, showed neuroprotective effects on APP/PS1 transgenetic mice and potential for AD treatment. Administration of forskolin can restore nest construction and sociability, decrease Aβ plaques in the hippocampus and cortex, and regulate the inflammatory response in microglia and astrocytes in APP/PS1 Tg mice (217).

4.8. Conclusion

To summarize, this study applied a meta-analysis approach to mRNA expression data to analyze the association between chemical/gene-induced DEGs and AD-induced DEGs. We identified positively associated chemicals/genes and negatively associated drugs/genes. Most highly associated gene and chemical perturbations are associated with other neurological diseases. This indicates the common mechanism and constructs under different neurological disorders and neurodegenerative diseases. It is reasonable to repurpose negatively associated drugs to treat AD,

as they may reverse the gene expression profile induced by AD. Some of these drugs are found in ongoing clinical trials and literature reports for AD treatment, supporting our prediction. The new potential therapeutic targets and repurposed drugs came from cardiovascular disease treatment, anti-inflammation, anti-oxidative stress, and anti-immune medications. Moreover, some repurposed drugs failed in clinical trials due to their limited effect within a specific subgroup and stage of AD patients. More specific clinical trials designed according to different subgroups of patients with optimum treatment regimens might help evaluate drug efficacy to AD. Furthermore, some highly associated targets are identified to play a critical role in the disease process.

5.0 Summary and Future Prospective

This study included four parts: 1) we applied a variety of computational chemistry and bioinformatics approaches to hit screening and lead the modification design process, including molecular docking, homology modeling, molecular dynamic simulation, binding free energy calculation, pharmacophore modeling, similarity search by diverse fingerprint, fragment-based drug design, scaffold hopping, QSAR, and *in silico* ADMET properties prediction; 2) we synthesized the compounds selected by virtual screening and economic considerations; 3) we set up *in vitro* assays to screen for the efficacy of potential treatment for MM and neurodegenerative diseases, cytotoxicity, specificity on p62 and some physicochemical properties of the compounds; 4) we identified one or two compounds with beneficial drug-like properties and potential for MM and neurodegenerative disease therapy through the *in vitro* screening assays to explore the

molecular mechanism underlying their therapeutic effects by signaling analysis using IB and confocal immunofluorescence microscope.

5.1. Summary and Plan for Multiple Myeloma Treatment

In the previous report, we measured the effect of our lead **XRK3F2** on rat models transferred with myeloma tumor cells. **XRK3F2** showed a significant effect on curing the bone fraction and lengthening the life of the test rats by bone micro-CT. However, the lead had some issues with their ADMET properties when we tried to push them into further studies or clinical trials. **XRK3F2** did not have a high efficacy in treating the diseases on cell models.

The chemical modification was applied to find compounds with a higher efficacy on therapeutic effects on *in vitro* models and better drug-like properties. We found compound **XIE106** had a similar effect on MM animal models and have a good druggable property. We demonstrated **XIE106** has a specific binding to p62ZZ. **XIE106** can induce apoptosis signaling but not autophagy flux in MM1.S cells, which results in tumor cell death. We also identify a compound 6.28 with a 10-folder anti-proliferative effect on MM cells compared to **XRK3F2**. Moreover, we investigated the signaling pathways behind its anti-cancer activity and found compound **6.28** can induce apoptosis signaling but not autophagy flux on MM1.S cells via interacting with p62ZZ.

For future studies, we may need to measure some of our selective compounds' ADME profiles by *in vitro* assays. There is also a need to send novel analogs, such as compound **6.28**, with *in vitro* high efficacy and good drug-like properties for animal studies to measure therapeutic effects on MM. The signaling studies of compound **6.28** on NF-κB signaling induced by TNFα are

still needed for new compounds that show beneficial anti-MM properties. Furthermore, we plan to investigate whether compound **6.28** and **XIE106** have an effect on curing the bone fraction by bone micro-CT on MM rat models.

5.2. Summary and Plan for Neurodegenerative Diseases Treatment

In the chapter of compounds' effect on neurodegenerative diseases, we established a model to screen the neuroprotective effects of our compounds on differentiated SH-SY5Y cells against the treatment of hydrogen peroxide. We found several compounds that have a moderate neuroprotective effect against oxidative stress. We chose compound **5.8** to investigate the signaling mechanisms behind it. We found that compound **5.8** induce p62 self-aggregation and autophagy flux. The levels of α-synuclein and tau were reduced by the treatment of compound **5.8**. P-tau and α-synuclein have the tendency to aggregate into insoluble fibrils, which are the component of Lewy bodies and NFTs that play an important role in the pathogenesis of PD and AD. Therefore, compound 5.8 might have a beneficial effect on treating AD or PD. However, to make that conclusion, we need to do more assays to measure the impact of compound **5.8** on the aggregation of α-synuclein, p-tau, or Aβ.

We propose to test some of our compounds by α-synuclein aggregation assay, a screening assay that is stable and widely used. In addition, the effect of compound **5.8** on the phosphorylation of tau, aggregation, and clearance of tau are strongly suggested to be investigated using IB and FM. It is also valuable to measure the generation, aggregation, and clearance of Aβ affected by compound **5.8**.

For future studies, we suggested that animal studies should be conducted for compound **5.8** or other compounds on neurodegenerative disease (AD or PD models). Behavioral studies are needed to represent the efficacy of compounds on neurodegenerative diseases. Beforehand, an acute toxicity test and PK/PD studies should be performed first on those animal models. An *in vivo* ADMET profile can be obtained in this process.

We suggested using a 5xFAD transgenic mice bearing five mutations, contains three in the APP695 gene (APP K670N/M671L, I716V, V717I) and two mutations in the presenilin 1 gene (PS1 M146L, L286V), which presents several disease characteristics, including high overexpression of $A\beta_{1-40}$ and $A\beta_{1-42}$ in the brain and cerebrospinal fluid, a dramatic plaque load, and beta-sheet formation accompanied by strong neuroinflammation of the cortex and hippocampus can be observed through histological analyses, as well as spatial and long-term memory deficits as analyzed by the Morris water maze (**Figure 66**).
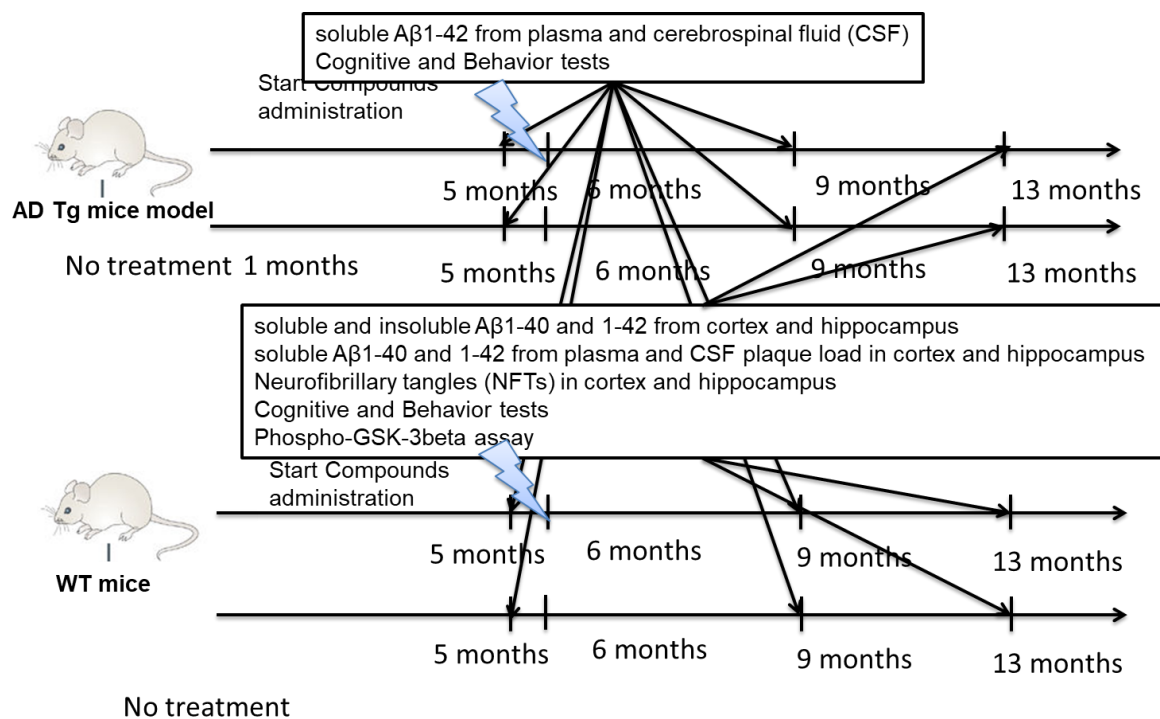
Figure 66. Strategy and Workflow Testing Compound in 5xFAD Transgenic Mice.

According to the disease-correlated characteristics in the mice model, we can measure the influence of our compound on these disease-related biomarkers. We plan to treat the mice, as shown in **Figure 66**. We will take some blood samples out for a short-time treatment of the compound to measure the soluble $A\beta_{1-40}$ and $A\beta_{1-42}$ plasma levels. The cognitive and behavioral study, such as the Morris water maze, can also be tested at the same time when we take out the blood samples. At the end of the study, all animals can be sacrificed for more bioassay tests. Pathological brain slices (section) were kept and stained to observe insoluble $A\beta_{1-42}$, CSF plaque load, and neurofibrillary tangles (NFTs) in the cortex and hippocampus. In addition, we can measure the level of soluble $A\beta_{1-40}$ and $A\beta_{1-42}$ in plasma and CSF. Cognitive and behavior studies should also be conducted on the animals, as they are one of the most important endpoints and biomarkers for neuron disease at the last stage before we can sacrifice them for other assays. We plan to observe amyloid deposition and gliosis in brain sections of the hippocampus and cortex

from 6-month-old 5XFAD mice from each group, and same age non-transgenic control mice were stained with anti-Aβ antibody, thioflavin S, anti-GFAP, and thiazine red and imaged by bright-field or confocal microscopy. The relative amounts of amyloid aggregation correlated with Aβ42 levels can be measured by ELISA at the same time.

5.3. Summary and Plan for the Interaction between compounds and p62ZZ.

We also propose to set up a binding assay specific for the p62 protein that can quantify and screen the binding affinity of compounds and the protein *in vitro.*

We expressed and purified full-length p62 protein from *E.coli*. We tried to set up different binding assays using this WT p62 protein, including SPR, radioligand competitive binding, and thermal stability assay. We did not get stable, solid, and confirmed binding affinity from these assays. First, we considered the folding system in *E.coli* is different from human beings, so we tried to use protein expressed and purified from Sf9 cells, but we still cannot get a stable result. We only get a good result using fresh-made p62 by SPR, but the background noise is still high. We get a stable and good result by radioligand saturated binding or competitive binding for the radio-labeled same compound. There might be three problems in the process. The p62 protein itself is unstable and self-aggregates in a buffer, making the binding site flexible and unstable. We can truncate the domains in p62 that promote its self-aggregation, such as PB1 and UBA. We can also use the p62-ZZ domain instead of the full-length p62 protein to do the binding assays. It might solve this self-aggregation problem. The radioligand competitive binding assay is mainly applied in measuring binding affinities to GPCRs. This might not be suitable for a cytosolic soluble protein, like p62. I may suggest trying to measure the binding affinity between our compound and the p62-ZZ domain by SPR in this case. A concern for this plan is that our compound might have some additional interactions with other domains and the existence of other domains in p62 may influence the shape and structure of binding site in ZZ domain.

5.4. Summary and Plan for Alzheimer's Genetic Association Analysis

This chapter applied a meta-analysis approach to mRNA expression data for AD individuals and models collected from the literature. The common DEGs shared by AD datasets are enriched in other neurological pathological signaling pathways. The association analysis was conducted comparing the chemical-induced DEGs and AD-induced DEGs to identify chemicals that are negatively associated with AD. Negatively genetic-associated drugs might have the potential to be repurposed for AD treatment or prevention. Some ongoing clinical trials could support some of our findings. Some of these drugs are found in the literature that are linked to AD. The new potential therapeutic targets and repurposed drugs might come from cardiovascular disease treatment or anti-inflammation, anti-oxidative stress, and anti-immune medications. In addition, some repurposed drugs failed in clinical trials due to their limited effect within a specific subgroup and stage of AD patients. The genetic association analysis might help to design more specific and selective clinical trials according to different subgroups of patients.

The discovery of negative or positive correlated gene perturbation might deepen our understanding of the molecular mechanism behind AD and provide a clue for future epigenetic therapy or novel therapeutic targets. In addition, a protein-protein interaction network was also built here for AD-related coding genes to identify the highly connected proteins, such as APP, HARS, RELA, LPAR1, LPAR3, AGTR1, PTEN, PSEN1, SOD1, HTT, MAPT, FGTR1, NTRK1, LCK, and PML, which might play a critical role in the disease progression. Signaling pathways for neurodegenerative diseases, inflammation and immune pathways, and lipid-regulation are also emphasized for their correlation with AD.

5.5. Future Plan for Chemical Modification.

We introduce diverse functional groups on Zone B of our p62ZZ ligands scaffold, but we did not explore Zone A sufficiently. It is a great suggestion to introduce asymmetric substituents on the benzyloxy rings. We can also introduce some other substituents with different sizes, hydrophilic, and electronic properties, such as nitroxide groups. In addition, we can also replace the benzene with heterocyclic rings, such as pyridine, to increase the solubility of our compounds.

Appendix A. Abbreviation

Here is the abbreviations and their full names mentioned in this dissertation:

Abbreviation	Full-name
5HT	Serotonergic synapse
AA	amino acid
AAPS	American Association of Pharmaceutical Scientists
Abbrevaition	Pathway Name
Abbrevaition	Pathway Name
ABL	Tyrosine-protein kinase ABL1
ACE	Angiotensin Converting Enzyme
ACE	Angiotensin Converting Enzyme
AchE	Acetyl cholinesterase
ACN	acetonitrile
ACS	American Cancer Society
AD	Alzheimer's disease
ADCC	Antibody-dependent cellular cytotoxicity
ADME	absorption, distribution, metabolism, and excretion
ADMET	absorption, distribution, metabolism, excretion, and toxicity
ADP	Adenosine diphosphate
ADR	Adrenergic signaling in cardiomyocytes
ADRA1	Alpha-1 adrenergic receptor
ADRA2	Alpha-2 adrenergic receptor
ADRB1	Beta-1 adrenergic receptor
ADRB2	Beta-2 adrenergic receptor
ADRB3	Beta-3 adrenergic receptor
AEBP1	AE binding protein 1
AGD	Amoebic gill disease
AGT	Angiotensinogen
AGTR	Angiotensin II receptor
AHNAK	AHNAK nucleoprotein
AKT	Protein kinase B
ÄKTA	a brand name
ALA	alanine
ALS	Amyotrophic lateral sclerosis

AMBRA	Augmentation Mammaplasty By Reverse Abdominoplasty
AMES	Ames Salmonella/microsome mutagenicity assay
AMP	Adenosine Monophosphate
AMPAR	Alpha-amino-3-hydroxy-5-methyl-4-isoxazolepropionic Acid Receptor
AMPK	AMP-activated protein kinase
ANOVA	analysis of variance
ANPR	Atrial natriuretic peptide receptor A
AP1S1	adaptor-related protein complex 1, sigma 1 subunit
APAF	Apoptotic protease-activating factor 1
API	active product ingredient
aPKCs	atypical protein kinases Cs
APN	Aminopeptidase N
APP	β-amyloid precursor protein
APRIL	Tumor necrosis factor ligand superfamily member 13
ARG	Tyrosine-protein kinase ABL2
ARVC	Arrhythmogenic right ventricular cardiomyopathy (ARVC)
ASN	Asparagine
ASP	Aspartic acid
ATCC	the American Type Culture Collection
Atg	autophagy-related protein
ATIII	Antithrombin-III
ATP	Adenosine tri-phosphate
ATP13A2	Polyamine-transporting ATPase 13A2
ATP2A2	ATPase, Ca++ transporting, cardiac muscle, slow twitch 2
ATP6V1G2	ATPase, H+ transporting, lysosomal 13kDa, V1 subunit G2
BACE	Beta-secretase 1
BAFF	Tumor necrosis factor ligand superfamily member 13B
BBB	Blood brain barrier
BCA	BCA protein assay
BCL-2	B-cell lymphoma 2
BCR	Breakpoint cluster region protein
BDNF	Brain-derived neurotrophic factor
Beclin-1	BCL-2-interacting protein
ADRBK1	*Beta-adrenergic receptor kinase 1*
AGFG1	*Arf-GAP domain and FG repeat-containing protein 1;*
BM	Bone marrow
AGTR1	*Type-1 angiotensin II receptor*
BMS	Bone marrow stromal
BMSC	Bone marrow stromal cells
BSA	Bovine serum albumin
ASPN	*Asporin*

CACN	Voltage-dependent L-type calcium channel
CACNG3	calcium channel, voltage-dependent, gamma subunit 3
ATN1	*Atrophin-1*
CALD1	caldesmon 1
cAMP	cyclic adenosine monophosphate
CBD	Corticobasal degeneration
CD	cluster of differentiation
CD44	CD44 molecule (Indian blood group)
CDC	complement dependent cytotoxicity
CBID	our database
CHO	Cholinergic synapse
CNS	central neural system
COX-2	Prostaglandin G/H synthase 2
CJD	Creutzfeldt-Jakob Disease
CQ	chloroquine
CR	Circadian rhythm
CML	chronic myelogenous leukemia
CNBP	Cellular nucleic acid-binding protein
CRE	*Cyperus rotundus rhizome* extract
CRBN	cerebronal
CRL	Cytokine receptor-like factor
CYLD	Ubiquitin carboxyl-terminal hydrolase CYLD
CYS	Cystein
DA	drug abuse
DAPI	4′,6-diamidino-2-phenylindole
DAPT	Dual antiplatelet therapy
CSF	cerebrospinal fluid
CTAB	Cetyl Trimethyl Ammonium Bromide
DDI	Drug-drug interaction
CM	cardiomyopathy
DISC	Death-inducingg signaling complex
DCM	dichloromethane
DD	drug drug
DMAG	17-dimethylaminoethylamino-17-demethoxygeldanamycin
DMEM	Dulbecco's Modified Eagle's Medium
DMF	Dimethylformamide
DMSO	Dimethyl Sulfoxide
DNA	Deoxyribonucleic Acid
DOI	Digital Object Identifier
DRPLA	Dentatorubral-pallidoluysian atrophy
DM	diabetes mellitus
Dvl2	Dishevelled protein

DSC	Differential scanning calorimeter
EDNRA	Endothelin-1 receptor
EDTA	Ethylenediamine tetraacetic acid
EGTA	Ethylene glycol tetraacetic acid
ELISA	enzyme-linked immunosorbent assay
EM	eletron microscope
EMBL	European Molecular Biology Laboratory
EMBO	European Molecular Biology Organization
ECM	extracellular material
ENC1	ectodermal-neural cortex 1 (with BTB-like domain)
ENSA	endosulfine alpha
EGFR	epidermal growth factor receptor
ER	Endoplasmic reticulum
ERK1	Mitogen-activated protein kinase 3
EMEM	Eagle's Minimum Essential Medium
FA	Fatty Acid
FAA	Flavone Acetic Acid
FAD	Flavin Adenine Dinucleotide
FADD	Fas-Associated Death Domain
FAS	Fetal Alcohol Syndrome
FBS	Fetal Bovine Serum
ESI	electrospray ionization
FDA	Food and Drug Administration
FGFR	Fibroblast growth factor receptor
EXD1	*piRNA biogenesis protein EXD1*
FII	Coagulation factor II (thrombin)
FIII	Coagulation factor III (tissue factor)
FITC	Fluorescein Isothiocyanate
FIX	Coagulation factor IX
FBXW7	*F-box/WD repeat-containing protein 7*
FM	Fluorescence microscope
FSHR	Follicle-Stimulating Hormone Receptor
FTD	Frontotemporal Dementia
FTLD	Frontotemporal Dementia
FUS	Feline Urological Syndrome
FV	Coagulation factor V (proaccelerin, labile factor)
FVIIa	Coagulation factor VIIa
FVIII	Coagulation factor VIII
Fxa	Coagulation factor Xa
FXI	Coagulation factor XI
FXIII	Coagulation factor XIII
GADPH	Glyceraldehyde-3-Phosphate Dehydrogenase

GC	Glucocorticoid
GCR	Glucocorticoid receptor
GDP	Guanosine Diphosphate
FGFR1	*Fibroblast growth factor receptor 1*
GEO	Gene Expression Omnibus
GFAP	Glial fibrillary acidic protein
GLU	glutamate
GLY	glysine
GBM	Glioblastoma Multiforme
GO	Gene Ontology
GPCR	G Protein-coupled Receptor
GPU	Graphics Processing Unit
GFP	Green Fluorescent Protein
GI	gastrointestinal
GSH	Glutathione
GSK3B	Glycogen synthase kinase 3 beta
GSS	Gerstmann-Straussler-Scheinker syndrome
GSSG	Glutathione disulfide
GNAQ	Guanine nucleotide-binding protein G(q) subunit alpha
GNAS	*Guanine nucleotide-binding protein G(s) subunit alpha isoforms Xlas*
GWAS	Genome-Wide Association Studies
GRN	Progranulin
HBA	hydrogen bond acceptor
HBD	hydrogen bond donor
GST	Glutathione-S-Transferase
GTP	guanosine triphosphate
HCM	Hypertrophic cardiomyopathy (HCM)
HCQ	hydroxychloroquine
HD	Huntington's disease
HDAC	Histone Deacetylase
GUSB	Glucuronidase Beta
HAP1	*Huntingtin-associated protein 1*
HARS	GTPase hRAS
HBB	Hemoglobin subunit beta
HBSS	Hank's Balanced Salt Solution
HEPES	4-(2-hydroxyethyl)-1-piperazineethanesulfonic acid
HERG	the human Ether-à-go-go-Related Gene
HMGCR	3-hydroxy-3-methylglutaryl-coenzyme A reductase
HF	heart failure
HOMER1	homer homolog 1 (Drosophila)
HIS	histine
HIV	human immunodeficiency virus

HPLC	High Performance Liquid Chromatography
HRH1	Histamine H1 receptor
HTR	serotonin receptor
HTS	highthroughput screening
HTT	Huntington
HLM	human liver microsome
IACUC	Institutional Animal Care and Use Committee
IB	immunoblotting
HMGCR	3-hydroxy-3-methylglutaryl-coenzyme A reductas
IF	immunofluoscrence
HOXA	Homeobox protein Hox-A
IHC	immunohistochemistry
IL-1	interleukin 1
IMAC	Immobilized Metal Affinity Chromatography
INSULIN	Insulin signaling pathway
IP	immunoprecipitation
HRAS	GTPase HRas
HRP	Horseradish Peroxidase
ITCH	Intrathoracic Chemohyperthermia
ITGB4	integrin, beta 4
ITPKB	inositol-trisphosphate 3-kinase B
IDR	iron-dependent repressor homolog
IGF	Insulin-like growth factor
IPA	Ingenuity Pathway Analysis
IPTG	Isopropyl-Beta-D-Thiogalactoside
IRB	Institutional Review Board
ITPKB	Inositol-trisphosphate 3-kinase B
JNK	c-Jun N-terminal kinase
JMC	journal of medicinal chemistry
KCN	Potassium channel
KIR	Keap1-interacting region
KO	Knock out
KD	Knock down
KEGG	Kyoto Encyclopedia of Genes and Genomes
KvCN	Potassium voltage-gated channel subfamily D member 3
LAMP	Lysosomal-associated membrane protein
LC3	Microtubule-associated protein light chain 3
LCK	*Tyrosine-protein kinase Lck*
LDS	Loeys-Dietz Syndrome
LRRK2	Leucine-rich repeat kinase 2
LEU	Leucine
M2AchR	M2 muscarinic acetylcholine receptor

M3AchR	M3 muscarinic acetylcholine receptor
LIR	LC3 interaction region
LLC	Limited Liability Corporation
MAPK	mitogen-activated protein kinase
LOAEL	Lowest Observed Adverse Effect Level
LRPPRC	leucine-rich pentatricopeptide-repeat motif containing protein
LTP	long-term potentiation
MCR	Mineralocorticoid receptor
MEK5	Dual specificity mitogen-activated protein kinase kinase 5
MEKK3	Mitogen-activated protein kinase kinase kinase 3
MAPT	*Microtubule-associated protein tau*
MGMT	Methyl Guanine Methyl Transferase
MARCKS	Myristoylated alanine-rich C-kinase substrate
mHTT	mutant Huntington
MD	molecular dynamic
MDCK	Madin-Darby Canine Kidney Cells
MM	Multiple myeloma
MEF	Mouse Embryonic Fibroblast
MMP-7	matrix metalloproteinase-7
MMSE	Minimum Mean Square Error
MIR	microsome
MSA	multiple system atrophy
MMK	Mitogen-activated protein kinase
mSOD1	mutant superoxide dismutase 1
mTOR	mammalian target of rapamycin
MTT	3-(4,5-dimethylthiazol-2-yl)-2,5-diphenyltetrazolium bromide
MW	molecular weight
MPAT	Microtubule-associated protein tau
NADP	Nicotinamide Adenine Dinucleotide Phosphate
NADPH	Nicotinamide Adenine Dinucleotide Phosphate Reduced
NBR	Neighbor of BRCA1 gene 1 protein
NCALD	neurocalcin delta
NCBI	National Center for Biotechnology Information
NCI	national cancer institute
ND	neurodegenerative diseases
NES	nuclear export system
MTD	maxium tolerant dose
NFTPD	Neurofibrillary Tangle Predominant Dementia
NF-κB	nuclear factor kappa-B
NGF	nerve growth factor
NAD	nicotinamide adenine dinucleotide

NIA	national institute of aging
NIH	national institute of health
NK	Natural killer
NLS	nuclear localization signal
NO	nitroxide
NFT	<u>Neurofibrillary Tangles</u>
Nrf2	nuclear factor erythroid 2–related factor 2
NMDA	N-Methyl-D-Aspartate
OLFM1	olfactomedin 1
NMR	<u>Nuclear Magnetic Resonance</u>
NOD	nonobese diabetic
NIK	NF-κB-inducing kinase
NY	new york
PAF	Platelet activating factor
OCL	osteoclast
OD	oribital
PB1	Phox-BEM1
PCA	principal component analysis
PD-L1	Programmed death ligand 1
PD	Parkinson's disease
PDB	Paget's disease of bone
PDE3	cGMP-inhibited 3',5'-cyclic phosphodiesterase
PDE4A4	phosphodiesterase-4A4
ONJ	Osteonecrosis of the jaw
PE	phosphatidylethanolamine
PEST	proline (P), glutamic acid (E), serine (S), and threonine (T)
PAGE	polyacrylamide gel electrophoresis
PAINS	Pan Assay Interference Compounds
PARP	Poly (ADP-ribose) polymerase
PBS	phosphate-buffered saline
PI3K	phosphatidylinositol-3-kinase
PI3K-AKT	PI3K-Akt signaling pathway
PINK1	PTEN-induced kinase 1
PCM	Prechordal Mesoderm
PDGF	Platelet-derived growth factor
PDGFC	*Platelet-derived growth factor C;*
PDGFR	platelet-derived growth factor receptor
PDGFRB	*Platelet-derived growth factor receptor beta;*
PLATELET	Platelet activation
PD	pharmacodynamic
PET	Polyethylene terephthalate
PLG	Plasminogen

PMCID	a unique reference number or identifier that is assigned to every article that is accepted into PMC
PMID	PubMed-Indexed for MEDLINE
PML	Progressive multifocal leukoencephalopathy
PMSF	Phenylmethanesulfonyl Fluoride
PN3	Sodium channel protein type 10 subunit alpha
POLG	DNA polymerase subunit gamma-1
PPAR	Peroxisome proliferator-activated receptor
PPI	Protein-protein interaction
PRO	Protein digestion and absorption
PS1	Presenilin-1
PSA	polar surface area
PVDF	Polyvinylidene fluoride or polyvinylidene difluoride
PVT	Portal Vein Thrombosis
PHB	Poly-B-Hydroxybutyrate
MDCK	The Madin-Darby canine kidney cells
QSAR	Quantitative structure–activity relationship models
RA	retonic acid
RAB15	RAB15, member RAS oncogene family
RAB6A	RAB6A, member RAS oncogene family
RANKL	receptor activator of nuclear factor kappa-B Ligand
RAP1GDS1	RAP1, GTP-GDP dissociation stimulator 1
PHP	Hypertext Preprocessor
RASL10A	RAS-like, family 10, member A
PK	pharmacokinetic
PKB	protein kinase B
PKC	protein kinase C
PKCSM	pharmacokinetic CSM
REN	Renin
PKPD	pharmacokinetic/pharmacodynamic
PML	*Protein PML;*
PTEN	*Phosphatase and tensin homolog*
RIP	receptor-interacting protein
RIPA	Radioimmunoprecipitation assay
PTK2B	*Protein-tyrosine kinase 2-beta;*
QPP	Quality Payment Program
RAB22A	*Ras-related protein Rab-22A; P*
RARA	Retinoic acid receptor alpha
RNA	Ribose Nucleic Acid
ROC	Receiver Operating Characteristic
ROS	Reactive Oxygen Species

RECAP	Retrosynthetic Combinatorial Analysis Procedure
RPM	Rotations Per Minute
RPMI	Roswell Park Memorial Institute
RELA	Nuclear factor kappaB subunit p65
RT	room temperture
RELA	*Transcription factor p65;*
REST	*RE1-silencing transcription factor;*
SAR	structure-activity relationship
RET	*Proto-oncogene tyrosine-protein kinase receptor Ret;*
SBMA	Spinal and Bulbar Muscle Atrophy
SCA	Spinocerebellar Ataxia
RFP	Red Fluorescent Protein
SCN	Sodium channel protein type 10 subunit alpha
SCN3B	sodium channel, voltage-gated, type III, beta subunit
SD	standard deviation
RIC8A	*Synembryn-A*
SLC17A7	solute carrier family 17 (sodium-dependent inorganic phosphate cotransporter), member 7
RMS	Root-Mean-Square
RMST	Root Mean Square Total
SNARE	"SNAP Receptors"
SOD	superoxide dismutase.
SPR	Surface Plasmon Resonance
SDS	sodium dodecyl sulfate
SEM	Standard Error of Mean
SER	serine
SYNGR1	synaptogyrin 1
TBS	TRAF6 binding domain
TBST	Tris-buffered saline Tween
SNP	Single-Nucleotide Polymorphism
SPARC	*SPARC;*
STARD9	*StAR-related lipid transfer protein 9;*
THR	Thyroid hormone signaling pathway
TLC	Thin Layer Chromatography
TNF-alpha	Tumor necrosis factor alpha
TPC2	two-pore calcium channel protein 2
TRADD	Tumor necrosis factor Receptor-Associated Death Domain
TRAF6	TNF receptor-associated factor 6
TRAP	Tartrate-Resistant Acid Phosphatase
TRIM36	tripartite motif containing 36
TrkA	Tropomyosin receptor kinase A

TRP	Inflammatory mediator regulation of TRP channels
TRPML	mucolipin
TSE	transmissible spongiform encephalopathies
TAB	TGF-beta-activated kinase 1 and MAP3K7-binding protein
UBA	ubiquitin-bounding domain
TCA	Tricarboxylic acid
uPA	Urokinase-type plasminogen activator
UPS	ubiquitin-proteasome system
USA	United States America
UV	ultraviolet
TEER	transepithelial electrical resistance
TERC	Thylakoid membrane protein TERC
VEGFR	Vascular smooth muscle contraction
TGA	thermal gravimetric analysis
THF	tetrahydrofuran
Vps	vacuolar protein sorting
vWF	Von Willebrand factor
TMS	Transcranial magnetic stimulation
TPSA	topical polar surface area
TRR	tRNA Arginine
TYR	tyrosine
WHO	World Health Organization
UBR	E3 ubiquitin-protein ligase UBR
WIPIs	WD repeat domain phosphoinositide-interacting 1 and 2
UFD	ubiquitin-fusion degradation
UPLC	Ultra Performance Liquid Chromatography
US	United States
USP	United States Pharmacopeia
VAL	valine
VCAM1	Vascular cell adhesion protein 1
VEGFA	*Vascular endothelial growth factor A;*
XBP-1	X-box-binding protein 1
ZZ	ZZ-type zinc finger domain
α-syn	α-Synuclein
SLAMF7	signaling lymphocytic activation molecule family 7
XRPD	powder X-Ray diffractometry
SCID	severe combined immunodeficiency

Appendix B. Chemical Characterization Spectrum

The structure of small molecules I synthesized in this study were confirmed by ^{1}H-NMR, ^{13}C-NMR, and MS. The detailed characterization spectrum information and the detailed synthesis procedure for each compound are listed below.

^{1}H-NMR and ^{13}C-NMR were recorded on a Bruker 400 MHz and a Bruker 600 MHz spectrometer in Salk Hall eight floor and BST10034. The NMR sample is prepared by dissolving compounds in appropriate solvent (DMSO-d6 or CDCl$_3$ e.g.). NMR data acquisition was performed at 25 °C (298.15 K) on a Bruker 600 MHz Avance III spectrometer (Bruker Biospin) equipped with a 5 mm BBO broadband (1H/19F/2D) z-gradient cryo-probe. The Topspin software (Bruker Biospin) was used for spectrometer control and data processing. Purity was determined by a Shimadzu HPLC instrument with a Hamilton reversed phase column (HxSil, C18, 3 µm, 2.1 mm × 50 mm (H2)); eluent A consisting of 5% CH$_3$CN in H$_2$O; eluent B consisting of 90% CH$_3$CN in H$_2$O; flow rate of 0.2 mL/min; UV detection, 254 and 214 nm.

3,4-bis((4-fluorobenzyl)oxy)benzaldehyde (**5.1, XIE5-1-24**).
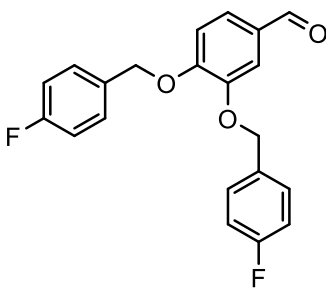
First, 3, 4-dihydroxybenzaldehyde (3.00 g, 21.7 mmol) was diluted with dry dimethylformamide (DMF, 50 mL). 1-(bromomethyl)-4-fluorobenzene (8.44 g, 44.7 mmol) was added slowly, followed by anhydrous K$_2$CO$_3$ (9.60 g, 69.4 mmol). The mixture was stirred at room temperature for 2 hours. Additional K$_2$CO$_3$ (2.40 g, 17.3 mmol) was added, and the mixture was heated to 70 °C for 30 minutes and then cooled to room

was added, and the mixture was heated to 70 °C for 30 minutes and then cooled to room

temperature. The mixture was partitioned between H_2O and EtOAc (120 mL each). The organic layer was separated, and the water layer was extracted with ether (3 × 50 mL). The pooled organic layers were washed with H_2O (2 × 50 mL) and saturated aqueous NaCl (50 mL). The pale, straw-colored extracts were dried over anhydrous sodium sulfate and concentrated to yield a white cream-colored solid (7.33 g, yield=95%) after washing with hexanes (75 mL) and drying. The product 3,4-bis((4-fluorobenzyl)oxy)benzaldehyde (**5.1, XIE5-1-24)** was characterized by ^{1}H NMR (600MHz, CDCl$_3$): 9.85 (s, 1H), 7.51-7.50 (d, J = 2Hz, 1H), 7.48-7.41 (m, 5H), 7.12-7.04 (m, 5H), 5.22-5.18 (d, J = 16.4Hz, 4H). ^{13}C NMR (151MHz, CDCl$_3$) δ 190.76-190.75 (d, J=1.5Hz), 163.41-163.37 (d, J = 6Hz), 161.77-161.73 (d, J = 6Hz), 154.04, 149.04, 132.22-132.20 (d), 131.89-131.87 (d, J = 3Hz), 130.44, 129.22-129.17 (d, J = 4.5Hz), 129.04-128.99 (d, J = 4.5Hz), 126.88, 115.71-115.60-115.56-115.46 (m), 113.08, 112.28, 70.37, 70.25.

3,4-bis((4-chlorobenzyl)oxy)benzaldehyde (**6-1, XIE5-1-84**).

First, 3, 4-dihydroxybenzaldehyde (5g, 36mmol) was diluted with dry dimethylformamide (DMF, 50 mL). 1-(bromomethyl)-4-chlorobenzene (15.6 g, 79mmol) was added slowly, followed by anhydrous K_2CO_3 (18g, 112mmol). The mixture was stirred at room temperature for 2 hours. Additional K_2CO_3 (5 g, 35mmol) was added, and the mixture was heated to 70 °C for 30 minutes and then cooled to room temperature. The mixture was partitioned between H_2O and ether (120 mL each). The organic layer was separated, and the water layer was extracted with ether (3 × 50 mL). The pooled organic layers were washed with H_2O (2 × 50 mL) and saturated aqueous NaCl (50 mL). The pale, straw-colored extracts were dried over anhydrous

sodium sulfate and concentrated to yield a white solid (8.39g, yield: 60%) after washing with hexanes (75 mL) and drying. The product was characterized by ^{1}H NMR (600MHz, CDCl$_3$): 9.850 (s, 1H), 7.498-7.448 (m, 2H), 7.425-7.362 (m, 8H), 7.041-7.021 (d, J = 8 Hz, 1H), 5.223-5.184 (d, J = 15.6Hz, 4H). ^{13}C NMR (151MHz, CDCl$_3$) δ 190.71, 153.88, 148.93, 134.91, 134.59, 134.04, 133.90, 130.46, 128.89, 128.80, 128.64, 128.45, 126.90, 113.01, 112.11, 70.19, 70.10.

3,4-bis((2,4-difluorobenzyl)oxy)benzaldehyde (**4.1, XIE5-1-85**)

First, 3, 4-dihydroxybenzaldehyde (6.1g, 44mmol) was diluted with dry dimethylformamide (DMF, 50 mL). 1-(bromomethyl)-2,4-difluorobenzene (18.63g, 11.6ml, 90mmol) was added slowly, followed by anhydrous K$_2$CO$_3$ (12g, 86.8mmol). The mixture was stirred at room temperature for 2 hours. Additional K$_2$CO$_3$ (3 g, 22mmol) was added, and the mixture was heated to 70 °C for 30 minutes and then cooled to room temperature. The mixture was partitioned between H$_2$O and ether (120 mL each). The organic layer was separated, and the water layer was extracted with EtOAc (3 × 50 mL). The pooled organic layers were washed with H$_2$O (2 × 50 mL) and saturated aqueous NaCl (50 mL). The pale, straw-colored extracts were dried over anhydrous sodium sulfate and concentrated to yield a white solid (10.03g, yield=61%) after washing with hexanes (75 mL) and drying. The product 3,4-bis((2,4-difluorobenzyl)oxy)benzaldehyde (**4.1, XIE5-1-85**) was characterized by ^{1}H NMR

(600MHz, CDCl$_3$): 9.862 (s, 1H), 7.598-7.574 (m, 4H), 7.356-7.305 (m, 3H), 7.143-7.155 (m, 2H), 5.262-5.202 (d, J = 24Hz, 4H). ^{13}C NMR (151MHz, CDCl$_3$) δ 190.71, 163.82-162.05 (dd, 2C), 161.54-59.64 (dt, 2C), 153.85, 148.92, 130.79-130.53 (dt, 2C), 130.71, 126.99, 119.71-119.25 (dt, 2C), 113.23-111.37 (dt, 2C), 104.13-103.79 (tri, 2C), 64.65-64.29 (dd, 2C).

3,4-bis(benzyloxy)benzaldehyde (**3.1, XIE5-1-86**).
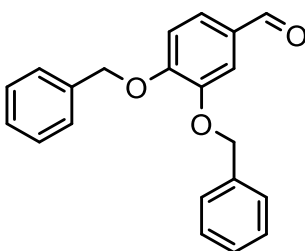
First, 3, 4-dihydroxybenzaldehyde (3.00 g, 21.7 mmol) was diluted with dry dimethylformamide (DMF, 50 mL). Benzyl bromide (7.65 g, 5.4ml, 44.7 mmol) was added slowly, followed by anhydrous K$_2$CO$_3$ (9.60 g, 69.4 mmol). The mixture was stirred at room temperature for 2 hours. Additional K$_2$CO$_3$ (2.40 g, 17.3 mmol) was added, and the mixture was heated to 70 °C for 30 minutes and then cooled to room temperature. The mixture was partitioned between H$_2$O and ether (120 mL each). The organic layer was separated, and the water layer was extracted with ether (3 × 50 mL). The pooled organic layers were washed with H$_2$O (2 × 50 mL) and saturated aqueous NaCl (50 mL). The pale, straw-colored extracts were dried over anhydrous sodium sulfate and concentrated to yield a white solid (4.7g, yield: 68%) after washing with hexanes (75 mL) and drying. The product 3,4-bis(benzyloxy)benzaldehyde (**3.1, XIE5-1-86**) was characterized by ^{1}H NMR (600MHz, CDCl$_3$): 9.837 (s, 1H), 7.519-7.345 (m, 12H), 7.061-7.040 (d, J = 8.4 Hz, 1H), 5.287-5.244 (d, J = 17.2 Hz, 4H). ^{13}C NMR (76 MHz, CDCl$_3$) δ 190.87, 190.86, 154.26, 149.19, 136.56, 136.24, 130.30, 128.68 (2C), 128.61 (2C), 128.14, 128.04, 127.33(2C), 127.08 (2C), 126.73, 113.08, 112.33, 70.97, 70.83. LC−MS (ESI): m/z 319.3 (M + H)$^+$.

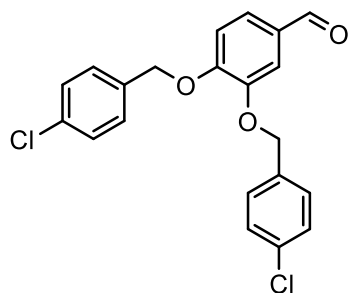3,4-bis((4-methylbenzyl)oxy)benzaldehyde (**7.1, XIE5-1-12/I4**).
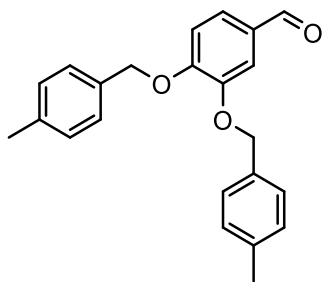
First, 3, 4-dihydroxybenzaldehyde (3g, 21.7mmol) was diluted with dry dimethylformamide (DMF, 50 mL). 1-(bromomethyl)-4-methylbenzene (8.32g, 45mmol) was added slowly, followed by anhydrous K_2CO_3 (10g, 70 mmol). The mixture was stirred at room temperature for 2 hours. Additional K_2CO_3 (2 g, 15 mmol) was added,

and the mixture was heated to 70 °C for 30 minutes and then cooled to room temperature. The mixture was partitioned between H_2O and ether (120 mL each). The organic layer was separated, and the water layer was extracted with ether (3 × 50 mL). The pooled organic layers were washed with H_2O (2 × 50 mL) and saturated aqueous NaCl (50 mL). The pale, straw-colored extracts were dried over anhydrous sodium sulfate and concentrated to yield a white solid (5.2g, yield: 70%). after washing with hexanes (75 mL) and drying. The product 3,4-bis((4-methylbenzyl)oxy)benzaldehyde (**7-1, XIE5-1-12**) was characterized by ^1H NMR (600MHz, CDCl$_3$): 9.822 (s, 1H), 7.498-7.493 (d, J = 2Hz, 1H), 7.433-7.428, 7.412-7.408 (dd, 1H), 7.383-7.339 (t, 3H), 7.220-7.194 (dd, 4H), 7.042-7.021 (d, J = 8.4 Hz, 1H), 5.241-5.196 (d, J = 18 Hz, 4H), 2.384 (s, 6H). ^{13}C NMR (101 MHz, CDCl3) δ 190.90, 154.35, 149.21, 137.88, 137.76, 133.5, 133.22 (2C), 130.19, 129.34 (2C), 129.27 (2C), 127.45 (2C), 127.18 (2C), 126.62, 113.10, 70.91, 70.78, 21.24. LC−MS (ESI): m/z 347.5 (M + H)$^+$.
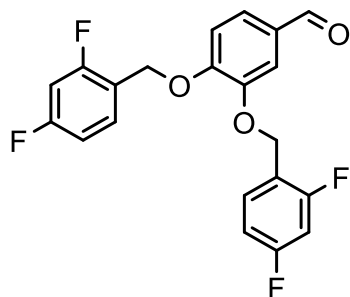
3,5-bis((4-chlorobenzyl)oxy)benzaldehyde (**8-1, XIE5-1-83**)
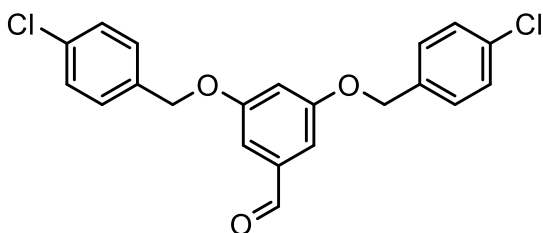
First, 3, 5-dihydroxybenzaldehyde (3g, 21.7mmol) was diluted with dry dimethylformamide (DMF, 50 mL). 1-(bromomethyl)-4-chlorobenzene (9.2 g, 45mmol) was added slowly, followed by anhydrous K_2CO_3 (10g, 70mmol). The mixture was stirred at room temperature for 2 hours. Additional K_2CO_3 (3 g, 22mmol) was added, and the mixture was heated to 70 °C for 30 minutes and then cooled to room temperature. The mixture was partitioned between H_2O and ether (120 mL each). The organic layer was separated, and the water layer was extracted with ether (3 × 50 mL). The pooled organic layers were washed with H_2O (2 × 50 mL) and saturated aqueous NaCl (50 mL). The pale, straw-colored extracts were dried over anhydrous sodium sulfate and concentrated to yield a white solid (7g, yield: 82%) after washing with hexanes (75 mL) and drying. The product was characterized by ^{1}H-NMR (CDCl$_3$): 9.925 (s, 1H), 7.394 (m, 8H), 7.123-7.117 (m, 2H), 6.845 (m, 1H), 5.090 (s, 4H). ^{13}C NMR (151 MHz, CDCl$_3$) δ 191.65, 160.15 (2C), 138.49 (2C), 134.67 (2C), 134.10, 128.90 (4C), 128.85 (4C), 108.66, 108.37 (2C), 69.60 (2C). LC−MS (ESI): m/z 319.3 (M + H)$^+$.

3,5-bis((4-methylbenzyl)oxy)benzaldehyde (**9.1, XIE5-1-82**)
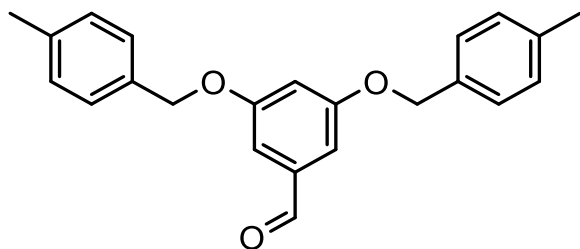
First, 3, 5-dihydroxybenzaldehyde (3g, 21.7mmol) was diluted with dry dimethylformamide (DMF, 50 mL). 1-(bromomethyl)-4-methylbenzene (8.32g, 45mmol) was added slowly, followed by anhydrous K_2CO_3 (10g, 70mmol). The mixture was stirred at room temperature for 2 hours. Additional K_2CO_3

(2 g, 14mmol) was added, and the mixture was heated to 70 °C for 30 minutes and then cooled to room temperature. The mixture was partitioned between H_2O and ether (120 mL each). The organic layer was separated, and the water layer was extracted with ether (3 × 50 mL). The pooled organic layers were washed with H_2O (2 × 50 mL) and saturated aqueous NaCl (50 mL). The pale, straw-colored extracts were dried over anhydrous sodium sulfate and concentrated to yield a white solid (4.5g, yield: 61%). after washing with hexanes (75 mL) and drying. The product was characterized by[1]H-NMR (CDCl$_3$): 9.919 (s, 1H), 7.354-7.335 (m, 4H), 7.242-7.223 (m, 4H), 7.127-7.122 (m, 2H), 6.879 (m, 1H), 5.073 (s, 4H), 2.936 (s, 6H). ^{13}C NMR (151 MHz, CDCl$_3$) δ 191.93, 160.43 (2C), 138.37 (2C), 138.08 (2C), 133.20, 129.37 (4C), 127.74 (4C), 108.72 (2C), 108.27, 70.34 (2C), 21.24 (2C).

N-(3,4-bis((4-fluorobenzyl)oxy)benzyl)-1-(furan-2-yl)methanamine (**5.8, XIE5-2-1**)

3,4-bis((4-fluorobenzyl)oxy)benzaldehyde (**5.1,** 356 mg, 1 mmol) was dissolved in dry ethanol, and furan-2-ylmethanamine (97.2mg, 1 mmol) wasadded in. The reaction mixture was stirred for 12 hours at 65 °C. The reaction solution was then cooled down to room temperature. $NaBH_4$ (57mg, 1 mmol) was added slowly in small portions, and the resulting solution was stirred for another 12 hours (143, 144). The solvent was evaporated in vacuum, and the residue was dissolved in water and extracted with ethyl acetate. The organic layers were combined and dried with Na_2SO_4, filtered, and evaporated in a vacuum. The residue was purified by a flash column to generate the desired product N-(3,4-bis((4-fluorobenzyl)oxy)benzyl)-1-(furan-2-yl)methanamine (**5.8, XIE5-2-1**), a white solid (43mg, yield: 10%). The structure was characterized by $^-$ ^{1}H-NMR (400Hz, DMSO-d^6): 7.546-7.545 (m, 1H), 7.501-7.450 (m, 4H), 7.219-7.174 (m, 4H), 7.057-7.053 (d, J = 1.6 Hz, 1H), 6.989-6.969 (d, J = 8 Hz, 1H), 6.835-6.831, 6.814-6.810 (dd, 1H), 6.389-6.377 (m, 1H), 6.212-6.205 (d, J = 2.8Hz, 1H), 5.078-5.064 (d, J = 4.8 Hz, 4H), 3.584-3.578 (d, J = 2.4 Hz, 4H). ^{13}C NMR (101 MHz, CDCl$_3$) δ 161.22 (2C), 159.77, 148.88, 147.77, 141.97, 134.13 (2C), 133.11-133.01 (t), 129.30-129.17 (dd, 4C), 121.27, 120.43, 115.48 (4C), 115.26, 113.72, 112.34, 70.91-70.67 (d, J = 24Hz, 2C), 55.22, 53.03-52.72 (d, J =31Hz). LC−MS (ESI): m/z 436.6 (M + H)$^+$

N-(3,4-bis((4-fluorobenzyl)oxy)benzyl)-1-(3-methoxyphenyl)methanamine(**5.14, XIE5-2-2**).

3,4-bis((4-fluorobenzyl)oxy)benzaldehyde (**5.1,** 356 mg, 1 mmol) was dissolved in dry ethanol, and furan-2-ylmethanamine (97.2mg, 1 mmol) was added in. The reaction mixture was stirred for 12 hours at 65 °C. The reaction solution was then cooled down to room temperature. NaBH$_4$ (57mg, 1 mmol) was added slowly in small portions, and the resulting solution was stirred for another 12 hours (143, 144). The solvent was evaporated in vacuum, and the residue was dissolved in water and extracted with ethyl acetate. The organic layers were combined and dried with Na$_2$SO$_4$, filtered, and evaporated in a vacuum. The residue was purified by a flash column to generate the desired product N-(3,4-bis((4-fluorobenzyl)oxy)benzyl)-1-(3-methoxyphenyl)methanamine(**5.14, XIE5-2-2**), a white solid (171mg, yield: 36%). The structure was characterized by ^{1}H-NMR (CDCl$_3$, 400Hz): 7.497-7.450 (m, 3H), 7.215-7.171 (m, 4H), 7.074-6.871 (m, 5H), 5.076-5.064 (d, J = 4.8 Hz, 4H), 3.733 (s, 3H), 3.592-3.572 (d, J = 8 Hz, 4H). LC−MS (ESI): m/z 476.2 (M + H)$^+$. ^{13}C NMR (76 MHz, CDCl$_3$) δ 160.81, 159.78, 148.91, 147.80, 141.88, 134.05, 133.13-133.02 (dd, 2C), 129.41, 129.32-129.15 (t, 4C), 121.30, 120.44, 115.50-115.22 (d, J= 21.28Hz, 4C), 115.30-115.20, 113.74 (2C), 112.37, 70.92, 70.69, 55.22 (2C), 52.99-52.68 (d, J=23.56Hz).

N-(3,4-bis((2,4-difluorobenzyl)oxy)benzyl)-1-(thiophen-2-yl)methanamine (**4.7, XIE5-2-3**)

3,4-bis((2,4-difluorobenzyl)oxy)benzaldehyde (**4-1,** 390 mg, 1 mmol) was dissolved in dry ethanol, and thiophen-2-ylmethanamine (113mg, 1 mmol) was added in. The reaction mixture was stirred for 12 hours at 65 °C. The reaction solution was then cooled down to room temperature. NaBH$_4$ (57mg, 1 mmol) was added slowly in small portions, and the resulting solution was stirred for another 12 hours (143, 144). The solvent was evaporated in vacuum, and the residue was dissolved in water and extracted with ethyl acetate. The organic layers were combined and dried with Na$_2$SO$_4$, filtered, and evaporated in a vacuum. The residue was purified by a flash column to generate the desired product N-(3,4-bis((2,4-difluorobenzyl)oxy)benzyl)-1-(thiophen-2-yl)methanamine (**4.7, XIE5-2-3**), a white solid (65mg, yield: 13%). The structure was characterized by ^{1}H-NMR (400MHz, DMSO-d): 7.576-7.551 (m, 2H), 7.389-7.379 (d, J=1H), 7.315-7.265 (m, 2H), 7.133-6.874 (m, 7H), 5.108-5.091 (d, J = 6.8Hz, 4H), 3.812 (s, 2H), 3.635 (s, 2H). LC−MS (ESI): m/z 488.1 (M + H)[+]. ^{13}C NMR (151 MHz, DMSO) δ 161.31-161.23 (d, J = 10.6Hz, 2C), 159.66-159.58 (d, J = 12.1Hz, 2C), 147.91, 146.71, 145.03, 134.26 (2C), 131.80 (m), 126.55, 124.39, 124.38, 121.04 (2C), 114.88-114.78 (d, J = 15.1Hz), 111.54-111.38 (dd), 104.12-103.78 (dd, 2C), 64.20-64.00 (d, J = 30Hz, 2C), 51.40, 46.62.

N-(3,4-bis((2,4-difluorobenzyl)oxy)benzyl)-3-morpholinopropan-1-amine (**4.11, XIE5-2-7**)

3,4-bis((2,4-difluorobenzyl)oxy)benzaldehyde (**4.1, 390mg, 1 mmol**) was dissolved in dry ethanol, and 3-morpholinopropan-1-amine (144mg, 1 mmol) was added in. The reaction mixture was stirred for 12 hours at 65 °C. The reaction solution was then cooled down to room temperature. NaBH$_4$ (57mg, 1 mmol) was added slowly in small portions, and the resulting solution was stirred for another 12 hours (143, 144). The solvent was evaporated in vacuum, and the residue was dissolved in water and extracted with ethyl acetate. The organic layers were combined and dried with Na$_2$SO$_4$, filtered, and evaporated in a vacuum. The residue was purified by a flash column to generate the desired product N-(3,4-bis((2,4-difluorobenzyl)oxy)benzyl)-3-morpholinopropan-1-amine (**4.11, XIE5-2-7**), a yellow solid (83mg, yield: 16%). The structure was characterized by ^{1}H NMR (DMSO-d^6): 7.584-7.529 (m, 2H), 7.316-7.271 (m, 2H), 7.234 (m, 1H), 7.116-7.095 (m, 3H), 6.998-6.978 (m, 1H), 5.117-5.110 (d, J = 2.8Hz, 4H), 3.858 (s, 2H), 3.542 (m, 4H), 2.723-2.711 (m, 2H), 2.325 (m, 6H), 1.697-1.662 (m, 2H). ^{13}C NMR (151 MHz, DMSO) δ 161.34 (m, 2C), 159.69 (2C), 147.87, 146.05, 131.79 (2C), 131.76, 120.29 (2C), 120.10, 115.78, 114.78 (2C), 111.57-111.43 (dd), 104.16-103.81 (t, 2C), 66.08 (2C), 64.12 (m, 2C), 55.79 (2C), 53.13, 48.57, 45.82, 39.95. LC−MS (ESI): m/z 519 (M + H)$^+$.

N-(3,4-bis((2,4-difluorobenzyl)oxy)benzyl)-1-(pyridin-2-yl)methanamine (**4.9, XIE5-2-10)**
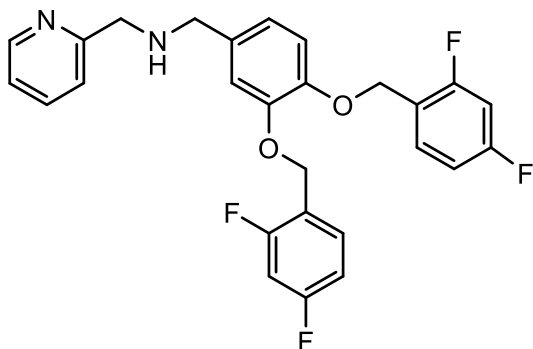
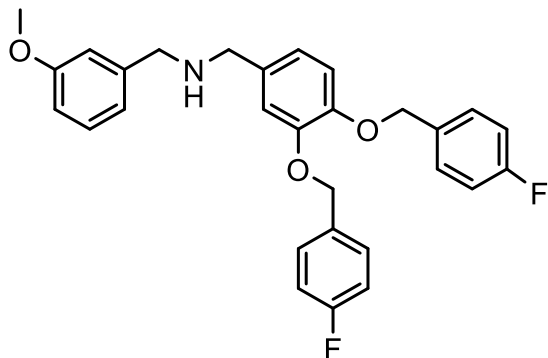3,4-bis((2,4-difluorobenzyl)oxy)benzaldehyde (**4.1,** 390 mg, 1 mmol) was dissolved in dry ethanol, and pyridin-2-ylmethanamine (108mg, 1 mmol) was added in. The reaction mixture was stirred for 12 hours at 65 °C. The reaction solution was then cooled down to room temperature. NaBH$_4$ (57mg, 1 mmol) was added slowly in small portions, and the resulting solution was stirred for another 12 hours (143, 144). The solvent was evaporated in vacuum, and the residue was dissolved in water and extracted with ethyl acetate. The organic layers were combined and dried with Na$_2$SO$_4$, filtered, and evaporated in a vacuum. The residue was purified by a flash column to generate the desired product N-(3,4-bis((2,4-difluorobenzyl)oxy)benzyl)-1-(pyridin-2-yl)methanamine (**4.9, XIE5-2-10)**, a white solid (48mg, yield: 10%). The structure was characterized by ^{1}H-NMR (400Hz, DMSO-d^6): 8.511 (s, 1H), 8.454-8.444 (d, *J* = 4 Hz, 1H), 7.742-7.725 (d, *J* = 6.8 Hz, 1H), 7.576-7.527 (m, 2H), 7.363-7.259 (m, 3H), 7.124-7.082 (m, 3H), 7.043-7.023 (m, 1H), 6.897-6.878 (d, *J* = 3.6 Hz, 1H), 5.103-5.089 (d, *J* = 5.6Hz, 4H), 3.657-3.616 (d, *J* = 16.4 Hz, 4H). ^{13}C NMR (151Hz, DMSO-d^6) δ 161.34 (t), 159.70 (2C), 159.62 (2C), 149.32, 148.11-147.83 (t), 146.74, 136.10, 135.73-135.63 (m, 2C), 134.30, 131.86 (m), 123.33 (m, 2C), 121.07, 120.60 (m), 114.94, 114.77, 111.55-111.41 (d, *J* = 21.1 Hz, 2C), 103.97 (t, 2C), 64.24-64.03 (d, *J* = 31.7 Hz, 2C), 51.75, 49.35
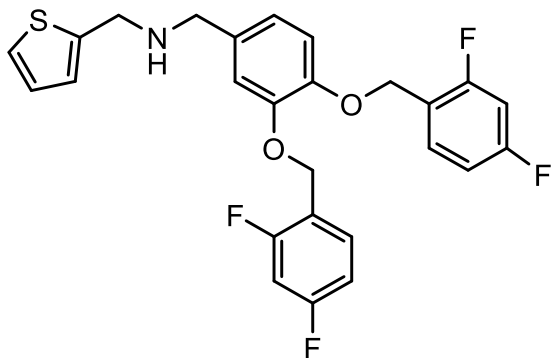
N-(3,4-bis((2,4-difluorobenzyl)oxy)benzyl)-1-(3,4,5-trimethoxyphenyl)methanamine (**4.15, XIE5-2-11**)

3,4-bis((2,4-difluorobenzyl)oxy)benzaldehyde (**4.1,** 195 mg, 0.5 mmol) was dissolved in dry ethanol, and 3,4,5-trimethoxyphenyl)methanamine (99mg, 0.5 mmol) was added in. The reaction mixture was stirred for 12 hours at 65 °C. The reaction solution was then cooled down to room temperature. NaBH$_4$ (29mg, 0.5 mmol) was added slowly in small portions, and the resulting solution was stirred for another 12 hours (143, 144). The solvent was evaporated in vacuum, and the residue was dissolved in water and extracted with ethyl acetate. The organic layers were combined and dried with Na$_2$SO$_4$, filtered, and evaporated in a vacuum. The residue was purified by a flash column to generate the desired product N-(3,4-bis((2,4-difluorobenzyl)oxy)benzyl)-1-(3,4,5-trimethoxyphenyl)methanamine (**4.15, XIE5-2-11**), a white solid (34mg, yield: 12%). The structure was characterized by ^{1}H-NMR (400Hz, DMSO-d^6): 7.577-7.454 (m, 2H), 7.306-7.262 (m, 2H), 7.135-7.026 (m, 4H), 6.908-6.889 (m, 1H), 6.651 (s, 2H), 5.099-5.089 (d, J = 4.0 Hz, 4H), 3.764 (s, 6H), 3.638 (s, 3H), 3.617-3.587 (d, J = 12.0 Hz, 4H). ^{13}C NMR (151Hz, DMSO-d^6) δ 163.03 (2C), 161.39-161.23 (t, 2C), 159.66-159.58 (d, J = 12.1 Hz), 152.64 (2C), 147.94, 146.64, 136.50, 135.91, 134.53, 131.86-131.79 (t, 2C), 121.07 (2C), 120.63-120.53 (dd), 114.90-114.77 (d, J = 19.6 Hz, 2C), 111.53-111.37 (m), 104.85 (2C), 104.09-103.75 (t, 2C), 64.21-64.00 (d, J = 12.0 Hz, 2C), 63.98, 59.92, 55.67, 52.15, 51.68.

N-(3,4-bis((2,4-difluorobenzyl)oxy)benzyl)-3-(1H-imidazol-1-yl)propan-1-amine (**4.10, XIE5-2-13**)

3,4-bis((2,4-difluorobenzyl)oxy)benzaldehyde (**4.1,** 195 mg, 0.5 mmol) was dissolved in dry ethanol, and 3-(1H-imidazol-1-yl)propan-1-amine (63mg, 0.5 mmol) was added in. The reaction mixture was stirred for 12 hours at 65 °C. The reaction solution was then cooled down to room temperature. NaBH$_4$ (28mg, 0.5 mmol) was added slowly in small portions, and the resulting solution was stirred for another 12 hours (143, 144). The solvent was evaporated in vacuum, and the residue was dissolved in water and extracted with ethyl acetate. The organic layers were combined and dried with Na$_2$SO$_4$, filtered, and evaporated in a vacuum. The residue was purified by a flash column to generate the desired product N-(3,4-bis((2,4-difluorobenzyl)oxy)benzyl)-3-(1H-imidazol-1-yl)propan-1-amine (**4.10, XIE5-2-13**), a white solid (50mg, yield: 20%). The structure was characterized by ^{1}H-NMR (DMSO-d^6): 7.585-7.523 (m, 3H), 7.314-7.265 (t, 2H), 7.132-7.103 (m, 4H), 7.035-7.014 (m, 1H), 6.885-6.871 (m, 2H), 5.100-5.088 (d, J = 4.8 Hz, 4H), 4.029-4.012-3.995 (t, J =6.8 Hz, 2H), 3.610 (s, 2H), 2.422-2.391 (m, 2H), 1.850-1.816 (m, 2H). ^{13}C NMR (151Hz, DMSO-d^6) δ 161.40-161.32 (d, J = 16Hz, 2C), 159.65-159.57 (m, 2C), 147.93, 146.71, 137.18, 131.84-131.80 (d, J = 6 Hz, 2C), 128.22, 121.11, 120.63, 120.53-120.45 (t, 2C), 119.26, 114.90-114.85 (d, J = 7.5 Hz, 2C), 111.54, 111.40, 104.10-103.76 (t, 2C), 64.21-64.02 (dd, 2C), 52.34, 48.56, 45.03-43.91 (d, J = 160 Hz), 30.71. LC−MS (ESI): m/z 500.5 (M + H)$^+$.
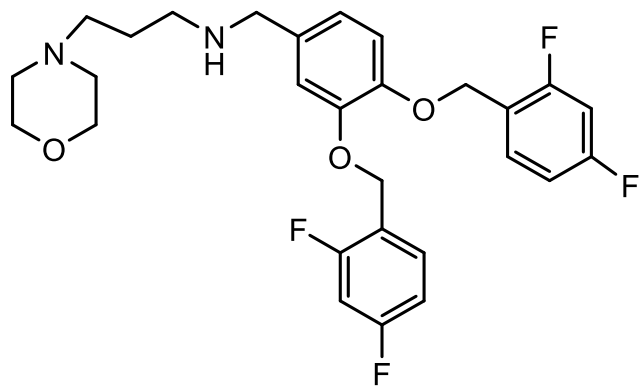
N-(3,4-bis((2,4-difluorobenzyl)oxy)benzyl)-1-(furan-2-yl)methanamine (**4.8, XIE5-2-14**)
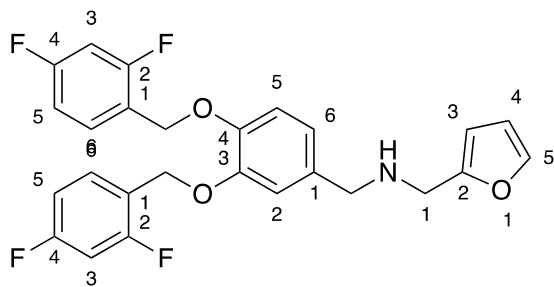
3,4-bis((2,4-difluorobenzyl)oxy)benzaldehyde (**4.8,** 195 mg, 0.5 mmol) was dissolved in dry ethanol, and furan-2-ylmethanamine (48mg, 0.5 mmol) was added in. The reaction mixture was stirred for 12 hours at 65 °C. The reaction solution

was then cooled down to room temperature. NaBH$_4$ (28mg, 0.5 mmol) was added slowly in small portions, and the resulting solution was stirred for another 12 hours (143, 144). The solvent was evaporated in vacuum, and the residue was dissolved in water and extracted with ethyl acetate. The organic layers were combined and dried with Na$_2$SO$_4$, filtered, and evaporated in a vacuum. The residue was purified by a flash column to generate the desired product N-(3,4-bis((2,4-difluorobenzyl)oxy)benzyl)-1-(furan-2-yl)methanamine (**4.8, XIE5-2-14**), a yellow solid (63mg, yield: 26%). The structure was characterized by ^{1}H-NMR (600MHz, CDCl$_3$): 7.537-7.460 (m, 2H), 7.400-7.394 (m, 1H), 7.023-7.018 (d, J = 2.0 Hz, 1H), 6.948-6.815 (m, 6H), 6.355-6.342 (m, 1H), 6.193-6.183 (m, 1H), 5.159-5.142 (d, J = 6.8 Hz, 4H), 3.780-3.735 (d, J = 18Hz, 4H). ^{13}C NMR (151MHz, CDCl$_3$) δ 161.96-161.31 (m, 2C), 159.73-159.65 (m, 2C), 152.78, 148.74, 147.69, 141.90, 133.81, 131.45, 130.82-130.71 (m, 2C), 121.81 (2C), 115.42, 111.41-111.24 (m, 2C), 110.16, 108.37, 107.20, 103.75-103.73 (d, J = 3 Hz, 2C), 64.87-64.70 (dd, 2C), 52.26, 45.13. LC−MS (ESI): m/z 472.3 (M + H)$^+$.

N-(3,4-bis((2,4-difluorobenzyl)oxy)benzyl)-1-(3-methoxyphenyl)methanamine (**4.16, XIE5-2-15**)

3,4-bis((2,4-difluorobenzyl)oxy)benzaldehyde (**4.1,** 195 mg, 0.5 mmol) was dissolved in dry ethanol, and (3-methoxyphenyl)methanamine (68mg, 0.5 mmol) was added in. The reaction mixture was stirred for 12 hours at 65 °C. The reaction solution was then cooled down to room temperature. NaBH$_4$ (30mg, 0.5 mmol) was added slowly in small portions, and the resulting solution was stirred for another 12 hours (143, 144). The solvent was evaporated in vacuum, and the residue was dissolved in water and extracted with ethyl acetate. The organic layers were combined and dried with Na$_2$SO$_4$, filtered, and evaporated in a vacuum. The residue was purified by a flash column to generate the desired product N-(3,4-bis((2,4-difluorobenzyl)oxy)benzyl)-1-(3-methoxyphenyl)methanamine (**4.16, XIE5-2-15**), a white solid (45mg, yield: 20%). The structure was characterized by ^{1}H-NMR (600MHz, CDCl$_3$): 7.524-7.489 (m, 2H), 7.290-7.258 (m, 2H), 6.937-6.828 (m, 9H), 5.166-5.151 (d, J = 6Hz, 4H), 3.844 (s, 3H), 3.789-3.759 (d, J = 12Hz, 4H). ^{13}C NMR (151Hz, CDCl$_3$) δ 163.61-163.51 (m, 2C), 161.96-161.86 (m, 2C), 161.45-161.32 (m), 159.78, 148.75, 147.60, 141.92, 134.50, 130.89-130.74 (m, 2C), 129.41, 121.63 (2C), 120.44, 115.44, 115.30, 113.67, 112.42, 111.41-111.25 (dd, 2C), 103.93-103.57 (m, 2C), 64.90-64.88 (d, J = 3Hz), 64.71-64.69 (d, J = 3Hz), 55.19, 53.02, 52.67. LC−MS (ESI): m/z 512.4 (M + H)$^+$.

N-(3,4-bis((4-fluorobenzyl)oxy)benzyl)-1-(thiophen-2-yl)methanamine (**5.7, XIE5-2-16**)
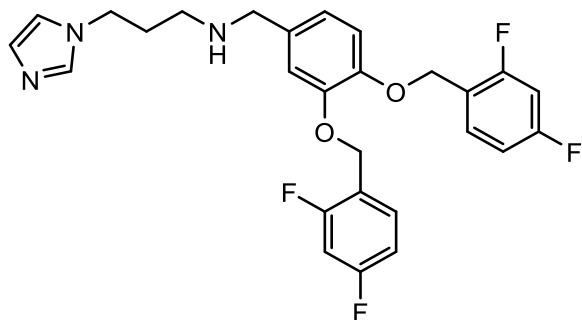

3,4-bis((4-fluorobenzyl)oxy)benzaldehyde (**5-1,** 178 mg, 0.5 mmol) was dissolved in dry ethanol, and thiophen-2-ylmethanamine (57mg, 0.5 mmol) was added in. The reaction mixture was stirred for 12 hours at 65 °C. The reaction solution was then cooled down to room temperature. $NaBH_4$ (28mg, 0.5 mmol) was added slowly in small portions, and the resulting solution was stirred for another 12 hours (143, 144). The solvent was evaporated in vacuum, and the residue was dissolved in water and extracted with ethyl acetate. The organic layers were combined and dried with Na_2SO_4, filtered, and evaporated in a vacuum. The residue was purified by a flash column to generate the desired product N-(3,4-bis((4-fluorobenzyl)oxy)benzyl)-1-(thiophen-2-yl)methanamine (**5.7, XIE5-2-16**), a white solid (93mg, yield: 40%). The structure was characterized by ^{1}H-NMR (150MHz, CDCl$_3$): 7.449-7.395 (m, 4H), 7.257-7.241 (m, 1H), 7.085-6.971 (m, 6H), 6.627-6.875 (m, 3H), 5.127-5.102 (d, J = 10 Hz, 4H), 3.978-9.976 (d, J = 0.8 Hz, 2H), 3.767 (s, 2H). ^{13}C NMR (600Hz, CDCl$_3$) 163.23 (2C), 161.60, 149.74, 148.89, 148.52, 147.90, 135.80, 135.58, 133.67, 133.00 (2C), 129.23 (4C), 123.40, 121.27, 115.29 (4C), 70.84-70.66 (d, J = 27.2 Hz, 2C), 52.77, 50.34. LC−MS (ESI): m/z 452.3 (M + H)$^+$.

N-(3,4-bis((4-fluorobenzyl)oxy)benzyl)-3-morpholinopropan-1-amine (**5.11, XIE5-2-17**)

3,4-bis((4-fluorobenzyl)oxy)benzaldehyde (**5.1,** 178 mg, 0.5 mmol) was dissolved in dry ethanol, and 3-morpholinopropan-1-amine (72mg, 0.5 mmol) was added in. The reaction mixture was stirred for 12 hours at 65 °C. The reaction solution was then cooled down to room temperature. $NaBH_4$ (28mg, 0.5 mmol) was added slowly in small portions, and the resulting solution was stirred for another 12 hours (143, 144). The solvent was evaporated in vacuum, and the residue was dissolved in water and extracted with ethyl acetate. The organic layers were combined and dried with Na_2SO_4, filtered, and evaporated in a vacuum. The residue was purified by a flash column to generate the desired product N-(3,4-bis((4-fluorobenzyl)oxy)benzyl)-3-morpholinopropan-1-amine (**5.11, XIE5-2-17**), a white solid (27mg, yield; 22%). The structure was characterized by ^{1}H NMR (600MHz, CDCl₃): 7.428-7.385 (m, 4H), 7.082-7.034 (m, 5H), 6.893-6.877 (m, 2H), 5.133-5.096 (d, J = 14.8, 4H), 3.762 (s, 2H), 3.633 (m, 4H), 2.745 (t, 2H), 2.451-2.416 (m, 6H), 1.768 (m, 2H). ^{13}C NMR (151Hz, CDCl3) δ 163.21, 161.58, 148.88, 148.12, 132.93-132.91 (d, J = 3Hz, 2C), 131.96, 129.31-129.13 (dd, 4C), 121.56, 115.42-115.39 (d, J = 4.5Hz, 4C), 115.28-115.25 (d, J = 4.5Hz), 115.12, 70.75-70.62 (d, J = 19.63Hz, 2C), 66.89 (2C), 57.33 (2C), 53.67, 52.96, 47.66, 25.48. LC−MS (ESI): m/z 483.3 (M + H)⁺.

N-(3,4-bis((4-fluorobenzyl)oxy)benzyl)-1-(pyridin-2-yl)methanamine (**5.9, XIE5-2-18**)

3,4-bis((4-fluorobenzyl)oxy)benzaldehyde (**5.1,** 178 mg, 0.5 mmol) was dissolved in dry ethanol, and pyridin-2-ylmethanamine (54mg, 0.5 mmol) was added in. The reaction mixture was stirred for 12 hours at 65 °C. The reaction solution was then cooled down to room temperature. NaBH$_4$ (28mg, 0.5 mmol) was added slowly in small portions, and the resulting solution was stirred for another 12 hours (143, 144). The solvent was evaporated in vacuum, and the residue was dissolved in water and extracted with ethyl acetate. The organic layers were combined and dried with Na$_2$SO$_4$, filtered, and evaporated in a vacuum. The residue was purified by a flash column to generate the desired product N-(3,4-bis((4-fluorobenzyl)oxy)benzyl)-1-(pyridin-2-yl)methanamine (**5.9, XIE5-2-18**), a white solid (23mg, yield; 20%). The structure was characterized by ^{1}H NMR (600MHz, CDCl$_3$): 8.55 (s, 1H), 8.50-8.49 (d, *J*= 4 Hz, 1H), 7.64-7.63 (d, *J* = 4Hz, 1H), 7.40-7.37 (m, 4H), 7.26-7.23 (m, 1H), 7.04-7.01 (t, 4H), 6.97 (d, 1H), 6.89-6.87 (d, *J*= 8 Hz, 1H), 6.85-6.83 (d, 1H), 5.09-5.07 (d, *J*= 8 Hz, 4H), 3.75-3.70 (d, *J*= 20 Hz, 4H), 1.76 (s, 1H). ^{13}C NMR (150Hz, CDCl$_3$) δ 163.24 (2C), 161.61, 149.75, 148.90-148.54 (d, *J*= 54 Hz), 147.91, 135.81-135.54 (d, *J*= 41 Hz), 133.62-133.06 (d, *J*= 84 Hz, 2C), 133.03-133.00 (d, *J*= 4.5 Hz), 132.98, 129.27-129.18 (t, 4C), 123.40, 121.28, 115.44-115.29 (d, *J*= 22.5 Hz, 4C), 115.21-115.12 (d, *J*= 13.5 Hz), 70.84-70.66 (d, *J*= 27.2 Hz, 2C), 52.76, 50.33.

N-(3,4-bis((4-fluorobenzyl)oxy)benzyl)-1-(3,4,5-trimethoxyphenyl)methanamine (**5.15, XIE5-2-19**)

3,4-bis((4-fluorobenzyl)oxy)benzaldehyde (**5.1,** 178 mg, 0.5 mmol) was dissolved in dry ethanol, and (3,4,5-trimethoxyphenyl)methanamine (99mg, 0.5 mmol) was added in. The reaction mixture was stirred for 12 hours at 65 °C. The reaction solution was then cooled down to room temperature. NaBH4 (29mg, 0.5 mmol) was added slowly in small portions, and the resulting solution was stirre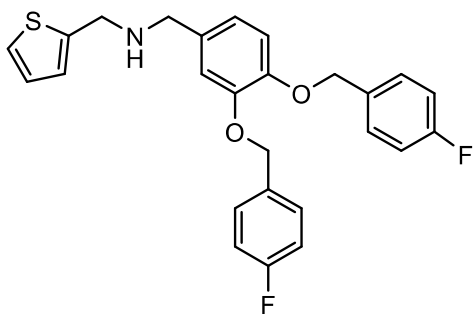d for another 12 hours (143, 144). The solvent was evaporated in vacuum, and the residue was dissolved in water and extracted with ethyl acetate. The organic layers were combined and dried with Na2SO4, filtered, and evaporated in a vacuum. The residue was purified by a flash column to generate the desired product N-(3,4-bis((4-fluorobenzyl)oxy)benzyl)-1-(3,4,5-trimethoxyphenyl)methanamine (**5.15, XIE5-2-19**), a white solid (89mg, yield: 34%). The structure was characterized by ^{1}H-NMR (600MHz, CDCl3): 7.430-7.396 (m, 4H), 7.081-7.003 (m, 5H), 6.932-6.892 (m, 2H), 6.583 (s, 2H), 5.116-5.104 (d, J = 4.8 Hz, 4H), 3.883-3.864 (d, J = 7.6 Hz, 9H), 3.753-3.739 (d, J = 6.4 Hz, 4H).^{13}C NMR (151Hz, CDCl3) δ 163.24-163.23 (d, J = 1.5 Hz, 2C), 161.60, 153.24, 148.88, 147.84, 136.86, 135.98, 133.95, 133.04-132.94 (m, 2C), 129.26-129.15 (t, 4C), 121.32, 115.43, 115.28-115.23 (t, 4C), 105.08-104.90 (d, J = 27.2 Hz), 70.86-70.72 (d, J = 21.1Hz, 2C), 60.87, 56.23, 56.10, 53.33, 52.79. LC−MS (ESI): m/z 536.1 (M + H)$^+$.

1-(benzo[d][1,3]dioxol-5-yl)-N-(3,4-bis((4-fluorobenzyl)oxy)benzyl)methanamine (**5.16, XIE5-2-20**)

3,4-bis((4-fluorobenzyl)oxy)benzaldehyde (**5.1,** 178 mg, 0.5 mmol) was dissolved in dry methanol, and benzo[d][1,3]dioxol-5-ylmethanamine (75mg, 0.5 mmol) was added in. The reaction mixture was stirred for 12 hours at 65 °C. The reaction solution was then cooled down to room temperature. NaBH4 (29mg, 0.5 mmol) was added slowly in small portions, and the resulting solution was stirred for another 12 hours (143, 144). The solvent was evaporated in vacuum, and the residue was dissolved in water and extracted with ethyl acetate. The organic layers were combined and dried with Na_2SO_4, filtered, and evaporated in a vacuum. The residue was purified by a flash column to generate the desired product 1-(benzo[d][1,3]dioxol-5-yl)-N-(3,4-bis((4-fluorobenzyl)oxy)benzyl)methanamine (**5.16, XIE5-2-20**), a white solid (34mg, yield: 28%). The structure was characterized by ^{1}H-NMR (600MHz, CDCl3): 7.475-7.446 (m, 4H), 7.221-7.173 (m, 4H), 7.056-7.051 (d, J = 2 Hz, 1H), 6.979 (s, 1H), 6.959 (s, 1H), 6.897-6.894 (d, 1H), 6.828-6.801 (m, 2H), 6.738-6.715 (dd, 1H), 5.967 (s, 2H), 5.076-5.062 (d, J = 5.6 Hz, 4H), 3.537-3.521 (d, J = 6.4 Hz, 4H). ^{13}C NMR (151 MHz, CDCl3) δ 162.49 (2C), 160.91-160.88 (d, J = 6 Hz), 148.04, 147.17, 146.79, 145.78, 134.79, 134.07, 133.60-133.58 (d, J = 3 Hz, 2C), 129.81-129.69 (d, J = 18 Hz, 4C), 120.92-120.58 (d, J=51Hz), 115.24-115.10 (d, J = 21 Hz, 4C), 114.48, 108.34, 107.81, 100.65, 69.53-69.37 (d, J = 18 Hz, 2C), 51.72, 51.52. LC−MS (ESI): m/z 490.7 (M + H)$^+$.
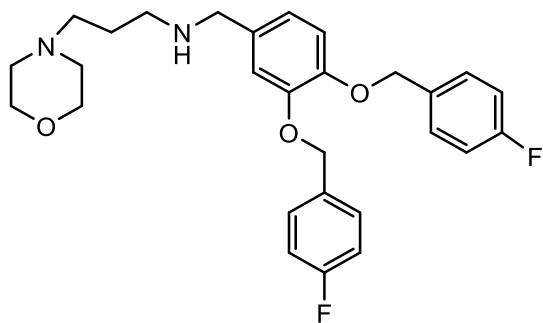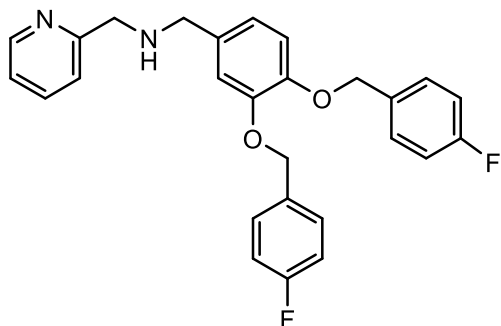
N-(3,4-bis((4-fluorobenzyl)oxy)benzyl)-3-(1H-imidazol-1-yl)propan-1-amine (**5.10, XIE5-2-21**)

3,4-bis((4-fluorobenzyl)oxy)benzaldehyde (**5.1,** 178 mg, 0.5 mmol) was dissolved in dry ethanol, and 3-(1H-imidazol-1-yl)propan-1-amine (63mg, 0.5 mmol) was added in. The reaction mixture was stirred for 12 hours at 65 °C. The reaction solution was then cooled down to room temperature. NaBH$_4$ (30mg, 0.5 mmol) was added slowly in small portions, and the resulting solution was stirred for another 12 hours (143, 144). The solvent was evaporated in vacuum, and the residue was dissolved in water and extracted with ethyl acetate. The organic layers were combined and dried with Na$_2$SO$_4$, filtered, and evaporated in a vacuum. The residue was purified by a flash column to generate the desired product N-(3,4-bis((4-fluorobenzyl)oxy)benzyl)-3-(1H-imidazol-1-yl)propan-1-amine (**5.10, XIE5-2-21**), a white solid (40mg, yield: 34%). The structure was characterized by ^{1}H-NMR (CDCl$_3$): 7.467-7.394 (m, 5H), 7.080-7.032 (m, 5H), 6.949-6.849 (m, 4H), 5.120-5.098 (d, J = 8.8 Hz, 4H), 4.053-4.036-4.019 (t, J = 6.8 Hz, 2H), 3.684 (s, 2H), 2.601-2.585-2.568 (t, J = 6.8 Hz, 2H), 1.952-1.918 (m, 2H). ^{13}C NMR (150Hz, CDCl3) δ 163.21, 161.58, 148.80, 148.00, 137.19, 133.14-132.96 (d, J = 27Hz, 2C), 129.36, 129.25-129.16 (m, 4C), 121.39, 118.87, 115.42-115.26 (dd, 4C), 115.33-115.15 (d, J = 27Hz), 70.79-70.66 (d, J = 19.5 Hz, 2C), 53.35, 45.43, 44.58, 31.03. LC−MS (ESI): m/z 464.5 (M + H)$^+$.

N-(3,4-bis((2,4-difluorobenzyl)oxy)benzyl)-4-fluoroaniline (**4.17, XIE5-2-22**)
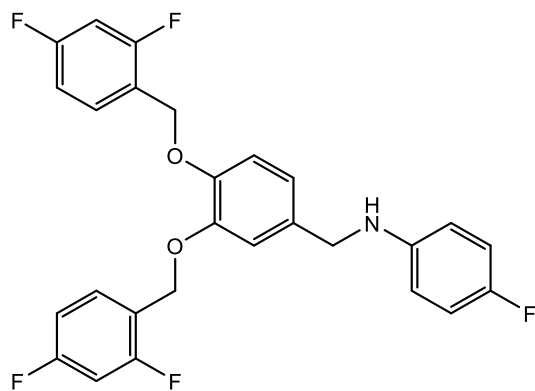
3,4-bis((2,4-difluorobenzyl)oxy)benzaldehyde (**4.1, 195 mg, 0.5 mmol**) was dissolved in dry ethanol, and 4-fluoroaniline (55mg, 0.5 mmol) was added in. The reaction mixture was stirred for 12 hours at 65 °C. The reaction solution was then cooled down to room temperature. NaBH$_4$ (30mg, 0.5 mmol) was added slowly in small portions, and the resulting solution was stirred for another 12 hours (143, 144). The solvent was evaporated in vacuum, and the residue was dissolved in water and extracted with ethyl acetate. The organic layers were combined and dried with Na$_2$SO$_4$, filtered, and evaporated in a vacuum. The residue was purified by a flash column to generate the desired product N-(3,4-bis((2,4-difluorobenzyl)oxy)benzyl)-4-fluoroaniline. White solid (20mg, yield: 9%). ^{1}H NMR (CDCl$_3$): 7.508- 7.455 (m, 2H), 7.014-6.828 (m, 9H), 6.575-6.542 (m, 3H), 5.145-5.139 (s, 4H), 4.223(s, 2H). ^{13}C NMR (151 MHz, CDCl$_3$) δ 163.61-163.53 (d, 2C), 161.96-161.88 (d, 2C), 156.70, 155.14, 148.82, 147.84, 144.38-144.37 (d, 2C), 133.29, 130.84-130.82-130.80-130.78-130.76-130.74-130.72 (m, 2C), 120.91, 120.37-120.35-120.28-120.25-120.23-120.15-120.13 (m, 2C), 115.73-115.58-115.50 (t, 2C), 114.60, 113.69-113.64 (d), 111.44-111.42-111.40-111.30-111.28-111.26 (m, 2C), 103.94-103.60 (pent, 2C), 64.85-64.68 (dd), 48.53. LC−MS (ESI): *m/z* 486.2 (M + H)$^+$.
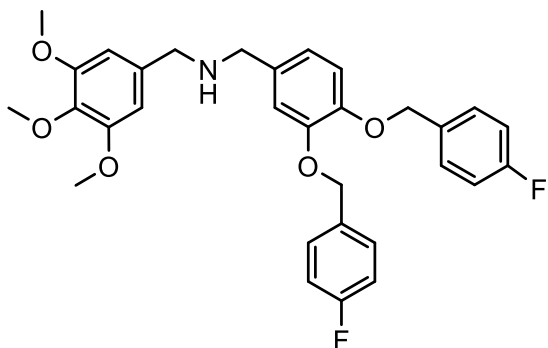
N-(3,4-bis((4-chlorobenzyl)oxy)benzyl)-1-(furan-2-yl)methanamine (**6.8, XIE5-2-31**)

3,4-bis((4-chlorobenzyl)oxy)benzaldehyde (**6-1, XIE5-1-84,** 198mg, 0.5 mmol) was dissolved in dry ethanol, and furan-2-ylmethanamine (48mg, 0.5 mmol) was added in. The reaction mixture was stirred for 12 hours at 65 °C. The reaction solution was then cooled down to room temperature. NaBH$_4$ (30mg, 0.5 mmol) was added slowly in small portions, and the resulting solution was stirred for another 12 hours (143, 144). The solvent was evaporated in vacuum, and the residue was dissolved in water and extracted with ethyl acetate. The organic layers were combined and dried with Na$_2$SO$_4$, filtered, and evaporated in a vacuum. The residue was purified by a flash column to generate the desired product N-(3,4-bis((4-chlorobenzyl)oxy)benzyl)-1-(furan-2-yl)methanamine (**6.8, XIE5-2-31**), a white solid (34mg, yield: 13%). ^{1}H-NMR (CDCl$_3$): 7.393-7.343 (m, 9H), 6.989 (m, 1H), 6.902-6.852 (m, 2H), 6.350 (m, 1H), 6.181-6.174 (d, J = 2.8 Hz, 1H), 5131-5.110 (d, J = 8.4 Hz, 4H), 3.770-3.720 (d, J = 20Hz, 4H). LC−MS (ESI): m/z 469.3 (M + H)$^+$. ^{13}C NMR (101 MHz, CDCl$_3$) δ 153.53, 148.74, 147.72, 141.90, 135.81, 135.75, 133.62 (2C), 133.61 (2C), 133.46, 128.73 (4C), 128.67 (2C), 121.51, 115.13, 115.08, 110.18, 107.23, 70.70, 70.47, 52.30, 45.15.
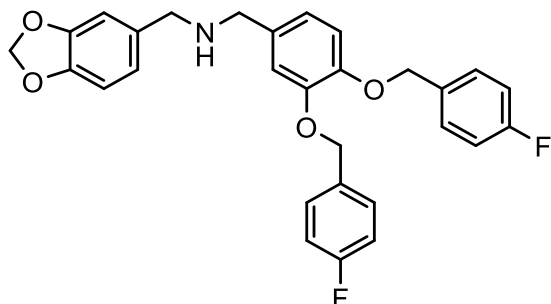
N-(3,4-bis((4-chlorobenzyl)oxy)benzyl)-1-(3-methoxyphenyl)methanamine (**6.14, XIE5-2-32**)

3,4-bis((4-chlorobenzyl)oxy)benzaldehyde (**6.1, XIE5-1-84,** 198mg, 0.5 mmol) was dissolved in dry ethanol, and (3-methoxyphenyl)methanamine (68mg, 0.5 mmol) was added in. The reaction mixture was stirred for 12 hours at 65 °C. The reaction solution was then cooled down to room temperature. NaBH$_4$ (30mg, 0.5 mmol) was added slowly in small portions, and the resulting solution was stirred for another 12 hours (143, 144). The solvent was evaporated in vacuum, and the residue was dissolved in water and extracted with ethyl acetate. The organic layers were combined and dried with Na$_2$SO$_4$, filtered, and evaporated in a vacuum. The residue was purified by a flash column to generate the desired product N-(3,4-bis((4-chlorobenzyl)oxy)benzyl)-1-(3-methoxyphenyl)methanamine (**6.14, XIE5-2-32**), a white solid (42mg, yield: 18%). ^{1}H-NMR (CDCl$_3$): 7.383-7.228 (m, 10H), 6.894-6.797 (m, 5H), 5.103-5.088 (d, J = 6Hz, 4H), 3.813 (s, 3H), 3.747-3.711 (d, J = 14.4 Hz, 4H). ^{13}C NMR (150Hz, CDCl$_3$) δ 158.70, 147.66, 146.56, 140.77, 134.78 (2C), 134.71, 132.96 (2C), 132.53, 128.38 (4C), 127.68, 127.63, 127.60 (2C), 120.27, 119.39, 114.02, 113.95, 112.69, 111.31, 69.63, 69.39, 54.16, 51.91, 51.59. LC−MS (ESI): m/z 509.1 (M + H)$^+$.

N-(3,4-bis((4-chlorobenzyl)oxy)benzyl)-1-(thiophen-2-yl)methanamine (**6.7, XIE5-2-33**)

3,4-bis((4-chlorobenzyl)oxy)benzaldehyde (**6.1, XIE5-1-84,** 198mg, 0.5 mmol) was dissolved in dry ethanol, and thiophen-2-ylmethanamine (57mg, 0.5 mmol) was added in. The reaction mixture was stirred for 12 hours at 65 °C. The reaction solution was then cooled down to room temperature. NaBH$_4$ (30mg, 0.5 mmol) was added slowly in small portions, and the resulting solution was stirred for another 12 hours (143, 144). The solvent was evaporated in vacuum, and the residue was dissolved in water and extracted with ethyl acetate. The organic layers were combined and dried with Na$_2$SO$_4$, filtered, and evaporated in a vacuum. The residue was purified by a flash column to generate the desired product N-(3,4-bis((4-chlorobenzyl)oxy)benzyl)-1-(thiophen-2-yl)methanamine (**6.7, XIE5-2-33**), a white solid (28mg, yield: 11%). ^{1}H-NMR (CDCl$_3$): 7.411-7.344 (m, 8H), 7.258-7.248 (d, J = 4Hz, 1H), 7.001-6.975 (m, 2H), 6.925-6.877 (m, 3H), 5.140-5.127 (d, J = 5.2 Hz, 4H), 3.975 (s, 2H), 3.764 (s, 2H). ^{13}C NMR (151Hz, CDCl$_3$) δ 148.72, 147.65, 144.06, 135.80 (2C), 135.73, 133.75 (2C), 133.60, 133.58, 128.69 (4C), 128.65 (4C), 126.64, 124.89, 124.41, 121.29, 115.05, 114.95, 70.68, 70.43, 52.24, 47.37.

N-(3,4-bis((4-chlorobenzyl)oxy)benzyl)-1-(pyridin-2-yl)methanamine (**6.9, XIE5-2-35**)

3,4-bis((4-chlorobenzyl)oxy)benzaldehyde (**6.1, XIE5-1-84,** 198mg, 0.5 mmol) was dissolved in dry ethanol, and pyridin-2-ylmethanamine (54mg, 0.5 mmol) was added in. The reaction mixture was stirred for 12 hours at 65 °C. The reaction solution was then cooled down to room temperature.

NaBH$_4$ (30mg, 0.5 mmol) was added slowly in small portions, and the resulting solution was stirred for another 12 hours (143, 144). The solvent was evaporated in vacuum, and the residue was dissolved in water and extracted with ethyl acetate. The organic layers were combined and dried with Na$_2$SO$_4$, filtered, and evaporated in a vacuum. The residue was purified by a flash column to generate the desired product N-(3,4-bis((4-chlorobenzyl)oxy)benzyl)-1-(pyridin-2-yl)methanamine (**6.9, XIE5-2-35**), a white solid (33mg, yield: 14%). ^{1}H NMR (CDCl$_3$): 8.582 (m, 2H), 7.678-7.660 (d, J = 7.2 Hz, 1H), 7.405-7.272 (m, 10H), 6.976 (s, 1H), 6.877-6.856 (m, 2H), 5.134-5.117 (d, J = 6.8Hz, 4H), 3.792-3.738 (d, 4H). ^{13}C NMR (151Hz, CDCl$_3$) δ 149.73, 148.74, 148.51, 147.74, 135.79, 135.74, 135.57 (2C), 133.70, 133.60, 133.58, 128.71 (4C), 128.66 (4C), 123.41, 121.28, 115.04, 114.95, 70.64, 70.46, 52.76, 50.34. LC−MS (ESI): m/z 480.3 (M + H)$^+$.

N-(3,4-bis((4-chlorobenzyl)oxy)benzyl)-1-(3,4,5-trimethoxyphenyl)methanamine (**6.15, XIE5-2-36**)

3,4-bis((4-chlorobenzyl)oxy)benzaldehyde (**6.1, XIE5-1-84,** 198mg, 0.5 mmol) was dissolved in dry methanol, and (3,4,5-trimethoxyphenyl)methanamine (99mg, 0.5 mmol) was added in. The reaction mixture was stirred for 12 hours at 65 °C. The reaction solution was then cooled down to room temperature. NaBH$_4$ (30mg, 0.5 mmol) was added slowly in small portions, and the resulting solution was stirred for another 12 hours (143, 144). The solvent was evaporated in vacuum, and the residue was dissolved in water and extracted with ethyl acetate. The organic layers were combined and dried with Na$_2$SO$_4$, filtered, and evaporated in a vacuum. The residue was purified by a flash column to generate the desired product N-(3,4-bis((4-chlorobenzyl)oxy)benzyl)-1-(3,4,5-trimethoxyphenyl)methanamine (**6.15, XIE5-2-36**), a white solid (30mg, yield: 12%). ^{1}H-NMR (CDCl$_3$):7.379-7.339 (m, 8H), 6.993 (s, 1H), 6.896 (m, 2H), 6.583 (s, 2H), 5.126-5.116 (d, J = 4Hz, 4H), 3.885-3.867 (d, J = 7.2 Hz, 9H), 3.750-3.740 (d, J = 4Hz, 4H). ^{13}C NMR (600Hz, CDCl$_3$) δ 152.18, 147.69, 146.63, 135.80, 135.00, 134.75, 134.66, 133.01 (2C), 132.57, 132.54, 127.64 (4C), 127.60 (4C), 120.28, 114.03, 114.02, 103.85, 76.26, 76.05, 75.84, 69.61, 69.48, 59.82, 55.05, 52.33, 51.75. LC−MS (ESI): m/z 569 (M + H)$^+$.

1-(benzo[d][1,3]dioxol-5-yl)-N-(3,4-bis((4-chlorobenzyl)oxy)benzyl)methanamine (**3.16, XIE5-2-37**)
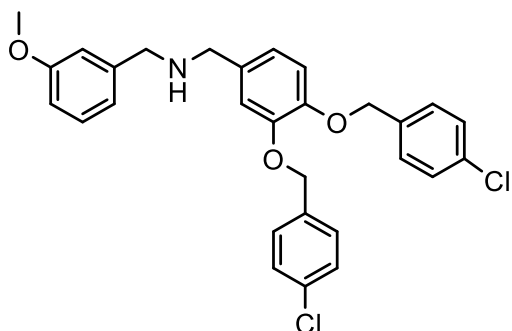

3,4-bis((4-chlorobenzyl)oxy)benzaldehyde (**6.1, XIE5-1-84,** 198mg, 0.5 mmol) was dissolved in dry methanol, and benzo[d][1,3]dioxol-5-ylmethanamine (75mg, 0.5 mmol) was added in. The reaction mixture was stirred for 12 hours at 65 °C. The reaction solution was then cooled down to room temperature. NaBH$_4$ (30mg, 0.5 mmol) was added slowly in small portions, and the resulting solution was stirred for another 12 hours (143, 144). The solvent was evaporated in vacuum, and the residue was dissolved in water and extracted with ethyl acetate. The organic layers were combined and dried with Na$_2$SO$_4$, filtered, and evaporated in a vacuum. The residue was purified by a flash column to generate the desired product 1-(benzo[d][1,3]dioxol-5-yl)-N-(3,4-bis((4-chlorobenzyl)oxy)benzyl)methanamine (**3.16, XIE5-2-37**), a white solid (78mg, yield: 31%). ^{1}H NMR (CDCl$_3$): 7.416-7.344 (m, 8H), 6.997 (s, 1H), 6.891-6.883 (m, 3H), 6.879-6.775 (m, 3H), 5.968 (s, 2H), 5.137-5.114 (d, J = 9.2 Hz, 4H), 3.719-3.698 (d, J = 8.4 Hz, 4H). ^{13}C NMR (600Hz, CDCl$_3$) δ 147.67, 146.55, 145.45, 140.90, 134.79, 133.48, 133.21, 132.55, 129.72, 128.35 (4C), 127.61, 120.55, 120.13, 119.36, 113.90, 112.60, 111.35, 107.60, 107.01, 102.70, 99.85, 69.64, 63.65, 54.13, 51.79. LC−MS (ESI): m/z 524.3 (M + H)$^+$.

N-(3,4-bis((4-chlorobenzyl)oxy)benzyl)-3-(1H-imidazol-1-yl)propan-1-amine (**6.10, XIE5-2-38**)
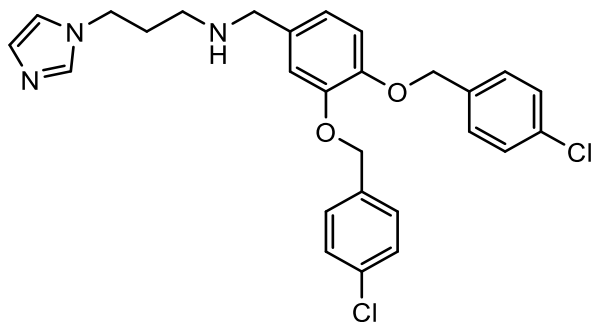
Compound **6.10** was prepared from 3-(1H-imidazol-1-yl)propan-1-amine and 3,4-bis((4-chlorobenzyl)oxy)benzaldehyde using **Method 2**. Yellow Oil (53mg, yield: 23%). ^{1}H-NMR (CDCl$_3$): 7.459-7.290 (m, 9H), 7.063 (s, 1H), 6.911-6.823 (m, 4H), 5.129-5.110 (d, J = 7.6 Hz, 4H), 4.044-4.010 (t, J = 6.8 Hz, 2H), 3.668 (s, 2H), 2.584-2.551 (t, J = 6.8 Hz, 2H), 1.931-1.897 (m, 2H). ^{13}C NMR (600Hz, CDCl$_3$) δ 148.63, 147.77, 137.20, 135.73, 135.71 (2C), 133.71, 133.59 (2C), 129.40 (4C), 128.65 (4C), 121.28, 118.84, 115.11, 115.02, 70.65, 70.49, 57.40, 53.49, 45.56, 44.61, 31.24. LC−MS (ESI): m/z 496.5 (M + H)$^+$.

N-(3,4-bis((4-chlorobenzyl)oxy)benzyl)-3-morpholinopropan-1-amine (**6.11, XIE5-2-39**)
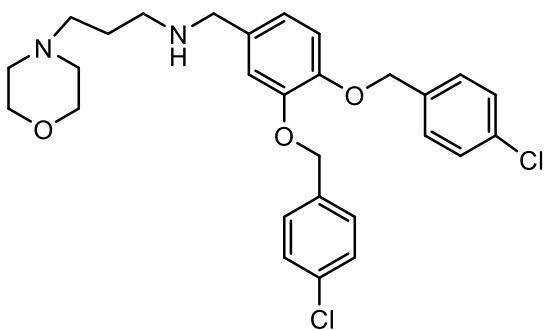
Compound **6.11** was prepared from 3-morpholinopropan-1-amine and 3,4-bis((4-chlorobenzyl)oxy)benzaldehyde using **Method 2**. White solid (34mg, 0.075mmol, yield: 15%). ^{1}H-NMR (CDCl$_3$): 7.401-7.332 (m, 8H), 6.965 (s, 1H), 6.877-6.859 (m, 2H), 5.126-5.105 (d, J = 8.4Hz, 4H), 3.712 (s, 6H), 3.490 (s), 2.683-2.649 (t, 2H), 2.452-2.391 (m, 6H), 1.729-1.694 (m, 2H). ^{13}C NMR (76 MHz, CDCl$_3$) δ 148.73, 148.69, 147.67, 136.09, 135.75, 135.63, 133.63 (2C),

130.49 (4C), 128.70, 128.66, 127.35, 121.24, 116.28, 115.14, 111.19, 70.73 (2C), 70.55 (2C), 67.00 (2C), 57.42 (2C), 53.81, 47.96, 23.09. LC−MS (ESI): m/z 515.5 (M + H)$^+$.

N-(3,4-bis(lbenzyloxy)benzyl)-1-(3-methoxyphenyl)methanamine (**3.14, XIE5-2-46**)
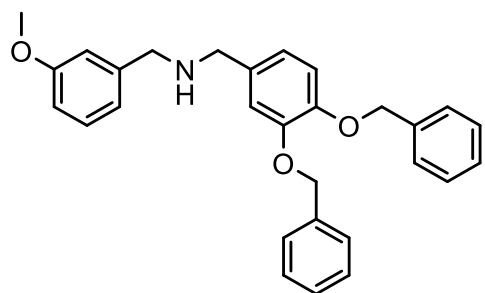
Compound **3.14** was prepared from 3,4-bis(benzyloxy)benzaldehyde and (3-methoxyphenyl)methanamine using **Method 2**. White solid (79mg, yield: 36%). ^{1}H-NMR (CDCl$_3$): 7.502-7.472 (m, 4H), 7.409-7.183 (m, 8H), 6.941-6.829 (m, 5H), 5.199-5.184 (d, J = 6Hz, 4H), 3.843 (s, 3H), 3.772-3.737 (d, J = 14Hz, 4H). ^{13}C NMR (600Hz, CDCl$_3$) δ 161.54, 148.00, 137.45, 137.36, 129.40, 129.13, 128.47, 127.78, 127.75, 127.40, 127.32, 121.16, 120.50, 115.15-115.13 (d), 113.68, 112.48, 71.45, 71.26, 55.23, 52.87, 52.65, 55.05, 52.33, 51.75. LC−MS (ESI): m/z 440.2 (M + H)$^+$.

N-(3,4-bis(benzyloxy)benzyl)-1-(pyridin-2-yl)methanamine (**3.9, XIE5-2-49**)
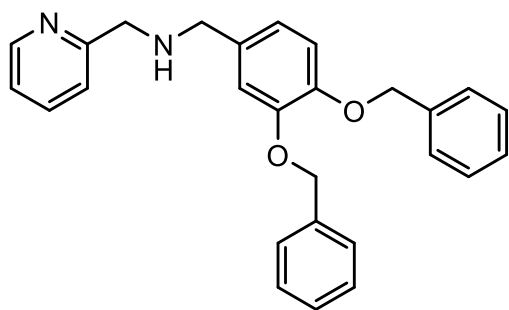
Compound **3.9** was prepared from 3,4-bis(benzyloxy)benzaldehyde and pyridin-2-ylmethanamine using **Method 2**. White solid (58mg, yield: 28%). ^{1}H-NMR (600MHz, CDCl$_3$): 8.563-8.528 (m, 2H), 7.687-7.669 (d, J = 7.2 Hz, 1H), 7.475-7.466 (m, 4H), 7.402-7.281 (m, 7H), 7.000-6.840 (m, 3H), 5.203-5.178 (d, J = 10 Hz, 4H), 3.774-3.733 (d, J =16.4 Hz, 4H). ^{13}C NMR (600MHz,

CDCl₃) δ 149.79, 148.97, 148.57, 148.15, 137.33, 137.28, 135.95, 135.09, 132.73, 128.46, 127.77-127.34 (d), 127.29, 123.40, 121.20, 115.11, 115.04, 71.37, 71.21, 52.60, 50.02. LC−MS (ESI): *m/z* 411.3 (M + H)⁺.

1-(benzo[d][1,3]dioxol-5-yl)-N-(3,4-bis((benzyloxy)benzyl)methanamine (**3.16, XIE5-2-51**)
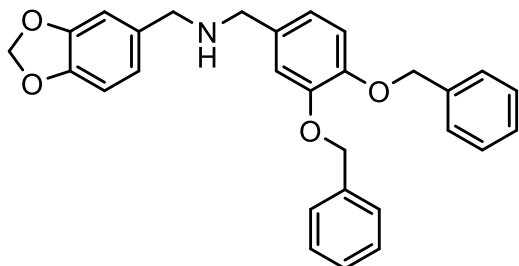
Compound **3.16** was prepared from 3,4-bis(benzyloxy)benzaldehyde and benzo[d][1,3]dioxol-5-ylmethanamine using **Method 2**. White solid (33mg, yield:15%). ¹H-NMR (600MHz, CDCl₃): 7.451-7.295 (m, 10H), 7.057 (s, 1H), 6.972-6.952 (m, 1H), 6.890 (s, 1H), 6.820-6.790 (m, 2H), 6.731-6.712 (m, 1H), 5.959 (s, 2H), 5.097-5.084 (d, *J* = 5.2 Hz, 4H), 3.529-3.517 (d, *J* = 4.8 Hz, 4H). ¹³C NMR (600Hz, DMSO-d⁶) δ 148.12, 147.13, 146.87, 145.74, 137.44, 137.37, 134.78, 133.89, 128.33, 127.70, 127.67, 127.51, 127.46, 120.90, 120.43, 114.32, 114.28, 108.32, 107.77, 100.61, 70.15, 70.00, 51.71, 51.52. LC−MS (ESI): *m/z* 454.2 (M + H)⁺.

N-(3,4-bis((benzyloxy)benzyl)-1-(furan-3-yl)methanamine (**3.8, XIE5-2-53**)
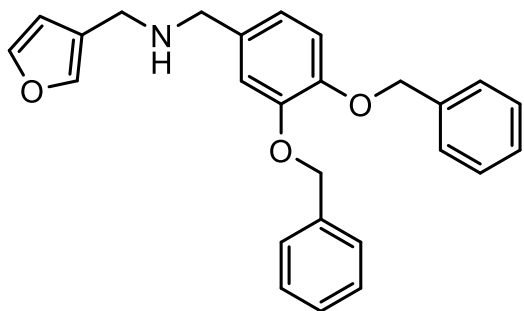
Compound **3.8** was prepared from 3,4-bis(benzyloxy)benzaldehyde and furan-2-ylmethanamine using **Method 2**. Yellow oil (30mg, yield: 15%). ¹H-NMR (400MHz, CDCl₃): 7.499-7.467 (m, 4H), 7.393-7.291 (m, 7H), 7.006-7.003 (d, *J* = 1.2 Hz, 1H), 6.937-845 (m, 2H), 6.347 (m, 1H), 6.173-6.166 (d, *J* = 2.8Hz, 1H), 5.196-5.178 (d, *J* = 7.2 Hz, 4H), 3.763-3.717 (d, J = 18.4 Hz, 4H). LC−MS (ESI): *m/z* 400.7 (M + H)⁺.

N-(3,4-bis(benzyloxy)benzyl)-1-(thiophen-2-yl)methanamine (**3.7, XIE5-2-54**)
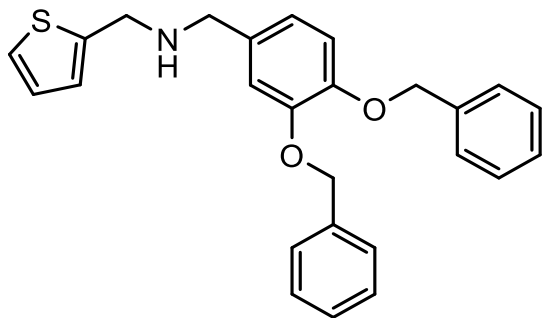
Compound **3.7** was prepared from 3,4-bis(benzyloxy)benzaldehyde and thiophen-2-ylmethanamine using **Method 2**. Yellow oil (15mg, yield: 7%). ^{1}H-NMR (600MHz, CDCl$_3$): 7.500-7.467 (m, 4H), 7.404-7.329 (m, 6H), 7.254-7.242 (m, 1H), 7.013-6.847 (m, 5H), 5.202-5.180 (d, J = 8.4 Hz, 4H), 3.962 (s, 2H), 3.757 (s, 2H). ^{13}C NMR (600MHz, CDCl$_3$) δ 148.98, 148.00, 144.01, 137.41, 137.33, 133.34, 128.45, 127.76-127.74 (d), 127.39, 127.30, 126.62, 124.97, 124.40, 121.15, 115.11, 71.43, 71.21, 52.28, 47.28. LC−MS (ESI): m/z 416.2 (M + H)$^+$.

N-(3,4-bis((4-methylbenzyl)oxy)benzyl)-1-(furan-3-yl)methanamine (**7.8, XIE5-2-58**)
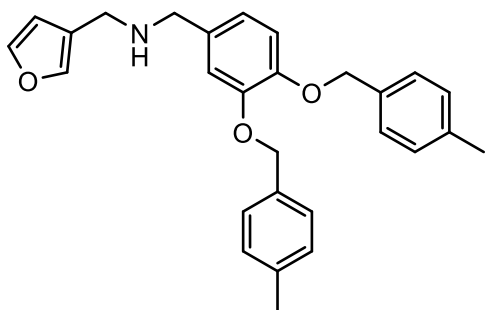
Compound **7.8** was prepared from 3,4-bis((4-methylbenzyl)oxy)benzaldehyde and furan-2-ylmethanamine using **Method 2**. Yellow oil (32mg, yield: 15%). ^{1}H-NMR (400MHz, CDCl$_3$): 7.392-7.340 (m, 5H), 7.197-7.178 (m, 4H), 6.977-6.974 (d, J = 1.2 Hz, 1H), 6.915-6.820 (m, 2H), 6.342 (m, 1H), 6.164-6.156 (d, J =3.2 Hz, 1H), 5.145-5.129 (d, J = 6.4 Hz, 4H), 3.744-3.698 (d, J = 18.4 Hz, 4H). LC−MS (ESI): m/z 428.2 (M + H)$^+$.

N-(3,4-bis((4-methylbenzyl)oxy)benzyl)-1-(3-methoxyphenyl)methanamine (**7.14, XIE5-2-61**)
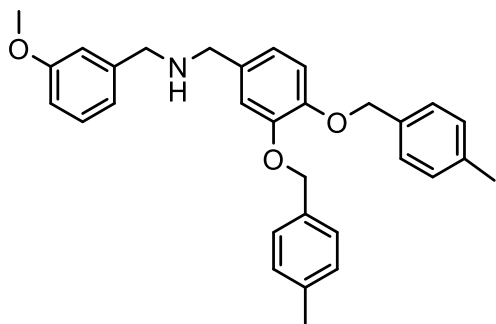
Compound **7.14** was prepared from 3,4-bis((4-methylbenzyl)oxy)benzaldehyde and (3-methoxyphenyl)methanamine using **Method 2**. White solid (46mg, yield: 21%). ^{1}H-NMR (CDCl$_3$): 7.374-7.175 (m, 10H), 7.931-7.823 (m, 5H), 5.148-5.129 (d, J = 7.6 Hz, 4H), 3.839 (s, 3H), 3.764-3.732 (d, J = 12.8Hz, 4H), 2.378-2.369 (d, J = 3.6 Hz, 6H). ^{13}C NMR (600Hz, CDCl$_3$) δ 159.73, 148.99, 148.07, 137.41, 137.40, 134.39, 134.31, 129.37, 129.11, 127.50, 127.39, 121.21, 120.61, 115.30, 115.14, 113.72, 112.63, 71.33, 71.13, 55.23 (2C), 52.85, 52.68, 52.51, 21.19 (2C). LC−MS (ESI): m/z 468.2 (M + H)$^+$.

N-(3,4-bis((4-methylbenzyl)oxy)benzyl)-3-(1H-imidazol-1-yl)propan-1-amine (**3.10, XIE5-2-64**)
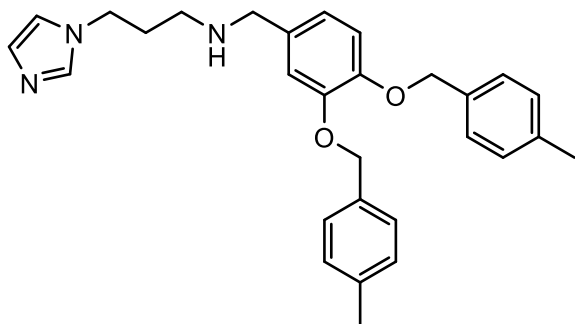
Compound **3.10** was prepared from 3,4-bis((4-methylbenzyl)oxy)benzaldehyde and 3-(1H-imidazol-1-yl)propan-1-amine using **Method 2**. White solid (77mg, yield :35%). ^{1}H-NMR (CDCl$_3$): 7.475 (s, 1H), 7.366-7.338 (m, 4H), 7.195-1.177 (m, 4H), 7.063 (s, 1H), 6.965 (s, 1H), 6.909-6.890 (m, 2H), 6.826-6.807 (m, 1H), 5.155-5.128 (d, J = 10.8 Hz, 4H), 4.042-4.025-4.008 (t, J = 6.8 Hz, 2H), 3.680 (s, 2H), 2.600-2.583-2.567 (t, J = 6.8 Hz, 2H), 2.378-2.364 (d, J = 6.4 Hz, 6H), 1.977-1.926 (m, 2H). ^{13}C NMR (600Hz, CDCl$_3$) δ 148.96, 148.26, 137.46, 137.43, 137.15, 134.27, 134.25, 132.18, 129.29, 129.13, 129.11, 127.42, 127.37, 121.29, 118.88, 115.34,

115.01, 71.26, 71.14, 53.22, 52.73, 45.23, 44.57, 30.82, 52.51, 21.19 (2C). LC−MS (ESI): *m/z* 456.2 (M + H)$^+$.

2-((3,5-bis((4-chlorobenzyl)oxy)benzyl)amino)ethan-1-ol (**8.25, XIE5-2-90**)
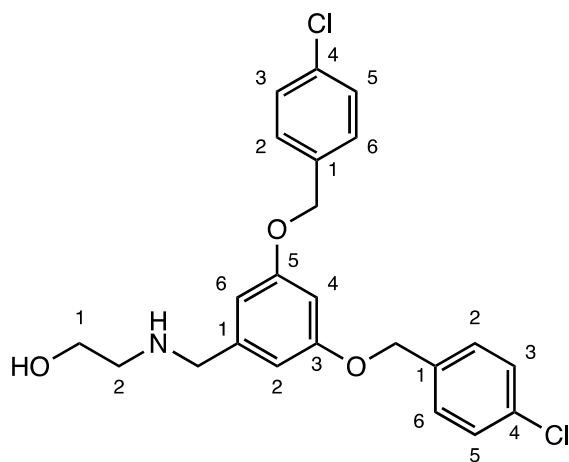
White solid (92mg, 21mmol, 21%).

^{1}H-NMR (CDCl$_3$): 7.37-7.28 (m, 8H), 6.78 (d, *J*= 8Hz, 2H), 6.54-6.53 (t, 1H), 5.01 (s, 4H), 4.58 (s, 1H), 4.35 (s, 1H), 4.04-3.99 (t, 2H), 3.84 (s, 2H), 2.92 (s, 2H). ^{13}C NMR (151 MHz, CDCl$_3$) δ 160.08, 135.12, 134.96, 133.90, 128.95, 128.88, 128.87, 128.83, 128.81, 128.76, 128.43, 108.58, 107.25, 102.72, 101.59, 69.42, 58.17, 49.10. LC−MS (ESI): *m/z* 432.2 (M + H)$^+$.

(E)-2-(3,4-bis((2,4-difluorobenzyl)oxy)benzylidene)hydrazine-1-carboximidamide (**4.28, XIE5-2-40**)

3,4-bis((4-chlorobenzyl)oxy)benzaldehyde (390mg, 1 mmol) was dissolved in dry methanol, and aminoguanidine hydrochloride salt (112mg, 1 mmol) was added. The reaction mixture was stirred for overnight at 70 ^{o}C. The reaction solution was cooled down to room temperature. The solvent was evaporated in vacuum, and the residue was purified by a column chromatography and eluted by chloroform and methanol to generate the desired product (E)-2-(3,4-bis((2,4-difluorobenzyl)oxy)benzylidene)hydrazine-1-carboximidamide, a white solid (**4.28**, 23mg, yield
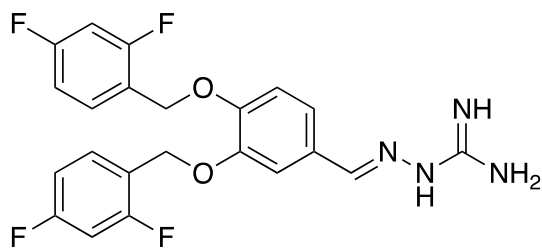
5%). The structure was confirmed by ^{1}H NMR (400MHz, DMSO-d6): 7.952 (s, 1H), 7.626-7.551(m, 3H), 7.333-7.266 (m, 2H), 7.194-7.075 (m, 4H), 5.164-5.131 (d, J = 13.2 Hz, 4H). ^{13}C NMR (300 MHz, DMSO-d6) δ 172.46, 161.41 (m, 2C), 159.56, 148.25, 144.77, 131.91-131.58 (m, 2C), 127.68 (2C), 121.92, 118.91 (m, 2C), 114.27, 111.60-111.53-111.46 (m, 2C), 104.17-104.06-104.00-103.90-103.83 (m, 2C), 78.07, 64.01, 63.95, 21.36.

(E)-2-(3,4-bis((4-chlorobenzyl)oxy)benzylidene)hydrazine-1-carboximidamide (**6.28, XIE5-1-25/XIE5-2-42/XIE5-2-68-3**)
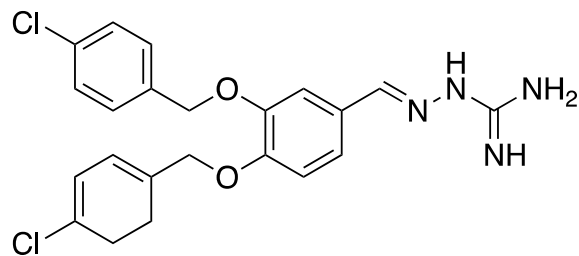
3,4-bis((4-chlorobenzyl)oxy)benzaldehyde (3.72g, 9.6 mmol) was dissolved in dry methanol, and aminoguanidine hydrochloride salt (1.12g, 10 mmol) was added. The reaction mixture was stirred for overnight at 70 °C. The reaction solution was cooled down to room temperature. The solvent was evaporated in vacuum, and the residue was purified by a column chromatography and eluted by chloroform and methanol to generate the desired product (E)-2-(3,4-bis((4-chlorobenzyl)oxy)benzylidene)hydrazine-1-carboximidamide, a white solid (**6.28**, 1.58g, yield 37.2%). The structure was confirmed by ^{1}H-NMR (300MHz, DMSO-d6): 8.006 (s, 1H), 7.715-7.710 (d, 1H), 7.523-7.448 (m, 9H), 7.310-7.277 (dd, 1H), 7.119-7.190 (d, 1H), 5.186 (s, 4H). ^{13}C NMR (300MHz, DMSO-d6) δ 155.81, 150.58, 148.74, 146.95, 136.53-136.43 (d), 132.97-132.91 (d), 130.04, 129.79, 128.93, 127.25, 123.20, 114.24, 112.15, 69.87, 69.55. LC−MS (ESI): m/z 443.5 (100%), 445.5 (M + H)[+]. ^{1}H NMR (300MHz, DMSO-d6): 8.297 (s, 1H), 7.914 (s, 1H),

7.496-7.423 (m, 9H), 7.104-7.087 (m, 1H), 7.010-6.996 (d, 1H), 6.241 (s, 1H), 5.957 (s, 1H), 5.168-5.131 (d, 4H).

(E)-2-(3,4-bis((4-fluorobenzyl)oxy)benzylidene)hydrazine-1-carboximidamide (**5.28, XIE5-2-43**)
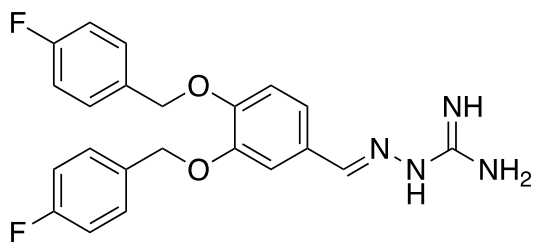
3,4-bis((4-chlorobenzyl)oxy)benzaldehyde (178mg, 0.5 mmol) was dissolved in dry methanol, and aminoguanidine hydrochloride salt (56mg, 0.5 mmol) was added. The reaction mixture was stirred for overnight at 70 °C. The reaction solution was cooled down to room temperature. The solvent was evaporated in vacuum, and the residue was purified by a column chromatography and eluted by chloroform and methanol to generate the desired product (E)-2-(3,4-bis((4-fluorobenzyl)oxy)benzylidene)hydrazine-1-carboximidamide, a white solid (**5.28**, 56mg, yield 26.2%). The structure was confirmed by ^{1}H NMR (400MHz, DMSO-d6): 7.886 (s, 1H), 7.526-7.455 (m, 5H), 7.234-7.179 (m, 4H), 7.055-7.010 (m, 2H), 5.880 (s, 1H), 5.358 (s, 2H), 5.136-5.079 (d, $J = 22.8$ Hz, 4H). LC−MS (ESI): m/z 408.5 (M + H)$^+$.

(E)-2-(3,4-bis(benzyloxy)benzylidene)hydrazine-1-carboximidamide (**XIE5-2-44**)

3,4-bis((4-chlorobenzyl)oxy)benzaldehyde (319mg, 1 mmol) was dissolved in dry methanol, and aminoguanidine hydrochloride salt (112mg, 1mmol) was added. The reaction mixture was stirred for overnight at 70 °C. The reaction solution was cooled down to room temperature. The solvent was evaporated in vacuum, and the residue was purified by a column chromatography and eluted by chloroform and methanol to generate the desired product (E)-2-(3,4-
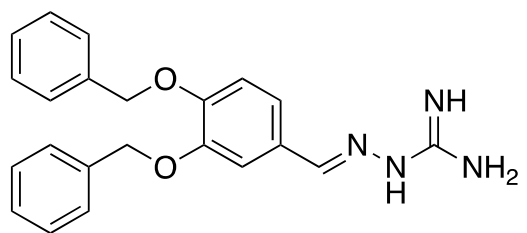
bis(benzyloxy)benzylidene)hydrazine-1-carboximidamide, a white solid (**XIE5-2-44**, 63mg, yield: 17%). The structure was confirmed by ^{1}H NMR (300MHz, DMSO-d6) δ 8.04 (s, 1H), 7.86 (s, 4H), 7.72 (d, J=1Hz, 1H), 7.50-7.49 (d, J=4Hz, 2H), 7.46-7.44 (d, J=5Hz, 2H), 7.41-7.37 (tetra, 4H), 7.35-7.31 (tetra, 2H), 7.27-7.25 (dd, 1H), 5.19-5.18 (d, J=3Hz, 4H). ^{13}C NMR (300MHz, DMSO-d6) δ 156.09, 150.03, 148.46, 145.61, 137.07-136.94 (d, J=39Hz, 2C), 128.38-128.38 (d, J=1Hz), 127.85-127.81 (d, J=12Hz, 2C), 127.76 (4C), 127.47 (4C), 122.24, 113.63, 111.32, 70.14, 69.85. LC−MS (ESI): *m/z* 375.2 (M + H)$^+$.

(E)-2-(3,4-bis((4-chlorobenzyl)oxy)benzylidene)hydrazine-1-carboximidamide (**7.28, XIE5-2-45/XIE5-1-53**)
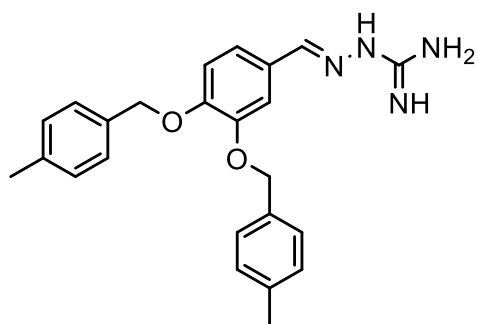
3,4-bis((4-chlorobenzyl)oxy)benzaldehyde (348mg, 1 mmol) was dissolved in dry methanol, and aminoguanidine hydrochloride salt (112mg, 1mmol) was added. The reaction mixture was stirred for overnight at 70 ºC. The reaction solution was cooled down to room temperature. The solvent was evaporated in vacuum, and the residue was purified by a column chromatography and eluted by chloroform and methanol to generate the desired product (E)-2-(3,4-bis(benzyloxy)benzylidene)hydrazine-1-carboximidamide, a white solid (**7.28**, 110mg, yield: 27%). The structure was confirmed by ^{1}H-NMR (DMSO): 8.038 (s, 1H), 7.682-7.677 (d, 1H), 7.375-7.315 (m, 5H), 7.261-7.236 (dd, 1H), 7.210-7.180 (m, 4H), 7.100-7.079 (d, *J* = 8.4 Hz, 1H), 5.121 (s, 4H), 2.315-2.307 (d, *J* = 2.4 Hz, 6H). LC−MS (ESI): *m/z* 403.2 (M + H)$^+$.

2-(3,4-bis((2,4-difluorobenzyl)oxy)phenyl)ethan-1-aminium chloride (**4.3, XIE5-2-70**)
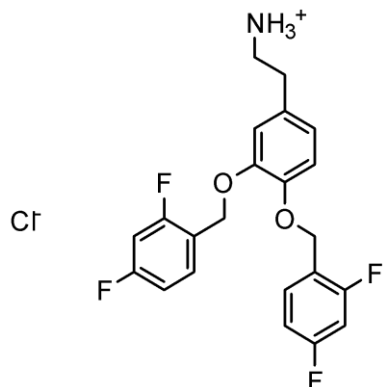
4-(2-aminoethyl)benzene-1,2-diol (1.53g, 10 mmol) was dissolved in THF (10ml) at 0 °C, sodium hydroxide aqueous solution (10.00 ml, 10 mmol, 1 mol/L). Then a solution of di-tert-butyl dicarbonate (2.18g, 10 mmol) in 10ml THF was added to the mixture at 0 °C dropwise by constant pressure funnel under vigorous stirring. The mixture was warmed to room temperature and stirred at room temperature overnight and then washed with water (50 mL x 3). The organic layer was dried over Na_2SO_4 and concentrated to afford the crude intermediate tert-butyl (3,4-dihydroxyphenethyl)carbamate **IM1** (2.15 g, 8.5 mmol, 85% yield) , which was used without further purification. (218)

The intermediate tert-butyl (3,4-dihydroxyphenethyl)carbamate **IM1** (2.15 g, 8.5 mmol) was dissolved in dry dimethylformamide (DMF, 50 mL). 1-(bromomethyl)-2,4-difluorobenzene (3.7g, 18 mmol) was added slowly, followed by anhydrous K_2CO_3 (3.8 g, 27mmol). The mixture was stirred at room temperature for 2 hours. Additional K_2CO_3 (1.2 g, 8.5 mmol) was added, and the mixture was heated to 70 °C for 30 minutes and then cooled to room temperature. The mixture was partitioned between H_2O and EtOAc (120 mL each). The organic layer was separated, and the water layer was extracted with ether (3×50 mL). The pooled organic layers were washed with H_2O (2×50 mL) and saturated aqueous NaCl (50 mL). The pale, straw-colored extracts were dried over anhydrous sodium sulfate and concentrated to yield a white cream-colored solid after washing with hexanes (75 mL) and drying. The intermediate tert-butyl (3,4-

bis(benzyloxy)phenethyl)carbamate **IM2 (**3.53g, 7mmol, yield=83%) was attained and confirmed by NMR.

The intermediate tert-butyl (3,4-bis(benzyloxy)phenethyl)carbamate **IM2** (3.53 g, 7 mmol) was dissolved in solvent (CH_2Cl_2) to make the reaction mixture. The hydrochloride gas was bubbled into the reaction mixture, and then reacted with starting material to get rid of the protection group. The reaction mixture was stirred at room temperature with hydrochloride gas bubbled in for about 40 min. Generation hydrochloride gas by slowly adding concentrated sulfuric acid (dropwise) into sodium chloride, the additional water in the generated HCl gas was then removed by concentrated sulfuric acid and lead to the reaction mixture in a three-necked bottle by tube. Stop generation of HCl gas, continue stirring at room temperature for about half an hour, then evaporate the solvent, add solvent to resuspend it and evaporate solvent for several times to remove extra hydrochloride. Too much residual hydrochloride will make the product not so stable in room temperature. Product 2-(3,4-bis((2,4-difluorobenzyl)oxy)phenyl)ethan-1-aminium chloride (2.9g, 6.6mmol, yield=95%, **4.3, XIE5-2-70**) was attained and then placed under vacuum overnight to remove solvent. Confirm the structure with ^{1}H-NMR (600MHz, CDCl_3): 7.964-7.959 (s, 3H), 7.589-7.520 (m, 2H), 7.328-7.270 (m, 2H), 7.139-7.046 (m, 4H), 6.832-6.817 (d, J = 9Hz, 1H), 5.114-5.087 (d, J = 10.8 Hz, 4H), 3.028-3.015 (m, 2H), 2.835-2.814 (m, 2H). ^{13}C NMR (151Hz, DMSO) δ 161.35-161.23 (m, 2C), 159.67-159.58 (d, J= 15Hz, 2C), 148.13, 146.83, 131.88-131.73 (m), 130.80 (2C), 121.75 (2C), 120.52-120.35, 115.50, 115.20, 111.60-111.40 (m, 2C), 104.15-103.81(m, 2C), 64.18-64.07 (dd, 2C), 39.03, 32.46. LC−MS (ESI): *m*/*z* 406.2 (M + H)[+], 388.8 (M-F)[+].

N-(3,4-bis((4-chlorobenzyl)oxy)phenethyl)acetamide (**6.5, XIE5-2-73**)

To a solution of 2-(3,4-bis((4-chlorobenzyl)oxy)phenyl)ethan-1-aminium chloride (**6.3,** 403mg, 1 mmol) and triethylamine (TEA, 125mg, 1.25mmol) in anhydrous dichloromethane (DCM, 4mL) was slowly added a solution of methylcarbamic chloride (103 mg,1.1mmol) in anhydrous DCM (3 mL). The mixture was then refluxed for 3 days. The reaction mixture was diluted with water (5mL) and extracted with DCM (8 mL × 3). The combined organic layers were subsequently washed with H_2O (10mL× 3) and brine (10 mL × 3), dried over anhydrous Na_2SO_4 and concentrated in vacuo (145). The crude product was purified on a silica gel column (CH_2Cl_2/MeOH = 19/1, v/v) to afford N-(3,4-bis((4-chlorobenzyl)oxy)phenethyl)acetamide (white solid, **6.5, XIE5-2-73**, 270 mg, 0.61mmol, 61% yield). The chemical structured was characterized by ^{1}H-NMR (CDCl$_3$): 7.371 (m, 8H), 6.892-6.872 (m, 1H), 6.790-6.730 (m, 2H), 5.389 (s, 1H), 5.118-5.107 (d, $J = 4.4$ Hz, 4H), 3.846-3.471 (m, 2H), 2.759-2.742-2.725 (t, $J = 6.8$ Hz, 2H), 1.941 (s, 3H). LC−MS (ESI): m/z 444.1 (M + H)$^+$

N-(3,4-bis((2,4-fluorobenzyl)oxy)phenethyl)acetamide (**4.5, XIE5-2-74**)

To a solution of 2-(3,4-bis((2,4-difluorobenzyl)oxy)phenyl)ethan-1-aminium chloride (**4.3, XIE5-2-70**, 406mg, 1 mmol) and triethylamine (TEA, 125mg, 1.25mmol) in anhydrous dichloromethane (DCM, 4mL) was slowly added a solution of methylcarbamic chloride (103 mg,1.1mmol) in anhydrous DCM (3 mL). The mixture was then refluxed for 3 days. The reaction mixture was diluted with water (5mL) and extracted with DCM (8 mL × 3). The combined organic layers were subsequently washed with H_2O (10mL× 3) and brine (10 mL × 3), dried over anhydrous Na_2SO_4 and concentrated in vacuo. The crude product was purified on a silica gel column (CH_2Cl_2/MeOH = 20/1, v/v) to afford (145) N-(3,4-bis((2,4-fluorobenzyl)oxy)phenethyl)acetamide (white solid, **4.5, XIE5-2-74,** 289mg, 0.64mmol, yield=64%). The chemical structured was characterized by ^{1}H-NMR (600MHz, CDCl$_3$): 7.514-7.484 (m, 2H), 6.943-6.775 (m, 7H), 5.421 (s, 1H), 5.143-5.137 (d, J = 2.8Hz, 4H), 3.522-3.474 (m, 2H), 2.781-2.765-2.748 (t, J = 6.8 Hz, 2H), 1.962 (s, 3H). ^{13}C NMR (151Hz, CDCl$_3$) δ 170.00, 162.01 (m, 2C), 159.73 (2C), 148.78, 147.40, 132.89 (2C), 130.93-130.74 (m), 122.16 (2C), 120.41-120.21 (t), 116.01, 115.70, 111.47-111.28 (m, 2C), 103.97-103.61 (m, 2C), 64.90-64.83 (dd, 2C), 40.65, 35.12, 23.36. LC−MS (ESI): m/z 448.0 (M + H)$^+$

N-(3,4-bis((4-fluorobenzyl)oxy)phenethyl)acetamide (**5.5, XIE5-2-75**)
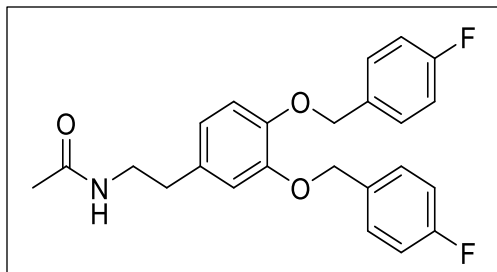
To a solution of 2-(3,4-bis((4-fluorobenzyl)oxy)phenyl)ethan-1-aminium chloride (**XIE5-1-90**, 333mg, 1 mmol) and triethylamine (TEA, 125mg, 1.25mmol) in anhydrous dichloromethane (DCM, 4mL) was slowly added a solution of methylcarbamic chloride (103 mg,1.1mmol) in anhydrous DCM (3 mL). The mixture was then refluxed for 3 days. The reaction mixture was diluted with water (5mL) and extracted with DCM (8 mL × 3). The combined organic layers were subsequently washed with H_2O (10Ml × 3) and brine (10 mL × 3), dried over anhydrous Na_2SO_4 and concentrated in vacuo. The crude product was purified on a silica gel column (CH_2Cl_2/MeOH = 20/1, v/v) to afford N-(3,4-bis((4-fluorobenzyl)oxy)phenethyl)acetamide (creamy white solid, **5.5, XIE5-2-75**, 210mg, 0.5mmol, yield=51%). The chemical structured was characterized by ^{1}H-NMR (600MHz, $CDCl_3$): 7.421-7.410 (m, 4H), 7.091-7.052 (m, 4H), 6.909-6.890 (m, 1H), 6.807-6.738 (m, 2H), 5.407 (s, 1H), 5.108-5.097 (d, J = 4.4 Hz, 4H), 3.489-3.458 (m, 2H), 2.763-2.746-2.729 (t, J = 6.8 Hz, 2H), 1.944 (s, 3H). ^{13}C NMR (151Hz, CDCl3) δ 169.99, 163.26, 161.63, 148.89, 147.53, 133.01-132.99 (d, J = 3Hz), 132.90-132.88 (d, J = 3Hz), 132.46 (4C), 129.24-129.17 (m), 121.76, 115.78, 115.50-115.46 (m, 4C), 115.34-115.31 (d, J =4.5Hz), 70.87, 70.73, 40.64, 35.12, 23.35, LC−MS (ESI): m/z 412.0 (M + H)+

N-(3,4-bis((4-fluorobenzyl)oxy)phenethyl)cyclohexanecarboxamide (**5.6, XIE5-2-77**)
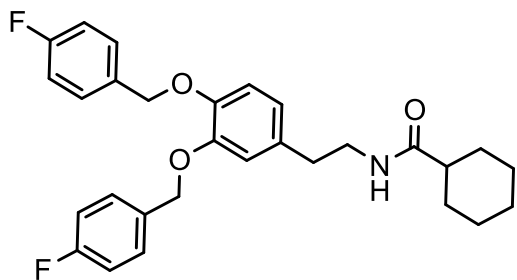
To a solution of 2-(3,4-bis((4-fluorobenzyl)oxy)phenyl)ethan-1-aminium chloride (**XIE5-1-91**, 368mg, 1 mmol) and triethylamine (TEA, 125mg, 1.25mmol) in anhydrous dichloromethane (DCM, 4mL) was slowly added a solution of cyclohexylcarbamic chloride (177 mg,1.1mmol) in anhydrous DCM (3 mL). The mixture was then refluxed for 3 days. The reaction mixture was diluted with water (5mL) and extracted with DCM (8 mL × 3). The combined organic layers were subsequently washed with H_2O (10mL× 3) and brine (10 mL × 3), dried over anhydrous Na_2SO_4 and concentrated in vacuo. The crude product was purified on a silica gel column (CH$_2$Cl$_2$/MeOH = 20/1, v/v) (145) to afford N-(3,4-bis((4-fluorobenzyl)oxy)phenethyl)cyclohexanecarboxamide (white solid, **5.6, XIE5-2-77,** 297mg, 0.62mmol, yield=62%). The chemical structure was confirmed by ^{1}H-NMR (CDCl$_3$): 7.379-7.360 (m, 8H), 6.887-6.867 (m, 1H), 6.805 (m, 1H), 6.744-6.742 (m, 1H), 5.408 (s, 1H), 5.103 (s, 4H), 3.482-3.466 (m, 2H), 2.754-2.737-2.720 (t, J = 6.8 Hz, 2H), 2.013-1.985 (m, 1H), 1.826-1.797 (m, 4H), 1.411-1.384 (m, 3H), 1.247-1.224 (m, 3H). ^{13}C NMR (151 MHz, CDCl$_3$) δ 176.09, 163.36, 161.64, 150.19, 148.94, 148.79, 147.45, 140.23, 138.84, 137.71, 132.66, 129.60, 129.20, 126.68, 123.38, 122.83, 115.44, 114.09, 113.88, 70.74, 70.14, 45.54, 40.33, 35.22, 29.67, 28.97, 25.70, 22.70. LC−MS (ESI): m/z 480.0 (M + H) $^+$

N-(3,4-bis((4-methylbenzyl)oxy)phenethyl)cyclohexanecarboxamide (**7.6, XIE5-2-78**)

To a solution of 2-(3,4-bis((4-methylbenzyl)oxy)phenyl)ethan-1-aminium chloride (360mg, 1 mmol) and triethylamine (TEA, 125mg, 1.25mmol) in anhydrous dichloromethane (DCM, 4mL) was slowly added a solution of cyclohexylcarbamic chloride (177 mg,1.1mmol) in anhydrous DCM (4 mL). The mixture was then refluxed for 3 days. The reaction mixture was diluted with water (5mL) and extracted with DCM (8 mL × 3). The combined organic layers were subsequently washed with H_2O (10mL× 3) and brine (10 mL × 3), dried over anhydrous Na_2SO_4 and concentrated in vacuo. The crude product was purified on a silica gel column (CH_2Cl_2/MeOH = 19/1, v/v) to afford N-(3,4-bis((2,4-difluorobenzyl)oxy)phenethyl)cyclohexanecarboxamide (white solid, **7.6, XIE5-2-78,** 283mg, 0.6mmol, yield=60%). The structure was confirmed by ^{1}H-NMR (600MHz, CDCl$_3$) δ 7.26 (s, 4H), 7.09-7.03 (m, 4H), 6.95 (d, J = 2Hz, 3H), 5.49 (s, 4H), 3.48-3.47 (d, J = 6Hz, 2H), 2.80-2.79 (d, J = 6Hz, 2H), 2.53 (t, 1H), 2.04-2.01 (m, 6H), 1.82-1.80 (m, 5H), 1.58-1.23 (m, 5H). ^{13}C NMR (151 MHz, CDCl$_3$) δ 176.19, 173.50, 173.38, 142.20, 140.85, 137.70, 126.66, 123.85, 123.46, 45.51, 43.03, 43.00, 40.15, 35.03, 29.65, 28.97, 25.72, 25.67, 25.32, 25.30. LC−MS (ESI): m/z 484.2 (M + H)[+]

N-(3,4-bis((2,4-difluorobenzyl)oxy)phenethyl)cyclohexanecarboxamide (**4.6, XIE5-2-79**)

To a solution of 2-(3,4-bis((2,4-difluorobenzyl)oxy)phenyl)ethan-1-aminium chloride (**4.3, XIE5-2-70**, 406mg, 1 mmol) and triethylamine (TEA, 125mg, 1.25mmol) in anhydrous dichloromethane (DCM, 4mL) was slowly added a solution of cyclohexylcarbamic chloride (177 mg,1.1mmol) in anhydrous DCM (4 mL). The mixture was then refluxed for 3 days. The reaction mixture was diluted with water (5mL) and extracted with DCM (8 mL × 3). The combined organic layers were subsequently washed with H$_2$O (10mL× 3) and brine (10 mL × 3), dried over anhydrous Na$_2$SO$_4$ and concentrated in vacuo. The crude product was purified on a silica gel column (CH$_2$Cl$_2$/MeOH = 19/1, v/v) to afford N-(3,4-bis((2,4-difluorobenzyl)oxy)phenethyl)cyclohexanecarboxamide (white solid, **4.6, XIE5-2-79,** 305mg, 0.59mmol, yield=59%). The structure was confirmed by ^{1}H-NMR (600MHz, CDCl$_3$): 7.513-7.459 (m, 2H), 6.940-6.765 (m, 7H), 5.425 (s, 1H), 5.134 (s, 4H), 3.515-3.468 (m, 2H), 2.776-2.742 (m, 2H), 2.056-2.027 (m, 1H), 1.839-1.781 (m, 4H), 1.451-1.371 (m, 3H), 1.283-1.230 (m, 3H). ^{1}H-NMR (CDCl$_3$): 7.48-7.45 (m, 2H), 7.29-7.26 (m, 1H), 6.91-6.74 (m, 7H), 5.40 (s, 1H), 5.11 (s, 4H), 3.48-3.45 (t, 2H), 2.74-2.72 (t, 2H), 2.00 (m, 1H), 1.81-1.67 (m, 5H), 1.39-1.21 (m, 5H). ^{13}C NMR (200Hz, CDCl$_3$) δ 176.08, 163.58 (d), 161.95, 161.46, 159.73, 159.68, 148.82, 147.31, 133.1, 130.88, 122.21, 120.31, 115.97, 115.74, 111.45, 111.26, 103.93, 103.76, 64.94, 45.55, 40.36, 35.22, 29.71, 25.73. ^{13}C NMR (151 MHz, CDCl$_3$) δ 176.05, 163.67, 163.62, 162.02, 161.94, 161.48, 161.43, 161.40, 161.35, 159.83, 148.83, 147.32, 133.12-130.75 (m), 122.22, 120.41, 120.34, 120.32, 120.22, 115.98, 115.76, 111.47-111.41 (m), 111.33-111.27 (m),

103.97, 103.94, 103.80-103.77 (d, J = 4.5Hz), 103.64-103.60 (d, J = 6Hz), 64.94, 64.81, 45.56, 40.36, 35.23, 29.71, 25.76, 25.71. LC−MS (ESI): m/z 516.0 (M + H)$^+$

N-(3,4-bis((4-chlorobenzyl)oxy)phenethyl)cyclohexanecarboxamide (**6.6, XIE5-2-80**)

To a solution of 2-(3,4-bis((4-chlorobenzyl)oxy)phenyl)ethan-1-aminium chloride (**6.3,** 403mg, 1 mmol) and triethylamine (TEA, 125mg, 1.25mmol) in anhydrous dichloromethane (DCM, 4mL) was slowly added a solution of cyclohexylcarbamic chloride (177 mg,1.1mmol) in anhydrous DCM (4 mL). The mixture was then refluxed for 3 days. The reaction mixture was diluted with water (5mL) and extracted with DCM (8 mL × 3). The combined organic layers were subsequently washed with H$_2$O (10mL× 3) and brine (10 mL × 3), dried over anhydrous Na$_2$SO$_4$ and concentrated in vacuo. The crude product was purified on a silica gel column (CH$_2$Cl$_2$/MeOH = 19/1, v/v) to afford N-(3,4-bis((4-chlorobenzyl)oxy)phenethyl)cyclohexanecarboxamide (**6.6, XIE5-2-80**, 303mg, 0.6mmol, yield=60%). The structure was confirmed by ^{1}H-NMR (600MHz, CDCl$_3$): 7.42-7.30 (m, 8H), 6.86-6.84 (d, J = 12Hz, 1H), 6.78-6.77 (d, J = 6Hz, 1H), 6.71-6.70 (dd, 1H), 5.08 (s, 4H), 3.45-3.44 (t, 2H), 2.72-2.70 (t, 2H), 1.98 (t, 1H), 1.38-1.36 (m, 2H), 1.26-1.21 (m, 8H). ^{13}C NMR (151 MHz, CDCl$_3$) δ 176.01, 148.80, 147.32, 135.76, 135.62, 133.69, 133.64, 132.69, 128.69 (2C), 128.68 (2C), 128.67 (2C), 128.65 (2C), 121.85, 115.61, 115.36, 70.72, 70.56, 45.54, 40.32, 35.22, 29.70 (2C), 25.73 (2C), 25.71, 0.01. LC−MS (ESI): m/z 512.2 (M + H)$^+$, 514.0 (M + 3H)$^+$

2-[2,3-bis-(tert-Butoxycarbonyl)guanidino]ethylamine (**XIE5-1-28B**, CAS Reg. No. 203258-44-
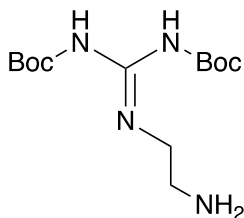
0) was prepared from Boc-protected methylisothiourea and 1,2-ethylenediamine using **Method 4**. Dissolve 1,3-Di-Boc-2-methylisothiourea (2.9g, 10mM) in THF (25ml), added the solution of 1,3-Di-Boc-2-methylisothiourea dropwise to a stirred solution of 1,2-ethylenediamine (1.44g, 1.6ml, 24mM) in THF/H_2O (40ml, 20:1, volume/volume). After stirred for 1h in 50°C, the reaction mixture was concentrated in vacuum, and the residue was partitioned between $CHCl_3$ and 10% aqueous $NaHCO_3$. The organic layer was dried by adding Na_2SO_4 and stirring for over 1h, filter out Na_2SO_4 and evaporated the solvent. The residue was then purified by chromatography on silica gel column using $CHCl_3$ (contain 1% TEA) to give product 2-[2,3-bis-(tert-Butoxycarbonyl)guanidino]ethylamine (**XIE5-1-28B**) 1.03g (yield=34%) as yellow oil (cited in JMC, 2001, vol 4-18-2955). The product structure was characterized by ^{1}H NMR (300 MHz, $CDCl_3$): δ 11.52 (s, 1 H), 8.68 (s, 1 H), 3.47 (m, 2 H), 2.86 (t, 2 H, J = 5.9 Hz), 1.51 (s, 9 H). ^{13}C NMR (300MHz, $CDCl_3$): δ 28.1 (3C), 28.3 (2C), 41.0, 43.4, 79.2, 153.2, 156.4, 163. LC-MS (ESI-MS): m/z 303.1 (M + H)[+].
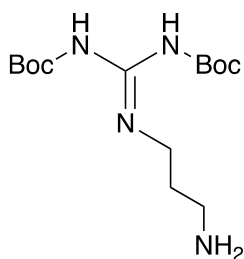
2-[2,3-bis-(tert-Butoxycarbonyl)guanidino]propylamine (**XIE5-1-29B**, CAS Reg. No. 214151-16-3) was prepared from Boc-protected methylisothiourea (2.9g, 10 mmol) and 1,3-diaminopropane (2.3 ml, 21 mmol) in THF/H_2O_2. Dissolve 1,3-Di-Boc-2-methylisothiourea (2.9g, 10mM) in THF (25ml), added the solution of 1,3-Di-Boc-2-methylisothiourea dropwise to a stirred solution of propane-1,3-diamine (2.3ml, 21mM) in THF/H_2O (40ml, 20:1, volume/volume). After stirred for 1h in 50°C, the reaction mixture was concentrated in vacuum, and the residue was

partitioned between CHCl₃ and 10% aqueous NaHCO₃. The organic layer was dried by adding

Na₂SO₄ and stirring for over 1h, filter out Na₂SO₄ and evaporated the solvent. The residue was

then purified by chromatography on silica gel column using CHCl₃ (contain 1% TEA) to give

product 2-[2,3-bis-(tert-Butoxycarbonyl)guanidino]propylamine (**XIE5-1-29B**)1.2g (yield=38%)

as colorless oil. The product structure was characterized by ^{1}H NMR (300 MHz, CDCl₃): δ 1.49

(s, 9H), 1.50 (s, 9H), 1.73 (t, J = 6.7Hz, 2H), 2.79 (t, J = 6.7Hz, 2H), 3.51 (m, J = 6.7Hz, 2H), 8.43

(s, 1H), 11.47 (s, 1H). LC-MS (ESI, m/z) 317.2 [M + H]$^+$
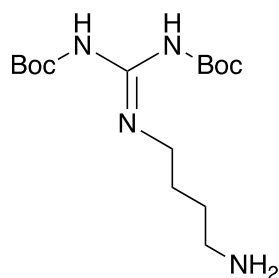
2-[2,3-bis-(tert-Butoxycarbonyl)guanidino]butylamine   [**XIE5-1-37B,**
CAS   Reg.   No.   128009-23-4]   was   prepared   from   Boc-protected
methylisothiourea and 1,4-diaminobutane using **Method 4**. Dissolve 1,3-
Di-Boc-2-methylisothiourea (2.9g, 10mM) in THF (25ml), added the
solution of 1,3-Di-Boc-2-methylisothiourea dropwise to a stirred solution

of 1,4-diaminobutane (1.9g, 2.16ml, 26mM) in THF/H₂O (40ml, 20:1, volume/volume). After

stirred for 1h in 50°C, the reaction mixture was concentrated in vacuum, and the residue was

partitioned between CHCl₃ and 10% aqueous NaHCO₃. The organic layer was dried by adding

Na₂SO₄ and stirring for over 1h, filter out Na₂SO₄ and evaporated the solvent. The residue was

then purified by chromatography on silica gel column using CHCl₃ (contain 1% TEA) to give

product 2-[2,3-bis-(tert-Butoxycarbonyl)guanidino]butylamine [**XIE5-1-37B**] 1.8g (yield=56%)

as yellow oil (cited in JMC, 2001, vol 4-18-2955). ^{1}H-NMR (400MHz, DMSO-d6): 8.37 (s, 1H),

3.42 (m, 2H), 2.78 (t, J = 7Hz, 2H), 2.12 (s, 2H), 1.44-1.67 (m, 22H). LC-MS (ESI, m/z) 331.2 [M

+ H]$^+$
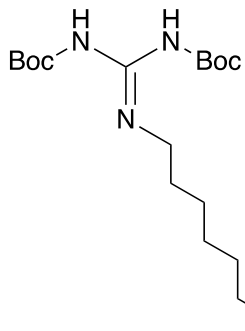
6-[2,3-bis-(tert-Butoxycarbonyl)guanidino]hexylamine (**XIE5-1-38B,** CAS Registry Number: 160677-41-8) was prepared from Boc-protected methylisothiourea and 1,6-diaminobutane using **Method 4**. Dissolve 1,3-Di-Boc-2-methylisothiourea (2.9g, 10mM) in THF (25ml), added the solution of 1,3-Di-Boc-2-methylisothiourea dropwise to a stirred solution of 1,6-diaminohexane (2.68g, 3ml, 23mM) in THF/H_2O (40ml, 20:1, volume/volume). After stirred for 1h in 50°C, the reaction mixture was concentrated in vacuum, and the residue was partitioned between $CHCl_3$ and 10% aqueous $NaHCO_3$. The organic layer was dried by adding Na_2SO_4 and stirring for over 1h, filter out Na_2SO_4 and evaporated the solvent. The residue was then purified by chromatography on silica gel column using $CHCl_3$ (contain 1% TEA) to give product 6-[2,3-bis-(tert-Butoxycarbonyl)guanidino]hexylamine (**XIE5-1-38B**) yellow oil (1.3g, yield=36%). The product structure was confirmed by ^{1}H-NMR (400MHz, DMSO-d6): 8.33 (s, 2H), 3.28-3.27 (m, 2H), 2.53 (s 1H), 2.53-2.50 (m, 4H), 1.48 (s, 9H), 1.40 (s, 9H), 1.27-1.38 (m, 6H). LC-MS (ESI, m/z) 359.3 [M + H]$^+$
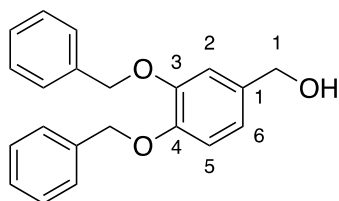
(3,4-bis(benzyloxy)phenyl)methanol (**3.2**, **XIE5-1-33A**) was prepared from 3,4-bis(benzyloxy)benzaldehyde (**3.1, XIE5-1-86**). To a solution of 3,4-bis(benzyloxy)benzaldehyde (**3.1, XIE5-1-86, 159mg, 0.5mmol**) in MeOH (5ml), add $NaBH_4$ (28mg, 0.5mmol). After stirring for 3 hours, the reaction mixture was concentrated in vacuum, and the residue was partitioned between $CHCl_3$ and 10% aqueous $NaHCO_3$. The organic layer was dried by adding

Na2SO4 and stirring for over 1h, filter out Na2SO4 and evaporated the solvent. The residue was recrystallized to give product (3,4-bis(benzyloxy)phenyl)methanol (**3.2**, **XIE5-1-33A,** 120mg, 0.39mmol, yield=78%). The product structure was characterized by ^{1}H-NMR (400MHz, DMSO-d6): 7.48-7.31 (m, 10H), 7.05 (d, J = 2Hz, 1H), 7.01-6.99 (d, J = 8Hz, 1H), 6.84-6.81 (dd, J = 4Hz, J = 8Hz, 1H), 5.12 (s, 4H), 4.40-4.39 (d, J = 4Hz, 1H). LC-MS (ESI, m/z) 321.5 [M + H]$^+$
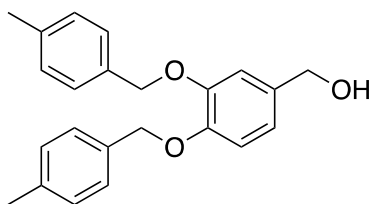
(3,4-bis((4-methylbenzyl)oxy)phenyl)methanol (**7.2, XIE5-1-55A**) was prepared from 3,4-bis((4-methylbenzyl)oxy)benzaldehyde (**7.1, XIE5-1-12/I4**). To a solution of 3,4-bis((4-methylbenzyl)oxy)benzaldehyde (**7.1, XIE5-1-12/I4**, 174mg, 0.5mmol) in MeOH (5ml), add NaBH4 (29mg, 0.5mmol). After stirring for 3 hours, the reaction mixture was concentrated in vacuum, and the residue was partitioned between CHCl3 and 10% aqueous NaHCO3. The organic layer was dried by adding Na2SO4 and stirring for over 1h, filter out Na2SO4 and evaporated the solvent. The residue was recrystallized to give product (3,4-bis((4-methylbenzyl)oxy)phenyl)methanol (**7.2, XIE5-1-55A**, 143mg, 0.41mmol, yield=82%). The product structure was characterized by ^{1}H-NMR (400MHz, DMSO-d6): 7.35-7.30 (t, 4H), 7.20-7.17 (t, J = 6Hz, 4H), 7.03-7.02 (d, J = 4Hz, 1H), 7.98-7.96 (d, J = 8Hz, 1H), 6.82-6.80 (dd, J = 8Hz, 1H), 5.05 (s, 5H, CH2+OH), 4.39-4.38 (d, J = 4Hz, 2H), 2.31-2.30 (d, J = 4Hz, 6H). LC-MS (ESI, m/z) 349.1 [M + H]$^+$
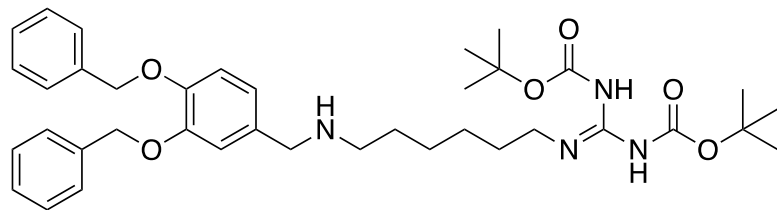
The intermediate di-tert-butyl (((6-((3,4-bis(benzyloxy)benzyl)amino)hexyl)amino)methylene)dicarbamate (**XIE5-1-54C**) was prepared from 3,4-bis(benzyloxy)benzaldehyde (**3.1, XIE5-1-86**) and 6-[2,3-bis-(tert-Butoxycarbonyl)guanidino]hexylamine (**XIE5-1-38B)** using **Method 2.** 3,4-bis(benzyloxy)benzaldehyde (**3.1, XIE5-1-86**, 318 mg, 1 mmol) was dissolved in dry ethanol, and 6-[2,3-bis-(tert-Butoxycarbonyl)guanidino]hexylamine (**XIE5-1-38B,** 360mg, 1mmol**)** was added in. The reaction mixture was stirred for 12 hours at 65 °C. The reaction solution was then cooled down to room temperature. NaBH4 (30mg, 0.5 mmol) was added slowly in small portions, and the resulting solution was stirred for another 12 hours (143, 144). The solvent was evaporated in vacuum, and the residue was dissolved in water and extracted with ethyl acetate. The organic layers were combined and dried with Na2SO4, filtered, and evaporated in a vacuum. The residue was purified by a flash column to generate the intermediate di-tert-butyl (((6-((3,4-bis(benzyloxy)benzyl)amino)hexyl)amino)methylene)dicarbamate (**XIE5-1-54C**), a white solid (328mg, 0.48mmol, yield: 48%). The structure was characterized by ^{1}H-NMR (400MHz, DMSO-d6): 7.48-7.30 (m, 11H), 7.09-7.07 (d, J=8Hz, 1H), 6.99-6.97 (d, J = 8Hz, 1H), 5.77 (s, 1H), 5.15-5.14 (d, J = 4Hz, 4H), 3.94 (s, 2H), 2.75-2.73-2.71 (t, J = 8Hz, 2H), 2.00 (s, 1H), 1.48-1.40 (d, J = 32Hz, 18H), 1.46 (m, 3H, CH2+NH), 1.28 (m, 6H), 1.20-1.12 (m, 2H).
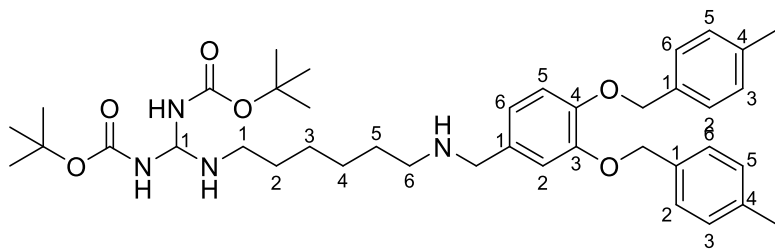
The intermediate di-tert-butyl (((6-((3,4-bis((4-methylbenzyl)oxy)benzyl)amino)hexyl)amino)methylene)dicarbamate (**XIE5-1-55C**) was prepared from 3,4-bis((4-methylbenzyl)oxy)benzaldehyde (**7.1, XIE5-1-12/I4**) and 6-[2,3-bis-(tert-Butoxycarbonyl)guanidino]hexylamine (**XIE5-1-38B)** using **Method 2.** 3,4-bis((4-methylbenzyl)oxy)benzaldehyde (**7.1, XIE5-1-12/I4,** 348 mg, 1 mmol) was dissolved in dry ethanol, and 6-[2,3-bis-(tert-Butoxycarbonyl)guanidino]hexylamine (**XIE5-1-38B, 360mg, 1mmol)** was added in. The reaction mixture was stirred for 12 hours at 70 °C. The reaction solution was then cooled down to room temperature. NaBH$_4$ (57mg, 1 mmol) was added slowly in small portions, and the resulting solution was stirred for another 12 hours (143, 144). The solvent was evaporated in vacuo, and the residue was dissolved in water and extracted with ethyl acetate. The organic layers were combined and dried with Na$_2$SO$_4$, filtered, and evaporated in a vacuum. The residue was purified by a flash column to generate the intermediate (((6-((3,4-bis((4-methylbenzyl)oxy)benzyl)amino)hexyl)amino)methylene)dicarbamate (**XIE5-1-55C**), a white solid (345mg, 0.5mmol, yield: 50%).

1-(2-((3,4-bis(benzyloxy)phenethyl)amino)ethyl)guanidine (**3.29, XIE1-4-3**)
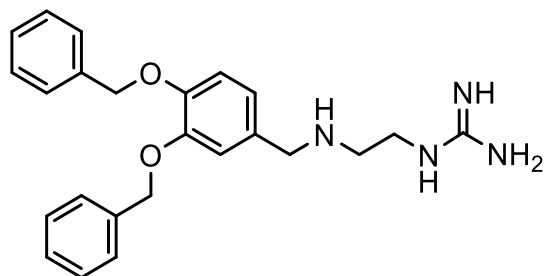
The intermediate di-tert-butyl (((2-((3,4-bis(benzyloxy)benzyl)amino)ethyl)amino)methylene)dicarbamate (**XIE5-1-94**) was prepared from 3,4-bis(benzyloxy)benzaldehyde (**3.1, XIE5-1-86**) and 2-[2,3-bis-(tert-Butoxycarbonyl)guanidino]ethylamine (**XIE5-1-28B**) using **Method 2.** 3,4-bis(benzyloxy)benzaldehyde (**3.1, XIE5-1-86**, 318 mg, 1 mmol) was dissolved in dry ethanol, and 2-[2,3-bis-(tert-Butoxycarbonyl)guanidino]ethylamine (**XIE5-1-28B,** 305mg, 1mmol**)** was added in. The reaction mixture was stirred for 12 hours at 65°C. The reaction solution was then cooled down to room temperature. NaBH$_4$ (30mg, 0.5 mmol) was added slowly in small portions, and the resulting solution was stirred for another 12 hours (143, 144). The solvent was evaporated in vacuum, and the residue was dissolved in water and extracted with ethyl acetate. The organic layers were combined and dried with Na$_2$SO$_4$, filtered, and evaporated in a vacuum. The residue was purified by a flash column to generate the intermediate di-tert-butyl (((2-((3,4-bis(benzyloxy)benzyl)amino)ethyl)amino)methylene)dicarbamate (**XIE5-1-94,** 297mg, 0.48mmol, yield=48%), a white solid.

The product 1-(2-((3,4-bis(benzyloxy)phenethyl)amino)ethyl)guanidine (**3.29, XIE1-4-3**) was prepared from di-tert-butyl (((2-((3,4-bis(benzyloxy)benzyl)amino)ethyl)amino)methylene)dicarbamate (**XIE5-1-94**) using **Method 5**. To a solution of the intermediate di-tert-butyl (((2-((3,4-

bis(benzyloxy)benzyl)amino)ethyl)amino)methylene)dicarbamate (**XIE5-1-94,** 297mg, 0.48mmol) in CH_2Cl_2, hydrochloride gas was bubbled into. The reaction mixture was stirred at room temperature with hydrochloride gas bubbled in for about 40 min. Stop generation of HCl gas, continue stirring at r.t. for about half an hour, then evaporate the solvent, add solvent to resuspend it and evaporate solvent for several times to remove extra hydrochloride. The solvent was evaporated under vacuo and the residue was collected as the product 1-(2-((3,4-bis(benzyloxy)phenethyl)amino)ethyl)guanidine (**3.29, XIE1-4-3,** 178mg, 0.39mmol, yield=83%). The product structure was characterized by ^{1}H-NMR (600MHz, MeOD): 7.482-7.433 (m, 4H), 7.399-7.317 (m, 6H), 7.077-7.056 (d, J = 12.6 Hz, 1H), 6.907-6.902 (d, 1H), 6.871-6.866-6.851-6.845 (dd, 1H), 5.192-5.169 (d, J = 13.8 Hz, 4H), 4.593 (s, 1H), 4.419 (s, 1H), 3.581-3.535 (m, 2H), 3.451-3.407 (m, 2H). ^{13}C NMR (151 MHz, CDCl$_3$) δ 191.93, 162.68, 160.43, 160.14, 138.08, 137.82, 133.65, 133.20, 129.38, 129.27, 129.23, 129.21, 129.19, 127.83, 127.75, 127.74, 108.72, 108.27, 106.87, 70.12, 61.42, 44.68, 38.02, 21.22. LC-MS (ESI, m/z) 405.3 [M + H]$^+$

1-(2-((3,4-bis((4-fluorobenzyl)oxy)benzyl)amino)ethyl)guanidine (**5.29, XIE5-1-27AT/XIE5-1-**
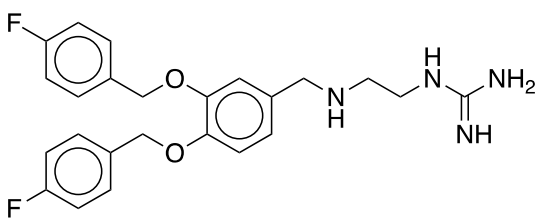
66) was prepared from the intermediate di-tert-butyl (((2-((3,4-bis((4-fluorobenzyl)oxy)benzyl)amino)ethyl)amino)methylene)dicarbamate (**XIE5-1-27A**). The intermediate di-tert-butyl (((2-((3,4-bis((4-fluorobenzyl)oxy)benzyl)amino)ethyl)amino)methylene)dicarbamate (**XIE5-1-27A**) was prepared from 3,4-bis((4-fluorobenzyl)oxy)benzaldehyde (**5-1, XIE5-1-24**) and 2-[2,3-bis-(tert-Butoxycarbonyl)guanidino]ethylamine (**XIE5-1-28B**) using **Method 2.** 3,4-bis((4-fluorobenzyl)oxy)benzaldehyde (**5-1, XIE5-1-24,** 356mg, 1mmol) was dissolved in dry ethanol,

and 2-[2,3-bis-(tert-Butoxycarbonyl)guanidino]ethylamine (**XIE5-1-28B,** 305mg, 1mmol) was added in. The reaction mixture was stirred for 12 hours at 65°C. The reaction solution was then cooled down to room temperature. $NaBH_4$ (30mg, 0.5 mmol) was added slowly in small portions, and the resulting solution was stirred for another 12 hours (143, 144). The solvent was evaporated in vacuum, and the residue was dissolved in water and extracted with ethyl acetate. The organic layers were combined and dried with Na_2SO_4, filtered, and evaporated in a vacuum. The residue was purified by a flash column to generate the intermediate di-tert-butyl (((2-((3,4-bis((4-fluorobenzyl)oxy)benzyl)amino)ethyl)amino)methylene)dicarbamate (**XIE5-1-27A,** 274mg, 0.42mmol, yield=42%), a white solid.

The product 1-(2-((3,4-bis((4-fluorobenzyl)oxy)benzyl)amino)ethyl)guanidine (**5.29, XIE5-1-27AT/XIE5-1-66**) was prepared from di-tert-butyl (((2-((3,4-bis((4-fluorobenzyl)oxy)benzyl)amino)ethyl)amino)methylene)dicarbamate (**XIE5-1-27A**) using **Method 5**. To a solution of the intermediate di-tert-butyl (((2-((3,4-bis((4-fluorobenzyl)oxy)benzyl)amino)ethyl)amino)methylene)dicarbamate (**XIE5-1-27A,** 274mg, 0.42mmol) in 10ml CH_2Cl_2, hydrochloride gas was bubbled into. The reaction mixture was stirred at room temperature with hydrochloride gas bubbled in for about 40 min. Stop generation of HCl gas, continue stirring at r.t. for about half an hour, then evaporate the solvent, add solvent to resuspend it and evaporate solvent for several times to remove extra hydrochloride. The solvent was evaporated under vacuo and the residue was collected as the product 1-(2-((3,4-bis((4-fluorobenzyl)oxy)benzyl)amino)ethyl)guanidine (**5.29, XIE5-1-27AT/XIE5-1-66,** 163mg, 0.36mmol, yield=86%). The structure was confirmed by ^{1}H-NMR (400MHz, $CDCl_3$):7.34 (s,1H), 7.32-7.30 (d, *J* = 8Hz, 4H), 7.17-7.13 (m, 5H), 6.95 (s, 2H), 6.89-6.87 (m, 1H), 6.83-6.77 (m, 1H),

5.10 (s, 4H), 4.36-4.34 (d, J = 8Hz, 2H), 3.32 (s, 2H), 2.43-2.33 (d, J = 40Hz, 2H), 1.25 (s, 1H).

LC-MS (ESI, m/z) 441.3 [M + H]$^+$

1-(6-((3,4-bis((4-methylbenzyl)oxy)benzyl)amino)hexyl)guanidine (**XIE5-1-55CT/XIE5-1-65**)
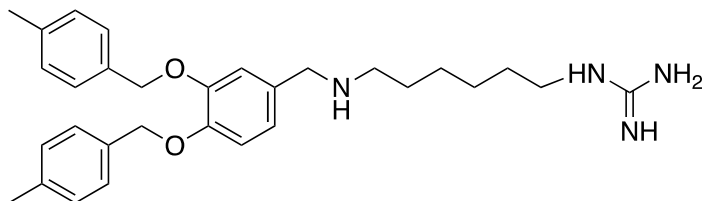
To a solution of the intermediate di-tert-butyl ((((6-((3,4-bis((4-methylbenzyl)oxy)benzyl)amino)hexyl)amino)methylene)dicarbamate (**XIE5-1-55C,** 345mg, 0.5mmol) in 10ml CH$_2$Cl$_2$, hydrochloride gas was bubbled into. The reaction mixture was stirred at room temperature with hydrochloride gas bubbled in for about 40 min. Stop generation of HCl gas, continue stirring at r.t. for about half an hour, then evaporate the solvent, add solvent to resuspend it and evaporate solvent for several times to remove extra hydrochloride. The solvent was evaporated under vacuo and the residue was collected as the product 1-(6-((3,4-bis((4-methylbenzyl)oxy)benzyl)amino)hexyl)guanidine (**XIE5-1-55CT/XIE5-1-65,** 196mg, 0.4mmol, yield=80%). The structure was confirmed ^{1}H-NMR (400MHz, CDCl$_3$): 9.28 (bs, 2H, NH$_2$), 7.70 (bs, 1H, NH), 7.45-7.31 (m, 6H), 7.29-7.28 (m, 2H), 7.02 (s, 1H), 6.48 (d, J = 4Hz, 1H), 5.19-5.03 (d, J = 64Hz, 4H), 3.94 (s, 2H, CH$_2$), 3.35 (s, 1H), 3.23 (m, 2H, CH$_2$), 2.75 (m, 2H, CH$_2$), 1.75 (s, 2H, CH$_3$), 1.49-1.28 (m, 9H, CH$_2$/NH). LC-MS (ESI, m/z) 489.3 [M + H]$^+$
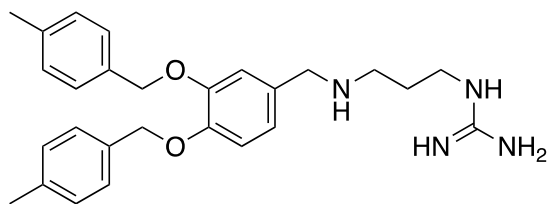
1-(3-((3,4-bis((4-methylbenzyl)oxy)benzyl)amino)propyl)guanidine (**XIE5-1-61BT/XIE5-1-67**)

To a solution of the intermediate di-tert-butyl (((3-((3,4-bis((4-methylbenzyl)oxy)benzyl)amino)propyl)amino)methylene)dicarbamate (**XIE5-1-61B, 267**mg, 0.4mmol) in 10ml CH_2Cl_2, hydrochloride gas was bubbled into. The reaction mixture was stirred at room temperature with hydrochloride gas bubbled in for about 40 min. Stop generation of HCl gas, continue stirring at r.t. for about half an hour, then evaporate the solvent, add solvent to resuspend it and evaporate solvent for several times to remove extra hydrochloride. The solvent was evaporated under vacuo and the residue was collected as the product 1-(3-((3,4-bis((4-methylbenzyl)oxy)benzyl)amino)propyl)guanidine (**XIE5-1-61BT/XIE5-1-67,** 147mg, yield=32%). The structure was confirmed by ^{1}H-NMR (400MHz, CDCl$_3$): 7.38 (s, 1H, NH), 7.36-7.33 (m, 4H), 7.21-7.14 (m, 6H), 7.01-6.99 (m, 1H), 6.91 (bs, 2H, NH$_2$), 5.15 (s, 4H, CH$_2$), 4.53 (s, 2H,CH$_2$), 4.39-4.28 (m, 2H, CH$_2$), 2.39-2.38 (d, *J* = 4Hz, 2H, CH$_3$), 2.37.-2.33 (m, 3H, CH$_2$/NH). LC-MS (ESI, m/z) 447.4 [M + H]$^+$

XIE5-1-24, 3,4-bis((4-fluorobenzyl)oxy)benzaldehyde
¹H-NMR

¹³C-NMR

190.76
190.74
163.41
163.37
161.77
161.74
154.04
149.04
132.22
132.20
131.89
131.87
130.44
129.23
129.17
129.04
128.99
126.88
115.71
115.60
115.56
115.46
113.08
112.28
77.23
77.02
76.81
70.38
70.25
0.00
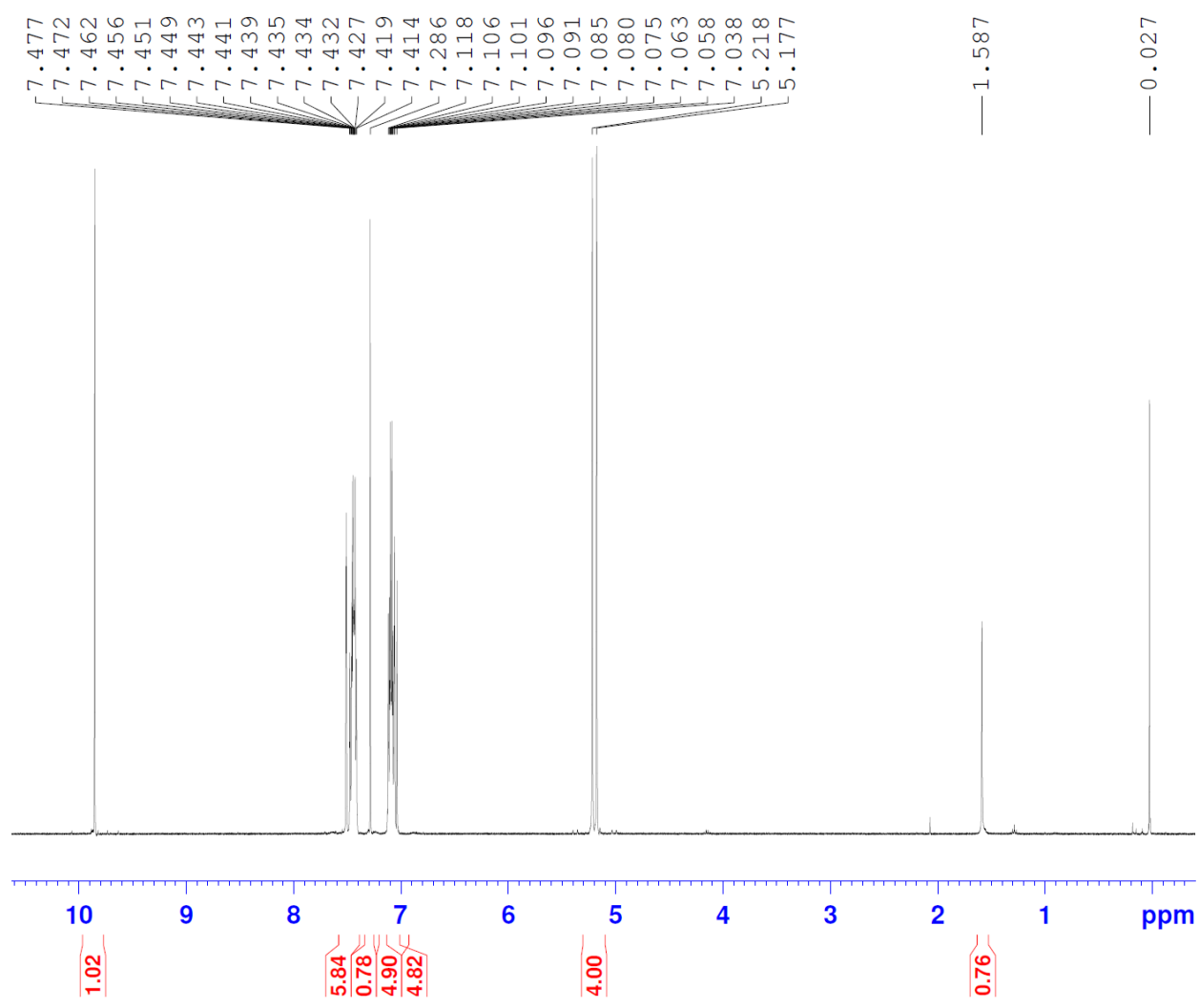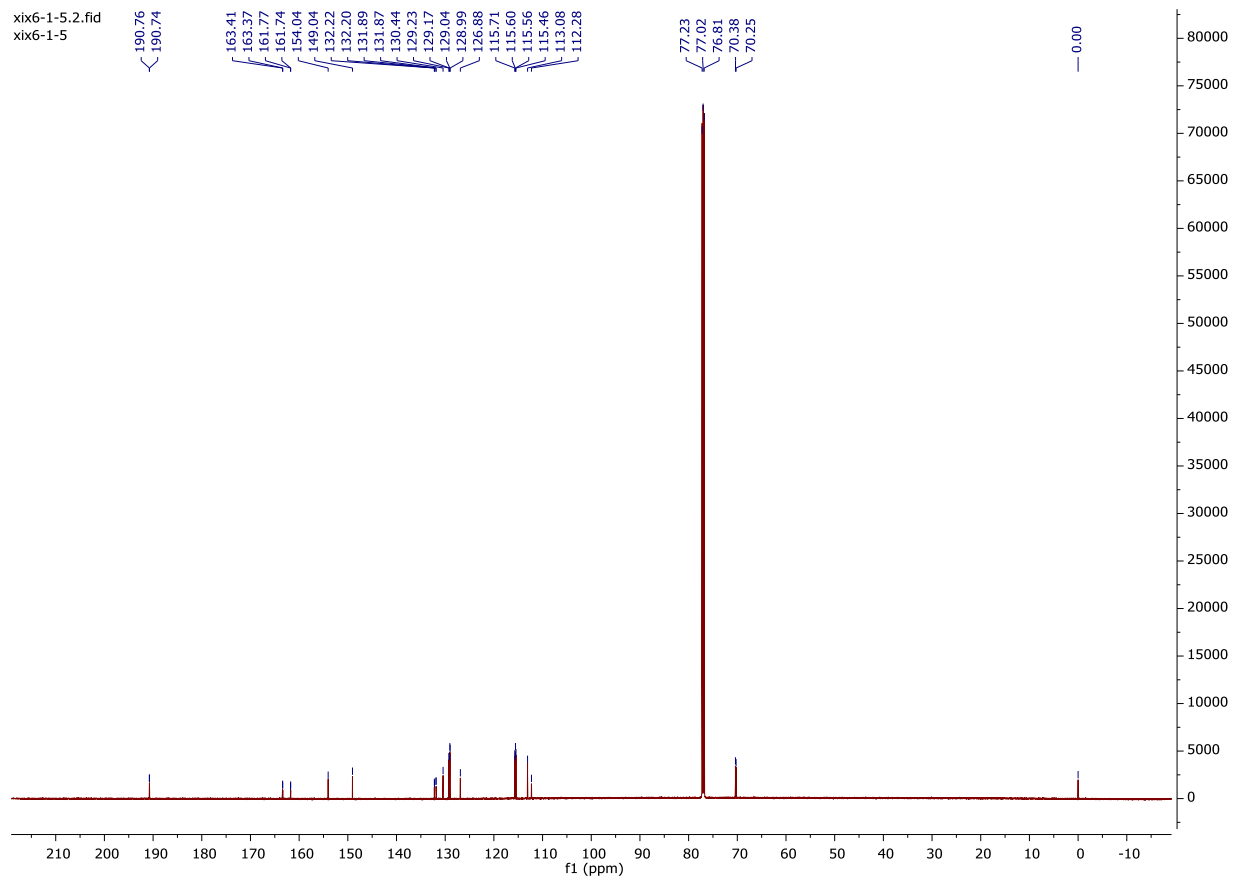
XIE5-1-84 (3,4-bis((4-chlorobenzyl)oxy)benzaldehyde)
^{1}H-NMR

9.850
7.498
7.493
7.473
7.453
7.448
7.402
7.401
7.389
7.384
7.362
7.287
7.041
7.021
5.223
5.184
1.589
0.026

10 9 8 7 6 5 4 3 2 1 ppm

1.03
2.01
8.07
1.34
1.12
4.00
3.61
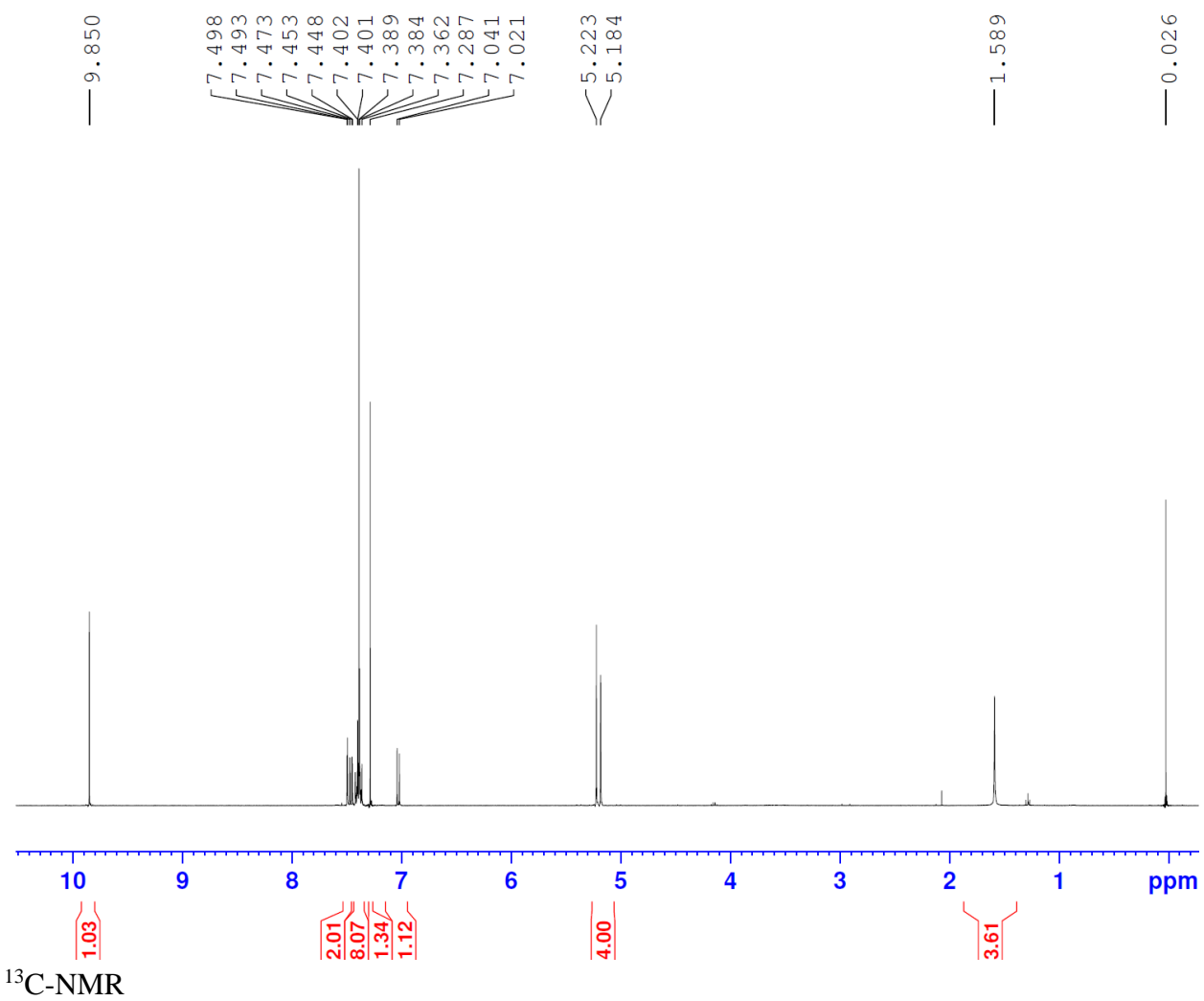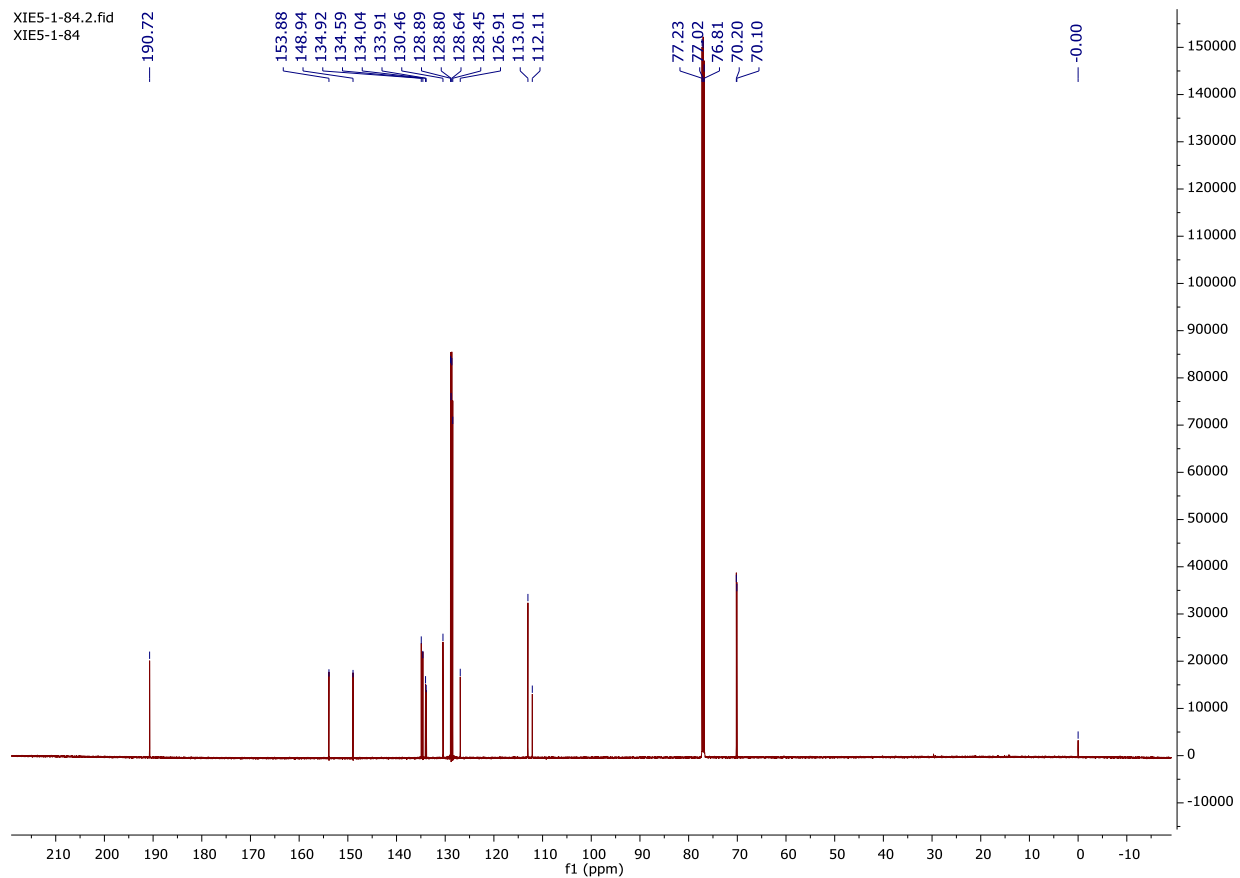
^{13}C-NMR

XIE5-1-85, 3,4-bis((2,4-difluorobenzyl)oxy)benzaldehyde
^{1}H-NMR

XIE5-1-3

9.862

7.598
7.579
7.574
7.377
7.356
7.331
7.325
7.305
7.299
7.143
7.136
7.120
7.115

5.262
5.202

3.330

2.520
2.515
2.511
2.507
2.502

0.010

10   9   8   7   6   5   4   3   2   1   0

1.17

4.04
3.02
2.12

2.00
1.94

^{13}C-NMR

331
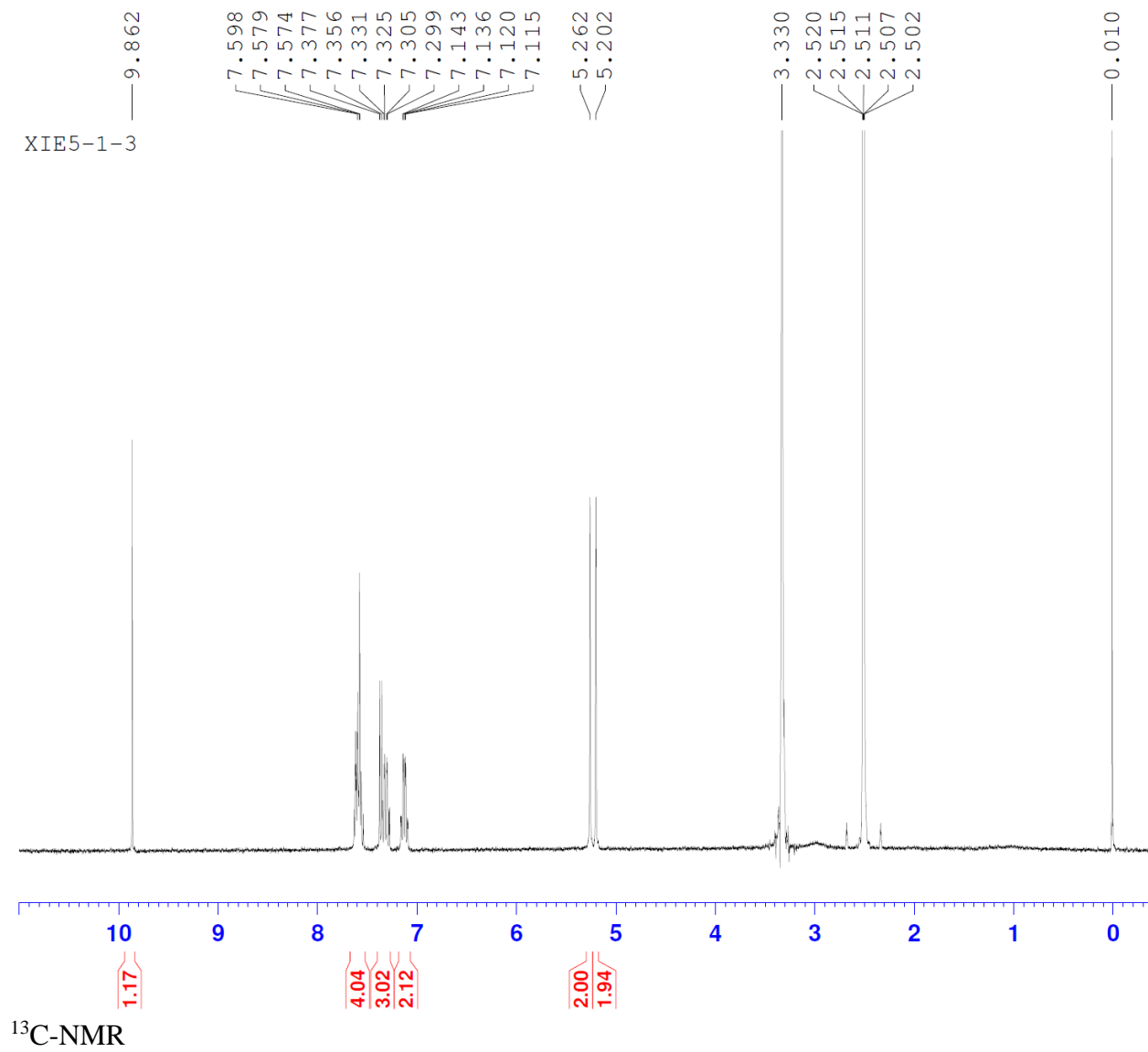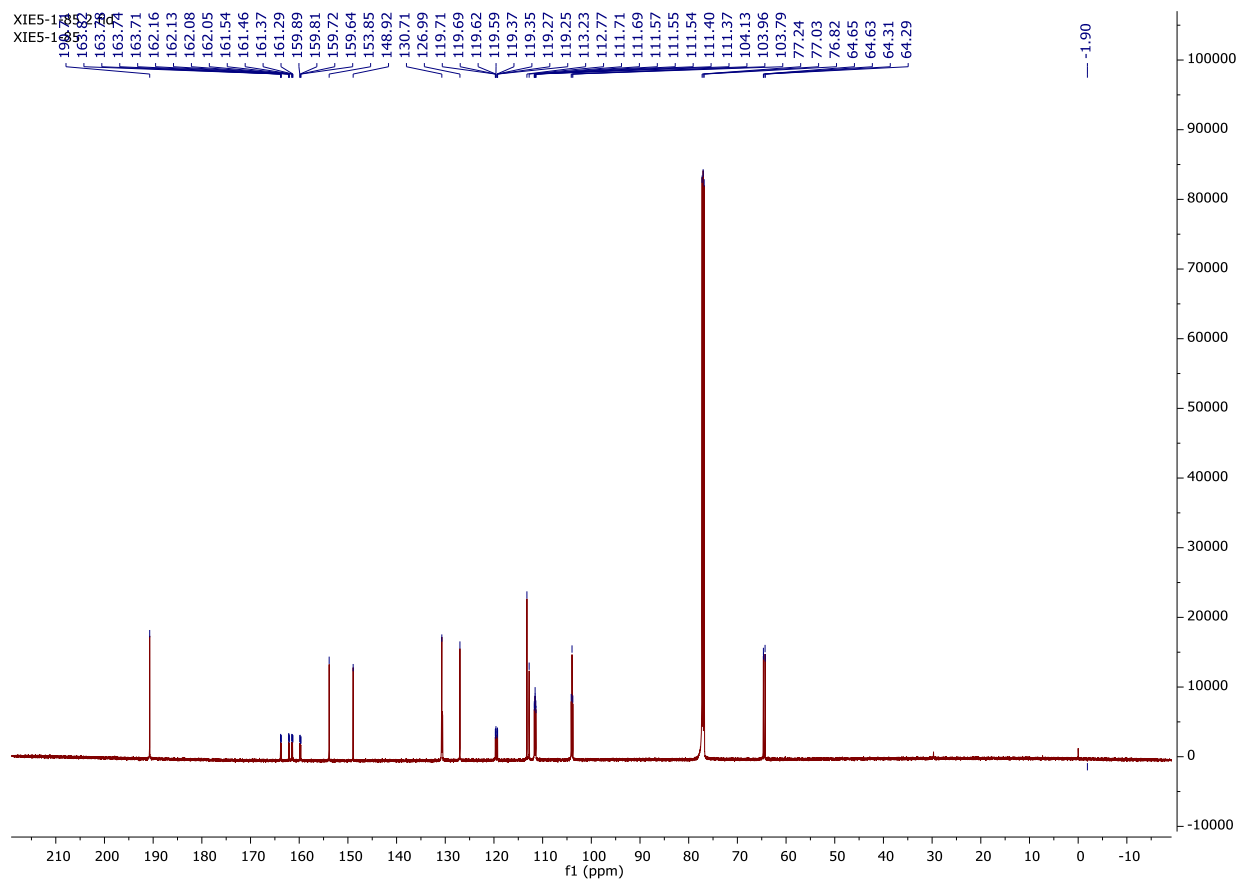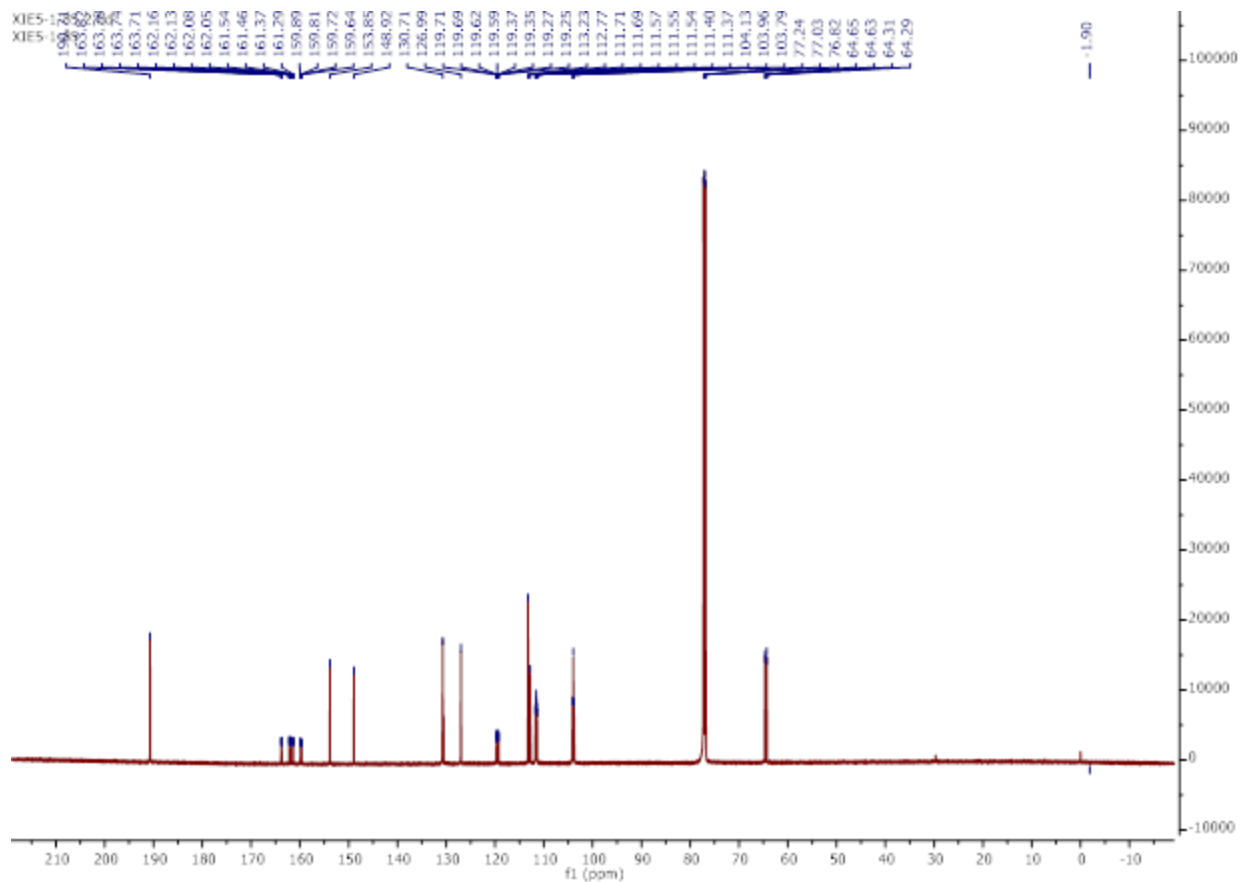
XIE5-1-86 (XIE5-1-8/XIE5-1-83), 3,4-bis(benzyloxy)benzaldehyde
^{1}H-NMR

XIE5-1-86

7.486 7.484 7.483 7.469 7.467 7.465 7.464 7.462 7.456 7.451 7.435 7.432 7.430 7.429 7.426 7.423 7.411 7.407 7.405 7.401 7.396 7.392 7.391 7.387 7.385 7.372 7.368 7.367 7.363 7.360 7.355 7.346 7.345 7.061 7.040 5.287 5.244

1.592

0.028

1.02   11.89 0.99 1.05   4.00   2.51

10 9 8 7 6 5 4 3 2 1 ppm

^{13}C-NMR

334

XIE5-1-86.2.fid
XIE5-1-86

190.87
190.86
154.26
149.19
136.56
136.24
130.30
128.68
128.61
128.14
128.04
127.33
127.08
126.73
113.08
112.33
77.29
77.08
76.87
70.97
70.83
0.04

XIE5-1-I4 (XIE5-1-12), 3,4-bis((4-methylbenzyl)oxy)benzaldehyde
^{1}H-NMR

XIE5-1-I4

9.822
7.498
7.493
7.433
7.428
7.412
7.408
7.383
7.362
7.338
7.287
7.220
7.214
7.199
7.194
7.042
7.021
5.241
5.196
2.384
1.593
0.028

10   9   8   7   6   5   4   3   2   1   ppm

1.00   10.92   3.76   5.61   2.95

^{13}C-NMR

336

XIE5-2-1, N-(3,4-bis((4-fluorobenzyl)oxy)benzyl)-1-(furan-2-yl)methanamine
^{1}H-NMR

XIE5-2-1-1

7.501
7.486
7.480
7.470
7.465
7.449
7.218
7.196
7.174
7.056
7.052
6.988
6.968
6.833
6.830
6.813
6.809
6.388
6.382
6.376
6.210
6.202
6.078
5.064

3.580
3.518

2.517
2.513
2.509
1.988

9.0 8.5 8.0 7.5 7.0 6.5 6.0 5.5 5.0 4.5 4.0 3.5 3.0 2.5 2.0 1.5 1.0 ppm

5.04 4.01 1.02 1.06 1.08 1.15 1.03 4.00 4.39

^{13}C-NMR

161.22
159.77
148.88
147.77
141.97
134.13
133.11
133.08
133.04
133.01
129.30
129.25
129.22
129.17
121.27
120.43
115.48
115.26
113.72
112.34
77.36
77.24
77.04
76.72
70.91
70.67
55.22
53.03
52.72
0.02

CDCl$_3$

2, 27
1
5
2
1
8
18
4, 31, 25, 3, 9
5, 24
10 11
25, 3, 9
30
26
17
16
29
2 0
6, 23
12
14
TMS

190 180 170 160 150 140 130 120 110 100 90 80 70 60 50 40 30 20 10 0
f1 (ppm)

XIE5-2-2, N-(3,4-bis((4-fluorobenzyl)oxy)benzyl)-1-(3-methoxyphenyl)methanamine
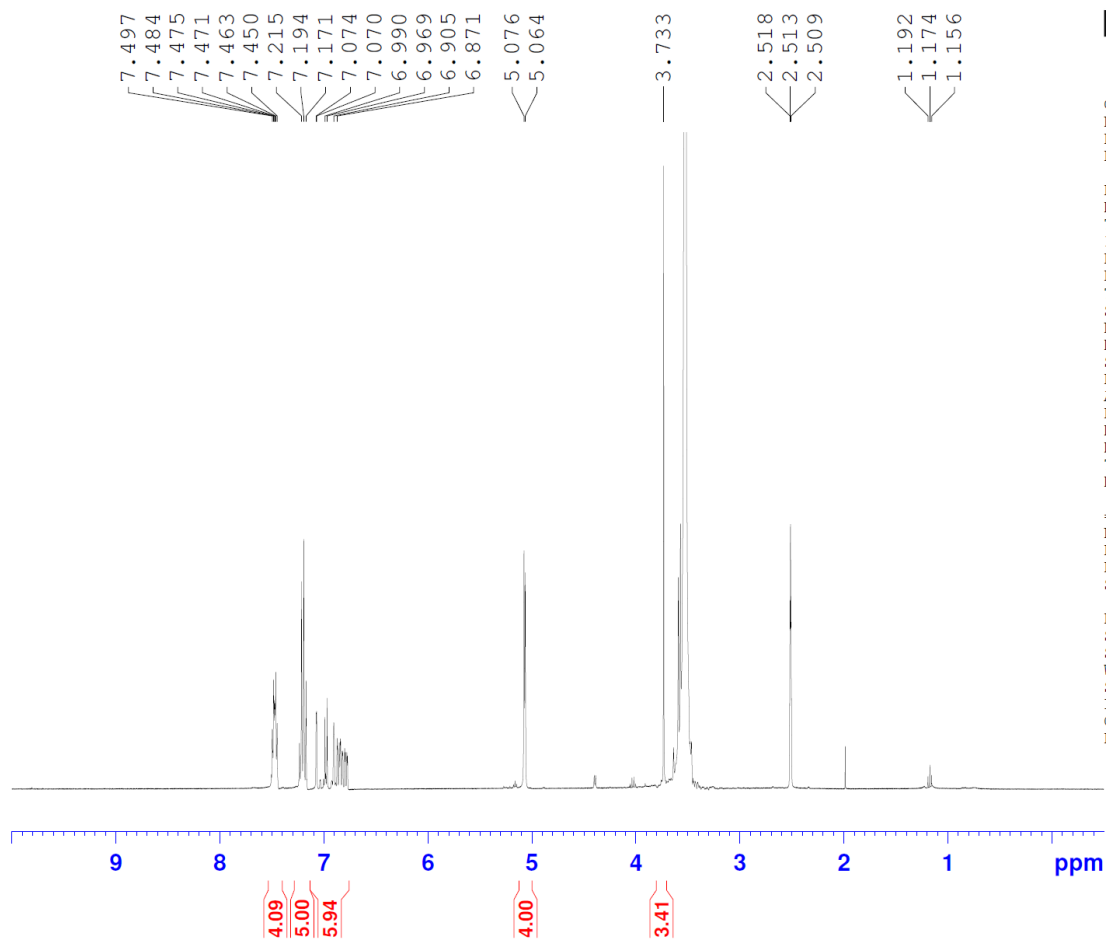
^{1}H-NMR

XIE5-2-2-1

7.497
7.484
7.475
7.471
7.463
7.450
7.215
7.194
7.171
7.074
7.070
6.990
6.969
6.905
6.871

5.076
5.064

3.733

2.518
2.513
2.509

1.192
1.174
1.156

9 8 7 6 5 4 3 2 1 ppm

4.09 5.00 5.94   4.00   3.41

^{13}C-NMR

XIE5-2-3, N-(3,4-bis((2,4-difluorobenzyl)oxy)benzyl)-1-(thiophen-2-yl)methanamine.

^{1}H-NMR

XIE5-2-3

7.567
7.560
7.551
7.389
7.379
7.315
7.290
7.265
7.123
7.107
7.086
7.047
7.027
6.977
6.968
6.957
6.933
6.892
6.874
5.108
5.091
3.812
3.635
3.364
2.517
0.014

2.74 1.09 2.08 7.97 4.00 2.15 2.05

^{13}C-NMR

342

XIE5-2-7, N-(3,4-bis((2,4-difluorobenzyl)oxy)benzyl)-3-morpholinopropan-1-amine

¹H-NMR

water

DMSO

7.57 7.56 7.55 7.55 7.54 7.30 7.28 7.28 7.23 7.11 7.11 7.10 7.10 7.09 6.99 6.98

5.11 5.10

3.86 3.54 3.53 3.52 3.17

2.31

1.70 1.68 1.67 1.66 1.65

0.00 TMS

2.16 2.00 1.03 2.88 1.15   3.90   2.04 4.29 1.10   2.17 5.77   1.94

f1 (ppm)
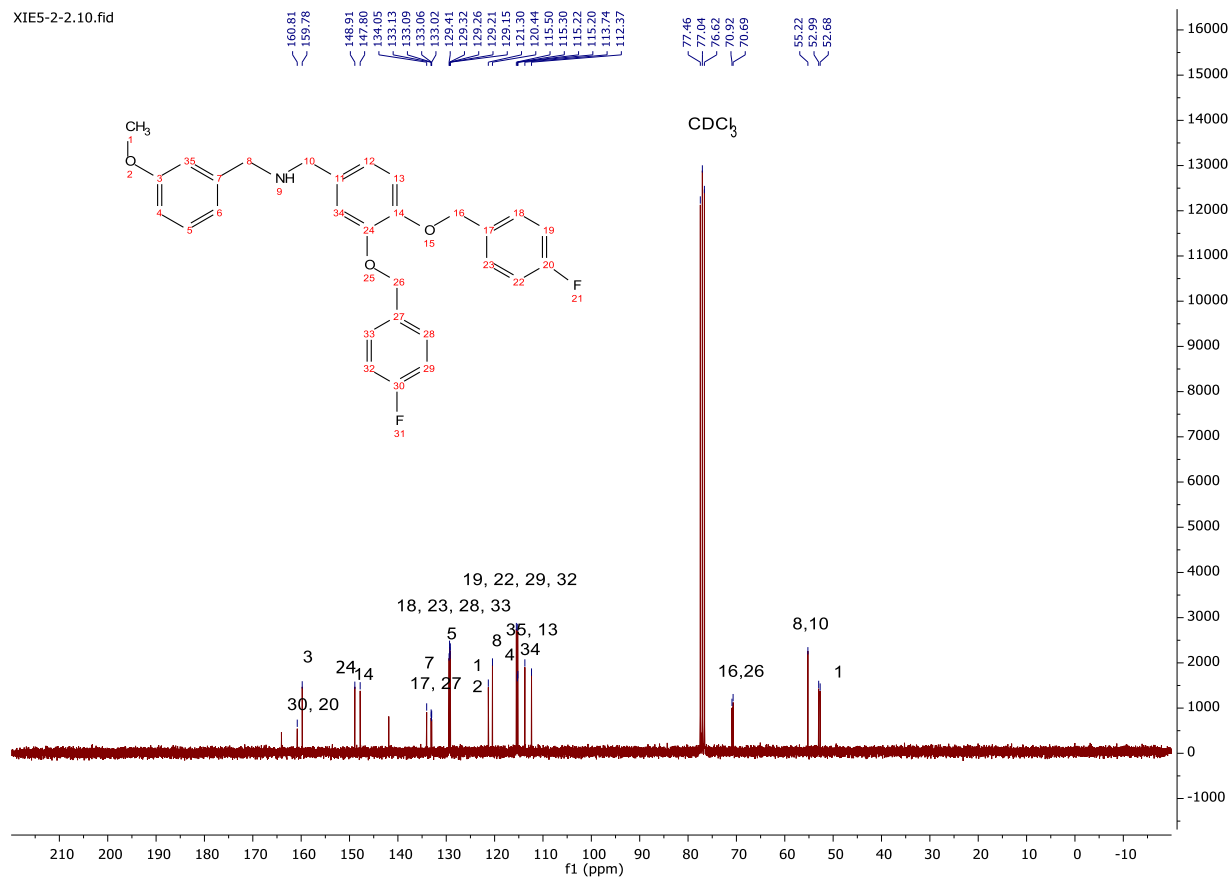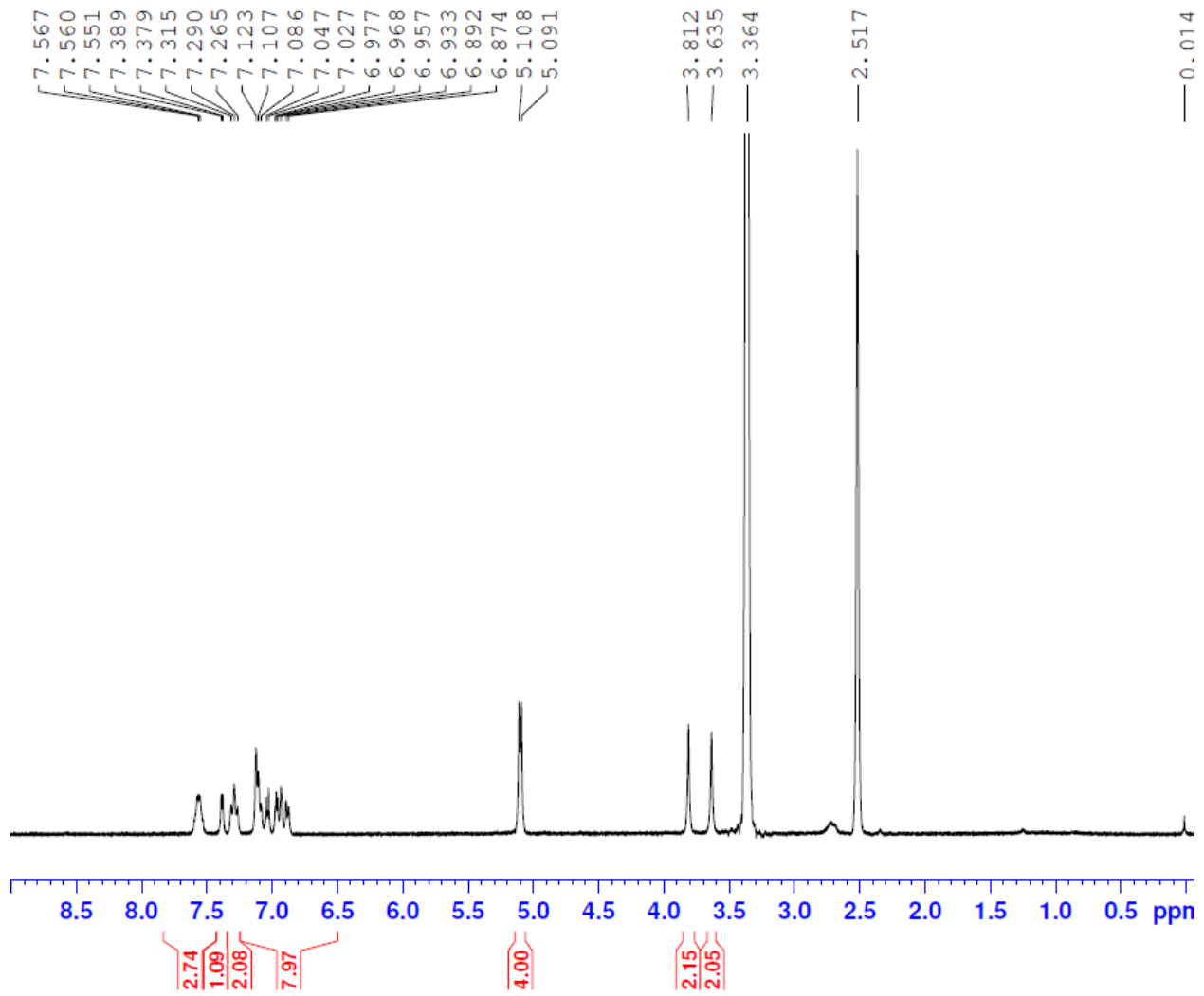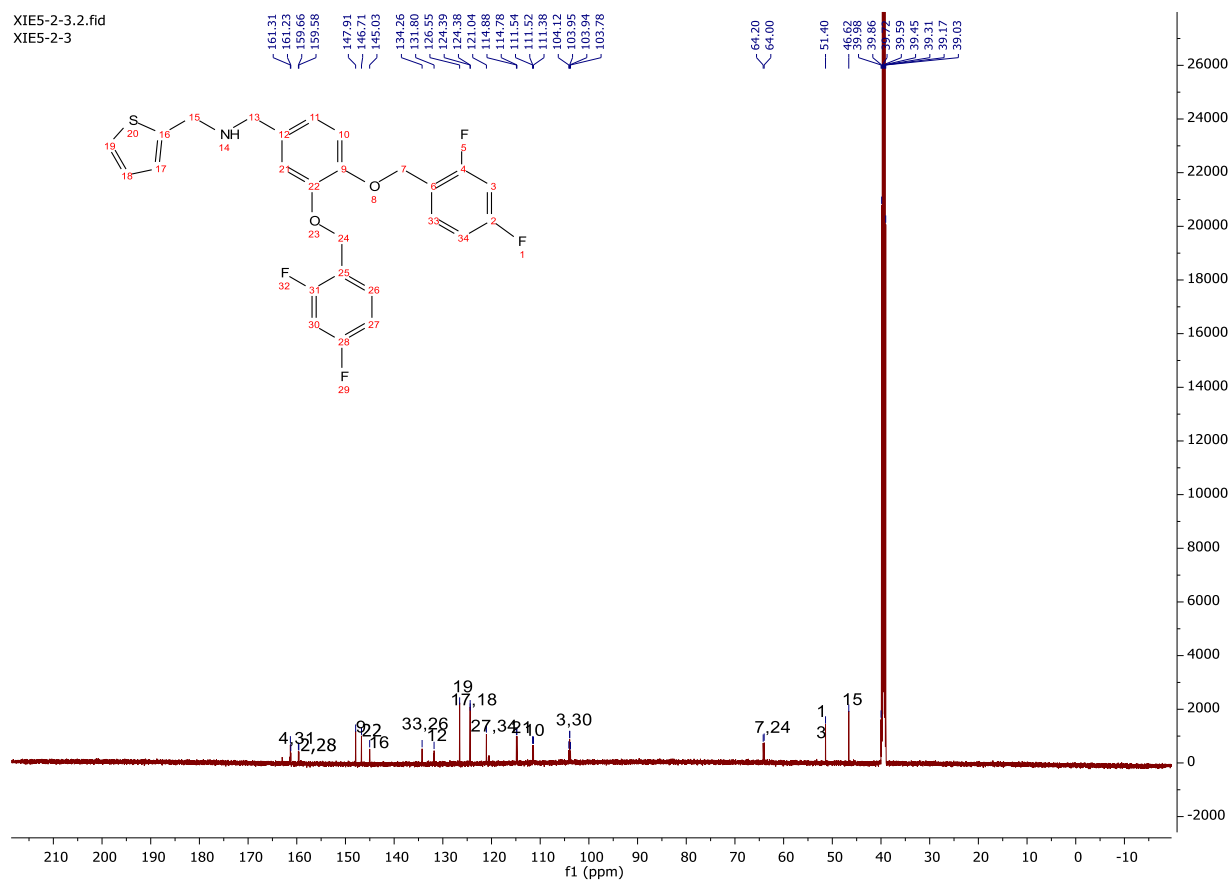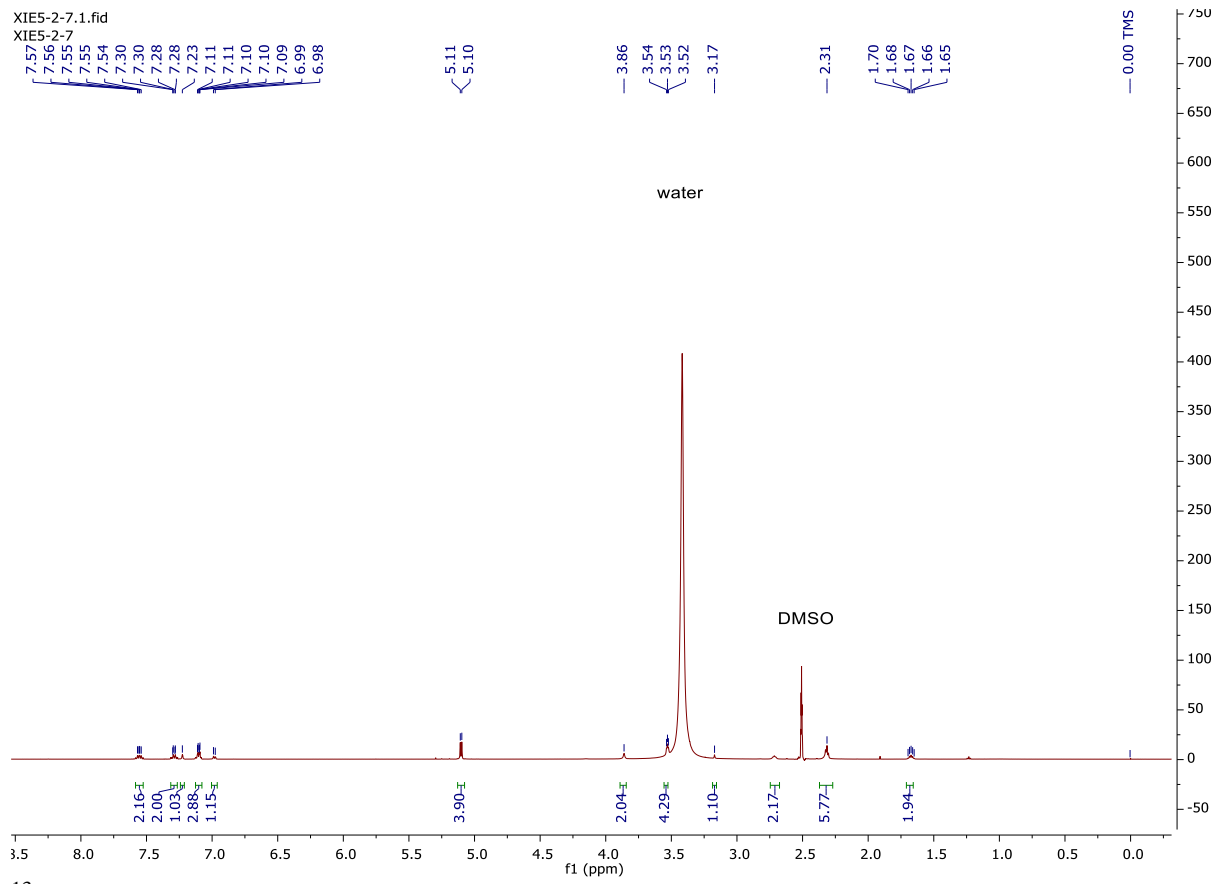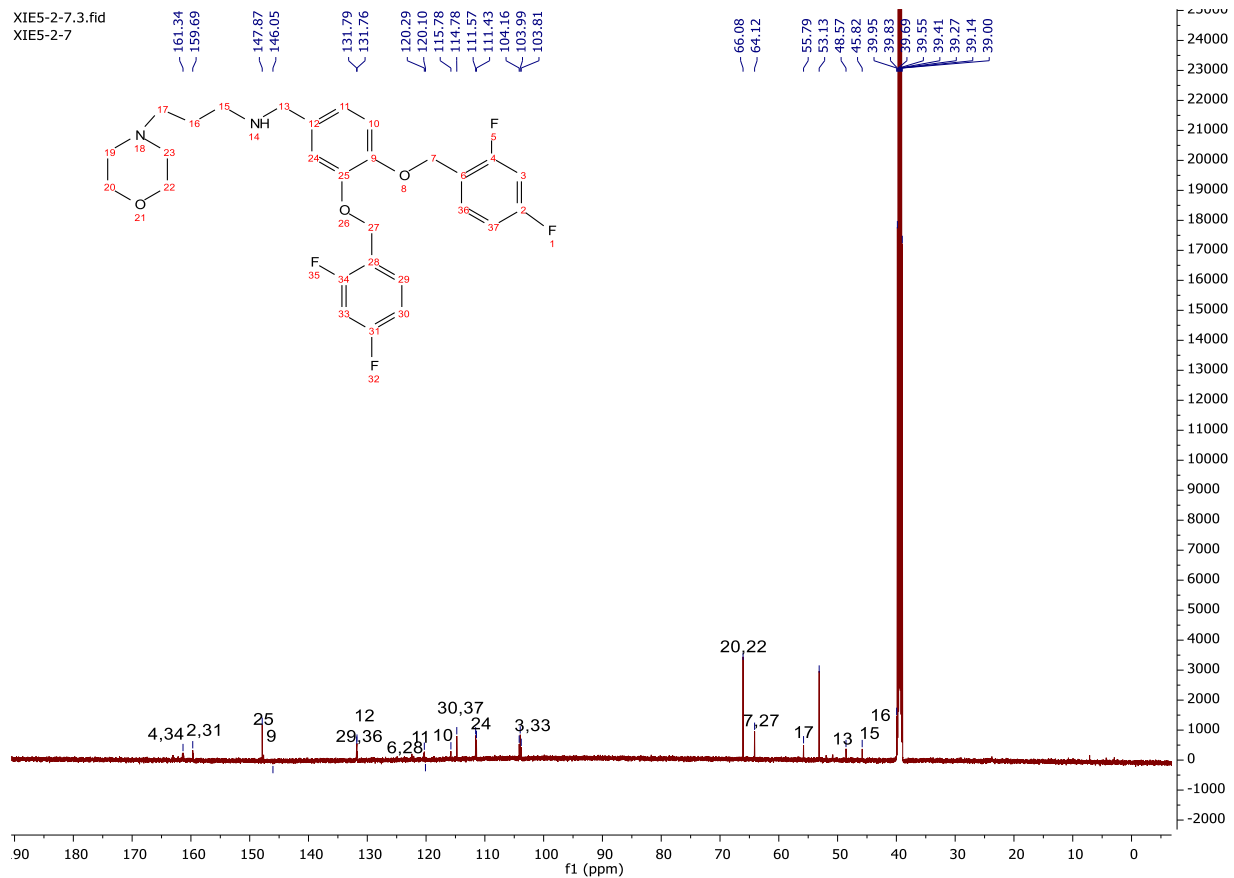
^{13}C-NMR

XIE5-2-10, N-(3,4-bis((2,4-difluorobenzyl)oxy)benzyl)-1-(345yridine-2-yl)methanamine
^{1}H-NMR

XIE5-2-10

7.560
7.545
7.527
7.363
7.352
7.345
7.333
7.307
7.284
7.259
7.124
7.103
7.082
7.043
7.023
6.897
6.878
5.103
5.089
3.657
3.616
2.517
0.010

8.5 8.0 7.5 7.0 6.5 6.0 5.5 5.0 4.5 4.0 3.5 3.0 2.5 2.0 1.5 1.0 0.5 ppm

1.00 1.01 | 1.05 2.25 1.10 2.14 3.11 1.14 1.05 | 4.09 | 4.14
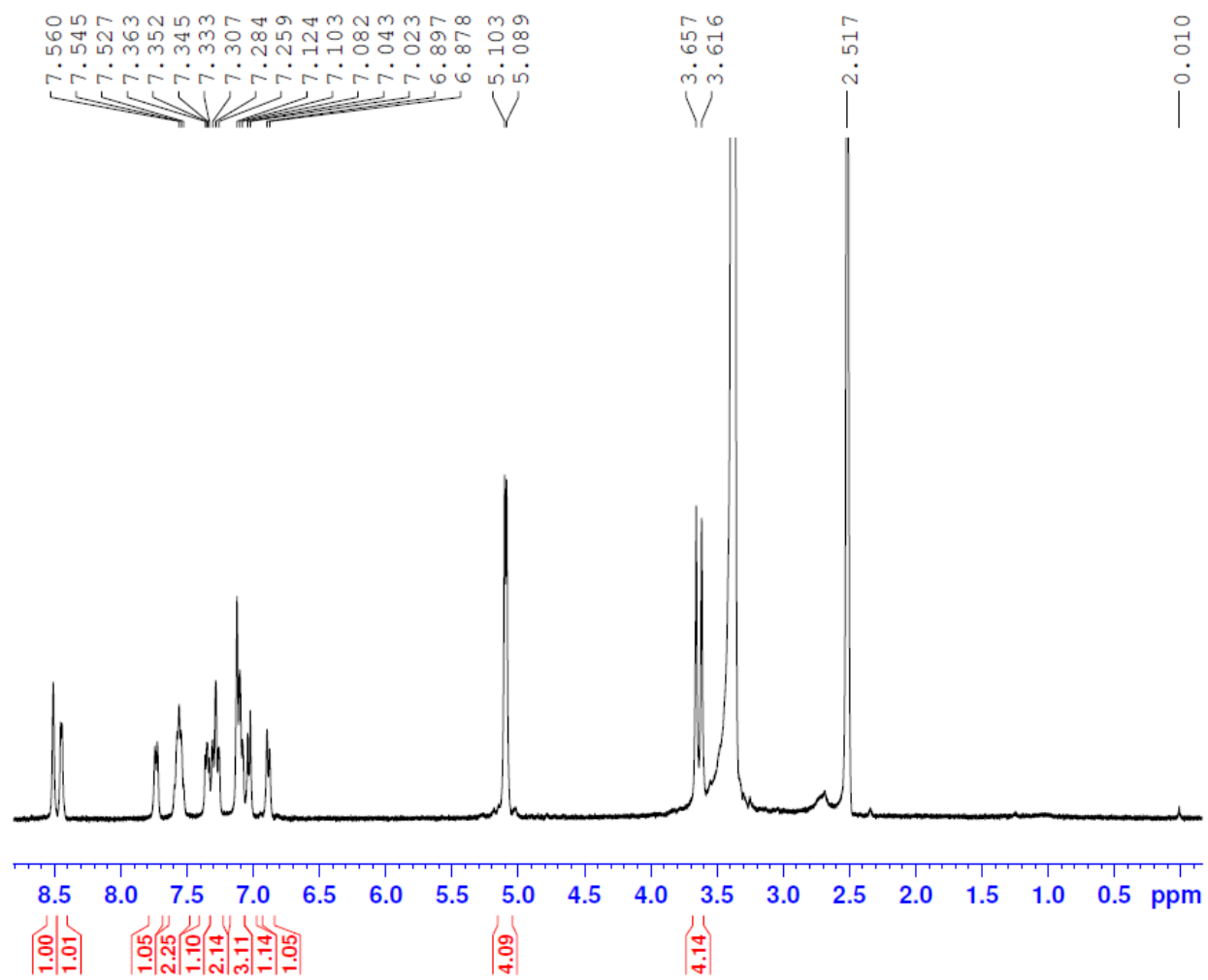
^{13}C-NMR

XIE5-2-10.2.fid
XIE5-2-10

161.34
159.70
159.62
149.32
148.11
147.98
147.83
146.74
136.10
135.73
135.63
134.30
131.86
123.33
121.07
120.60
114.94
114.77
111.55
111.41
103.97

64.24
64.03

51.75
49.35
39.99
39.87
39.73
39.59
39.45 TMS
39.45
39.31
39.17
39.03

16
2,29
4,32
23
20
9
12
27
18
30
17
6,26
11
19
28,35
22
10
3,31
7.25
15
13

70000
65000
60000
55000
50000
45000
40000
35000
30000
25000
20000
15000
10000
5000
0

180   170   160   150   140   130   120   110   100   90   80   70   60   50   40   30   20   10   0
f1 (ppm)
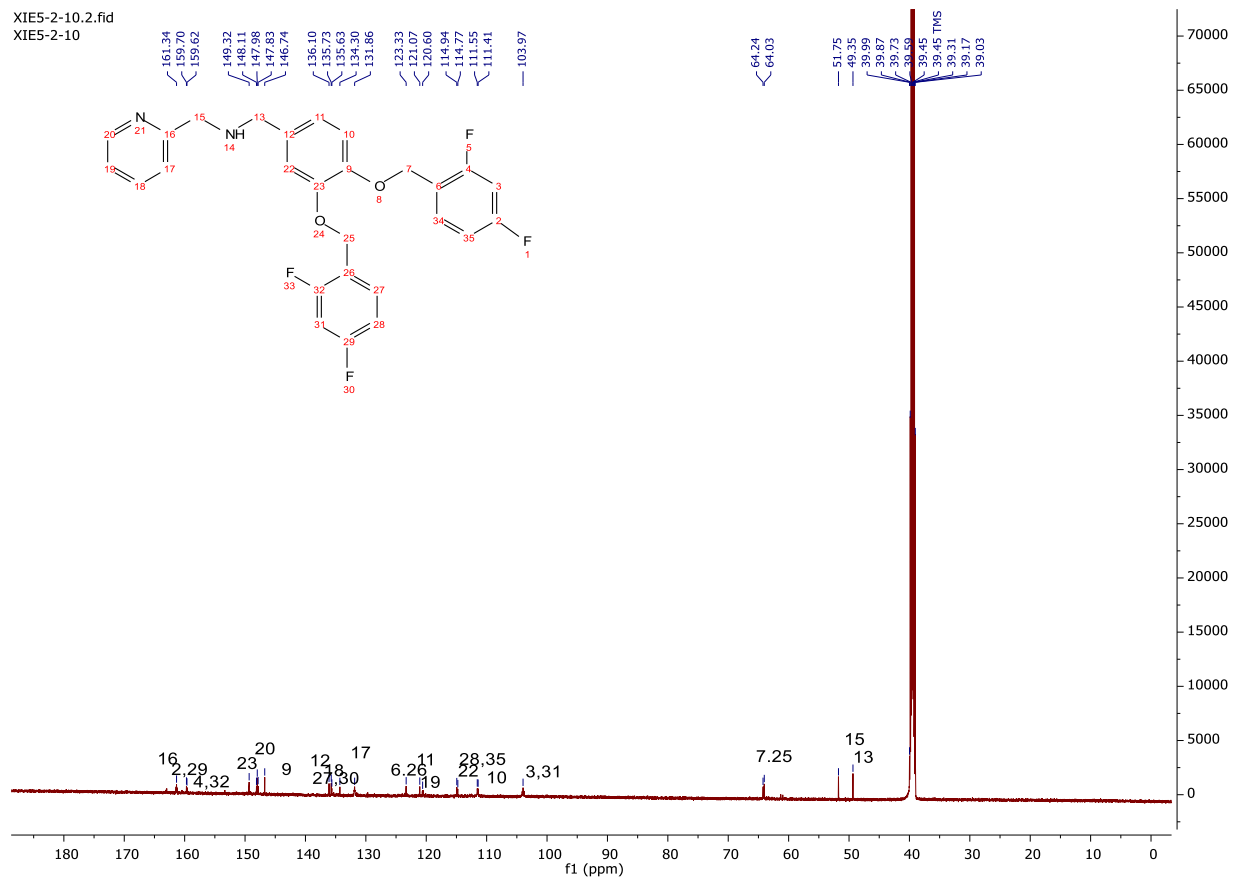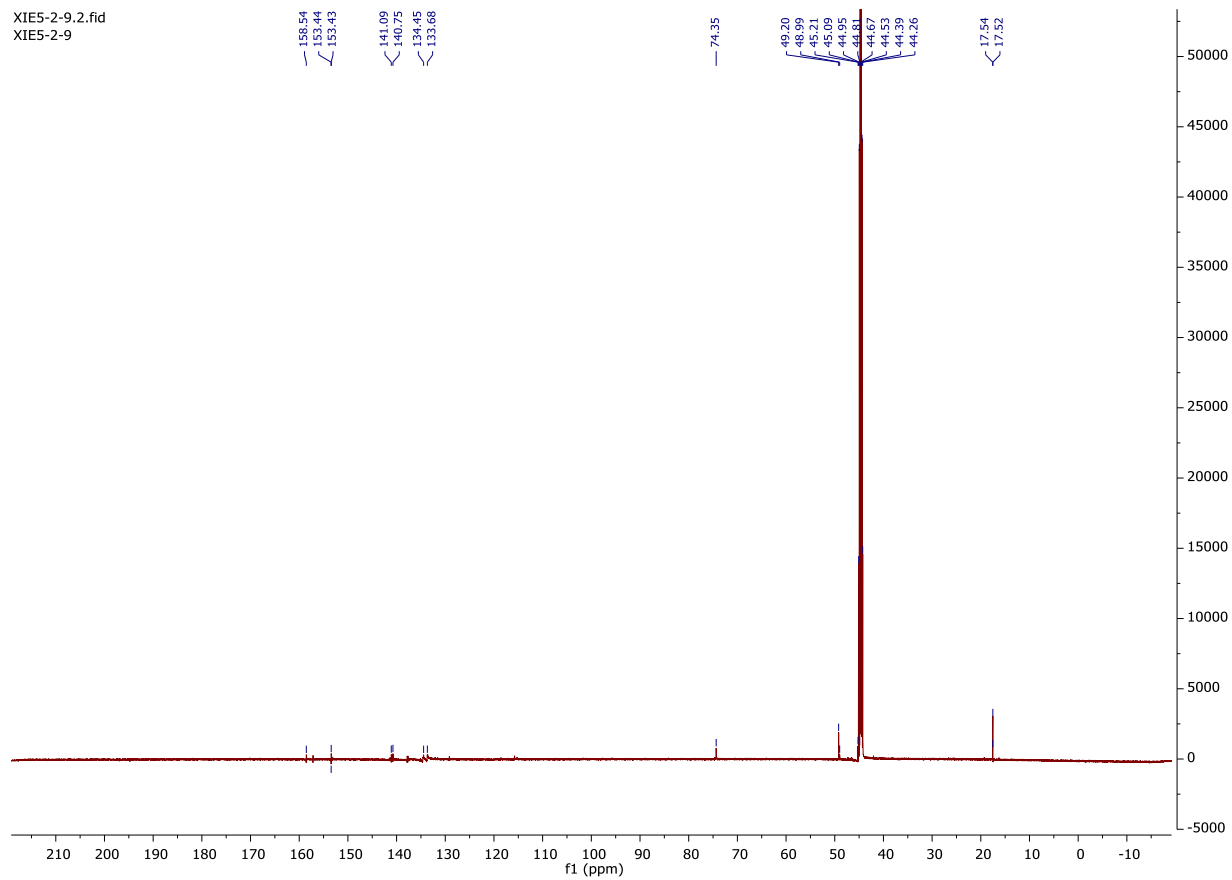
XIE5-2-11, N-(3,4-bis((2,4-difluorobenzyl)oxy)benzyl)-1-(3,4,5-trimethoxyphenyl)methanamine ^{1}H-NMR

XIE5-2-11-1

7.561
7.545
7.306
7.283
7.262
7.135
7.103
7.083
7.046
7.026
6.908
6.889
6.651

5.099
5.089

3.764
3.638
3.617
3.587
3.386

2.517

-0.049

8.0 7.5 7.0 6.5 6.0 5.5 5.0 4.5 4.0 3.5 3.0 2.5 2.0 1.5 1.0 0.5 ppm

2.16 2.10 3.99 1.06 1.99   4.00   6.10 7.01
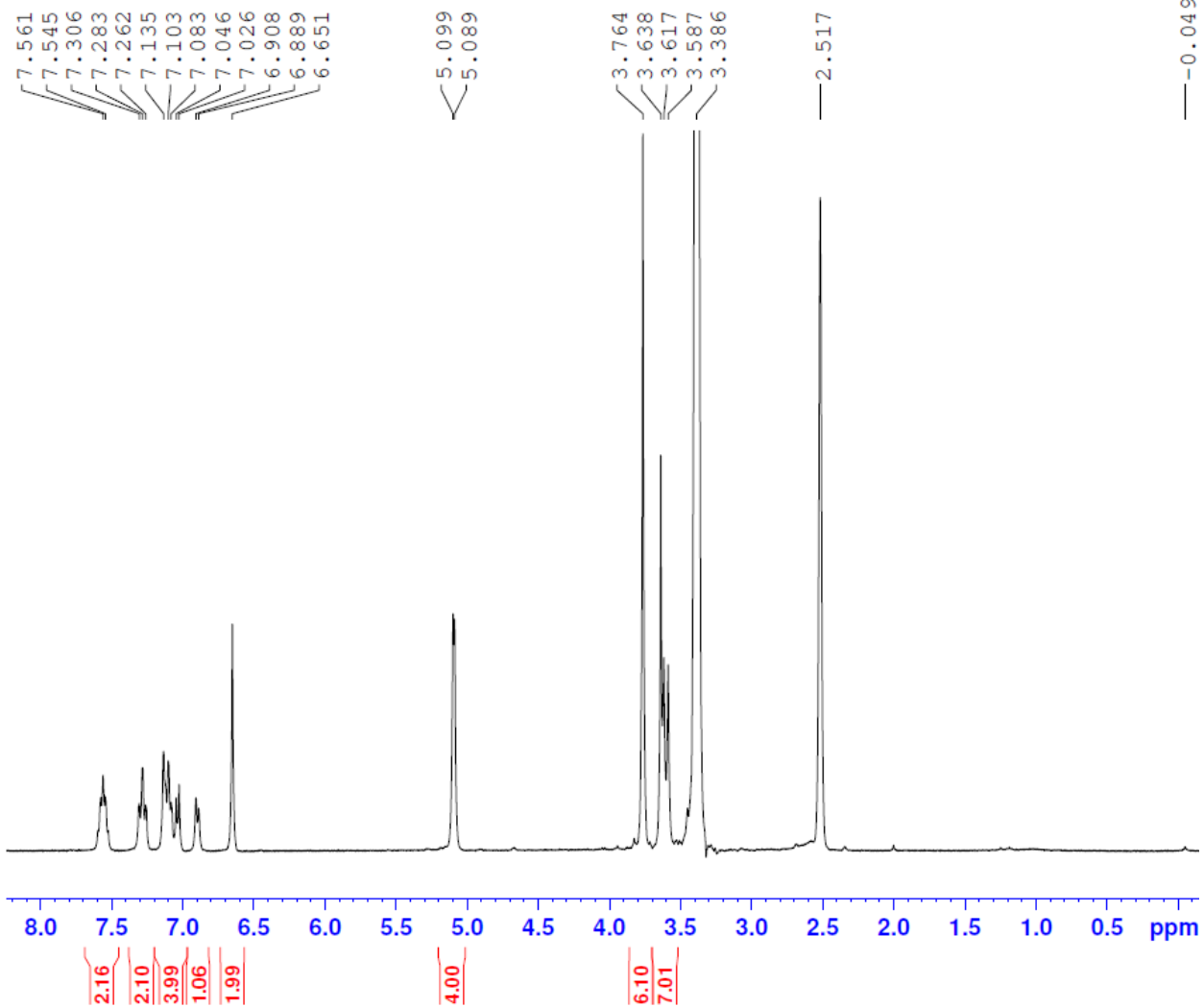
^{13}C-NMR

XIE5-2-13, N-(3,4-bis((2,4-difluorobenzyl)oxy)benzyl)-3-(1H-imidazol-1-yl)propan-1-amine
^{1}H-NMR

XIE5-2-13

7.523 7.314 7.289 7.265 7.132 7.103 7.035 7.014 6.885 6.871
5.100 5.088
4.132 4.119 4.029 4.012 3.995 3.610 3.361 3.190 3.177
2.422 2.406 2.391 1.850 1.834 1.816
0.013

3.01 2.07 3.88 1.07 1.99   4.00   0.58 2.04 2.09 1.38   2.05   2.10

^{13}C-NMR

XIE5-2-14, N-(3,4-bis((2,4-difluorobenzyl)oxy)benzyl)-1-(furan-2-yl)methanamine
^{1}H-NMR

XIE5-2-14

7.516 7.500 7.497 7.481 7.287 7.023 7.018 6.948 6.928 6.907 6.904 6.902 6.899 6.896 6.893 6.890 6.887 6.884 6.875 6.872 6.868 6.863 6.854 6.850 6.847 6.844 6.841 6.837 6.825 6.821 6.815 6.354 6.350 6.347 6.342 6.193 6.191 6.185 6.183 5.159 5.142 3.780 3.735 1.618 0.026

1.00 0.46 0.93 0.57 2.85 0.49 0.49 1.99 1.86 2.84

¹³C-NMR

XIE5-2-14.3.fid
XIE5-2-14

161.96
161.85
161.39
161.37
159.65
152.78
148.74
147.69
141.90
130.82
130.78
130.75
130.71
121.81
115.42
111.41
111.38
111.27
111.24
110.16
103.75
103.73
77.24
77.02
76.81
64.87
64.85
64.72
64.70
52.26
45.13
0.00
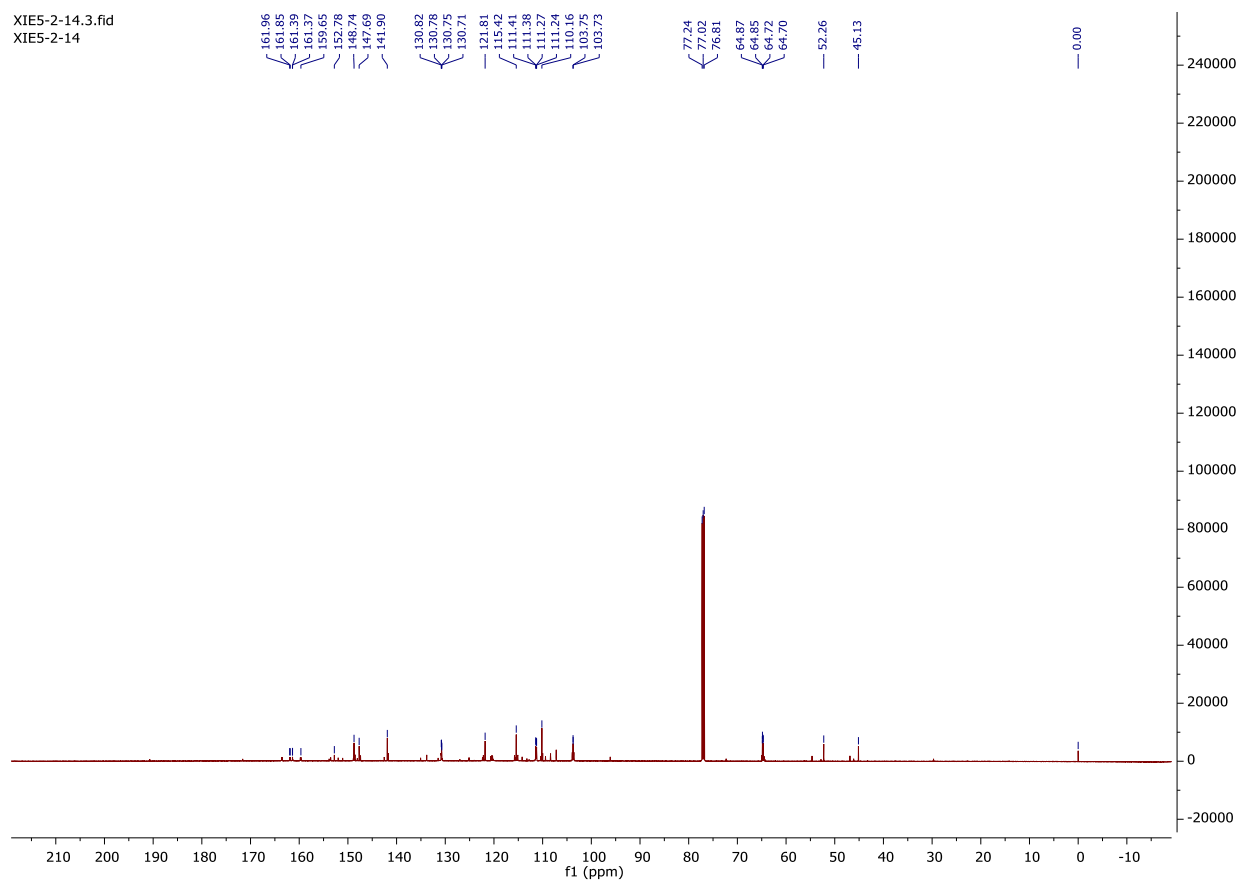
XIE5-2-15, N-(3,4-bis((2,4-difluorobenzyl)oxy)benzyl)-1-(3-methoxyphenyl)methanamine
^{1}H-NMR

XIE5-2-15

7.524
7.507
7.489
7.290
7.278
7.258
7.043
6.937
6.924
6.889
6.875
6.869
6.849
6.828

5.166
5.151

3.844
3.824
3.789
3.759

1.639

0.035

2.04 1.75 1.06 9.17   4.00   3.57 3.94   2.31

9.0 8.5 8.0 7.5 7.0 6.5 6.0 5.5 5.0 4.5 4.0 3.5 3.0 2.5 2.0 1.5 1.0 0.5 ppm

^{13}C-NMR

XIE5-2-15

161.96
161.93
161.88
161.45
161.40
161.37
159.78
159.75
159.71
159.67
148.75
147.60
141.92
134.50
130.84
130.80
130.79
129.41
121.62
120.43
115.44
115.29
113.67
112.42
111.41
111.39
111.28
111.25
103.76
103.74
77.28
77.07
76.86
64.90
64.88
64.71
64.69
55.19
53.07
53.02
52.67

160 150 140 130 120 110 100 90 80 70 60 50 40 30 20

XIE5-2-16, N-(3,4-bis((4-fluorobenzyl)oxy)benzyl)-1-(thiophen-2-yl)methanamine
^{1}H-NMR

7.257
7.253
7.244
7.241
7.085
7.081
7.063
7.059
7.041
7.037
7.014
7.010
6.992
6.984
6.980
6.971
6.927
6.924
6.918
6.898
6.880
6.875
5.127
5.102
3.978
3.976
3.767
1.608
0.027

3.89
3.27
5.97
3.17
4.00
2.17
2.25

^{13}C-NMR

XIE5-2-16

163.23
161.60
149.74
148.89
148.52
147.90
135.80
135.58
133.67
133.06
133.04
133.00
132.98
129.27
129.23
129.22
129.18
123.40
121.27
115.43
115.29
77.32
77.11
76.90
70.84
70.66
52.77
50.34

170 160 150 140 130 120 110 100 90 80 70 60 50 ppm
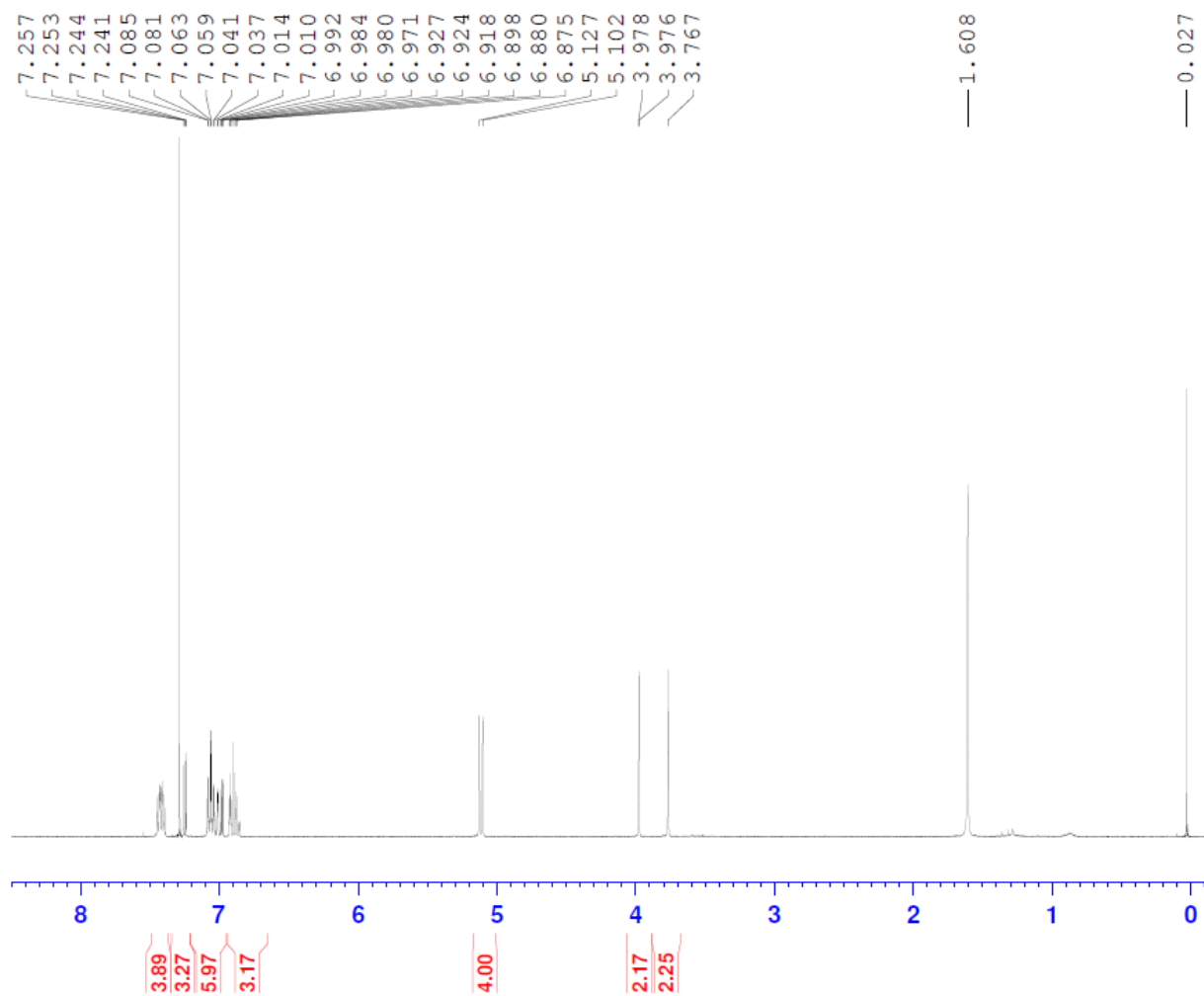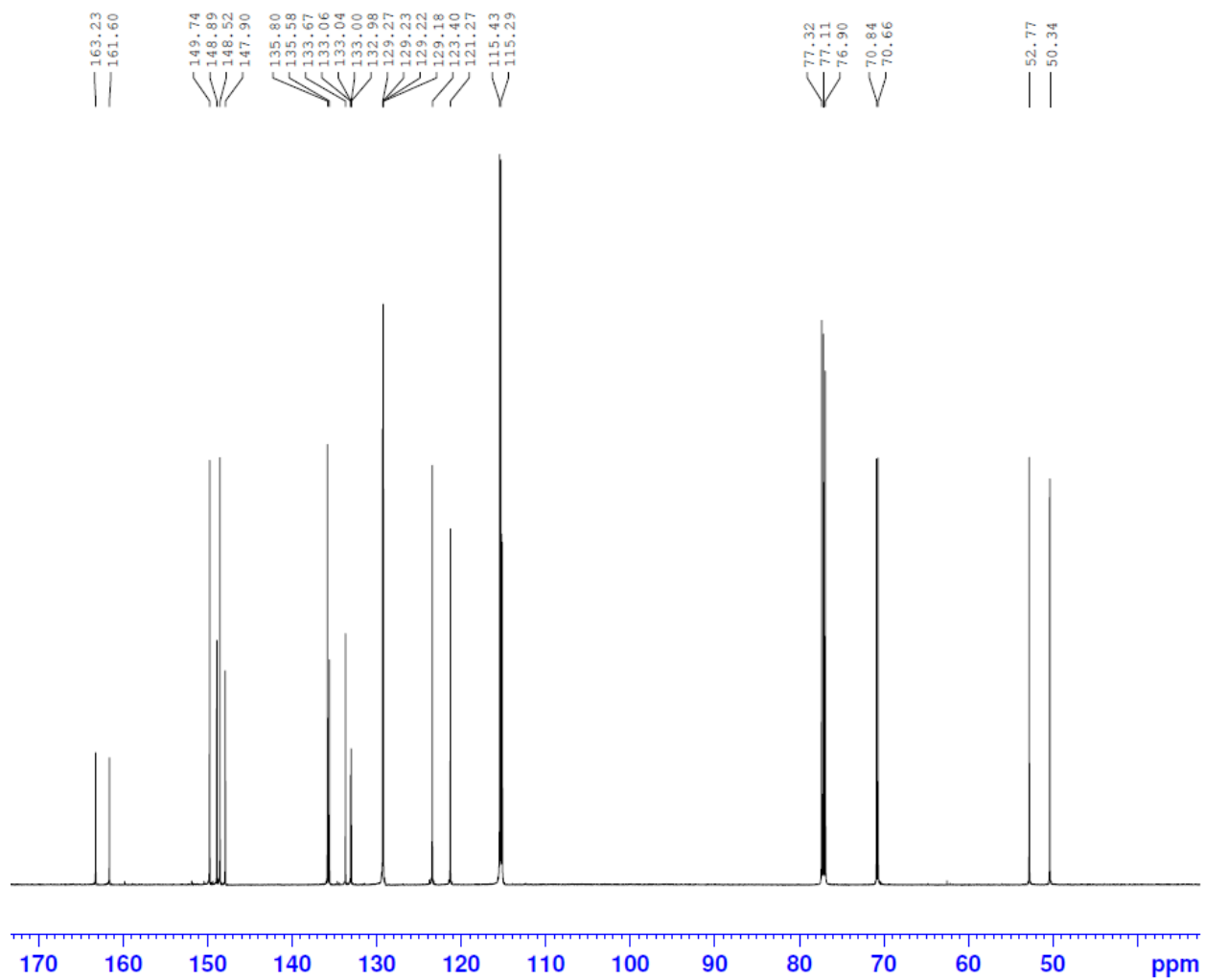
XIE5-2-17, N-(3,4-bis((4-fluorobenzyl)oxy)benzyl)-3-morpholinopropan-1-amine
^{1}H-NMR

358

XIE5-2-17

7.428
7.421
7.415
7.407
7.400
7.399
7.385
7.286
7.082
7.078
7.060
7.056
7.038
7.034
6.893
6.882
6.877
5.133
5.096
3.762
2.745
2.451
2.434
2.416
1.768
0.022

8.5 8.0 7.5 7.0 6.5 6.0 5.5 5.0 4.5 4.0 3.5 3.0 2.5 2.0 1.5 1.0 0.5 pp

4.00 0.77 4.96 2.02 4.05 2.21 4.01 3.45 6.31 2.14
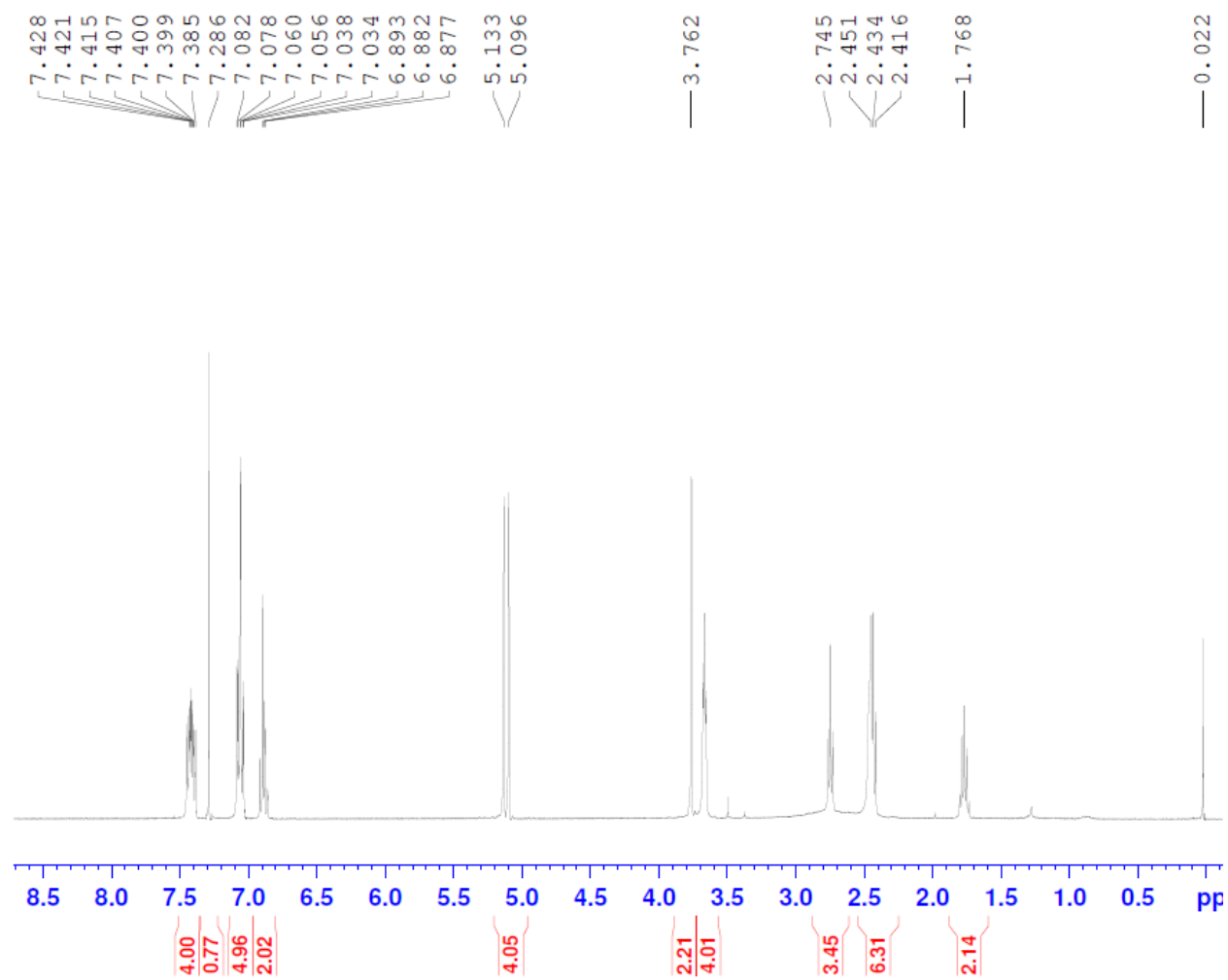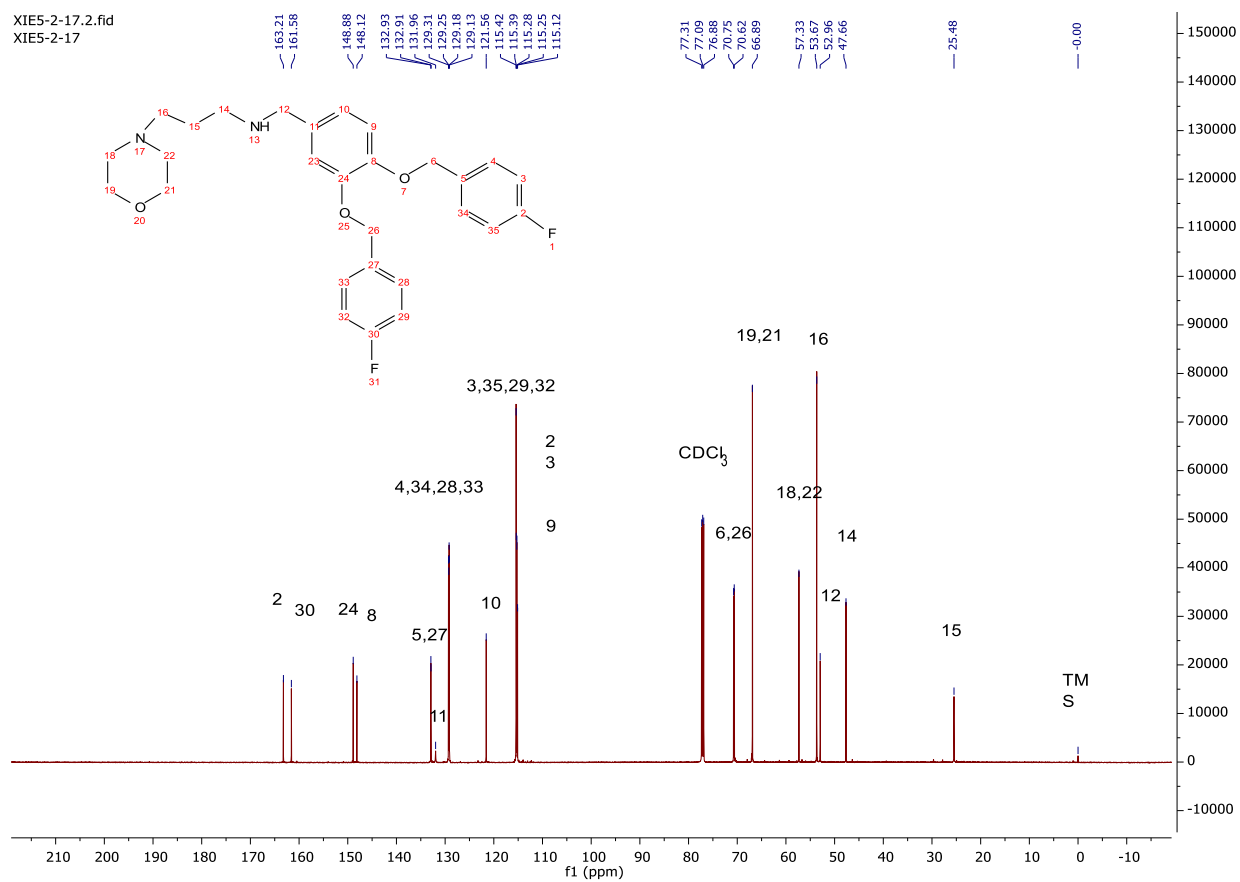
^{13}C-NMR

XIE5-2-18, N-(3,4-bis((4-fluorobenzyl)oxy)benzyl)-1-(360yridine-2-yl)methanamine
^{1}H-NMR

XIE5-2-18.1.fid
XIE5-2-18

8.55
8.51
8.50
7.65
7.63
7.41
7.39
7.38
7.37
7.26
7.25
7.25
7.24
7.04
7.03
7.03
7.01
6.97
6.89
6.88
6.85
6.83
5.09
5.07
3.76
3.71

0.90
0.96
1.13
4.74
1.28
4.28
1.50
2.27
4.22
1.83
1.90

f1 (ppm)
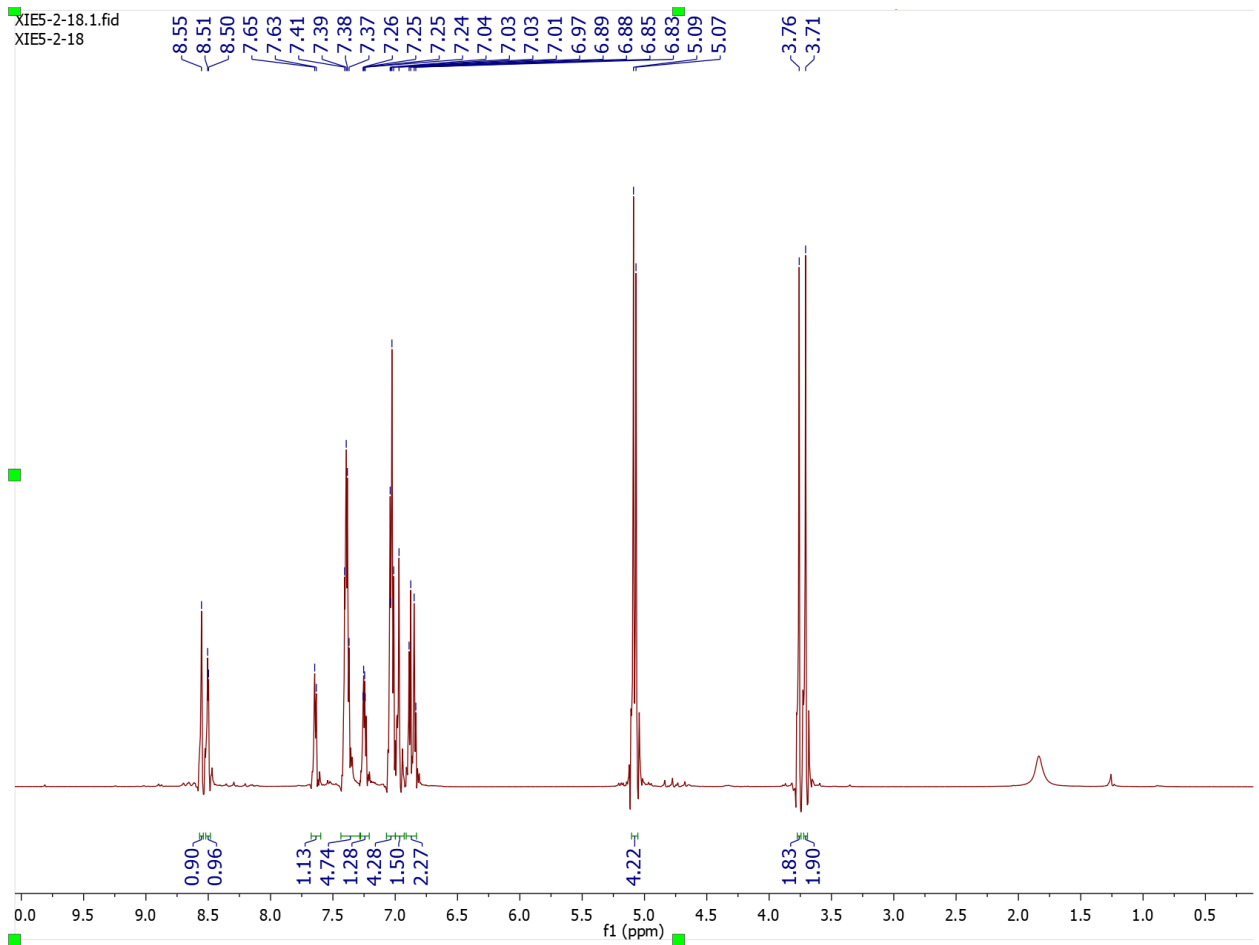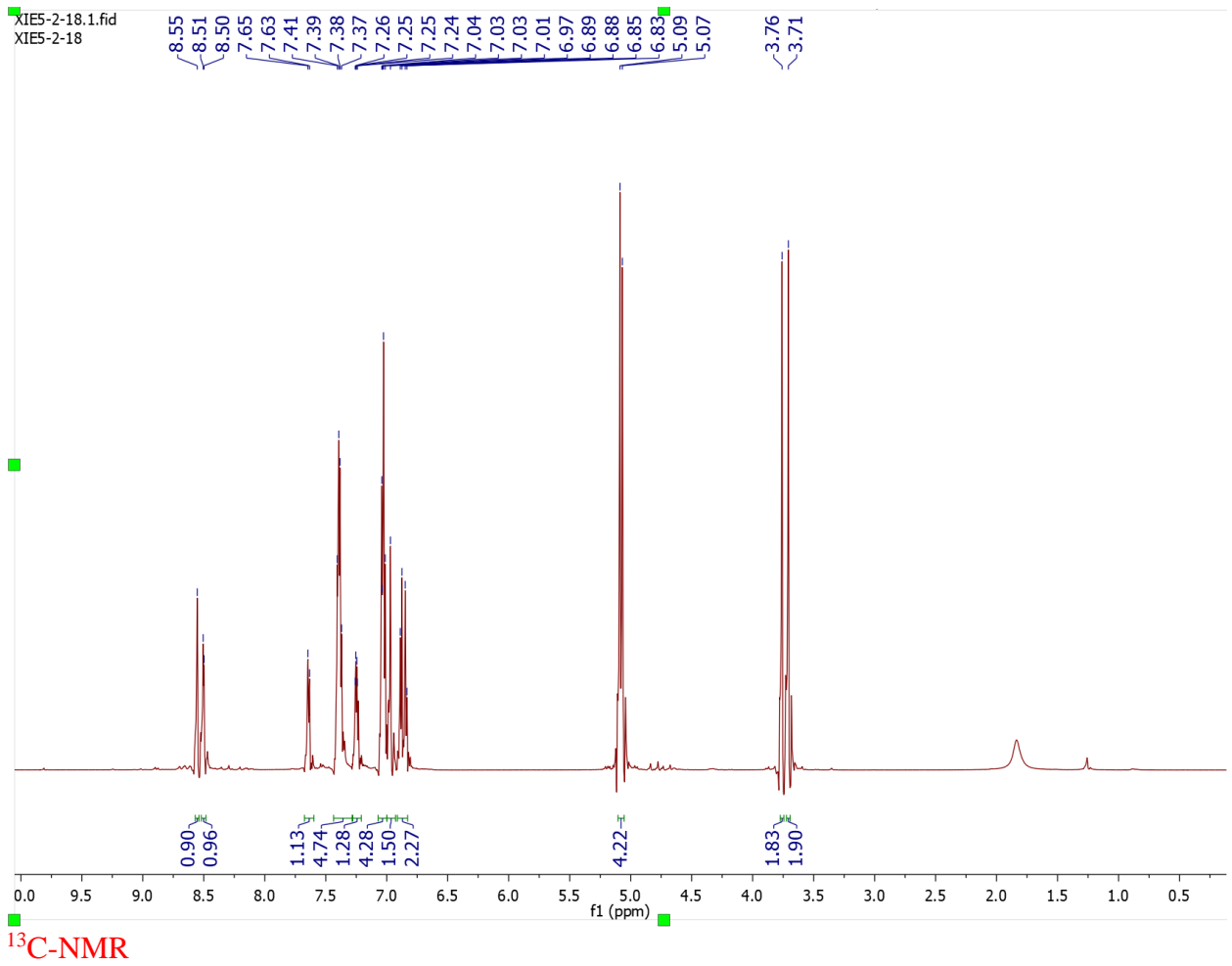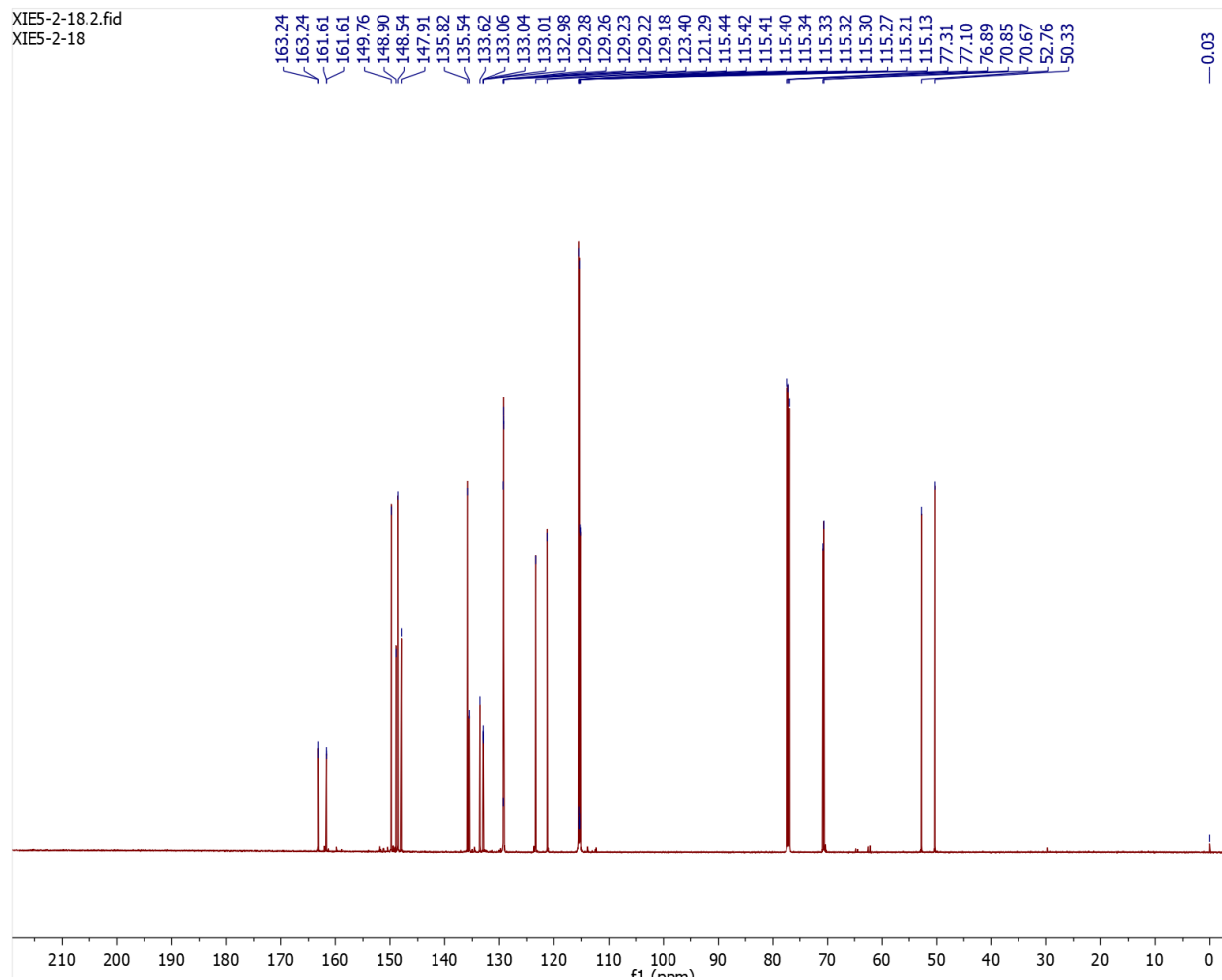
13C-NMR

XIE5-2-19, N-(3,4-bis((4-fluorobenzyl)oxy)benzyl)-1-(3,4,5-trimethoxyphenyl)methanamine
^{1}H-NMR

7.405
7.404
7.397
7.396
7.287
7.081
7.076
7.065
7.059
7.054
7.038
7.008
7.003
6.932
6.911
6.897
6.892
6.583
5.116
5.104

3.882
3.864
3.753
3.739

1.662

0.027

8.0 7.5 7.0 6.5 6.0 5.5 5.0 4.5 4.0 3.5 3.0 2.5 2.0 1.5 1.0 0.5 ppm

3.92 0.58 4.91 1.98 1.97 4.00 8.87 4.06

13C-NMR

XIE5-2-19

163.24
163.23
161.60
153.24
148.88
147.84
136.86
135.98
133.95
133.04
133.02
132.96
132.94
129.38
129.26
129.20
129.15
121.32
115.43
115.28
115.26
115.23
105.08
104.90
77.23
77.02
76.81
70.86
70.72
60.87
56.23
56.10
53.33
52.79
41.01
29.70
1.02
-0.00

180 160 140 120 100 80 60 40 20 0
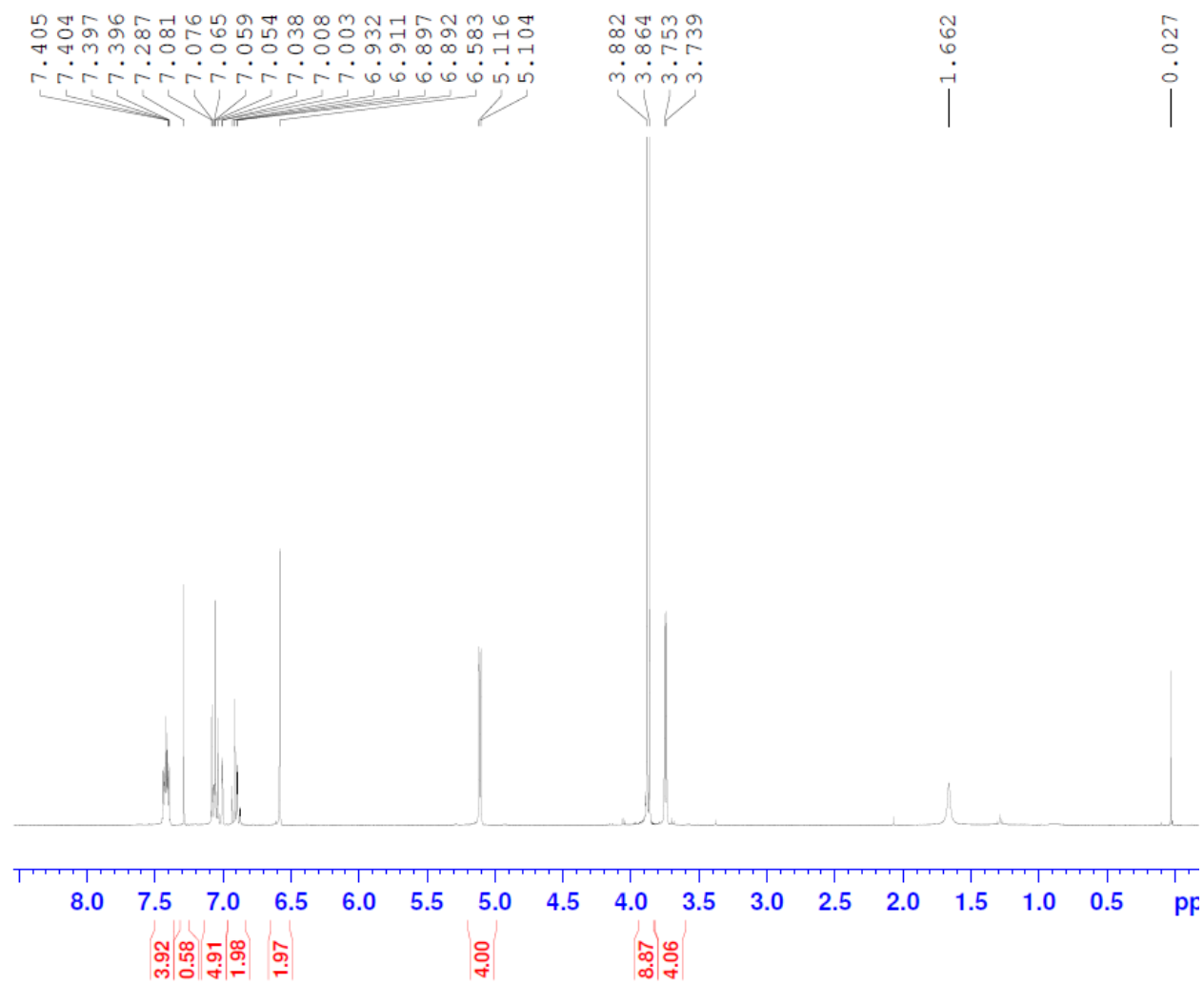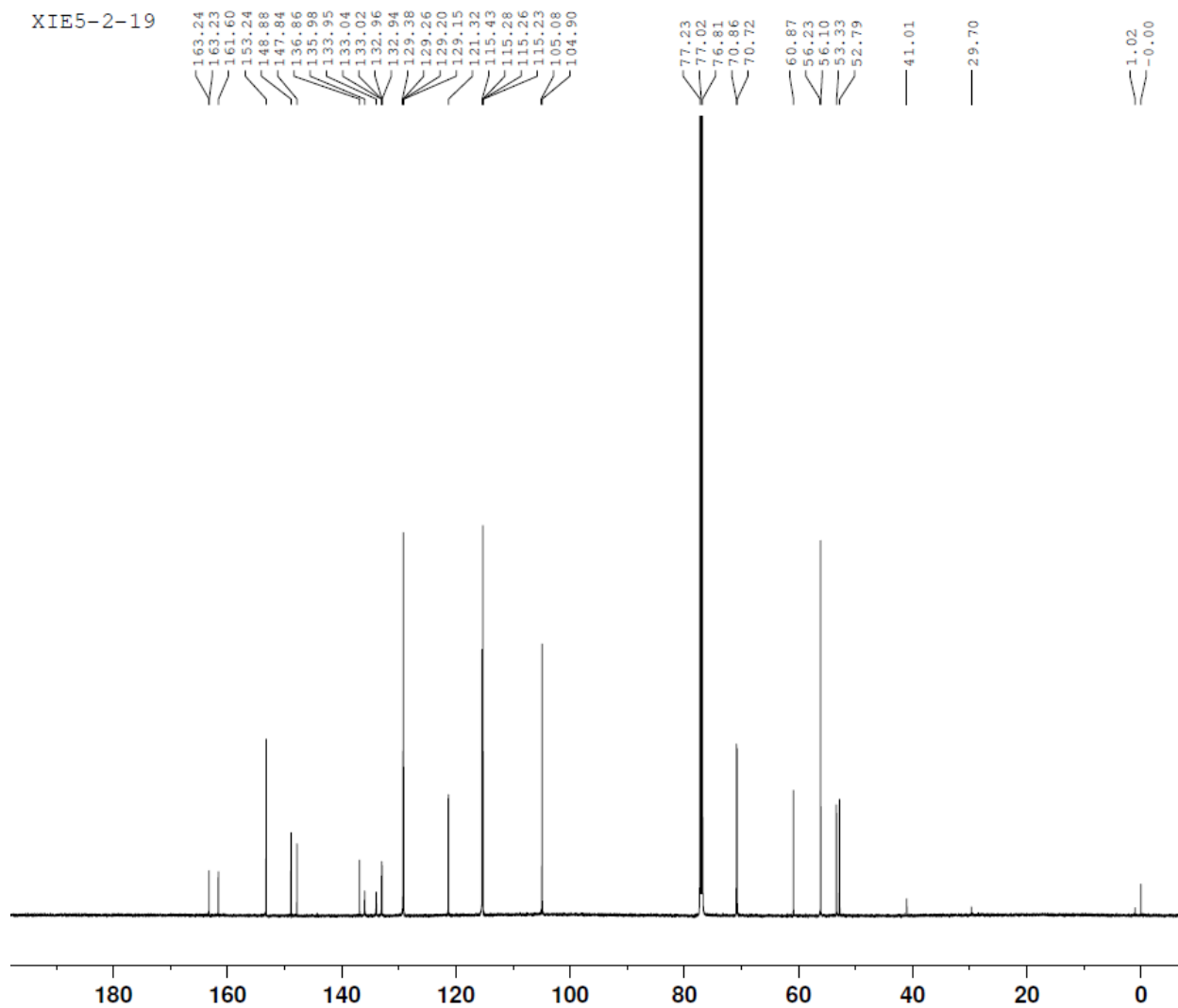
XIE5-2-20, 1-(benzo[d][1,3]dioxol-5-yl)-N-(3,4-bis((4-fluorobenzyl)oxy)benzyl)methanamine
^{1}H-NMR

XIE5-2-20

7.461
7.446
7.221
7.217
7.198
7.195
7.176
7.173
7.056
7.051
6.979
6.959
6.897
6.894
6.828
6.809
6.738
5.076
5.062
3.537
3.521
3.359
2.499
-0.005

8.0 7.5 7.0 6.5 6.0 5.5 5.0 4.5 4.0 3.5 3.0 2.5 2.0 1.5 1.0 0.5 ppm

4.07
4.21
1.11
1.16
1.05
2.02
1.09
2.12
4.05
4.14

^{13}C-NMR

XIE5-2-21, N-(3,4-bis((4-fluorobenzyl)oxy)benzyl)-3-(1H-imidazol-1-yl)propan-1-amine
^{1}H-NMR

XIE5-2-21

7.437
7.429
7.423
7.415
7.407
7.401
7.394
7.287
7.080
7.075
7.070
7.058
7.054
7.037
7.032
6.949
6.945
6.914
6.901
6.898
6.894
6.853
6.849
5.120
5.098
4.053
4.036
4.019
3.684
2.601
2.584
2.568
1.952
1.935
1.918
0.024

9.0 8.5 8.0 7.5 7.0 6.5 6.0 5.5 5.0 4.5 4.0 3.5 3.0 2.5 2.0 1.5 1.0 0.5 ppm

4.93 0.47 4.96 3.96   4.00   2.06   2.04   2.07   2.34

^{13}C-NMR

163.21
161.58
148.80
148.00
137.19
133.14
132.96
129.36
129.25
129.21
129.20
129.15
129.10
121.39
118.87
115.52
115.42
115.41
115.32
115.28
115.26
115.14
77.29
77.08
76.87
70.79
70.66
57.40
53.35
45.43
44.58
31.03
29.69
-0.00

190 180 170 160 150 140 130 120 110 100 90 80 70 60 50 40 30 20 ppm

XIE5-2-22, N-(3,4-bis((2,4-difluorobenzyl)oxy)benzyl)-4-fluoroaniline
¹H-NMR

XIE5-2-22

9.877
7.503
7.499
7.482
7.476
7.471
7.455
7.286
7.014
7.012
6.947
6.946
6.942
6.919
6.898
6.897
6.896
6.892
6.884
6.875
6.866
6.853
6.828
6.575
6.564
6.552
6.542
5.145
5.142
5.139
4.223
1.590
0.025

10   9   8   7   6   5   4   3   2   1   ppm

2.26
2.75
9.28
2.51
4.00
2.36
5.84
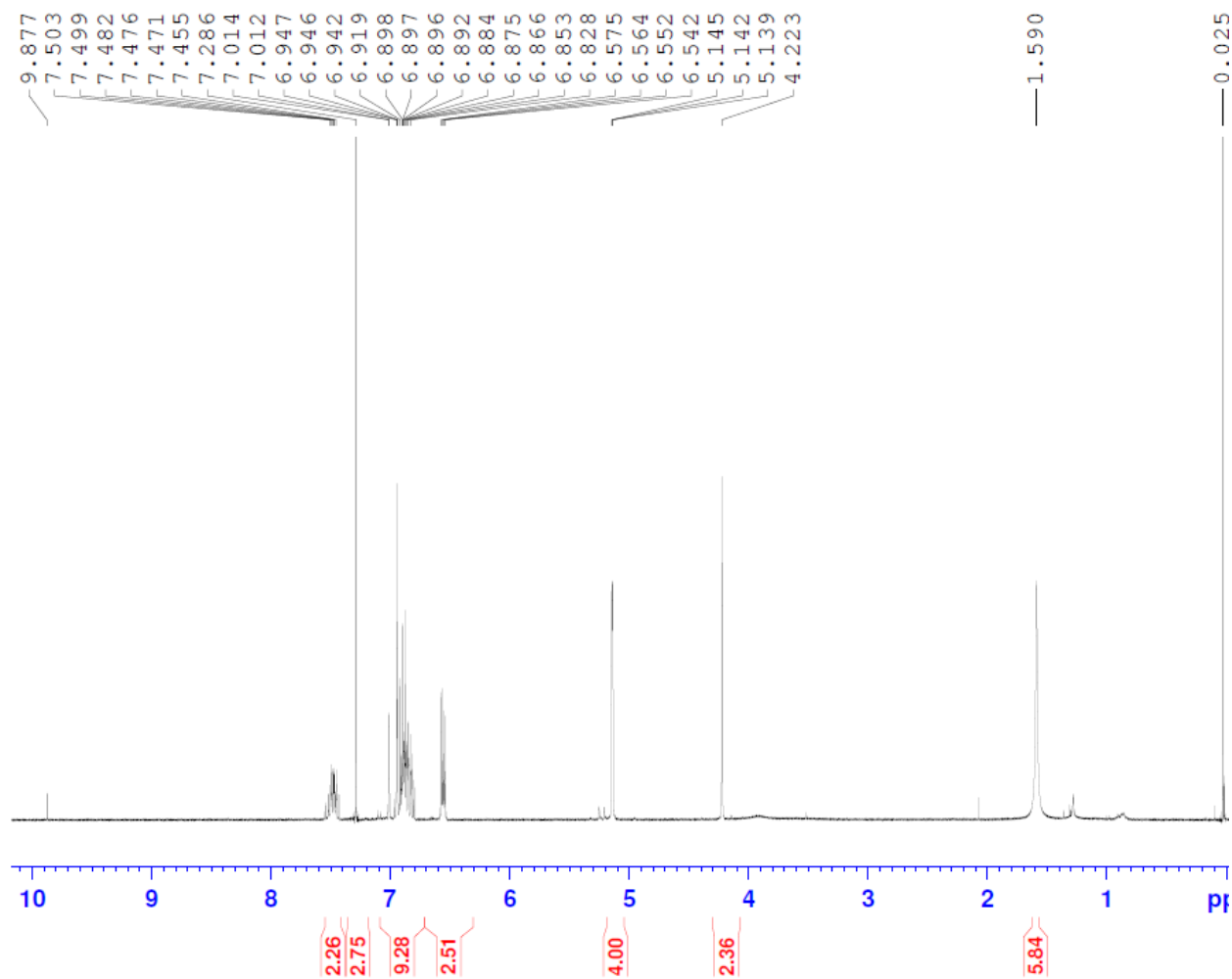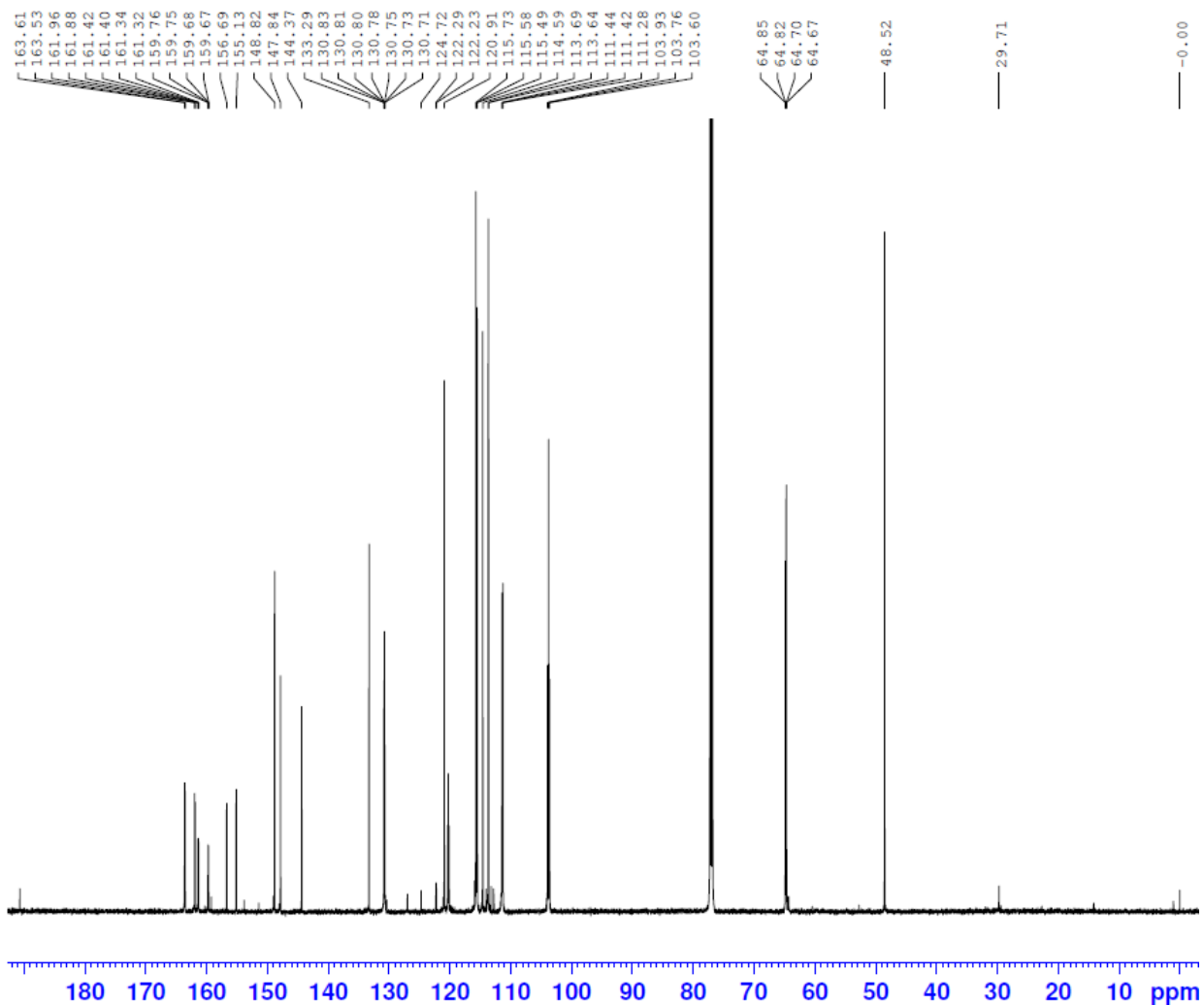
^{13}C-NMR

XIE5-2-31, N-(3,4-bis((4-chlorobenzyl)oxy)benzyl)-1-(furan-2-yl)methanamine
^{1}H-NMR

XIE5-2-31

7.370
7.364
7.359
7.343
7.291
6.989
6.902
6.881
6.872
6.852
6.350
6.181
6.174

5.131
5.110

3.770
3.720

1.722
1.492
1.475
1.457
1.288

0.032

8.68 0.75 1.01 2.01 0.98 0.94 4.00 3.77 2.29

^{13}C-NMR

372

XIE5-2-32, N-(3,4-bis((4-chlorobenzyl)oxy)benzyl)-1-(3-methoxyphenyl)methanamine
^{1}H-NMR

7.383
7.362
7.349
7.335
7.315
7.290
7.268
7.247
7.228
6.974
6.894
6.861
6.816
6.797

5.103
5.088

3.813
3.747
3.711

2.013
1.971
1.952
1.925

0.005

8.5 8.0 7.5 7.0 6.5 6.0 5.5 5.0 4.5 4.0 3.5 3.0 2.5 2.0 1.5 1.0 0.5 p

9.95
1.10
4.78

4.00

2.94
3.94

4.35

0.75

^{13}C-NMR

158.70 147.66 146.56 140.77 134.78 134.71 132.96 132.53 132.51 128.38 127.68 127.63 127.60 120.27 119.39 114.02 113.95 112.69 111.31 76.29 76.08 75.87 69.63 69.39 54.16 51.91 51.59 39.12 38.98 38.84 28.66 −0.00

XIE5-2-33, N-(3,4-bis((4-chlorobenzyl)oxy)benzyl)-1-(thiophen-2-yl)methanamine
^{1}H-NMR

XIE5-2-33-1

7.411
7.390
7.373
7.364
7.344
7.291
7.258
7.248
7.001
6.988
6.975
6.925
6.914
6.883
6.877
5.140
5.127
5.115
4.617
3.975
3.764
1.637
1.288
0.032

10.24
1.91
2.97
4.00
1.77
2.01
4.90
4.15
1.61

9.0 8.5 8.0 7.5 7.0 6.5 6.0 5.5 5.0 4.5 4.0 3.5 3.0 2.5 2.0 1.5 1.0 0.5 ppm
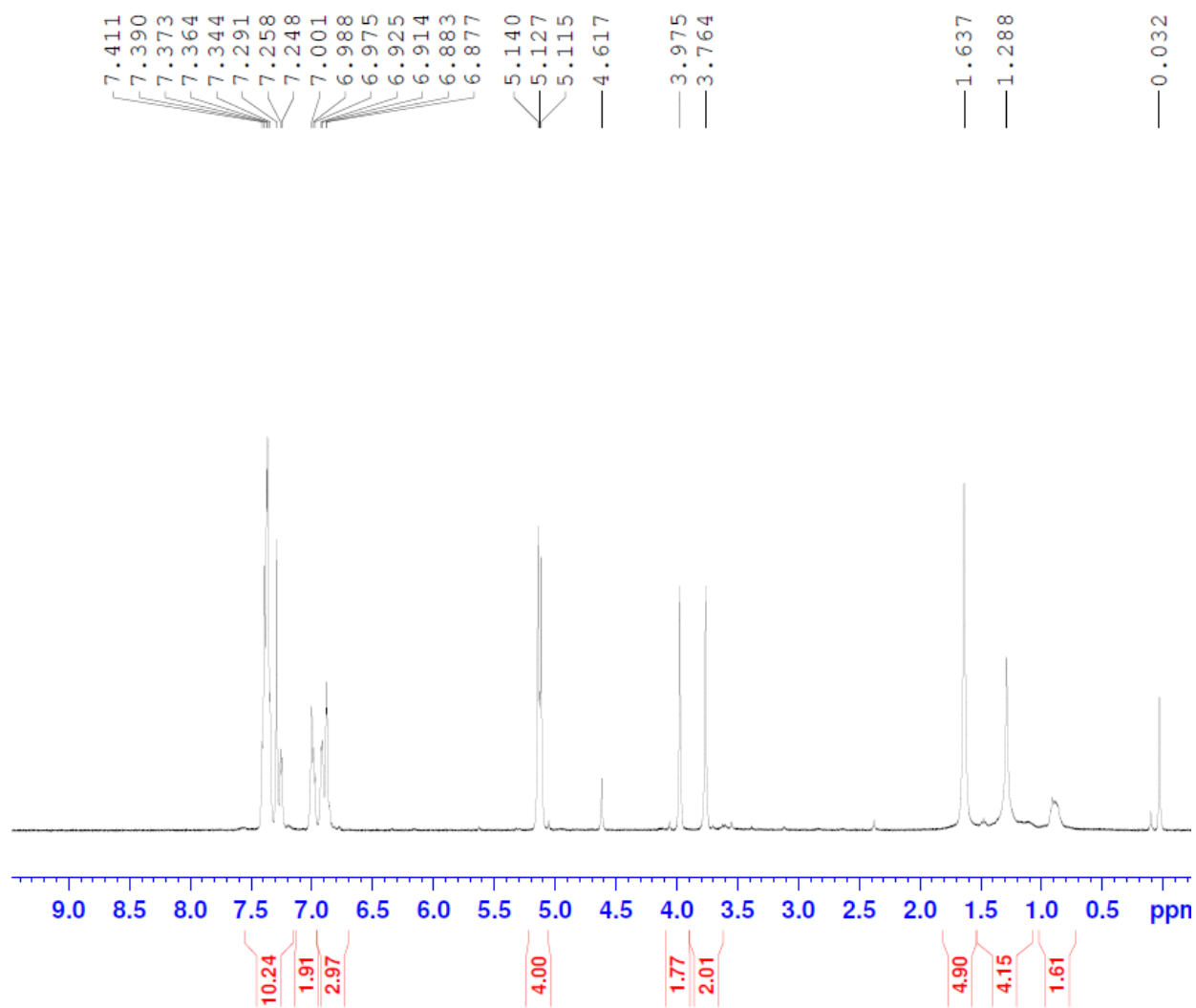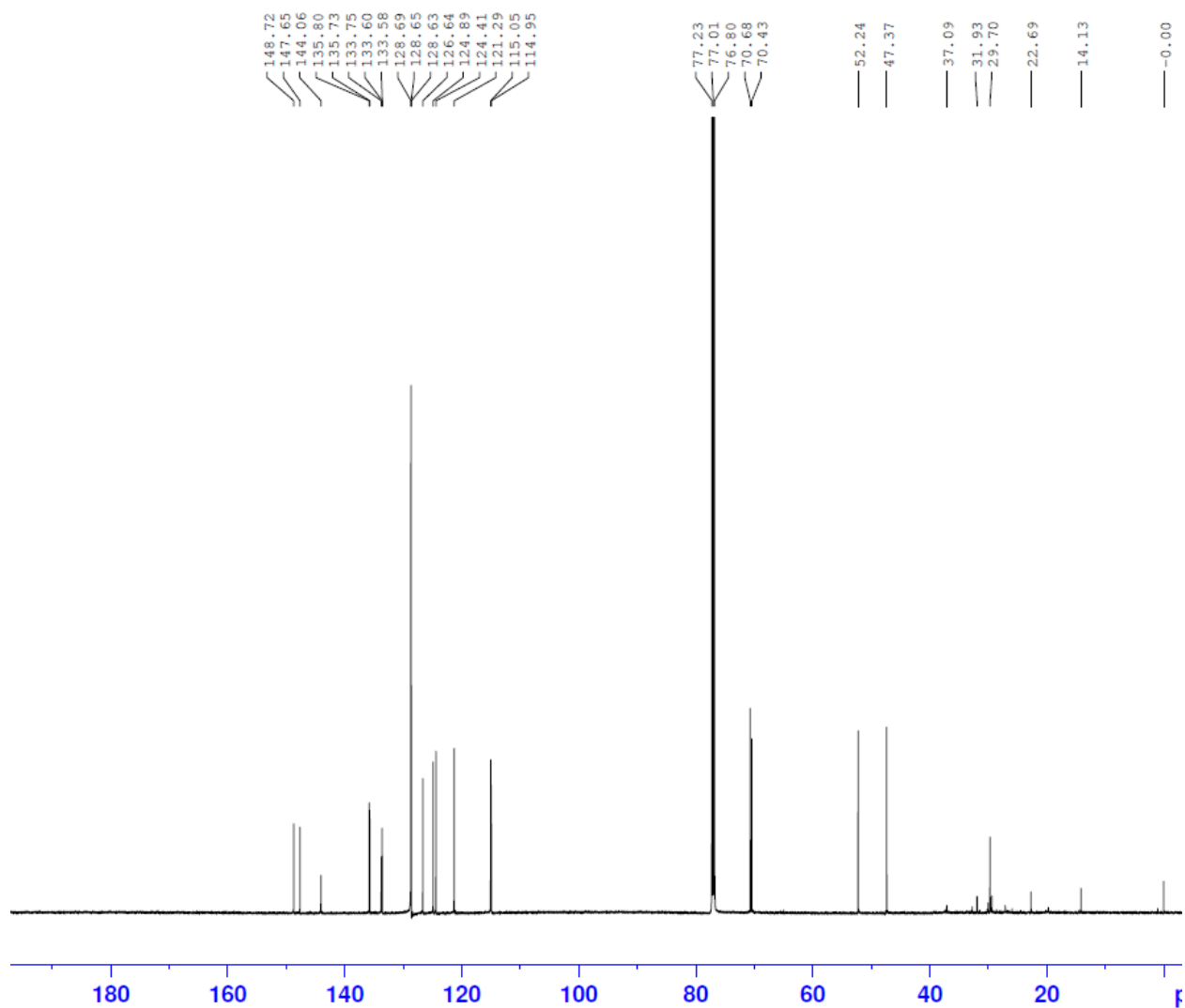
^{13}C-NMR

XIE5-2-35, N-(3,4-bis((4-chlorobenzyl)oxy)benzyl)-1-(377yridine-2-yl)methanamine
^{1}H-NMR

XIE5-1-35

8.582
7.678
7.660
7.405
7.385
7.375
7.362
7.341
7.290
7.272
6.976
6.909
6.888
6.877
6.856

5.134
5.117

3.792
3.738

1.632
1.287

0.030

8.5 8.0 7.5 7.0 6.5 6.0 5.5 5.0 4.5 4.0 3.5 3.0 2.5 2.0 1.5 1.0 0.5 ppm

1.99   1.06 0.39 3.08   4.00   4.11   5.95

^{13}C-NMR

378
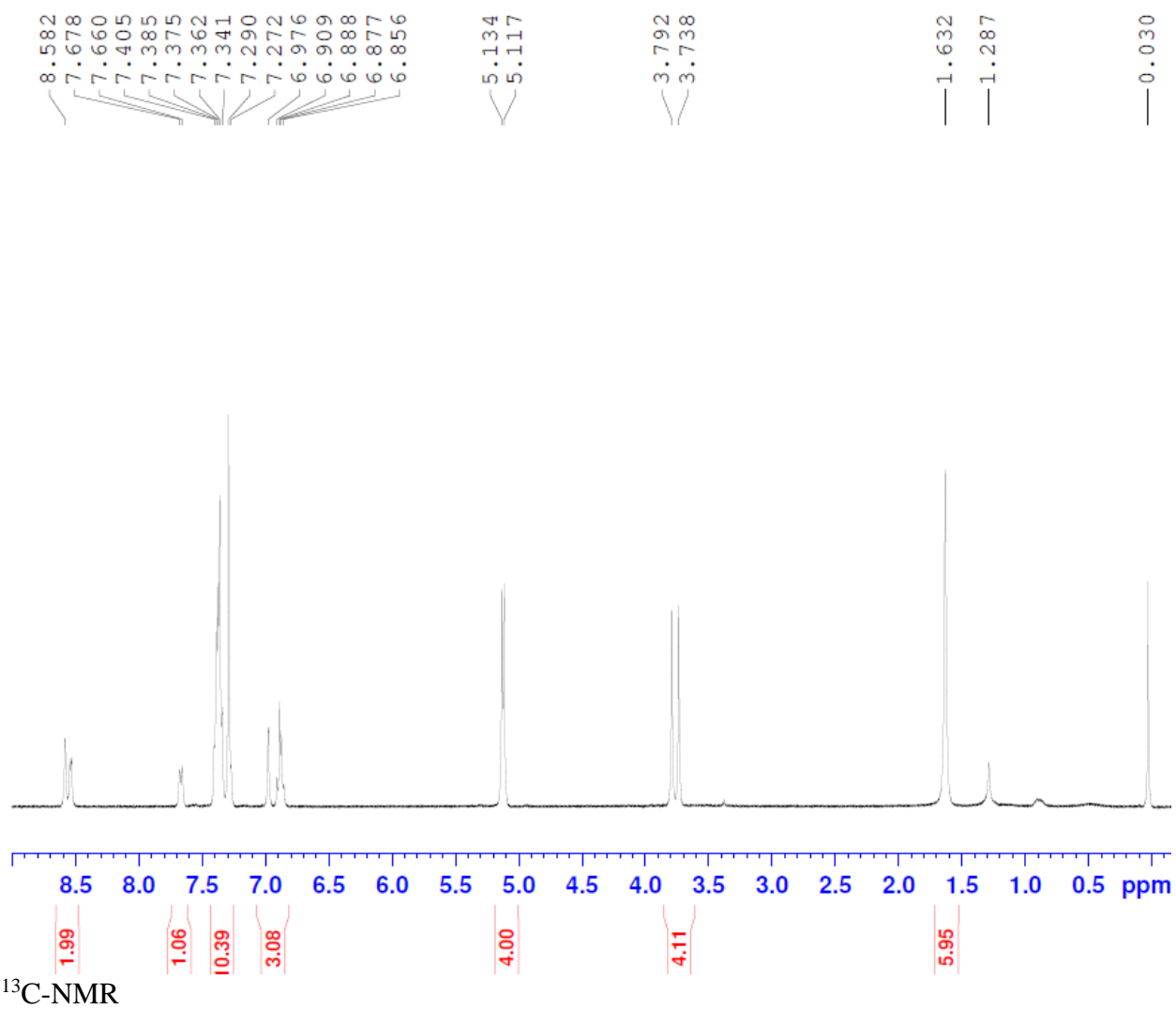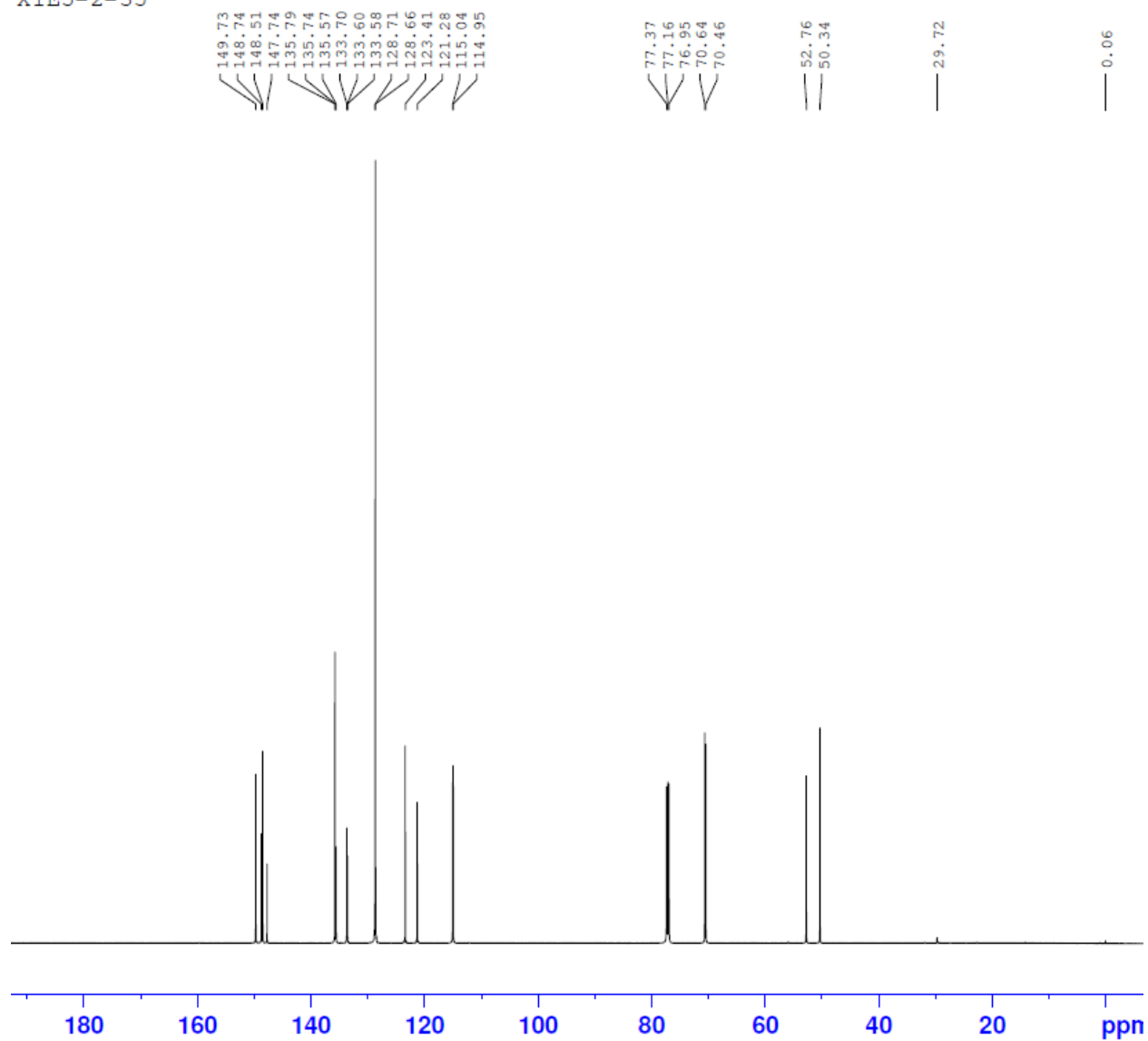
XIE5-2-36, N-(3,4-bis((4-chlorobenzyl)oxy)benzyl)-1-(3,4,5-trimethoxyphenyl)methanamine
^{1}H-NMR

7.379
7.373
7.360
7.338
7.291
6.993
6.896
6.582

5.126
5.116

3.885
3.867
3.750
3.740

1.607
1.286

0.910
0.894

0.031

8.5 8.0 7.5 7.0 6.5 6.0 5.5 5.0 4.5 4.0 3.5 3.0 2.5 2.0 1.5 1.0 0.5

9.21 1.07 1.97 2.06   4.00   8.81 4.08   4.78 2.03 0.89

^{13}C-NMR

XIE5-2-36

152.18
147.69
146.63
135.80
135.00
134.75
134.66
133.01
132.57
132.54
127.64
127.60
120.28
114.03
114.02
103.85
76.26
76.05
75.84
69.61
69.48
59.82
55.05
52.33
51.75
28.66
-0.00

180 160 140 120 100 80 60 40 20
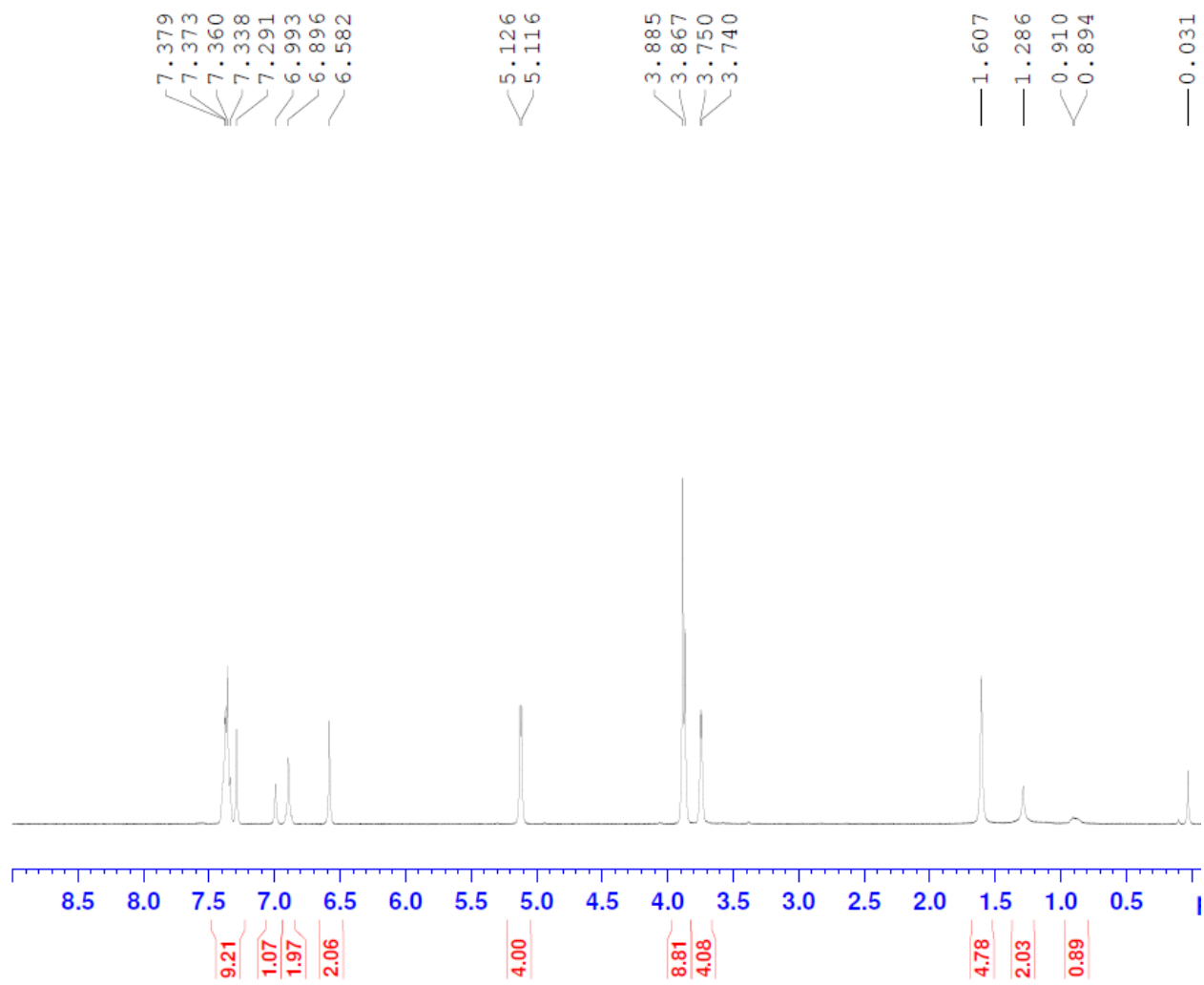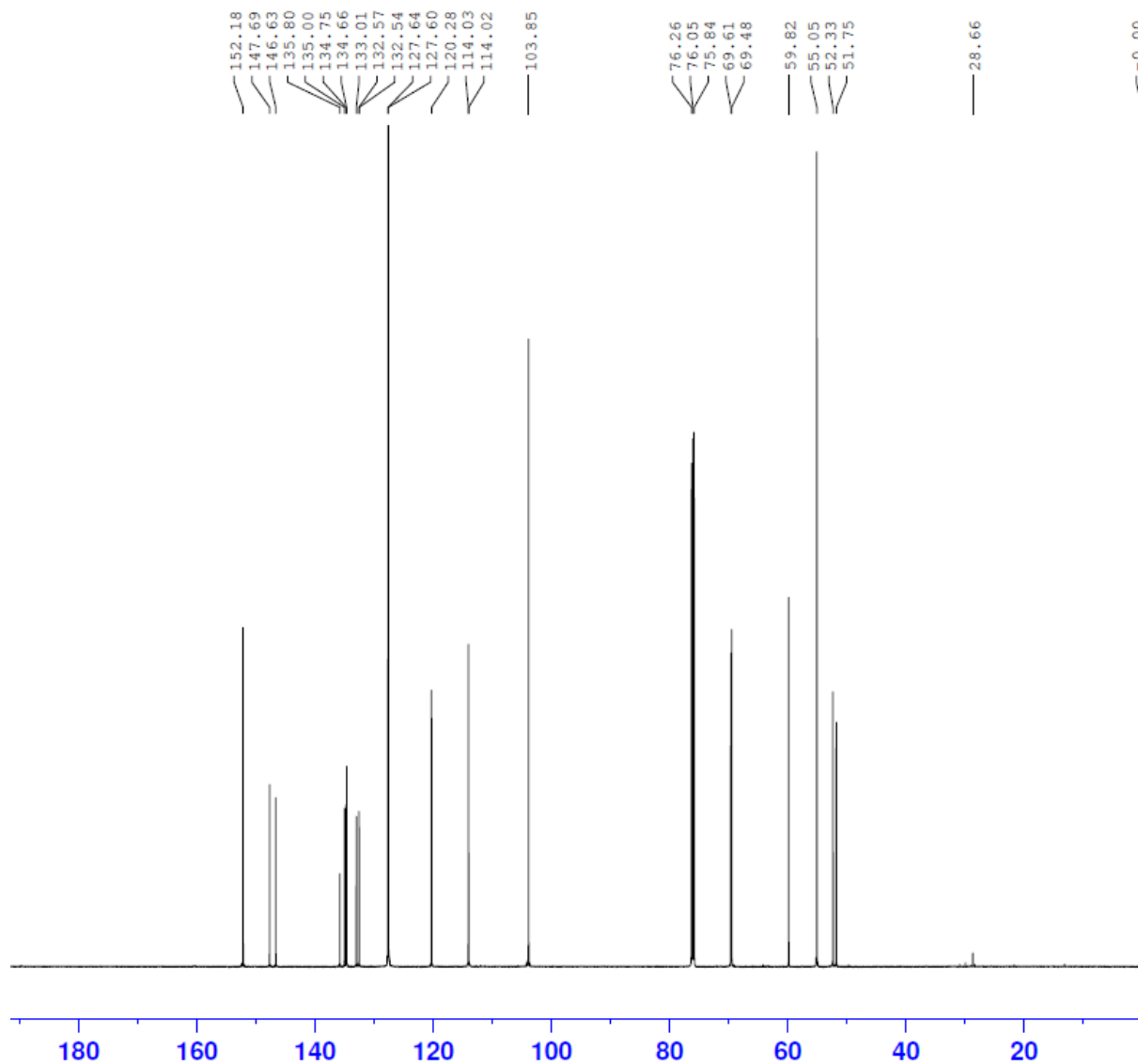
XIE5-2-37, 1-(benzo[d][1,3]dioxol-5-yl)-N-(3,4-bis((benzyloxy)benzyl)methanamine
^{1}H-NMR

XIE5-1-37

7.526
7.509
7.492
7.299
7.290
7.279
7.259
7.047
7.044
6.960
6.940
6.928
6.890
6.876
6.870
6.862
6.851
6.829
6.823
5.167
5.152
3.845
3.791
3.761
1.660
1.294
0.037

8.5 8.0 7.5 7.0 6.5 6.0 5.5 5.0 4.5 4.0 3.5 3.0 2.5 2.0 1.5 1.0 0.5 ppr

1.99 1.55 1.11 9.14 4.00 3.25 3.75 2.05 0.44
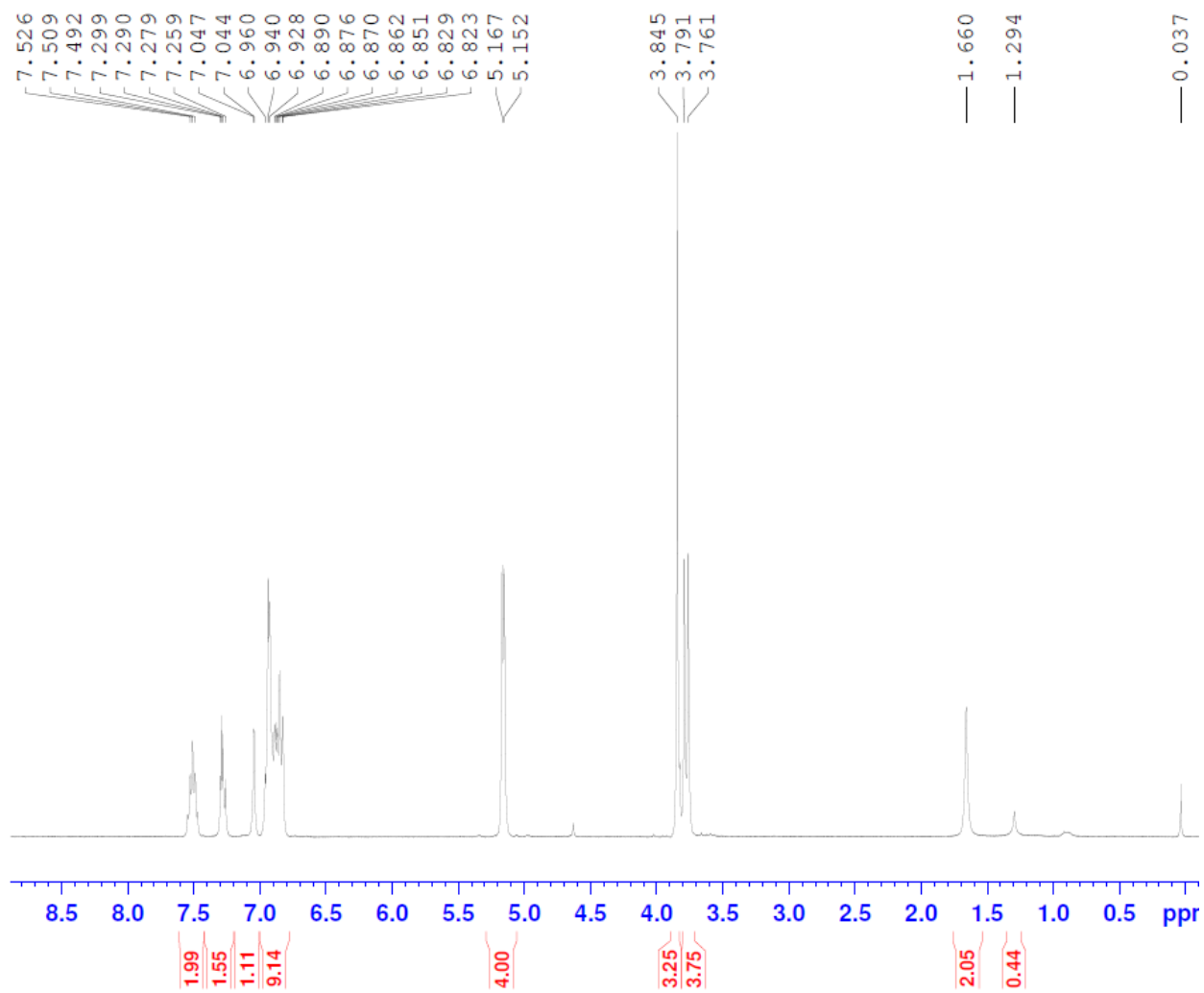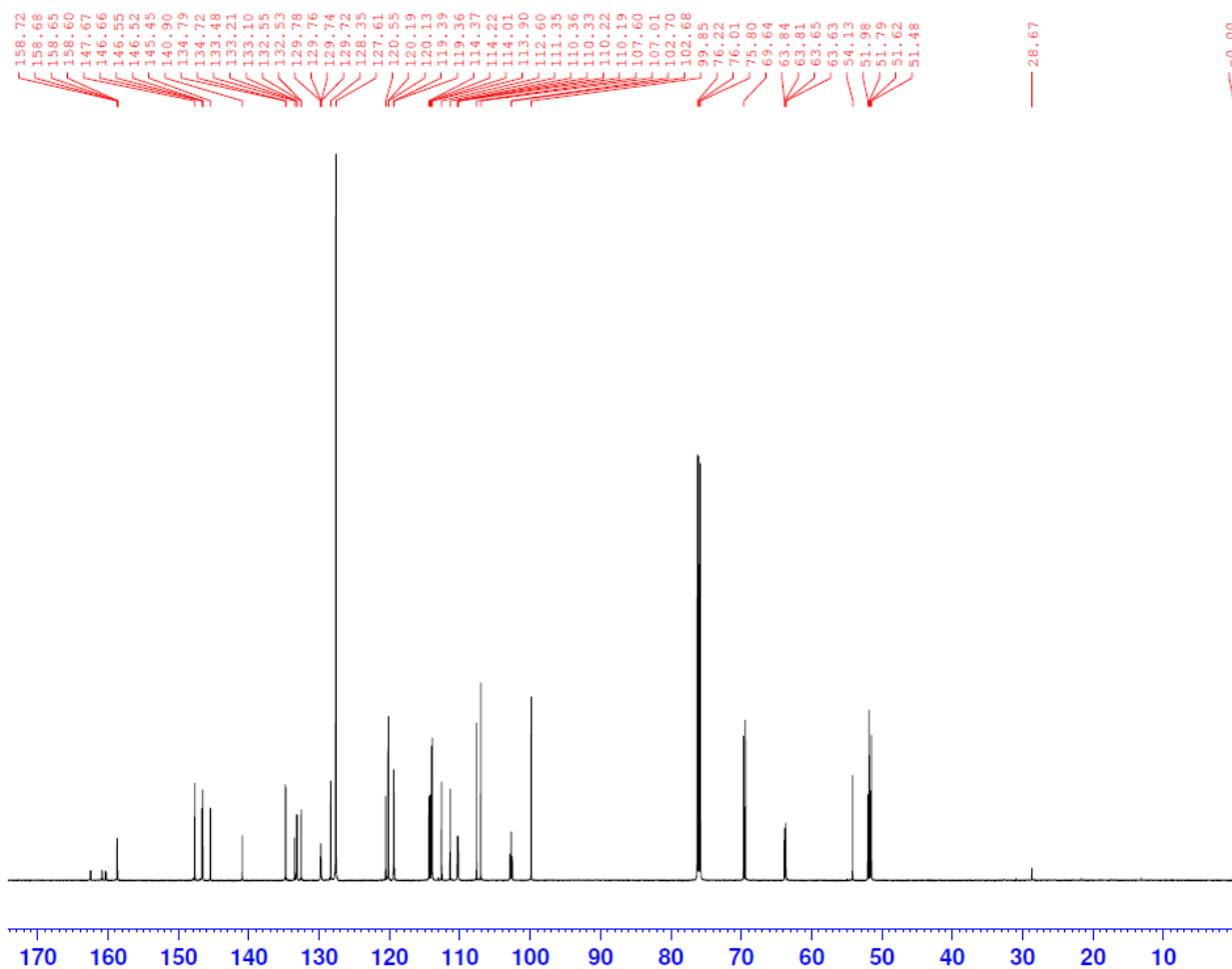
^{13}C-NMR

XIE5-2-37

XIE5-2-38, N-(3,4-bis((4-chlorobenzyl)oxy)benzyl)-3-(1H-imidazol-1-yl)propan-1-amine
^{1}H-NMR

XIE5-2-38

7.459
7.392
7.355
7.350
7.334
7.290
7.063
6.911
6.896
6.878
6.843
6.823

5.129
5.110

4.044
4.027
4.010
3.668

2.584
2.568
2.551
1.931
1.914
1.897

1.284

0.027

9   8   7   6   5   4   3   2   1

9.17 1.03 3.92   4.00   1.99 2.06   1.99 2.23 1.66 0.92
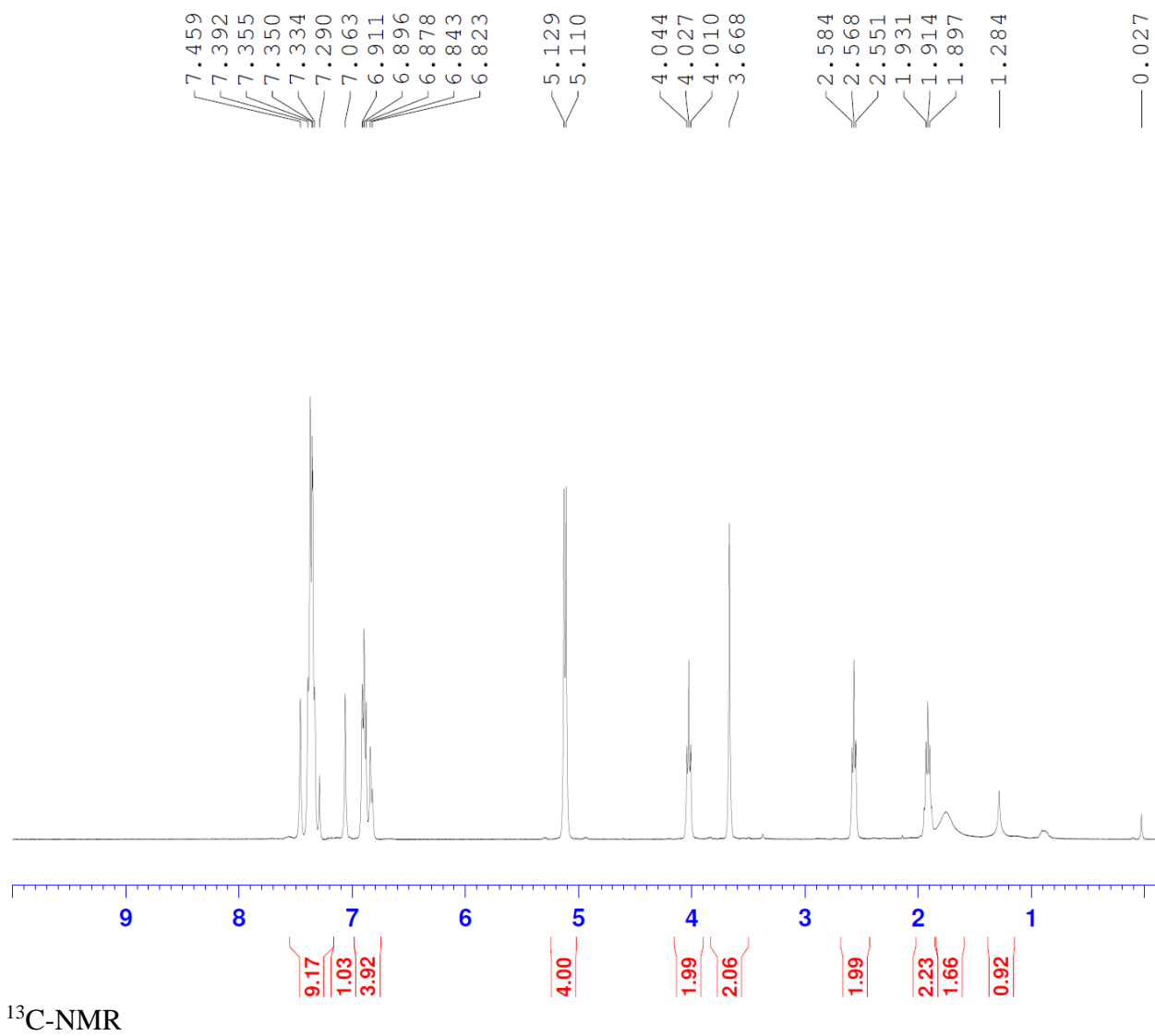
^{13}C-NMR

xix5-2-38
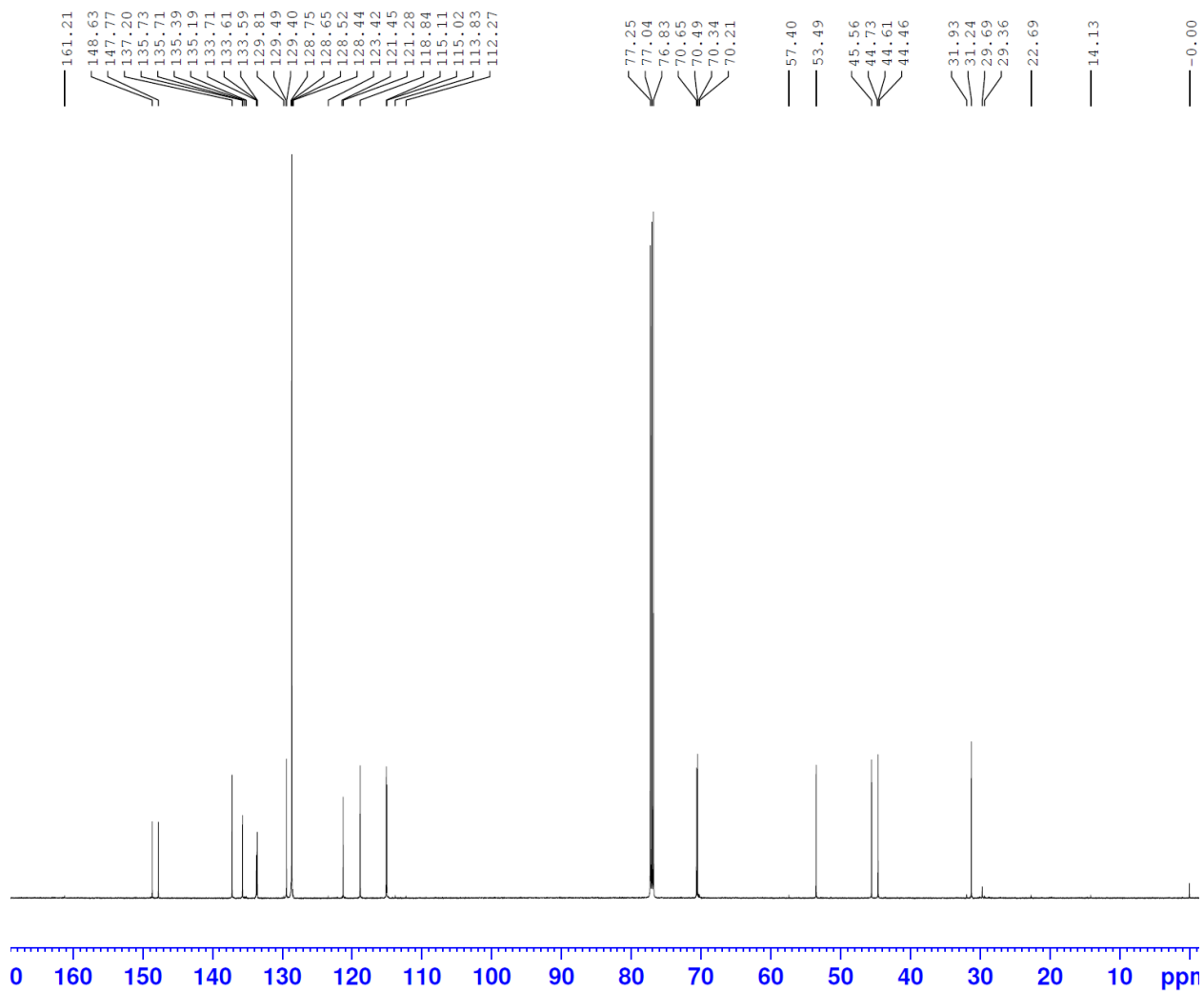
XIE5-2-39, N-(3,4-bis((4-chlorobenzyl)oxy)benzyl)-3-morpholinopropan-1-amine
^{1}H-NMR

XIE5-1-39

7.401 7.400 7.379 7.365 7.361 7.357 7.354 7.339 7.333 7.332 7.290 6.965 6.962 6.877 6.863 6.859 5.126 5.105 3.712 3.490 2.683 2.666 2.649 2.452 2.428 2.410 2.391 1.958 1.729 1.711 1.694 1.285 0.028

8.21 0.99 1.98 4.00 6.05 0.36 2.10 5.96 2.40 2.16 1.34
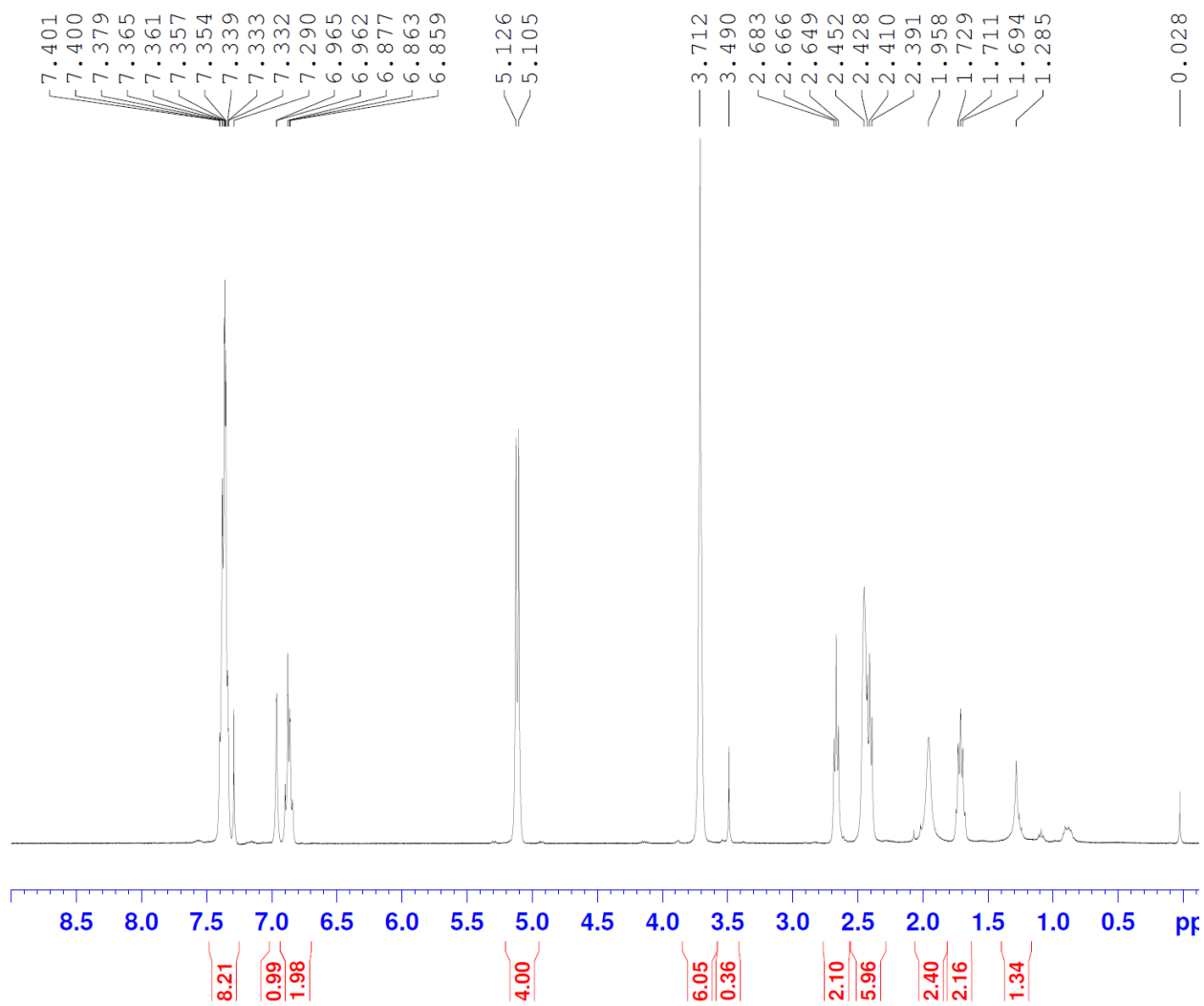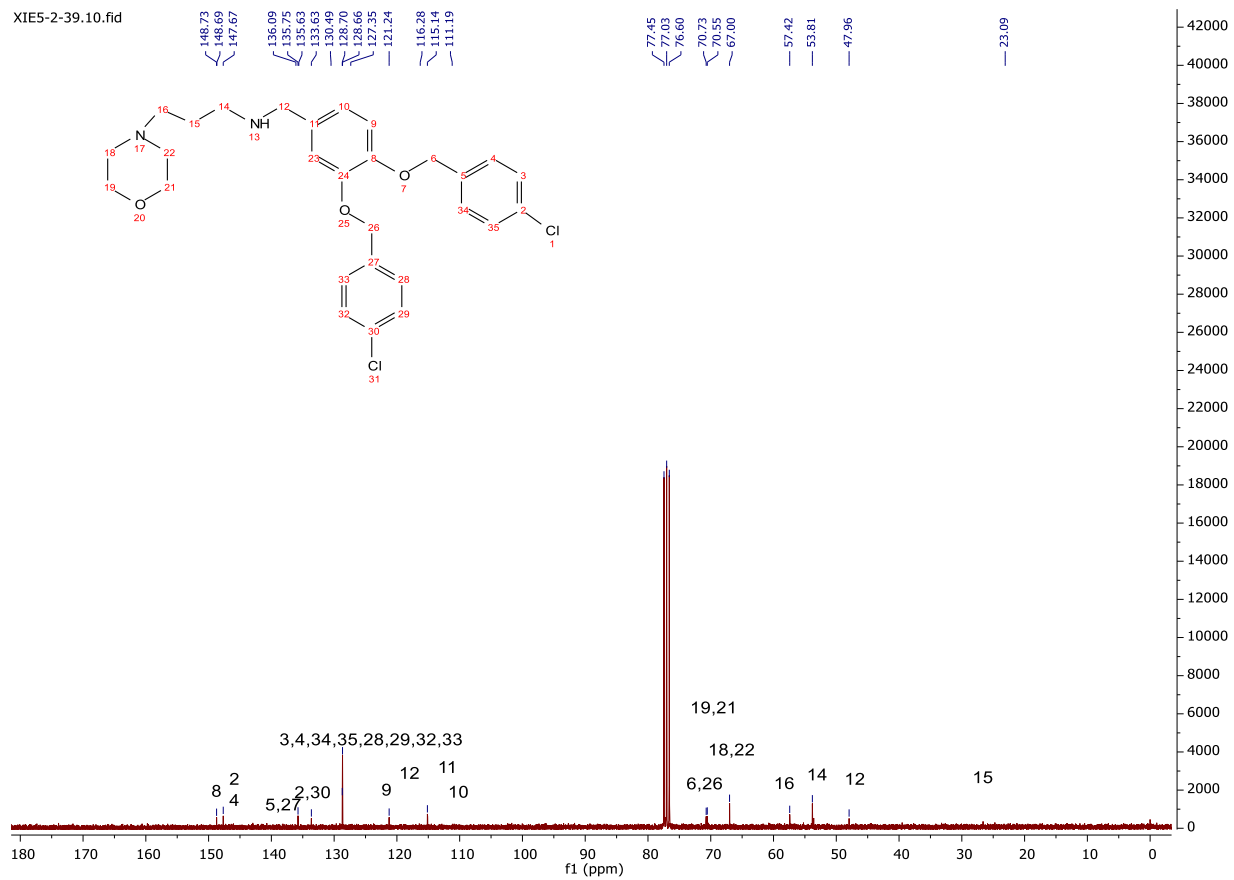
^{13}C-NMR

XIE5-2-40, €-2-(3,4-bis((2,4-difluorobenzyl)oxy)benzylidene)hydrazine-1-carboximidamide
^{1}H-NMR

9.85
8.32
8.00
7.67
7.61
7.60
7.58
7.57
7.57
7.56
7.55
7.53
7.32
7.31
7.31
7.31
7.30
7.30
7.29
7.29
7.28
7.28
7.25
7.25
7.24
7.24
7.13
7.12
7.11
7.11
7.10
5.16
5.14
3.36

2.50

1.89

0.00

1.00
1.18
1.31
4.21
4.26
4.90

4.10

^{13}C-NMR

172.46
161.41
148.75
148.25
145.65
144.77
135.35
131.91
127.68
121.92
114.27
112.85
111.60
111.46
104.17
104.06
104.00
103.83
99.14
86.61
76.32
64.07
64.01
63.99
61.06
43.38
39.99
39.87
39.73
39.59
39.45
39.31
39.17
39.04
21.36
0.08

f1 (ppm)
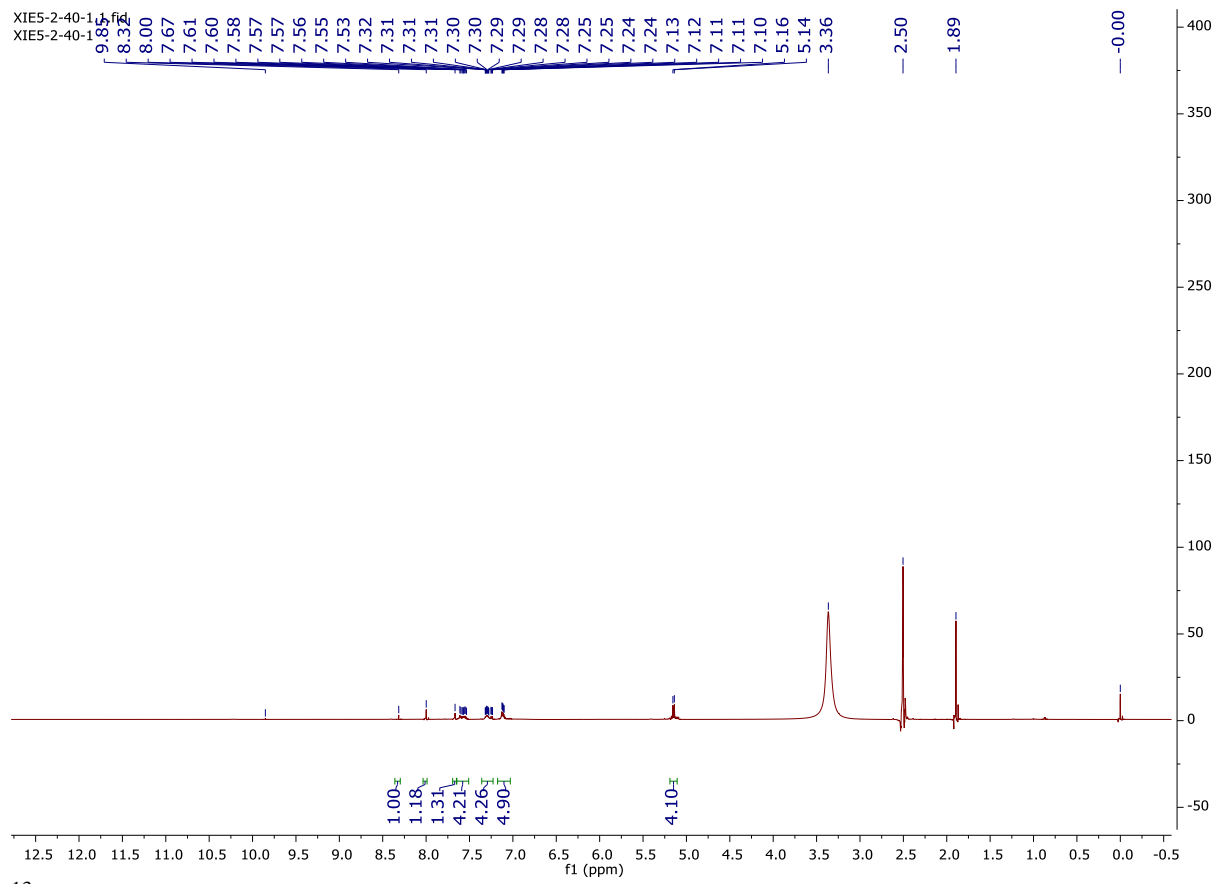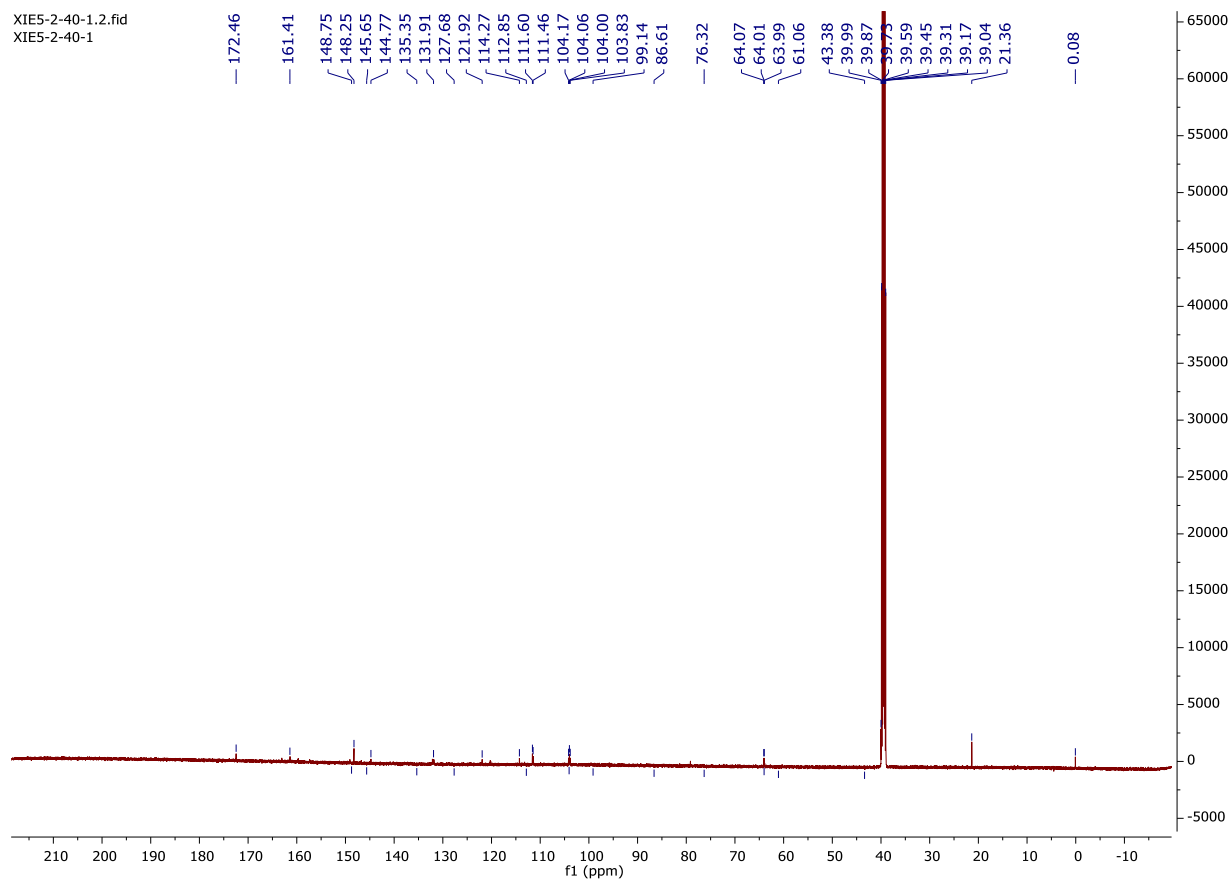
XIE5-1-25 (same as XIE5-2-42/XIE5-2-67-4/XIE5-2-68-3)
€-2-(3,4-bis((4-chlorobenzyl)oxy)benzylidene)hydrazine-1-carboximidamide
^{1}H-NMR
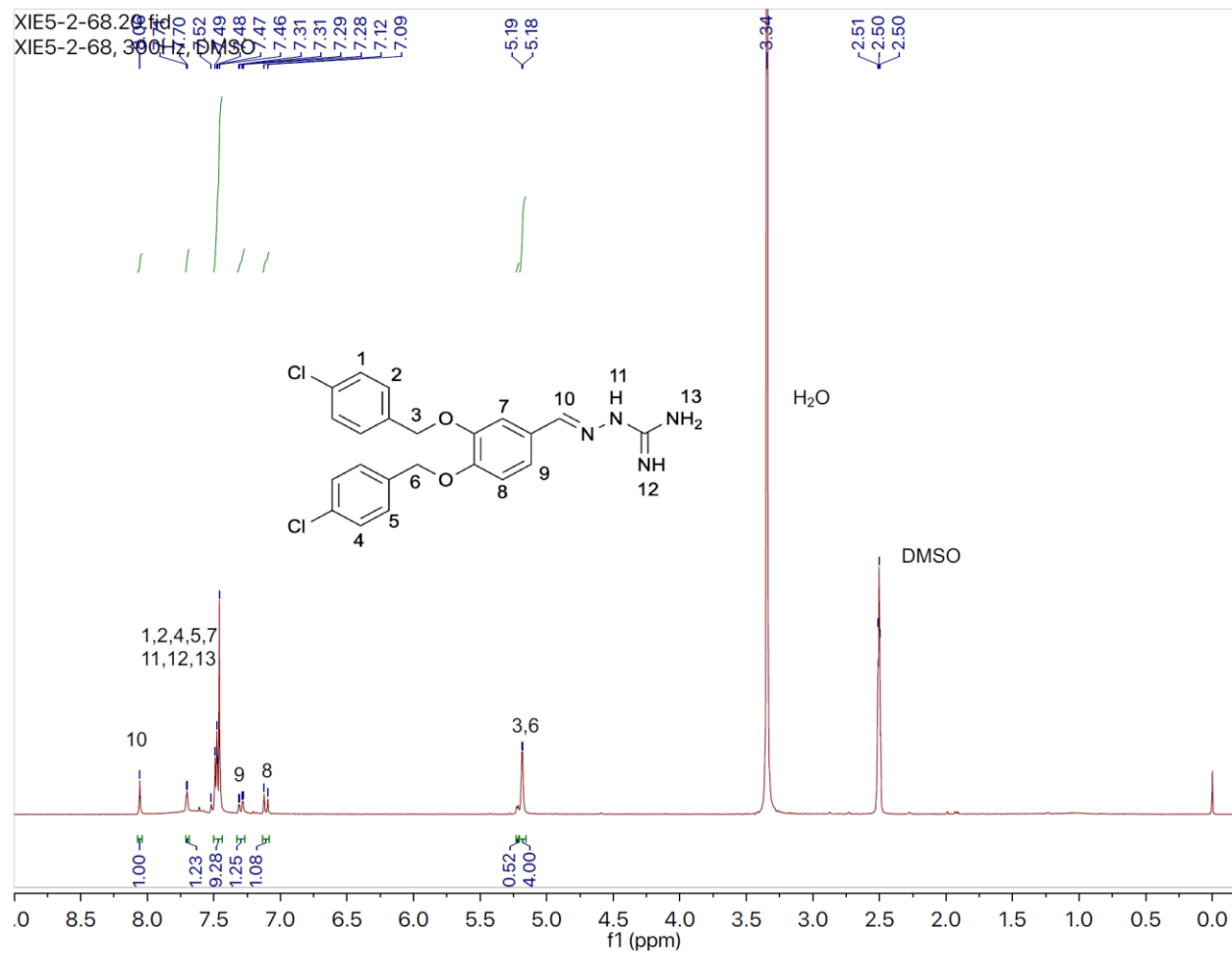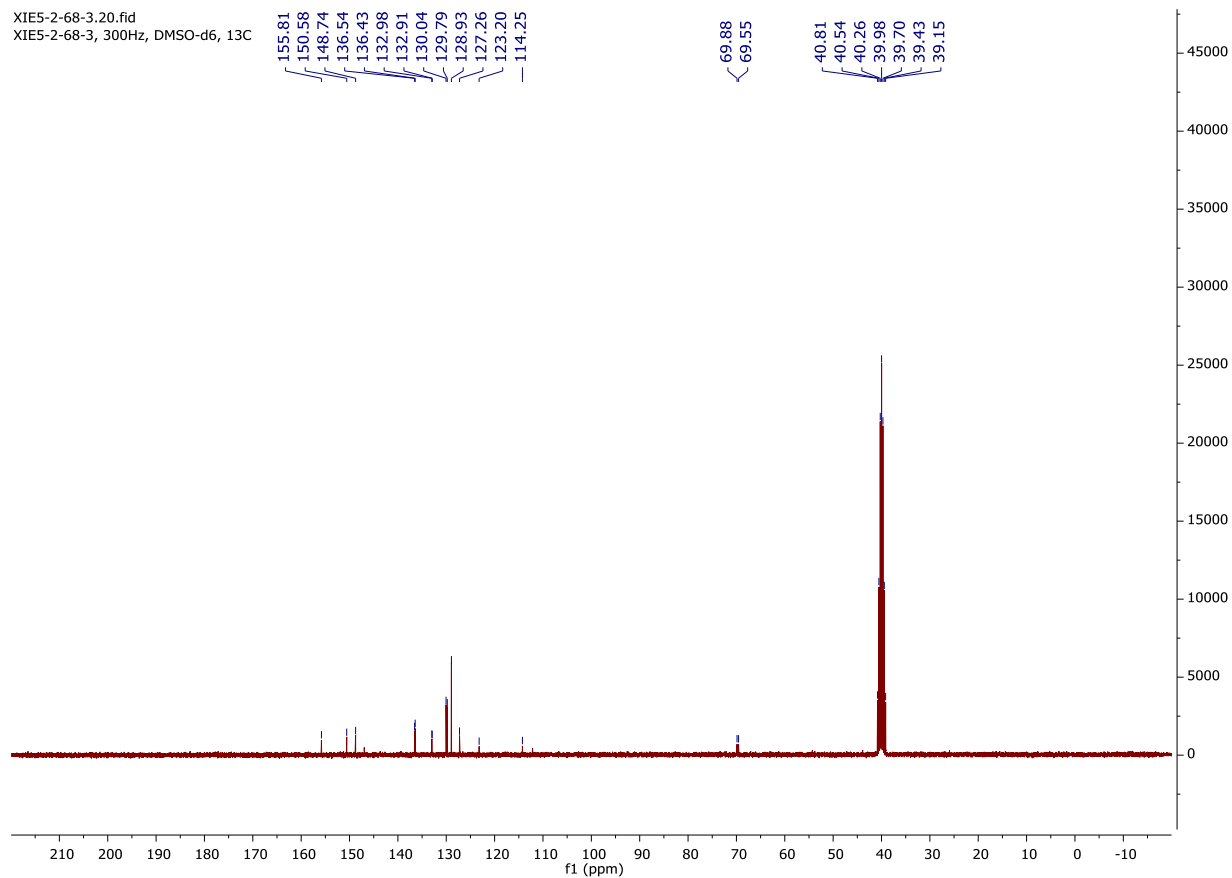
^{13}C-NMR

XIE5-2-43, €-2-(3,4-bis((4-fluorobenzyl)oxy)benzylidene)hydrazine-1-carboximidamide
^{1}H-NMR

¹³C-NMR

7.508 7.504 7.490 7.476 7.468 7.455 7.234 7.223 7.218 7.211 7.206 7.201 7.195 7.189 7.179 7.055 7.051 7.010 6.989 5.880 5.358 5.136 5.097

3.330

2.502 2.497 2.493

-0.005

0.21 1.04 4.83 4.00 2.08 1.73 1.78 3.99 10.67

8.5 8.0 7.5 7.0 6.5 6.0 5.5 5.0 4.5 4.0 3.5 3.0 2.5 2.0 1.5 1.0 0.5 p

XIE5-2-42

175.71
159.37
148.34
148.21
143.39
136.30
136.16
132.37
132.35
130.05
129.40
129.36
129.20
128.34
128.25
120.72
114.06
111.03
79.13
78.92
78.70
69.22
39.64
39.50
39.36
23.77

200 180 160 140 120 100 80 60 40 20
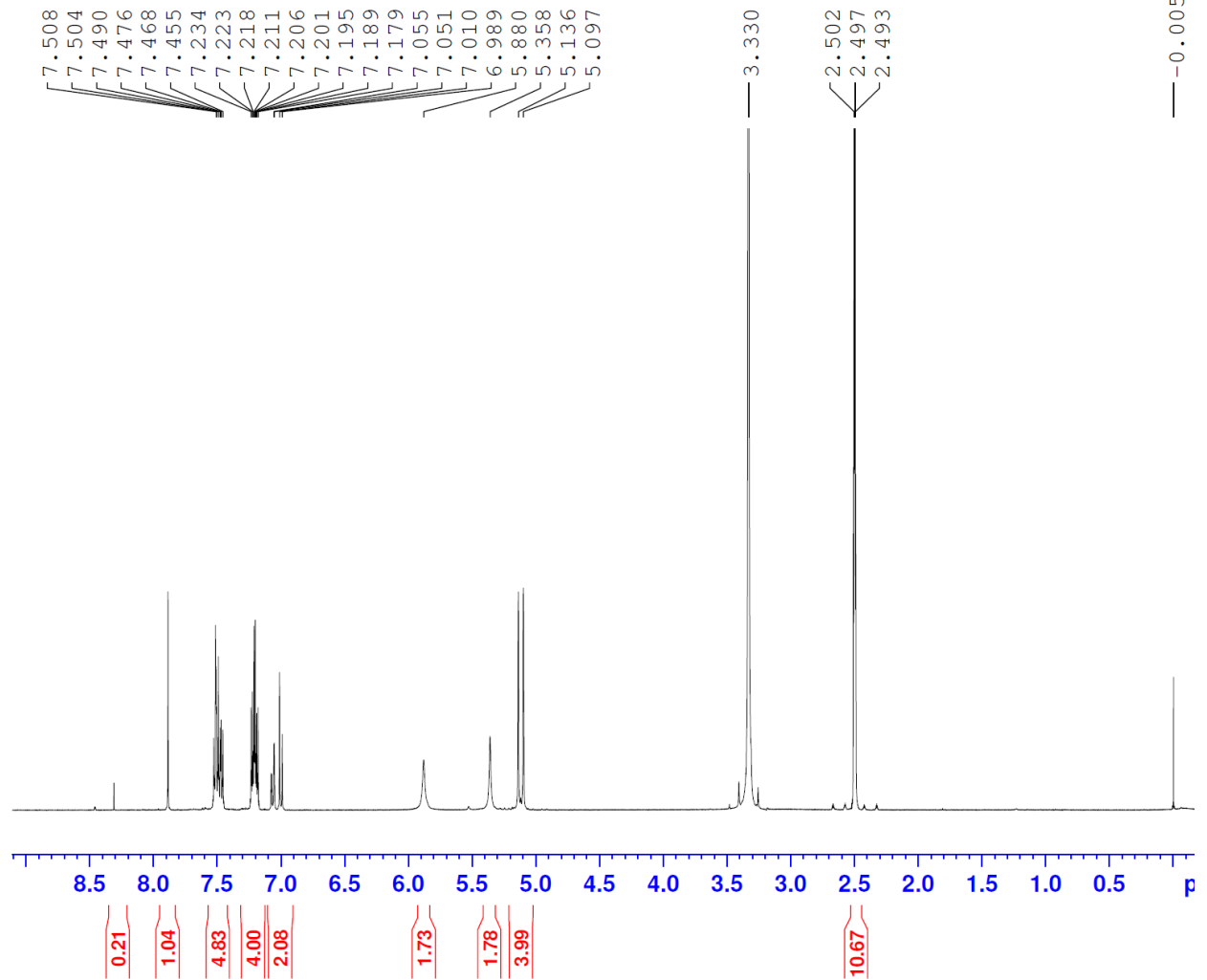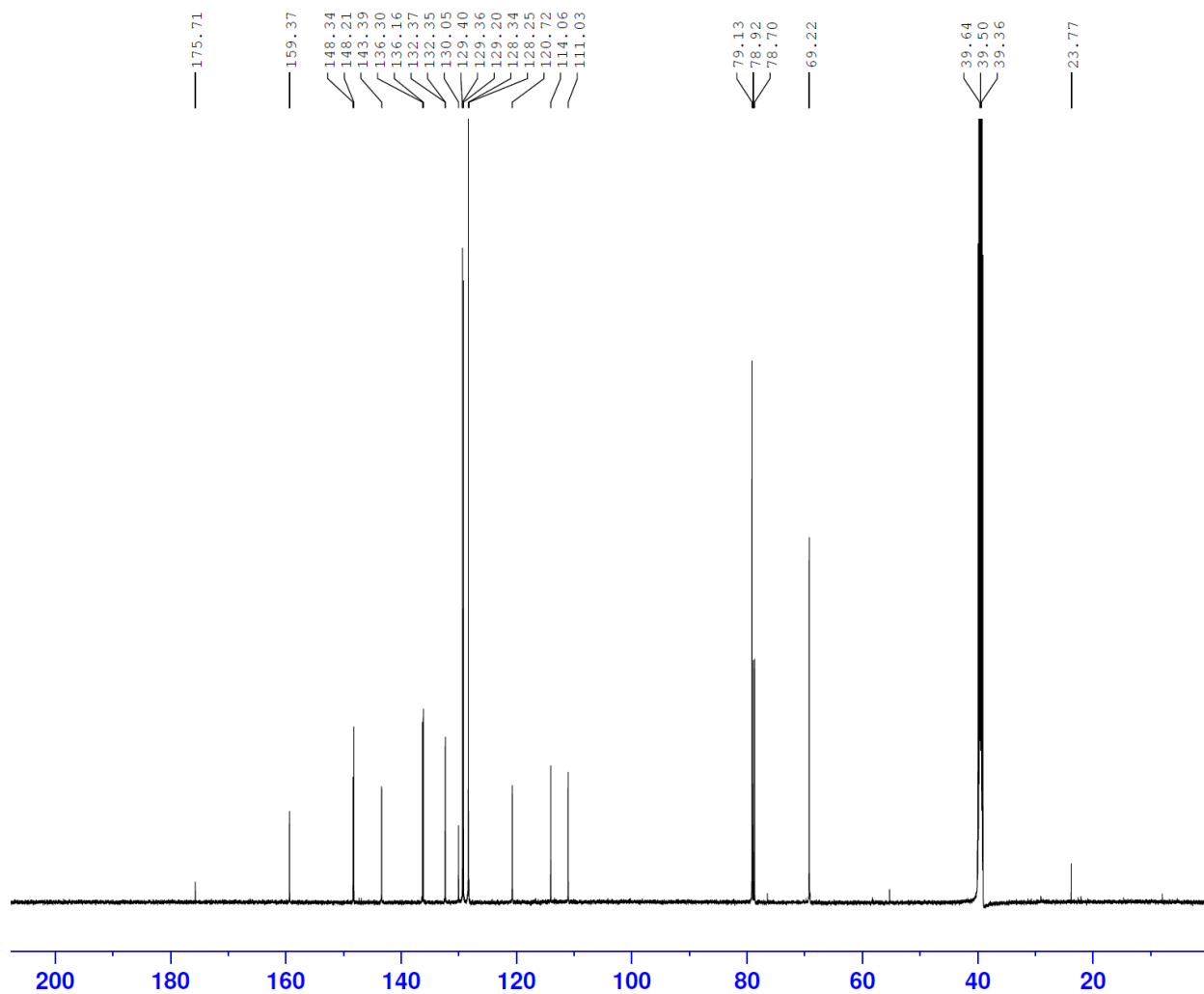
XIE5-2-44, €-2-(3,4-bis(benzyloxy)benzylidene)hydrazine-1-carboximidamide
^{1}H-NMR

XIE5-2-44

8.332
7.989
7.691
7.650
7.629
7.612
7.592
7.585
7.573
7.556
7.326
7.316
7.301
7.283
7.277
7.268
7.247
7.142
7.131
7.110
5.173
5.149
4.126
4.118
4.095
4.089
4.081
4.057
4.039
4.017
3.957
3.944
2.517
2.127
2.108
1.855
1.246
1.212
1.193
0.982
0.964
0.946
0.884
0.868
0.013

| 0.28 | 1.44 | 4.49 | 4.36 | 2.99 | 4.00 | 9.54 | 4.77 | 2.12 |

9   8   7   6   5   4   3   2   1   ppm
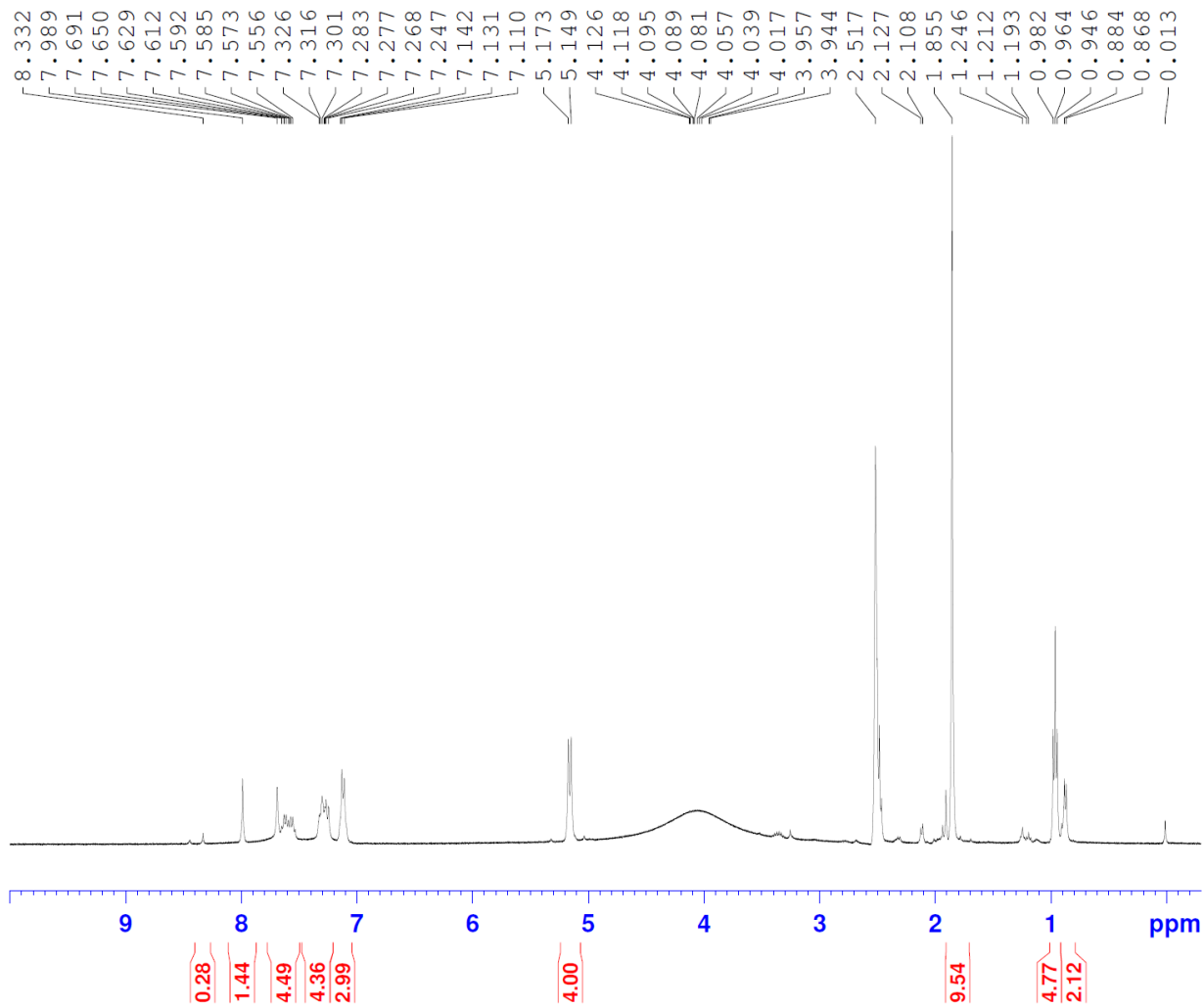
13C-NMR

XIE5-2-44

XIE5-2-46, N-(3,4-bis(lbenzyloxy)benzyl)-1-(3-methoxyphenyl)methanamine
^{1}H-NMR

XIE5-2-46

7.502 7.487 7.472 7.409 7.391 7.373 7.349 7.332 7.314 7.291 7.275 7.255 7.202 7.183 7.019 6.941 6.922 6.875 6.852 6.829 5.199 5.184 3.843 3.808 3.772 3.739 2.385 2.378 1.647 1.300 0.043

3.61 7.08 0.36 1.04 4.86 4.00 2.92 3.96 0.56 1.98
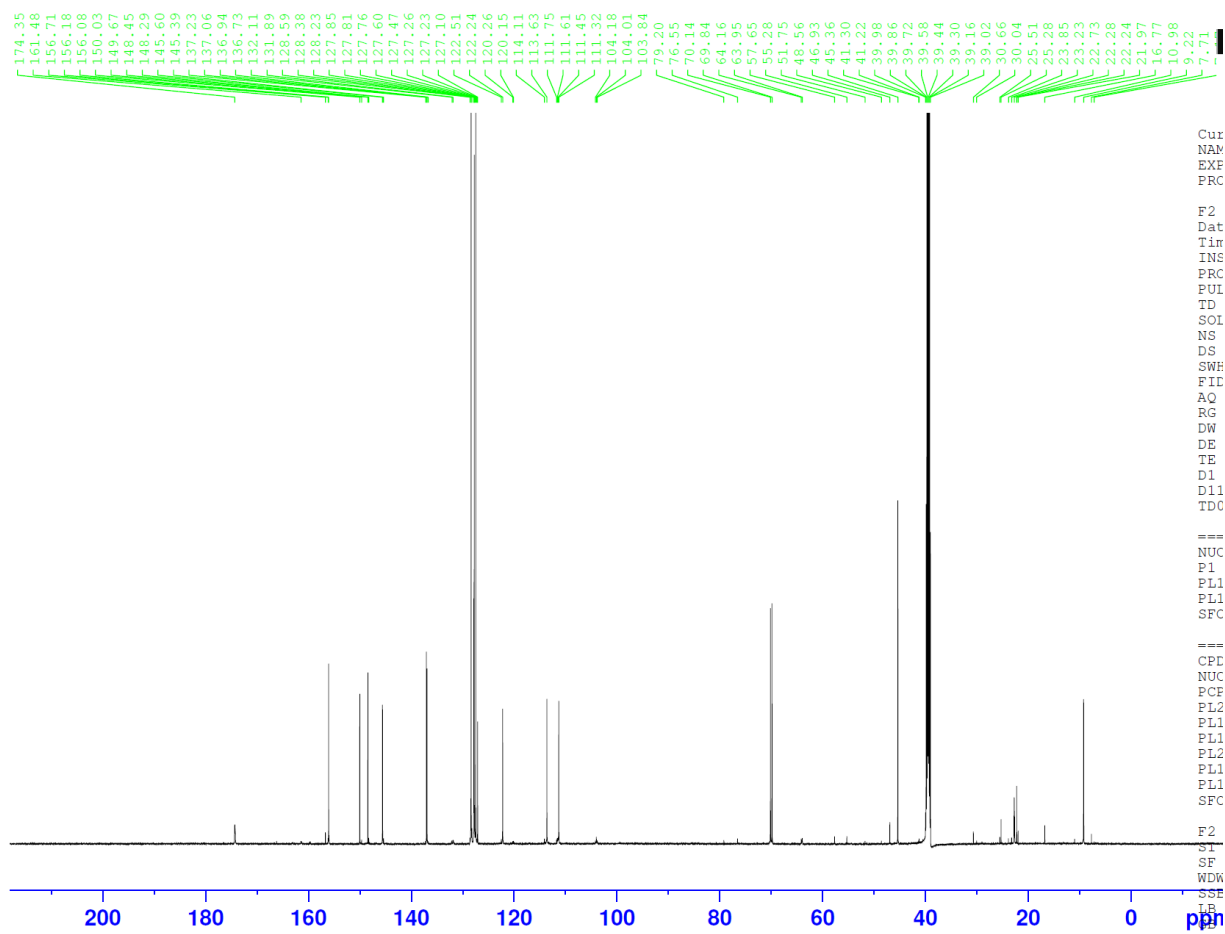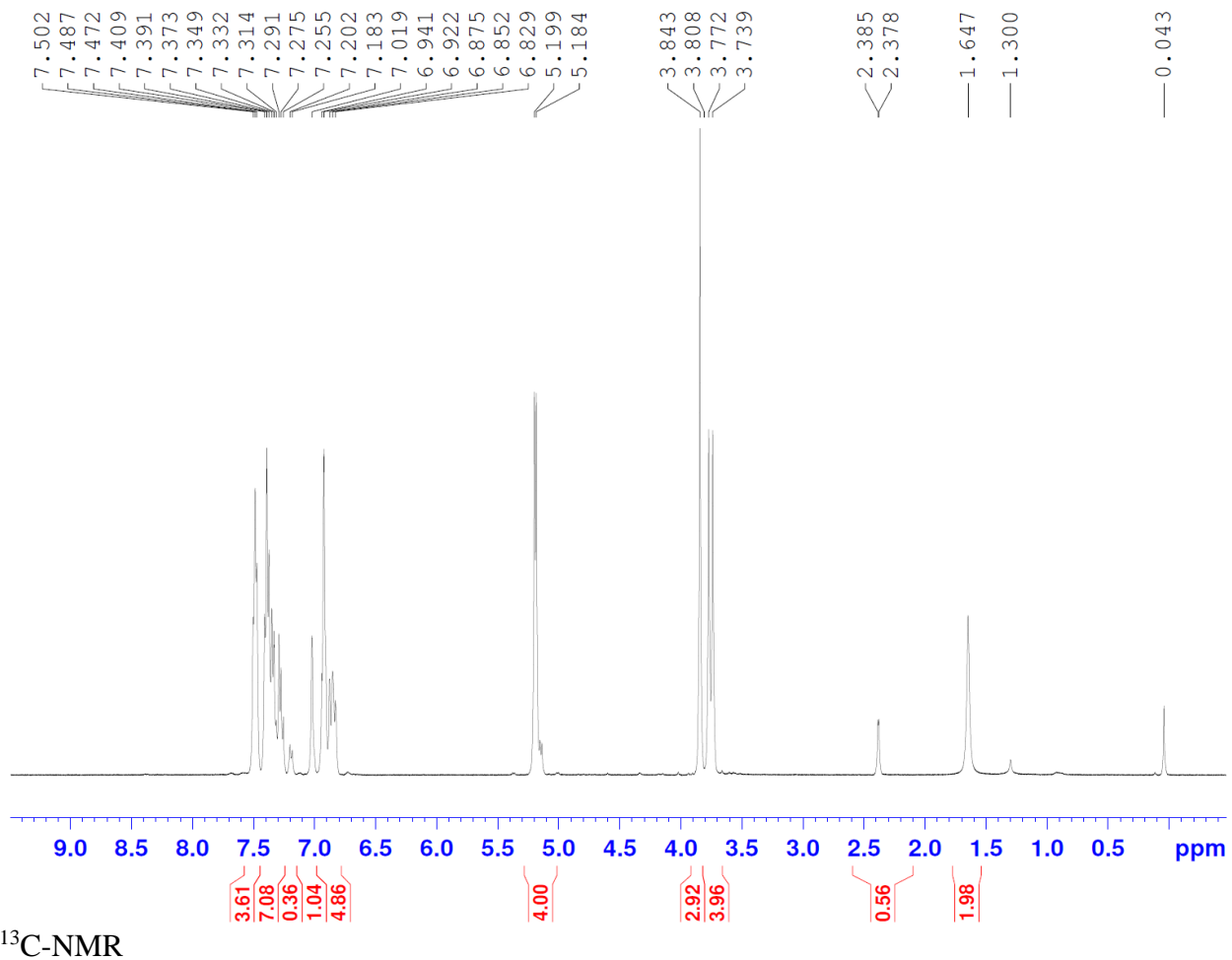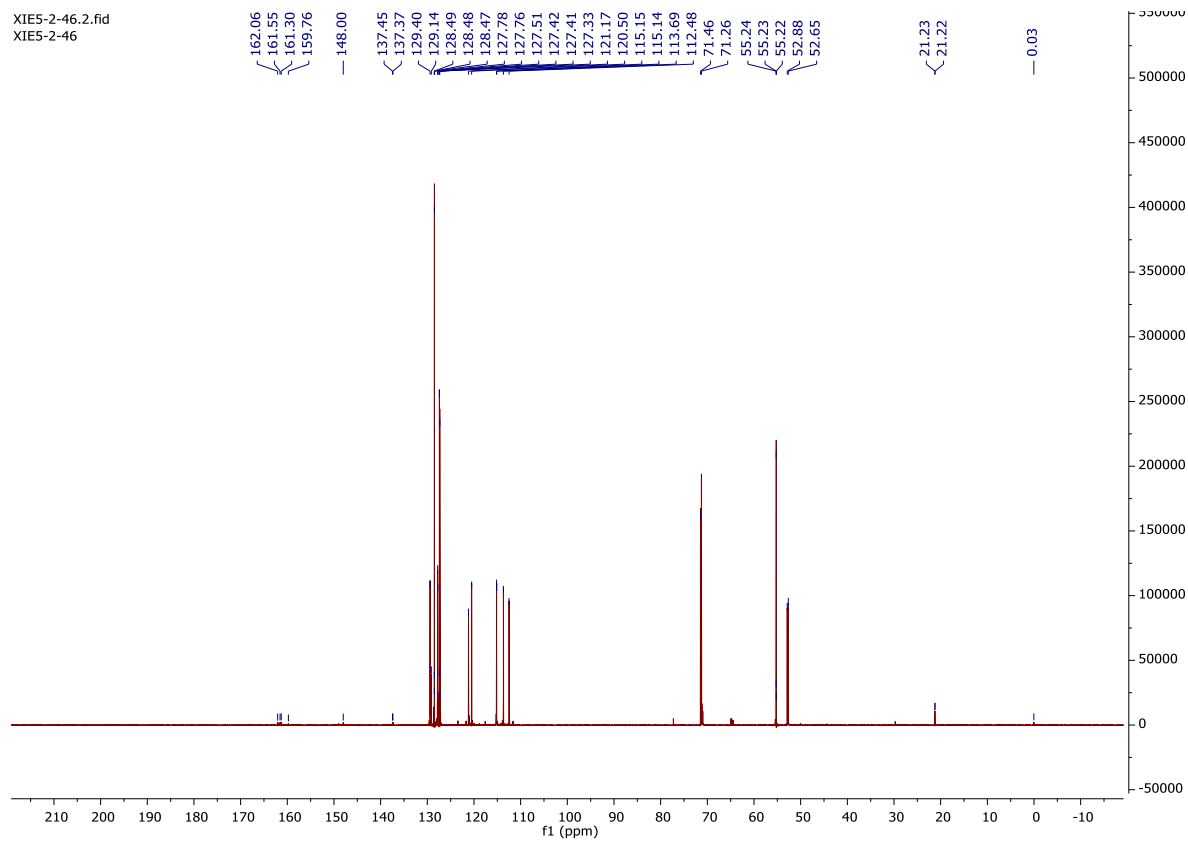
13C-NMR

XIE5-2-49, N-(3,4-bis(benzyloxy)benzyl)-1-(397yridine-2-yl)methanamine

^{1}H-NMR

XIE5-2-49

8.537
8.528
7.687
7.669
7.475
7.466
7.402
7.384
7.366
7.342
7.327
7.291
7.281
7.000
6.934
6.914
6.859
6.840
5.202
5.178
3.774
3.733
1.899
0.033

9.0 8.5 8.0 7.5 7.0 6.5 6.0 5.5 5.0 4.5 4.0 3.5 3.0 2.5 2.0 1.5 1.0 0.5 ppm

1.00 0.54 1.96 3.68 1.49 2.00 1.97 1.45

¹³C-NMR

149.79
148.98
148.57
148.15
137.33
137.28
135.96
128.48
128.46
127.77
127.35
127.29
123.40
121.21
115.12
115.04
77.24
77.03
76.82
71.38
71.22
52.60
50.03
-0.00

f1 (ppm)
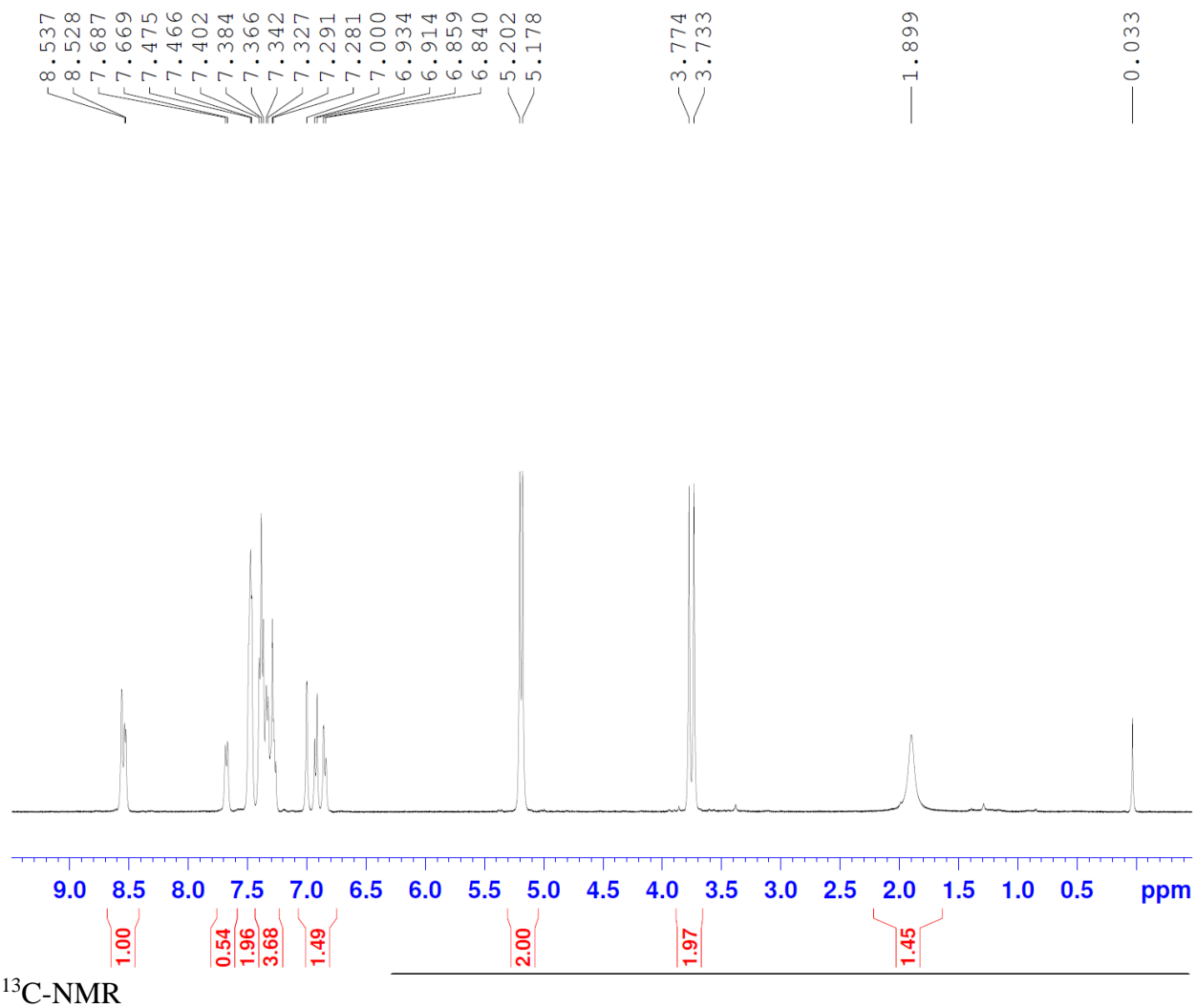
XIE5-2-51, 1-(benzo[d][1,3]dioxol-5-yl)-N-(3,4-bis((benzyloxy)benzyl)methanamine
^{1}H-NMR

XIE5-2-51

7.434
7.417
7.375
7.364
7.359
7.346
7.313
7.301
7.295
7.057
6.972
6.952
6.890
6.819
6.801
6.790
6.731
6.712
5.959
5.097
5.084
3.529
3.517
3.334
2.490
-0.012

8.5 8.0 7.5 7.0 6.5 6.0 5.5 5.0 4.5 4.0 3.5 3.0 2.5 2.0 1.5 1.0 0.5 p

9.97 1.03 1.03 1.08 2.07 1.10 2.20 4.00 4.25 4.29

^{13}C-NMR

400

160.68, 149.46, 148.32, 148.12, 147.24, 147.13, 146.87, 145.97, 145.74, 137.44, 137.37, 134.78, 133.89, 132.78, 132.40, 128.33, 128.32, 127.70, 127.67, 127.58, 127.51, 124.46, 124.36, 120.90, 120.87, 120.43, 114.32, 114.28, 108.45, 108.41, 108.32, 108.27, 108.21, 108.06, 107.77, 105.91, 101.48, 100.75, 100.61, 70.15, 70.00, 69.88, 69.83, 63.32, 63.22, 51.71, 51.57, 51.52, 39.98, 39.86, 39.72, 39.58, 39.44, 39.30, 39.16, 39.02

Current Data Parameters
NAME   XIE5-2-51
EXPNO   3
PROCNO   1

F2 - Acquisition Parameters
Date_   20190228
Time   0.30
INSTRUM   spect
PROBHD   5 mm CPTCI 1H-
PULPROG   zgpg30
TD   65536
SOLVENT   DMSO
NS   1300
DS   4
SWH   35971.223 Hz
FIDRES   0.548877 Hz
AQ   0.9109504 sec
RG   5792.6
DW   13.900 usec
DE   16.00 usec
TE   298.0 K
D1   2.00000000 sec
D11   0.03000000 sec
TD0   1

======== CHANNEL f1 ========
NUC1   13C
P1   12.00 usec
PL1   -1.50 dB
PL1W   99.34774780 W
SFO1   150.9178988 MHz

======== CHANNEL f2 ========
CPDPRG[2   waltz16
NUC2   1H
PCPD2   80.00 usec
PL2   4.00 dB
PL12   24.62 dB
PL13   27.00 dB
PL2W   7.00000000 W
PL12W   0.06068732 W
PL13W   0.03508311 W
SFO2   600.1324005 MHz

F2 - Processing parameters
SI   32768
SF   150.9028845 MHz
WDW   EM
SSB   0
LB   1.00 Hz
GB   0
PC   1.40

XIE5-2-53 (solvent, impurity), N-(3,4-bis((benzyloxy)benzyl)-1-(furan-3-yl)methanamine
^{1}H-NMR

7.499
7.483
7.467
7.393
7.373
7.348
7.331
7.314
7.291
7.006
7.003
6.937
6.917
6.864
6.845
6.347
6.173
6.166
5.196
5.178

3.763
3.717
3.612
3.594

1.730
1.481
1.463
1.446
1.298

0.041

BRUKER

Current Data Parameters
NAME   XIE5-2-53
EXPNO   1
PROCNO   1

F2 - Acquisition Parameters
Date_   20180914
Time   0.12
INSTRUM   spect
PROBHD   5 mm PABBO BB-
PULPROG   zg30
TD   65536
SOLVENT   CDCl3
NS   16
DS   2
SWH   8223.685 Hz
FIDRES   0.125483 Hz
AQ   3.9846387 sec
RG   128
DW   60.800 usec
DE   6.50 usec
TE   298.3 K
D1   1.00000000 sec

======== CHANNEL f1 ========
NUC1   1H
P1   12.19 usec
PLW1   11.98999977 W
SFO1   400.1324710 MHz

F2 - Processing parameters
SI   65536
SF   400.1300000 MHz
WDW   no
SSB   0
LB   0 Hz
GB   0
PC   1.00

9.0 8.5 8.0 7.5 7.0 6.5 6.0 5.5 5.0 4.5 4.0 3.5 3.0 2.5 2.0 1.5 1.0 0.5 ppm

3.97 7.35 1.02 2.03 1.00 0.94 4.00 3.86 0.53 2.01 0.66

^{13}C-NMR

XIE5-2-54, N-(3,4-bis(benzyloxy)benzyl)-1-(thiophen-2-yl)methanamine
^{1}H-NMR

402

XIE5-2-54

7.500 7.484 7.467 7.404 7.388 7.371 7.347 7.329 7.310 7.290 7.254 7.242 7.013 6.992 6.983 6.971 6.936 6.916 6.867 6.847 5.202 5.180

3.962 3.757

1.693 1.630 1.496 1.478 1.461 1.332 1.292 0.917 0.909 0.892

0.036

CNEP FDTIPPTSNDSFARDDTD =NPPS FSSWSLGP

3.90 8.18 5.00 3.91 1.95 2.01 2.35 0.78 2.30 1.23

¹³C-NMR

148.98
148.00
137.42
137.33
133.34
128.53
128.49
128.47
128.45
128.44
128.41
127.76
127.74
127.42
127.41
127.40
127.39
127.38
127.33
127.30
127.29
127.28
127.27
126.62
124.97
124.40
121.15
115.11
77.23
77.02
76.81
71.43
71.21
52.28
47.29
0.00

XIE5-2-58, N-(3,4-bis((4-methylbenzyl)oxy)benzyl)-1-(furan-3-yl)methanamine
^{1}H-NMR

7.392
7.390
7.373
7.355
7.340
7.290
7.197
7.178
6.977
6.974
6.915
6.894
6.839
6.820
6.342
6.164
6.156
5.648
5.145
5.129

3.744

2.379

1.717
1.603
1.497
1.479
1.461

0.035

4.99
1.45
4.00
1.00
2.19
1.06
1.02
4.00
3.92
6.18
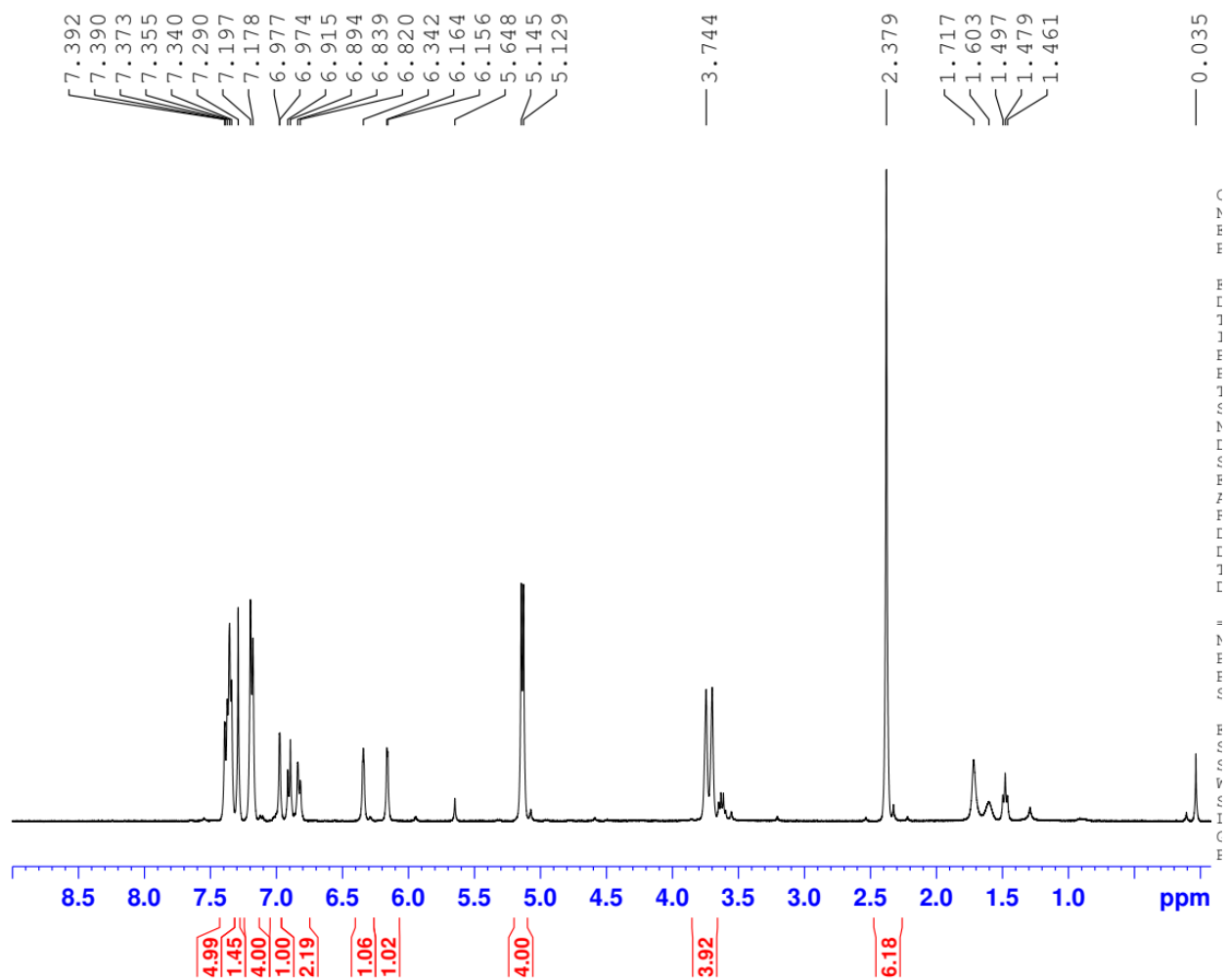
^{13}C-NMR

XIE5-2-61 (need further purification),
N-(3,4-bis((4-methylbenzyl)oxy)benzyl)-1-(3-methoxyphenyl)methanamine
^{1}H-NMR

405

7.34
7.33
7.32
7.31
7.26
7.23
7.22
7.17
7.16
7.15
7.00
7.00
6.92
6.90
6.88
6.86
6.83
6.83
5.12
5.10
3.81
3.74
3.71
2.35
2.33
-0.00

3.99
1.64
3.97
0.83
3.01
1.19
3.74
2.99
3.90
5.66
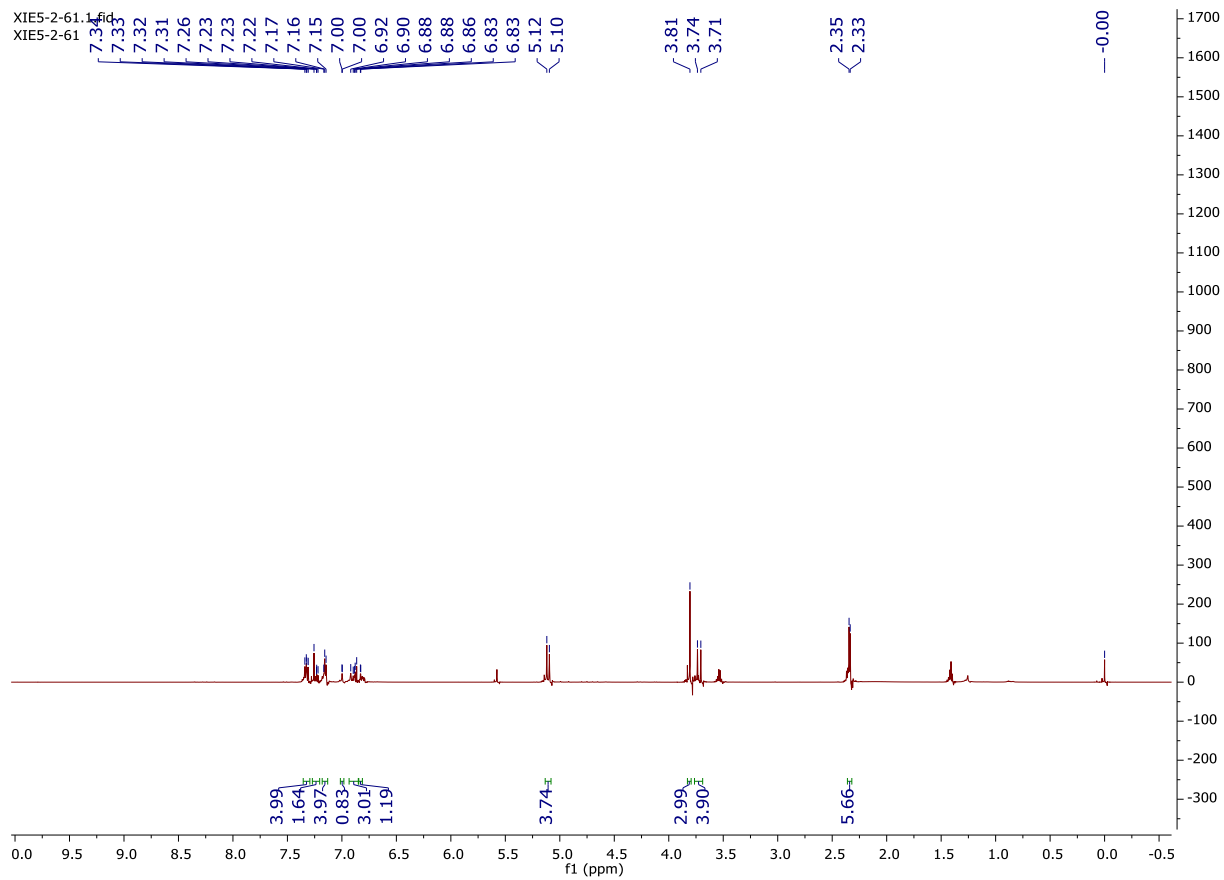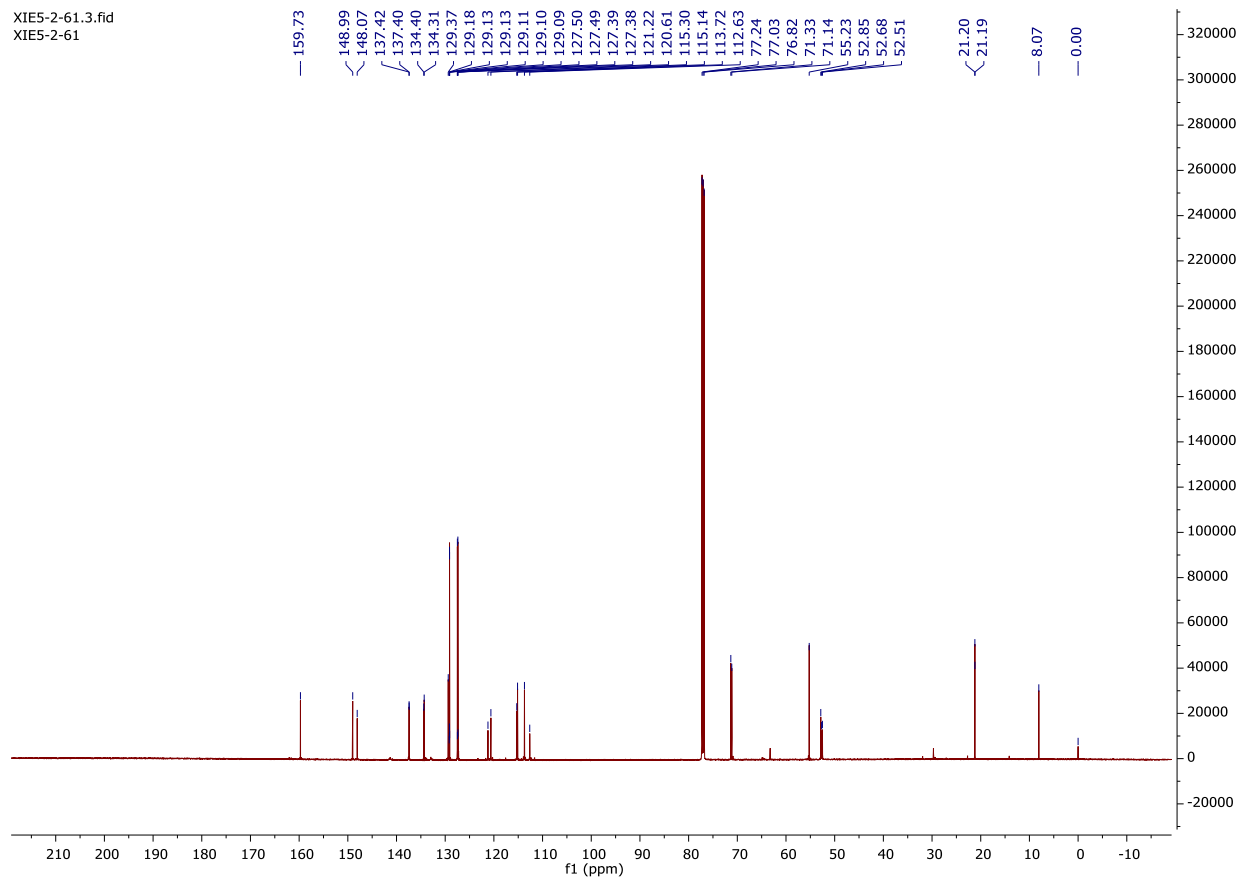
^{13}C-NMR

XIE5-2-64, N-(3,4-bis((4-methylbenzyl)oxy)benzyl)-3-(1H-imidazol-1-yl)propan-1-amine
^{1}H-NMR

XIE5-2-64

7.475
7.366
7.356
7.348
7.338
7.290
7.195
7.188
7.177
7.063
6.965
6.909
6.899
6.890
6.826
6.807
5.155
5.128
4.042
4.025
4.008
3.680
3.511
2.583
2.378
2.364
1.977
1.960
1.943
1.926
1.440
1.422
1.404
1.287
1.271
0.029

1.11
5.21
3.92
1.05
1.01
1.95
1.02
4.00
2.00
2.08
1.90
2.07
6.04
6.06
0.77

^{13}C-NMR

XIE5-2-64

161.45

148.96
148.26
137.46
137.43
137.15
134.27
134.25
132.18
129.29
129.13
129.11
127.42
127.37
121.29
118.88
115.34
115.01

77.28
77.06
76.85
71.26
71.14

53.22
52.73

45.23
44.57
40.95

30.82

21.19

7.91

-0.00

170 160 150 140 130 120 110 100 90 80 70 60 50 40 30 20 10 ppm

XIE5-2-70, 2-(3,4-bis((2,4-difluorobenzyl)oxy)phenyl)ethan-1-aminium chloride
^{1}H-NMR

7.959
7.589
7.571
7.559
7.541
7.520
7.328
7.308
7.303
7.293
7.289
7.270
7.139
7.125
7.104
7.088
7.082
7.066
7.054
7.051
7.046
6.832
6.817
5.114
5.087
3.403
3.028
3.015
2.835
2.814
2.796
2.512
0.009

9   8   7   6   5   4   3   2   1   ppm

2.92 2.19 1.97 3.87 1.10   4.00   2.06 2.16
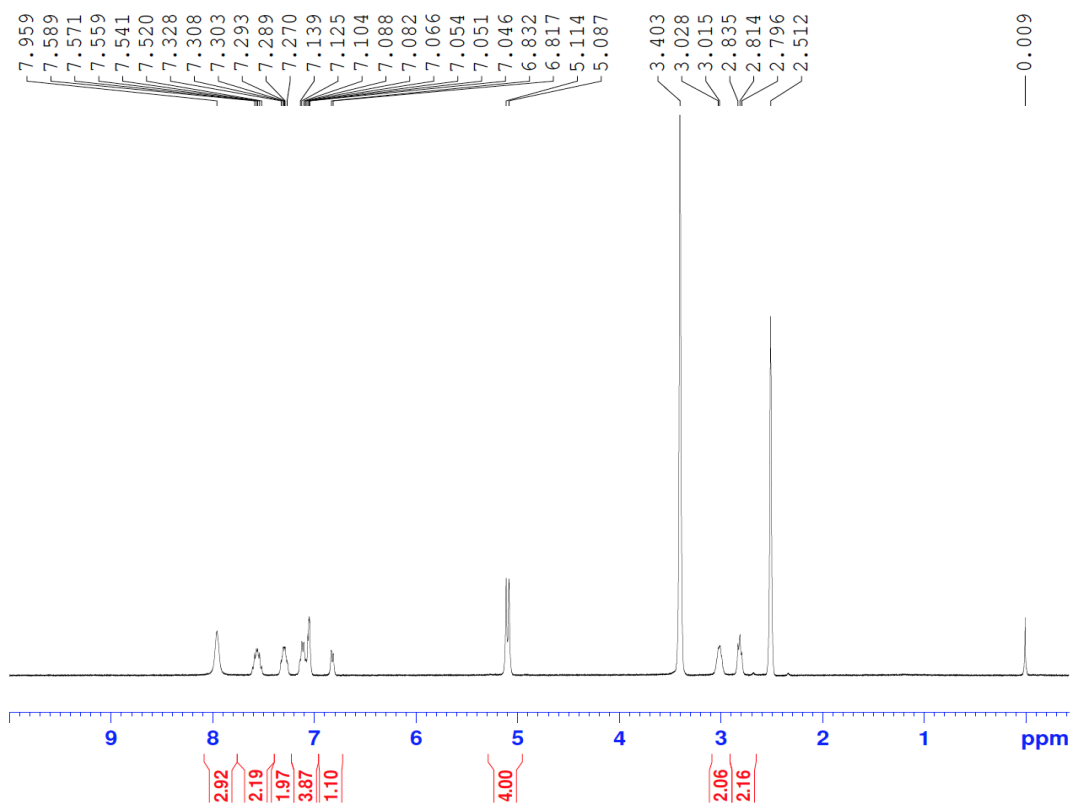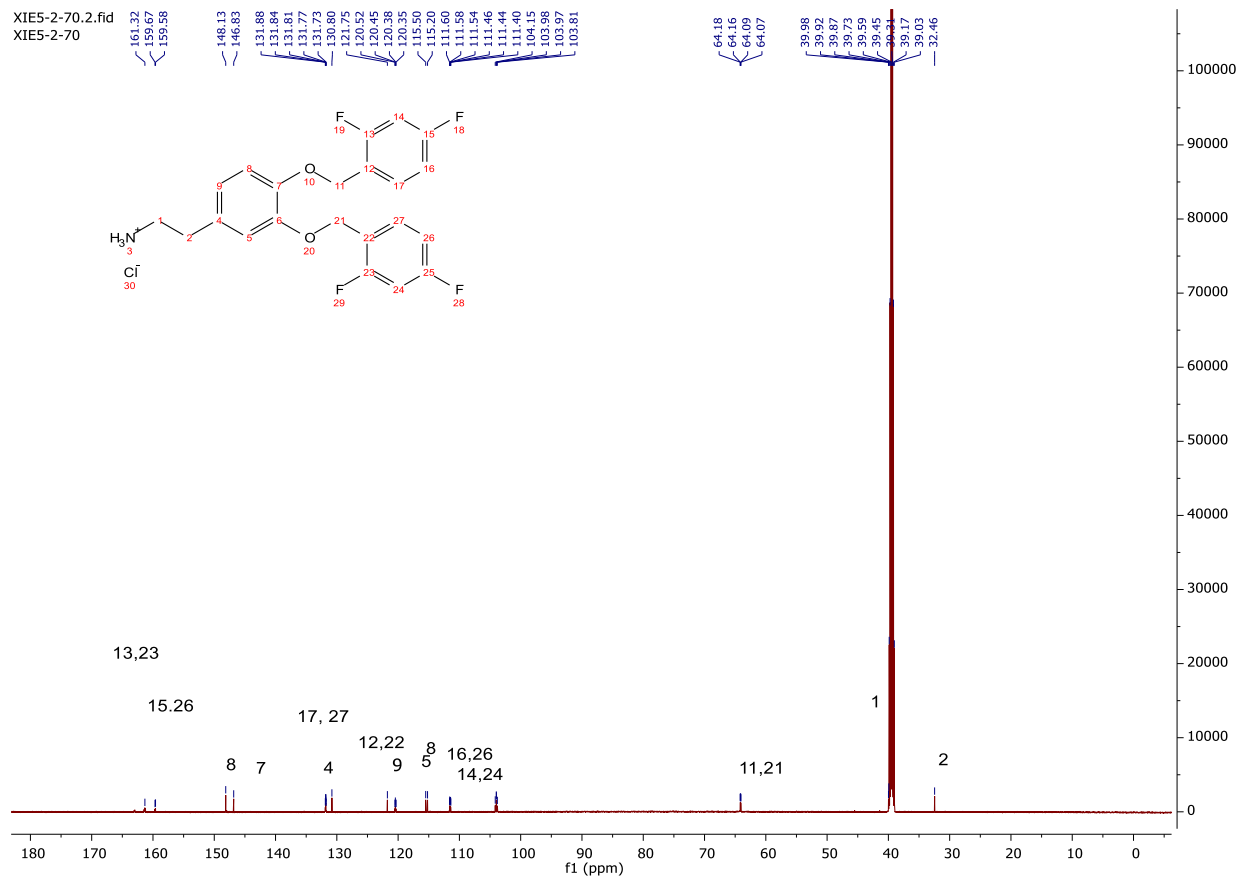
^{13}C-NMR

XIE5-2-73, *N*-(3,4-bis((4-chlorobenzyl)oxy)phenethyl)acetamide
^{1}H-NMR
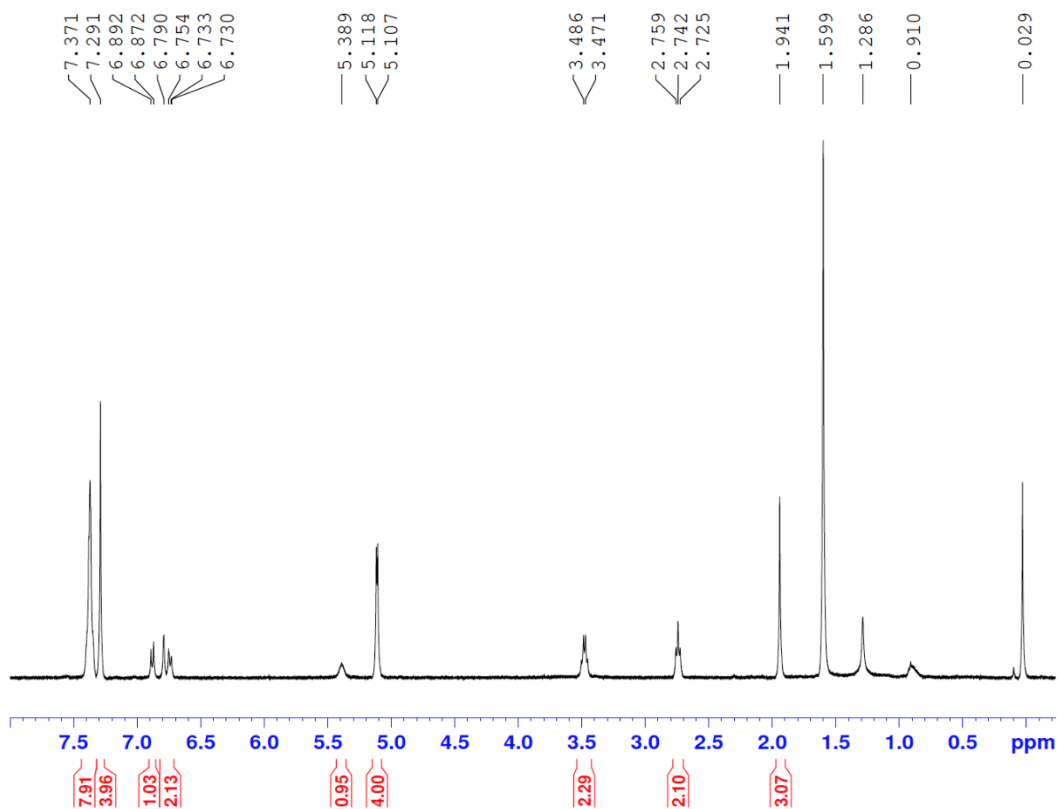
XIE5-3-73

¹³C-NMR

XIE5-2-74, N-(3,4-bis((2,4-fluorobenzyl)oxy)phenethyl)acetamide
¹H-NMR

XIE5-3-73

^{13}C-NMR

XIE5-2-74, N-(3,4-bis((2,4-fluorobenzyl)oxy)phenethyl)acetamide
^{1}H-NMR

XIE5-3-74

7.514
7.511
7.499
7.490
7.484
7.290
6.943
6.923
6.896
6.888
6.879
6.849
6.795
6.775
5.422
5.421
5.143
5.137
3.522
3.506
3.490
3.474
2.781
2.765
2.748
1.962
1.600
1.285
0.029

9.0 8.5 8.0 7.5 7.0 6.5 6.0 5.5 5.0 4.5 4.0 3.5 3.0 2.5 2.0 1.5 1.0 0.5 pp

2.07 3.99 6.97 1.19 4.00 2.48 2.33 3.05 9.76 1.81 0.84
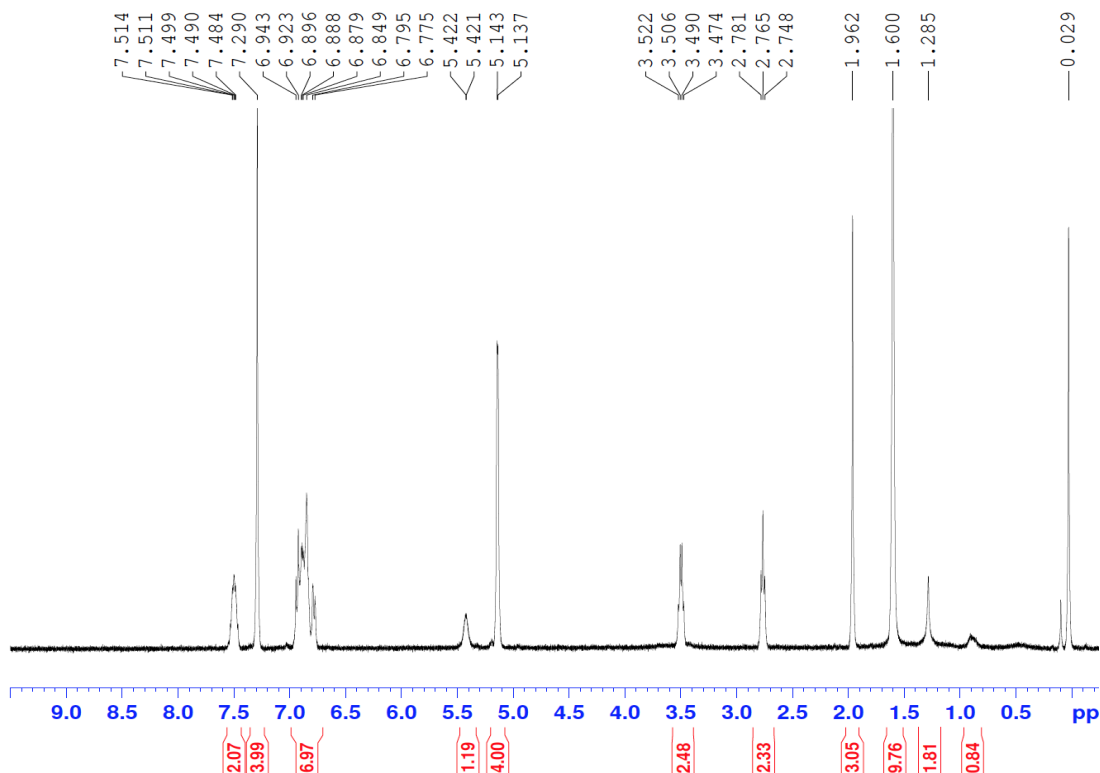
^{13}C-NMR

XIE5-3-74.2.fid
XIE5-3-74

170.00
162.01
159.73
148.78
147.40
132.90
130.93
130.89
130.87
130.83
130.81
130.78
130.74
122.16
120.31
120.28
116.01
115.70
111.47
111.44
111.42
111.33
111.30
111.28
103.97
103.95
103.80
103.78
103.64
103.61
77.23
77.02
76.81
64.91
64.88
64.86
64.83
40.66
35.13
23.36
0.00

210 200 190 180 170 160 150 140 130 120 110 100 90 80 70 60 50 40 30 20 10 0 -10
f1 (ppm)
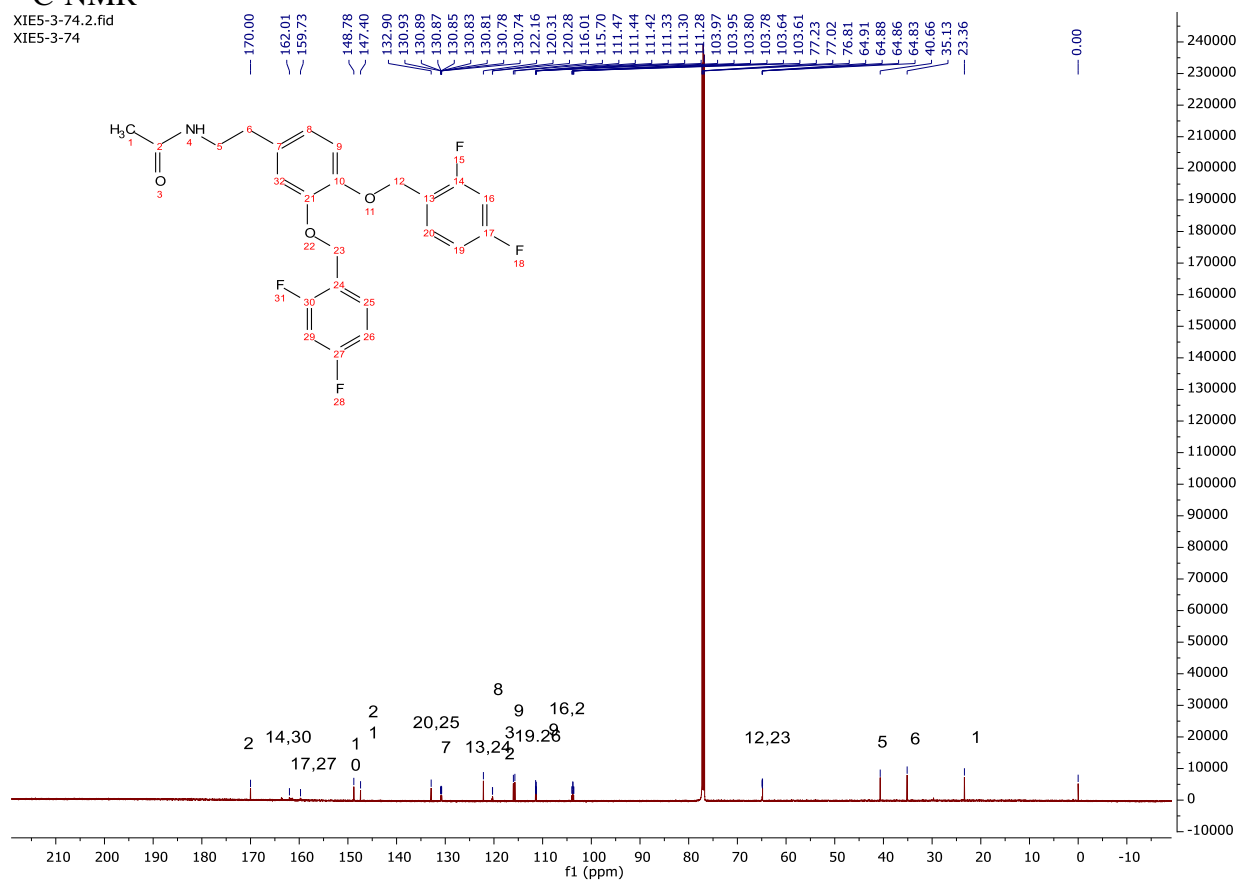
XIE5-2-75, *N*-(3,4-bis((4-fluorobenzyl)oxy)phenethyl)acetamide
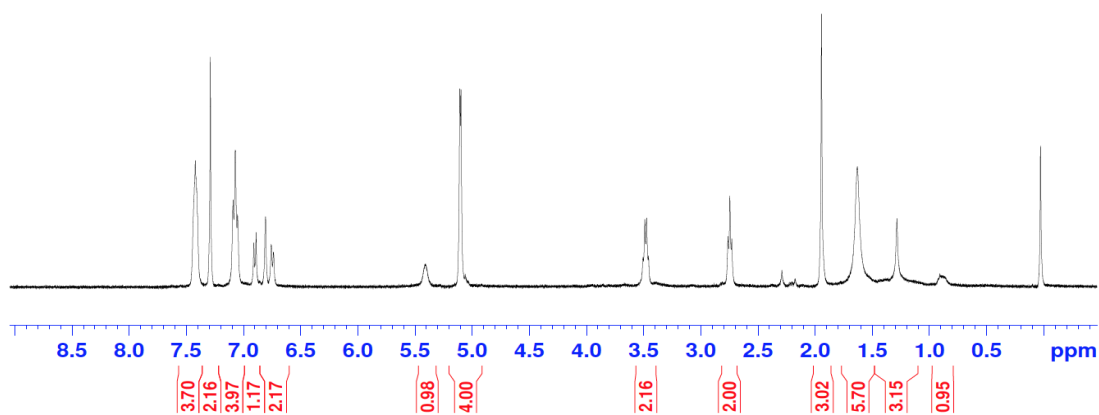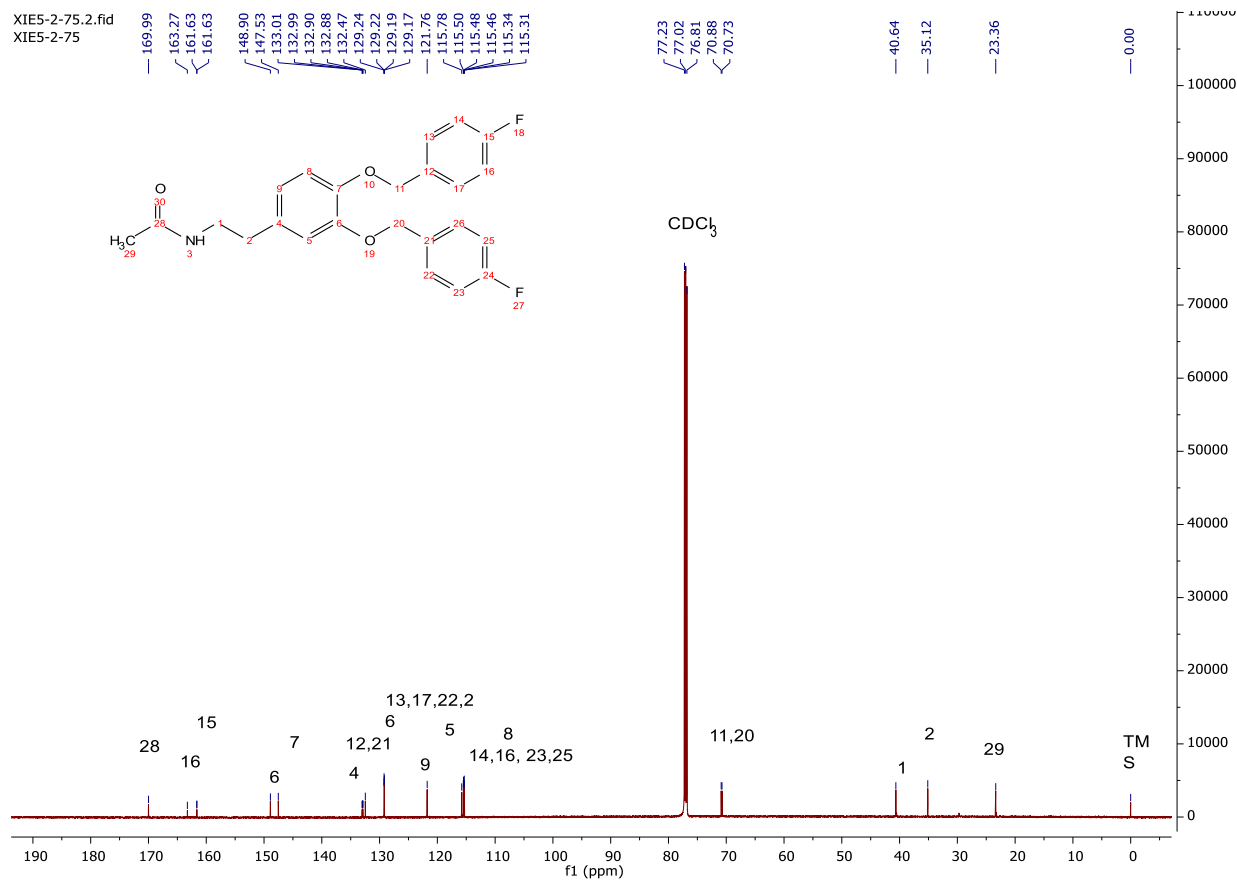
¹H-NMR

¹³C-NMR

XIE5-2-77, N-(3,4-bis((4-fluorobenzyl)oxy)phenethyl)cyclohexanecarboxamide
^{1}H-NMR

^{13}C-NMR

XIE5-2-78
^{1}H-NMR

7.26 CDCl3
7.09
7.08
7.04
7.03
6.95
6.95

5.49

3.48
3.47

2.80
2.79
2.53
2.53
2.04
2.03
2.02
2.02
2.01
1.82
1.81
1.80
1.80
1.58
1.57
1.56
1.55
1.28
1.26
1.26
1.23

0.00

3,4,34,35

28,29,32,33

9,10,23

6,26

13

12

17

1,31

18-22

4.00

2.02
2.08
3.01

4.00

2.31

2.00
1.14

6.11
5.50

5.19

8.0   7.5   7.0   6.5   6.0   5.5   5.0   4.5   4.0   3.5   3.0   2.5   2.0   1.5   1.0   0.5   0.0
f1 (ppm)

^{13}C-NMR

176.19
173.50
173.38
142.20
140.85
137.70
126.66
123.85
123.46
77.24
77.02
76.81
45.51
43.03
43.00
40.15
35.03
29.65
28.97
25.72
25.67
25.32
25.30
0.00

170000
160000
150000
140000
130000
120000
110000
100000
90000
80000
70000
60000
50000
40000
30000
20000
10000
0
-10000

f1 (ppm)

XIE5-2-79, N-(3,4-bis((2,4-difluorobenzyl)oxy)phenethyl)cyclohexanecarboxamide
^{1}H-NMR

^{13}C-NMR

XIE5-3-79.2.1.1r
XIE5-3-79
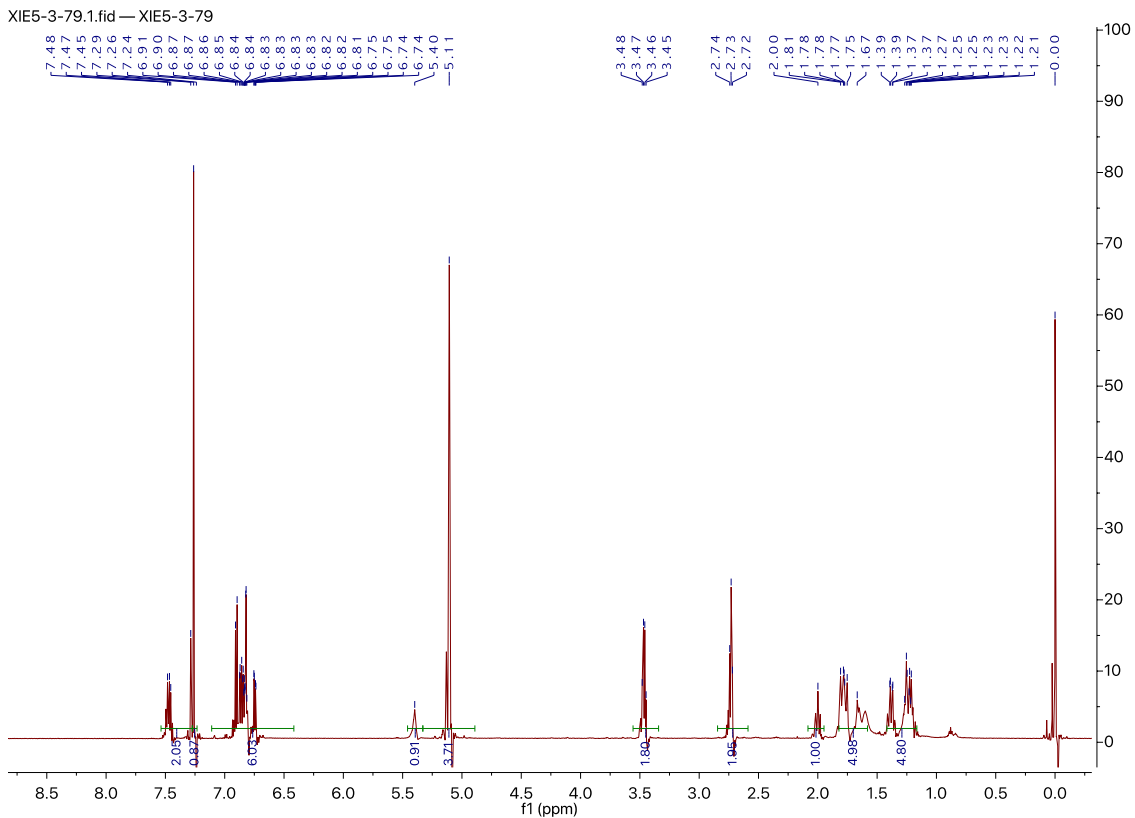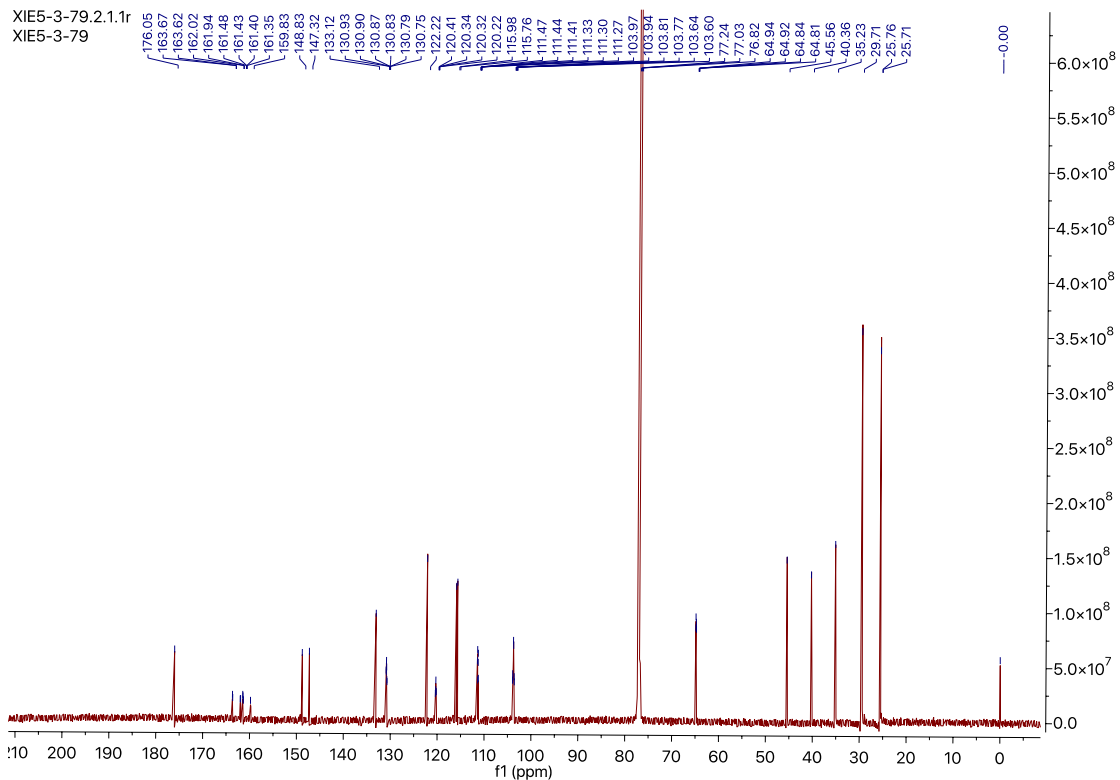
XIE5-2-80, N-(3,4-bis((4-chlorobenzyl)oxy)phenethyl)cyclohexanecarboxamide

^{1}H-NMR

XIE5-3-80.1.fid
XIE5-3-80

7.37
7.35
7.34
7.34
7.33
7.32
7.26
6.86
6.84
6.78
6.77
6.71
6.70
6.70
6.70

5.08

3.46
3.45
3.44
3.43

2.72
2.71
2.70

1.98
1.79
1.77
1.75
1.38
1.36
1.26
1.23
1.22
1.21

7.70
1.00
1.02
1.03
4.00
2.09
2.05
1.17
1.97
8.61

^{13}C-NMR

XIE5-3-80.2.fid
XIE5-3-80

176.01

148.80
147.32
135.76
135.62
133.69
133.64
132.69
128.69
128.68
128.67
128.65
121.85
115.61
115.36

77.23
77.02
76.81
70.72
70.56

45.54
40.32
35.22
29.70
25.73
25.71

-0.01
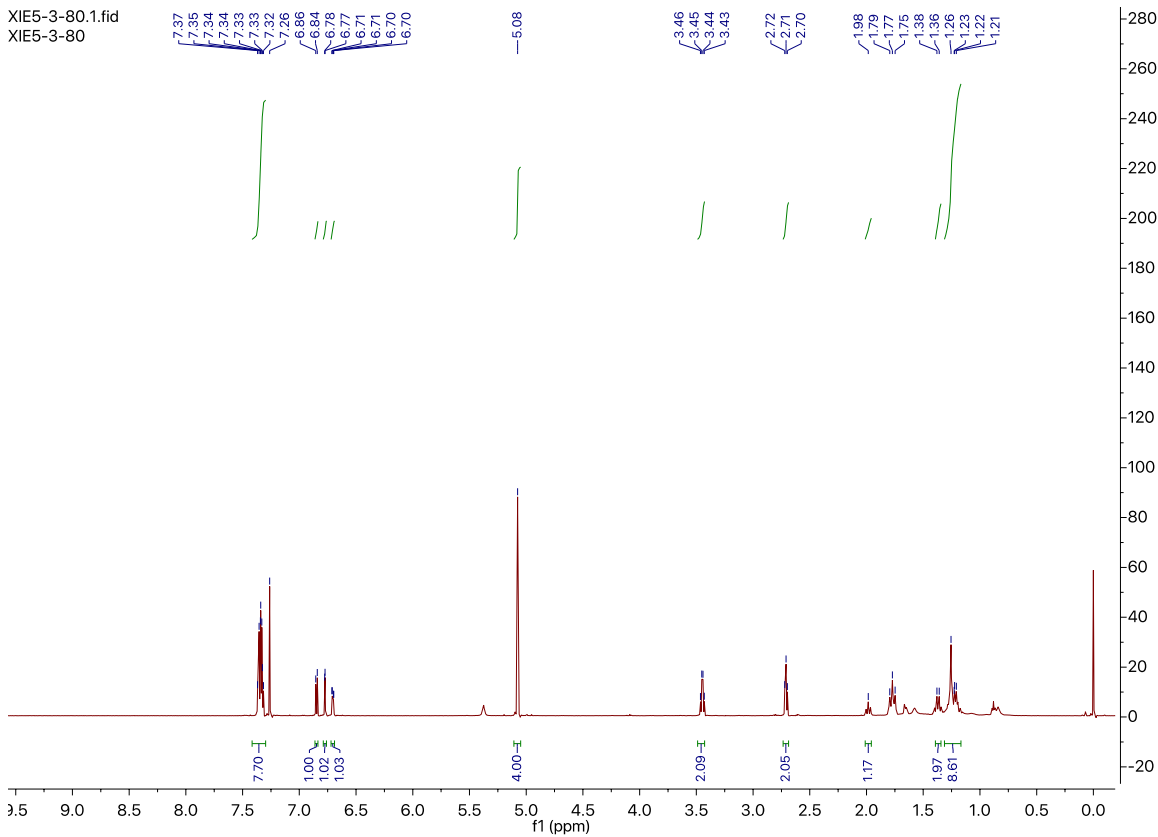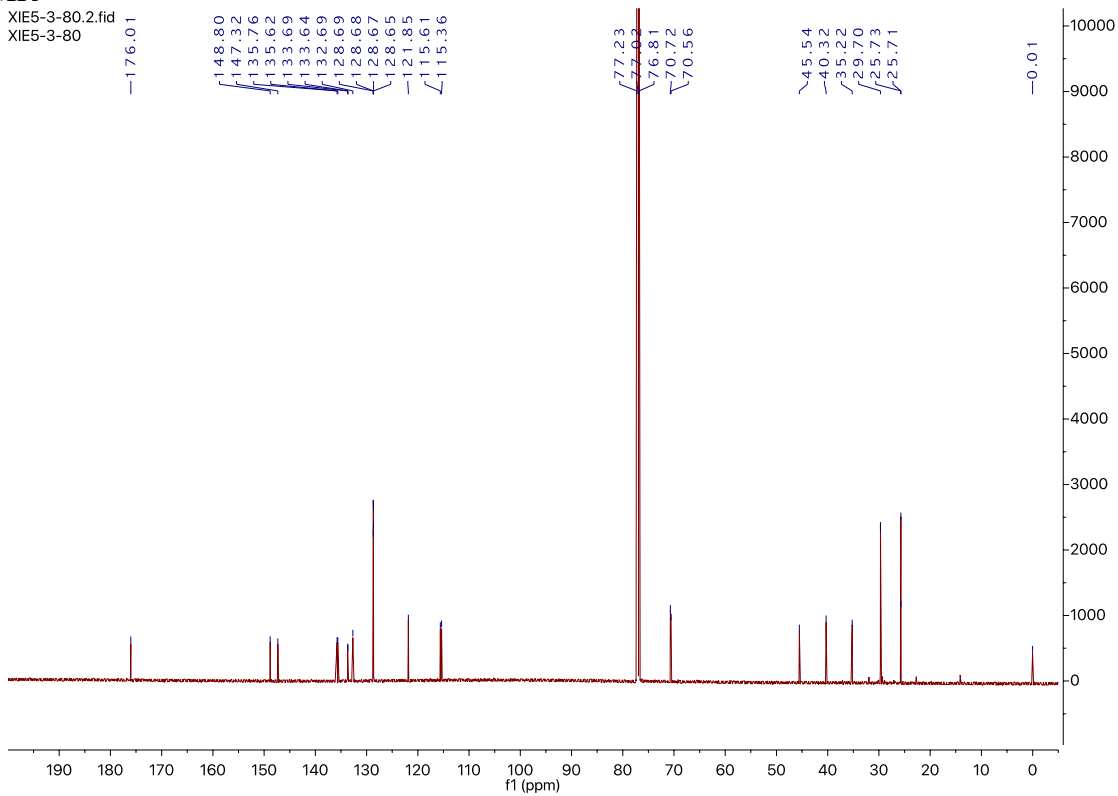
XIE5-1-83, 3,5-bis((4-chlorobenzyl)oxy)benzaldehyde

421

¹H-NMR

XIE5-3-83.1.fid — XIE5-3-83
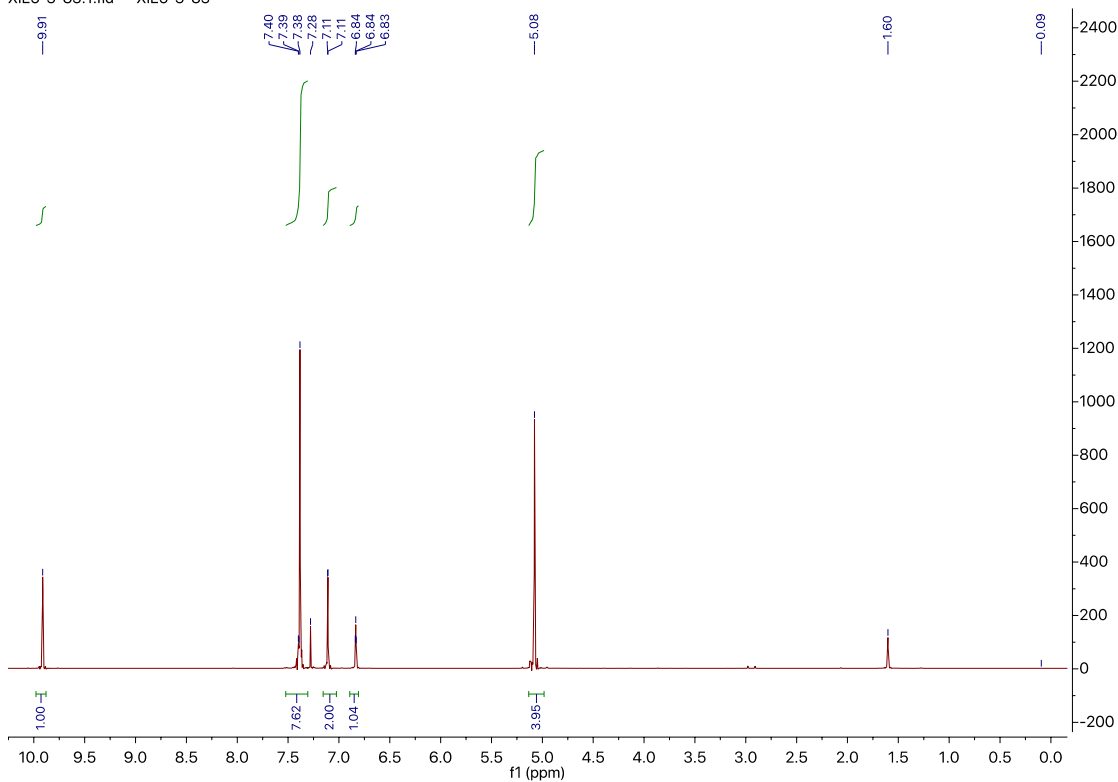
¹³C-NMR

XIE5-3-83.2.fid — XIE5-3-83
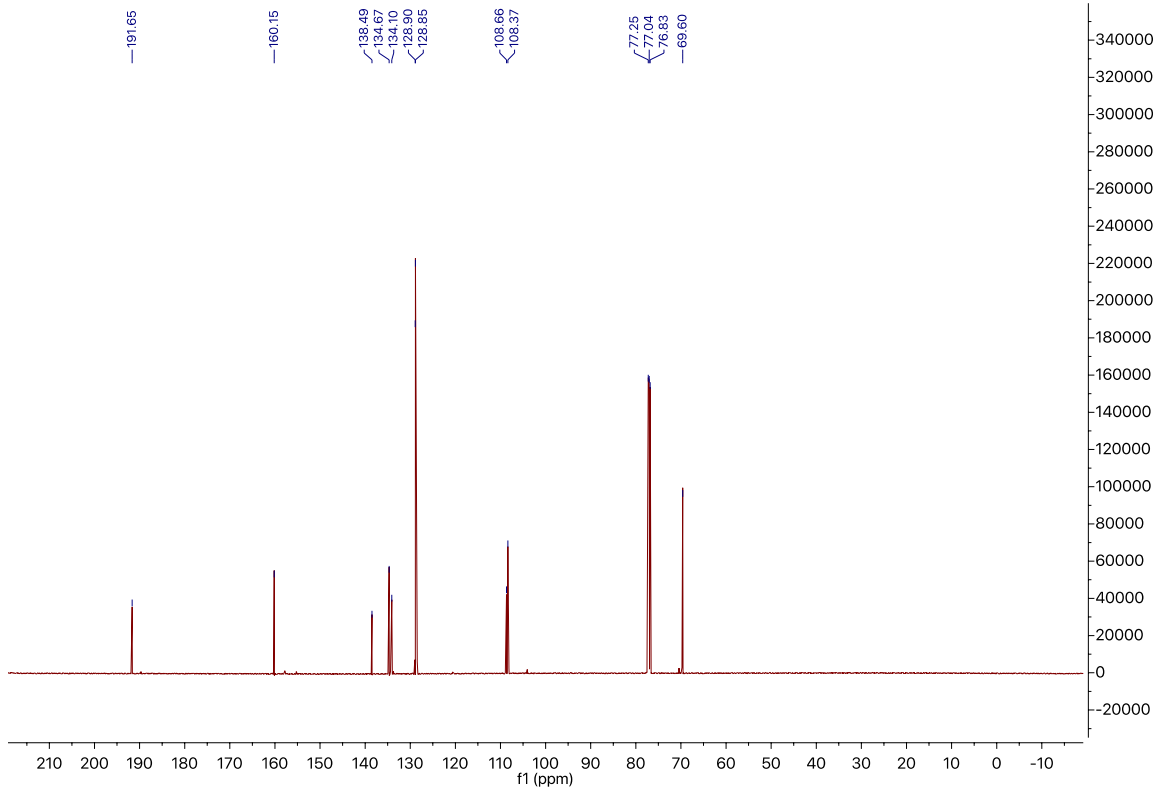
XIE5-1-82, 3,5-bis((4-methylbenzyl)oxy)benzaldehyde

^{1}H-NMR

XIE5-3-84.1.fid — XIE5-3-84

9.91
7.34
7.33
7.28
7.23
7.22
7.12
7.11
6.87
5.06
2.39
1.59
0.10

1.00
4.00
4.03
2.10
1.22
4.08
6.11
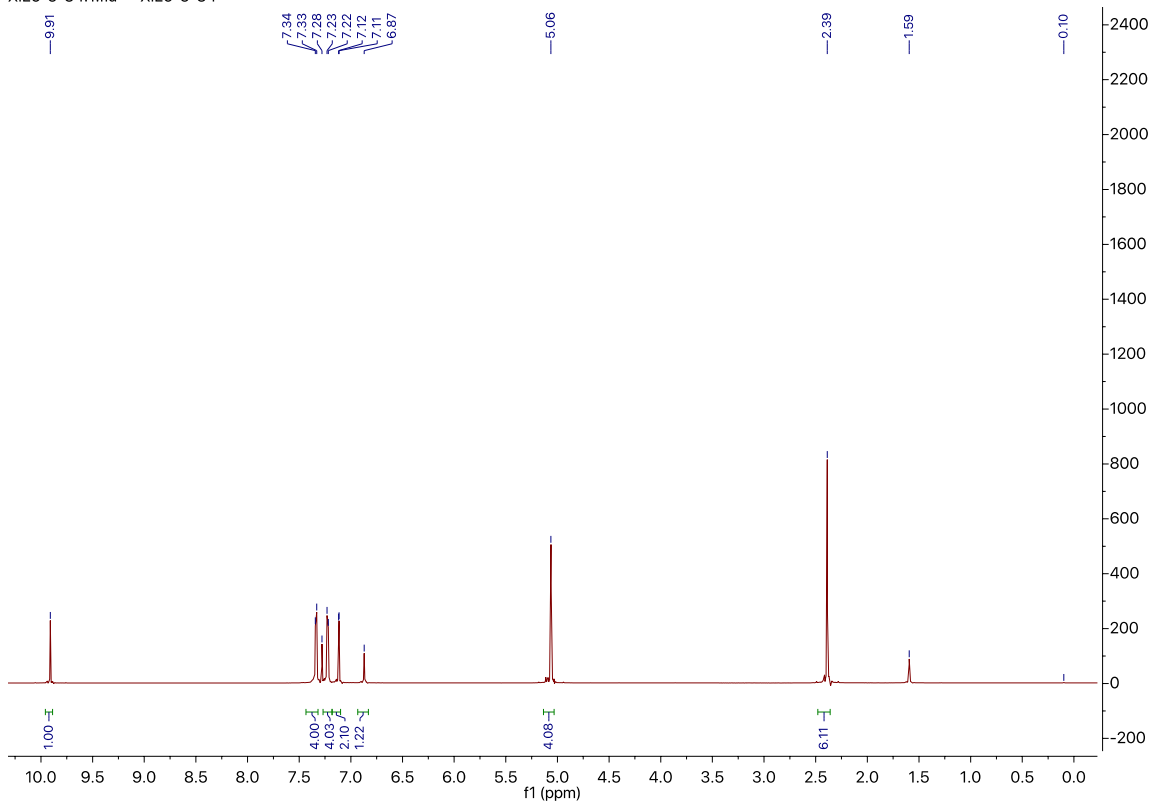
^{13}C-NMR

XIE5-3-84.2.fid — XIE5-3-84

191.93
160.43
138.37
138.08
133.20
129.37
127.74
108.72
108.27
70.34
21.24
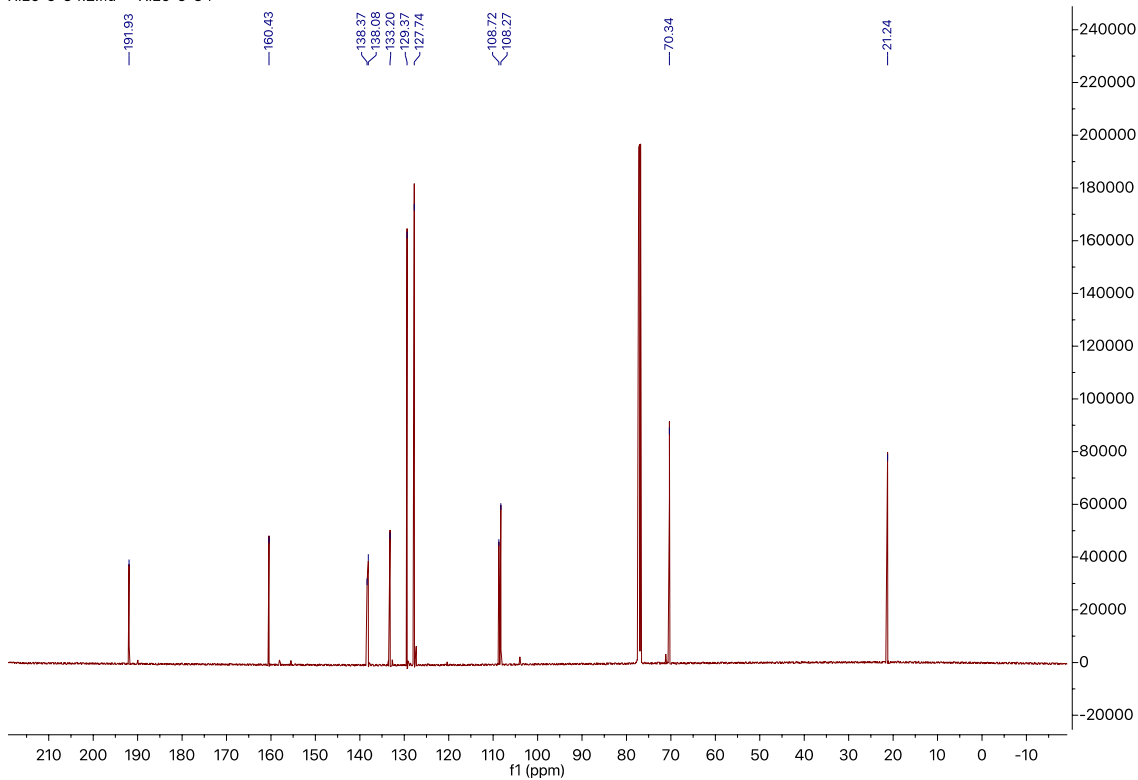
XIE5-2-89, N1-(3,5-bis((4-methylbenzyl)oxy)benzyl)ethane-1,2-diamine

423

¹H-NMR

XIE5-3-89.3.fid
XIE5-3-89

9.91

8.20

7.32
7.31
7.28
7.20
7.19
7.17
6.97
6.97
6.67
6.67

5.06
5.01

3.98
3.80
3.78
3.76

3.22
3.21
3.20

2.37

1,21

3,4,25,26,
18,19,22,2
3

24

9,13

29

6,16

12

11

27

0.91

1.00

8.01

1.24

2.02

4.89

1.87

1.68

1.87

6.12

1.5 11.0 10.5 10.0 9.5 9.0 8.5 8.0 7.5 7.0 6.5 6.0 5.5 5.0 4.5 4.0 3.5 3.0 2.5 2.0 1.5 1.0 0.5 0.0 -0.5 -1.0
f1 (ppm)

¹³C-NMR

424

162.68
160.14

138.37
138.28
138.08
137.82
133.20
133.65
129.38
129.27
129.23
129.21
127.75
127.74

108.27
106.87
104.91

77.25
77.04
76.83
70.34
70.12

61.42
57.07
50.79

21.22

CH₃

CDCl₃

8 14

10

5,17

2,20

3,26,22,1

9

4,25,18,23

9, 10, 24

8,16

11

f1 (ppm)

XIE5-2-90, 2-((3,5-bis((4-chlorobenzyl)oxy)benzyl)amino)ethan-1-ol
^{1}H-NMR

7.37
7.37
7.36
7.35
7.34
7.33
7.33
7.33
7.31
7.29
7.28
7.28
6.78
6.78
6.54
6.53
6.53
5.01
4.58
4.35
4.04
4.01
3.99
3.84
2.92
-0.09

f1 (ppm)

8.03
1.89
1.00
3.86
0.62
1.02
2.19
1.97
1.83

^{13}C-NMR

160.08
135.12
134.96
133.90
128.95
128.88
128.87
128.83
128.81
128.76
128.43
108.58
107.25
102.72
101.59
77.24
77.03
76.82
69.42
58.17
49.10

f1 (ppm)
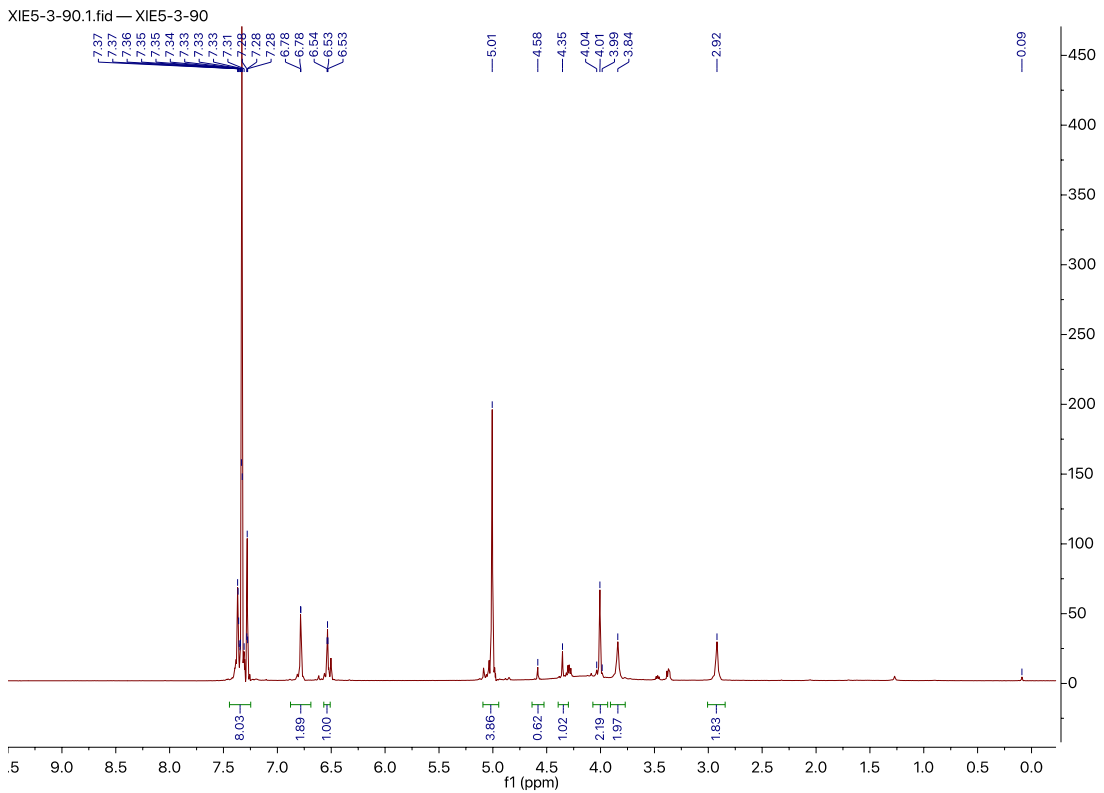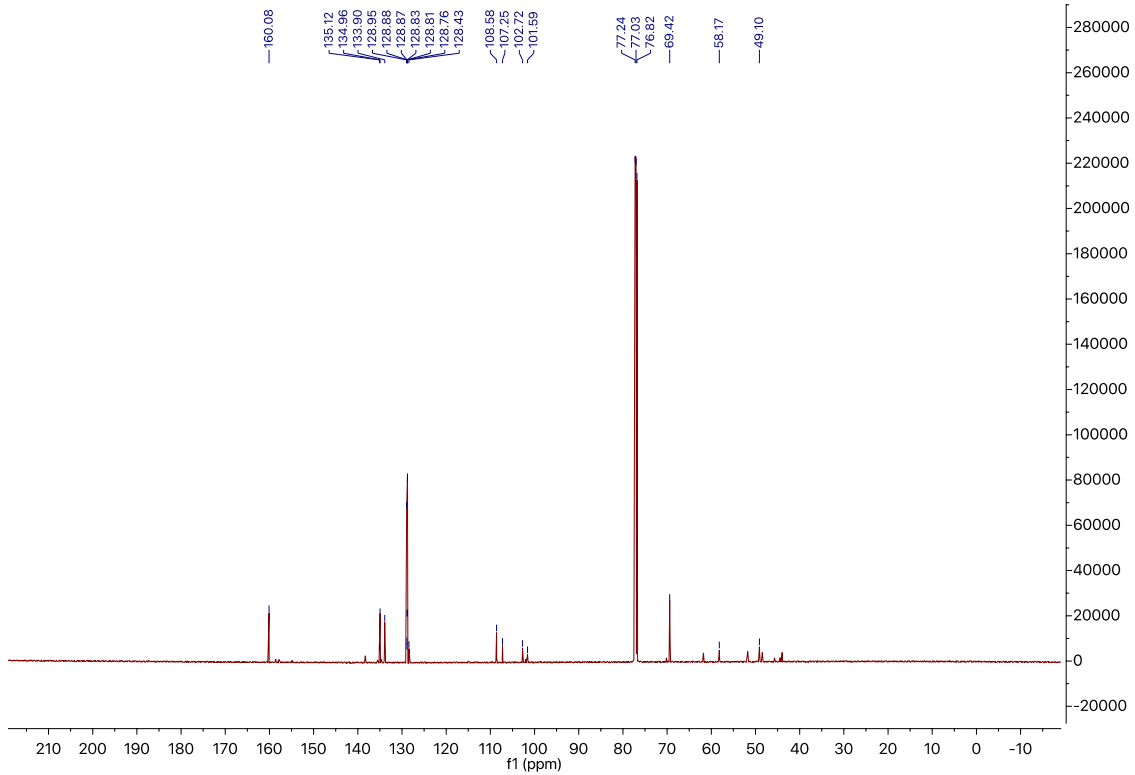
Appendix C. Drug-Dose Response Curves in MTT Assay

We determined the IC_{50} values for the antiproliferative effects of each compound on three different multiple myeloma cell lines. Each data was replicated in three wells. The detailed methods used for MTT assays were mentioned on Page 105 of this dissertation. The IC_{50} values were summarized in **Table 4** to **Table 10** on Page 106 to Page 118. The dose-dependent curves for each compound were listed below.

XIE5-2-1
Anti-proliferative effects on multiple myeloma cell lines
MM1.S. cells
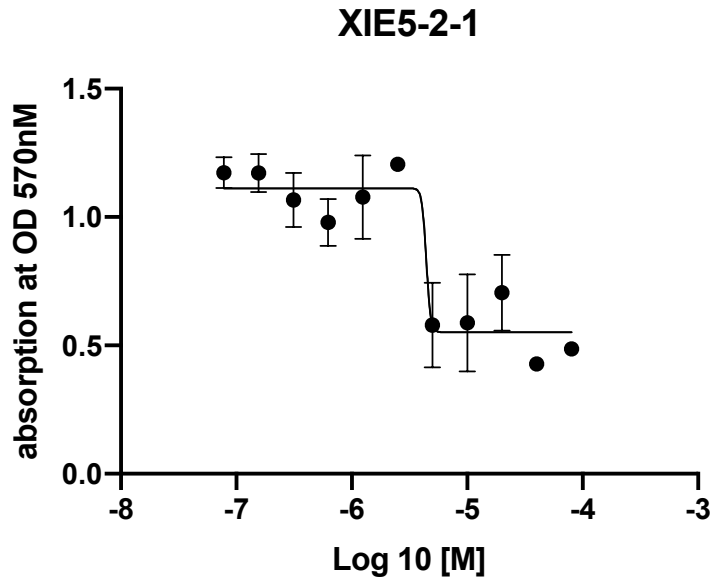
XIE5-2-1

	IC50
XIE5-2-1	~ 4.426e-006

RPMI8226 cells
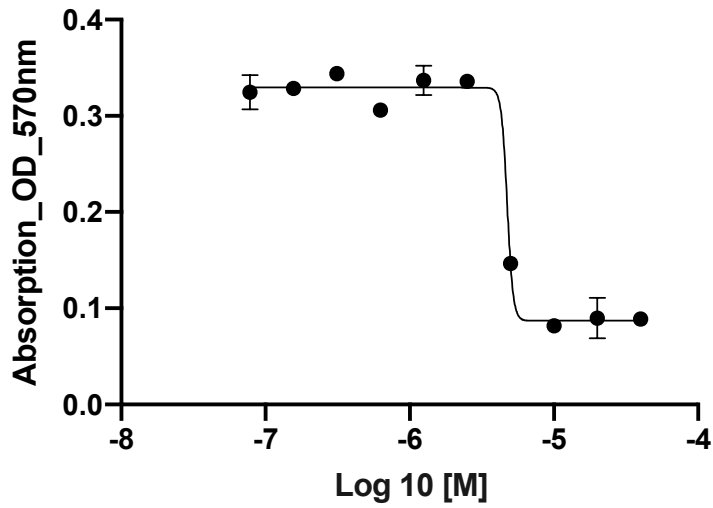
XIE5-2-1

	IC50
XIE5-2-1	~ 4.743e-006

U266 cells
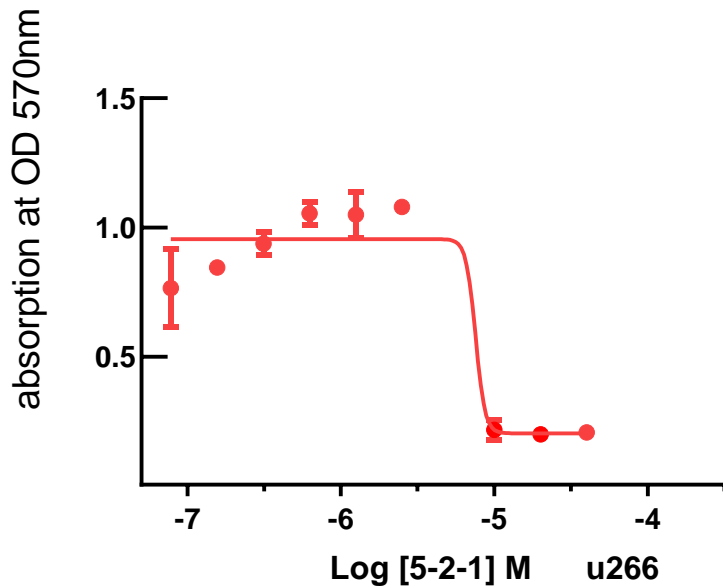
	XIE5-2-1
IC50	~ 7.534e-006

Neuro-protective effects on differentiated SH-SY5Y cells against hydrogen peroxide

Neuroprotective effect against H_2O_2 induced toxicity
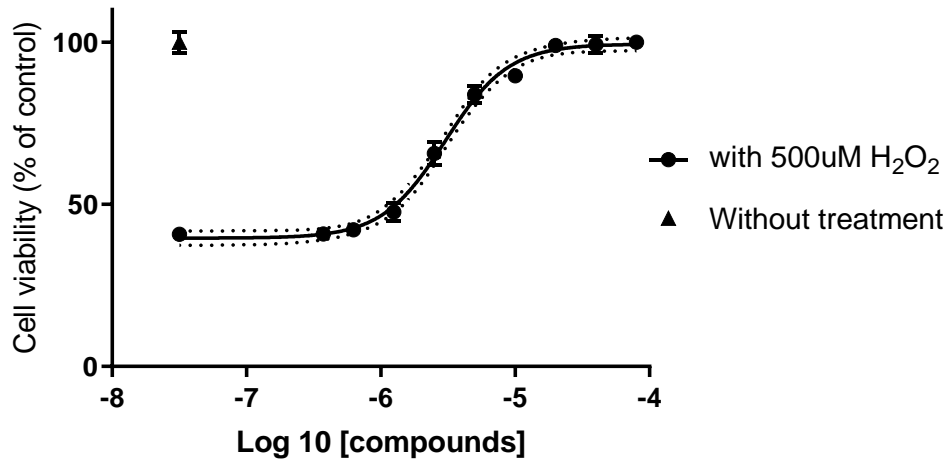
	with 500uM H_2O_2
IC50	3.014e-006

XIE5-2-2

Anti-proliferative effects on multiple myeloma cell lines
MM1.S. cells
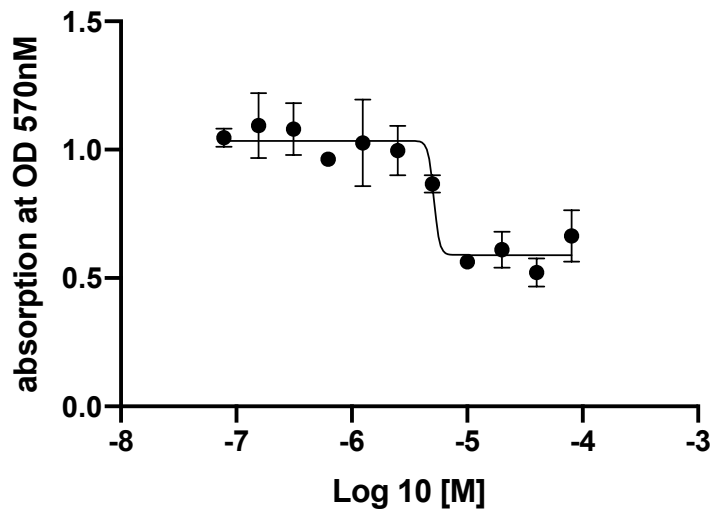
XIE5-2-2

	IC50
XIE5-2-2	~ 5.144e-006

RPMI8226 cells
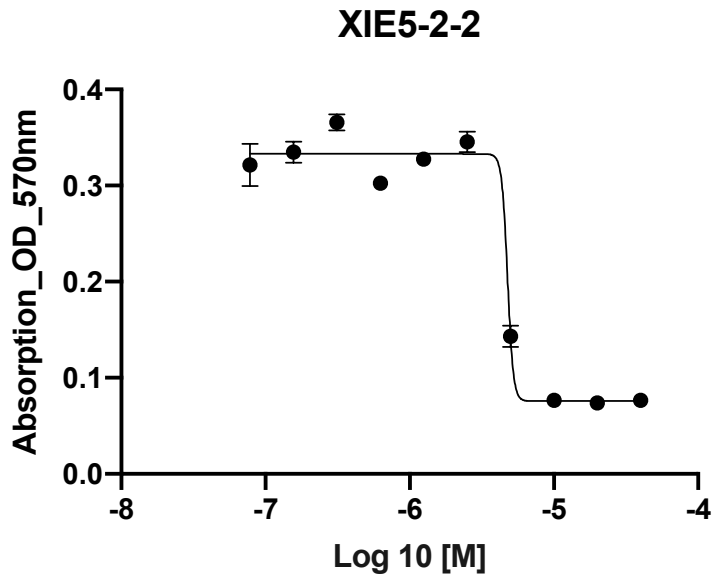
XIE5-2-2

	IC50
XIE5-2-2	~ 4.767e-006

U266 cells
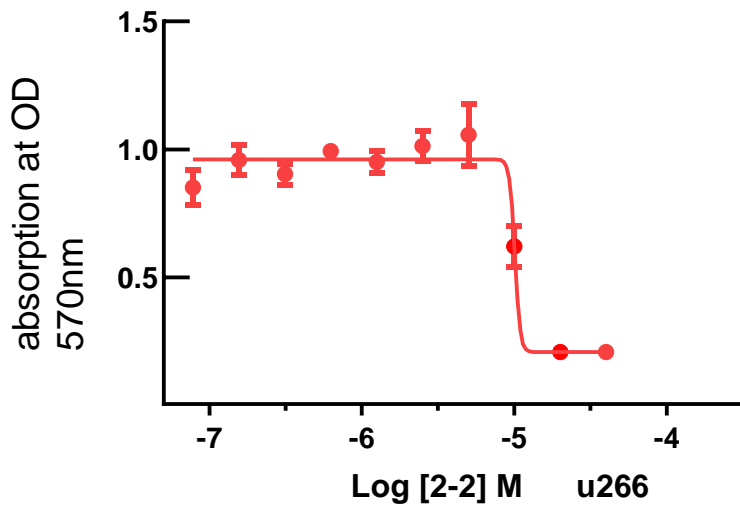
	5-2-2
IC50	~ 1.008e-005

Neuro-protective effects on differentiated SH-SY5Y cells against hydrogen peroxide
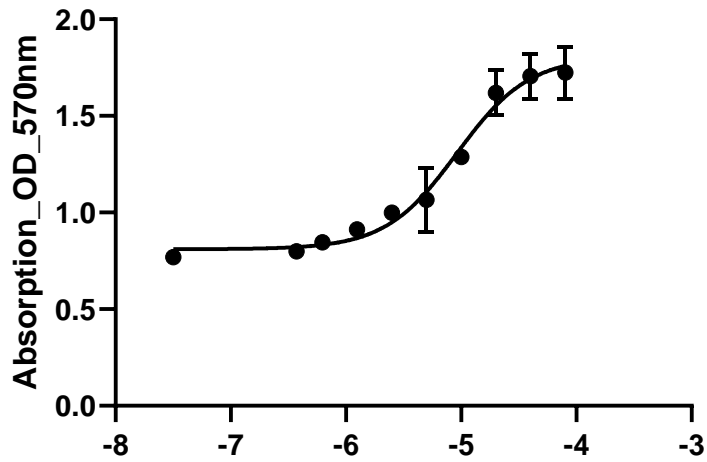
XIE5-2-2

	IC50
XIE5-2-2	9.218e-006

XIE5-2-3 (4.7)
Anti-proliferative effects on multiple myeloma cell lines
MM1.S. cells
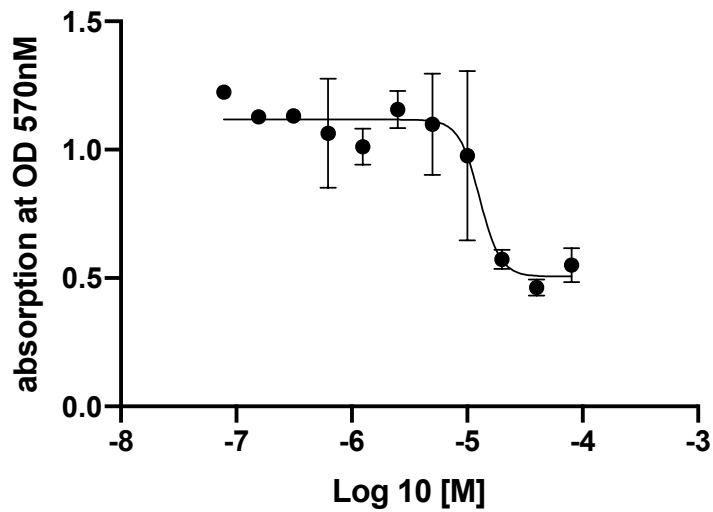
XIE5-2-3

	IC50
XIE5-2-3	1.283e-005

RPMI8226 cells

U266 cells

	5-2-3
IC50	1.351e-005

Neuro-protective effects on differentiated SH-SY5Y cells against hydrogen peroxide

XIE5-2-3

	IC50
XIE5-2-3	1.314e-005

XIE5-2-7

Anti-proliferative effects on multiple myeloma cell lines
MM1.S. cells

XIE5-2-7

	IC50
XIE5-2-7	1.567e-006

XIE5-2-7

	IC50
XIE5-2-7	3.059e-006

RPMI8226 cells

XIE5-2-7
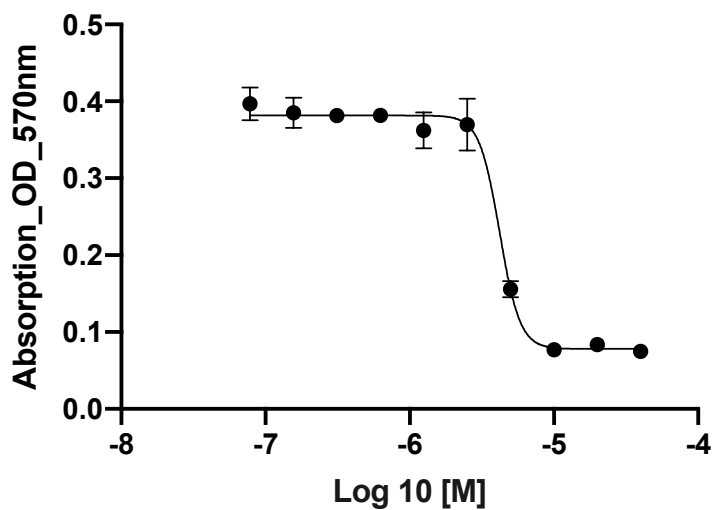
	IC50
XIE5-2-7	4.200e-006

U266 cells
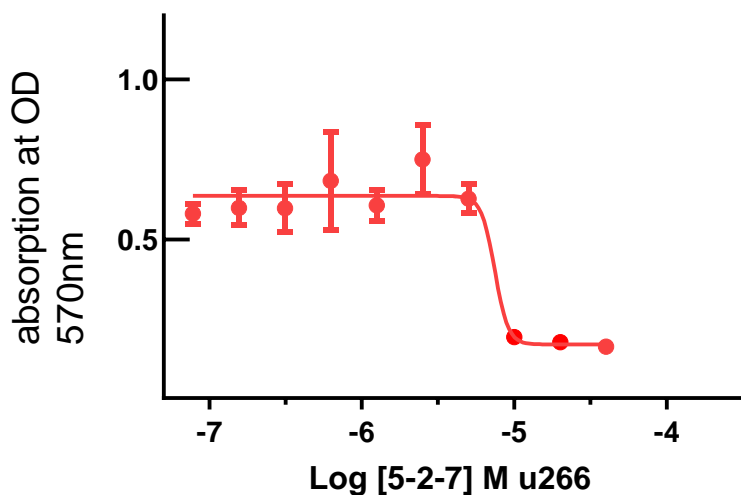
	5-2-7
IC50	7.437e-006

Neuro-protective effects on differentiated SH-SY5Y cells against hydrogen peroxide
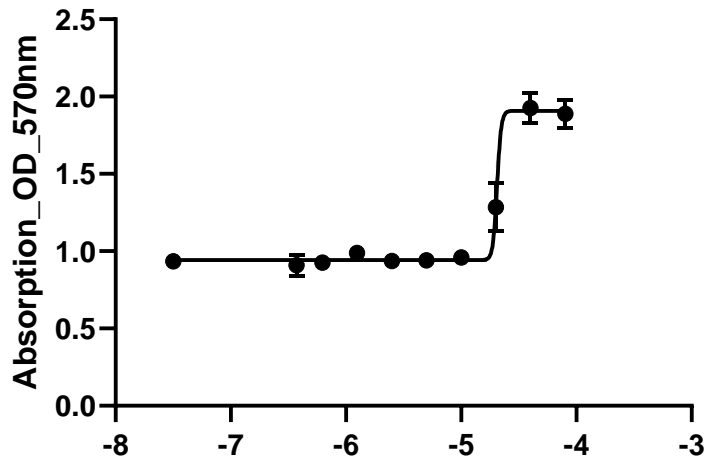
XIE5-2-7

	IC50
XIE5-2-7	~ 2.050e-005

XIE5-2-9

Anti-proliferative effects on multiple myeloma cell lines
MM1.S. cells

XIE5-2-9
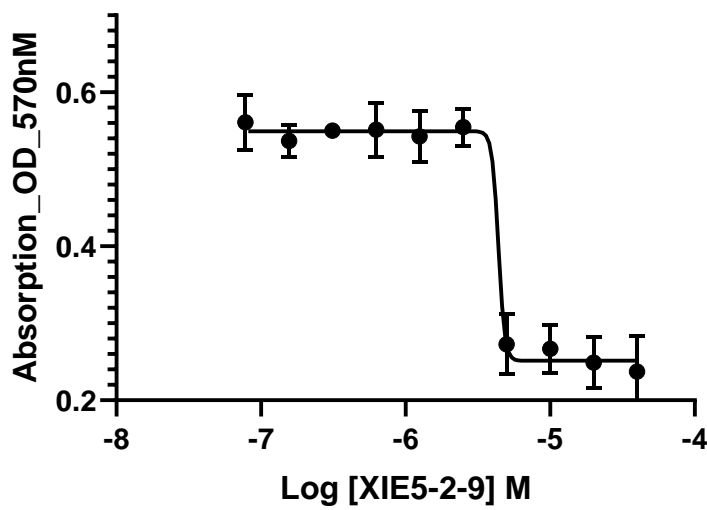
	IC50
XIE5-2-9	~ 4.397e-006

XIE5-2-9
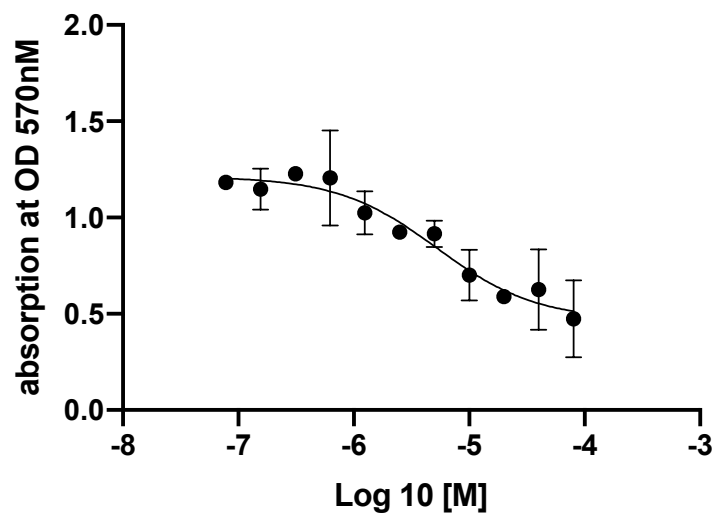
	IC50
XIE5-2-9	5.264e-006

RPMI8226 cells

XIE5-2-9
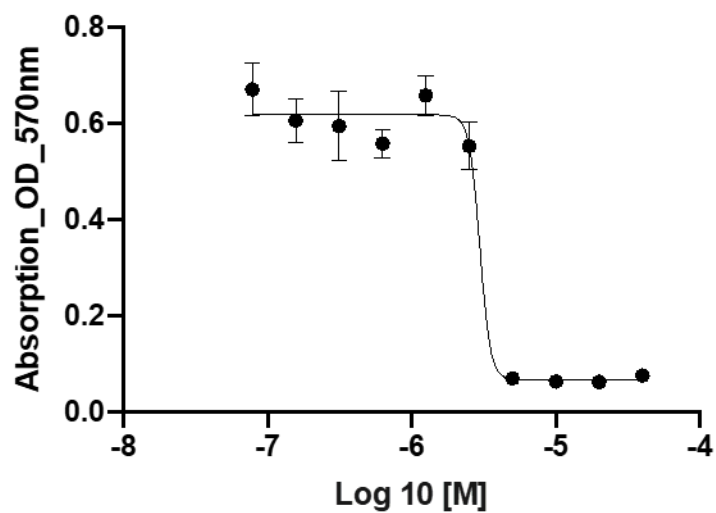
	IC50
XIE5-2-9⁻	2.968e-006

U266 cells

Log [5-2-9] M   u266

	5-2-9
IC50	~ 4.914e-006
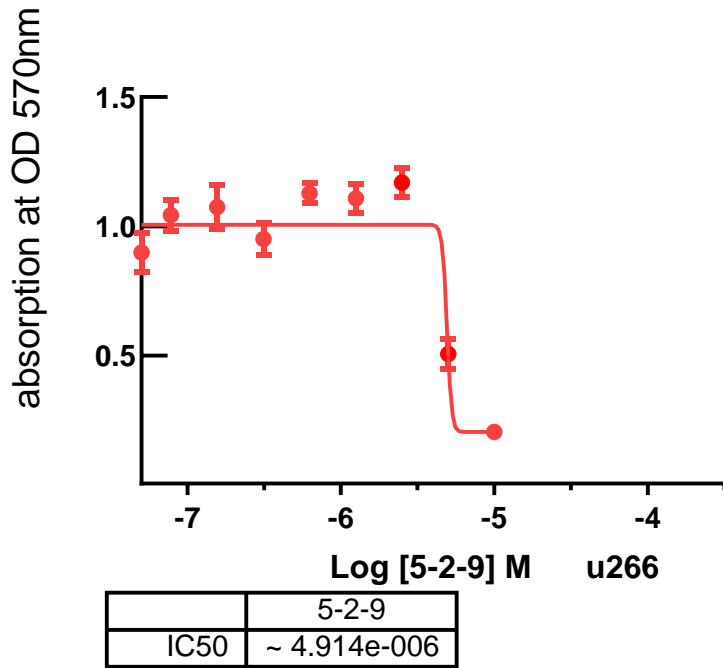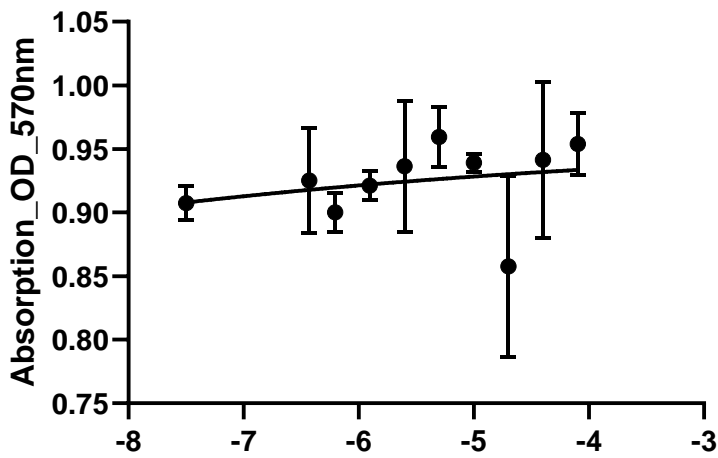
SH-SY5Y

XIE5-2-9

XIE5-2-10
Anti-proliferative effects on multiple myeloma cell lines
MM1.S. cells

XIE5-2-10
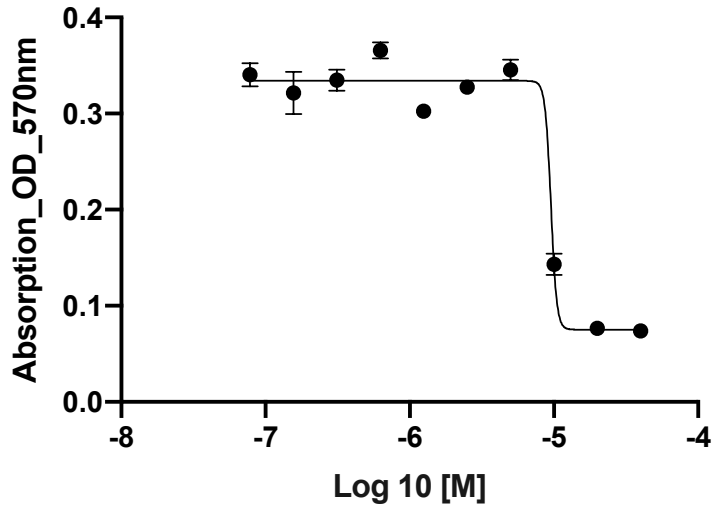
	IC50
XIE5-2-10	~ 9.532e-006

RPMI8226 cells

XIE5-2-10
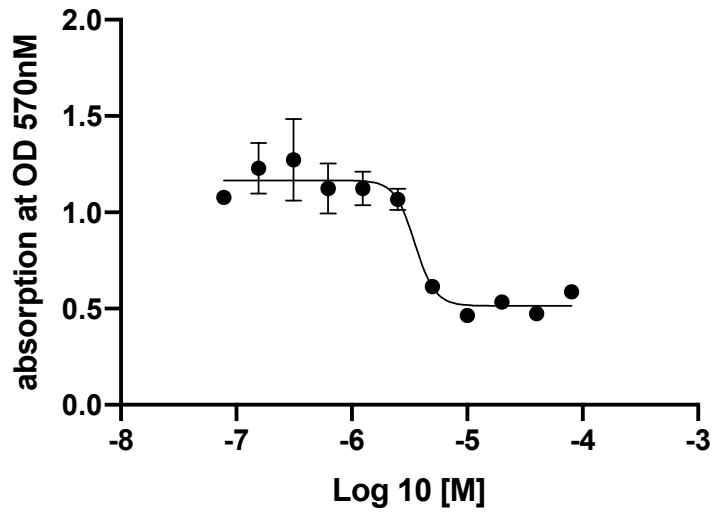
	IC50
XIE5-2-10	3.522e-006

U266 cells
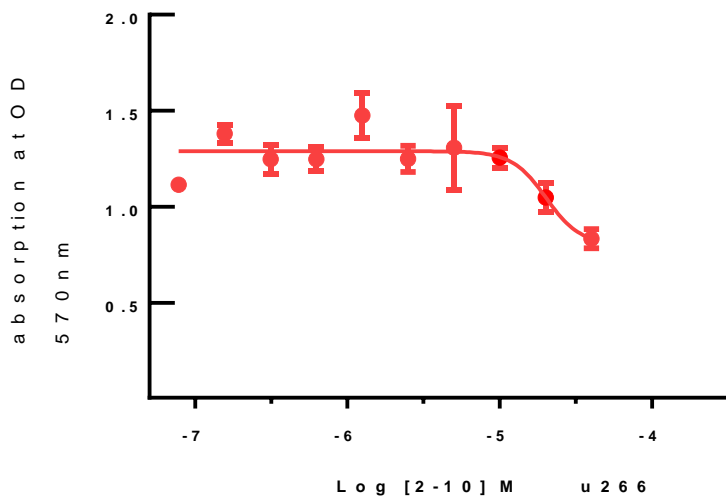
	2-10
IC50	2.012e-005

Neuro-protective effects on differentiated SH-SY5Y cells against hydrogen peroxide

XIE5-2-10
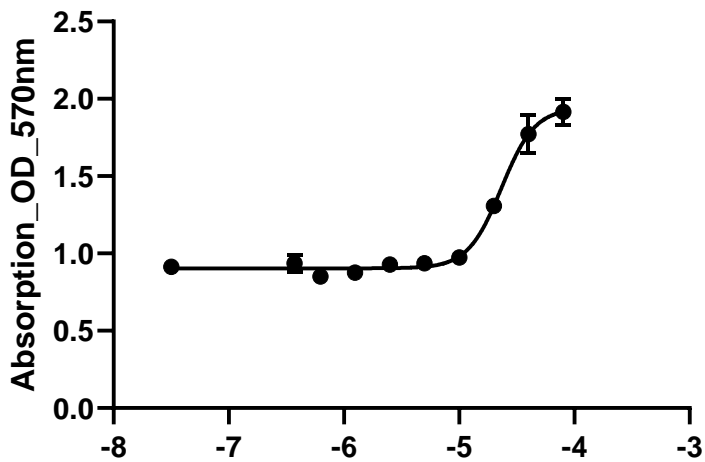
	IC50
XIE5-2-10	2.327e-005

XIE5-2-11

Anti-proliferative effects on multiple myeloma cell lines
MM1.S. cells

XIE5-2-11
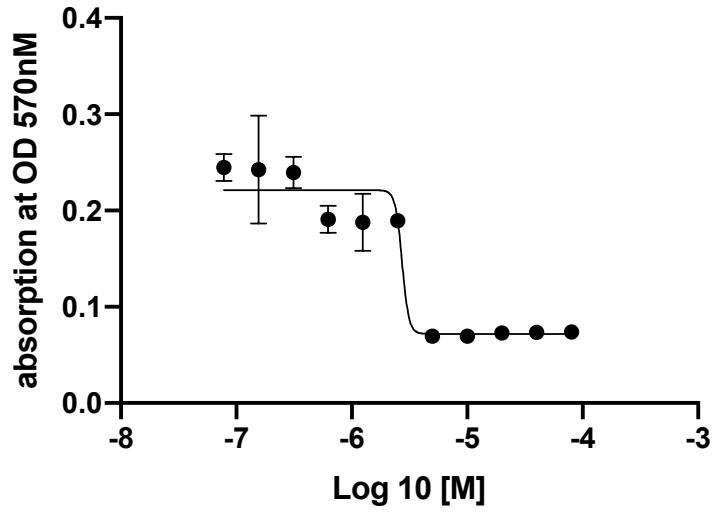
	IC50
XIE5-2-11	~ 2.730e-006

RPMI8226 cells

XIE5-2-11
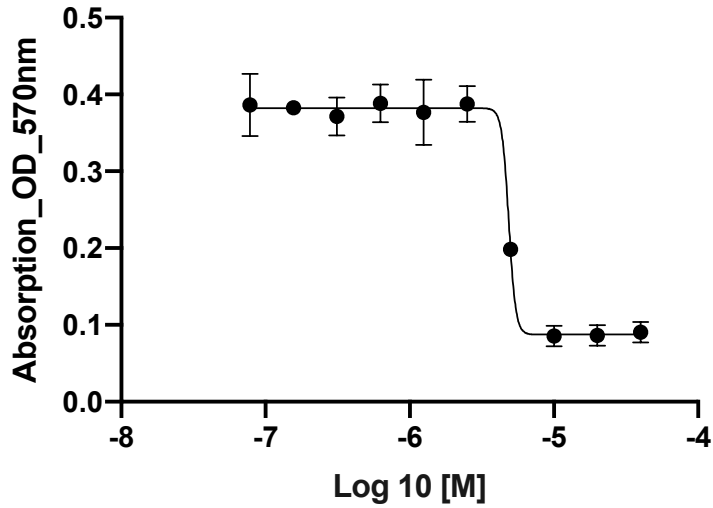
	IC50
XIE5-2-11	~ 4.863e-006

U266 cells
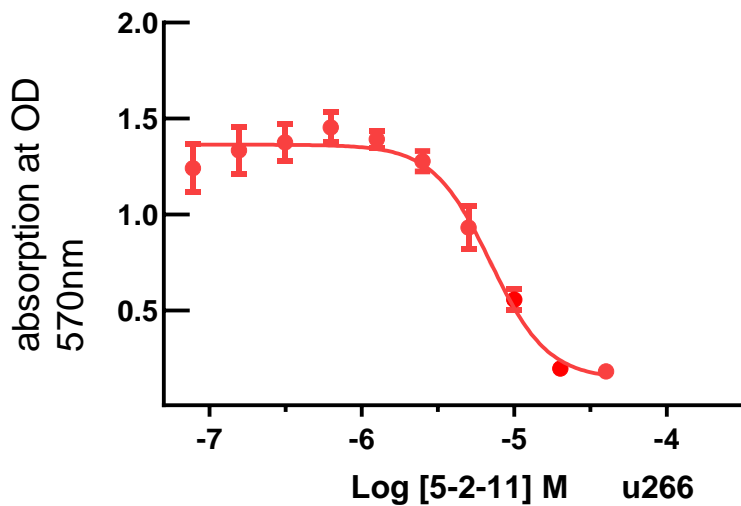
440

	5-2-11
IC50	6.950e-006

Neuro-protective effects on differentiated SH-SY5Y cells against hydrogen peroxide

XIE5-2-11

	IC50
XIE5-2-11	~ 9.834e-006
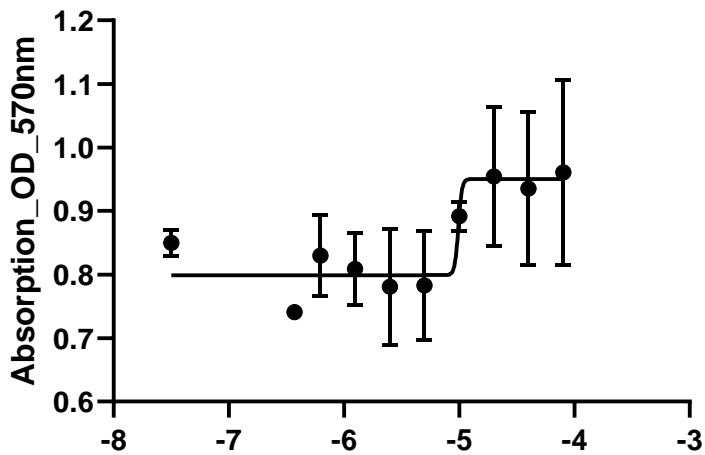
XIE5-2-13

Anti-proliferative effects on multiple myeloma cell lines
MM1.S. cells

XIE5-2-13
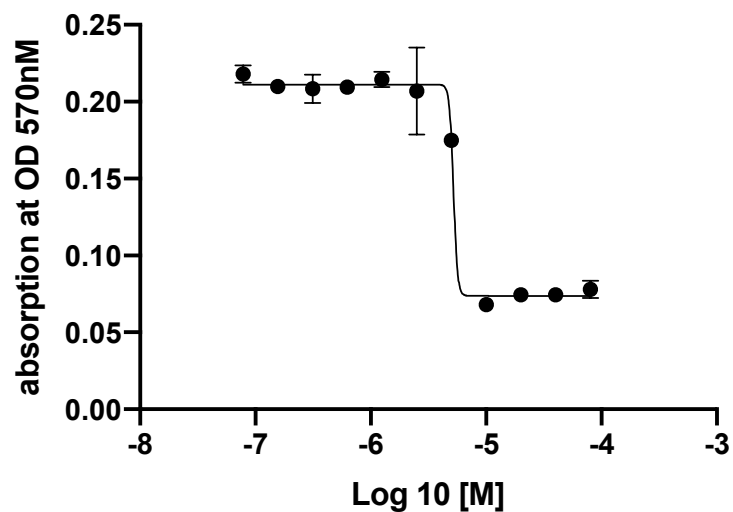
	IC50
XIE5-2-13	~ 5.209e-006

RPMI8226 cells

MTT_RPMI8226_XIE5-2-13

	IC50
XIE5-2-13	~ 4.913e-006

U266 cells
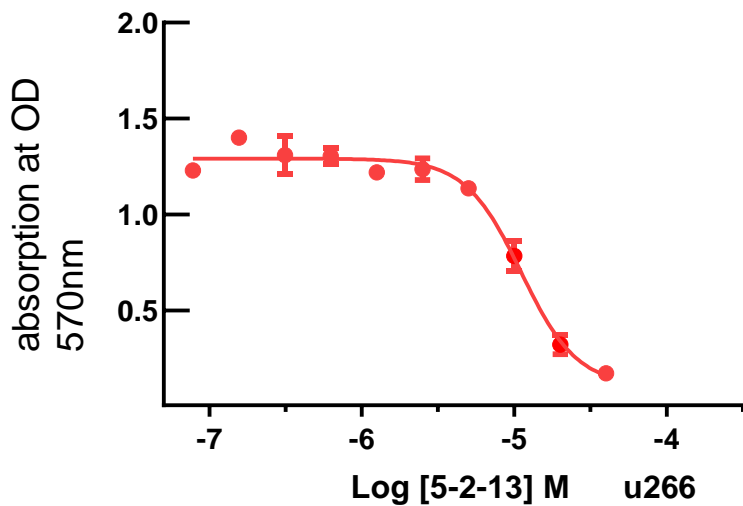
	5-2-13
IC50	1.107e-005

Neuro-protective effects on differentiated SH-SY5Y cells against hydrogen peroxide

XIE5-2-13
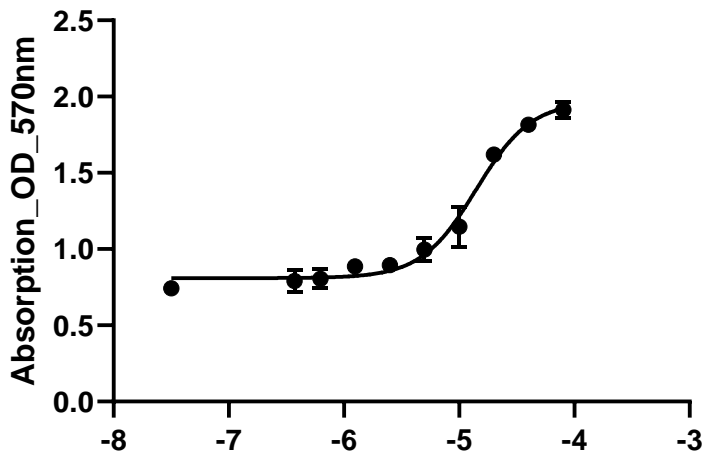
	IC50
XIE5-2-13	1.403e-005

XIE5-2-14
Anti-proliferative effects on multiple myeloma cell lines
MM1.S. cells

XIE5-2-14
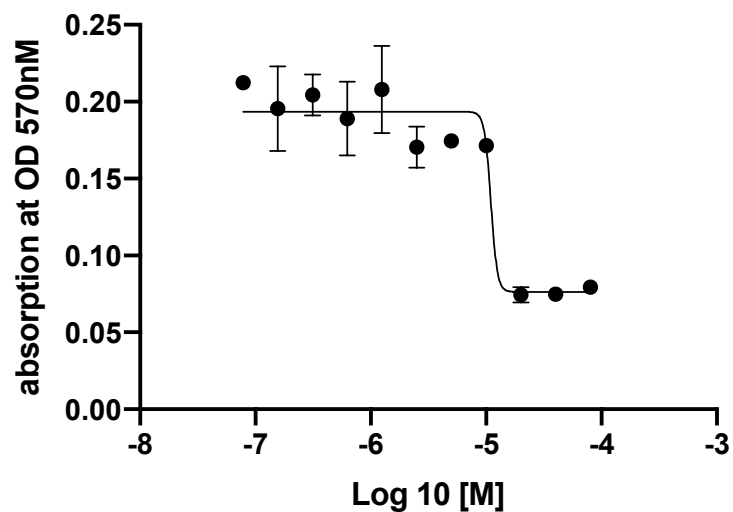
	IC50
XIE5-2-14	~ 1.098e-005

RPMI8226 cells

MTT_RPMI8226_XIE5-2-14
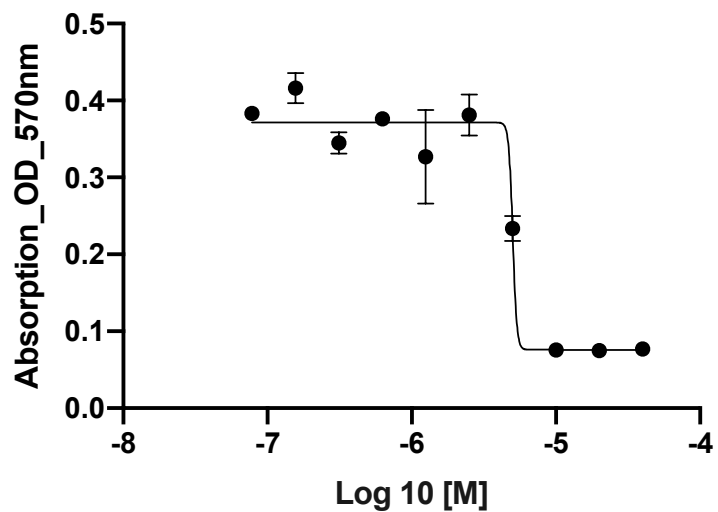
	IC50
XIE5-2-14	~ 5.021e-006

U266 cells
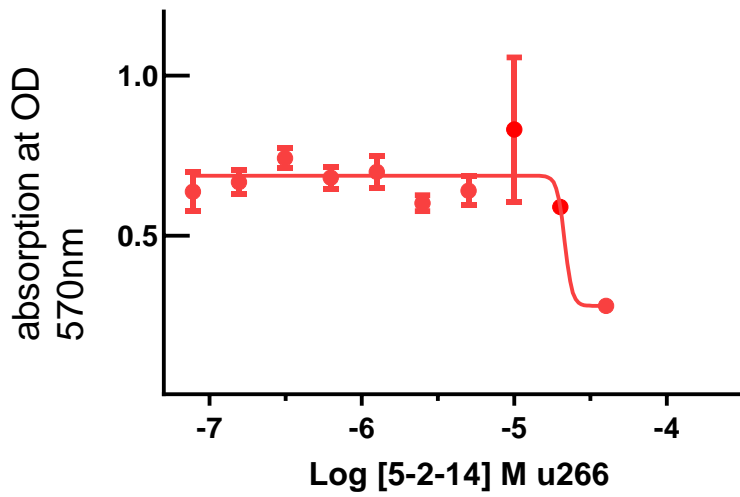
	5-2-14
IC50	~ 2.135e-005

Neuro-protective effects on differentiated SH-SY5Y cells against hydrogen peroxide

XIE5-2-14

	IC50
XIE5-2-14	8.064e-006

XIE5-2-15
Anti-proliferative effects on multiple myeloma cell lines
MM1.S. cells

XIE5-2-15
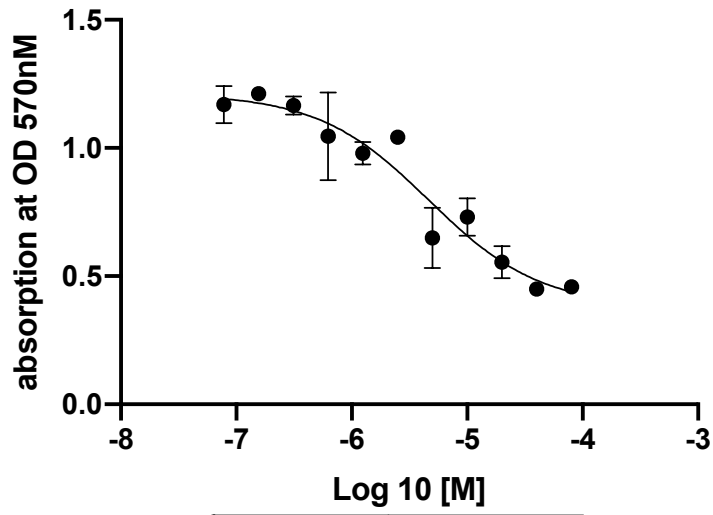
	IC50
XIE5-2-15	4.674e-006

RPMI8226 cells

XIE5-2-15

	IC50
XIE5-2-15	~ 5.328e-006

U266 cells
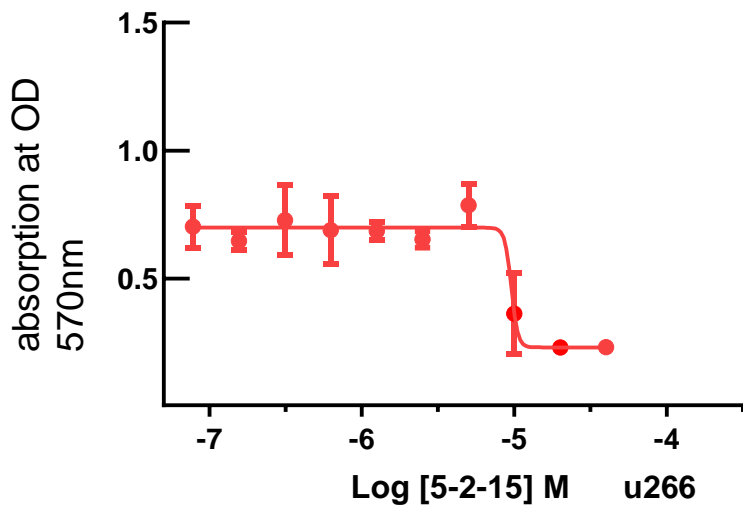
	5-2-15
IC50	~ 9.552e-006

Neuro-protective effects on differentiated SH-SY5Y cells against hydrogen peroxide

XIE5-2-15

	IC50
XIE5-2-15	1.423e-005
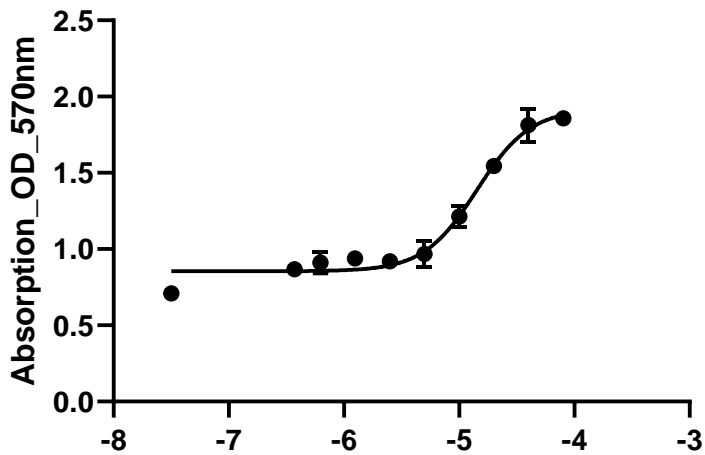
XIE5-2-16
Anti-proliferative effects on multiple myeloma cell lines
MM1.S. cells

XIE5-2-16
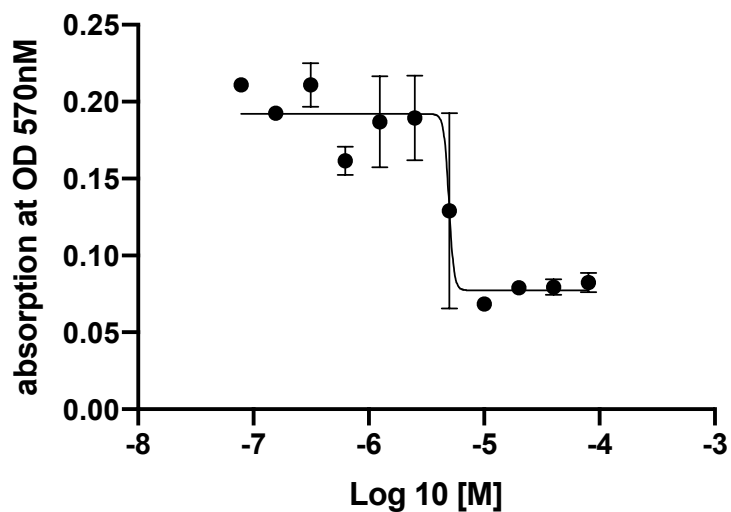
	IC50
XIE5-2-16	~ 4.950e-006

RPMI8226 cells

MTT_RPMI8226_XIE5-2-16
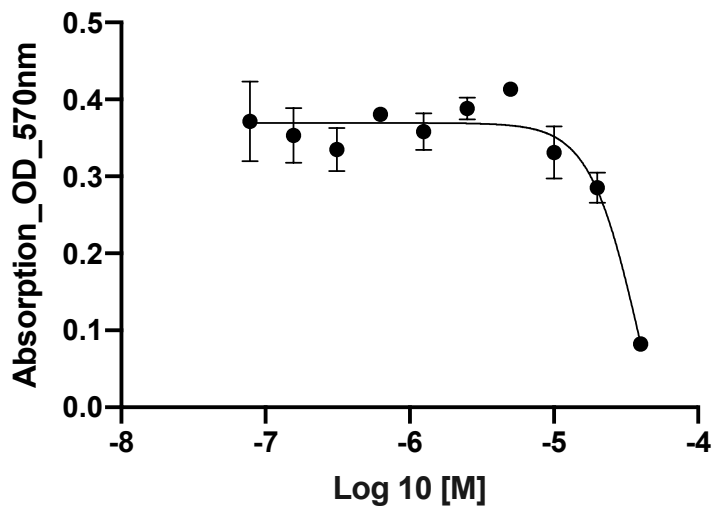
	IC50
XIE5-2-16	3.904e-005

U266 cells
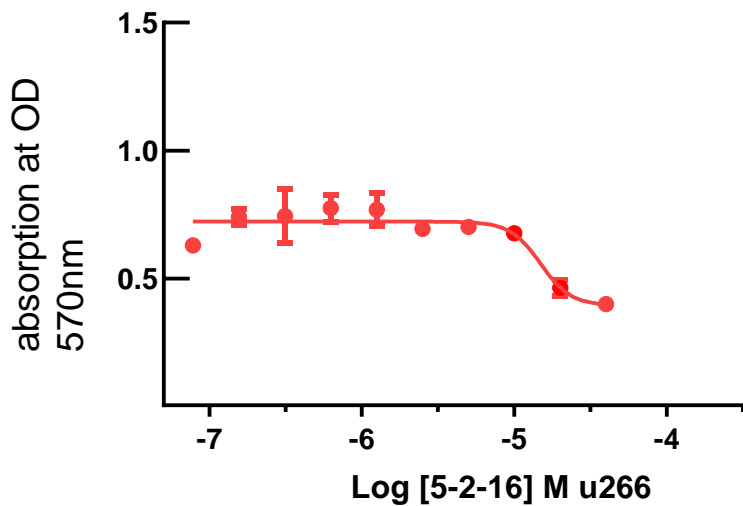
	5-2-16
IC50	1.483e-005

Neuro-protective effects on differentiated SH-SY5Y cells against hydrogen peroxide

XIE5-2-16
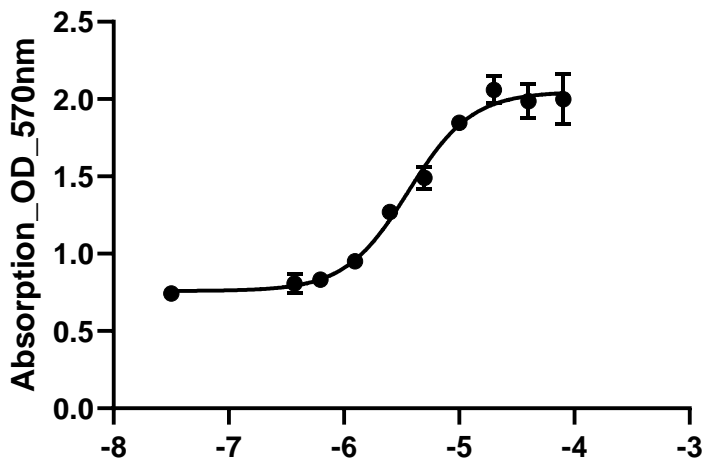
	IC50
XIE5-2-16	3.624e-006

XIE5-2-17

Anti-proliferative effects on multiple myeloma cell lines
MM1.S. cells

XIE5-2-17
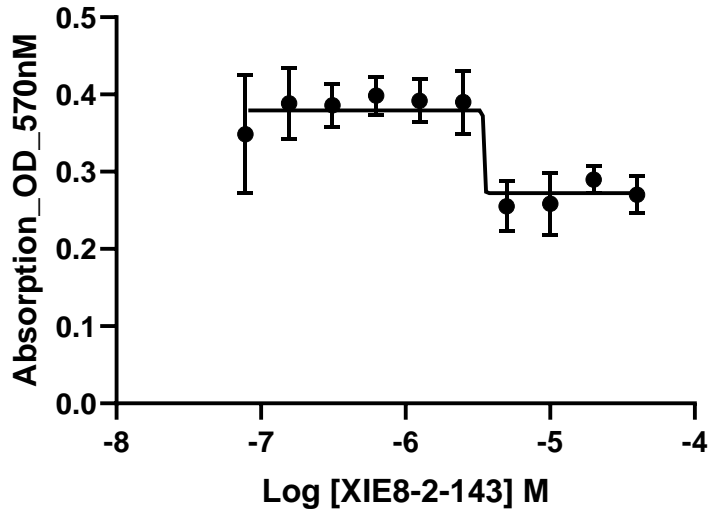
	IC50
XIE5-2-17	~ 3.500e-006

XIE5-2-17
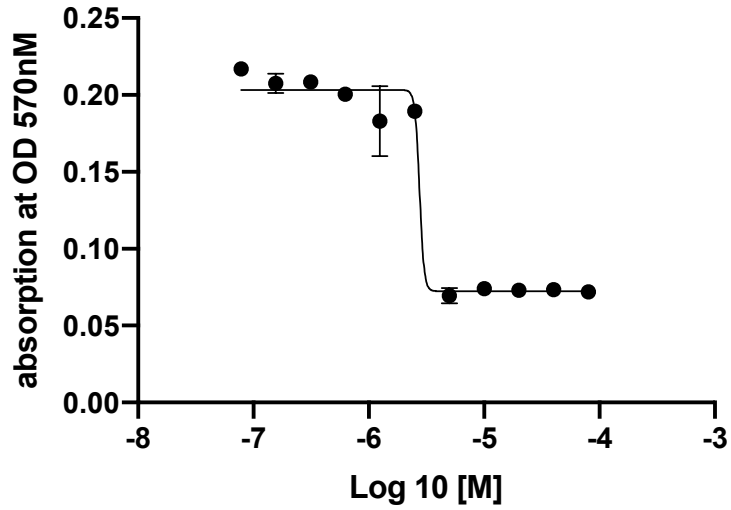
	IC50
XIE5-2-17	~ 2.754e-006

RPMI8226 cells

MTT_RPMI8226_XIE5-2-17
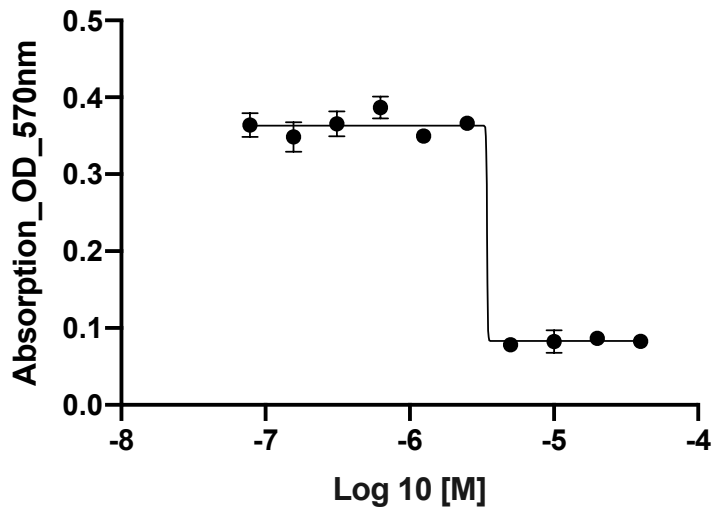
	IC50
XIE5-2-17	~ 3.437e-006

U266 cells

XIE5-2-18

Anti-proliferative effects on multiple myeloma cell lines
MM1.S. cells

XIE5-2-18
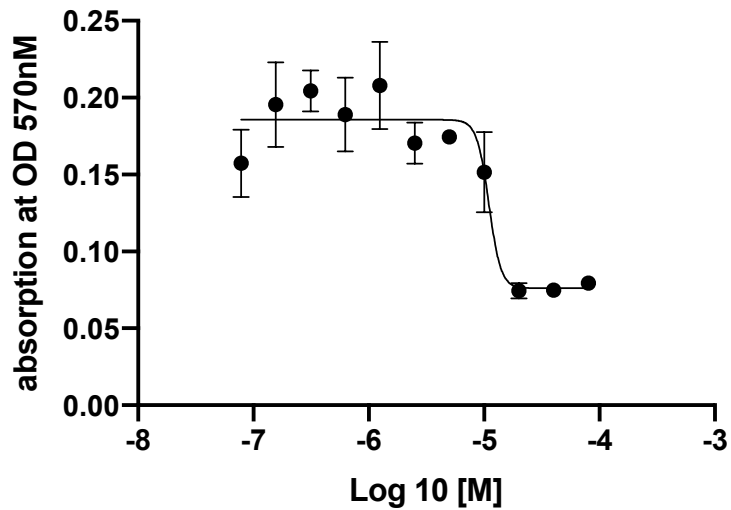
	IC50
XIE5-2-18	1.098e-005

RPMI8226 cells

451
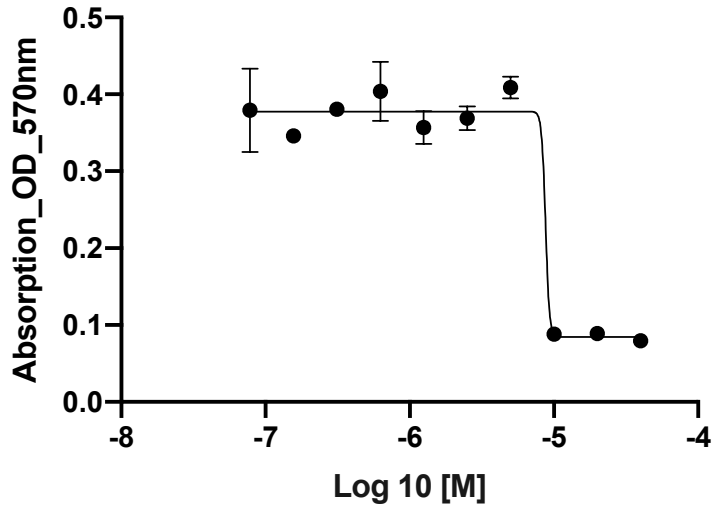
XIE5-2-18

	IC50
XIE5-2-18	~ 8.747e-006

U266 cells
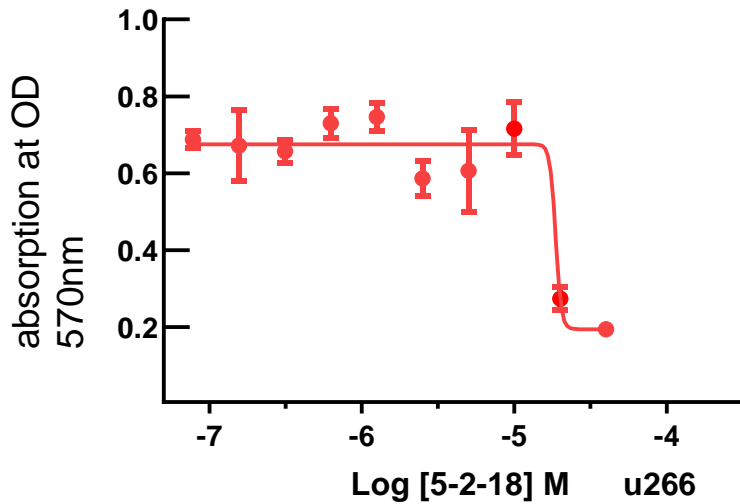
	5-2-18
IC50	~ 1.866e-005

Neuro-protective effects on differentiated SH-SY5Y cells against hydrogen peroxide

XIE5-2-18
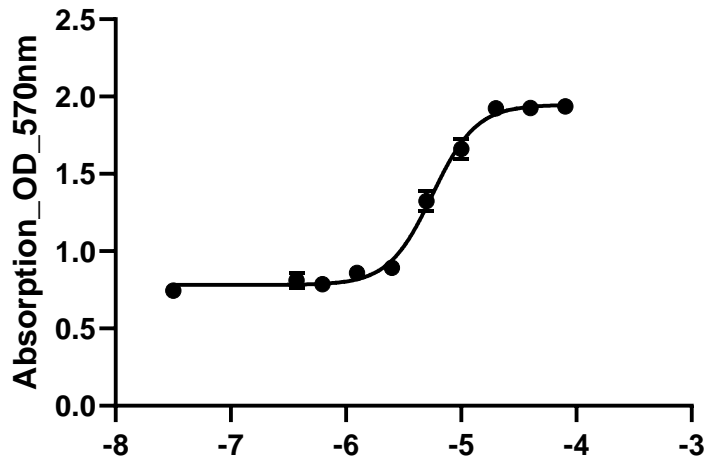
	IC50
XIE5-2-18	5.618e-006

XIE5-2-19

Anti-proliferative effects on multiple myeloma cell lines
MM1.S. cells

XIE5-2-19
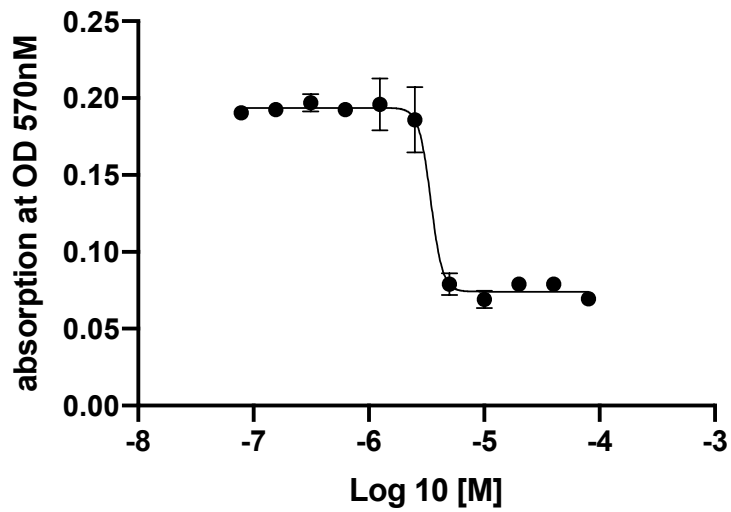
	IC50
XIE5-2-19	3.434e-006

RPMI8226 cells

XIE5-2-19
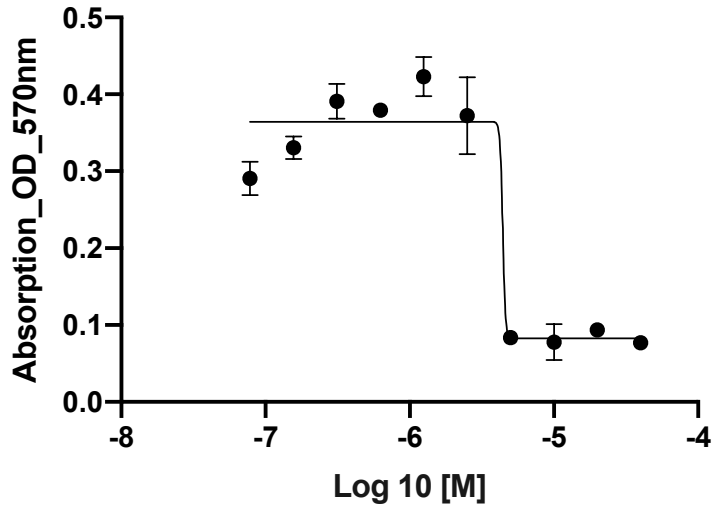
	IC50
XIE5-2-19	~ 4.416e-006

U266 cells
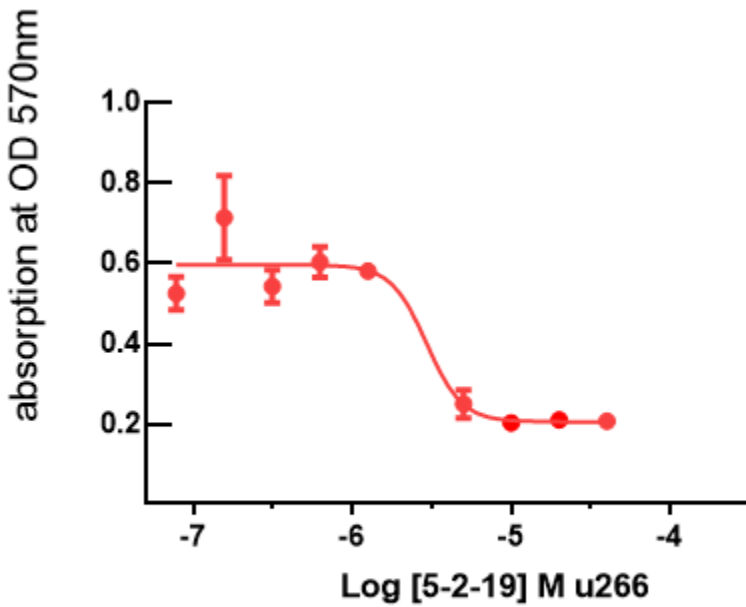
	5-2-19
IC50	2.928e-006

Neuro-protective effects on differentiated SH-SY5Y cells against hydrogen peroxide

XIE5-2-19
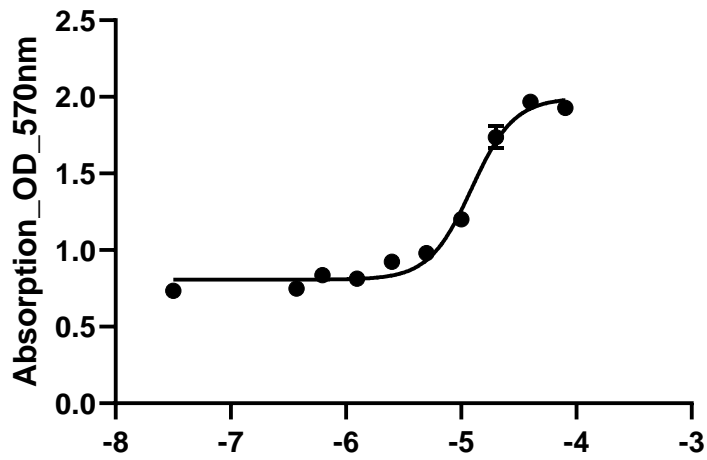
	IC50
XIE5-2-19	1.229e-005

XIE5-2-20

Anti-proliferative effects on multiple myeloma cell lines
MM1.S. cells

XIE5-2-20
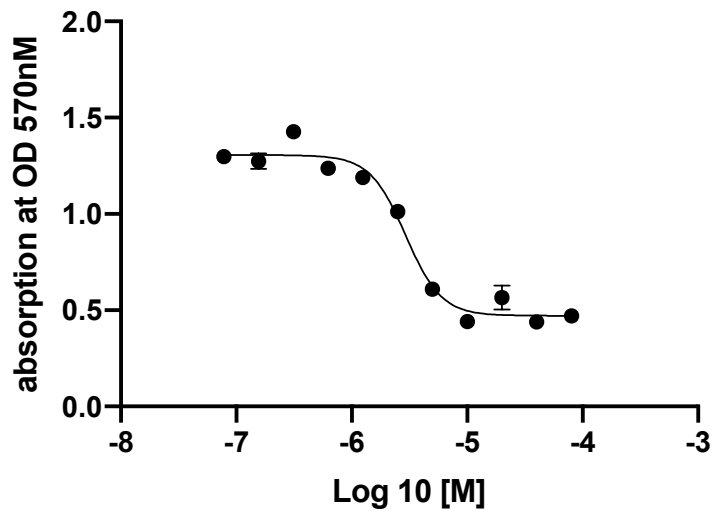
	IC50
XIE5-2-20	2.935e-006

RPMI8226 cells

XIE5-2-20
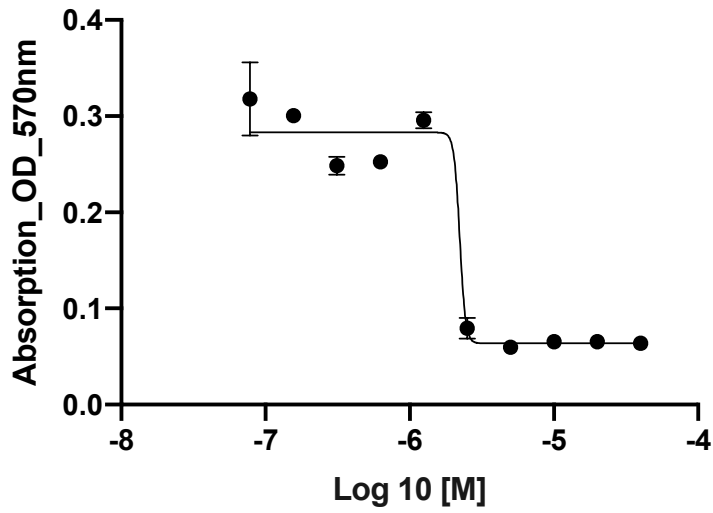
	IC50
XIE5-2-20	2.223e-006

U266 cells
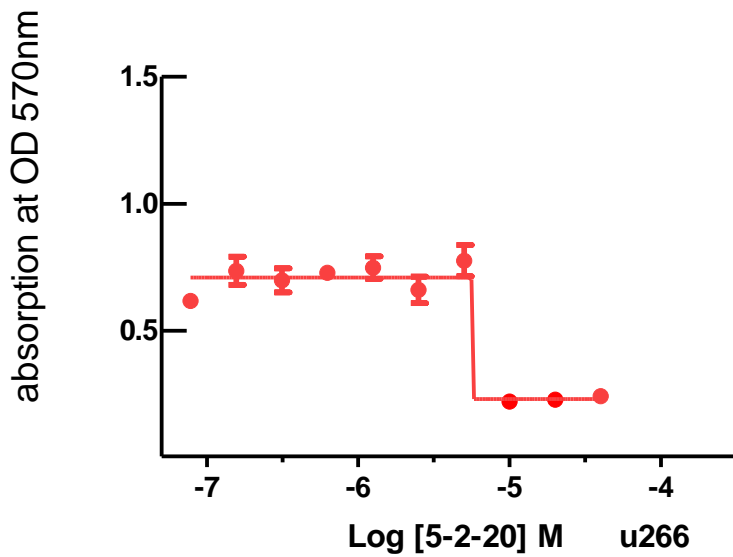
	5-2-20
IC50	~ 5.676e-006

Neuro-protective effects on differentiated SH-SY5Y cells against hydrogen peroxide

XIE5-2-20
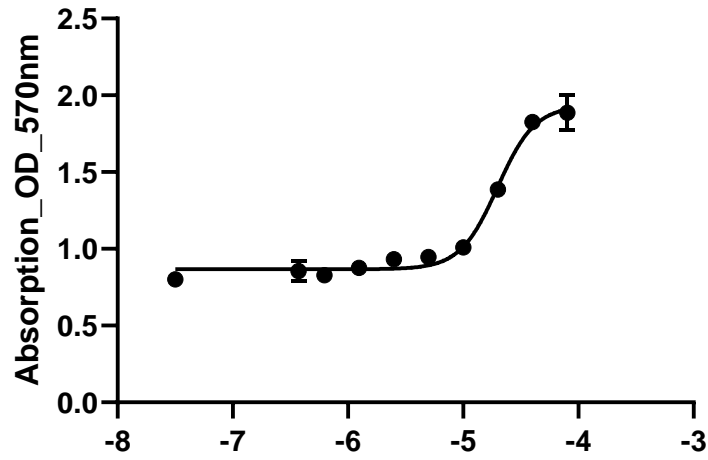
	IC50
XIE5-2-51	1.985e-005

XIE5-2-21

Anti-proliferative effects on multiple myeloma cell lines
MM1.S. cells

XIE5-2-21
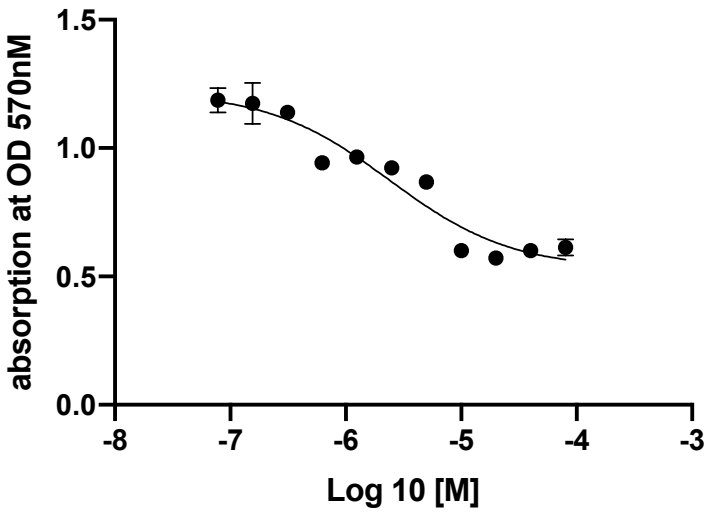
	IC50
XIE5-2-21	2.402e-006

RPMI8226 cells

XIE5-2-21
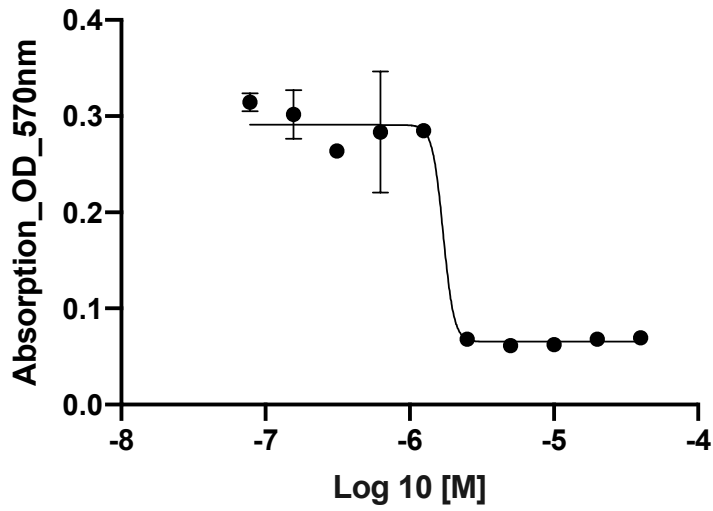
	IC50
XIE5-2-21	1.705e-006

U266 cells
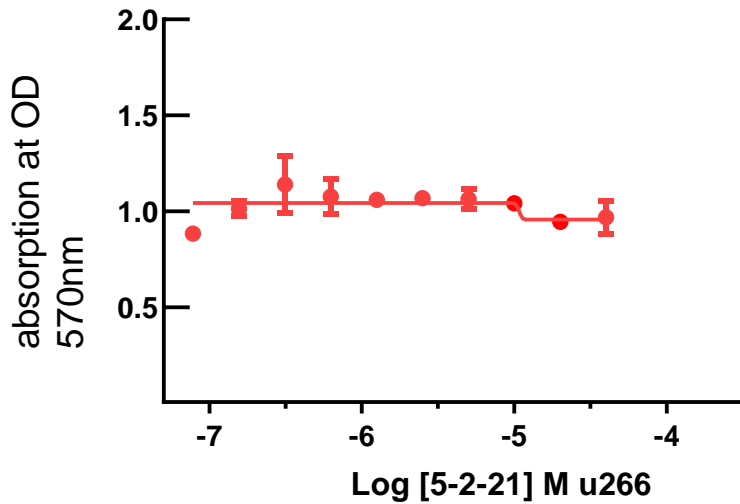
	5-2-21
IC50	~ 1.074e-005

Neuro-protective effects on differentiated SH-SY5Y cells against hydrogen peroxide

XIE5-2-22
Anti-proliferative effects on multiple myeloma cell lines
MM1.S. cells

XIE5-2-22
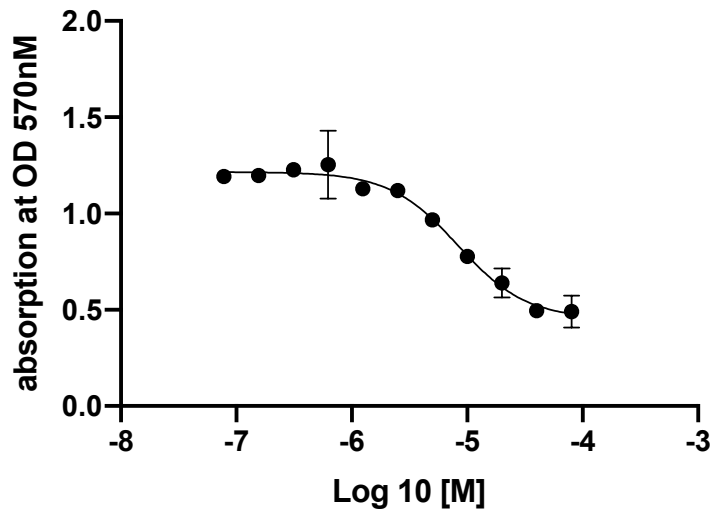
	IC50
XIE5-2-22	8.323e-006

RPMI8226 cells

XIE5-2-22
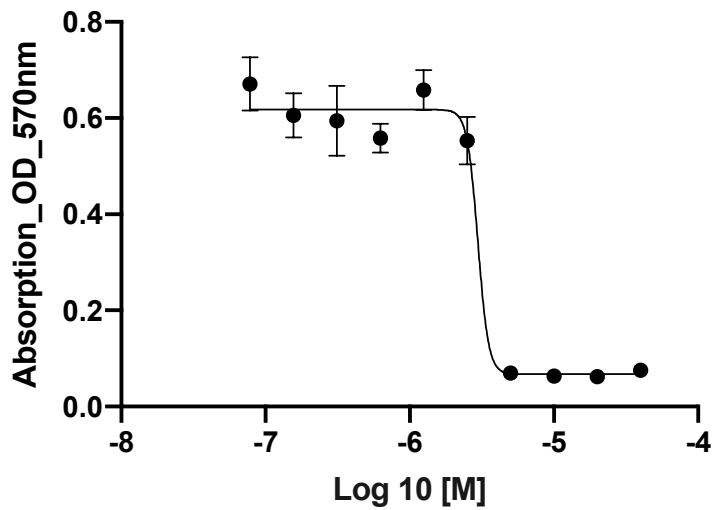
	IC50
XIE5-2-22	2.968e-006

U266 cells

Neuro-protective effects on differentiated SH-SY5Y cells against hydrogen peroxide

XIE5-2-31
Anti-proliferative effects on multiple myeloma cell lines
MM1.S. cells

XIE5-2-31
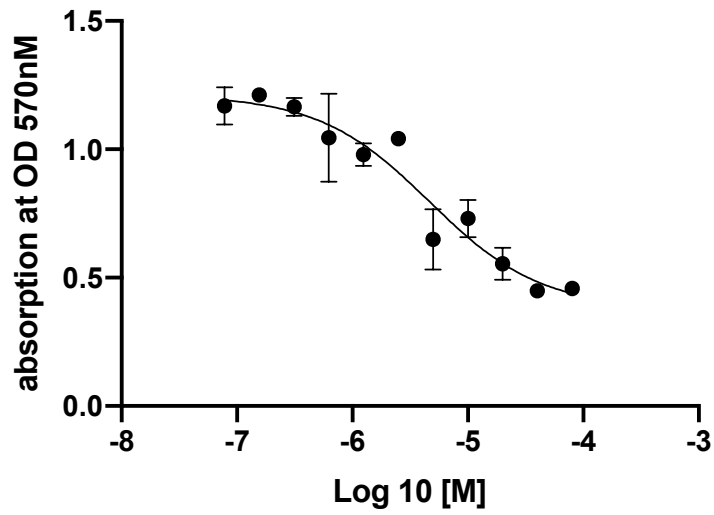
	IC50
XIE5-2-31	4.674e-006

RPMI8226 cells

XIE5-2-31
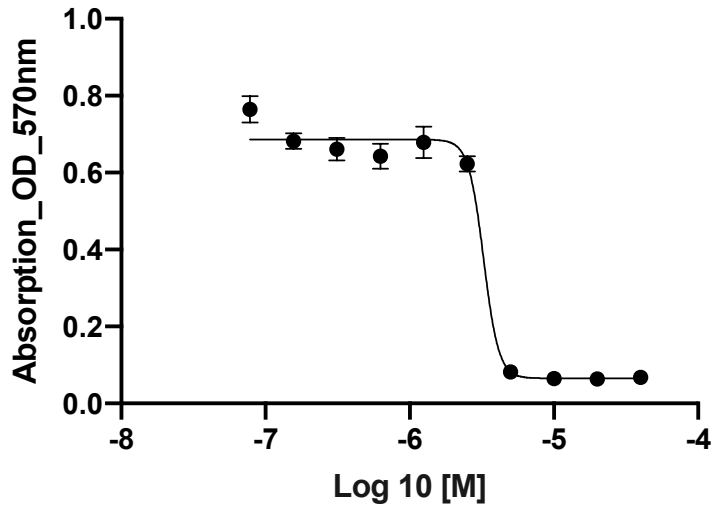
	IC50
XIE5-2-31	3.253e-006

U266 cells
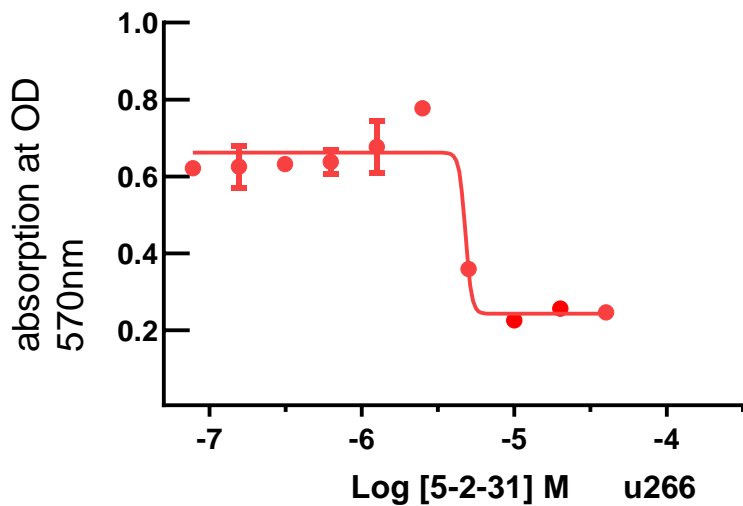
	5-2-31
IC50	~ 4.780e-006

Neuro-protective effects on differentiated SH-SY5Y cells against hydrogen peroxide
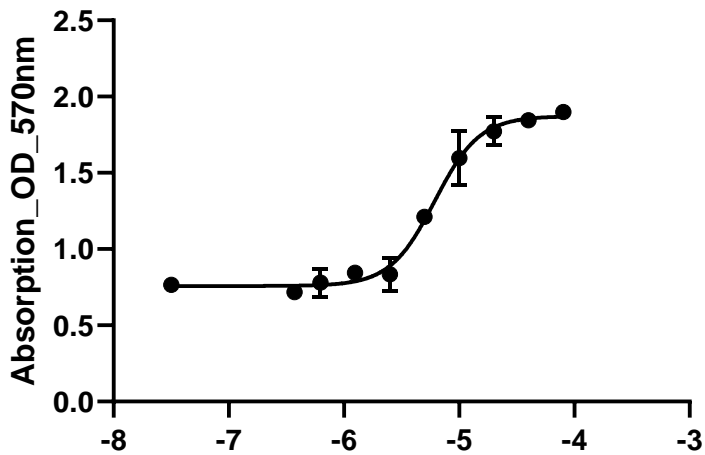
XIE5-2-31

	IC50
XIE5-2-31	6.132e-006

XIE5-2-32
Anti-proliferative effects on multiple myeloma cell lines
MM1.S. cells

XIE5-2-32
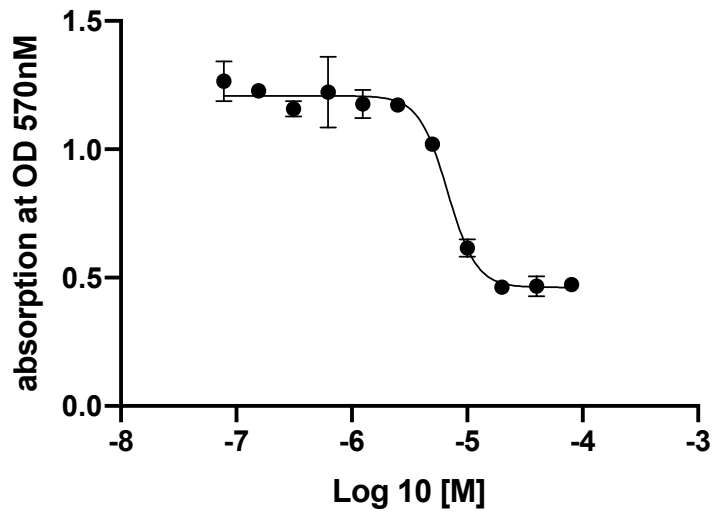
	IC50
XIE5-2-32	6.771e-006

RPMI8226 cells

XIE5-2-32
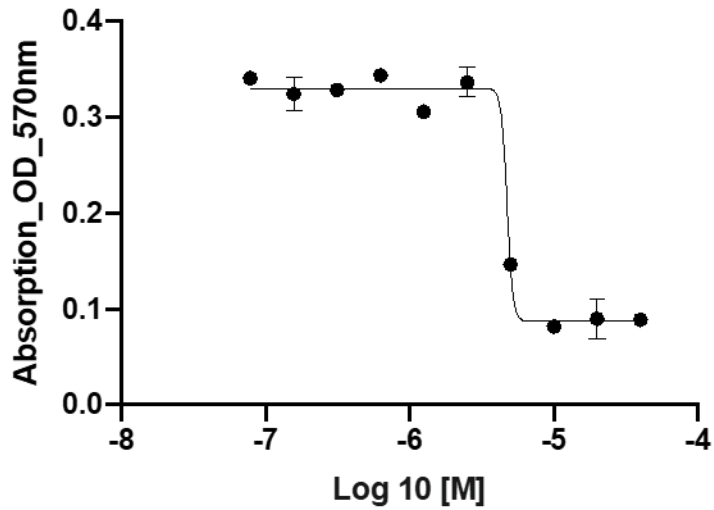
	IC50
XIE5-2-32	~ 4.743e-006

U266 cells
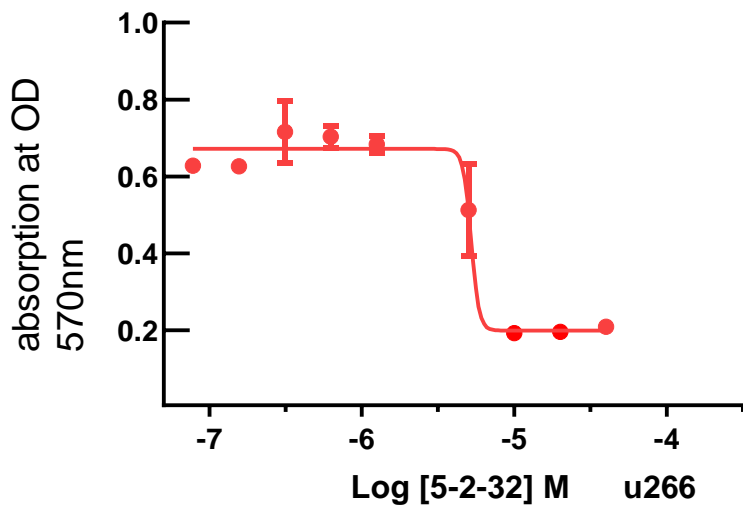
	5-2-32
IC50	~ 5.209e-006

Neuro-protective effects on differentiated SH-SY5Y cells against hydrogen peroxide

XIE5-2-32
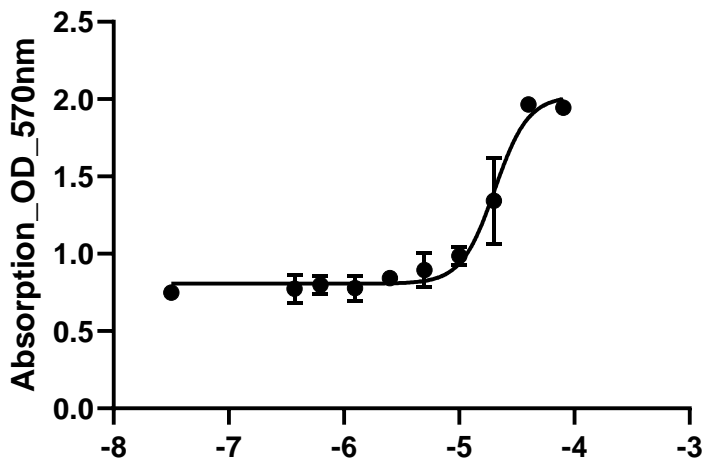
	IC50
XIE5-2-32	2.033e-005

XIE5-2-33
Anti-proliferative effects on multiple myeloma cell lines
MM1.S. cells

XIE5-2-33
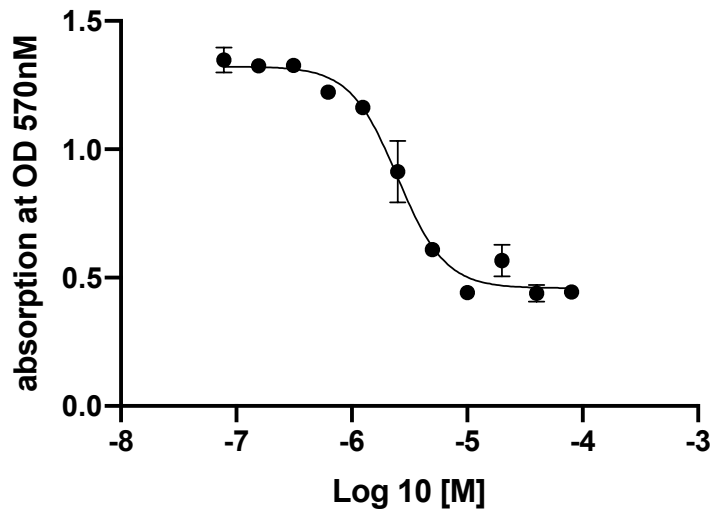
	IC50
XIE5-2-33	2.497e-006

RPMI8226 cells

XIE5-2-33
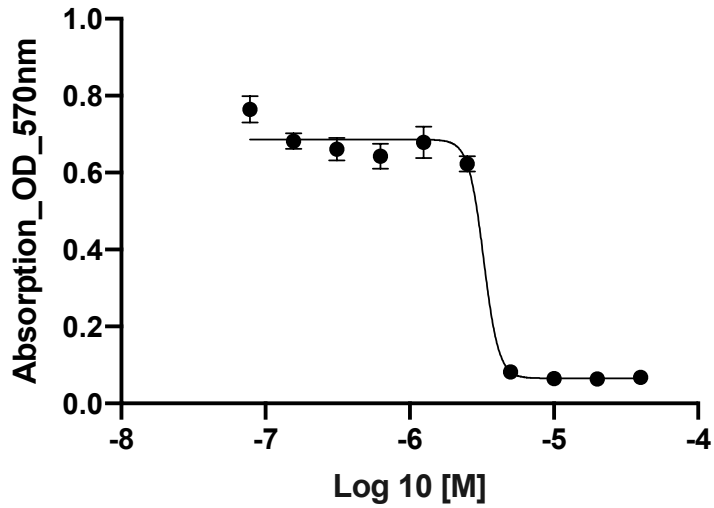
	IC50
XIE5-2-33	3.253e-006

U266 cells
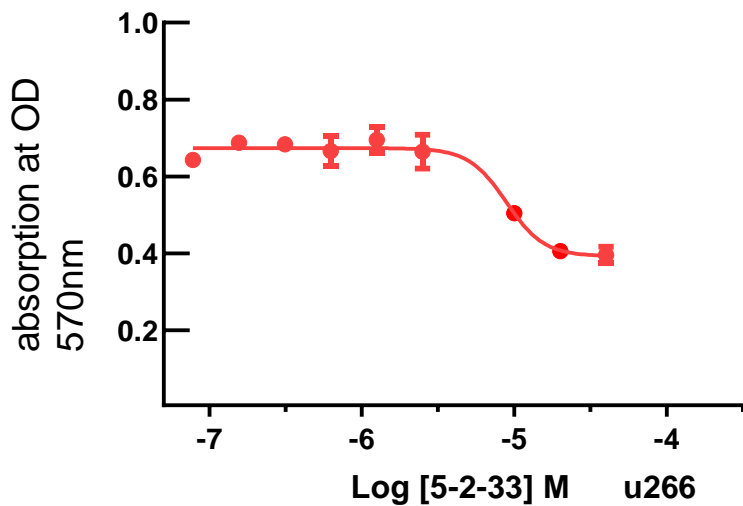
	5-2-33
IC50	8.859e-006

Neuro-protective effects on differentiated SH-SY5Y cells against hydrogen peroxide

XIE5-2-33
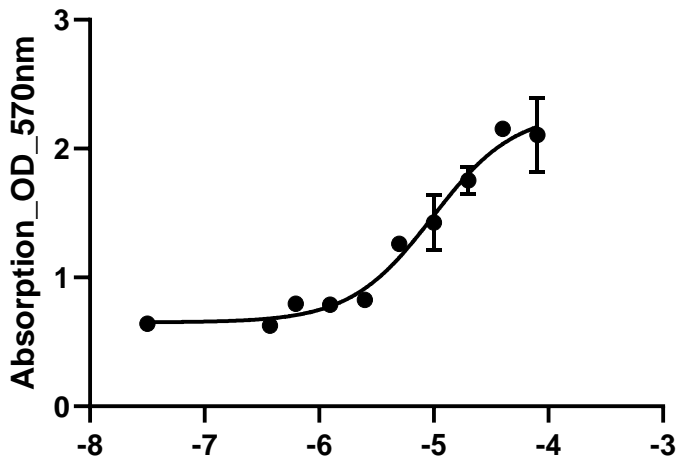
	IC50
XIE5-2-33	9.767e-006

XIE5-2-35
Anti-proliferative effects on multiple myeloma cell lines
MM1.S. cells

XIE5-2-35
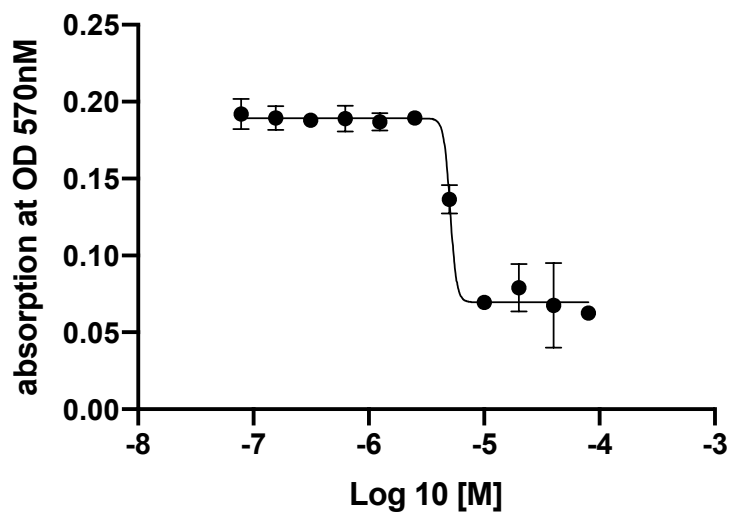
	IC50
XIE5-2-35	~ 5.076e-006

RPMI8226 cells

MTT_RPMI8226_XIE5-2-35
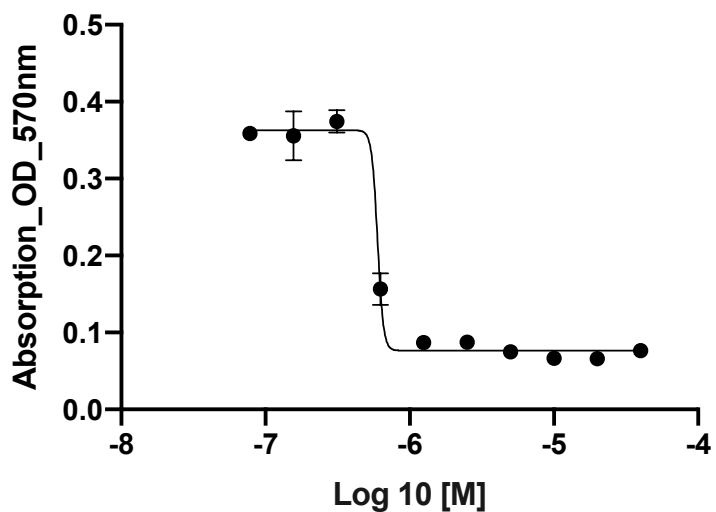
	IC50
XIE5-2-35	~ 5.982e-007

U266 cells
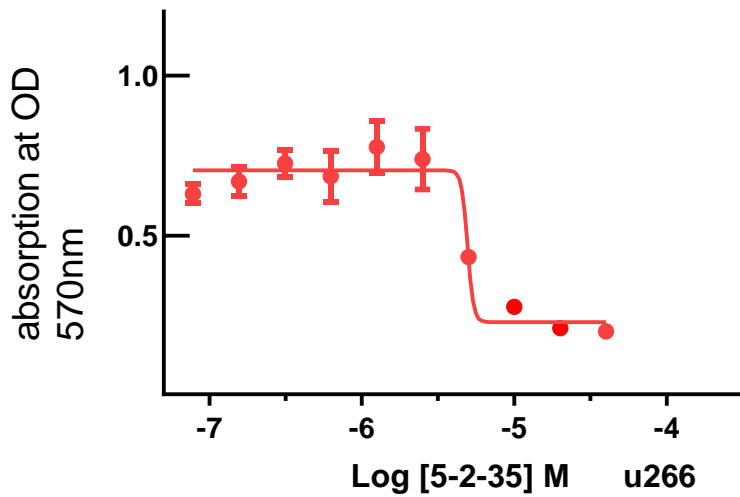
	5-2-35
IC50	~ 4.935e-006

Neuro-protective effects on differentiated SH-SY5Y cells against hydrogen peroxide

XIE5-2-35
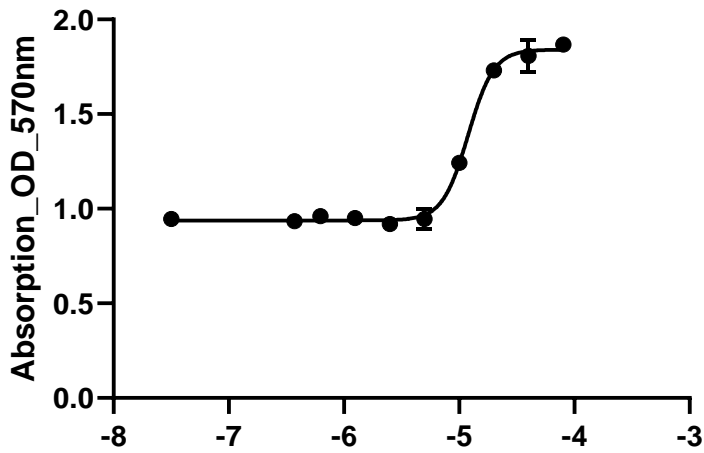
	IC50
XIE5-2-35	1.197e-005

XIE5-2-36
Anti-proliferative effects on multiple myeloma cell lines
MM1.S. cells

XIE5-2-36
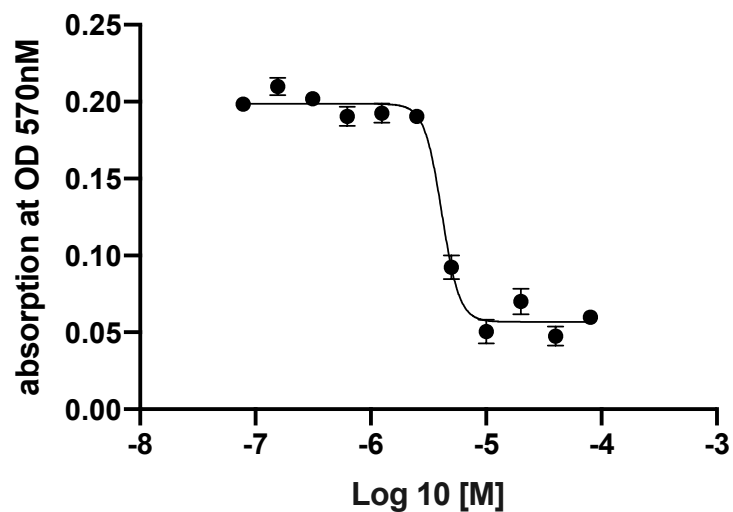
	IC50
XIE5-2-36	4.123e-006

RPMI8226 cells

MTT_RPMI8226_XIE5-2-36
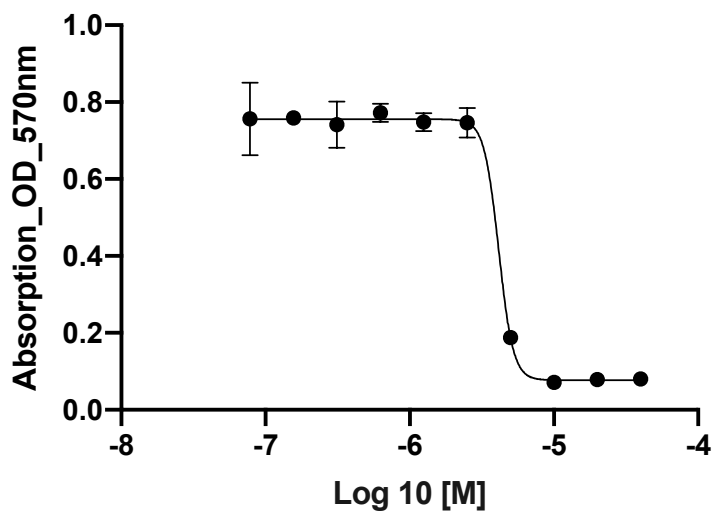
	IC50
XIE5-2-36	4.138e-006

U266 cells
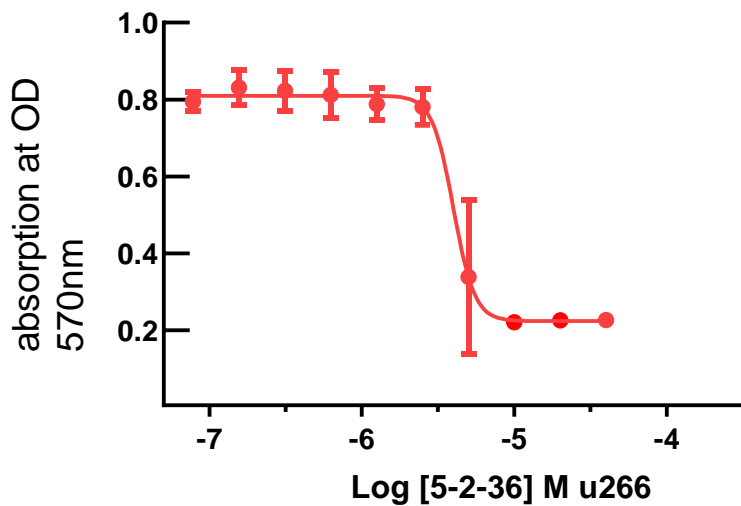
	5-2-36
IC50	3.989e-006

Neuro-protective effects on differentiated SH-SY5Y cells against hydrogen peroxide

XIE5-2-37
Anti-proliferative effects on multiple myeloma cell lines
MM1.S. cells

	IC50
XIE5-2-37	8.459e-006
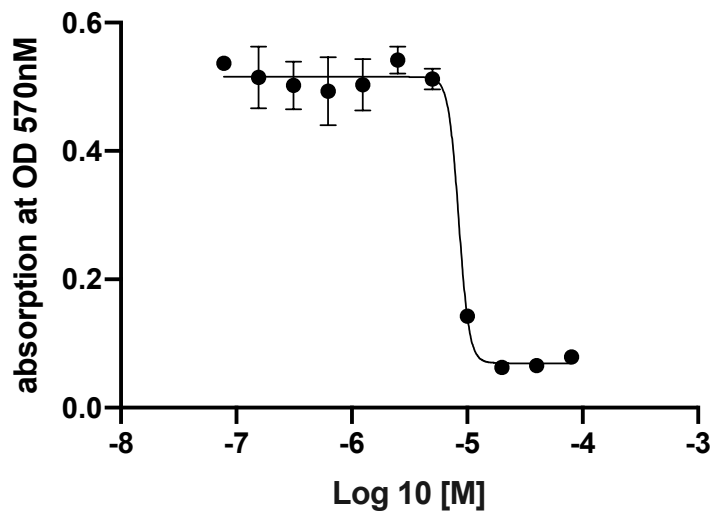
RPMI8226 cells

XIE5-2-37
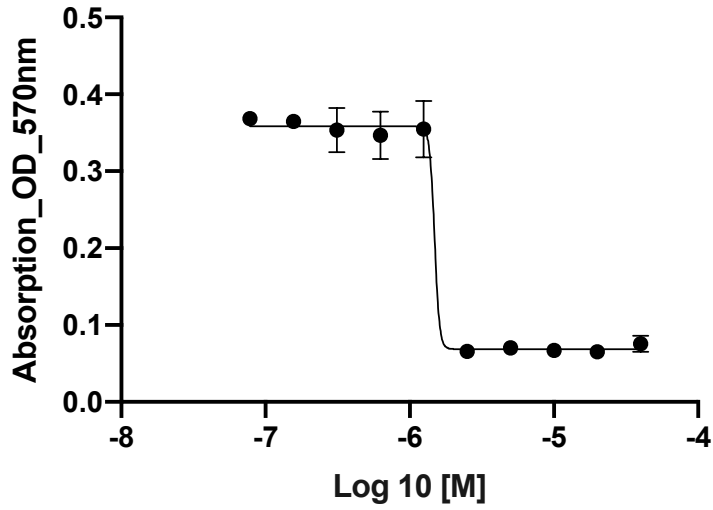
	IC50
XIE5-2-37	~ 1.486e-006

U266 cells

Neuro-protective effects on differentiated SH-SY5Y cells against hydrogen peroxide
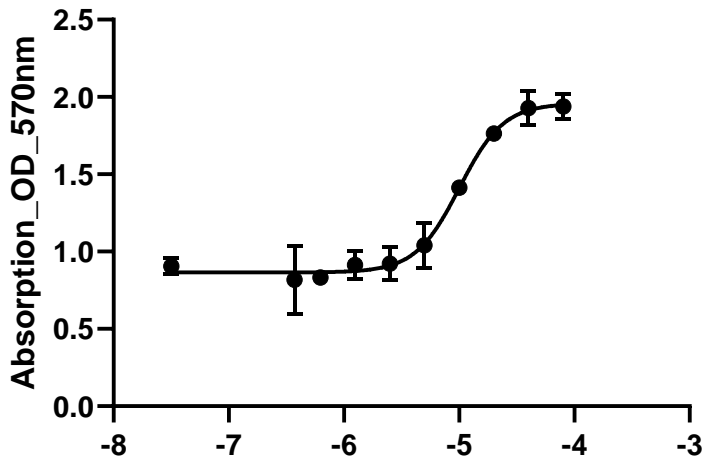
XIE5-2-37

	IC50
XIE5-2-37	1.004e-005

XIE5-2-38
Anti-proliferative effects on multiple myeloma cell lines
MM1.S. cells

XIE5-2-38
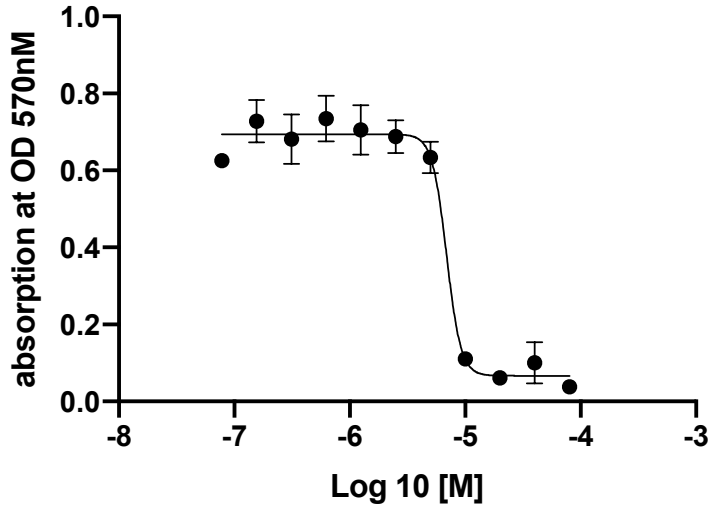
	IC50
XIE5-2-38	6.900e-006

RPMI8226 cells

XIE5-2-38
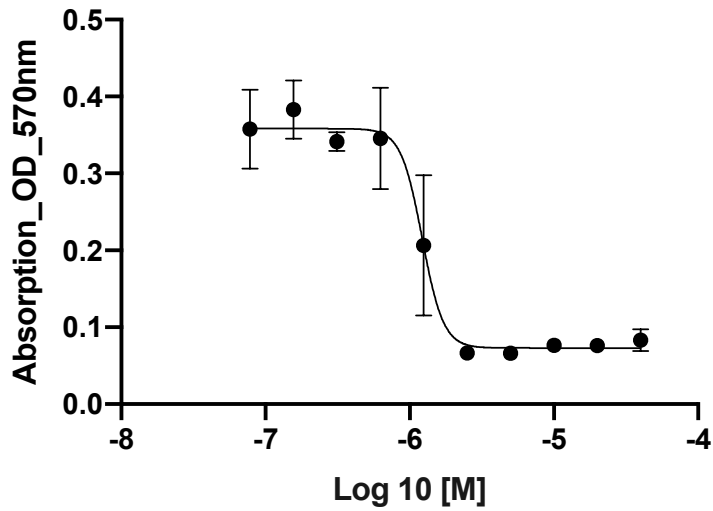
	IC50
XIE5-2-38	1.220e-006

U266 cells
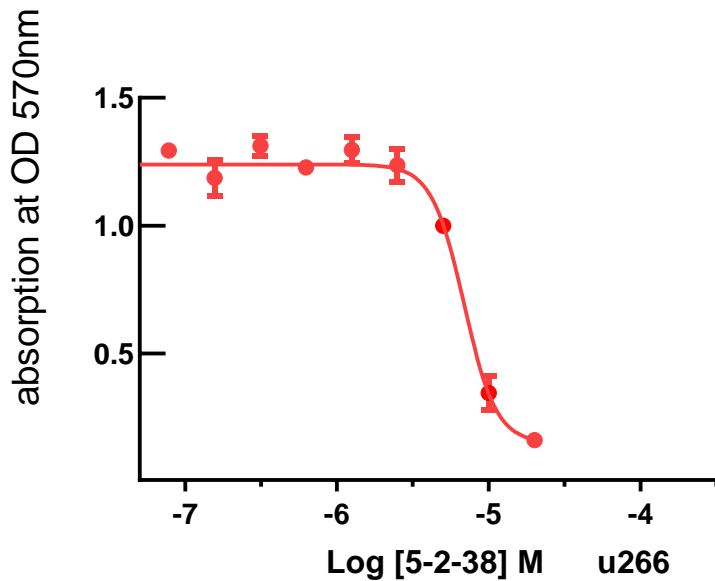
	5-2-38
IC50	6.862e-006

Neuro-protective effects on differentiated SH-SY5Y cells against hydrogen peroxide

XIE5-2-38
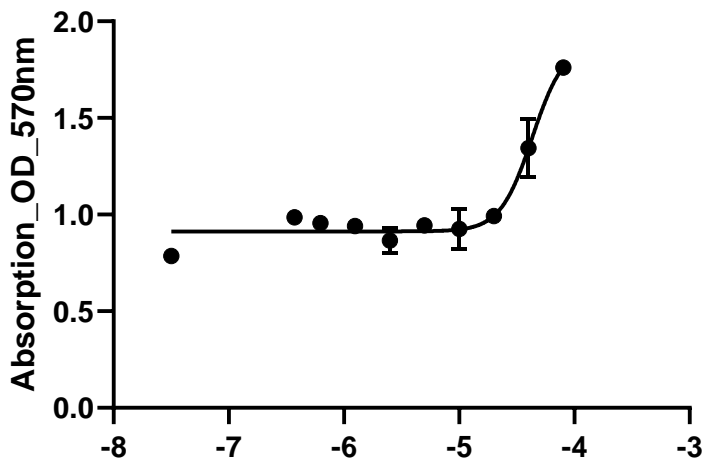
	IC50
XIE5-2-38	4.305e-005

XIE5-2-39
Anti-proliferative effects on multiple myeloma cell lines
MM1.S. cells

XIE5-2-39
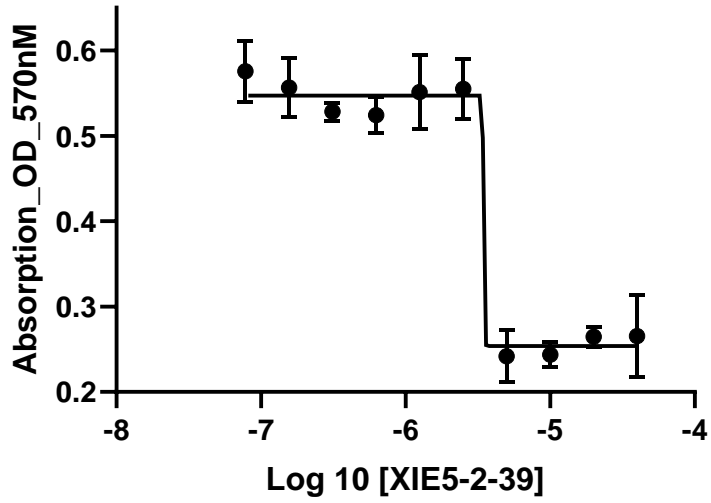
	IC50
XIE5-2-39	3.469e-006

XIE5-2-39
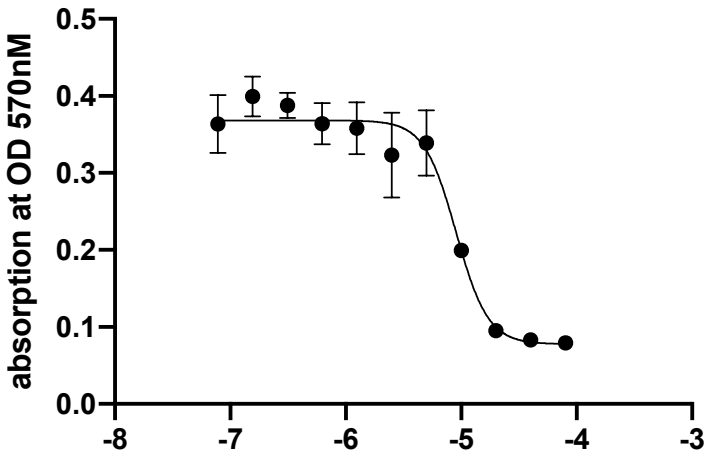
	IC50
XIE5-2-39	9.036e-006

RPMI8226 cells

XIE5-2-39
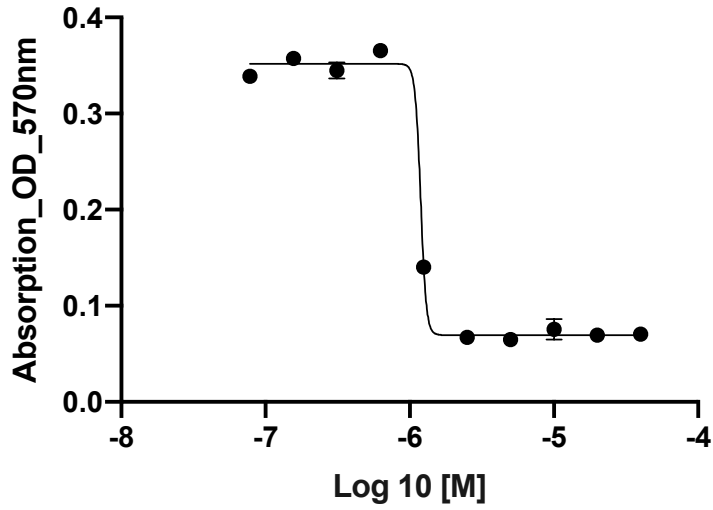
	IC50
XIE5-2-39	~ 1.191e-006

U266 cells
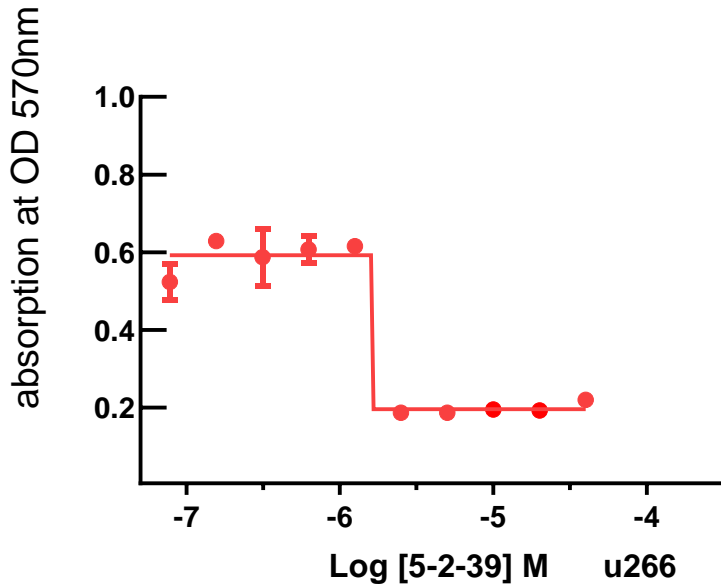
	5-2-39
IC50	~ 1.629e-006

Neuro-protective effects on differentiated SH-SY5Y cells against hydrogen peroxide

XIE5-2-39
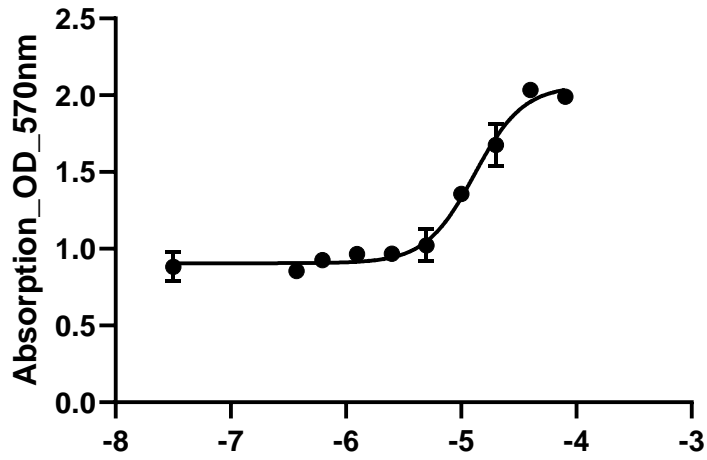
	IC50
XIE5-2-39	1.304e-005

XIE5-2-40

Anti-proliferative effects on multiple myeloma cell lines
MM1.S. cells
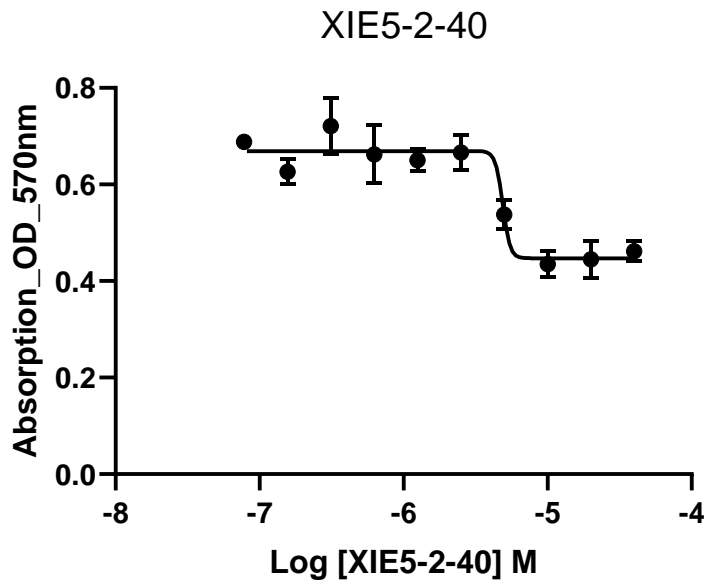
XIE5-2-40

	IC50
XIE5-2-40	~ 4.894e-006

RPMI8226 cells
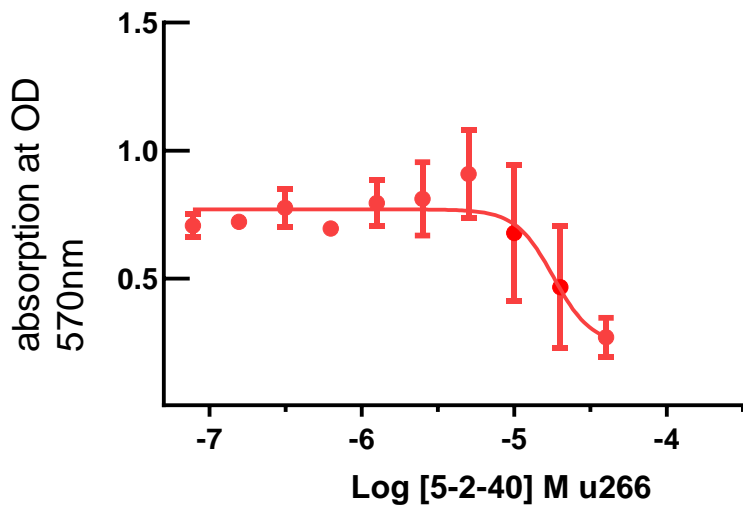
U266 cells

	5-2-40
IC50	1.802e-005

Neuro-protective effects on differentiated SH-SY5Y cells against hydrogen peroxide

XIE5-1-23
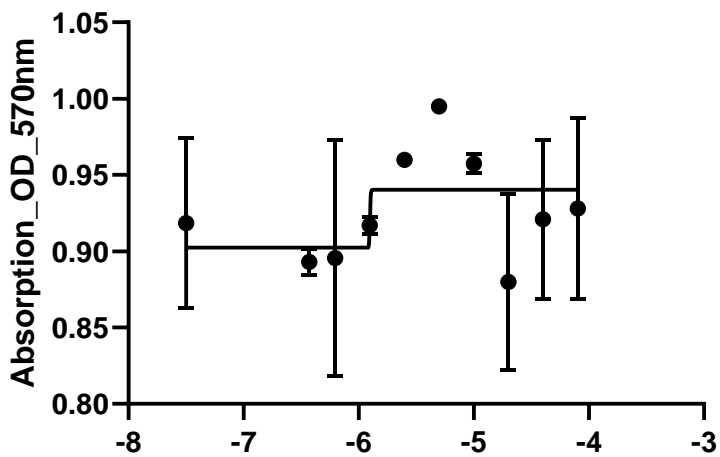
XIE5-2-42/XIE5-2-68-3
Anti-proliferative effects on multiple myeloma cell lines
MM1.S. cells

RPMI8226 cells
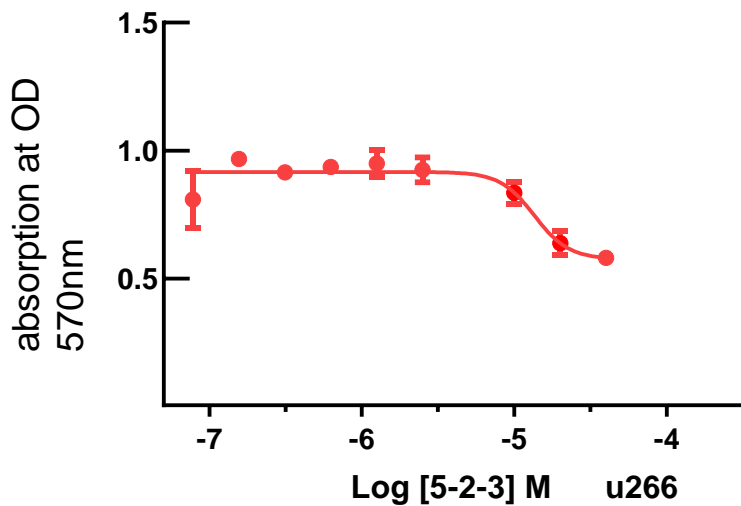
U266 cells

	25
IC50	1.607e-006
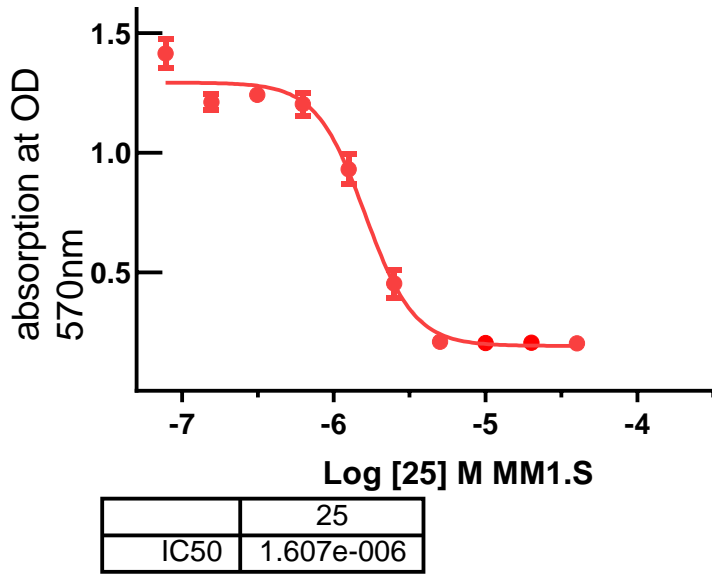
Neuro-protective effects on differentiated SH-SY5Y cells against hydrogen peroxide

XIE5-2-43
Anti-proliferative effects on multiple myeloma cell lines
MM1.S. cells
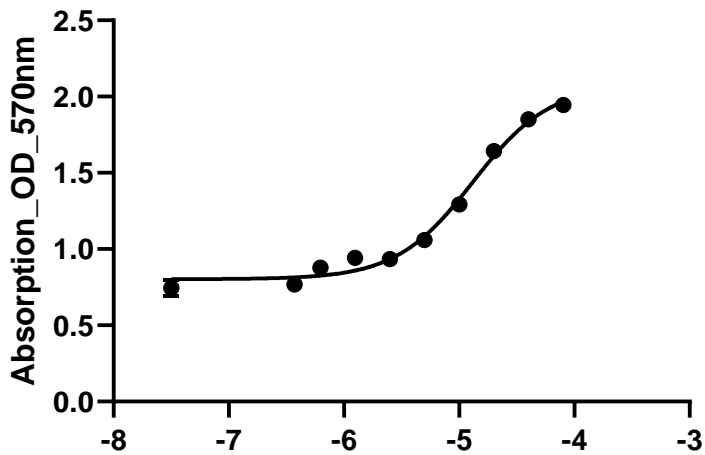

XIE5-2-43
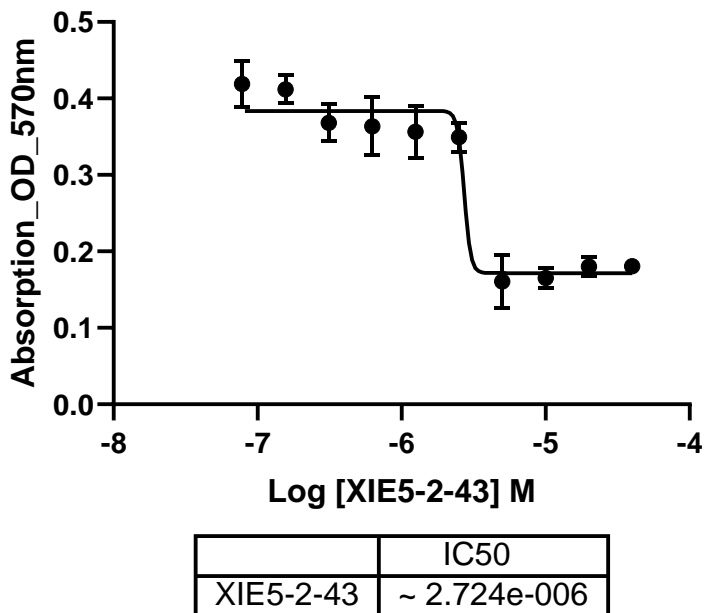
	IC50
XIE5-2-43	~ 2.724e-006

RPMI8226 cells

U266 cells

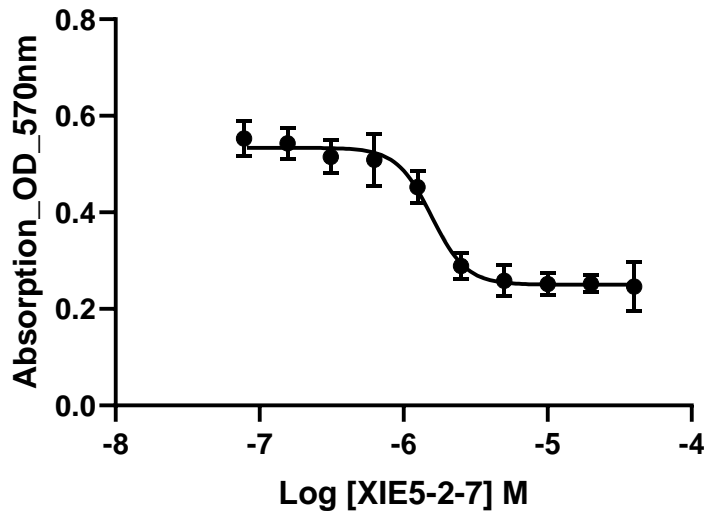Neuro-protective effects on differentiated SH-SY5Y cells against hydrogen peroxide

XIE5-2-44
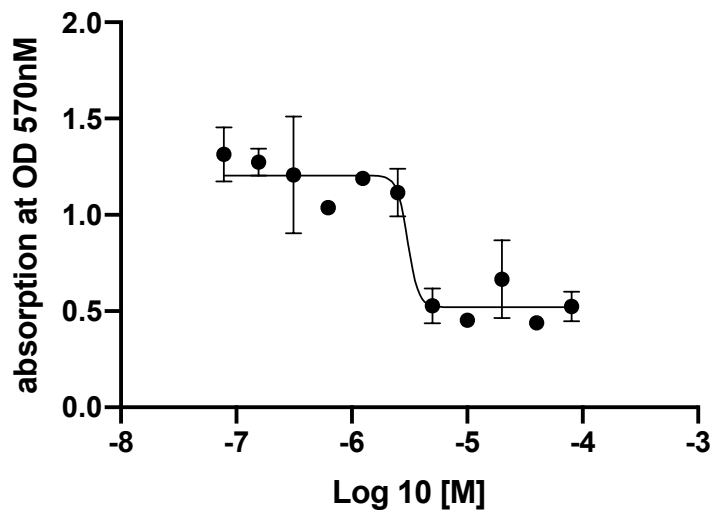Anti-proliferative effects on multiple myeloma cell lines
MM1.S. cells

RPMI8226 cells
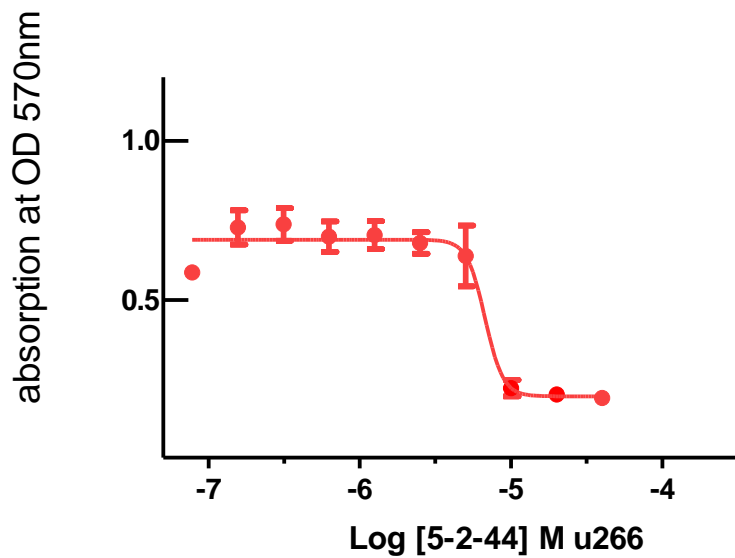
U266 cells

	5-2-44
IC50	6.724e-006

Neuro-protective effects on differentiated SH-SY5Y cells against hydrogen peroxide

XIE5-2-45
Anti-proliferative effects on multiple myeloma cell lines
MM1.S. cells

XIE5-2-45
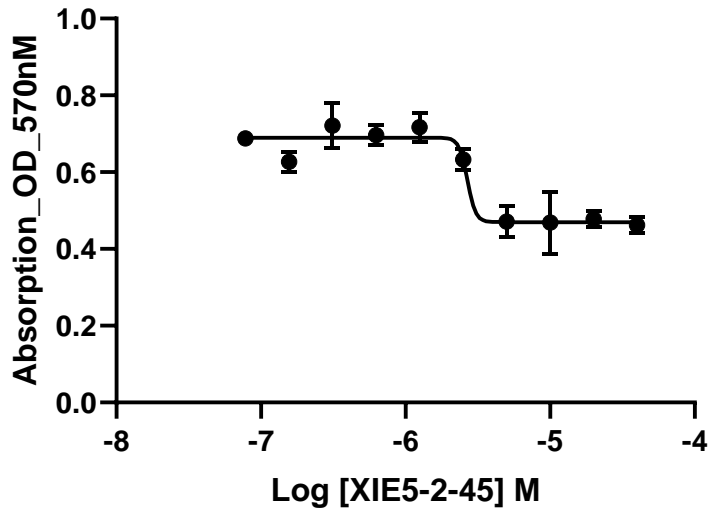
	IC50
XIE5-2-45	~ 2.682e-006

RPMI8226 cells

U266 cells

Neuro-protective effects on differentiated SH-SY5Y cells against hydrogen peroxide

XIE5-2-46
Anti-proliferative effects on multiple myeloma cell lines
MM1.S. cells

XIE5-2-46
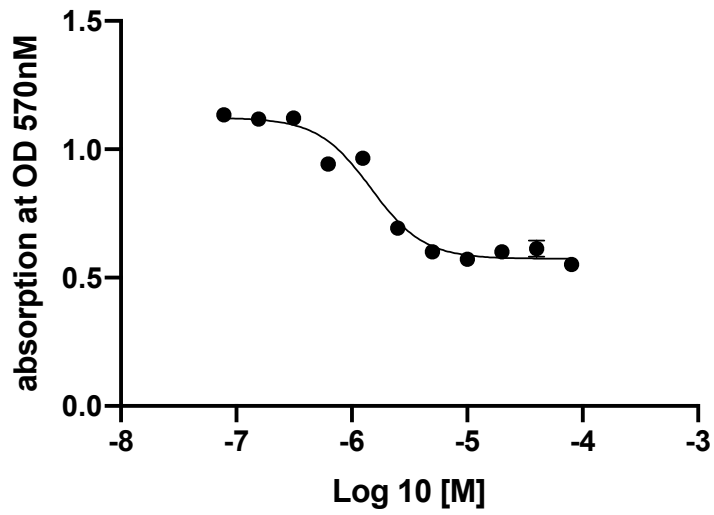
	IC50
XIE5-2-46	1.466e-006

RPMI8226 cells

XIE5-2-46
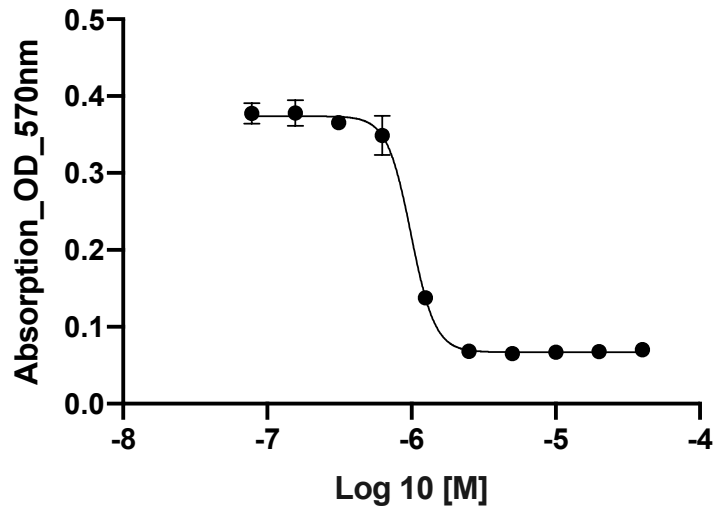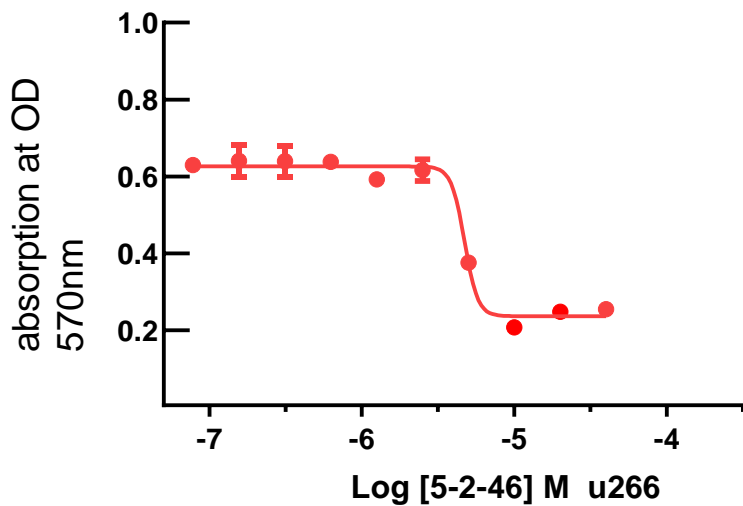
	IC50
XIE5-2-46	9.912e-007

U266 cells

	5-2-46
IC50	4.717e-006

Neuro-protective effects on differentiated SH-SY5Y cells against hydrogen peroxide

XIE5-2-49
Anti-proliferative effects on multiple myeloma cell lines
MM1.S. cells

XIE5-2-49

	IC50
XIE5-2-49	~ 4.242e-006
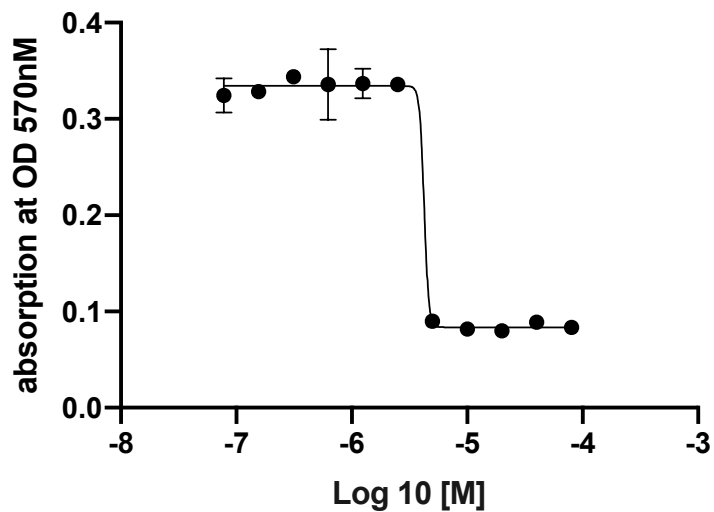
RPMI8226 cells

XIE5-2-49
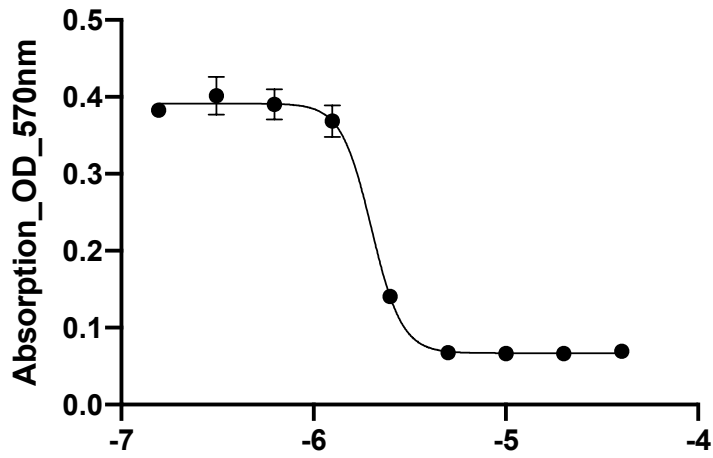
	IC50
XIE5-2-49	1.999e-006

U266 cells
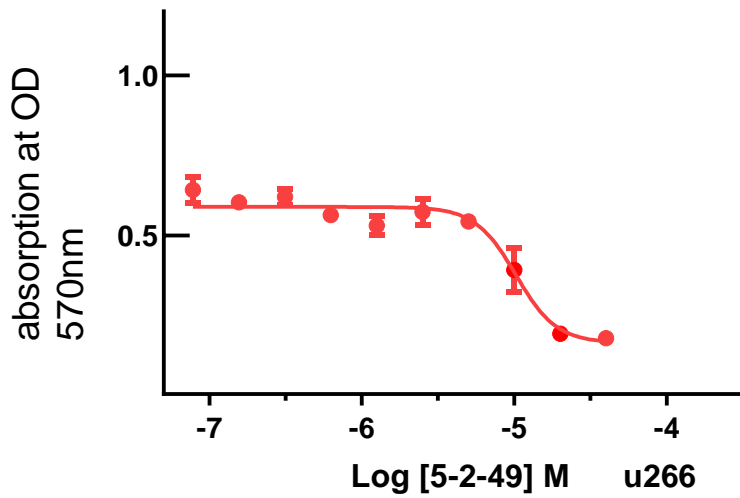
	5-2-49
IC50	1.023e-005

Neuro-protective effects on differentiated SH-SY5Y cells against hydrogen peroxide
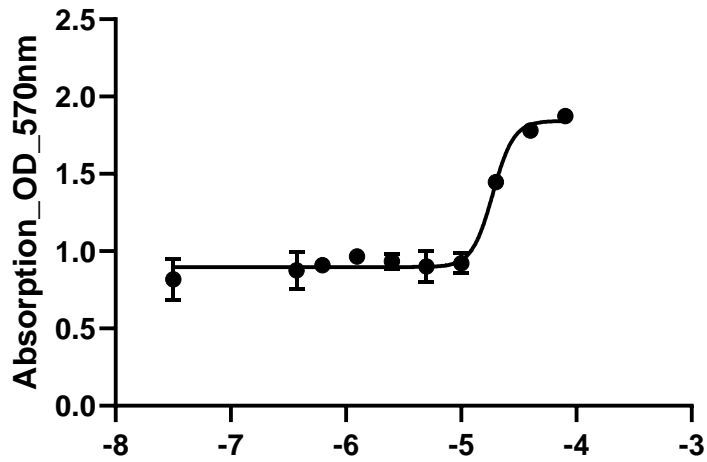
XIE5-2-49

	IC50
XIE5-2-49	1.880e-005

XIE5-2-51

Anti-proliferative effects on multiple myeloma cell lines
MM1.S. cells

XIE5-2-51
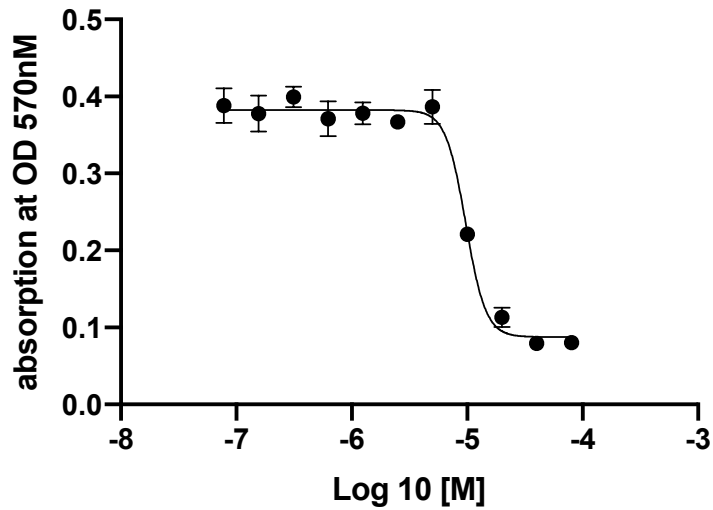
	IC50
XIE5-2-51	9.724e-006

RPMI8226 cells

U266 cells

Neuro-protective effects on differentiated SH-SY5Y cells against hydrogen peroxide

XIE5-2-53
Anti-proliferative effects on multiple myeloma cell lines
MM1.S. cells

XIE5-2-53
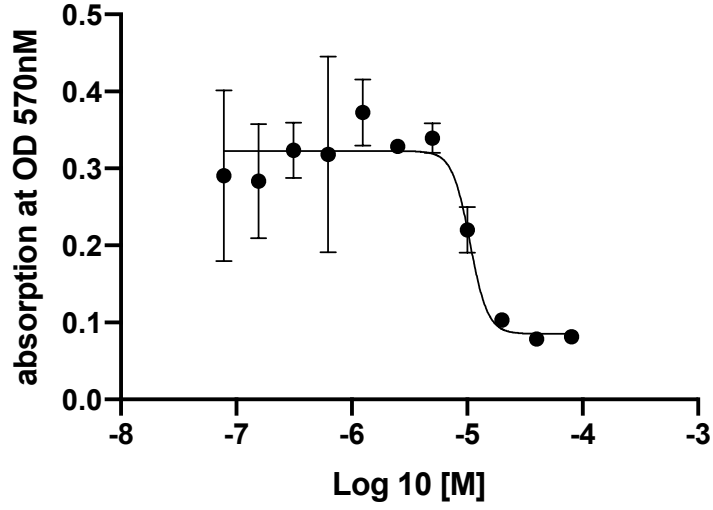
	IC50
XIE5-2-53	1.057e-005

RPMI8226 cells

U266 cells
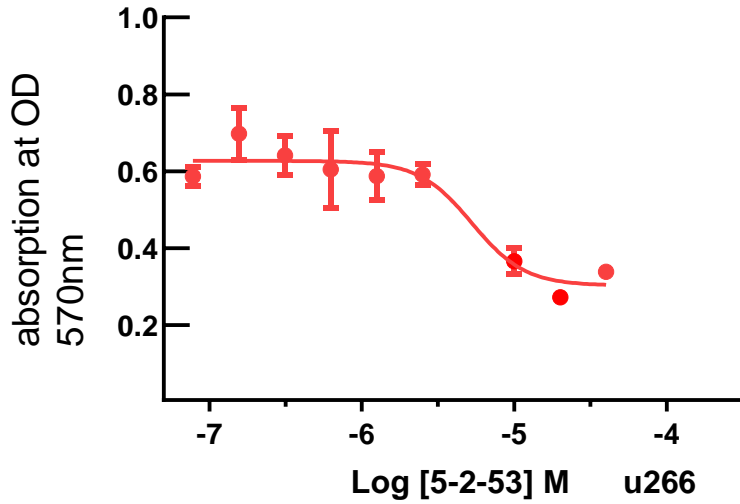
	5-2-53
IC50	5.275e-006

Neuro-protective effects on differentiated SH-SY5Y cells against hydrogen peroxide
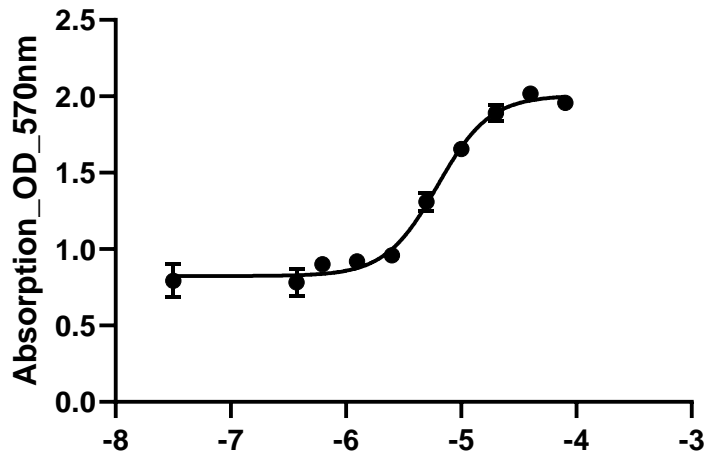
XIE5-2-53

	IC50
XIE5-2-53	6.225e-006

XIE5-2-55
Anti-proliferative effects on multiple myeloma cell lines
MM1.S. cells

XIE5-2-54

Log 10 [M]
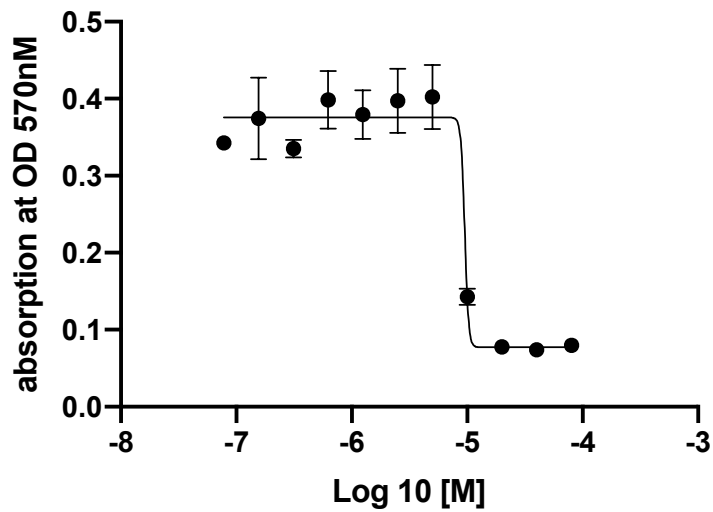
	IC50
XIE5-2-54	~ 9.534e-006

RPMI8226 cells

XIE5-2-54
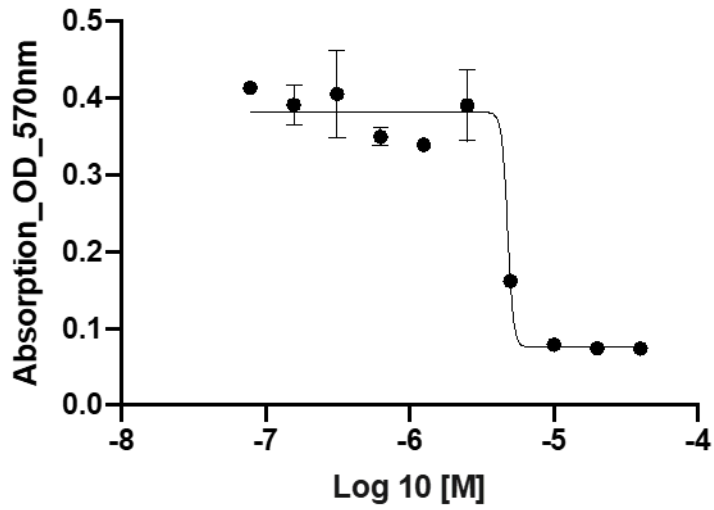
	IC50
XIE5-2-54	~ 4.783e-006

U266 cells
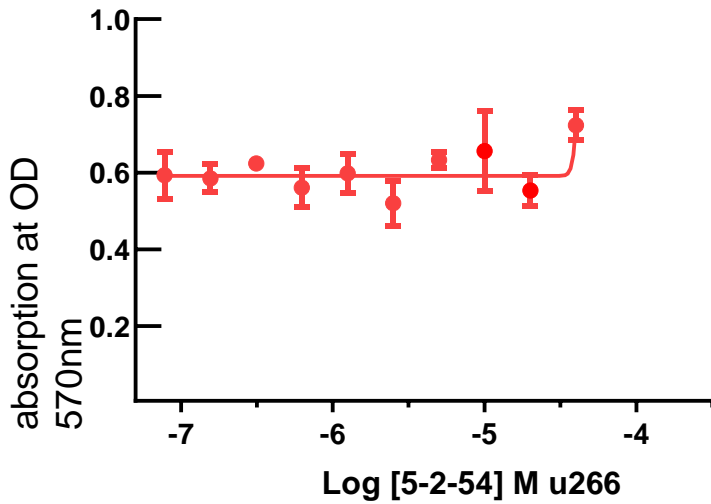
	5-2-54
IC50	~ 4.081e-005

Neuro-protective effects on differentiated SH-SY5Y cells against hydrogen peroxide

XIE5-2-55
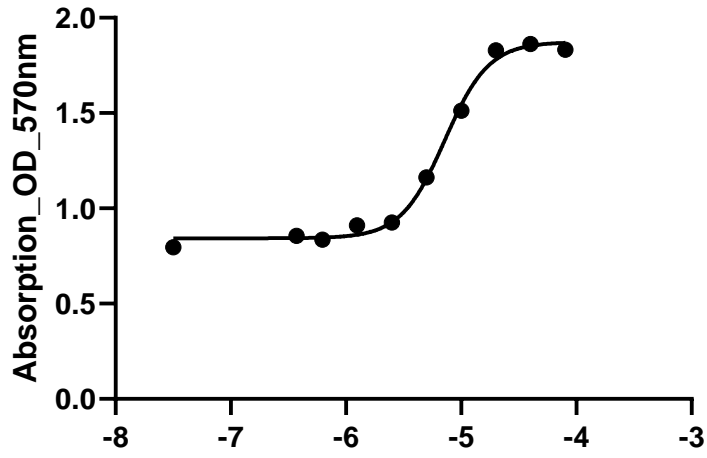
	IC50
XIE5-2-55	7.211e-006

XIE5-2-58
Anti-proliferative effects on multiple myeloma cell lines
MM1.S. cells

RPMI8226 cells

U266 cells

Neuro-protective effects on differentiated SH-SY5Y cells against hydrogen peroxide

XIE5-2-58
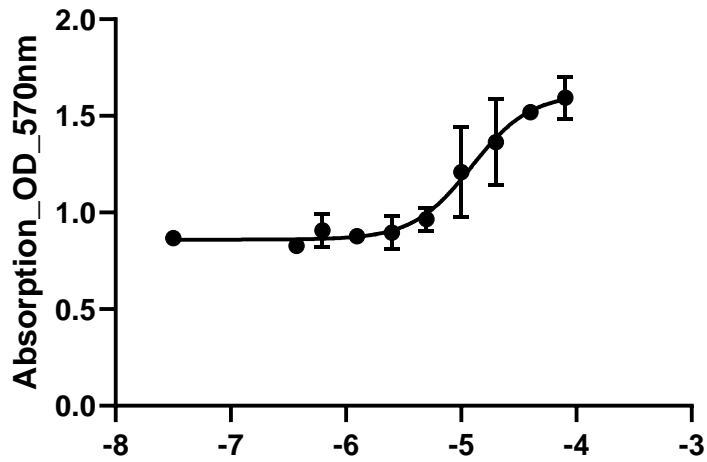
	IC50
XIE5-2-58	1.229e-005

XIE5-2-59
Anti-proliferative effects on multiple myeloma cell lines
MM1.S. cells

RPMI8226 cells

U266 cells
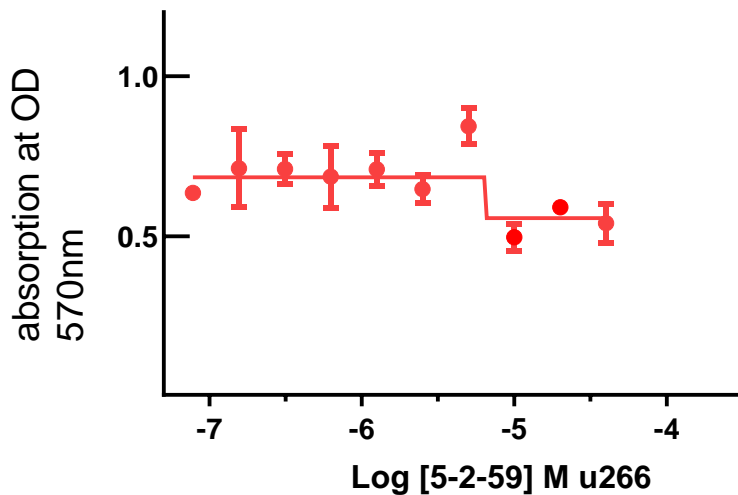
	5-2-59
IC50	~ 6.520e-006

Neuro-protective effects on differentiated SH-SY5Y cells against hydrogen peroxide

XIE5-2-59
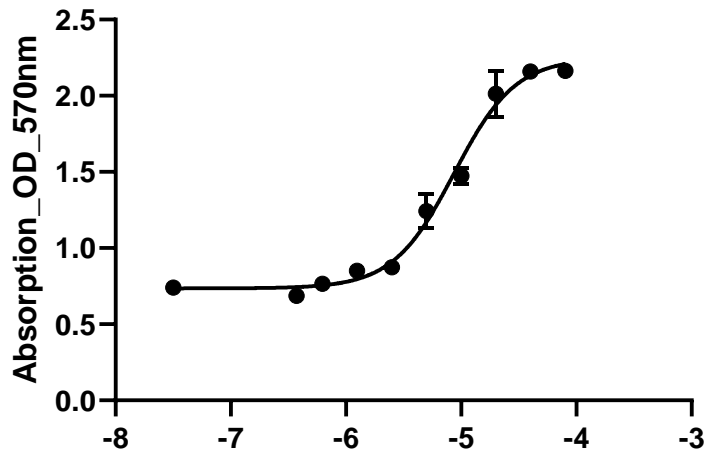
	IC50
XIE5-2-59	8.691e-006

XIE5-2-61
Anti-proliferative effects on multiple myeloma cell lines
MM1.S. cells
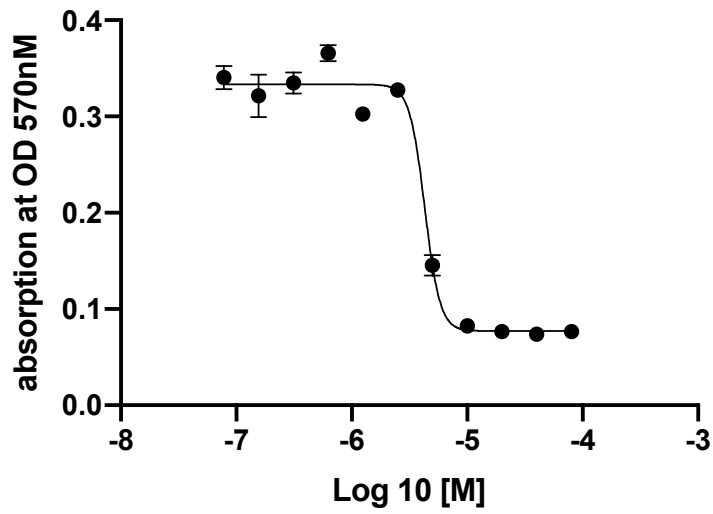
	IC50
XIE5-2-61	4.291e-006

RPMI8226 cells
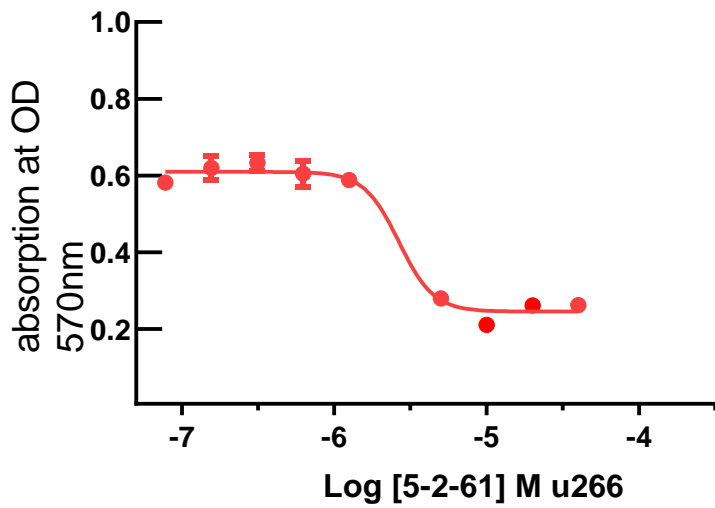
U266 cells

	5-2-61
IC50	2.652e-006

Neuro-protective effects on differentiated SH-SY5Y cells against hydrogen peroxide

XIE5-2-64
Anti-proliferative effects on multiple myeloma cell lines
MM1.S. cells

	IC50
XIE5-2-64	~ 4.749e-006
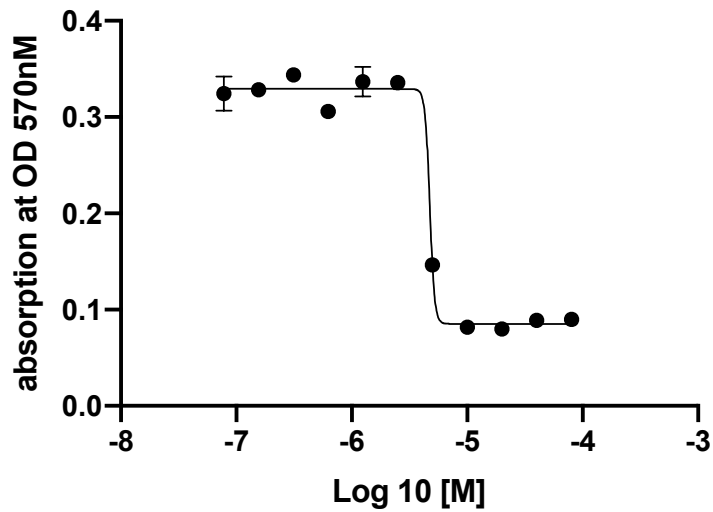
RPMI8226 cells
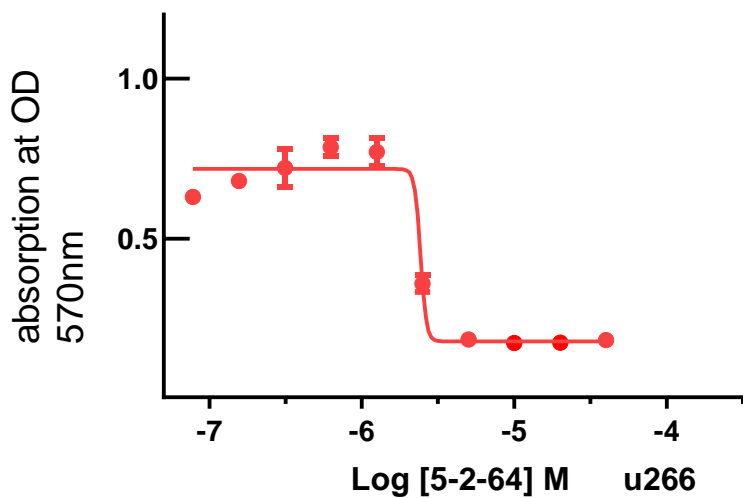
U266 cells

	5-2-64
IC50	~ 2.426e-006

Neuro-protective effects on differentiated SH-SY5Y cells against hydrogen peroxide

XIE5-2-70
Anti-proliferative effects on multiple myeloma cell lines
MM1.S. cells

RPMI8226 cells
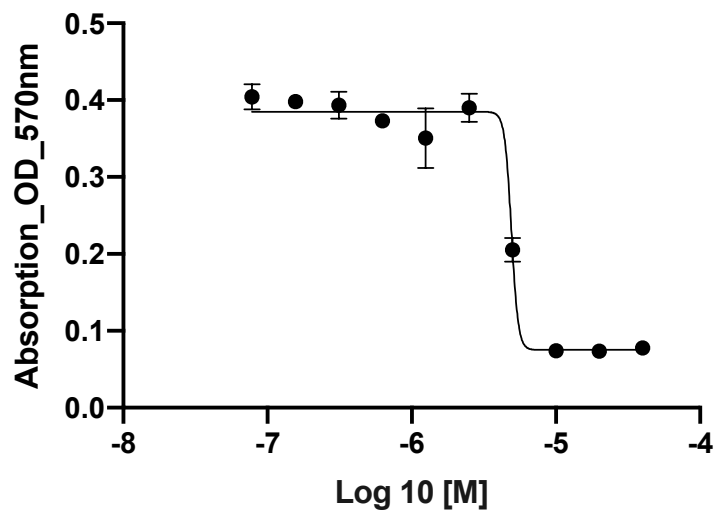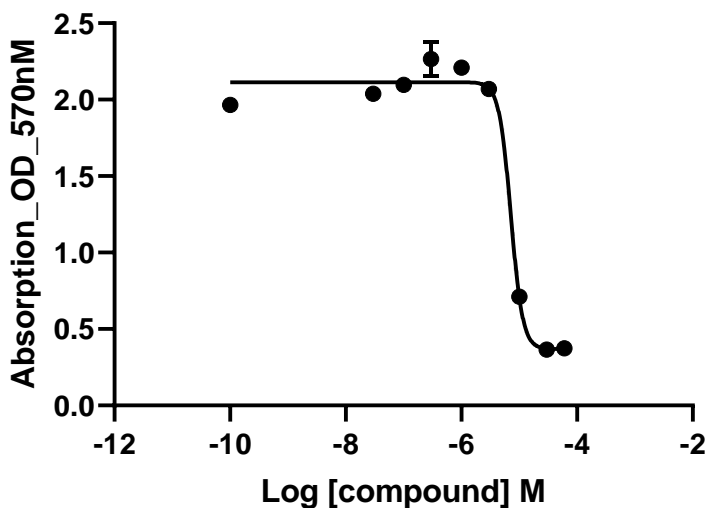

	IC50
XIE5-2-70	7.179e-006

U266 cells
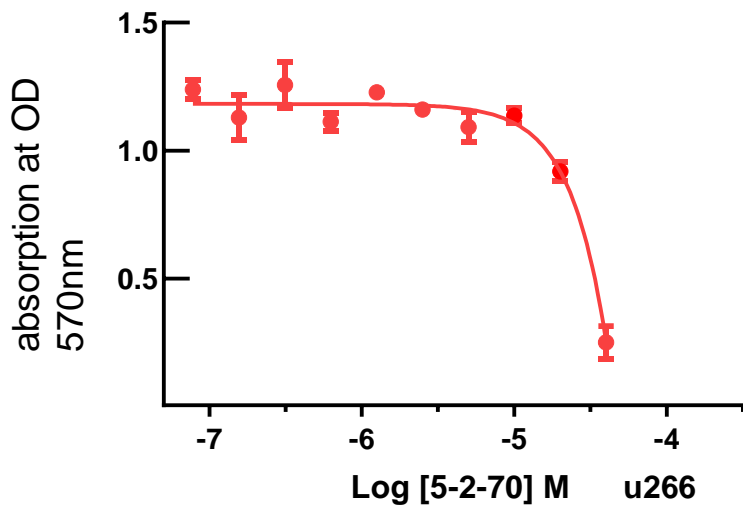
	5-2-70
IC50	~ 0.0009846

Neuro-protective effects on differentiated SH-SY5Y cells against hydrogen peroxide

XIE5-2-73

Anti-proliferative effects on multiple myeloma cell lines

U266 cells

XIE5-2-73
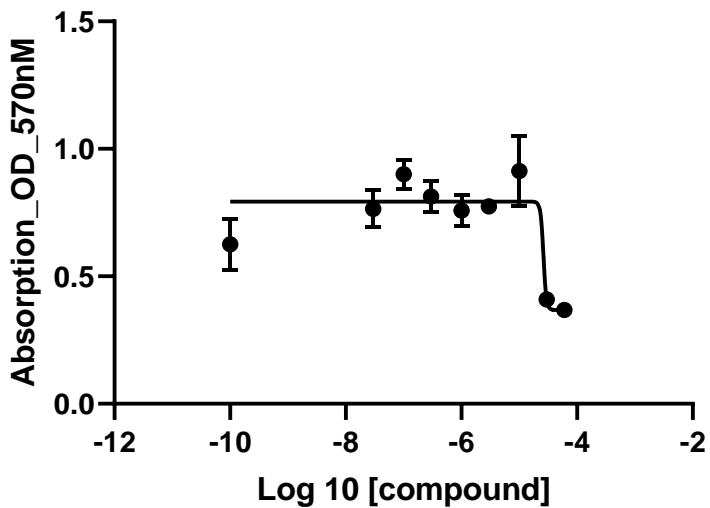
	IC50
XIE5-2-73	~ 2.626e-005

XIE5-2-74

Anti-proliferative effects on multiple myeloma cell lines
MM1.S. cells
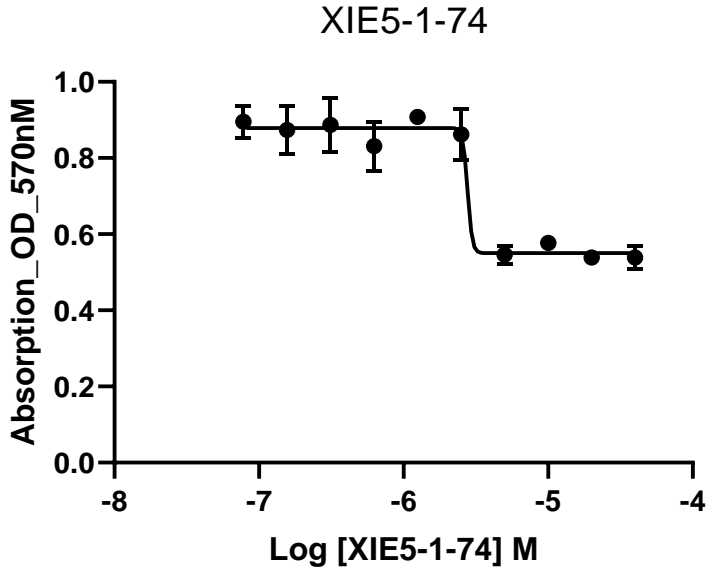
XIE5-1-74

	IC50
XIE5-1-74	~ 2.778e-006

RPMI8226 cells

U266 cells

Neuro-protective effects on differentiated SH-SY5Y cells against hydrogen peroxide

XIE5-1-74
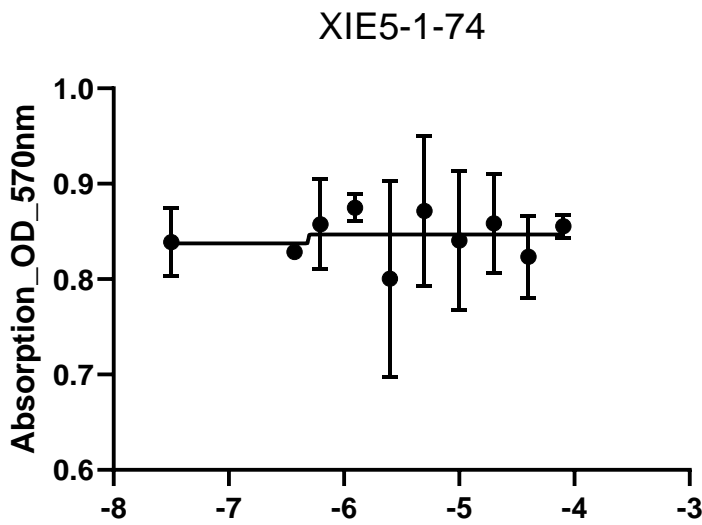
XIE5-2-80

Anti-proliferative effects on multiple myeloma cell lines
MM1.S. cells

XIE5-2-80
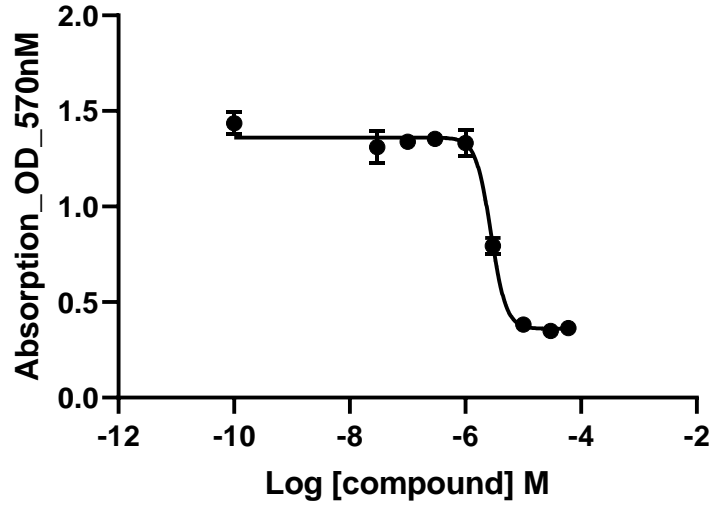
	IC50
XIE5-2-80	2.768e-006

RPMI8226 cells

U266 cells

XIE5-2-80
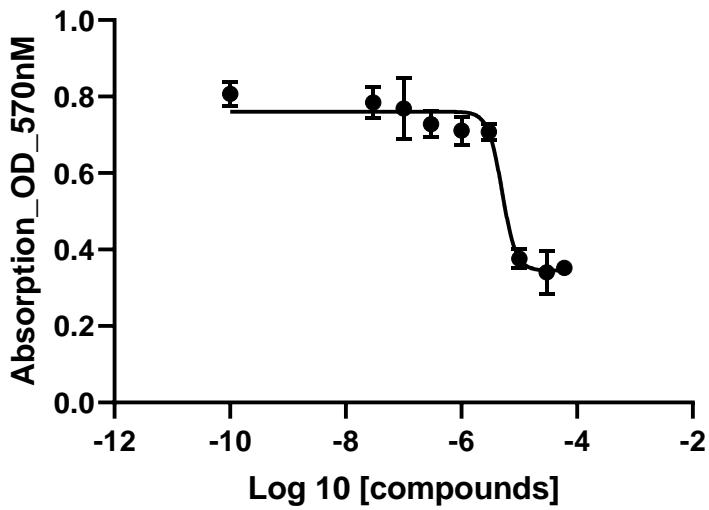
	IC50
XIE5-2-80	5.042e-006

Neuro-protective effects on differentiated SH-SY5Y cells against hydrogen peroxide
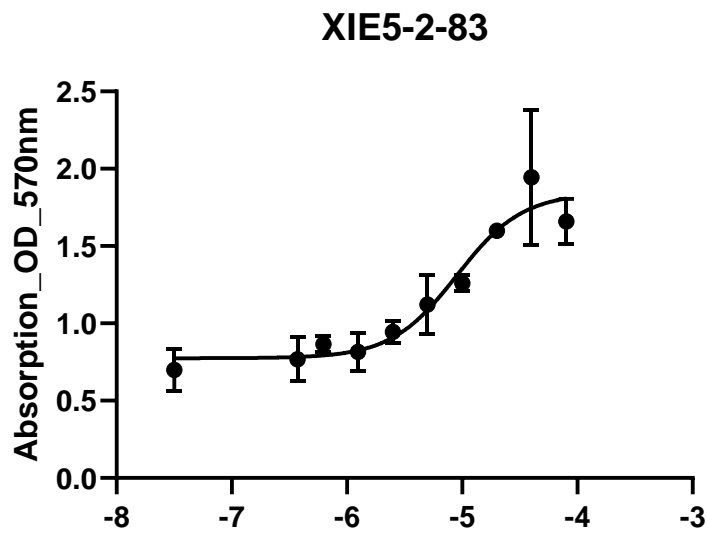
XIE5-2-83

	IC50
XIE5-2-83	8.973e-006

XIE5-2-85
Anti-proliferative effects on multiple myeloma cell lines
MM1.S. cells

RPMI8226 cells
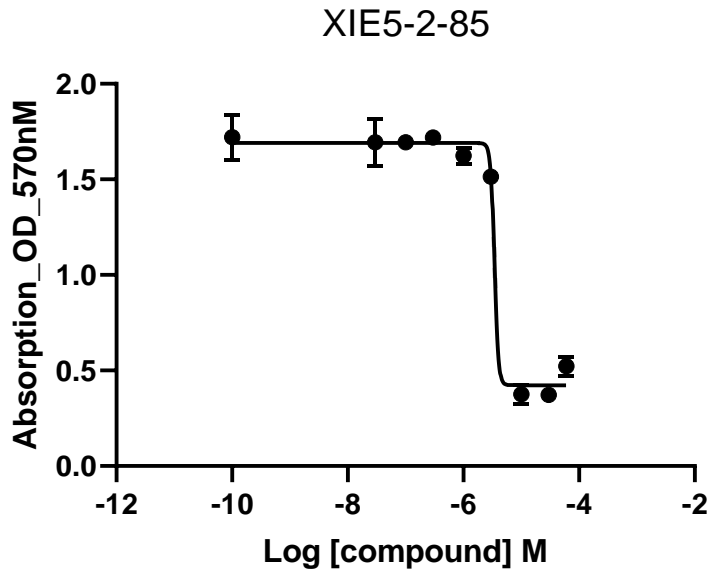
XIE5-2-85

	IC50
XIE5-2-85	~ 3.455e-006

U266 cells
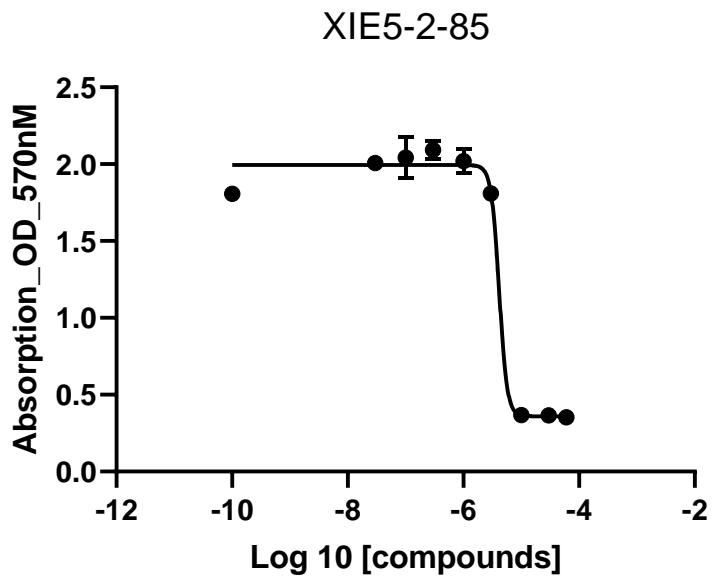
XIE5-2-85

	IC50
XIE5-2-85	4.154e-006

Neuro-protective effects on differentiated SH-SY5Y cells against hydrogen peroxide

XIE5-2-85
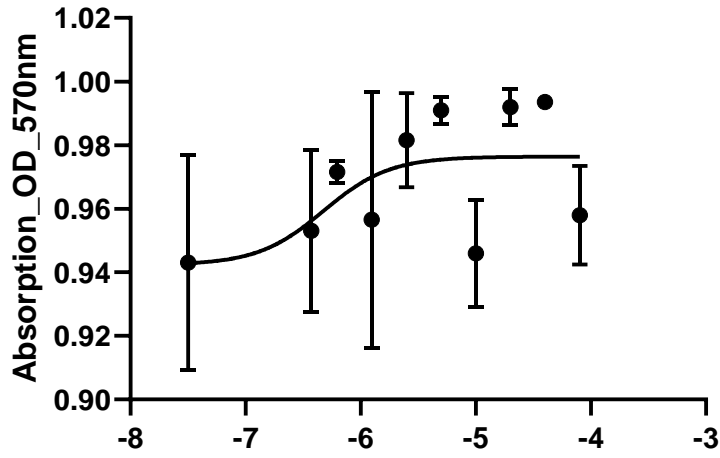
XIE5-2-87
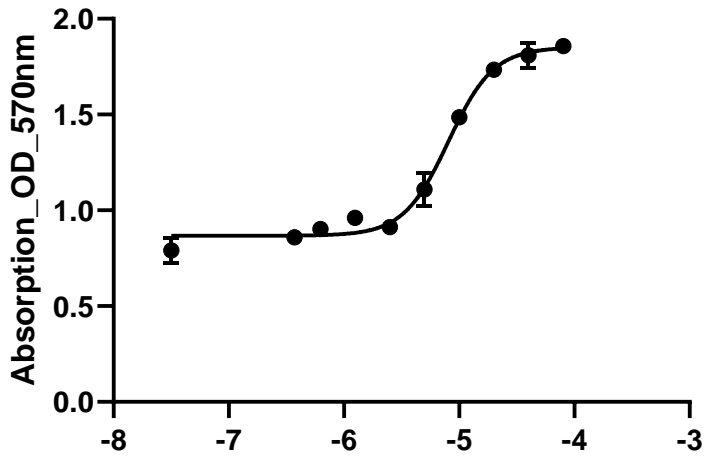Anti-proliferative effects on multiple myeloma cell lines
MM1.S. cells

RPMI8226 cells

XIE5-2-87
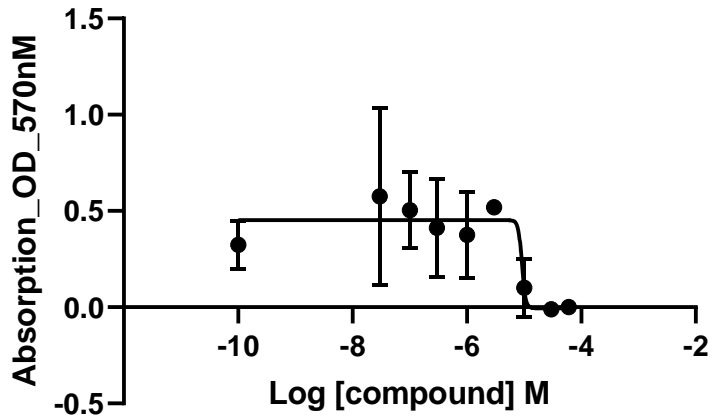
	IC50
XIE5-2-87	~ 9.174e-006

U266 cells

Neuro-protective effects on differentiated SH-SY5Y cells against hydrogen peroxide

XIE5-2-88

497

RPMI8226 cells

XIE5-2-88

	IC50
XIE5-2-88	~ 8.755e-006

U266 cells

XIE5-2-88
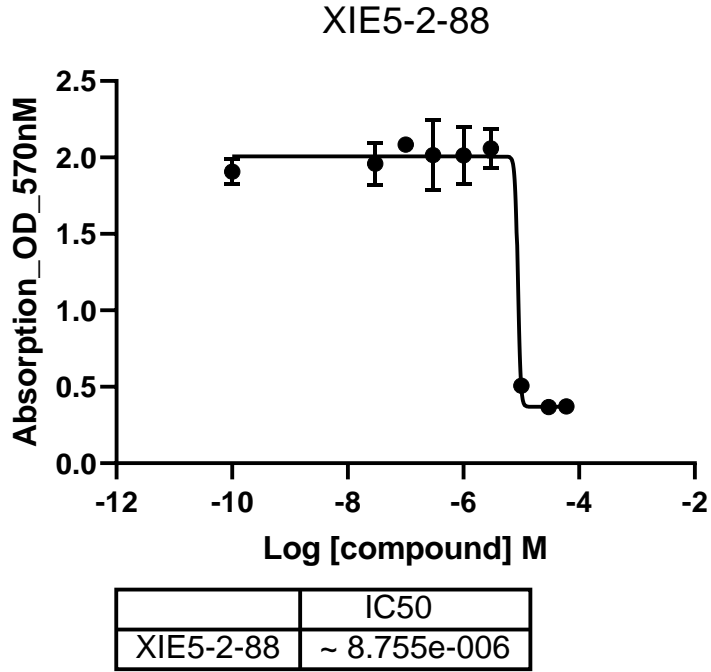
	IC50
XIE5-2-88	3.274e-006
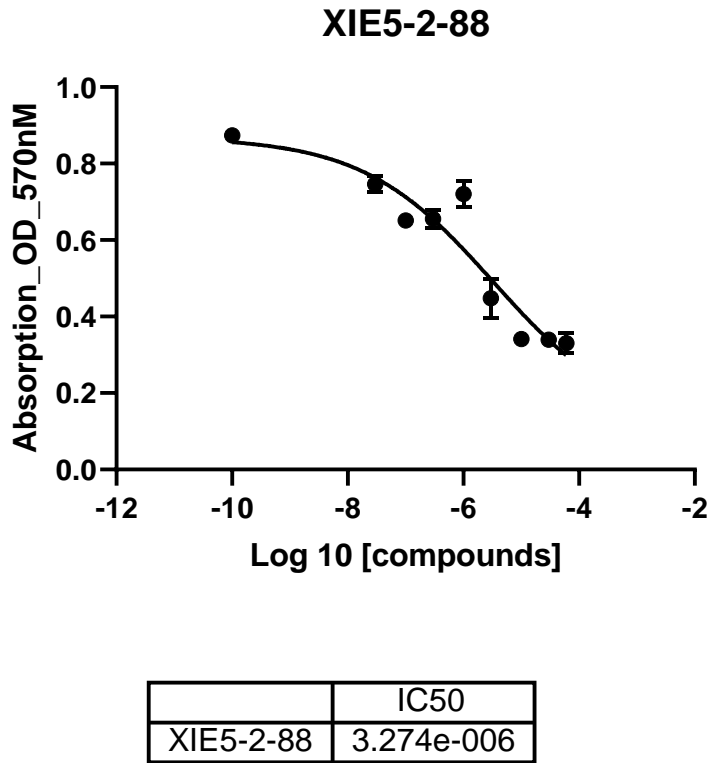
XIE5-1-33A
Anti-proliferative effects on multiple myeloma cell lines
MM1.S. cells
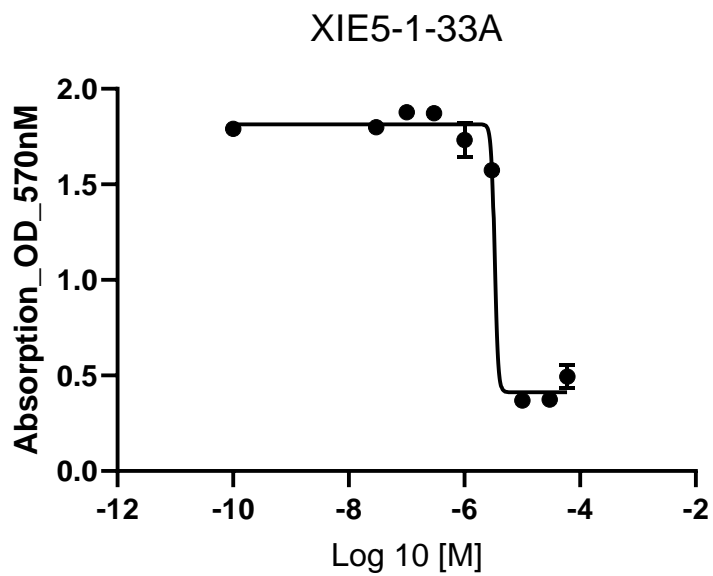
XIE5-1-33A

	IC50
XIE5-1-33A	~ 3.342e-006

RPMI8226 cells
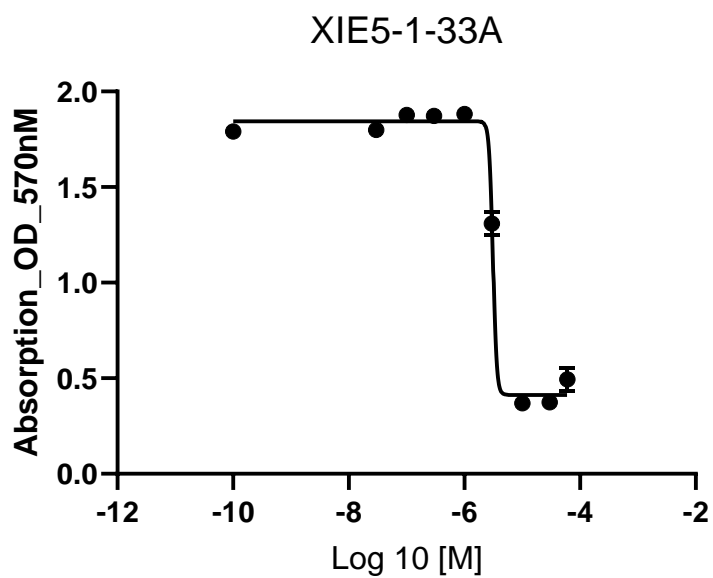
XIE5-1-33A

	IC50
XIE5-1-33A	~ 3.118e-006

U266 cells

XIE5-1-33A
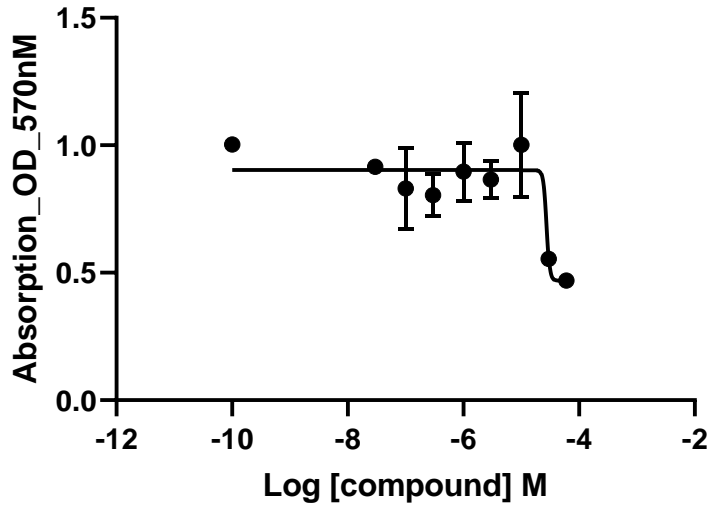
	IC50
XIE5-1-33A	~ 2.743e-005

Neuro-protective effects on differentiated SH-SY5Y cells against hydrogen peroxide

XIE5-1-33A
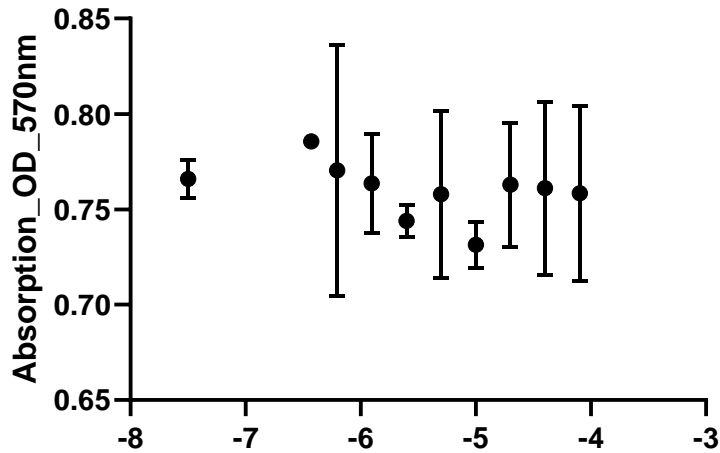
XIE5-1-64/54CT
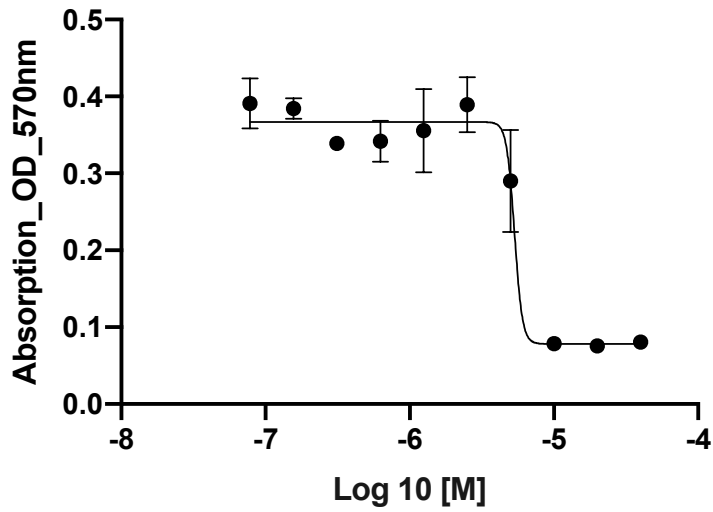Anti-proliferative effects on multiple myeloma cell lines
MM1.S. cells

RPMI8226 cells

Neuro-protective effects on differentiated SH-SY5Y cells against hydrogen peroxide

XIE5-1-54CT
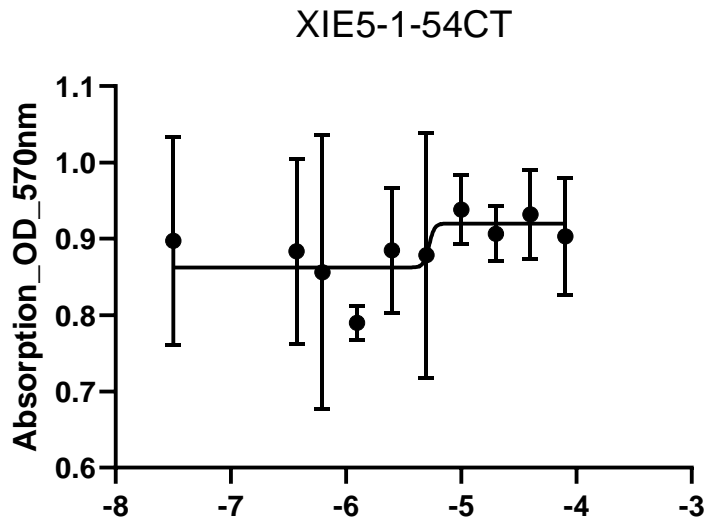
XIE5-1-65/55CT
Anti-proliferative effects on multiple myeloma cell lines
MM1.S. cells
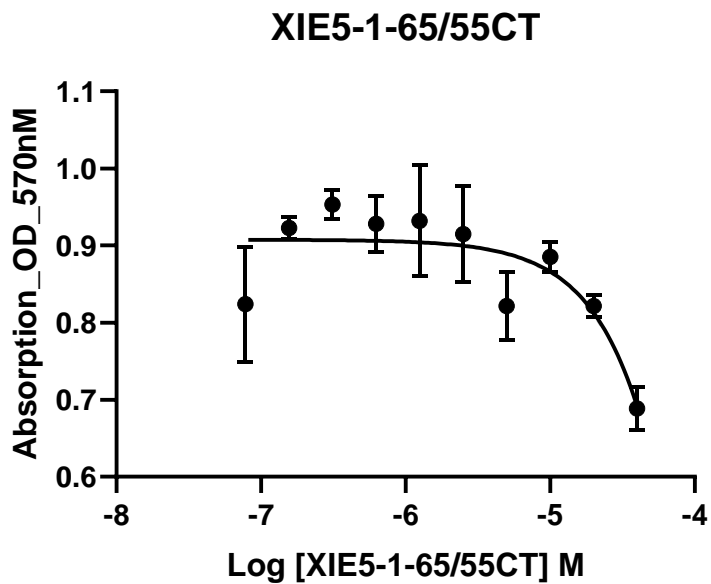
XIE5-1-65/55CT

	IC50
XIE5-1-65/55CT	~ 0.003140

RPMI8226 cells

XIE5-1-65/55CT
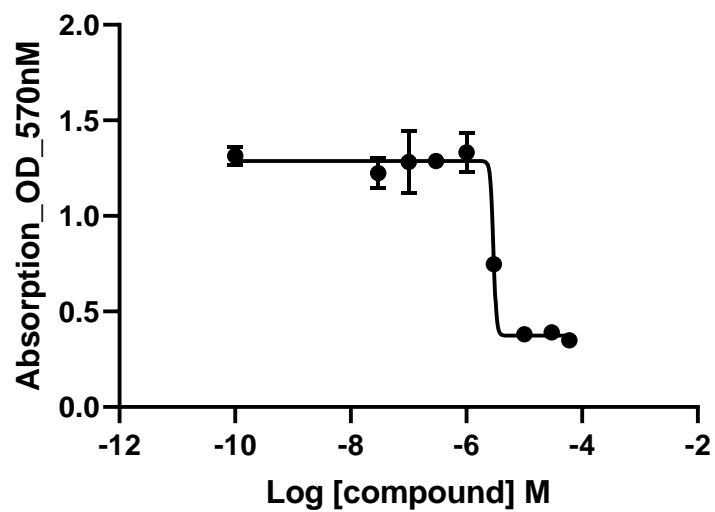
	IC50
XIE5-1-65/55CT	~ 2.934e-006

U266 cells

Neuro-protective effects on differentiated SH-SY5Y cells against hydrogen peroxide

XIE5-1-67/61BT
Anti-proliferative effects on multiple myeloma cell lines
MM1.S. cells

XIE5-1-67/61BT
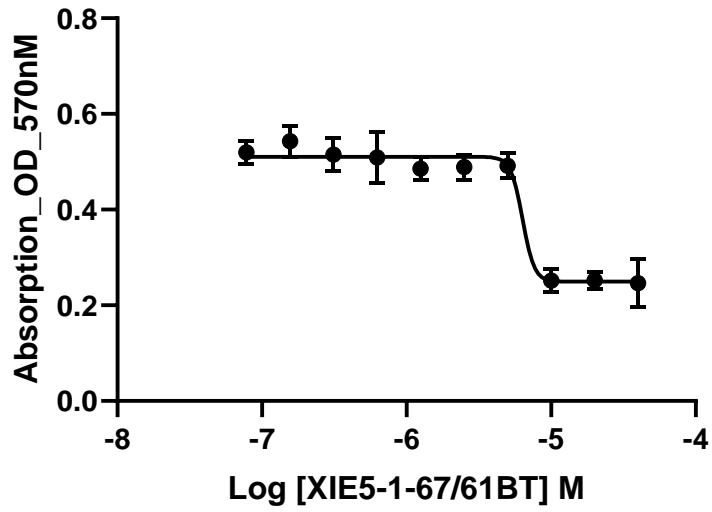
	IC50
XIE5-1-67/61BT	6.359e-006

RPMI8226 cells

U266 cells

Neuro-protective effects on differentiated SH-SY5Y cells against hydrogen peroxide

XIE5-1-68/26BT
Anti-proliferative effects on multiple myeloma cell lines
MM1.S. cells

## XIE5-1-68/2BT
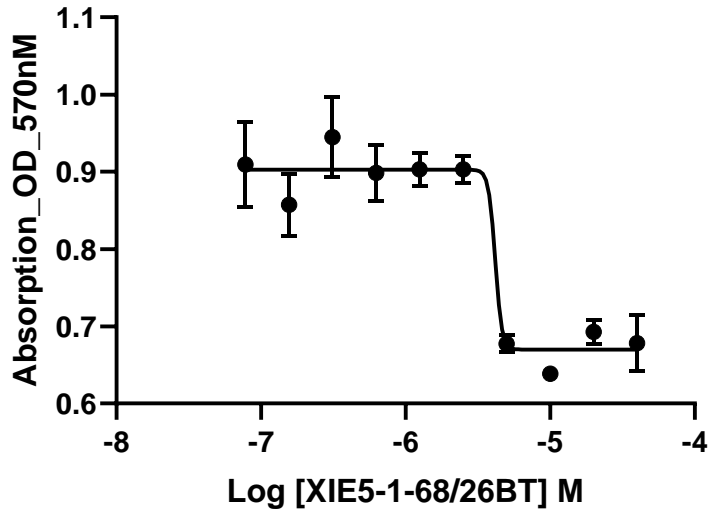
	IC50
XIE5-1-68/2BT	~ 4.179e-006

RPMI8226 cells

XIE5-1-26BT/68
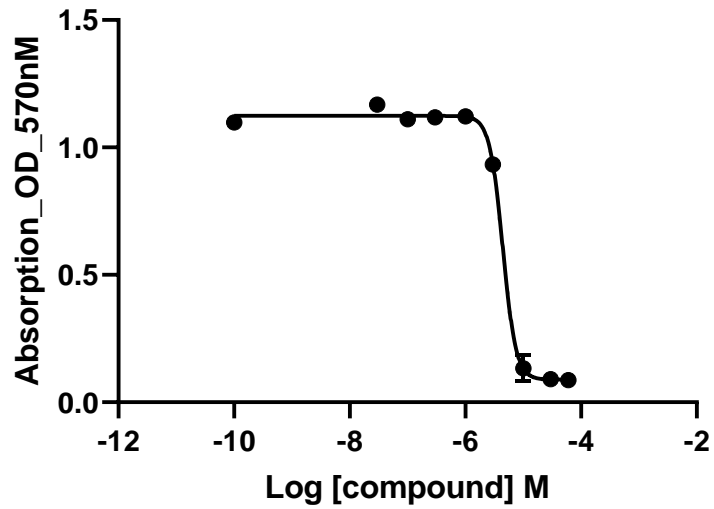
	IC50
XIE5-1-26BT/68	4.431e-006

XIE5-1-82
Anti-proliferative effects on multiple myeloma cell lines
MM1.S. cells

RPMI8226 cells

XIE5-1-82
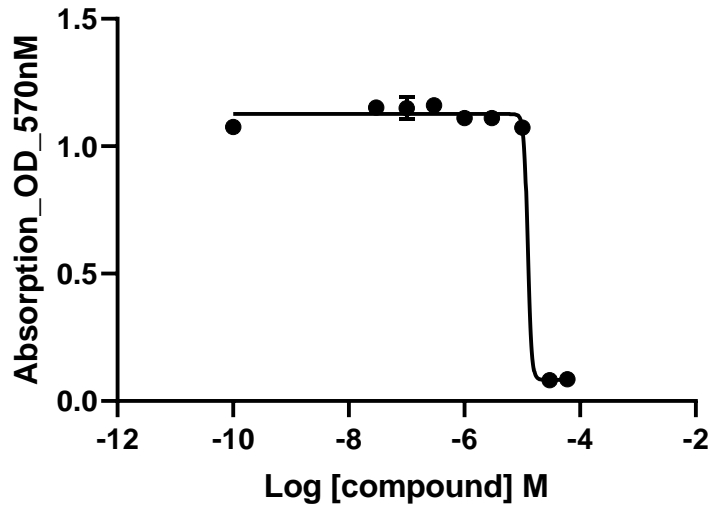
	IC50
XIE5-1-82	~ 1.247e-005

U266 cells

Neuro-protective effects on differentiated SH-SY5Y cells against hydrogen peroxide

XIE5-1-83
Anti-proliferative effects on multiple myeloma cell lines
MM1.S. cells

RPMI8226 cells

XIE5-1-83
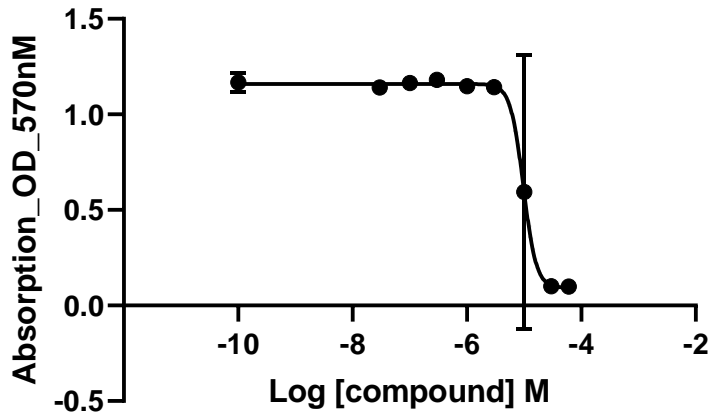
	IC50
XIE5-1-83	9.686e-006

U266 cells

Neuro-protective effects on differentiated SH-SY5Y cells against hydrogen peroxide
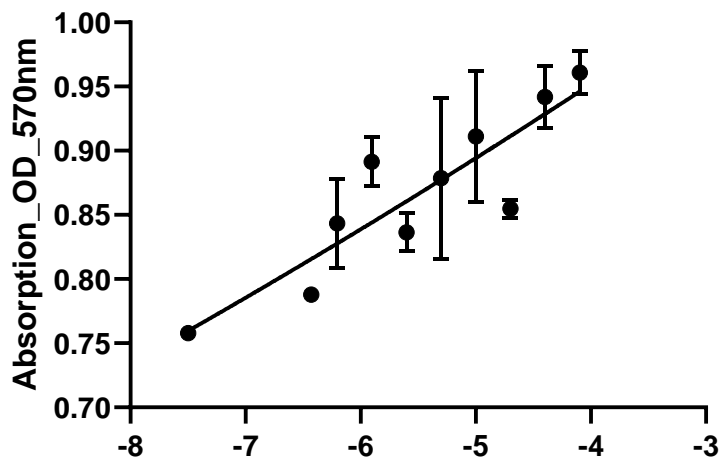
XIE5-1-83

	IC50
XIE5-1-83	~ 42164457230548

XIE106
Anti-proliferative effects on multiple myeloma cell lines
MM1.S. cells
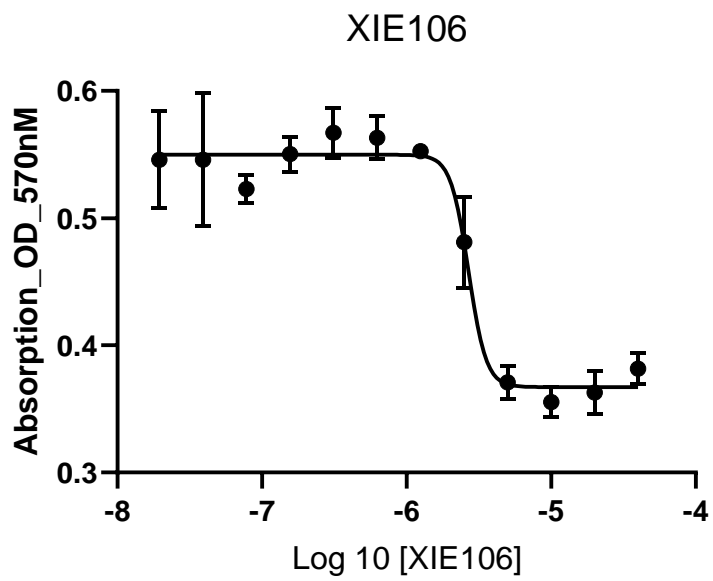
XIE106

	IC50
XIE106	2.686e-006

RPMI8226 cells

U266 cells

Neuro-protective effects on differentiated SH-SY5Y cells against hydrogen peroxide

Appendix D. Table of FDA-Approved MM Medications

We summarized the FDA-approved multiple myeloma medications with their drug name, approved date, company, brand name, adverse effects, mechanism of actions, and their mechanism of drug resistance in the following table. As all of them have drug resistance issues and severe side effects, there is still a need for new medications to treat multiple myeloma.

Appendix Table 1 Current Available Drugs in the Market for Multiple Myeloma Treatment.

Class	Drug Name	Approved Date	Company	Brand Name	Side Effects	Note or Mechanism of Action	Mechanism of drug resistance
Proteasome inhibitor	Bortezomib	2003	Millennium Pharmaceuticals,	Velcade	Gastrointestinal, transient cytopenias, fatigue, and peripheral neuropathy hypokalemia, hypertension, nerve damage. Serious cardiac dysfunction in approximately 5%	Inhibition of the activity of the 26S proteasome; Inhibition of NF-κB activity; induction of apoptosis by activation caspase-8 and caspase-9; downregulates the expression of adhesion molecules on PCM cells	Upregulation of the proteasomal system; point mutations of the PSMB5 gene and overexpression of the proteasome β5 subunit; modification and loss of 8p21; mutations and lo expression in the XBP1 gene; suppression; increased expression of the MARCKS protein; ABCB1 overexpression; overexpression CXCR4 gene; overexpression of proteins involved in protection from oxidative stress; overexpression of MAF; XBP1 suppression
	Carfilzomib	2012	Amgen Medical Information	Kyprolis			
	Ixazomib	2015	Takeda Pharmaceuticals	Ninlaro			
Immunotherapy	Thalidomide	1997	Celgene	Thalomid	Sedation, fatigue, rash, bradycardia, peripheral neuropathy, and constipation. Deep venous thrombosis is a serious adverse event necessitating routine prophylaxis with aspirin or other anticoagulant in all patients. Teratogen	Targeting PCM cells in the BM microenvironment; changing CRBN; triggering caspase-8-mediated apoptosis and enhancing caspase-8-mediated PCM cell apoptosis; triggering caspase-9- mediated MM cell killing; anti-angiogenic activity	Downregulation of CRBN expression; deregulation of IRF4 expression
	Lenalidomide	2004	Celgene	Revlimid	Fatigue, rash, thrombocytopenia, and neutropenia.		

	Pomal idomi de	2013	Celgene	Pomalyst	Deep venous thrombosis is a serious adverse event necessitating routine prophylaxis with aspirin or other anticoagulant in all patients. Diarrhea and leg cramps with long-term use. Teratogen		
Glucoco rticoid	Dexa metha sone	1958	Dexcel Pharma Technologies Ltd	Ozurdex, DexPak	Heartburn, indigestion, mood change, Problem with falling sleep, Increased appetite and weight gain	Induction of apoptosis of PCM cells; reduction in mitochondrial transmembrane potential, caspase 3 and poly (ADP ribose) polymerase cleavage	Functional defect of the glucocorticoid receptor; increased secretion of pro-survival cytokines BM microenvironment, overexpression of the oncogenes FGFR3 and MYC, epigenetic inactivation of RASD1, a GTPase member of Ras superfamily RASD1
	Mitox snteo ne			Novantrone			
	Predn isolon e	1995	Sciele Drug Safety	Pred Mild			
Chemoth erapy	Cyclo phosp hamid e	1959	Baxter Healthcare	Cytoxan	Infection, nausea, vomiting, hair loss, tummy upsets	DNA damage, immunostimulatory activity by inhibiting interleukin-6, interaction with dendritic cells, immunogenic effects in tumor microenvironment; topoisomerase II inhibition	Up-regulation of P-gp, increased ABCG2 expression, RECQ1 over-expression, overexpression of Bcl-xL
	Melp halan	1964	Spectrum Pharmaceutica ls, Inc.				
	Etopo side	1983	Bristol-Myers Squibb	VP-16			
	Melp halan flufen amide	2021	Oncopeptides Inc	Pepaxto		On February 26, 2021, the Food and Drug Administration granted accelerated approval to melphalan flufenamide (Pepaxto, Oncopept ides AB) in combination with dexamethasone for adult patients with relapsed or refractory multiple myeloma who have received at least four prior lines of therapy and whose disease is refractory to drugs	
	Benda musti ne	2008	Cephalon Inc.	Treanda	fatigue, rash, headache, constipation, and cytopenias		
	cispla tin	1978	WG Critical	CDDP	leukopenia, neuritic pain, and constipation		
	Vincri stine	2012	Acrotech Biopharm LLC	VinCRIStine Sulfate	hair loss, sensory loss, paresthesia, difficulty in walking, slapping gait, loss of deep–	Natural product	The mechanism of action of vincristine sulfate has been related to the inhibition of microtubule formation

					tendon reflexes, and muscle wasting		in mitotic spindle, resulting in an arrest of dividing cells at the metaphase stage.
Anthracyclines	Doxorubicin	1974	Pfizer, Inc	Adriamycin	Infection, nausea, vomiting, hair loss, tummy upsets	nucleotide base intercalation and cell membrane lipid binding activities of doxorubicin. Intercalation inhibits nucleotide replication and action of DNA and RNA polymerases. The interaction of doxorubicin with topoisomerase II to form DNA-cleavable complexes appears to be an important mechanism of doxorubicin HCl cytocidal activity	
	Liposomal doxorubicin	1995	Ortho Biotech	Doxil			
	Pirarubicin	1999	Pfizer Inc				
Bisphosphonates for bone disease	zoledronic acid	2001	Novartis	Zometa	a rare but serious side effect called osteonecrosis of the jaw (ONJ)	Myeloma cells can weaken and even break bones. Drugs called bisphosphonates can help bones stay strong by slowing down this process. They can also help reduce pain in the weakened bone(s). Sometimes, pain medicines such as NSAIDs or narcotics will be given along with bisphosphonates to help control or lessen the pain.	
	pamidronate	1991	Bedford Laboratories®	Aredia			
	denosumab	2010	Amgen Inc	Xgeva, Prolia			
HDAC inhibitors	Panobinostat	2015	Novartis Pharmaceuticals Corporation	Farydak	Diarrhea, thrombocytopenia, fatigue		
CD38	daratumumab and hyaluronidase	2020	Janssen Biotech, Inc.	Darzalex Faspro	coughing, wheezing, trouble breathing, tightness in the throat, a runny or stuffy nose, feeling dizzy or lightheaded, headache, rash, and nausea, fatigue, anemia,	Antibody-dependent cellular cytotoxicity (ADCC), complement-dependent cytotoxicity (CDC), macrophage-mediated phagocytosis, and apoptosis via Fc-mediated crosslinking; stimulatory effects on immune cells, particularly NK cells	Downregulation of CD38 expression [135]; upregulation of CD55 and CD59 on the PCM cells
	Isatuximab	2020	sanofi-aventis U.S. LLC	SAR650984			
	Daratumumab	2015	Janssen Biotech, Inc.	Darzalex			
SLAMF7	Elotuzumab	2015	Bristol-Myers Squibb	Sarclisa	Infusion-related reactions, fatigue, infections, fever, chills, feeling dizzy or lightheaded, rash, wheezing, trouble		

					breathing, tightness in the throat, or a runny or stuffy nose, fatigue, fever, loss of appetite, diarrhea, constipation, cough, nerve damage resulting in weakness or numbness in the hands and feet (peripheral neuropathy), upper respiratory tract infections, and pneumonia		
Antibody-drug conjugates	Belantamab mafodotin-blmf	2020	GlaxoSmithKline	Blenrep			
Nuclear export inhibitor	Selinexor	2019	Karyopharm Therapeutics Inc	Xpovio	low platelet counts, low white blood cell counts, diarrhea, nausea, vomiting, not feeling hungry, weight loss, low blood sodium levels, and infections like bronchitis or pneumonia.	The nucleus of a cell holds most of the cell's genetic material (DNA) needed to make the proteins the cell uses to function and stay alive. A protein called XPO1 helps carry other proteins from the nucleus to other parts of the cell.	
PD-1	Pembrolizumab	2014	Merck	KEYTRUDA			
PDL-1	Durvalumab	2017	AstraZeneca, FiercePharma	IMFINZI			

Note: The data from this table were collected from the American Cancer Society website (71), the FDA label for each drug, and literature reports (70, 72, 74, 75).

Appendix E. Table of Drug Candidates in AD Clinical Trials

This section shows a table for the drug candidates in the clinical trials to treat Alzheimer's disease.

Some of them have a mechanism similar to what we proposed in this study.

Appendix Table 2. Drug Candidates in Alzheimer's clinical trials

Drug Candidate	Developing Phase	Administration	Clinical trial ID
(-)-Huperzine A	Clinical trial - Phase II/III	oral/tablet, extended-release	NCT01282619
(+)-Phenserine	Clinical trial		PMID: 18300284
2-(3-Isoxazolyl)-3,6,7,9-tetrahydroimidazol[4,5-d]pyrano[4,3-b]pyridine	Discontinued		
AAB-003	Clinical trial - Phase I	intravenous	NCT01193608
ACN-288	Clinical trial - Phase II	oral	NCT01018875
ABT-384	Clinical trial - Phase II		NCT01137526
ABT239	Clinical trial		PMID: 15608078
ABT418	Clinical trial		PMID: 10229057
AC-1204	Clinical trial - Phase II/III	oral	NCT01741194
Acitretin	Clinical trial - Phase II	oral	NCT01078168
Aducanumab	Clinical trial - Phase I	intravenous/infusion	NCT01397539
Aftobetin	Clinical trial		Link
AGN-229666	Clinical trial - Phase II	ophthalmic	NCT01754766
Aleplasinin	Clinical trial - Phase I		NCT00739037
Alfatradiol	Clinical trial		

Allotetrahydroprogesterone	Clinical trial - Phase I	intravenous/injection	NCT02221622
Alvameline	Discontinued		
Ampalex	Clinical trial - Phase II	oral	NCT00001662
Arecoline	Discontinued		PMID: 8841150
Arundic acid	Clinical trial - Phase II		NCT00083421
ATP	Clinical trial - Phase II	intravenous/infusion	NCT02279511
Avagacestat	Clinical trial - Phase II	oral/capsule	NCT00890890
AZD1446	Clinical trial - Phase II	oral/capsule	NCT01039701
AZD1446	Clinical trial - Phase II	oral/capsule	NCT01125683
AZD5213	Clinical trial - Phase I		NCT01121302
AZD5213	Clinical trial - Phase II		NCT01548287
BAN2401	Clinical trial - Phase II		NCT01767311
BAN2401	Clinical trial - Phase II		NCT01767311
Bapineuzumab	Clinical trial - Phase I	intravenous/infusion	NCT00397891
Bapineuzumab	Clinical trial - Phase I	intravenous/infusion	PMID: 20505438
Bapineuzumab	Clinical trial - Phase II	intravenous	NCT00174525
Bapineuzumab	Clinical trial - Phase III	intravenous	NCT00574132
Bapineuzumab	Clinical trial - Phase II	intravenous	NCT00606476
Bapineuzumab	Clinical trial - Phase II	intravenous	NCT00112073
Bapineuzumab	Clinical trial - Phase II	subcutaneous/injection	NCT00663026
Bapineuzumab	Clinical trial - Phase II	subcutaneous/injection	NCT01254773
BCI-632	Clinical trial - Phase I		Link
BCI-838	Clinical trial - Phase I	oral	Link
Begacestat	Clinical trial - Phase I		NCT00479219

Benfotiamine	Clinical trial - Phase II		NCT02292238
Besipirdine	Discontinued		PMID: 8624122
Bexarotene	Clinical trial - Phase II		NCT01782742
BI1034020	Clinical trial - Phase I		Link
Bifeprunox	Clinical trial - Phase III	oral	NCT00160147
BMS299897	Preclinical		
Bradanicline	Clinical trial - Phase I	oral/capsule	NCT01254448
Brexpiprazole	Clinical trial - Phase III	oral	NCT01922258
Bryostatin 1	Clinical trial - Phase II	intravenous	NCT00606164
Bupropion	Clinical trial - Phase III	oral/tablet	NCT01047254
Capeserod	Clinical trial - Phase I		PMID: 15975071
Caprospinol	Approved		
Carvedilol	Clinical trial - Phase IV	oral	NCT01354444
Cebaracetam	Discontinued		
Cerlapirdin	Clinical trial - Phase II	oral	NCT00895895
CHF5074	Clinical trial - Phase I	oral/capsule	NCT00954252
CHF5074	Clinical trial - Phase II	oral/tablet	NCT01303744
Citalopram	Clinical trial - Phase III		NCT00898807
Clioquinol	Clinical trial		
Crenezumab	Clinical trial - Phase II	subcutaneous/injection	NCT01343966
CTS21166	Clinical trial - Phase I	intravenous	NCT00621010
CX717	Clinical trial - Phase II		Link
D-Pinitol	Clinical trial - Phase II		NCT01928420
Dapsone	Clinical trial - Phase II		Link
DAPT	Preclinical		PMID: 16192379
Davunetide	Clinical trial - Phase II	intravenous	NCT00404014

Distigmine	Approved		
DMP543	Discontinued		
Donepezil	FDA approved	oral/tablet	Drug label
Drinabant	Clinical trial - Phase I/II		NCT00380 302
DSP-8658	Preclinical		PMID: 23197723
DWP09031	Clinical trial - Phase I	oral	NCT01522 586
E2012	Clinical trial - Phase I		Link
E2212	Clinical trial - Phase I	oral	NCT01221 259
E2609	Clinical trial - Phase I	oral	NCT01294 540
Efaroxan	Discontinued		Link
Encenicline	Clinical trial - Phase II	oral/capsule	NCT01073 228
Encenicline	Clinical trial - Phase III	oral/tablet	NCT01969 136
Epigallocatechin	Clinical trial - Phase II/III		NCT00951 834
Epothilone D	Clinical trial - Phase I	intravenous	NCT01492 374
Eptastigmine	Discontinued		
Escitalopram	Clinical trial	oral	NCT00702 780
Etazolate	Clinical trial - Phase II	oral/capsule	NCT00880 412
EVP-0962	Clinical trial - Phase II	oral	NCT01661 673
Exenatide	Clinical trial - Phase II		NCT01255 163
Facinicline	Clinical trial - Phase II	oral	NCT00454 870
Facinicline	Clinical trial - Phase II	oral	NCT00884 507
Filgrastim	Clinical trial - Phase I/II	subcutaneous	NCT01617 577
FK960	Discontinued		
FK962	Clinical trial - Phase II		NCT00087 724
Gabapentin	Clinical trial		NCT00018 291
Galantamine	FDA approved	oral/capsule, extended release	Drug label

Galantamine	FDA approved	oral/tablet	Drug label
Ganstigmine	Clinical trial	oral	PMID: 12782920
Gantenerumab	Clinical trial - Phase III	subcutaneous	NCT01224106
Gemfibrozil	Clinical trial	oral	NCT02045056
GSI-136	Clinical trial - Phase I	oral	NCT00718731
GSK239512	Clinical trial - Phase II	oral/tablet	NCT01009255
GSK2647544	Clinical trial - Phase I	oral	NCT01702467
GT1061	Clinical trial - Phase I	oral	PMID: 15665418
GTS-21	Clinical trial - Phase II	oral	NCT00414622
HF0220	Clinical trial - Phase II		NCT00357357
HPP854	Clinical trial - Phase I	oral	NCT01482013
Ibutamoren	Clinical trial - Phase II	oral	NCT00074529
Idalopirdine	Clinical trial - Phase III	oral/tablet	NCT02006654
Idebenone	Approved	oral	Drug label
Insulin Detemir	Clinical trial - Phase II	nasal	NCT01547169
Insulin lispro	Clinical trial		NCT01636596
Insulin_(HUMAN)	Clinical trial - Phase II/III	nasal	NCT01767909
Interferon beta-1a	Clinical trial - Phase II	subcutaneous/injection	NCT01075763
Irdabisant	Clinical trial - Phase I		Link
Isotretinoin	Clinical trial - Phase I/II		NCT01560585
Ispronicline	Clinical trial - Phase II	oral	NCT00501111
Itameline	Discontinued		
ITI-009	Preclinical		Link
JNJ-54861911	Clinical trial - Phase I	oral	NCT01827982
KHK6640	Clinical trial - Phase I		NCT02127476

Ladostigil	Clinical trial - Phase II	oral	NCT01354 691
Latrepirdine	Clinical trial - Phase III	oral/tablet	NCT00829 374
Lecozotan	Clinical trial - Phase II/III	oral	NCT00277 810
Leteprinim	Clinical trial - Phase I	oral	PMID: 12770610
Leuprorelin	Clinical trial - Phase III		NCT00231 946
Li+	Clinical trial - Phase II	oral/tablet	NCT01055 392
Liraglutide	Clinical trial - Phase II	subcutaneous/inj ection	NCT01843 075
Liraglutide	Clinical trial		NCT01469 351
Lornoxicam	Clinical trial - Phase II	oral/tablet	NCT01117 948
LY2811376	Clinical trial - Phase I	oral/capsule	NCT00838 084
LY2886721	Clinical trial - Phase I		NCT01133 405
LY2886721	Clinical trial - Phase I/II	oral/capsule	NCT01561 430
LY3002813	Clinical trial - Phase I	intravenous	NCT01837 641
LY3002813	Clinical trial - Phase I	subcutaneous	NCT01837 641
Masitinib	Clinical trial - Phase II	oral	NCT00976 118
Masitinib	Clinical trial - Phase III		NCT01872 598
MCI225	Clinical trial - Phase II		Link
MEDI1814	Clinical trial - Phase I	intravenous/inje ction	NCT02036 645
MEDI1814	Clinical trial - Phase I	subcutaneous/inj ection	NCT02036 645
MEM1003	Clinical trial - Phase II	oral	NCT00257 673
MEM1414	Clinical trial	oral	Link
Memantine	FDA approved	oral/tablet	Drug label
Metformin	Clinical trial - Phase II		NCT01965 756
Metformin	Clinical trial - Phase II		NCT01965 756

Name	Drug Status	Route&Delivery	Source
Methanesulfonyl fluoride	Clinical trial - Phase I	oral	Link
Methylene blue	Clinical trial - Phase II	oral/capsule	NCT00515333
Methylphenidate	Clinical trial - Phase II	oral/tablet	NCT01117181
Mibampator	Clinical trial - Phase II		NCT00051909
Mifepristone	Clinical trial - Phase I/II	oral	NCT00105105
Milameline	Discontinued		PMID: 10188788
Mimopezil	Clinical trial - Phase II	oral/capsule	NCT00423228
Mimopezil	Clinical trial - Phase II	subcutaneous/implant	NCT00423228
Minocycline	Clinical trial - Phase II		NCT01463384
Mixture of IgG1	Clinical trial - Phase III	intravenous	NCT01736579
MK 0952	Clinical trial - Phase II		NCT00362024
MK-0249	Clinical trial - Phase II	oral/tablet	NCT00420420
MK-8931	Clinical trial - Phase III	oral/tablet	NCT01953601
MK-8931	Clinical trial - Phase II/III	oral/tablet	NCT01739348
MK-8931	Clinical trial - Phase I	oral/capsule	NCT01496170
MSDC-0160	Clinical trial - Phase II	oral/capsule	NCT01374438
Name	Drug Status	Route&Delivery	Source
Nefiracetam	Clinical trial - Phase II		NCT00001933
Nelonicline	Clinical trial - Phase II		NCT00948909
Neramexane	Clinical trial - Phase III	oral	NCT00090116
NGD 97-1	Discontinued		
NGX267	Clinical trial - Phase I		Link
Nicotinamide	Clinical trial - Phase I/II	oral/tablet	NCT00580931
Nilvadipine	Clinical trial - Phase III	oral/tablet	NCT02017340

Nilvadipine	Clinical trial		PMID: 18097255
Nitroflurbiprofen	Clinical trial - Phase I	oral	Link
NSA-789	Clinical trial - Phase I	oral	NCT00795730
Octahydroaminoacridine	Clinical trial - Phase II	oral/tablet	NCT01569516
ODM-102	Clinical trial - Phase I		NCT01839019
ORM-12741	Clinical trial - Phase II	oral	Link
OSI754	Clinical trial - Phase I		NCT01013610
Paliroden	Clinical trial - Phase II	oral	NCT00285025
PBT2	Clinical trial - Phase II	oral	NCT00471211
PF-03654746	Clinical trial - Phase I	oral/capsule	NCT01028911
PF-05297909	Clinical trial - Phase I	oral	NCT01462851
PF04447943	Clinical trial - Phase II	oral/tablet	NCT00930059
PF04494700	Clinical trial - Phase III	oral	NCT02080364
PF04494700	Clinical trial - Phase II	oral	NCT00141661
PF04995274	Clinical trial - Phase I		NCT01091272
Pimavanserin	Clinical trial - Phase II	oral/tablet	NCT02035553
Pioglitazone	Clinical trial - Phase III	oral/tablet	NCT01931566
Pioglitazone	Clinical trial - Phase II	oral	NCT00982202
Ponezumab	Clinical trial - Phase I	intravenous/infusion	NCT00607308
Ponezumab	Clinical trial - Phase II	intravenous	NCT00945672
Ponezumab	Clinical trial - Phase I	intravenous/infusion	NCT00733642
Ponezumab	Clinical trial - Phase I	intravenous/infusion	PMID: 23334070
Ponezumab	Clinical trial - Phase II	intravenous	NCT00722046

Ponezumab	Clinical trial - Phase I	intravenous/infusion	NCT01125631
Posatirelin	Discontinued		PMID: 7484061
Pozanicline	Clinical trial - Phase II		NCT00069849
PPI1019	Clinical trial - Phase I/II	intravenous	NCT00100334
Pramipexole	Clinical trial - Phase II	oral/liquid	NCT01388478
Prazosin	Clinical trial	oral/capsule	NCT01126099
Propentofylline	Clinical trial - Phase III	oral/capsule	PMID: 9298634
PRX03140	Clinical trial - Phase II		NCT00672945
PRX07034	Clinical trial - Phase I		Link
Quilostigmine	Discontinued		
R4996	Clinical trial		Link
Radequinil	Clinical trial - Phase II	oral/tablet	NCT00359944
Raloxifene	Clinical trial - Phase II/III	oral	NCT00065767
Rasagiline	Clinical trial		
Resveratrol	Clinical trial - Phase III	oral/capsule	NCT00743743
RG7129	Clinical trial - Phase I		Link
Rilapladib	Clinical trial - Phase II	oral	NCT01428453
Riluzole	Clinical trial - Phase II	oral/tablet	NCT01703117
Risperidone	Clinical trial		NCT00018291
Rivastigmine	FDA approved	oral/capsule	Drug label
Rivastigmine	FDA approved	transdermal/patch	Drug label
RO5508887	Clinical trial - Phase I	oral	NCT01461967
RO6926496	Clinical trial - Phase I		Link
Rosiglitazone	Clinical trial - Phase III	oral	NCT00428090
Sabcomeline	Clinical trial - Phase III		Link
sabeluzole	Discontinued		PMID: 9260731

SAM-315	Clinical trial - Phase I	oral	NCT00474552
SAM-760	Clinical trial - Phase I	oral/capsule	NCT01159496
SAR110894	Clinical trial - Phase I	oral	NCT01266525
Saracatinib	Clinical trial - Phase II		NCT02167256
Saracatinib	Clinical trial - Phase I	oral	NCT01864655
Sargramostim	Clinical trial - Phase II	subcutaneous/injection	NCT01409915
SB271046	Discontinued		
SB742457	Clinical trial - Phase II		NCT00708552
SB742457	Clinical trial - Phase II	oral	NCT00710684
Scyllo-Inositol	Clinical trial - Phase II	oral	NCT00568776
Scyllo-Inositol	Clinical trial - Phase II	oral	NCT00934050
Semagacestat	Clinical trial - Phase III	oral/tablet	NCT00594568
Semagacestat	Clinical trial - Phase III	oral/tablet	NCT00594568
Sembragiline	Clinical trial - Phase II	oral	NCT01677754
SGS742	Clinical trial - Phase II	oral	NCT00093951
SL251188	Discontinued		
Smilagenin	Clinical trial - Phase II		NCT00130429
Solanezumab	Clinical trial - Phase II	intravenous	NCT00329082
Solanezumab	Clinical trial - Phase III	intravenous	NCT00904683
Solanezumab	Clinical trial - Phase II	intravenous	NCT00329082
SRA-444	Clinical trial - Phase I	oral	NCT00499200
SSR180711	Clinical trial - Phase II		NCT00602680
ST 101	Clinical trial - Phase II	oral/tablet	NCT00842673

ST 101	Clinical trial - Phase II	oral/tablet	NCT00842816
T817MA	Clinical trial - Phase II	oral	NCT00663936
Tacrine	FDA approved	oral/capsule	Drug label
Talsaclidine	Discontinued		PMID: 12762134
Tamibarotene	Clinical trial - Phase II	oral/tablet	NCT01120002
Tarenflurbil	Clinical trial - Phase III	oral	NCT00105547
Tazomeline	Discontinued		
Tesofensine	Clinical trial - Phase II	oral	NCT00153010
Thalidomide	Clinical trial - Phase II/III		NCT01094340
Tideglusib	Clinical trial - Phase I/II	oral	NCT01049399
Tideglusib	Clinical trial - Phase II	oral/suspension	NCT01350362
TPI287	Clinical trial - Phase I	intravenous/infusion	NCT01966666
Tramiprosate	Clinical trial - Phase III		NCT00088673
Tricaprylin	Clinical trial - Phase II		NCT00142805
TRx0237	Clinical trial - Phase II	oral/tablet	NCT01626391
TRx0237	Clinical trial - Phase III	oral/tablet	NCT01689246
TTP4000	Clinical trial - Phase I	subcutaneous/injection	NCT01548430
Vanutide cridificar	Clinical trial - Phase II	intramuscular	NCT00498602
Varenicline	Clinical trial - Phase II	oral/tablet	NCT00744978
Vitamin E	Clinical trial - Phase III	oral/capsule	NCT00235716
VP025	Clinical trial - Phase I		Link
Xaliproden	Clinical trial - Phase III	oral	NCT00103649
Xanomeline	Discontinued	transdermal/patch	PMID: 11790638
Zanapezil	Discontinued		

Appendix E. Predicted ADME Properties by Pkcsm

The predicted properties related to absorption and distribution calculated by pkCSM (http://biosig.unimelb.edu.au/pkcsm/) were listed in **Table 32. Table 33** shows the metabolism and excretion properties predicted by pkCSM. The predicted properties of our in-house compounds about toxicity calculated by pkCSM were listed in **Table 34**.

Table 32 listed commonly used absorption properties, including water solubility (log mol/L), Caco-2 permeability (>0.9, high permeability), intestinal absorption (<30, poor absorption), skin permeability (log Kp >-2.5, poor permeability), P-gp substrate and inhibitor, as well as distribution-related parameters, involving volume of distribution at steady state (VDss< -0.15, low; VDss > 0.45, high), fraction unbound with plasma protein (fu<0.01, high plasma protein binding), capacity to pass blood-brain barrier (logBB>0.3, readily cross BBB, logBB<-1, poorly distributed in brain) and distribute in CNS (logPS>-2 can penetrate CNS, logPS <-3 cannot penetrate CNS).

From **Table 32,** most of absorption and distribution related properties are within the acceptable range for drugs. Only a few compounds have a poor aqueous solubility (**3-4**, XIE5-2-73, <-7 log(mol/L)). Also, some compounds with guanidine groups, such as XIE5-1-23, XIE1-4-3, XIE5-1-27AT, XIE5-1-25, and XIE5-2-45 that with a score below 0, are in lack of ability to cross the caco-2 cell membranes, indicating a potential problem for permeability for analogs with this functional group. As for drug distribution, some of our compounds has a very high plasma protein binding affinity, in which fraction unbound is less than 0.01 (larger than 99% binding),

suggesting a potential risk of using these compounds with other high plasma protein binding drugs together, due to toxicity problem caused by a large fluctuation of plasma concentration of drugs. On the other side, a few compounds are observed with a low possibility to penetrate BBB (logBB<-1) to get into CNS (log PS <-3). Analogs with guanidine groups occupies a majority of these compounds, including XIE5-2-40, XIE5-1-27AT, XIE5-1-65, XIE5-1-68/26BT, XIE5-1-67/61BT, and XIE5-1-65/55CT. These compounds might not be a good choice for CNS-acting drug candidates.

Appendix Table 3 Predicted Absorption/Distribution Properties for p62 Ligands by pkCSM.

Name	ID	Water solubility	Caco2	Intestinal absorption (human)	Skin Permeability	P-gp substrate	P-gp I inhibitor	P-gp II inhibitor	VDss	Fraction unbound	BBB	CNS
XIE5-1-8	3.1	-5.92	2.30	93.51	-2.64	No	No	Yes	-0.19	0.00	0.46	-1.15
XIE5-1-33A	3.2	-5.58	2.29	91.24	-2.64	No	No	Yes	-0.19	0.00	0.42	-1.42
XIE5-2-54/55	3.7	-6.12	1.06	89.58	-2.74	Yes	Yes	Yes	0.26	0.08	0.73	-0.55
XIE5-2-51	3.16	-5.34	1.07	92.00	-2.74	Yes	Yes	Yes	-0.17	0.15	0.35	-0.55
XIE5-2-49	3.9	-6.04	1.10	92.30	-2.74	Yes	Yes	Yes	0.51	0.05	0.18	-0.98
XIE5-2-64	3.10	-3.16	0.45	93.02	-2.74	Yes	Yes	Yes	0.45	0.01	0.13	-0.82
XIE5-2-53	3.8	-6.55	1.04	91.48	-2.73	Yes	Yes	Yes	0.45	0.04	0.37	-1.11
XIE5-2-46	3.14	-5.69	1.08	89.03	-2.74	Yes	Yes	Yes	-0.30	0.10	0.38	-0.82
XIE1-4-3	3.29	-3.41	-0.17	76.24	-2.74	Yes	Yes	Yes	1.72	0.00	-0.62	-2.73
XIE5-1-23	3.28	-3.39	-0.08	83.52	-2.73	Yes	Yes	Yes	1.36	0.00	-0.47	-2.39
XIE5-1-64/XIE5-1-54CT	3.31	-4.55	0.84	79.41	-2.74	Yes	Yes	Yes	1.86	0.00	-0.92	-2.79
XIE62PY1-9 (NSC173162)	3.25	-5.84	1.02	90.71	-2.74	Yes	Yes	Yes	0.49	0.00	0.18	-2.46
XIE5-1-11	4.1	-5.36	1.18	96.42	-2.74	No	Yes	Yes	-0.63	0.17	-0.05	-1.41
XIE5-2-85	4.2	-4.51	1.43	94.47	-2.74	No	Yes	Yes	-0.58	0.22	-0.07	-1.44
XIE5-2-70	4.3	-5.29	1.64	91.33	-2.65	No	No	Yes	0.43	0.00	0.36	-1.40
lp1-66	4.4	-5.53	1.65	90.09	-2.74	Yes	Yes	Yes	-0.93	0.17	-0.77	-2.85
XIE5-1-74/XIE5-2-74	4.5	-5.51	1.40	92.57	-2.74	Yes	Yes	Yes	-0.80	0.17	-0.80	-1.34
XIE5-2-79	4.6	-5.27	1.18	91.89	-2.74	Yes	Yes	Yes	-0.83	0.16	-0.28	-0.86
XIE5-2-3	4.7	-5.70	0.97	88.33	-2.74	Yes	Yes	Yes	-0.35	0.19	0.96	-0.76
XIE5-2-7	4.11	-5.17	0.91	92.75	-2.74	Yes	Yes	Yes	0.79	0.21	-0.19	-1.55
XIE5-2-10	4.9	-5.18	1.00	92.94	-2.74	Yes	Yes	Yes	0.04	0.26	0.09	-1.41
XIE5-2-11	4.15	-3.74	1.27	91.18	-2.74	Yes	Yes	Yes	-0.82	0.37	-0.61	-3.08

XIE5-2-13	4.10	-3.07	0.55	92.07	-2.74	Yes	Yes	Yes	-0.12	0.14	-0.14	-0.91
XIE5-2-14	4.8	-5.57	0.99	91.86	-2.74	Yes	Yes	Yes	0.08	0.21	0.01	-1.28
XIE5-2-15	4.16	-3.86	1.23	89.48	-2.74	Yes	Yes	Yes	-0.85	0.35	-0.46	-0.94
LP1-20b	4.13	-4.55	1.16	91.21	-2.74	Yes	Yes	Yes	-0.69	0.33	-0.58	-0.81
XIE5-2-22	4.17	-5.41	1.04	89.79	-2.74	Yes	Yes	Yes	-0.38	0.17	0.12	-1.12
XIE5-2-40	4.28	-3.60	0.02	88.26	-2.73	Yes	Yes	Yes	0.79	0.21	-1.30	-3.11
lp1-9a	4.25	-5.17	1.16	91.34	-2.74	Yes	Yes	Yes	-0.07	0.26	-0.46	-3.17
LP1-17b	4.21	-5.93	1.23	89.98	-2.74	Yes	Yes	Yes	0.01	0.13	1.03	-0.77
LP1-17a	4.12	-5.54	1.22	90.77	-2.74	Yes	Yes	Yes	-0.42	0.22	0.97	-0.67
LP1-19a	4.18	-5.58	1.22	91.44	-2.74	Yes	Yes	Yes	-0.47	0.22	1.01	-0.70
LP1-19b	4.19	-4.40	1.08	89.17	-2.74	Yes	Yes	Yes	-0.74	0.34	1.04	-0.76
LP1-20a	4.20	-5.94	1.19	91.45	-2.74	Yes	Yes	Yes	0.47	0.16	0.81	-1.43
Lp1-21a	4.32	-3.79	1.62	92.85	-2.74	No	Yes	Yes	-0.90	0.33	-0.68	-3.06
lp1-22b	4.24	-5.63	1.18	87.59	-2.74	Yes	Yes	Yes	0.17	0.21	0.92	-1.13
lp1-21b	4.23	-5.60	1.22	90.63	-2.74	Yes	Yes	Yes	0.08	0.18	0.73	-1.11
XIE5-1-24	5.1	-5.62	1.12	96.44	-2.72	No	No	Yes	-0.33	0.08	0.19	-1.38
XIE5-2-87	5.2	-5.78	1.13	91.54	-2.72	No	No	Yes	-0.51	0.03	-0.16	-1.52
XIE5-1-91	5.3	-5.80	1.12	92.06	-2.73	No	No	Yes	0.08	0.05	-0.24	-1.48
lp1-64	5.4	-6.69	1.57	89.94	-2.74	Yes	Yes	Yes	-0.71	0.00	-0.49	-2.69
XIE5-2-77	5.6	-5.88	1.12	91.92	-2.74	Yes	Yes	Yes	-0.57	0.08	-0.17	-0.81
XIE5-2-75	5.5	-6.26	1.32	92.41	-2.74	Yes	Yes	Yes	-0.57	0.01	-0.52	-1.32
XIE5-2-16	5.7	-5.11	0.99	89.73	-2.73	Yes	Yes	Yes	-0.08	0.12	1.19	-1.11
XIE5-2-17	5.11	-5.19	0.86	92.78	-2.75	Yes	Yes	Yes	1.19	0.13	-0.08	-1.53
XIE5-2-18	5.9	-4.91	0.97	93.11	-2.74	Yes	Yes	Yes	0.38	0.18	0.08	-1.39
XIE5-2-19	5.15	-4.39	1.19	91.03	-2.74	Yes	Yes	Yes	-0.67	0.26	-0.35	-2.91
XIE5-2-21	5.10	-3.08	0.76	92.57	-2.74	Yes	Yes	Yes	0.04	0.08	0.00	-0.95
XIE5-2-1	5.8	-4.72	0.97	91.66	-2.71	Yes	Yes	Yes	0.46	0.14	0.17	-1.71
XIE5-2-2	5.14	-4.40	1.15	89.32	-2.74	Yes	Yes	Yes	-0.64	0.23	-0.20	-0.93
LP1-16B	5.13	-5.83	1.00	90.21	-2.73	Yes	Yes	Yes	0.09	0.12	0.09	-1.07
XIE5-2-20	5.16	-4.41	0.93	91.25	-2.74	Yes	Yes	Yes	-0.53	0.25	0.21	-0.81
XIE5-2-43	5.28	-3.44	0.01	90.30	-2.74	Yes	Yes	Yes	0.86	0.08	-0.90	-2.50
XIE5-1-27AT	5.29	-3.49	-0.01	83.01	-2.74	Yes	Yes	Yes	1.18	0.09	-1.10	-2.89
LP1-10a	5.26	-5.69	1.08	90.03	-2.75	Yes	Yes	Yes	0.70	0.08	-0.41	-2.52
LP1-15a	5.27	-5.65	1.00	90.19	-2.70	Yes	Yes	Yes	1.20	0.04	-0.51	-2.50
XIE62PY1-31/XRK3F2	5.25	-5.45	1.09	91.00	-2.74	Yes	Yes	Yes	0.14	0.10	-0.39	-2.59
LP1-10b	5.21	-6.21	0.92	88.36	-2.73	Yes	Yes	Yes	0.34	0.05	1.00	-0.71
LP1-11b	5.12	-5.80	0.92	90.11	-2.73	Yes	Yes	Yes	-0.15	0.14	0.97	-0.63
LP1-12b	5.20	-5.97	0.89	90.84	-2.72	Yes	Yes	Yes	0.79	0.08	0.81	-1.39
LP1-13a	5.18	-5.85	0.92	90.82	-2.73	Yes	Yes	Yes	-0.19	0.14	1.02	-0.66
LP1-13b	5.22	-5.52	1.14	91.06	-2.74	Yes	Yes	Yes	0.07	0.09	0.72	-1.03
LP1-14a	5.23	-6.58	1.15	90.01	-2.74	Yes	Yes	Yes	-0.12	0.01	0.57	-0.93
LP1-14b	5.24	-6.92	1.11	87.84	-2.74	Yes	Yes	Yes	0.07	0.03	0.76	-0.98

LP1-15b	5.19	-5.33	1.12	89.88	-2.74	Yes	Yes	Yes	-0.75	0.19	0.89	-0.64
XIE5-1-13	6.1	-6.65	1.08	94.45	-2.67	No	No	Yes	0.04	0.00	0.32	-1.32
XIE5-2-88	6-2	-6.47	1.04	89.35	-2.63	No	Yes	Yes	-0.06	0.00	0.33	-1.44
lp1-67	6.4	-8.01	1.48	87.75	-2.73	Yes	Yes	Yes	-0.21	0.00	0.00	-1.68
XIE5-2-80	6.6	-6.89	1.07	89.92	-2.73	Yes	Yes	Yes	-0.19	0.00	-0.03	-0.75
XIE5-2-73	6.5	-7.25	1.23	90.22	-2.71	Yes	Yes	Yes	-0.10	0.00	-0.03	-1.25
XIE5-2-33	6.7	-6.45	0.87	86.36	-2.72	Yes	Yes	Yes	0.36	0.06	0.85	-0.67
XIE5-2-39	6.11	-5.51	0.81	90.78	-2.74	Yes	Yes	Yes	1.61	0.08	0.05	-1.46
XIE5-2-35	6.9	-5.69	0.92	91.11	-2.73	Yes	Yes	Yes	0.72	0.11	0.21	-1.33
XIE5-2-36	6.15	-6.13	1.09	88.83	-2.74	Yes	Yes	Yes	-0.25	0.13	0.14	-2.02
XIE5-2-38	6.10	-3.16	0.45	90.10	-2.74	Yes	Yes	Yes	0.43	0.00	0.10	-0.82
XIE5-2-31	6.8	-6.19	0.88	89.89	-2.70	Yes	Yes	Yes	0.71	0.07	0.25	-1.19
XIE5-2-32	6.14	-5.94	1.06	87.13	-2.73	Yes	Yes	Yes	-0.16	0.11	0.29	-0.85
XIE5-2-9	6.13	-6.25	0.87	90.15	-2.74	Yes	Yes	Yes	0.83	0.06	-0.07	-1.14
XIE5-2-37	6.16	-5.29	0.88	89.25	-2.74	Yes	Yes	Yes	-0.21	0.18	0.34	-0.74
XIE5-1-25	6.28	-3.53	-0.30	85.75	-2.73	Yes	Yes	Yes	1.46	0.04	-0.83	-2.17
XIE62PY1-32	6.25	-6.40	0.99	87.75	-2.71	Yes	Yes	Yes	0.64	0.00	0.14	-2.22
XIE5-1-12	7.1	-6.19	1.08	97.36	-2.66	No	No	Yes	0.08	0.02	0.34	-1.32
XIE5-1-54A	7.2	-5.93	1.04	92.26	-2.61	No	Yes	Yes	-0.02	0.00	0.36	-1.44
XIE5-1-65	7.4	-3.36	0.55	80.00	-2.74	Yes	Yes	Yes	1.34	0.00	-1.20	-2.75
XIE5-2-78	7.6	-6.67	1.08	92.84	-2.73	Yes	Yes	Yes	-0.16	0.01	-0.01	-0.75
XIE5-2-76	7.5	-6.78	1.23	93.14	-2.71	Yes	Yes	Yes	-0.06	0.00	-0.01	-1.25
XIE5-2-59	7.7	-5.99	1.12	89.82	-2.73	Yes	Yes	Yes	0.27	0.06	1.06	-0.76
XIE5-2-64	7.10	-3.16	0.45	93.02	-2.74	Yes	Yes	Yes	0.45	0.00	0.13	-0.82
XIE5-2-58	7.8	-5.99	0.87	92.60	-2.68	Yes	Yes	Yes	0.79	0.09	0.33	-1.32
XIE5-2-61	7.14	-5.84	1.06	90.05	-2.73	Yes	Yes	Yes	-0.15	0.11	0.32	-0.85
XIE5-2-45	7.28	-3.44	-0.07	84.33	-2.73	Yes	Yes	Yes	1.54	0.05	-0.53	-2.25
XIE5-1-68/26BT	7.29	-3.30	0.50	76.92	-2.74	Yes	Yes	Yes	0.80	0.01	-1.28	-2.75
lp1-25a	7.26	-4.84	0.79	93.13	-2.76	Yes	Yes	Yes	1.53	0.09	0.06	-2.28
LP1-62	7.27	-4.89	0.83	92.88	-2.75	Yes	Yes	Yes	1.65	0.11	-0.03	-2.28
XIE5-1-67/61BT	7.30	-3.34	0.52	77.74	-2.74	Yes	Yes	Yes	1.06	0.00	-1.14	-2.75
XIE5-1-65/55CT	7.31	-3.36	0.55	80.00	-2.74	Yes	Yes	Yes	1.34	0.00	-1.20	-2.75
Lp1-24b	7.25	-5.41	0.86	93.26	-2.73	Yes	Yes	Yes	0.81	0.09	-0.01	-2.33
Lp1-25b	7.21	-6.26	0.88	90.32	-2.71	Yes	Yes	Yes	0.85	0.01	1.06	-0.67
LP1-51	7.20	-6.19	0.85	91.76	-2.65	Yes	Yes	Yes	1.28	0.03	0.83	-1.32
XIE5-1-83	8.1	-6.47	1.10	93.72	-2.70	No	No	Yes	-0.02	0.04	0.00	-1.28
XIE5-1-82	9.1	-6.05	1.11	96.64	-2.69	No	No	Yes	0.02	0.05	0.03	-1.28
XIE5-2-83	8.2	-6.56	1.28	91.50	-2.69	Yes	Yes	Yes	0.17	0.00	0.06	-1.21
XIE5-2-84	9.2	-6.04	1.28	94.42	-2.69	Yes	Yes	Yes	0.21	0.00	0.08	-1.21
QYQ1-152	10.33	-6.35	1.09	94.85	-2.70	No	No	Yes	-0.39	0.00	0.26	-1.22
QYQ1-156-2	10.34	-6.61	1.08	92.83	-2.75	Yes	Yes	Yes	-0.23	0.00	0.04	-2.18

XIE62LP1-59	10.27	-5.94	1.14	90.77	-2.74	Yes	Yes	Yes	0.67	0.26	-0.56	-3.07
lp1-56	10.25	-5.17	1.16	91.34	-2.74	Yes	Yes	Yes	-0.07	0.26	-0.46	-3.17
Lp1-58	10.21	-5.64	1.25	88.72	-2.74	Yes	Yes	Yes	-0.10	0.18	1.01	-0.68
LP1-60	10.20	-5.71	1.22	90.16	-2.74	Yes	Yes	Yes	0.34	0.20	0.79	-1.33
lp1-85	9.25	-5.07	1.26	92.19	-2.71	Yes	Yes	Yes	0.75	0.09	-0.27	-2.35
XIE5-2-89	9.26	-4.56	1.19	92.02	-2.78	Yes	Yes	Yes	1.46	0.09	-0.20	-2.30
XIE5-2-90	8.25	-6.52	1.00	88.95	-2.71	Yes	Yes	Yes	0.71	0.01	0.04	-2.25
LP1-63	11.27	-3.67	1.51	91.67	-2.90	No	No	No	1.37	0.26	-0.12	-1.85
Lp1-53	11.26	-3.40	1.49	92.22	-2.91	No	No	No	1.22	0.27	-0.07	-1.86
LP1-52	11.25	-3.71	0.99	92.13	-2.89	No	No	No	0.59	0.21	-0.02	-1.88
lp1-54	11.21	-5.11	1.30	89.38	-2.79	Yes	Yes	Yes	0.85	0.03	0.84	-0.97
Lp1-55	11.20	-4.38	1.34	90.85	-2.84	No	Yes	No	1.02	0.15	0.66	-1.62

Note: Water solubility (log mol/L) <-7, low solubility; Caco2 permeability>0.9, high permeability; Intestinal absorption (human) <30, poor absorption; Skin Permeability (logKp) >-2.5, poor permeability; VDss (volume of distribution, human) < -0.15, low; VDss > 0.45, high; Fraction unbound (human, Fu) > 90, high plasma protein binding; BBB permeability (logBB)>0.3 readily cross BBB; logBB<-1, poorly distributed in brain; CNS permeability (logPS) >-2, can penetrate CNS; <-3 cannot penetrate CNS.

As listed in **Table 33**, the metabolism properties are represented by different effect of compounds on Cytochrome P450 (CYP450) monooxygenases is a large family of enzymes that catalyze the oxidation and metabolism of many endogenous as well as xenobiotics molecules. Compounds that are predicted to be CYP450 enzymes inhibitors might influence the metabolism of substrates whose metabolism were catalyzed by this enzyme, causing one of the major concerns of drug-drug interaction. Renal organic cation transporter 2 (OCT2), a primarily renal uptake transporter located on the basolateral side of proximal tubule cells in kidney, plays a critical role in the excretion as well as renal clearance of cationic drugs and endogenous compounds. Total drug clearance is measured by the constant CL_{total}, as a conjunction of hepatic (liver and biliary

metabolism) and renal clearance (kidney excretion). It plays a key role in predicting dosing to achieve steady-state concentration. Total drug clearance of compounds was given in log ml/min/kg.

Appendix Table 4 Predicted Metabolism/Excretion Properties for p62 Ligands by pkCSM.

Internal Name	ID	CYP2D6 substrate	CYP3A4 substrate	CYP1A2 blocker	CYP2C19 blocker	CYP2C9 blocker	CYP2D6 blocker	CYP3A4 blocker	Total Clearance	Renal OCT2 substrate
XIE5-1-8	3.1	No	Yes	Yes	Yes	Yes	No	No	0.191	No
XIE5-1-33A	3.2	No	Yes	Yes	Yes	Yes	No	No	0.209	No
XIE5-2-54	3.7	No	Yes	Yes	Yes	Yes	Yes	Yes	1.233	No
XIE5-2-51	3.16	No	Yes	No	Yes	Yes	No	Yes	1.124	No
XIE5-2-49	3.9	No	Yes	Yes	Yes	Yes	Yes	Yes	1.139	No
XIE5-2-64	3.10	No	Yes	No	Yes	Yes	Yes	Yes	1.225	No
XIE5-2-53	3.8	No	Yes	Yes	Yes	Yes	Yes	Yes	1.162	No
XIE5-2-46	3.14	No	Yes	No	No	No	Yes	Yes	1.025	No
XIE1-4-3	3.29	No	Yes	No	Yes	Yes	Yes	Yes	0.779	No
XIE5-1-23	3.28	No	Yes	Yes	Yes	Yes	Yes	Yes	0.533	No
XIE5-1-64/ XIE5-1-54CT	3.31	No	Yes	Yes	No	Yes	Yes	Yes	0.948	No
XIE62PY1-9 NSC173162	3.25	No	Yes	Yes	Yes	Yes	Yes	Yes	1.047	No
XIE5-1-11	4.1	No	Yes	Yes	Yes	Yes	No	Yes	0.508	No
XIE5-2-85	4.2	No	Yes	Yes	Yes	Yes	No	Yes	0.009	No
XIE5-2-70	4.3	No	Yes	Yes	Yes	Yes	Yes	No	0.981	No
lp1-66	4.4	No	Yes	No	Yes	Yes	No	Yes	0.132	No
XIE5-1-74/XIE5-2-74	4.5	No	Yes	No	Yes	Yes	No	Yes	0.137	No
XIE5-2-79	4.6	No	Yes	No	Yes	Yes	No	Yes	0.343	No
XIE5-2-3	4.7	No	Yes	No	No	No	No	Yes	1.097	No
XIE5-2-7	4-	No	Yes	No	No	No	No	Yes	0.938	No
XIE5-2-10	4.9	No	Yes	No	No	No	No	Yes	0.915	No
XIE5-2-11	4-	No	Yes	No	No	No	No	Yes	0.836	No
XIE5-2-13	4.10	No	Yes	No	Yes	Yes	Yes	Yes	0.977	No
XIE5-2-14	4.8	No	Yes	No	No	No	No	Yes	1.02	No
XIE5-2-15	4.13	No	Yes	No	No	No	No	Yes	0.806	No
LP1-20b	4.17	No	Yes	No	Yes	Yes	No	Yes	0.259	No
XIE5-2-22	4.4	No	Yes	No	No	No	No	Yes	1.022	No
XIE5-2-40	4.28	No	Yes	No	Yes	Yes	No	Yes	0.313	No
lp1-9a	4.25	No	Yes	No	Yes	Yes	No	Yes	0.774	No

LP1-17b	4.21	No	Yes	No	No	No	No	Yes	0.89	No
LP1-17a	4.12	No	Yes	No	No	No	No	Yes	0.917	No
LP1-19a	4.18	No	Yes	No	No	No	No	Yes	0.965	No
LP1-19b	4.19	No	Yes	No	No	No	No	Yes	0.803	No
LP1-20a	4.20	No	Yes	No	No	Yes	No	Yes	0.936	No
Lp1-21a	4.32	No	Yes	No	Yes	Yes	No	Yes	0.724	Yes
lp1-22b	4.24	No	Yes	No	No	No	No	Yes	1.006	No
lp1-21b	4.23	No	Yes	No	No	Yes	No	Yes	0.63	Yes
XIE5-1-24	5.1	No	Yes	Yes	Yes	Yes	No	Yes	0.038	No
XIE5-2-87	5.2	No	Yes	Yes	Yes	Yes	No	Yes	0.067	No
XIE5-1-91	5.3	No	Yes	Yes	Yes	Yes	Yes	Yes	0.899	No
lp1-64	5.4	No	Yes	No	Yes	Yes	No	Yes	0.376	No
XIE5-2-77	5.6	No	Yes	No	Yes	Yes	No	Yes	0.597	No
XIE5-2-75	5.5	No	Yes	No	Yes	Yes	No	No	0.212	No
XIE5-2-16	5.7	No	Yes	Yes	Yes	No	Yes	Yes	1.24	No
XIE5-2-17	5.11	Yes	Yes	No	Yes	No	Yes	Yes	1.083	No
XIE5-2-18	5.9	No	Yes	No	No	No	Yes	Yes	1.062	No
XIE5-2-19	5.15	No	Yes	No	No	No	No	Yes	0.959	No
XIE5-2-21	5.10	No	Yes	No	No	No	No	Yes	0.988	No
XIE5-2-11	5.8	No	Yes	No	No	No	No	Yes	0.836	No
XIE5-2-1	5.8	No	Yes	Yes	No	No	Yes	Yes	1.136	No
XIE5-2-2	5.14	No	Yes	No	No	No	No	Yes	0.928	No
LP1-16B	5.13	Yes	Yes	No	Yes	No	Yes	Yes	1.154	No
XIE5-2-20	5.28	No	Yes	No	No	No	No	Yes	1.126	No
XIE5-2-43	5.29	No	Yes	No	Yes	Yes	No	Yes	0.438	No
XIE5-1-27AT	5.26	No	Yes	No	Yes	Yes	No	Yes	0.683	No
LP1-10a	5.27	No	Yes	No	Yes	Yes	No	Yes	0.878	No
LP1-15a	5-	No	Yes	Yes	No	Yes	Yes	Yes	0.947	No
XIE62PY1-31/XRK3F2	5.25	No	Yes	No	Yes	Yes	Yes	Yes	0.952	No
LP1-10b	5.12	No	Yes	No	Yes	No	Yes	Yes	1.288	No
LP1-11b	5-	Yes	Yes	No	Yes	No	Yes	Yes	1.054	No
LP1-12b	5.20	No	Yes	No	No	No	Yes	Yes	1.074	No
LP1-13a	5.22	Yes	Yes	No	Yes	No	Yes	Yes	1.103	No
LP1-13b	5.23	No	Yes	No	No	No	Yes	Yes	0.853	No
LP1-14a	5.24	No	Yes	No	Yes	Yes	No	Yes	0.195	No
LP1-14b	5-	No	Yes	No	Yes	Yes	No	Yes	1.33	No
LP1-15b	5.19	No	Yes	Yes	Yes	Yes	No	Yes	0.021	No
XIE5-1-13	6.1	No	Yes	Yes	Yes	Yes	No	Yes	-0.293	No
XIE5-2-88	6-2	No	Yes	Yes	Yes	Yes	No	Yes	-0.26	No
	6.3	No	Yes	Yes	Yes	No	Yes	Yes	0.972	No
lp1-67	6.4	No	Yes	No	Yes	Yes	No	Yes	-0.549	No
XIE5-2-80	6.6	No	Yes	No	Yes	Yes	No	Yes	-0.476	No
XIE5-2-73	6.5	No	Yes	No	Yes	Yes	No	Yes	-0.401	No

XIE5-2-33	6.7	Yes	Yes	No	No	No	Yes	Yes	1.313	No
XIE5-2-39	6.11	Yes	Yes	No	Yes	No	Yes	Yes	1.162	No
XIE5-2-35	6.9	No	Yes	No	No	No	Yes	Yes	1.14	No
XIE5-2-36	6.15	No	Yes	No	No	No	No	Yes	1.036	No
XIE5-2-38	6.10	No	Yes	No	Yes	Yes	Yes	Yes	1.2	Yes
XIE5-2-31	6.8	No	Yes	No	No	Yes	Yes	Yes	1.241	No
XIE5-2-32	6.14	No	Yes	No	Yes	No	Yes	Yes	1.004	No
XIE5-2-9	6.13	No	Yes	No	No	Yes	Yes	Yes	1.098	No
XIE5-2-37	6.16	No	Yes	No	Yes	No	Yes	Yes	1.206	No
XIE5-1-25	6.28	No	Yes	No	Yes	Yes	No	Yes	0.513	No
XIE62PY1-32	6.25	No	Yes	Yes	Yes	Yes	Yes	Yes	1.024	No
XIE5-1-12	7.1	No	Yes	Yes	Yes	Yes	No	Yes	0.234	No
XIE5-1-54A	7.2	No	Yes	Yes	Yes	Yes	No	Yes	0.213	No
	7.3	No	Yes	Yes	Yes	No	Yes	Yes	0.998	No
XIE5-1-65	7.4	No	Yes	Yes	Yes	Yes	Yes	Yes	1.048	No
XIE5-2-78	7.6	No	Yes	No	Yes	Yes	No	Yes	0.716	No
XIE5-2-76	7.5	No	Yes	No	Yes	Yes	No	Yes	0.438	No
XIE5-2-59	7.7	Yes	Yes	No	No	No	Yes	Yes	1.357	No
XIE5-2-64	7.10	No	Yes	No	Yes	Yes	Yes	Yes	1.225	No
XIE5-2-58	7.8	No	Yes	No	No	No	Yes	Yes	1.24	No
XIE5-2-61	7.14	No	Yes	No	No	No	Yes	Yes	1.03	No
XIE5-2-45	7.28	No	Yes	No	Yes	Yes	No	Yes	0.538	No
XIE5-1-68/26BT	7.29	No	Yes	Yes	Yes	Yes	Yes	Yes	0.797	No
lp1-25a	7.26	No	Yes	Yes	No	No	Yes	Yes	1.013	No
LP1-62	7.27	No	Yes	Yes	No	No	Yes	Yes	1.073	No
XIE5-1-67/61BT	7.30	No	Yes	Yes	Yes	Yes	Yes	Yes	0.847	No
XIE5-1-65/55CT	7.31	No	Yes	Yes	Yes	Yes	Yes	Yes	1.048	No
Lp1-24b	7.25	No	Yes	Yes	No	No	Yes	Yes	1.084	No
Lp1-25b	7.21	No	Yes	No	No	No	Yes	Yes	1.133	No
LP1-51	7.20	No	Yes	No	No	No	Yes	Yes	1.178	No
XIE5-1-83	8.1	No	Yes	Yes	No	No	Yes	No	0.973	Yes
XIE5-1-82	9.1	No	Yes	Yes	No	No	Yes	No	0.914	No
XIE5-2-83	8.2	No	Yes	Yes	No	No	Yes	No	0.986	No
XIE5-2-84	9.2	Yes	Yes	Yes	No	No	Yes	Yes	1.033	No
QYQ1-152	10.33	Yes	Yes	Yes	No	No	Yes	Yes	1.076	Yes
QYQ1-156-2	10.34									
XIE62LP1-59	10.27	No	Yes	Yes	Yes	Yes	No	Yes	-0.233	No
lp1-56	10.25	No	Yes	Yes	Yes	Yes	No	Yes	0.325	No
Lp1-58	10.21	No	Yes	Yes	Yes	Yes	No	Yes	-0.246	No
LP1-60	10.20	No	Yes	Yes	Yes	Yes	No	Yes	0.298	No
lp1-85	9.25	No	Yes	Yes	Yes	Yes	No	Yes	0.677	No
XIE5-2-89	9.26	No	Yes	Yes	Yes	Yes	No	Yes	0.416	No

XIE5-2-90	8.25	No	Yes	No	No	Yes	No	Yes	0.749	No
		No	Yes	No	Yes	Yes	No	Yes	0.774	No
LP1-63	11.27	No	Yes	No	No	No	No	Yes	0.834	No
Lp1-53	11.26	No	Yes	No	No	No	No	Yes	0.88	No
LP1-52	11.25	Yes	Yes	No	No	No	Yes	Yes	1.109	No
lp1-54	11.21	Yes	Yes	No	Yes	Yes	Yes	Yes	1.037	No
Lp1-55	11.20	No	Yes	Yes	Yes	Yes	Yes	Yes	0.971	No

Note: Total clearance (log ml/min/kg)

The predicted toxicity properties were listed in **Table 34**. The Ames Salmonella/microsome mutagenicity (AMES) assay is widely applied to evaluate the potential mutagenesis in bacteria. The positive results in AMES test indicates a mutagenic and therefore carcinogenic potential of a compound. Only a few compounds are predicted to have this problem.

Maximum tolerated dose (log mg/kg/day) offers a threshold of toxic dose of a drug candidate in humans, which is helpful in determining the recommended initial dose for pharmaceuticals in phase I clinical trials. For a specific compound, a maximum tolerated dosage less than or equal to 0.477 is considered to be low, whereas larger than 0.477 is relatively high. Here some of our compounds are predicted to have a low maximum tolerated dose. Especially, the compounds with amino-guanidine groups that has the lowest values of maximum tolerated dose here (XIE5-2-40, XIE1-4-3, XIE5-1-23, XIE5-1-64, XIE5-1-25, XIE5-2-43, XIE5-1-27AT, XIE5-1-68 and XIE5-1-65). A few compounds with a cyclohexane group (LP1-10B/XIE106 and LP1-25B) are predicted with a low maximum tolerated dose, which indicate a concern of toxicity in rat.

The inhibition of potassium channel in heart encoded by hERG is one of major cause of long QT syndrome, which lead to cardiac arrythmia. Similar as the results predicted by Schrödinger QikProp package, most of our compounds are predicted to be hERG II inhibitors, indicating a potential cardiac toxicity issue in future studies. The standard oral rat acute toxicity of

532

a drug candidate was represented by lethal dosage value (LD$_{50}$), the amount of a drug given all at once that lead to death of 50% of test animals. The model is build based on over 10,000 compounds tested in rats (log mol/kg). Another concern in chronic-use drugs is the toxicity caused by long-time exposure to a low or moderate dose of drugs. To solve this concern, the lowest dosage of drug candidate that will lead to observed adverse effect by chronic treatment, as well as the highest dosage that results in no observed adverse effects are necessary to be measured. For a given molecule, the predicted log lowest observed adverse effect in log (mg/kg_bw/day) will be generated. This value needs to be interpreted in conjunction with bioactive concentration and treatment length of a compound. Skin sensitization is a potential adverse effect for dermally applied product.

Drug induced hepatoxicity is a major safety concern for drug candidate. It predicts whether a compound is likely to induce liver injury or affect the normal function of liver. Some of our compounds are predicted to be hepatoxic, indicating a safety concern for them to apply *in vivo*. T.Pyriformis (a protozoa bacteria) toxicity are frequently considered as a toxic endpoint for drug development. For a given compound, negative logarithm of a concentration required to inhibit 50% of bacteria growth in log µg/L is generated, with a value larger than -0.5 to be indicated as toxic. According to the prediction, except for some intermediates, most of our compound do not have this toxic problem. As for minnow toxicity, a log LC50 (lethal concentration) value is predicted, with a log LC50 below -0.3 are considered as high acute toxicity from the Flathead Minnows.

Appendix Table 5 Predicted Toxicity Properties for p62 Ligands by pkCSM

Internal Name	ID	AMES	Max. tolerated dose	hERG I	hERG II	Oral Rat Acute	Oral Rat Chronic Toxicity	Hepato	Skin Sens	T.Pyriformis	Minnow

		toxicity	(human)	blocker	blocker	Toxicity (LD50)	(LOAEL)	xicity	itisation	toxicity	toxicity
XIE5-1-8	3.1	No	0.874	No	Yes	2.125	2.137	Yes	No	0.474	-0.626
XIE5-1-33A	3.2	No	0.868	No	Yes	2.124	2.105	Yes	No	0.477	-0.329
XIE5-2-54/55	3.7	Yes	0.709	No	Yes	2.686	2.051	Yes	No	0.29	0.664
XIE5-2-51	3.16	No	0.67	No	Yes	2.826	1.027	Yes	No	0.286	0.421
XIE5-2-49	3.9	Yes	1.026	No	Yes	2.64	1.867	Yes	No	0.296	-1.424
XIE5-2-64	3.10	Yes	0.497	Yes	Yes	2.806	1.167	No	No	0.285	-1.49
XIE5-2-53	3.8	Yes	0.756	No	Yes	2.74	1.799	Yes	No	0.302	2.58
XIE5-2-46	3.14	No	0.435	No	Yes	2.576	1.924	Yes	No	0.286	0.94
XIE1-4-3	3.29	No	-0.046	Yes	Yes	2.332	2.238	No	No	0.285	4.861
XIE5-1-23	3.28	No	-0.084	No	Yes	2.502	2.277	No	No	0.285	2.923
XIE5-1-64 XIE5-1-54CT	3.31	No	0.268	Yes	Yes	2.255	1.842	Yes	No	0.29	3.507
XIE62PY1-9 (NSC173162)	3.25	No	0.753	No	Yes	2.286	1.876	Yes	No	0.406	2.654
XIE5-1-11	4.1	No	1.006	No	Yes	2.828	1.204	Yes	No	0.306	-2.802
XIE5-2-85	4.2	No	0.849	No	Yes	2.65	1.3	Yes	No	0.295	-1.501
XIE5-2-70	4.3	No	0.814	No	Yes	2.175	2.057	Yes	No	0.478	-0.339
lp1-66	4.4	No	0.805	No	Yes	2.867	1.246	Yes	No	0.286	-2.445
XIE5-1-74 XIE5-2-74	4.5	No	0.869	No	Yes	2.617	1.468	Yes	No	0.291	-1.258
XIE5-2-79	4.6	No	0.614	No	Yes	2.451	1.153	Yes	No	0.287	-3.323
XIE5-2-3	4.7	No	0.621	No	Yes	2.529	0.728	Yes	No	0.287	-3.477
XIE5-2-7	4.11	No	0.345	No	Yes	2.448	1.856	Yes	No	0.288	-0.414
XIE5-2-10	4.9	No	0.749	No	Yes	2.812	1.13	Yes	No	0.287	-2.453
XIE5-2-11	4.16	No	0.397	No	Yes	2.65	0.621	Yes	No	0.285	-1.788
XIE5-2-13	4.10	No	0.346	No	Yes	2.673	0.738	Yes	No	0.285	-2.714
XIE5-2-14	4.8	No	0.718	No	Yes	2.695	1.006	Yes	No	0.289	-2.463
XIE5-2-15	4.13	No	0.487	No	Yes	2.629	0.84	Yes	No	0.285	-1.32

LP1-20b	4.17	No	0.72	No	Yes	2.552	0.886	Yes	No	0.285	-1.785
XIE5-2-22	4.4	No	0.256	No	Yes	2.579	0.686	Yes	No	0.285	-5.97
XIE5-2-40	4.28	No	-0.321	No	Yes	2.489	2.494	Yes	No	0.285	0.929
lp1-9a	4.25	No	0.783	No	Yes	2.565	1.239	Yes	No	0.296	1.012
LP1-17b	4.21	No	0.309	No	Yes	2.464	1.134	Yes	No	0.29	-3.923
LP1-17a	4.12	No	0.56	No	Yes	2.68	0.805	Yes	No	0.286	-4.211
LP1-19a	4.18	No	0.545	No	Yes	2.577	0.836	Yes	No	0.286	-4.37
LP1-19b	4.19	No	0.65	No	Yes	2.53	0.887	Yes	No	0.285	-1.394
LP1-20a	4.20	No	0.569	No	Yes	2.825	1.228	Yes	No	0.301	-1.674
Lp1-21a	4.32	No	0.178	No	Yes	2.776	0.793	Yes	No	0.285	-4.642
lp1-22b	4.24	No	0.802	No	Yes	2.326	1.397	Yes	No	0.288	-0.95
lp1-21b	4.23	No	0.882	No	Yes	2.438	1.454	Yes	No	0.295	-0.272
XIE5-1-24	5.1	No	0.858	No	Yes	2.479	1.318	No	No	0.389	-1.445
XIE5-2-87	5.2	No	0.98	No	Yes	2.294	1.559	No	No	0.404	-0.912
XIE5-1-91	5.3	No	0.887	No	Yes	2.367	1.582	No	No	0.39	-1.054
lp1-64	5.4	No	0.729	No	Yes	2.483	1.442	Yes	No	0.301	-1.271
XIE5-2-77	5.6	No	0.462	No	Yes	2.39	1.279	Yes	No	0.292	-1.787
XIE5-2-75	5.5	No	0.796	No	Yes	2.254	1.623	Yes	No	0.343	-0.096
XIE5-2-16	5.9	No	0.134	Yes	Yes	2.646	0.685	Yes	No	0.285	-3.36
XIE5-2-17	5.11	No	0.326	Yes	Yes	2.498	1.823	Yes	No	0.297	1.124
XIE5-2-18	5.9	No	0.783	Yes	Yes	2.727	1.282	Yes	No	0.29	-1.33
XIE5-2-19	5.15	No	0.481	No	Yes	2.545	0.78	Yes	No	0.285	-0.405
XIE5-2-21	5.10	No	0.331	Yes	Yes	2.5	1.041	Yes	No	0.285	-2.766
XIE5-2-11	5.1	No	0.397	No	Yes	2.65	0.621	Yes	No	0.285	-1.788
XIE5-2-1	5.8	No	0.192	Yes	Yes	2.955	1.052	Yes	No	0.286	-0.808
XIE5-2-2	5.7	No	0.532	No	Yes	2.547	0.964	Yes	No	0.285	-0.093
LP1-16B	5.13	No	0.275	Yes	Yes	2.505	0.893	Yes	No	0.285	-4.575
XIE5-2-20	5.28	No	0.545	No	Yes	2.485	0.615	Yes	No	0.285	-2.608
XIE5-2-43	5.29	No	-0.325	Yes	Yes	2.504	2.396	Yes	No	0.285	2.126
XIE5-1-27AT	5.26	No	-0.206	No	Yes	2.312	2.465	Yes	No	0.285	3.796
LP1-10a	5.27	No	0.719	No	Yes	2.319	1.472	Yes	No	0.377	1.862
LP1-15a	5.26	No	0.655	No	Yes	2.447	1.183	Yes	No	0.393	1.17
XIE62PY1-31/XRK3F2	5.25	No	0.791	No	Yes	2.346	1.475	Yes	No	0.347	1.604
LP1-10b	5.21	No	0.232	Yes	Yes	2.519	1.082	Yes	No	0.295	-2.043

LP1-11b	5.27	No	0.545	Yes	Yes	2.53	0.905	Yes	No	0.287	-2.046
LP1-12b	5.20	No	0.569	Yes	Yes	2.784	1.349	Yes	No	0.332	-0.044
LP1-13a	5.22	No	0.506	Yes	Yes	2.44	0.923	Yes	No	0.286	-2.166
LP1-13b	5.23	No	0.826	No	Yes	2.315	1.447	Yes	No	0.326	0.546
LP1-14a	5.24	No	0.992	No	Yes	2.352	1.545	Yes	No	0.375	0.843
LP1-14b	5.18	No	0.928	No	Yes	2.292	1.487	Yes	No	0.318	0.251
LP1-15b	5.19	No	0.763	No	Yes	2.546	0.917	Yes	No	0.286	0.054
XIE5-1-13	6.1	No	0.782	No	Yes	2.405	1.12	No	No	0.467	-2.306
XIE5-2-88	6-2	No	0.828	No	Yes	2.338	1.225	No	No	0.517	-1.265
lp1-67	6.4	No	0.435	No	Yes	2.215	1.128	Yes	No	0.316	-1.722
XIE5-2-80	6.6	No	0.276	No	Yes	2.442	1.081	Yes	No	0.297	-2.649
XIE5-2-73	6.5	No	0.57	No	Yes	2.128	1.299	Yes	No	0.385	-0.548
XIE5-2-33	6.7	Yes	0.492	Yes	Yes	2.481	0.576	Yes	No	0.291	-2.316
XIE5-2-39	6.11	No	0.381	Yes	Yes	2.565	1.649	No	No	0.303	0.36
XIE5-2-35	6.9	No	0.769	Yes	Yes	2.749	1.084	Yes	No	0.292	-2.191
XIE5-2-36	6.15	No	0.342	No	Yes	2.54	0.517	Yes	No	0.286	-0.505
XIE5-2-38	6.10	Yes	0.507	Yes	Yes	2.81	0.713	Yes	No	0.285	-1.925
XIE5-2-31	6.8	Yes	0.656	Yes	Yes	2.622	0.845	Yes	No	0.301	-1.508
XIE5-2-32	6.14	No	0.372	No	Yes	2.592	0.635	Yes	No	0.286	-0.193
XIE5-2-9	6.13	No	0.813	Yes	Yes	2.776	1.036	Yes	No	0.29	-1.484
XIE5-2-37	6.16	No	0.449	Yes	Yes	2.5	0.422	Yes	No	0.286	-3.371
XIE5-1-25	6.28	No	-0.03	Yes	Yes	2.606	2.131	No	No	0.285	1.773
XIE62PY1-32	6.25	No	0.724	No	Yes	2.459	1.149	Yes	No	0.436	1.519
XIE5-1-12	7.1	No	0.768	No	Yes	2.215	2.126	No	No	0.487	-1.871
XIE5-1-54A	7.2	No	0.827	No	Yes	2.161	2.096	Yes	No	0.532	-0.829
XIE5-1-65	7.4	No	0.092	Yes	Yes	2.645	3.208	No	No	0.285	0.257
XIE5-2-78	7.6	No	0.248	No	Yes	2.418	1.472	Yes	No	0.299	-2.213
XIE5-2-76	7.5	No	0.56	No	Yes	2.042	1.863	Yes	No	0.4	-0.112
XIE5-2-59	7.7	Yes	0.453	Yes	Yes	2.445	1.19	Yes	No	0.287	-3.372
XIE5-2-64	7.10	Yes	0.497	Yes	Yes	2.806	1.167	No	No	0.285	-1.49
XIE5-2-58	7.8	Yes	0.658	Yes	Yes	2.643	1.129	Yes	No	0.306	-0.725
XIE5-2-61	7.14	No	0.358	No	Yes	2.646	1.917	Yes	No	0.286	0.243
XIE5-2-45	7.28	No	-0.041	Yes	Yes	2.594	2.038	No	No	0.285	2.208
XIE5-1-68/26BT	7.29	Yes	0.214	Yes	Yes	2.613	3.357	No	No	0.285	3.893

lp1-25a	7.26	Yes	0.577	Yes	Yes	2.45	1.292	Yes	No	0.355	1.825
LP1-62	7.27	Yes	0.52	Yes	Yes	2.459	1.38	Yes	No	0.336	1.089
XIE5-1-67/61BT	7.30	Yes	0.195	Yes	Yes	2.636	3.442	No	No	0.285	3.133
XIE5-1-65/55CT	7.31	No	0.092	Yes	Yes	2.645	3.208	No	No	0.285	0.257
Lp1-24b	7.25	No	0.64	Yes	Yes	2.375	1.33	Yes	No	0.379	1.162
Lp1-25b	7.21	Yes	0.159	Yes	Yes	2.548	1.819	Yes	No	0.304	-2.053
LP1-51	7.20	No	0.574	Yes	Yes	2.747	1.531	Yes	No	0.356	-0.372
XIE5-1-83	8.1	Yes	0.648	No	Yes	2.534	1.536	Yes	No	0.904	1.59
XIE5-1-82	9.1	Yes	0.584	No	Yes	2.448	1.503	No	No	0.952	1.897
XIE5-2-83	8.2	Yes	0.711	No	Yes	2.389	1.515	No	No	0.957	1.907
XIE5-2-84	9.2	No	0.375	No	Yes	2.743	1.547	Yes	No	0.611	-2.018
QYQ1-152	10.33	No	0.626	No	Yes	3.155	1.278	Yes	No	0.802	0.328
QYQ1-156-2	10.34										
XIE62LP1-59	10.27	No	0.84	No	Yes	2.406	1.094	No	No	0.445	-2.273
lp1-56	10.25	No	0.82	No	Yes	2.21	2.189	No	No	0.465	-1.838
Lp1-58	10.21	Yes	0.836	No	Yes	2.132	1.137	No	No	0.574	-1.889
LP1-60	10.20	Yes	0.815	No	Yes	1.995	1.875	No	No	0.593	-1.454
lp1-85	9.25	Yes	0.868	No	Yes	2.121	1.935	No	No	0.382	-2.369
XIE5-2-89	9.26	Yes	0.86	No	Yes	2.216	2.035	Yes	No	0.363	0.463
XIE5-2-90	8.25	No	0.718	No	Yes	2.563	1.192	Yes	No	0.305	0.77
		No	0.783	No	Yes	2.565	1.239	Yes	No	0.296	1.012
LP1-63	11.27	No	0.375	No	Yes	2.425	1.219	Yes	No	0.29	-3.641
Lp1-53	11.26	No	0.562	No	Yes	2.77	1.303	Yes	No	0.299	-1.56
LP1-52	11.25	Yes	0.443	Yes	Yes	2.511	0.83	No	No	0.306	-0.569

lp1-54	11.21	Yes	0.355	Yes	Yes	2.716	0.794	No	No	0.289	-0.667
Lp1-55	11.20	No	0.598	No	Yes	2.534	0.967	Yes	No	0.436	1.494

Before testing some ADMET properties *in vitro*, we performed a rapid ADME properties prediction using the QikProp package in Schrodinger software. Many drug candidates fail in late-stage clinical trials due to poor ADME properties, which significantly enhances the cost of novel drug development. The accurate identification of poor druggable candidates early on can rapidly reduce costs and resources and streamline the overall drug discovery and development process. Usually, *in vitro* ADME high throughput screening is applied to eliminate unfavorable drug candidates. However, there are some disadvantages like expensive costs and labor-intensive experimental procedures. Suppose we can predict ADME properties by their structures. In that case, we can escape from synthesis and *in vitro* measurement of those compounds with poor ADME properties that might eventually fail in clinical trials.

In this project, we applied QikProp to predict ADME properties for all the compounds we designed and synthesized and listed all our p62 ligands' predicted properties in **Table 13.** I retained the table with full content and all the properties in supporting information as there might be too much information to put in the main text. In **Table 13,** I only kept some important predicted ADMET properties, involving plasma protein binding (QplogKhsa, -1.5 to 1.5), blood-brain barrier penetration (QplogBB, -3.0 to 1.2), predicted central nervous system (CNS) activity (-- to ++), hERG K+ channel blockade (QPlogHERG, concern below -5), apparent Caco-2 permeability (QPPCaco, < 25 nm/sec poor, > 500 nm/sec great), apparent MDCK permeability (QPPMDCK, < 25 nm/sec poor, > 500 nm/sec great), skin permeability (QplogKp, Kp in cm/h), max transdermal

538

transport rate (jm, mg/cm^2-hr), human oral absorption in GI (% oral absorption, < 25% is poor), and aqueous solubility (QplogS). The software provides the range of most currently available drugs on the market for some predicted properties as normal druggable properties range. If a compound has property outside that range, there might be a PK/PD problem in future studies of this compound that would require more attention to perform chemical modifications or formulations to mitigate potential problems.

As shown in **Table 13**, we found that most of the properties are in the acceptable range for the majority of the analogs, which means the compounds are predicted to have a good PK/PD profile. Some of the compounds have several outlier ADME properties, which is not acceptable for druggable compounds in future studies. We will not consider them a priority when performing our animal studies. The properties that are outside the acceptable range are highlighted in red. For CNS activity, more than half of the compounds have CNS activity. As for aqueous solubility, some compounds' solubility is not good; QplogS less than -10 represents a solubility less than 0.1µg/ml. The overall water solubility for other compounds seems to be beneficial for drug candidates; therefore, those compounds will be our prior choice for further animal studies.

Appendix Table 6 Predicted ADME Properties for p62 Ligands by Schrodinger Module

Compound	CNS	QplogS	QPlogHERG	QPPCaco	QplogBB	QPP MDCK	Qplog Kp	Qplog Khsa	% Oral absorption	Jm
PY1-31 (XRKF2)	1	-7.66	-9.21	383.03	-0.56	691.66	-2.33	1.13	97	0
PY1-33 (XRK3)	-1	-5.67	-8.35	377.52	-0.70	241.23	-2.72	0.64	100	0
LP1-9a	1	-7.47	-8.40	377.69	-0.32	1918.25	-2.75	1.06	96	0
LP1-9b	1	-6.83	-8.64	377.47	-0.51	680.84	-2.54	0.96	94	0
LP1-11b	1	-10.11	-10.34	1564.14	0.33	3165.00	-0.54	2.08	100	0
LP1-12b	1	-10.04	-9.41	1385.29	0.32	2775.73	-1.41	2.04	100	0
LP1-13b	0	-9.66	-8.11	4873.49	-0.07	9771.71	0.37	1.69	100	0

LP1-14b	0	-11.77	-8.87	4761.69	-0.44	9529.78	0.88	2.22	100	0
LP1-15b	0	-12.00	-9.48	4761.63	-0.12	10000.0	1.16	2.25	100	0
LP1-17a	1	-10.36	-10.09	1412.13	0.40	5745.09	-0.83	2.06	100	0
LP1-17b	1	-10.45	-9.06	1478.96	0.43	6039.51	-1.51	2.14	100	0
LP1-19a	1	-10.86	-10.26	1346.47	0.30	5456.80	-0.76	2.19	100	0
LP1-19b	2	-11.51	-10.08	1849.53	0.67	10000.0	-0.62	2.32	100	0
LP1-20a	2	-10.02	-8.99	1385.09	0.46	5626.22	-1.65	2.00	100	0
Lp1-21a	1	-12.24	-10.81	406.39	-0.61	1495.16	-1.60	2.32	100	0
lp1-22b	1	-11.26	-9.43	1849.51	0.37	9894.04	-0.92	2.28	100	0
Lp1-24b	0	-6.92	-8.52	416.66	-0.71	212.45	-2.60	1.14	95	0
Lp1-25b	1	-9.79	-8.73	1638.13	0.12	933.07	-1.49	2.30	100	0
LP1-51	1	-9.80	-8.97	1382.74	0.07	776.88	-1.64	2.20	100	0
LP1-52	1	-4.11	-7.12	394.54	-0.20	634.48	-3.31	0.28	94	0
Lp1-53	1	-2.92	-7.86	85.44	0.13	134.31	-5.49	0.30	80	0
lp1-54	2	-6.68	-7.34	1521.02	0.52	2730.09	-2.28	1.27	100	0
Lp1-55	2	-6.01	-7.13	1906.67	0.68	3229.37	-2.16	1.10	100	0
lp1-56	1	-7.67	-8.52	298.61	-0.47	1488.01	-2.95	1.07	94	0
Lp1-58	2	-10.09	-8.63	1536.94	0.51	8097.68	-1.65	2.07	100	0
LP1-60	2	-9.50	-8.53	1788.91	0.65	8839.57	-1.60	1.90	100	0
LP1-63	1	-3.35	-8.03	85.44	0.04	134.32	-5.39	0.42	82	0
lp1-64	1	-9.25	-9.32	554.67	-0.31	1032.07	-2.18	1.56	100	0
lp1-65	-2	-9.95	-7.76	1657.85	-1.04	854.38	-0.59	1.96	100	0
lp1-66	1	-7.99	-8.43	554.73	-0.20	1255.98	-2.49	1.31	89	0
lp1-67	1	-9.53	-9.15	554.67	-0.22	1603.63	-2.27	1.64	94	0
XIE5-1-8	-1	-7.26	-8.16	1222.55	-0.97	614.72	-0.59	1.02	100	0
XIE5-1-11	0	-8.21	-7.45	1352.27	-0.49	6450.52	-1.11	1.04	100	0
XIE5-1-12	-1	-7.52	-7.31	1329.81	-0.91	673.21	-1.11	1.15	100	0
XIE5-1-13	0	-7.59	-7.50	1122.56	-0.68	3107.44	-1.17	1.06	100	0
XIE5-1-21A	-2	-12.04	-9.36	155.12	-1.35	733.44	-3.12	2.19	94	0
XIE5-1-23	-2	-5.30	-8.91	43.24	-1.95	18.36	-6.17	0.50	78	0
XIE5-1-25	-2	-7.26	-9.06	43.88	-1.75	103.33	-6.32	0.84	73	0
XIE5-1-28	-1	-7.26	-8.16	1222.55	-0.97	614.72	-0.59	1.02	100	0
XIE5-1-30	-2	-2.38	-5.41	19.48	-1.71	7.75	-6.93	-0.47	31	0
XIE5-1-31	1	-0.22	-3.06	145.00	-0.24	67.88	-5.59	-0.51	66	0
XIE5-1-37B	-2	-3.48	-5.64	70.15	-1.23	30.97	-5.74	0.17	59	0
XIE5-1-38B	-2	-4.99	-5.94	58.10	-1.56	25.26	-7.85	0.68	79	0
XIE5-1-39B	-2	-5.86	-6.26	58.10	-1.78	25.26	-7.66	0.92	83	0
XIE5-1-43	-2	-2.71	-5.99	59.02	-1.15	25.69	-5.70	-0.05	67	0
XIE5-1-44	-2	-2.71	-5.99	59.02	-1.15	25.69	-5.70	-0.05	67	0
XIE5-1-45	-2	-2.38	-5.41	19.48	-1.71	7.75	-6.93	-0.47	31	0

XIE5-1-49	-2	-5.30	-8.91	43.24	-1.95	18.36	-6.17	0.50	78	0
XIE5-1-50	-2	-5.30	-8.91	43.24	-1.95	18.36	-6.17	0.50	78	0
XIE5-1-51A	-1	-7.26	-8.16	1222.55	-0.97	614.72	-0.59	1.02	100	0
XIE5-1-54C	-2	-4.99	-5.94	58.10	-1.56	25.26	-7.85	0.68	79	0
XIE5-1-55C	-2	-4.99	-5.94	58.10	-1.56	25.26	-7.85	0.68	79	0
XIE5-1-58	-2	-3.52	-5.45	69.17	-1.13	30.50	-5.85	0.31	61	0
XIE5-1-59	-2	-3.48	-5.64	70.15	-1.23	30.97	-5.74	0.17	59	0
XIE5-1-61	-2	-12.99	-8.58	495.00	-2.30	231.34	-0.95	2.83	100	0
XIE5-1-65	-2	-9.21	-9.34	50.31	-2.51	21.62	-5.89	1.63	85	0
XIE5-1-66	-2	-7.15	-8.95	48.03	-1.85	73.32	-6.25	0.87	74	0
XIE5-1-67	-2	-7.90	-9.00	50.31	-2.19	21.62	-6.18	1.28	78	0
XIE5-1-68	-2	-7.47	-8.87	50.31	-2.07	21.62	-6.28	1.16	76	0
XIE5-2-70	1	-6.22	-8.92	493.26	-0.38	254.96	-2.16	1.12	95	0
XIE5-2-1	1	-8.37	-9.47	1558.28	0.35	3152.24	-0.88	1.60	100	0
XIE5-2-2	1	-10.44	-10.13	1107.39	0.05	2179.00	-0.97	2.12	100	0
XIE5-2-3	2	-9.94	-9.49	1660.48	0.65	10000.0	-1.05	1.87	100	0
XIE5-2-7	1	-8.55	-10.11	234.22	0.40	911.60	-3.74	1.51	86	0
XIE5-2-10	1	-9.55	-9.62	1223.84	0.38	6406.66	-1.17	1.76	100	0
XIE5-2-13	1	-9.81	-9.87	678.62	-0.18	2601.98	-1.49	1.71	100	0
XIE5-2-14	2	-9.02	-9.34	1662.91	0.57	8923.58	-1.01	1.66	100	0
XIE5-2-15	1	-9.14	-9.24	1107.46	0.12	2651.63	-1.28	1.86	100	0
XIE5-2-32	1	-10.73	-9.96	1107.32	0.14	3385.58	-1.07	2.20	100	0
XIE5-2-61	1	-11.05	-10.32	1107.36	-0.23	611.09	-1.03	2.35	100	0
XIE5-2-62	1	-9.68	-9.99	1061.16	-0.16	583.58	-1.11	2.04	100	0
XIE5-2-49	1	-8.70	-10.40	909.19	-0.24	493.79	-0.85	1.73	100	0
XIE5-2-35	1	-9.80	-9.96	1056.42	0.18	3219.50	-1.07	1.91	100	0
XIE5-2-18	1	-9.20	-9.89	1061.14	0.11	2080.87	-1.02	1.80	100	0
XIE5-2-16	2	-8.93	-9.31	1621.72	0.48	5936.63	-0.96	1.77	100	0
XIE5-2-33	2	-9.72	-9.51	1378.28	0.46	7741.33	-1.14	1.88	100	0
XIE5-2-55	1	-8.94	-10.12	1500.66	0.18	1530.95	-0.57	1.84	100	0
XIE5-2-59	1	-9.13	-9.24	1632.66	0.23	1677.01	-1.10	1.96	100	0
XIE5-2-58	1	-8.20	-9.13	1635.28	0.13	931.32	-1.03	1.76	100	0
XIE5-2-53	1	-8.01	-10.01	1502.60	0.08	849.92	-0.51	1.64	100	0
XIE5-2-31	1	-8.66	-9.30	1380.47	0.36	4299.04	-1.09	1.67	100	0
XIE5-2-17	1	-7.87	-10.01	235.27	0.29	451.86	-3.64	1.49	100	0
XIE5-2-39	1	-8.46	-10.07	234.22	0.37	699.09	-3.68	1.59	87	0
XIE5-2-47	1	-7.44	-10.60	227.92	0.02	122.45	-3.31	1.42	95	0
XIE5-2-60	1	-7.93	-9.82	235.27	0.04	126.72	-3.80	1.68	100	0
XIE5-2-64	1	-9.30	-9.66	681.67	-0.54	361.70	-1.53	1.89	100	0
XIE5-2-52	1	-8.80	-10.44	660.41	-0.57	349.52	-1.04	1.63	100	0
XIE5-2-38	1	-9.82	-9.91	678.66	-0.22	1995.50	-1.41	1.81	100	0

| XIE5-2-21 | 1 | -9.23 | -9.85 | 681.65 | -0.29 | 1289.72 | -1.37 | 1.70 | 100 | 0 |

Note: QP log K= Serum Protein Binding = QplogKhsa (-1.5 / 1.5); QP log BB for brain/blood = QplogBB (-3.0 / 1.2); Predicted CNS Activity = CNS (-- to ++); HERG K+ Channel Blockage: log IC50 = QPlogHERG (concern below -5); Apparent Caco-2 Permeability (nm/sec) = QPPCaco (<25 poor, >500 great); Apparent MDCK Permeability (nm/sec) = QPPMDCK (<25 poor, >500 great); QP log Kp for skin permeability = QplogKp (Kp in cm/hr); Jm, max transdermal transport rate = jm (micrograms/cm^2-hr); % Human Oral Absorption in GI (+-20%) = Percent Human Oral Absorption (<25% is poor);

For the hERG (the human Ether-à-go-go-Related Gene) inhibition prediction results, we found that most of our compounds were predicted to be hERG blockers with IC_{50} less than 10µM, which means they might have potential cardiac toxicity problems. hERG encodes an alpha subunit of a potassium ion channel. We referred to the ion channel as hERG. hERG regulates the repolarizing potassium current in cardiac action potential, which plays a role in mediating heartbeats. When the hERG's function to coordinate cardiac action potential is inhibited by drug or gene mutation, it will lead to a potentially fatal disease known as long QT syndrome. Previous studies found a number of drugs on the market interact with hERG, lengthening the QT and resulting in a ventricular tachyarrhythmia called *torsades de pointes*. Thus, hERG inhibition is an important point that should be avoided in the drug development process. Our compounds are predicted to be hERG inhibitors, which is not a positive property for a drug candidate. If the prediction is accurate, this might be a major problem that our chemical modification must avoid in our future studies. We could choose to synthesize analogs with no hERG inhibitions later if it became a problem in animal studies.

Permeability of compounds is generally good, with a few ones that have some outliers that are predicted to have problems in skin permeability and MDCK assays. Overall, most of our

analogs did not show problems in predictions of passing Caco-2 cells, blood-brain barriers, skin, transdermal membranes, and MDCK system, which predict scores within the acceptable range of currently available drugs. Moreover, the predicted oral absorption rate is high for all of our in-house compounds, indicating a positive property of our compounds.

Another problem found in this prediction is that nearly one-third of our compounds had a plasma protein binding beyond the average druggable range (-1.5 to 1.5), which is larger than 1.5, indicating a potential of high plasma protein binding rate, a drug distribution issue that may cause drug-drug interaction problems when two drugs with high plasma protein binding are combined to use. The plasma concentration of the free drugs might be influenced by other agents or factors that affect the free plasma protein level, which is dangerous in clinical use. In this case, we did not have any *in vivo* data that shows this problem so far. If this problem occurs in our animal studies, we will choose compounds without that distribution problem for synthesis and further experimental validation.

As the prediction results might be biased or inaccurate if we apply one software to test our compounds, we implemented the other two software packages to predict the ADMET properties of our p62 analogs. The predicted results and its analysis are listed in **Appendix F. Predicted ADME Profile for p62-ZZ Ligands by pkCSM**.

Appendix F. Evaluation of Residues

This is a list of evaluation of residues for the homology model using ProCheck.

Residue [4 :LEU] (-44.83, 114.42) in Allowed region
Residue [15 :ASP] (73.54, 28.78) in Allowed region
Residue [39 :ALA] (-71.43, -67.29) in Allowed region
Residue [40 :GLY] (-91.08, -60.66) in Allowed region
Residue [41 :PRO] (-87.95,-166.28) in Allowed region
Residue [67 :TYR] (-116.41,-173.09) in Allowed region
Residue [74 :LEU] (-76.23, 14.38) in Allowed region
Residue [78 :SER] (-156.82, 24.33) in Allowed region
Residue [101 :GLU] (67.93, 63.76) in Allowed region
Residue [104 :GLU] (-82.77, -64.56) in Allowed region
Residue [106 :ARG] (45.44, 69.95) in Allowed region
Residue [109 :HIS] (-68.85, -80.40) in Allowed region
Residue [116 :GLU] (81.91, 149.45) in Allowed region
Residue [129 :ASP] (-50.48, 165.45) in Allowed region
Residue [131 :CYS] (-128.00, 79.76) in Allowed region
Residue [135 :VAL] (-76.47, -76.39) in Allowed region
Residue [143 :SER] (69.73, -25.81) in Allowed region
Residue [147 :ASP] (-29.00, 130.09) in Allowed region
Residue [162 :GLY] (-55.93, -80.70) in Allowed region
Residue [164 :THR] (-171.57,-173.53) in Allowed region
Residue [166 :LEU] (-109.61,-110.88) in Allowed region
Residue [176 :SER] (-97.13,-153.28) in Allowed region
Residue [194 :GLY] (-157.24, 120.90) in Allowed region
Residue [205 :ASN] (-90.50,-165.86) in Allowed region
Residue [209 :ARG] (-83.44, -36.53) in Allowed region
Residue [229 :SER] (-105.22,-113.32) in Allowed region
Residue [233 :SER] (-145.48, 87.83) in Allowed region
Residue [247 :ALA] (-154.64,-149.53) in Allowed region
Residue [261 :HIS] (-71.88, 31.91) in Allowed region
Residue [270 :PRO] (-55.74, 106.82) in Allowed region
Residue [283 :SER] (-75.18, 21.19) in Allowed region
Residue [284 :SER] (-149.71, -45.29) in Allowed region
Residue [304 :THR] (-66.78, 92.23) in Allowed region
Residue [318 :SER] (-109.18, 81.04) in Allowed region
Residue [319 :GLU] (-101.42,-168.55) in Allowed region
Residue [320 :GLY] (-72.63, -75.70) in Allowed region
Residue [328 :SER] (-105.00,-122.01) in Allowed region
Residue [342 :SER] (48.26, 64.91) in Allowed region

Residue [345 :GLU] (53.99,-172.90) in Allowed region
Residue [355 :SER] (81.28, 14.34) in Allowed region
Residue [385 :HIS] (-70.80, 97.86) in Allowed region
Residue [389 :GLU] (59.06, 178.55) in Allowed region
Residue [42 :GLY] (161.94, -72.46) in Outlier region
Residue [123 :HIS] (-82.68,-160.37) in Outlier region
Residue [132 :ASN] (147.28, -93.11) in Outlier region
Residue [133 :GLY] (124.86, -71.06) in Outlier region
Residue [136 :VAL] (43.76, 167.28) in Outlier region
Residue [226 :SER] (-43.43, 73.28) in Outlier region
Residue [262 :GLY] (178.01, -27.32) in Outlier region
Residue [321 :ARG] (165.74, 157.64) in Outlier region
Residue [363 :GLY] (-160.24, 101.54) in Outlier region
Number of residues in favoured region   (~98.0% expected) : 387 (88.4%)
Number of residues in allowed region   (~2.0% expected) : 42 (9.6%)
Number of residues in outlier region   :   9 (2.1%)

Appendix G. Table of Drug Candidates in MM Clinical Trials

This table shows the drug candidates in the clinical trials to treat multiple myeloma. No one has the same mechanism as our p62 compounds.

Appendix Table 7. Drug Candidates in Multiple Myeloma Clinical Trials

Name	Type	Drug Status	Source	Recruitment Status	Therapeutic Drug Target	Effect
Armodafinil	Small molecule	Clinical trial - Phase III	NCT01160380	Completed		
ENMD-2076	Small molecule	Clinical trial - Phase I	NCT00806065	Completed	Aurora-A	Inhibition
					Aurora-B	Inhibition
Pazopanib	Small molecule	Clinical trial - Phase II	NCT00256880	Completed		
Riviciclib	Small molecule	Clinical trial - Phase I/II	NCT00882063	Completed	CDK1 (p34)	Inhibition
					CDK4	Inhibition
					CDK9	Inhibition
XL999	Small molecule	Clinical trial - Phase II	NCT00304590	Terminated	PDGF-R-alpha	Inhibition
					PDGF-R-beta	Inhibition
ABT-737	Small molecule	Preclinical	PMID: 17016430		Bcl-2	Inhibition
					Bcl-W	Inhibition

					Bcl-XL	Inhibition
Onyvax-O	Small molecule	Clinical trial				
Acalabrutinib	Small molecule	Clinical trial - Phase I	NCT02211014	Recruiting		
Atacicept	Biologic	Clinical trial - Phase I	PMID: 19789533		APRIL(TNFSF13)	Inhibition
					BAFF(TNFSF13B)	Inhibition
KW2478	Small molecule	Clinical trial - Phase I	NCT00457782	Completed	HSP90	Inhibition
Spebrutinib	Small molecule	Preclinical	Link			
Paclitaxel	Small molecule	Clinical trial - Phase II	NCT01646762	Active, not recruiting		
Sunitinib	Small molecule	Clinical trial - Phase II	NCT00514137	Completed		
Pyroxamide	Small molecule	Clinical trial - Phase I	NCT00042900	Completed	HDAC1	Inhibition
Selumetinib	Small molecule	Clinical trial - Phase II	NCT01085214	Completed		
Daratumumab	Biologic	Clinical trial - Phase II	NCT01985126	Active, not recruiting	CD38	Inhibition
Noscapine	Small molecule	Clinical trial - Phase I/II	NCT00912899	Completed	Tubulin (in microtubules)	Inhibition
Brostallicin	Small molecule	Clinical trial - Phase I/II	NCT00060203	Completed		
Epothilone D	Small molecule	Preclinical	PMID: 16030145			
XL139	Small molecule	Clinical trial - Phase I	NCT00884546	Completed		
Dexamethasone	Small molecule	Clinical trial - Phase II	NCT02402725	Withdrawn	GCR	Activation

Inebilizumab	Biologic	Clinical trial - Phase I	NCT00983619	Active, not recruiting	CD19	Inhibition
Curcumin	Small molecule	Clinical trial	NCT00113841	Completed		
Manumycin A	Small molecule	Preclinical	PMID: 17985347		FTase	Inhibition
IPH2101	Biologic	Clinical trial - Phase II	NCT00999830	Completed	KIR2DL1	Inhibition
			NCT01222286	Completed	KIR2DL3	Inhibition
			NCT01248455	Terminated	KIR2DL2	Unspecified
Samalizumab	Biologic	Clinical trial - Phase I/II	NCT00648739	Completed	CD200 (OX-2)	Inhibition
Perifosine	Small molecule	Clinical trial - Phase II	NCT00375791	Completed	AKT(PKB)	Inhibition
Vandetanib	Small molecule	Clinical trial - Phase II	NCT00047788	Completed		
PIM447	Small molecule	Clinical trial - Phase I/II	NCT02144038	Completed		
Idelalisib	Small molecule	Clinical trial - Phase I	NCT00710528	Completed		
Tefinostat	Small molecule	Clinical trial - Phase I	NCT00820508	Completed		
Phorbol 12-myristate 13-acetate	Small molecule	Clinical trial - Phase I	NCT00004058	Terminated		
CC-122	Small molecule	Clinical trial - Phase I	NCT01421524	Recruiting		
Imatinib	Small molecule	Clinical trial - Phase II	PMID: 16321825			
Retaspimycin	Small molecule	Clinical trial - Phase I	NCT00113204	Completed		
Marizomib	Small molecule	Clinical trial - Phase I	NCT00461045	Active, not recruiting	Proteasome (20S core)	Inhibition

Drug	Type	Stage	Identifier	Status	Target	Action
RG7598	Biologic	Clinical trial - Phase I	NCT01432353	Completed		
rhMBL	Biologic	Clinical trial - Phase I	NCT00388999	Completed		
Carfilzomib	Small molecule	Clinical trial - Phase I/II	NCT00531284	Active, not recruiting	PSMB5	Inhibition
Carfilzomib	Small molecule	Clinical trial - Phase II	NCT00511238	Completed	PSMB5	Inhibition
Citarinostat	Small molecule	Clinical trial - Phase I	NCT02400242	Recruiting		
Inebilizumab	Biologic	Clinical trial - Phase I	NCT01377116	Recruiting	CD19	Inhibition
Aldesleukin	Biologic	Clinical trial - Phase II	NCT00616720	Completed	IL-2R alpha chain	Activation
					IL-2R beta chain	Activation
Venetoclax	Small molecule	Clinical trial - Phase I	NCT01794520	Recruiting		
Sapanisertib	Small molecule	Clinical trial - Phase I	NCT01118689	Completed	TORC1	Inhibition
					TORC2	Inhibition
MOR202	Biologic	Clinical trial - Phase I/II	NCT01421186	Recruiting		
Zastumotide	Biologic	Clinical trial - Phase II/III	NCT00090493	Completed		
Vatalanib	Small molecule	Clinical trial - Phase II	NCT00165347	Completed	VEGFR-1	Inhibition
					VEGFR-2	Inhibition
Natalizumab	Biologic	Clinical trial - Phase I/II	NCT00675428	Terminated	ITGA4	Inhibition
Siltuximab	Biologic	Clinical trial - Phase II	NCT00402181	Completed	IL-6	Inhibition
Pomalidomide	Small molecule	FDA approved	Drug label	204026		

Romidepsin	Biologic	Clinical trial - Phase II	NCT00066638	Completed	HDAC1	Inhibition
Bortezomib	Small molecule	FDA approved	Drug label	21602	Proteasome (20S core)	Inhibition
(R)-Etodolac	Small molecule	Clinical trial - Phase II	NCT00293111	Terminated		
DS-3032	Small molecule	Clinical trial - Phase I	NCT02579824	Not yet recruiting		
Ricolinostat	Small molecule	Clinical trial - Phase I	NCT01323751	Active, not recruiting		
RO5126766	Small molecule	Clinical trial - Phase I	NCT02407509	Recruiting		
Dacetuzumab	Biologic	Clinical trial - Phase I	NCT00079716	Completed	CD40(TNFRSF5)	Inhibition
Lucatumumab	Biologic	Clinical trial - Phase I	NCT00231166	Completed	CD40(TNFRSF5)	Inhibition
Telomestatin	Small molecule	Preclinical	PMID: 14760100			
Bendamustine	Small molecule	Clinical trial - Phase II	NCT01849848	Completed	Caspase-3	Activation
					DNA	Inhibition
BI-505	Biologic	Clinical trial - Phase I	NCT01025206	Completed		
Darinaparsin	Small molecule	Clinical trial - Phase II	NCT00423644	Active, not recruiting		
Gallium	Small molecule	Approved	Drug label		FGF1	Inhibition
Muparfostat	Small molecule	Clinical trial - Phase II			FGF2	Inhibition
					Heparanase 1	Inhibition
					VEGF-A	Inhibition
Bryostatin 1	Small molecule	Clinical trial - Phase II	NCT00002907	Completed		

[2-(5-Chloro-2-fluoro-phenyl)pteridin-4-yl]-(4-pyridyl)amine	Small molecule	Preclinical	PMID: 15569984			
Melphalan	Small molecule	FDA approved	Drug label	20207		
Anti-HM1.24	Biologic	Discontinued	PMID: 9376601		BST2	Activation
R4733	Small molecule	Clinical trial - Phase II	NCT01251172	Terminated		
Cabozantinib	Small molecule	Clinical trial - Phase I	NCT01582295	Active, not recruiting		
TAS-120	Small molecule	Clinical trial - Phase I/II	NCT02052778	Recruiting		
PRLX93936	Small molecule	Clinical trial - Phase I/II	NCT01695590	Recruiting		
BHQ-880	Biologic	Clinical trial - Phase II	NCT01302886	Completed		
Delanzomib	Small molecule	Clinical trial - Phase I/II	NCT01023880	Terminated	Proteasome (20S core)	Inhibition
Tositumomab	Biologic	Clinical trial - Phase II	NCT00135200	Active, not recruiting	CD20	Unspecified
MLN3897	Small molecule	Preclinical	PMID: 17715391			
CUDC-907	Small molecule	Clinical trial - Phase I	NCT01742988	Recruiting		
Givinostat	Small molecule	Clinical trial - Phase II	NCT00792740	Terminated	HDAC2	Inhibition
Daratumumab	Biologic	Clinical trial - Phase IV	NCT02477891	Recruiting	CD38	Inhibition
BI 836909	Small molecule	Clinical trial - Phase I	NCT02514239	Recruiting		

Luminespib	Small molecule	Clinical trial - Phase I/II	NCT00708292	Completed	HSP90	Inhibition
Dovitinib	Small molecule	Clinical trial - Phase II	NCT01058434	Completed	FGFR1	Inhibition
					FGFR3	Inhibition
					FLT3	Inhibition
					PDGF-R-beta	Inhibition
					VEGFR-1	Inhibition
					VEGFR-2	Inhibition
Rigosertib	Small molecule	Clinical trial - Phase I	NCT00861510	Completed		
Atiprimod	Small molecule	Clinical trial - Phase I/II	NCT00086216	Completed	Caspase-3	Activation
					Caspase-9	Activation
					PLA2G1B	Inhibition
					PLC-beta1	Inhibition
Dalantercept	Biologic	Clinical trial - Phase I	NCT00996957	Completed		
Ardenermin	Biologic	Discontinued			BAFF-R	Activation
Filanesib	Small molecule	Clinical trial - Phase I/II	NCT00821249	Completed	KNSL1	Inhibition
Carfilzomib	Small molecule	FDA approved	Drug label	202714	PSMB5	Inhibition
Lorvotuzumab mertansine	Biologic	Clinical trial - Phase I	NCT00346255	Completed	NCAM1	Inhibition
					Tubulin beta	Inhibition
Filgrastim	Biologic	Clinical trial - Phase III	NCT01908621	Recruiting	G-CSF receptor	Activation
Beta-alethine	Small molecule	Clinical trial - Phase I/II	NCT00006466	Active, not recruiting		
MDX-1105	Biologic	Clinical trial - Phase I	NCT01452334	Withdrawn		

Tivantinib	Small molecule	Clinical trial - Phase II	NCT01447914	Completed		
CC-223	Small molecule	Clinical trial - Phase I/II	NCT01177397	Active, not recruiting		
Bevacizumab	Biologic	Clinical trial - Phase II	NCT00482495	Completed	VEGF-A	Inhibition
Talmapimod	Small molecule	Clinical trial - Phase II	NCT00087867	Completed	p38alpha (MAPK14)	Inhibition
N-Methylpyrrolidone	Small molecule	Clinical trial - Phase I	NCT02468687	Recruiting		
Pamidronic Acid	Small molecule	FDA approved	Drug label	20036	FDPS	Inhibition
Bardoxolone methyl	Small molecule	Clinical trial - Phase I	NCT00508807	Completed	IKK-beta	Inhibition
					PPAR-gamma	Inhibition
Masitinib	Small molecule	Clinical trial - Phase II	NCT00866138	Active, not recruiting	Lyn	Inhibition
					PDGF-R-beta	Inhibition
					Tyk2	Inhibition
Ibrutinib	Small molecule	Clinical trial - Phase II	NCT01478581	Active, not recruiting	Btk	Inhibition
VTP195183	Small molecule	Clinical trial - Phase I/II	NCT00234169	Completed		
Methoxy polyethylene glycol-epoetin beta	Biologic	Clinical trial - Phase II	NCT00360347	Completed	Epo receptor	Activation
Cyclophosphamide	Small molecule	FDA approved	Drug label	12142	DNA	Inhibition
ALT-801	Biologic	Clinical trial - Phase I/II	NCT01670994	Terminated		
Vemurafenib	Small molecule	Clinical trial - Phase II	NCT01524978	Active, not recruiting		

Ridaforolimus	Small molecule	Clinical trial - Phase I	NCT00060645	Completed	mTOR	Inhibition
Elsilimomab	Biologic	Clinical trial	PMID: 16113665			
Balixafortide	Small molecule	Clinical trial - Phase I/II	NCT01413568	Completed		
Balixafortide	Small molecule	Clinical trial - Phase II	NCT01105403	Completed		
Imetelstat	Biologic	Clinical trial - Phase II	NCT01242930	Completed	TERC	Inhibition
Rabacfosadine	Small molecule	Clinical trial - Phase I/II	NCT00499239	Terminated		
EDO-S101	Small molecule	Clinical trial - Phase I	NCT02576496	Recruiting		
ALT-803	Biologic	Clinical trial - Phase I/II	NCT01885897	Recruiting		
Troxacitabine	Small molecule	Clinical trial - Phase II	PMID: 17325846			
Olaptesed pegol	Biologic	Clinical trial - Phase II	NCT01521533	Completed		
Ibandronic acid	Small molecule	Clinical trial	PMID: 17615253		FDPS	Inhibition
Alvocidib	Small molecule	Clinical trial - Phase II	NCT00047203	Completed	CDK1 (p34)	Inhibition
			PMID: 16503551		CDK2	Inhibition
					CDK4	Inhibition
					CDK5	Inhibition
					CDK6	Inhibition
					CDK7	Inhibition
					CDK9	Inhibition
Etidronic acid	Small molecule	Clinical trial	PMID: 8258043			
Ancestim	Biologic	Clinical trial - Phase II	NCT00001750	Completed	c-Kit	Activation

Panobinostat	Small molecule	Clinical trial - Phase II/III	NCT00445068	Terminated	HDAC1	Inhibition
					HDAC3	Inhibition
					HDAC6	Inhibition
					HDAC9	Inhibition
Acadesine	Small molecule	Clinical trial - Phase II	Link			
Myelovax	Small molecule	Clinical trial	Link			
Zoledronic acid	Small molecule	FDA approved	Drug label	21223	FDPS	Inhibition
Pevonedistat	Small molecule	Clinical trial - Phase I	NCT00722488	Completed	APP-BP1	Inhibition
SL-401	Biologic	Preclinical	Link			
ABBV-838	Biologic	Clinical trial - Phase I	NCT02462525	Recruiting		
Tacedinaline	Small molecule	Clinical trial - Phase II	NCT00005624	Completed		
CB-5083	Small molecule	Clinical trial - Phase I	NCT02223598	Recruiting		
Lexibulin	Small molecule	Clinical trial - Phase II	NCT00664378	Terminated	Tubulin (in microtubules)	Inhibition
Daratumumab	Biologic	FDA approved	Drug label	761036	CD38	Inhibition
AT7519M	Small molecule	Clinical trial - Phase I/II	NCT01183949	Completed	CDK1 (p34)	Inhibition
					CDK2	Inhibition
					CDK3	Inhibition
					CDK4	Inhibition
					CDK6	Inhibition
					CDK7	Inhibition
					CDK9	Inhibition

Burixafor	Small molecule	Clinical trial - Phase II	NCT01018979	Completed		CXCR4	Inhibition
SF1126	Small molecule	Clinical trial	Link			PI3K cat class IA (p110-alpha)	Inhibition
Vismodegib	Small molecule	Clinical trial - Phase I	NCT01330173	Completed			
AR-42	Small molecule	Clinical trial - Phase I	NCT01129193	Active, not recruiting			
Abexinostat	Small molecule	Clinical trial - Phase I	NCT00562224	Completed			
Pembrolizumab	Biologic	Clinical trial - Phase I	NCT01953692	Recruiting			
Antithymocyte globulin	Biologic	Clinical trial - Phase I	NCT00545519	Completed		CD1a	Unspecified
Tosedostat	Small molecule	Clinical trial - Phase I/II	NCT00689000	Completed		PMID: 20733120	
Temozolomide	Small molecule	Clinical trial	Link			DNA	Inhibition
Figitumumab	Biologic	Clinical trial - Phase I	NCT01536145	Completed			
Panobinostat	Small molecule	FDA approved	Drug label		205353	HDAC1	Inhibition
						HDAC3	Inhibition
						HDAC6	Inhibition
						HDAC9	Inhibition
Gallium maltolate	Small molecule	Clinical trial - Phase I/II	NCT00050687	Terminated			
Epipropidine	Small molecule	Discontinued	PMID: 13952366				
Dalotuzumab	Biologic	Clinical trial - Phase I	NCT00701103	Completed		IGF-1 receptor	Inhibition
Pegfilgrastim	Biologic	Clinical trial - Phase II	NCT00067639	Completed		G-CSF receptor	Activation

Siplizumab	Biologic	Clinical trial - Phase II	NCT00113646	Terminated	CD2	Inhibition
CC-115	Small molecule	Clinical trial - Phase I	NCT01353625	Active, not recruiting		
Sotatercept	Biologic	Clinical trial - Phase II	NCT00747123	Completed	Activin beta A	Inhibition
Motexafin gadolinium	Small molecule	Clinical trial - Phase II	NCT00096837	Completed	TXNRD1	Inhibition
BIW-8962	Biologic	Clinical trial - Phase I	NCT00775502	Terminated		
Elotuzumab	Biologic	Clinical trial - Phase I/II	NCT00726869	Terminated	CRACC	Inhibition
Lenalidomide	Small molecule	Clinical trial - Phase II	NCT01054144	Active, not recruiting	TNF-alpha	Inhibition
OPB31121	Small molecule	Clinical trial - Phase I	NCT00511082	Recruiting		
BrevaRex	Biologic	Clinical trial	Link		MUC1	Inhibition
Fenofibrate	Small molecule	Clinical trial - Phase II	NCT01965834	Active, not recruiting		
Lestaurtinib	Small molecule	Clinical trial - Phase II	NCT00242827	Terminated	JAK2	Inhibition
GSK2857916	Biologic	Clinical trial - Phase I	NCT02064387	Recruiting		
Ruxolitinib	Small molecule	Clinical trial - Phase II	NCT00639002	Completed	JAK1	Inhibition
					JAK2	Inhibition
BMS-387032	Small molecule	Clinical trial - Phase I	NCT00446342	Completed	CDK2	Inhibition
					CDK7	Inhibition
					CDK9	Inhibition
CPI-0610	Small molecule	Clinical trial - Phase I	NCT02157636	Recruiting		

2-Methoxyestradiol	Small molecule	Clinical trial - Phase II	NCT00592579	Completed		
Enzastaurin	Small molecule	Clinical trial - Phase II	NCT00718419	Completed	PKC-beta	Inhibition
Isatuximab	Biologic	Clinical trial - Phase I	NCT01084252	Recruiting		
Emepepimut-S	Biologic	Clinical trial - Phase II	NCT01094548	Completed		
Melphalan	Small molecule	FDA approved	Drug label	14691		
MFGR1877S	Biologic	Clinical trial - Phase I	NCT01122875	Completed		
Triapine	Small molecule	Clinical trial			Ribonucleotide reductase	Inhibition
Clodronic acid	Small molecule	Clinical trial	PMID: 11442499			
Cabozantinib	Small molecule	Clinical trial - Phase I/II	NCT01866293	Active, not recruiting		
Azacitidine	Small molecule	Clinical trial - Phase II	NCT00412919	Terminated		
LY2812176	Biologic	Clinical trial - Phase I	NCT01457417	Completed		
As2O3	Small molecule	Clinical trial - Phase II	NCT00017433	Active, not recruiting		
Aflibercept	Biologic	Clinical trial - Phase II	NCT00437034	Terminated	VEGF-A	Inhibition
Danusertib	Small molecule	Clinical trial - Phase II	NCT00872300	Terminated		
TIC10	Small molecule	Clinical trial - Phase I	NCT02609230	Recruiting		
TAK-901	Small molecule	Clinical trial - Phase I	NCT00807677	Completed	Aurora-B	Inhibition

Drug	Type	Phase	NCT/PMID	Status	Target	Action
Semaxanib	Small molecule	Clinical trial - Phase II	NCT00006013	Completed	VEGFR-1	Inhibition
					VEGFR-2	Inhibition
Milatuzumab-doxorubicin conjugate	Biologic	Clinical trial - Phase I/II	NCT01101594	Completed		
BI-505	Biologic	Clinical trial - Phase II	NCT01838369	Terminated		
Plitidepsin	Small molecule	Clinical trial - Phase II	NCT00229203	Completed	PMID: 20530693	
Oprozomib	Small molecule	Clinical trial - Phase I/II	NCT01416428	Active, not recruiting		
AMG 224	Biologic	Clinical trial - Phase I	NCT02561962	Recruiting		
Imexon	Small molecule	Clinical trial - Phase I/II	NCT00327249	Completed	Caspase-3	Activation
			PMID: 20571355		Caspase-8	Activation
					Caspase-9	Activation
Ixazomib citrate	Small molecule	Clinical trial - Phase III	NCT02181413	Active, not recruiting		
Afuresertib	Small molecule	Clinical trial - Phase II	NCT01445587	Withdrawn		
Atezolizumab	Biologic	Clinical trial - Phase I	NCT02784483	Recruiting		
Anakinra	Biologic	Clinical trial - Phase II	NCT00635154	Completed	IL-1RI	Inhibition
Dasatinib	Small molecule	Clinical trial - Phase II	NCT00429949	Completed	BCR/ABL fusion protein	Inhibition
					c-Src	Inhibition
Fenretinide	Small molecule	Clinical trial - Phase I	NCT00104923	Active, not recruiting		
Ixazomib citrate	Small molecule	Clinical trial - Phase I/II	NCT00932698	Completed		

Semustine	Small molecule	Clinical trial - Phase II	PMID: 329977			
Entinostat	Small molecule	Clinical trial - Phase I	NCT00015925	Completed	HDAC1	Inhibition
Canfosfamide	Small molecule	Clinical trial - Phase II	NCT01148108	Completed		
Dinaciclib	Small molecule	Clinical trial - Phase II	NCT01096342	Completed		
Indatuximab ravtansine	Biologic	Clinical trial - Phase I/II	NCT01001442	Active, not recruiting		
Pembrolizumab	Biologic	Clinical trial - Phase II	NCT02636010	Recruiting		
Tocilizumab	Biologic	Preclinical	PMID: 8917348		IL-6 receptor	Inhibition
Milatuzumab	Biologic	Clinical trial - Phase I/II	NCT00421525	Completed	CD74	Inhibition
CC-220	Small molecule	Clinical trial - Phase I/II	NCT02773030	Not yet recruiting		
Simvastatin	Small molecule	Clinical trial - Phase II	NCT00399867	Completed	HMDH	Inhibition
PF-04878691	Small molecule	Clinical trial - Phase II	NCT00276159	Terminated		
Sorafenib	Small molecule	Clinical trial - Phase II	NCT00253578	Completed	B-Raf	Inhibition
					c-Kit	Inhibition
					c-Raf-1	Inhibition
					FLT3	Inhibition
					PDGF-R-beta	Inhibition
					RET	Inhibition
					VEGFR-1	Inhibition
					VEGFR-2	Inhibition
					VEGFR-3	Inhibition
Nivolumab	Biologic	Clinical trial - Phase I	NCT01592370	Recruiting		

Seliciclib	Small molecule	Preclinical	Link		CDK2	Inhibition
Denosumab	Biologic	Clinical trial - Phase III	NCT00330759 NCT00950911 NCT01345019	Completed Completed Active, not recruiting	Interactions (1) RANKL(TNFSF11)	 Inhibition
Acronine	Small molecule	Discontinued	PMID: 6616497			
Selinexor	Small molecule	Clinical trial - Phase I	NCT01607892	Active, not recruiting		
Durvalumab	Biologic	Clinical trial - Phase I	NCT02616640	Recruiting		
Evofosfamide	Small molecule	Clinical trial - Phase I/II	NCT01522872	Active, not recruiting		
Ulocuplumab	Biologic	Clinical trial - Phase I	NCT01359657	Completed		
IPH2101	Biologic	Clinical trial - Phase I	Link		KIR2DL1	Inhibition
			NCT00552396 PMID: 23033266	Completed	KIR2DL3 KIR2DL2	Inhibition Unspecified
LY2812176	Biologic	Clinical trial - Phase I	NCT01457417	Completed		
Resveratrol	Small molecule	Clinical trial - Phase II	NCT00920556	Terminated		
VEL0230	Small molecule	Clinical trial - Phase I	Link			
Ficlatuzumab	Biologic	Clinical trial - Phase I	NCT00725634	Completed		
Dinaciclib	Small molecule	Clinical trial - Phase II	NCT01096342	Completed		
Indatuximab ravtansine	Biologic	Clinical trial - Phase I/II	NCT01001442	Active, not recruiting		

Pembrolizumab	Biologic	Clinical trial - Phase II	NCT02636010	Recruiting		
Tocilizumab	Biologic	Preclinical	PMID: 8917348		IL-6 receptor	Inhibition
Milatuzumab	Biologic	Clinical trial - Phase I/II	NCT00421525	Completed	CD74	Inhibition
CC-220	Small molecule	Clinical trial - Phase I/II	NCT02773030	Not yet recruiting		
Simvastatin	Small molecule	Clinical trial - Phase II	NCT00399867	Completed	HMDH	Inhibition
PF-04878691	Small molecule	Clinical trial - Phase II	NCT00276159	Terminated		
Sorafenib	Small molecule	Clinical trial - Phase II	NCT00253578	Completed	B-Raf	Inhibition
					c-Kit	Inhibition
					c-Raf-1	Inhibition
					FLT3	Inhibition
					PDGF-R-beta	Inhibition
					RET	Inhibition
					VEGFR-1	Inhibition
					VEGFR-2	Inhibition
					VEGFR-3	Inhibition
Nivolumab	Biologic	Clinical trial - Phase I	NCT01592370	Recruiting		
Seliciclib	Small molecule	Preclinical	Link		CDK2	Inhibition
Denosumab	Biologic	Clinical trial - Phase III	NCT00330759	Completed	Interactions (1)	
			NCT00950911	Completed		
			NCT01345019	Active, not recruiting	RANKL(TNFSF11)	Inhibition
Acronine	Small molecule	Discontinued	PMID: 6616497			
Selinexor	Small molecule	Clinical trial - Phase I	NCT01607892	Active, not recruiting		

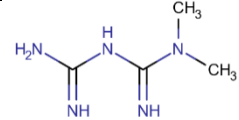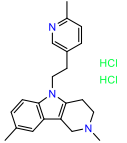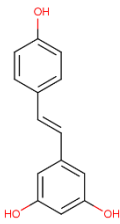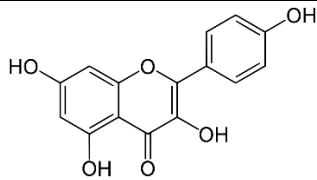|						
Durvalumab	Biologic	Clinical trial - Phase I	NCT02616640	Recruiting		
Evofosfamide	Small molecule	Clinical trial - Phase I/II	NCT01522872	Active, not recruiting		
Ulocuplumab	Biologic	Clinical trial - Phase I	NCT01359657	Completed		
IPH2101	Biologic	Clinical trial - Phase I	NCT00552396	Completed	KIR2DL1	Inhibition
			PMID: 23033266		KIR2DL3	Inhibition
					KIR2DL2	Unspecified
LY2812176	Biologic	Clinical trial - Phase I	NCT01457417	Completed		
Resveratrol	Small molecule	Clinical trial - Phase II	NCT00920556	Terminated		
CWP232291	Small molecule	Clinical trial - Phase I	NCT02426723	Recruiting		
ABC294640	Small molecule	Clinical trial - Phase I/II	NCT02757326	Not yet recruiting		
Fluphenazine	Small molecule	Clinical trial - Phase I/II	NCT00335647	Completed		
Tipifarnib	Small molecule	Clinical trial - Phase II	NCT00012350	Completed	FTase	Inhibition
BKT140	Small molecule	Clinical trial - Phase I/II	NCT01010880	Completed		
1D09C3	Biologic	Preclinical	PMID: 17409435			
Ixazomib citrate	Small molecule	Clinical trial - Phase II	NCT02168101	Recruiting		
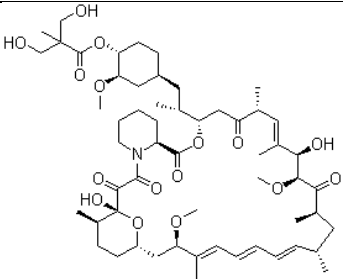
Appendix H. Table of Autophagy Modulators
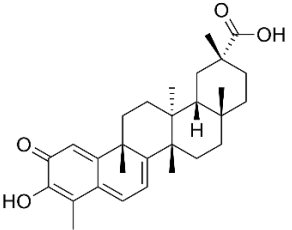
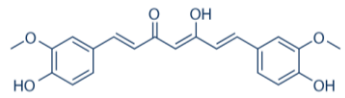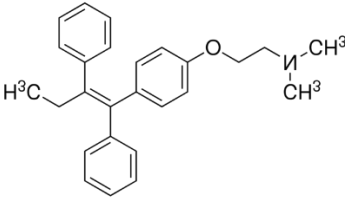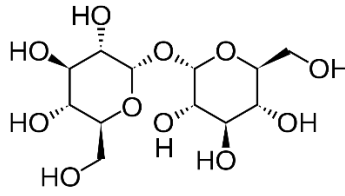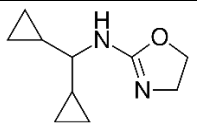This is the tables of autophagy inducers and inhibitors with their structure, target, mechanism of action, and the reference
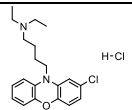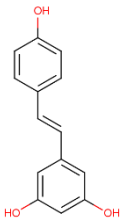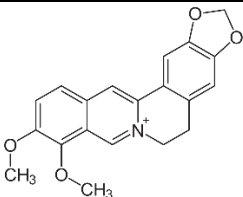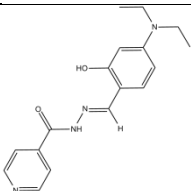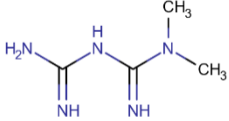
Appendix Table 8. Autophagy Inducers that has Effect on Neurodegenerative Disorders
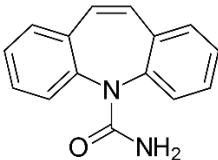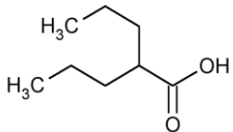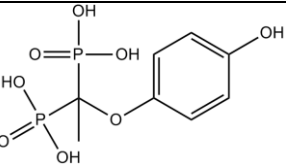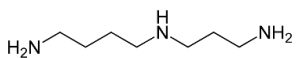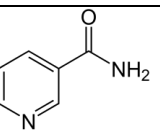
Auto phagy step	Target	Compound	Structure	Disease	References	Effect
Induc tion	mTOR inhibiti on	Rapamycin		AD, PD, HD, ALS, FTLD-U	Caccamo et al. 2010, J. Biol. Chem., 285(17), 13107-13120.; Caccamo et al. 2011, J. Biol. Chem. 286(11), 8924-8932. Spilman et al. 2010, PloS one, 5(4), e9979. Malagelada et al. 2010, Journal of Neuroscience, 30(3), 1166-1175. Ravikumar et al. 2004, Nature genetics, 36(6), 585-595; Zhang et al. 2011, *Autophagy, 7*(4), 412-425. Cortes et al. 2012, Journal of Neuroscience, 32(36), 12396-12405.	
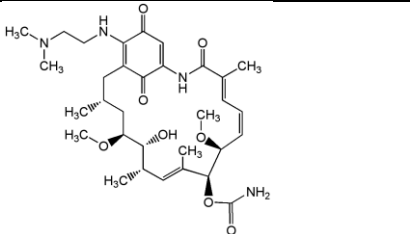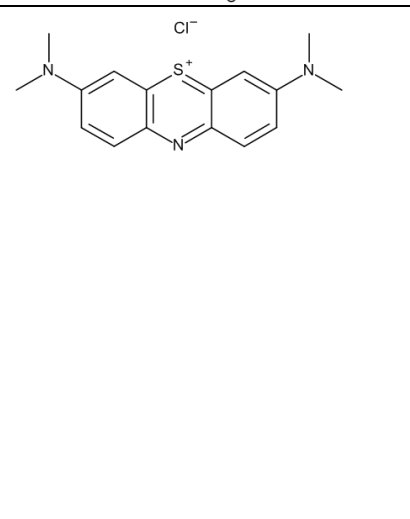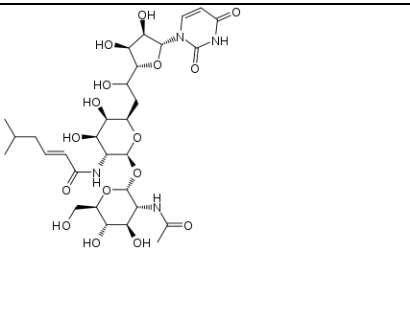
		CCI-779		PD, HD	Ravikumar et al., 2004, Nature genetics, 36(6), 585-595.	
		Metformin		AD	Kickstein et al., 2010, Proceedings of the National Academy of Sciences, 107(50), 21830-21835.	Clinical trial phase II
		Latrepirdine		AD, HD	Steele and Gandy, 2013, Autophagy, 9(4), 617-618.	Clinical trial phase III
		Resveratrol		AD	Vingtdeux et al., 2010, Journal of Biological Chemistry, 285(12), 9100-9113.	Clinical trial phase III
		Kaempferol		PD	Filomenin et al., 2012, Neurobiology of aging, 33(4), 767-785.	
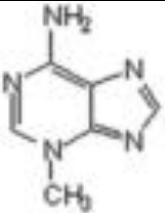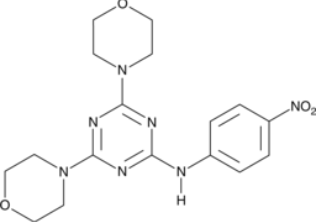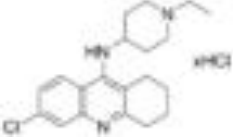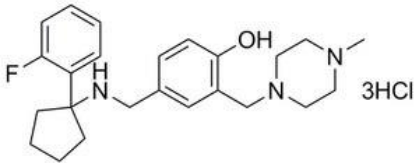
		Celastrol		PD	Deng et al., 2013, Neurochemistry international, 63(1), 1-9.	
		Curcumin		PD	Jiang et al., 2013, Journal of NeuroImmune Pharmacology, 8(1), 356-369.	
		Tamoxifen		FTLD-U		
	AMPK activation	Lithium	Li	AD, ALS	Forlenza et al., 2012, Drugs & aging, 29(5), 335-342; Fornai et al., 2008, Autophagy, 4(4), 527-530.	Clinical trial phase II inositol monophosphatase (IMPase) inhibitors
		Trehalose		FTLD-U, ALS, HD	Zhang et al., 2014, Autophagy, 10(4), 588-602. Tanaka et al., 2004, Nature medicine, 10(2), 148-154	
		Rilmenidine		HD	Rose et al., 2010, Human molecular genetics, 19(11), 2144-2153.	Imidazoline-1 receptors (I1R)
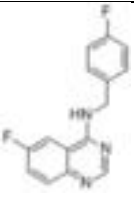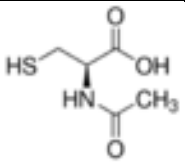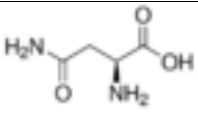
						agonists
		10-NCP		HD	Tsvetkov et al., 2010, Proceedings of the National Academy of Sciences, 107(39), 16982-16987.	AKT inhibitor
		Resveratrol		PD	Khan, et al., 2010, Brain research, 1328, 139-151; Chen, et al., 2009, Proceedings of the National Academy of Sciences, 106(10), 3907-3912; Jin et al., 2008, European journal of pharmacology, 600(1), 78-82.	
		Berberine		Krabbe's disease	Arzamastsev et al., 2013, US patent, US8440683B2, US20130226133A1	
		RSVA314		AD	Vingtdeux et al., 2011, Journal of Biological Chemistry, 285(12), 9100-9113.	
		RSVA405		AD	Vingtdeux et al., 2011, Journal of Biological Chemistry, 285(12), 9100-9113.	
		Metformin		HD,AD	Ma et al., 2007, Neuroscience letters, 411(2), 98-103. Gupta et al., 2011, Neuropharmacology, 60(6), 910-920.	
Initiation	BECN1	Beclin-1 expression regulation		PD	Spencer et al., 2009, J Neurosci. 28; 29(43): 13578–13588.	
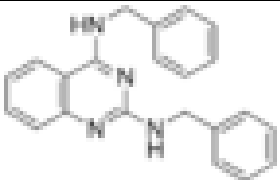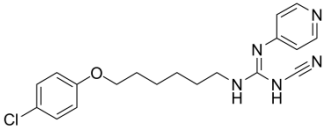
			Structure	Disease	Reference	Clinical status
		Beclin-1 biomimetics		AD	Shoji-Kawata et al., 2013, Nature, 494(7436), 201-206.	
	IP3 level and inositol level regulation	Carbamazepine		FTLD-U, ALS	Sarkar, et al., 2006, Autophagy, 2(2), 132-134.	
		Valproic Acid		FTLD-U, ALS	Sarkar et al., 2006, Autophagy, 2(2), 132-134; Duarte-Silva et al., 2014, The Cerebellum, 13(6), 713-727.	
	inositol monophosphatase (IMPase) inhibitors	L-690,330		FTLD-U, ALS	Sarkar, et al., 2006, Autophagy, 2(2), 132-134.	
Fusion and degradation	Histone Acetyl-Transferase	Spermidine		FTLD-U	Yamashima et al., 2012, The Journal of clinical investigation, 118(8), 2796-2807.	
	lysosomal function	Nicotinamide		AD	Liu et al., 2013, Neurobiology of aging, 34(6), 1564-1580.	Clinical trial phase I
	TFEB	TFEB expression regulation		PD	Decressac et al., 2013, Proceedings of the National Academy of Sciences, 110(19), E1817-E1826.	
	calpain inhibitors	calpastatin	protein	AD	Trinchese et al., 2008, The Journal of clinical investigation, 118(8), 2796-2807.	

Hsp 90 inhibitor	17-DMAG		SCA3	Silva-Fernandes et al., 2014, Neurotherapeutics, 11(2), 433-449	clear Mutant ataxin-3
Nitric oxide synthase, brain (NOS1), Guanylate cyclase soluble subunit alpha-2 (GUCY1A2)	Methylthioninium chloride		AD	Congdon et al., 2012, Autophagy, 8(4), 609-622.	clear Tau
glycosylation of newly synthesized insulin receptor	Tunicamycin		PD	Fouillet et al., 2012, Autophagy, 8(6), 915-926	Protects dopaminergic neuron on a toxicological model
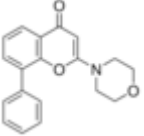
Appendix Table 9. The List of Autophagy Inhibitors
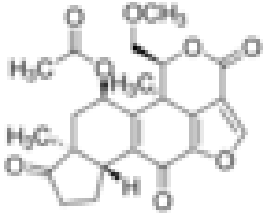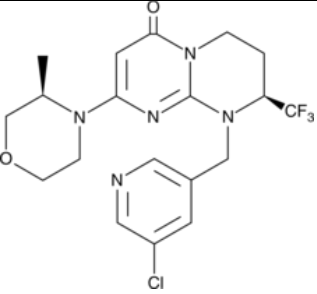
Image	Name	Properties and Actions	Reference
	Autophagy Inhibitor, 3-MA - CAS 5142-23-4	Autophagy Inhibitor, 3-MA, CAS 5142-23-4, is a cell-permeable autophagic sequestration blocker that protects cerebellar granule cells from apoptosis following serum/potassium deprivation., Autophagy Inhibitor, 3-MA, CAS 5142-23-4, is a cell-permeable autophagic sequestration blocker. Acts as an inhibitor of III PI3-Kinase.	(219)
	mTOR Activator, MHY1485	CAS Number: 326914-06-1, is a cell-permeable activator of mTOR that inhibits autophagy by suppressing the fusion between autophagosomes and lysosomes.	(220)
	Autophagy Inhibitor VII	A cell-permeable, potent lysosome targeted autophagy inhibitor with reduced toxicity. OM: Supplied as HCl salt. After EA, will suitably recommend the changes.	
	ARN5187	A cell-potent dual inhibitor of REV-ERBβ and autophagy. Relieves REV-ERB-mediated transcriptional repression and elicits stronger apoptotic induction in cancer cells.	(220)
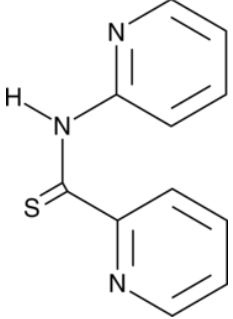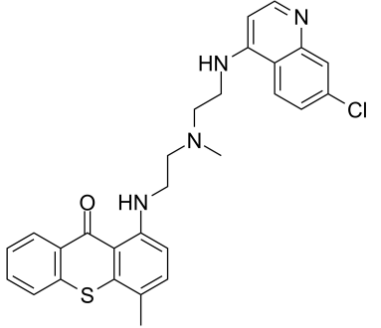
	Spautin-1	A quinazolin compound that acts as a specific and potent inhibitor of autophagy and promotes Vps34 PI 3-kinase complex degradation by blocking the activity of USP 10 (IC_{50} = 580 nM) and USP 13 (IC_{50} = 690 nM) deubiquitinating enzymes	(221)
	N-Acetyl-L-cysteine	Antioxidant and mucolytic agent. Increases cellular pools of free radical scavengers. Reported to prevent apoptosis in neuronal cells but induce apoptosis in smooth muscle cells. Inhibits HIV replication. May serve as a substrate for microsomal glutathione transferase.	(222, 223)
	L-Asparagine	BioReagent, suitable for cell culture, suitable for insect cell culture	(224, 225)
	Bafilomycin A1	A specific inhibitor of vacuolar type H^+-ATPase (V-ATPase) in animal cells, plant cells and microorganisms.	
	Catalase from human erythrocytes	Catalase activates the decomposition of hydrogen peroxide, a reactive oxygen species, into water and oxygen. It functions as a natural antioxidant, protecting cells against oxidative damage to proteins, lipids and nucleic acids. Catalase has also been used to study the role reactive oxygen species play in gene expression and apoptosis. Each subunit of the tetramer contains iron bound to a protoheme IX group. The enzyme also strongly binds NADP, which is in close proximity to the heme group. Catalase activity is constant over the pH range of 4.0-8.5. The pI is found to be 5.4. Optimum pH for catalytic activity is 7.0. The enzyme activity is inhibited by 3-amino-1-H-1,2,4 triazole, cyanide, azide, hydroxylamine, cyanogen bromide, 2-mercaptoethanol, dithiothreitol,	

		dianisidine, and nitrate. Incubation of catalase with ascorbate or ascorbate/Cu2+ results in degradation of the catalase molecule.	
	Chloroquine diphosphate salt solid	Standard anti-malarial drug. Substrate for MRP in multidrug resistant cell line and inhibits photoaffinity labeling of MRP by quinoline-based photoactive drug IAAQ (N-[4-[1-hydroxy-2-(dibutylamino)ethyl]quinolin-8-yl]-4-azidosalicylamide).	(226) (227)
	DBeQ	DBeQ is a potent and specific inhibitor of ATPase p97, an integral component of the ubiquitin-fusion degradation (UFD) pathway. DBeQ inhibits the degradation of ubiquitinated proteins, the endoplasmic reticulum-associated degradation pathway, and autophagosome maturation. The compound also potently inhibits cellular proliferation and induces caspase 3/7 activity and apoptosis.	
	E-64d protease inhibitor		
	GMX1778	GMX1778 (CHS-828) is a competitive inhibitor of nicotinamide phosphoribosyltransferase (NAMPT) that exhibits a potent anticancer activity both *in vitro* and *in vivo*. GMX1778 exerts a cytotoxic effect by decreasing the cellular level of NAD+. GMX1778 increases intracellular ROS in cancer cells but does not induce ROS in normal cells.	(228)
	Leupeptin BioUltra, microbial	Inhibitor of serine and cysteine proteases. Inhibits plasmin, trypsin, papain, calpain, and cathepsin B. Does not inhibit pepsin, cathepsins A and D, thrombin, or α-chymotrypsin. Effective concentration 10-100 μM. There have been numerous	

		studies using leupeptin to protect against hearing loss caused by acoustic overstimulation or the ototoxic antibiotic gentamicin. (Loss of cochlear hair cells is believed to be mediated by calpain.)	
	LY-294,002 hydrochloride solid	Specific cell permeable phosphatidylinositol 3-kinase inhibitor.	(229)
	Pepstatin A microbial	Pepstatin A is an inhibitor of acid proteases (aspartyl peptidases). It forms a 1:1 complex with proteases such as pepsin, renin, cathepsin D, bovine chymosin, and protease B (*Aspergillus niger*). The inhibitor is highly selective and does not inhibit thiol proteases, neutral proteases, or serine proteases. Solubilized γ-secretase and retroviral protease are also inhibited by Pepstatin A. It has been used to characterize proteases from several sources.	
	SBI-0206965	SBI-0206965 is a potent and selective inhibitor of the serine/threonine autophagy-initiating kinases ULK1 and ULK2 with selectivity for ULK1. SBI-0206965 has an IC_{50} value of 108 nM for ULK1, compared to 711nM for ULK2. Tumor cells require autophagy to remove misfolded proteins or damaged cellular organelles. SBI-0206965 was shown to suppress autophagy induced by mTOR inhibition. mTOR signaling is often hyperactive in many tumors and can drive proliferation, so mTOR inhibitors are being investigated as anticancer agents. However, mTOR inhibition also results in activation of the ULK1-dependent autophagy survival response, and most results with mTOR inhibitors have been at best cytostatic. SBI-0206965 synergizes with mTOR inhibition to induce apoptosis and cell death.	(230)

573

	Spautin-1	Spautin-1 inhibits the activity of two ubiquitin-specific peptidases, USP10 and USP13, causing an increase in proteasomal degradation of class III PI3 kinase complexes, which have been shown to regulate autophagy.	(221) (231)
	Thapsigargin solid film	Potent, cell-permeable, IP$_3$-independent intracellular calcium releaser. Blocks the transient increase in intracellular Ca^{2+}induced by angiostatin and endostatin. Induces apoptosis by disrupting intracellular free Ca^{2+} levels; incorporated into chemotherapeutic prodrug formulations.	
	Wortmannin from *Penicillium funiculosum*	Wortmannin is a potent and specific phosphatidylinositol 3-kinase (PI3-K) inhibitor with an IC$_{50}$ of 2-4 nM. Inhibition of PI3-K/Akt signal transduction cascade enhances the apoptotic effects of radiation or serum withdrawal and blocks the antiapoptotic effect of cytokines. Inhibition of PI3-K by wortmannin also blocks many of the short-term metabolic effects induced by insulin receptor activation.	(232)
	SAR405	Vacuolar Protein Sorting Protein 18 and 34 (Vps18 and Vps34) inhibitor	(233)

	NSC185058	autophagy-related gene 4 (ATG4) inhibitor	(234)
	ROC--325	ROC-325 is a potent and orally active autophagy inhibitor with a strong anticancer activity. ROC-325 induces the deacidification of lysosomes, accumulation of autophagosomes, and disrupted autophagic flux. ROC-325 also induces renal cell carcinoma apoptosis.	(235, 236)

Appendix Table 10. Application of Autophagy Modulator for Cancer Treatment.

Treatment(87)	Phase	Indication	Trial ID
HCQ + sunitinib malate	I	Adult solid neoplasm	NCT00813423
HCQ + vorinostat	I	Malignant solid tumor	NCT01023737
HCQ + sirolimus or vorinostat	I	Advanced cancers	NCT01266057
HCQ + Protein kinase B (Akt) inhibitor MK-2206 dihydrochloride (MK2206)	I	Advanced cancers	NCT01480154
HCQ	I	Estrogen receptor positive breast cancer	NCT02414776
HCQ + gemcitabine	I/II	Advanced adenocarcinoma	NCT01506973
HCQ + Interleukin 2(IL-2)	I/II	Renal cell carcinoma	NCT01550367
HCQ + vorinostat	I/II	Colorectal cancer	NCT02316340
HCQ + gemcitabine/carboplatin	I/II	Small cell lung cancer	NCT02722369
HCQ + capecitabine	II	Pancreatic carcinoma	NCT01494155
HCQ	II	Prostate cancer	NCT00726596
HCQ + rapamycin	II	Sarcoma	NCT01842594
HCQ + Rapamycin	I	Lymphaglioleiomyomatosis	NCT01687179
CQ	II	Glioblastoma Multiforme (GBM)	NCT01894633
CQ + Carmustine	II	GBM	NCT01894633
CQ + radiotherapy	II	GBM	NCT01894633

CQ + radiotherapy	II	Brain metastasis	NCT01894633
CQ + vemurafenib	II	BRAF^{V600E} Brain tumor	NCT01894633
(-)-gossypol + androgen deprivation therapy	II	metastatic prostate cancer	NCT00666666
Vorinostat + Tamoxifen	II	hormone-therapy resistant breast cancer	NCT00365599
HCQ + Abraxane and gemcitabine	II	Pancreatic carcinoma	NCT01978184

Appendix I. Reagents and Antibodies.

This is the detailed information about the reagent, material, and antibodies we used in this study. Some details are not listed in the main context.

Recombinant human TNF-α (210-TA) was from R&D Systems. FBS (F0926) was from Sigma-Aldrich (St. Louis, MO). hiFBS (heat-inactivated Fetal Bovine Serum) was prepared by thaw FBS and heat at 56 °C in a water bath for 30 min.

Specific antibodies against SQSTM1/p62 were purchased from Abcam (ab56416). Antibody against RIP1 (610459) was from BD Bioscience. Anti-LC-3B antibody (NB100-2220) was from Novus Biologicals. Antibodies against p-T202/Y204-ERK (4370), ERK (4695), p-S473-AKT (9271), AKT (9272), p-Thr180/Tyr182-p38 MAPK (9211), p38 MAPK (9212), p-Ser32/36IκBα (9246), IKBα (9242), p-T389-p70 S6 kinase (9234), p70 S6 kinase (9202), caspase-3 (9662), and caspase-8 (9746) were from Cell Signaling Technology. Antibody against caspase-8 (GTX100905) was from GeneTex. Antibody against caspase-10 (M059-3) was from MBL. Specific antibody against β-actin (A1978) was from Sigma-Aldrich. Goat anti-rabbit IgG-FITC (F-2765), Texas red goat anti-mouse IgG-Texas red (T6390) were from Invitrogen (Carlsbad, CA). Goat anti-rabbit IgG-HRP (7074) and goat anti-mouse IgG-HRP (7076) secondary antibodies were from Promega (Madison, WI). Goat Anti-Mouse IgG H&L (Alexa Fluor® 647) (ab150115) and Goat Anti-Rabbit IgG H&L (Alexa Fluor® 488) (ab150077) from Abcam. GAPDH (D4C6R) Mouse monoclonal antibody (97166), β3-Tubulin (D71G9) XP® Rabbit monoclonal antibody (5568), and MAP2 (D5G1) XP® Rabbit monoclonal antibody (8707) from Cell Signaling Technology. Anti-Tau rabbit monoclonal antibody (ab47579) from Abcam. A-synuclein mouse monoclonal antibody sc-12767 (211), β-Amyloid mouse monoclonal

antibody (B-4; sc-28365), and β-Amyloid oligomer mouse monoclonal antibody (D-11; sc-374527) from Santa Cruz Biotechnology.

All chemical reagents are brought from Sigma, Fisher, TCI America, Tocris Bioscience, and other vendors. All-trans retinoic acid (RA) 50mg were obtained from Sigma. Resuspend 50 mg RA in 33.3 ml 95% EtOH and keep in a dark bottle at 4°C as 5mM RA stock solution. RA is sensitive to heat, light, and air. B-27 Supplement was brought from Fisher and store at -20 °C. Potassium chloride was brought from Sigma. The 1M stock solution is prepared by adding 500ml water to 39.6g KCl, going through a sterile filter, and storing at room temperature. 1g Dibutyryl cyclic Adenosine Monophosphate (db-cAMP) were brought from Sigma. The 1M db-cAMP solution by resuspending 1g db-cAMP into 2.04ml water and store it at -20 °C. Brain-derived neurotrophic factor (BDNF) was brought from Fisher and stored at -80 °C.

All reagents were purchased from commercial sources and used without further purification. Analytical thin-layer chromatography (TLC) was performed on SiO_2 plates on alumina. Visualization was accomplished by UV irradiation at 254 nm. Flash column chromatography was performed using the Biotage Isolera flash purification system with SiO2 60 (particle size 0.040−0.055 mm, 230−400 mesh). ^{1}H-NMR and ^{13}C-NMR were recorded on a Bruker 400 MHz and a Bruker 600 MHz spectrometer. Splitting patterns are indicated as follows: s, singlet; d, doublet; t, triplet; m, multiplet; br, broad peak. The purity of all final derivatives for biological testing was confirmed to be >95% as determined using the following conditions: a Shimadzu HPLC instrument with a Hamilton reversed-phase column (HxSil, C18, 3 μm, 2.1 mm $\times$ 50 mm (H^2)); eluent A consisting of 5% CH_3CN in H_2O; eluent B composed of 90% CH_3CN in H_2O; flow rate of 0.2 mL/min; UV detection, 254 and 214 nm.

Recombinant human TNF-α (210-TA) was from R&D Systems. FBS (F0926) was from Sigma-Aldrich (St. Louis, MO). Specific antibodies against SQSTM1/p62 were purchased from Abcam (ab56416). Antibody against RIP1 (610459) was from BD Bioscience. Anti-LC-3B antibody (NB100-2220) was from Novus Biologicals. Antibodies against p-T202/Y204-ERK (4370), ERK (4695), p-S473-AKT (9271), AKT (9272), p-Thr180/Tyr182-p38 MAPK (9211), p38 MAPK (9212), p-Ser32/36IκBα (9246), IKBα (9242), p-T389-p70 S6 kinase (9234), p70 S6 kinase (9202), caspase-3 (9662), and caspase-8 (9746) were from Cell Signaling Technology. Antibody against caspase-8 (GTX100905) was from GeneTex. Antibody against caspase-10 (M059-3) was from MBL. Specific antibody against β-actin (A1978) was from Sigma-Aldrich. Goat anti-rabbit IgG-FITC (F-2765), Texas red goat anti-mouse IgG-Texas red (T6390) were from Invitrogen (Carlsbad, CA). Goat anti-rabbit IgG-HRP (7074), and goat anti-mouse IgG-HRP (7076) secondary antibodies were from Promega (Madison, WI). Goat Anti-Mouse IgG H&L (Alexa Fluor® 647) (ab150115) and Goat Anti-Rabbit IgG H&L (Alexa Fluor® 488) (ab150077) from Abcam.

Tris base (Promega; Catlog # H5131), Tris-HCl (JTBaker; Catlog # 4103-04), Methyl cellulose (Sigma; Catlog # P3143-100ML), Filter plates (UniFilter 96 GF/B or GF/C, PerkinElmer) (Part No. 6005174), MicroScint 0 (PerkinElmer; Reorder #. 6013611), MicroScint 20 (PerkinElmer, 6013621), TopSeal tape (PerkinElmer; Part #. 6005185), 96-well plate (Falcon; Ref #. 353077), NaN_3 (Fisher, Cat. S227I-500), Glutathione disulfide (GSSG, Fisher, Cat. AC34384-0050), Glutathione (GSH, Fisher, cat. BP2521-1), $ZnCl_2$ (Fisher, cat. ICN208679)

Multiple myeloma (MM) cell lines

MM1.S and RPMI8226 cells were kindly provided by Dr. Deborah L. Galson (University of Pittsburgh Cancer Institute). U266, SH-SY5Y, HEK293 cells, and BJ normal human fibroblasts were obtained from American Type Culture Collection (ATCC). Cell lines were maintained in an appropriate growth medium with 10% fetal bovine serum (FBS) and sub-cultured twice per week. MM1.S, RPMI8226, and U266 cell lines were authenticated by Short Tandem Repeat (STR) profiling utilizing 16 different STR loci. These studies were conducted using protocols approved by the University of Pittsburgh's IRB and Indiana University's IRB.

HEK293 cells were obtained from American Type Culture Collection (ATCC). Cell lines were maintained in an appropriate growth medium with 10% fetal bovine serum (FBS) and sub-cultured twice per week.

Culture Media

Eagle's Minimum Essential Medium (EMEM, Gibco Laboratories, Grand Island, NY, 670086)

RPMI-1640 Medium (Gibco Laboratories, Grand Island, NY)

Gibco™ Penicillin-Streptomycin (Pen/Strep, 10,000 u/ml, 15140148)

Gibco™ Neurobasal™ Medium (Gibco Laboratories, Grand Island, NY, 21103049)

Cell Type	Media
BJ	EMEM + 10% FBS + Glutamine + Pen/Strep
U266	RPMI-1640 Medium + 10% FBS + Glutamine + Pen/Strep
RPMI8226	RPMI-1640 Medium + 10% FBS + Glutamine + Pen/Strep
MM1.R and MM1.S	RPMI-1640 Medium + 10% FBS + Glutamine + Pen/Strep

Starvation medium for MM cell lines	RPMI-1640 Medium + 2% FBS + Glutamine + Pen/Strep
HEK293 cells	EMEM+10% FBS+ Glutamine + Pen/Strep
Starvation medium for HEK293	EMEM+2% FBS+ Glutamine + Pen/Strep

Appendix J. Computational Aided Drug Design Tools

This section summarized some computational-aided drug design tools we applied in this study. Some of them are developed by our center members, and some of them are collected and generated by myself.

Appendix J. 1. Database Construction

MMPlatform is derived from our established web-interface molecular database prototype CBID (www.CBLIgand.org/CBID) (237). It is constructed with a MySQL (http://www.mysql.com) database and an apache (http://www.apache.org/) web server, and implemented with our developed chemogenomics tools.

An accessible and easy-to-use web interface was offered with an effective and efficient search engine for the detailed data on multiple myeloma, written in PHP language

(http://www.php.net/). MMPlatform provides two types of structure query function for retrieval of bioactivity information: substructure and similarity. Open Babel (238) is utilized as the structural searching engine, and JME (239) supplies the input interface for search. Users can either draw a chemical structure or upload and submit a file containing the structure of a small molecule in the format of SMILES, sdf., mol., or cdx. After submission, the search will be performed automatically at the server side with GPU accelerating computing approach, and the results can be retrieved and shown to the user side on a new page, containing the structure of the compound, target name, and the corresponding reference link.

Data collection and contents.

We have data-mined MM-related genes, proteins, pathways, compounds with bioassays from public databases and literature, and have integrated them into our MMPlatform. The current version of MMPlatform is comprised of the following features and we will keep updating our information for multiple myeloma, and involve additional sections of data in the future.

Multiple Myeloma treatment. We collected information of multiple myeloma drugs from public database, including DrugBank (240) (www.drugbank.ca/), ClinicalTrials.gov (clinicaltrials.gov/), PubChem (241) (pubchem.ncbi.nlm.nih.gov/),

Multiple Myeloma related genes/proteins. We collected proteins as potential targets for multiple myeloma treatment based on the information of multiple myeloma drugs that are FDA-approved or currently in the clinical trials. These targets information were collected from literature, patents, and some public databases, such as DrugBank (240) (www.drugbank.ca/), ClinicalTrials.gov (clinicaltrials.gov/), PubChem (241) (pubchem.ncbi.nlm.nih.gov/), Cancer.gov (242) (www.cancer.gov/), Therapeutic Target Database (http://bidd.nus.edu.sg/group/cjttd/) and ChemBL (https://www.ebi.ac.uk/chembl/). These MM-

related target genes and proteins were mapped to UniProtKB. The crystal structures of these target proteins are downloaded from PDB (https://www.rcsb.org/) according to the speUniprot ID for further online docking program construction

MM-related pathways. MM-related pathways were achieved via the publicly available database Kyoto Encyclopedia of Genes and Genomes (KEGG) [16, 17] (http://www.genome.jp/kegg/) and commercial software or database Ingenuity Pathway Analysis (IPA) and MetaCore.

Chemicals of MM target proteins. Besides MM drugs of FDA approved or in clinical trials, chemicals that directly interact with the MM targets were also archived in our database. The compounds were from journal articles and archived in CHEMBL (243) (www.ebi.ac.uk/chembl/) with their corresponding bioassays.

Appendix J. 2. Poly-pharmacology Analysis Tools.

At present, one of the challenges is how to identify druggable targets and efficiently exploit these for the development of selective nontoxic cancer therapies to overcome the major drawbacks of conventional cytotoxic cancer chemotherapy (244). On the other hand, small molecules with desired properties are considered as top priorities for MM drug design. The MMPlatform provides chemogenomics and cheminformatics data to explore the potential multiple myeloma targets or off-targets, ADME (absorption, distribution, metabolism, excretion), and toxicity prediction (http://www.cbligand.org/Tox), as well as molecular properties, the properties explorer (http://www.cbligand.org/OP/Property_Explorer.php) and drug-likeness calculations. The chemogenomics tools based on state-of-the-art machine learning algorithms

developed by our group have been implemented on the MMPlatform to assist multiple myeloma drug design and target identification, as showed below.

HTDocking

We constructed an online high-throughput docking program (HTDocking, http://www.cbligand.org/MM/docking_search.php) in our MM*Platform*. HTDocking online program aims to explore multiple druggable protein targets and small molecule interactions and their potential pharmacology. Files for the structures of MM target proteins were downloaded from Protein Data Bank. AutoDock Vina is utilized in HTDocking program, which offers a multi-facet capability, high-performance rate, and enhanced accuracy to facilitate effortless usage (245). It can provide 3-5 predicted binding affinity values (ΔG values) from different poses for each compound in a binding pocket of a protein (246). The best binding affinity value is considered by docking score. The calculation of docking score is pK_i = -log (predicted Ki), where the predicted $K_i = \exp^{(\Delta G*1000/(1.987191*298.15))}$. According to the docking score of a queried compound from each protein structure, we can rank the potential MM targets. A higher docking score means a good binding affinity indicating that the protein could be a candidate target for a small molecule.

TargetHunter

A web-interfaced target identification program, TargetHunter (http://cbligand.org/TargetHunter), was built in MM*Platform* to predict the targets or off-targets of compounds (247). TargetHunter predicts targets for small molecules by a powerful data-mining algorithm (TAMOSIC), which is based on the principle that compounds with structural similarities have similar physicochemical properties and potentially similar biological profiles. What's more, the Tanimoto threshold as an important parameter of TAMOSIC can exclude irrelevant targets (248). There are five prominent features of TargetHunter: (a) User-friendly

interface; (b) History data retrieval; (c) Multiple options of specific databases and fingerprints; (d) High accuracy; € Bioassay finder or Bioassay GeoMap function to easily find the potential collaborators who may already have the bioassays established for predicted targets validation.

Appendix J. 3. Docking Results

Some docking results we didn't discuss in the main context are also listed here.

The length of the guanidine group is equal to the three-carbon chain. If the guanidine group is replaced by shorter groups, the length of compound is reduced, and the amine hand of the compound will not steep into the pocket in the PB1 domain. The loss of interaction with residues in PB1 might influence the activity of compound **4.22** with an isopropyl group, but the interactions with Cys151, Cys154, and Asp149 might compromise this deprivation. However, this difference in interactions with different domains in p62 might induce different downstream signaling pathways. In addition, compound **6.3** in **Figure 27B** and **3.1** in **Figure 27C** showed that neither an amine nor aldehyde is long enough to keep the benzene in the best position and angle for a face-to-face π-π stacking with Tyr148 and His160 and at the same time maintain interactions with Cys151, Cys154, and Asp149. More specificially, **6.3** is likely to form parallel-displaced stacking and **3.1** has slightly T-shaped stacking with His160 and Tyr148. According to the virtual screening results, **6.3** and **3.1** have relatively low binding affinity to p62.
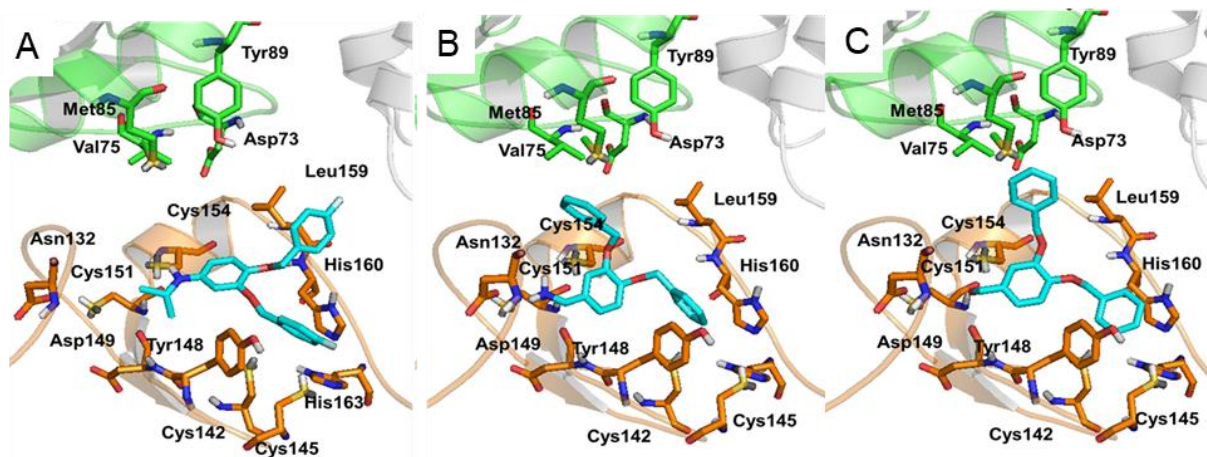
Appendix Figure 1. The Docking Poses of Compounds with Short Side Chain.

(A) The docking pose of **4.22** with p62. (B) The docking pose of **6.3** with p62. (C) The docking pose of **3.1** with p62. The compounds are represented by cyan sticks. The ZZ domain is in orange and PB1 domain is in green.

Bibliography

1.   Zhao W, Eiseman JL, Beumer JH, Xie X-Q, Yang P, Myint K-Z, Wang L, Feng Z, Windle JJ, Roodman GD, Kurihara N. A Novel Sequestosome-1/p62 ZZ Domain Inhibitor Induces New Bone Formation In The Presence Of Myeloma In Vivo. Blood. 2013;122(21):684.

2.   Komatsu M, Kageyama S, Ichimura Y. p62/SQSTM1/A170: physiology and pathology. Pharmacological research. 2012;66(6):457-62.

3.   Du Y, Wooten MC, Wooten MW. Oxidative damage to the promoter region of SQSTM1/p62 is common to neurodegenerative disease. Neurobiology of disease. 2009;35(2):302-10.

4.   Moscat J, Diaz-Meco MT, Wooten MW. Signal integration and diversification through the p62 scaffold protein. Trends in biochemical sciences. 2007;32(2):95-100.

5.   Kuusisto E. Role of the p62 protein in the formation of neuropathological cytoplasmic inclusions: University of Kuopio; 2004.

6.   Salminen A, Kaarniranta K, Haapasalo A, Hiltunen M, Soininen H, Alafuzoff I. Emerging role of p62/sequestosome-1 in the pathogenesis of Alzheimer's disease. Progress in neurobiology. 2012;96(1):87-95.

7.   Swat MJ, Moodie S, Wimalaratne SM, Kristensen NR, Lavielle M, Mari A, Magni P, Smith MK, Bizzotto R, Pasotti L, Mezzalana E, Comets E, Sarr C, Terranova N, Blaudez E, Chan P, Chard J, Chatel K, Chenel M, Edwards D, Franklin C, Giorgino T, Glont M, Girard P, Grenon P, Harling K, Hooker AC, Kaye R, Keizer R, Kloft C, Kok JN, Kokash N, Laibe C, Laveille C, Lestini G, Mentre F, Munafo A, Nordgren R, Nyberg HB, Parra-Guillen ZP, Plan E, Ribba B, Smith G, Troconiz IF, Yvon F, Milligan PA, Harnisch L, Karlsson M, Hermjakob H, Le Novere N. Pharmacometrics Markup Language (PharmML): Opening New Perspectives for Model Exchange in Drug Development. CPT Pharmacometrics Syst Pharmacol. 2015;4(6):316-9. doi: 10.1002/psp4.57. PubMed PMID: 26225259; PMCID: PMC4505825.

8.   Lee SJ, Pfluger PT, Kim JY, Nogueiras R, Duran A, Pagès G, Pouysségur J, Tschöp MH, Diaz-Meco MT, Moscat J. A functional role for the p62–ERK1 axis in the control of energy homeostasis and adipogenesis. EMBO Reports. 2010;11(3):226-32. doi: 10.1038/embor.2010.7. PubMed PMID: PMC2838704.

9.   Yan XY, Zhang Y, Zhang JJ, Zhang LC, Liu YN, Wu Y, Xue YN, Lu SY, Su J, Sun LK. p62/SQSTM1 as an oncotarget mediates cisplatin resistance through activating RIP1‐NF‐κB pathway in human ovarian cancer cells. Cancer Science. 2017;108(7):1405-13. doi: 10.1111/cas.13276. PubMed PMID: PMC5497928.

10.   Ofengeim D, Yuan J. Regulation of RIP1 kinase signaling at the crossrods of inflammation and cell death2013.

11.   Duran A, Amanchy R, Linares Juan F, Joshi J, Abu-Baker S, Porollo A, Hansen M, Moscat J, Diaz-Meco Maria T. p62 Is a Key Regulator of Nutrient Sensing in the mTORC1 Pathway. Molecular Cell. 2017;44(1):134-46. doi: 10.1016/j.molcel.2011.06.038.

12.   Adamik J, Silbermann R, Marino S, Sun Q, Anderson JL, Zhou D, Xie X-Q, Roodman GD, Galson DL. XRK3F2 Inhibition of p62-ZZ Domain Signaling Rescues Myeloma-

Induced GFI1-Driven Epigenetic Repression of the Runx2 Gene in Pre-osteoblasts to Overcome Differentiation Suppression. Frontiers in Endocrinology. 2018;9(344). doi: 10.3389/fendo.2018.00344.

13. Teramachi J, Silbermann R, Yang P, Zhao W, Mohammad KS, Guo J, Anderson JL, Zhou D, Feng R, Myint KZ, Maertz N, Beumer JH, Eiseman JL, Windle JJ, Xie XQ, Roodman GD, Kurihara N. Blocking the ZZ domain of sequestosome1/p62 suppresses myeloma growth and osteoclast formation in vitro and induces dramatic bone formation in myeloma-bearing bones in vivo. Leukemia. 2015;30:390. doi: 10.1038/leu.2015.229 https://www.nature.com/articles/leu2015229#supplementary-information.

14. Silbermann R, Zhou D, Teramachi J, Xie X-Q, Roodman GD, Kurihara N. The p62-ZZ Domain Inhibitor XRK3F2 Alters Myeloma-Induced Suppression of Osteoblast Differentiation and Is Highly Cytotoxic to Myeloma Cells in Combination with Bortezomib. Blood. 2014;124(21):2083.

15. Silbermann R, Adamik J, Zhou D, Xie X-Q, Kurihara N, Roodman GD, Galson DL. p62-ZZ Domain Signaling Inhibition Rescues MM-Induced Epigenetic Repression at the Runx2 promoter and Allows Osteoblast Differentiation of MM Patient Pre-Osteoblasts In Vitro. Blood. 2016;128(22):4410.

16. Yoo YD, Mun SR, Ji CH, Sung KW, Kang KY, Heo AJ, Lee SH, An JY, Hwang J, Xie X-Q, Ciechanover A, Kim BY, Kwon YT. N-terminal arginylation generates a bimodal degron that modulates autophagic proteolysis. Proceedings of the National Academy of Sciences. 2018;115(12):E2716-E24. doi: 10.1073/pnas.1719110115.

17. Cha-Molstad H, Lee SH, Kim JG, Sung KW, Hwang J, Shim SM, Ganipisetti S, McGuire T, Mook-Jung I, Ciechanover A, Xie X-Q, Kim BY, Kwon YT. Regulation of autophagic proteolysis by the N-recognin SQSTM1/p62 of the N-end rule pathway. Autophagy. 2018;14(2):359-61. doi: 10.1080/15548627.2017.1415190.

18. Cha-Molstad H, Yu JE, Feng Z, Lee SH, Kim JG, Yang P, Han B, Sung KW, Yoo YD, Hwang J, McGuire T, Shim SM, Song HD, Ganipisetti S, Wang N, Jang JM, Lee MJ, Kim SJ, Lee KH, Hong JT, Ciechanover A, Mook-Jung I, Kim KP, Xie X-Q, Kwon YT, Kim BY. p62/SQSTM1/Sequestosome-1 is an N-recognin of the N-end rule pathway which modulates autophagosome biogenesis. Nature Communications. 2017;8(1):102. doi: 10.1038/s41467-017-00085-7.

19. Jin Z, Li Y, Pitti R, Lawrence D, Pham VC, Lill JR, Ashkenazi A. Cullin3-based polyubiquitination and p62-dependent aggregation of caspase-8 mediate extrinsic apoptosis signaling. Cell. 2009;137(4):721-35.

20. Moscat J, Diaz-Meco MT, Albert A, Campuzano S. Cell signaling and function organized by PB1 domain interactions. Molecular cell. 2006;23(5):631-40.

21. Sanz L, Diaz‑Meco MT, Nakano H, Moscat J. The atypical PKC‑interacting protein p62 channels NF‑κB activation by the IL‑1‑TRAF6 pathway. The EMBO journal. 2000;19(7):1576-86.

22. Moscat J, Diaz-Meco MT. p62 at the crossroads of autophagy, apoptosis, and cancer. Cell. 2009;137(6):1001-4.

23. Geetha T, Jiang J, Wooten MW. Lysine 63 polyubiquitination of the nerve growth factor receptor TrkA directs internalization and signaling. Molecular cell. 2005;20(2):301-12.

24. Rechsteiner M, Rogers SW. PEST sequences and regulation by proteolysis. Trends in biochemical sciences. 1996;21(7):267-71.

25. Ebrahimi-Fakhari D, Wahlster L, Hoffmann GF, Kölker S. Emerging role of autophagy in

pediatric neurodegenerative and neurometabolic diseases. Pediatric research. 2013;75(1-2):217-26.

26. Kaltschmidt B, Kaltschmidt C. NF-κB in the Nervous System. Cold Spring Harbor Perspectives in Biology. 2009;1(3):a001271. doi: 10.1101/cshperspect.a001271. PubMed PMID: PMC2773634.

27. Nakamura K, Kimple AJ, Siderovski DP, Johnson GL. PB1 Domain Interaction of p62/Sequestosome 1 and MEKK3 Regulates NF-κB Activation. Journal of Biological Chemistry. 2010;285(3):2077-89. doi: 10.1074/jbc.M109.065102.

28. Ramesh Babu J, Lamar Seibenhener M, Peng J, Strom A-L, Kemppainen R, Cox N, Zhu H, Wooten Michael C, Diaz-Meco María T, Moscat J, Wooten Marie W. Genetic inactivation of p62 leads to accumulation of hyperphosphorylated tau and neurodegeneration. Journal of Neurochemistry. 2008;106(1):107-20. doi: 10.1111/j.1471-4159.2008.05340.x.

29. Puri R, Suzuki T, Yamakawa K, Ganesh S. Hyperphosphorylation and Aggregation of Tau in Laforin-deficient Mice, an Animal Model for Lafora Disease. The Journal of Biological Chemistry. 2009;284(34):22657-63. doi: 10.1074/jbc.M109.009688. PubMed PMID: PMC2755673.

30. Rodriguez A, Durán A, Selloum M, Champy M-F, Diez-Guerra FJ, Flores JM, Serrano M, Auwerx J, Diaz-Meco MT, Moscat J. Mature-onset obesity and insulin resistance in mice deficient in the signaling adapter p62. Cell Metabolism. 2006;3(3):211-22. doi: https://doi.org/10.1016/j.cmet.2006.01.011.

31. Hadi TMA. The role of p62 in osteoclastogenesis and paget's disease of bone. (Doctoral dissertation) Retrieved from: https://scholarscompass.vcu.edu/etd/33122014.

32. !!! INVALID CITATION !!!

33. Wooten MW, Seibenhener ML, Mamidipudi V, Diaz-Meco MT, Barker PA, Moscat J. The atypical protein kinase C-interacting protein p62 is a scaffold for NF-κB activation by nerve growth factor. Journal of Biological Chemistry. 2001;276(11):7709-12.

34. Wooten MW, Geetha T, Seibenhener ML, Babu JR, Diaz-Meco MT, Moscat J. The p62 scaffold regulates nerve growth factor-induced NF-κB activation by influencing TRAF6 polyubiquitination. Journal of Biological Chemistry. 2005;280(42):35625-9.

35. Zheng C, Geetha T, Gearing M, Ramesh Babu J. Amyloid β‐abrogated TrkA ubiquitination in PC12 cells analogous to Alzheimer's disease. Journal of neurochemistry. 2015;133(6):919-25.

36. Geetha T, Zheng C, McGregor WC, White BD, Diaz-Meco MT, Moscat J, Babu JR. TRAF6 and p62 inhibit amyloid β-induced neuronal death through p75 neurotrophin receptor. Neurochemistry international. 2012;61(8):1289-93.

37. Coulson E, May L, Sykes A, Hamlin A. The role of the p75 neurotrophin receptor in cholinergic dysfunction in Alzheimer's disease. The Neuroscientist. 2009.

38. Katsuragi Y, Ichimura Y, Komatsu M. Regulation of the Keap1–Nrf2 pathway by p62/SQSTM1. Current Opinion in Toxicology. 2016;1:54-61. doi: https://doi.org/10.1016/j.cotox.2016.09.005.

39. Komatsu M, Kurokawa H, Waguri S, Taguchi K, Kobayashi A, Ichimura Y, Sou Y-S, Ueno I, Sakamoto A, Tong KI, Kim M, Nishito Y, Iemura S-i, Natsume T, Ueno T, Kominami E, Motohashi H, Tanaka K, Yamamoto M. The selective autophagy substrate p62 activates the stress responsive transcription factor Nrf2 through inactivation of Keap1. Nature Cell Biology. 2010;12:213. doi: 10.1038/ncb2021

https://www.nature.com/articles/ncb2021#supplementary-information.

40. Jiang T, Harder B, Rojo de la Vega M, Wong PK, Chapman E, Zhang DD. p62 links autophagy and Nrf2 signaling. Free radical biology & medicine. 2015;88(0 0):199-204. doi: 10.1016/j.freeradbiomed.2015.06.014. PubMed PMID: PMC4628872.

41. Ichimura Y, Komatsu M. Activation of p62/SQSTM1–Keap1–Nuclear Factor Erythroid 2-Related Factor 2 Pathway in Cancer. Frontiers in Oncology. 2018;8(210). doi: 10.3389/fonc.2018.00210.

42. Inami Y, Waguri S, Sakamoto A, Kouno T, Nakada K, Hino O, Watanabe S, Ando J, Iwadate M, Yamamoto M, Lee M-S, Tanaka K, Komatsu M. Persistent activation of Nrf2 through p62 in hepatocellular carcinoma cells. The Journal of Cell Biology. 2011;193(2):275.

43. Lippai M, #xf3, nika, #x151, w P, #xe9, ter. The Role of the Selective Adaptor p62 and Ubiquitin-Like Proteins in Autophagy. BioMed Research International. 2014;2014:11. doi: 10.1155/2014/832704.

44. Kanninen K, Heikkinen R, Malm T, Rolova T, Kuhmonen S, Leinonen H, Ylä-Herttuala S, Tanila H, Levonen A-L, Koistinaho M, Koistinaho J. Intrahippocampal injection of a lentiviral vector expressing Nrf2 improves spatial learning in a mouse model of Alzheimer's disease. Proceedings of the National Academy of Sciences. 2009;106(38):16505-10. doi: 10.1073/pnas.0908397106.

45. Liddell J. Are Astrocytes the Predominant Cell Type for Activation of Nrf2 in Aging and Neurodegeneration? Antioxidants. 2017;6(3):65. PubMed PMID: doi:10.3390/antiox6030065.

46. Rusten TE, Stenmark H. p62, an autophagy hero or culprit? Nature Cell Biology. 2010;12:207. doi: 10.1038/ncb0310-207.

47. Diaz-Meco MT, Moscat J. The atypical PKCs in inflammation: NF-κB and beyond. Immunological reviews. 2012;246(1):154-67. doi: 10.1111/j.1600-065X.2012.01093.x. PubMed PMID: PMC3531713.

48. Puissant A, Fenouille N, Auberger P. When autophagy meets cancer through p62/SQSTM1. American Journal of Cancer Research. 2012;2(4):397-413. PubMed PMID: PMC3410580.

49. Wei W, Li M, Wang J, Nie F, Li L. The E3 Ubiquitin Ligase ITCH Negatively Regulates Canonical Wnt Signaling by Targeting Dishevelled Protein. Molecular and Cellular Biology. 2012;32(19):3903-12. doi: 10.1128/MCB.00251-12. PubMed PMID: PMC3457526.

50. Rosenberg T, Gal-Ben-Ari S, Dieterich DC, Kreutz MR, Ziv NE, Gundelfinger ED, Rosenblum K. The roles of protein expression in synaptic plasticity and memory consolidation. Frontiers in Molecular Neuroscience. 2014;7:86. doi: 10.3389/fnmol.2014.00086. PubMed PMID: PMC4228929.

51. Liu WJ, Ye L, Huang WF, Guo LJ, Xu ZG, Wu HL, Yang C, Liu HF. p62 links the autophagy pathway and the ubiquitin–proteasome system upon ubiquitinated protein degradation. Cellular & Molecular Biology Letters. 2016;21:29. doi: 10.1186/s11658-016-0031-z. PubMed PMID: PMC5415757.

52. Lippai M, Lőw P. The Role of the Selective Adaptor p62 and Ubiquitin-Like Proteins in Autophagy. BioMed Research International. 2014;2014:832704. doi: 10.1155/2014/832704. PubMed PMID: PMC4075091.

53. Nezis IP, Stenmark H. p62 at the Interface of Autophagy, Oxidative Stress Signaling, and

Cancer. Antioxidants & Redox Signaling. 2011;17(5):786-93. doi: 10.1089/ars.2011.4394.

54.   Nixon RA. The role of autophagy in neurodegenerative disease. Nat Med. 2013;19(8):983-97. doi: 10.1038/nm.3232.

55.   Vidal RL, Matus S, Bargsted L, Hetz C. Targeting autophagy in neurodegenerative diseases. Trends in pharmacological sciences. 2014;35(11):583-91.

56.   Soto C. Unfolding the role of protein misfolding in neurodegenerative diseases. Nature Reviews Neuroscience. 2003;4(1):49-60.

57.   van de Donk NWCJ, Moreau P, Plesner T, Palumbo A, Gay F, Laubach JP, Malavasi F, Avet-Loiseau H, Mateos M-V, Sonneveld P. Clinical efficacy and management of monoclonal antibodies targeting CD38 and SLAMF7 in multiple myeloma. Blood. 2015:blood-2015-10-646810.

58.   Tanji K, Zhang HX, Mori F, Kakita A, Takahashi H, Wakabayashi K. p62/sequestosome 1 binds to TDP‐43 in brains with frontotemporal lobar degeneration with TDP‐43 inclusions. Journal of neuroscience research. 2012;90(10):2034-42.

59.   Seneci P. Molecular Targets in Protein Misfolding and Neurodegenerative Disease: Academic Press; 2014.

60.   Puissant A, Fenouille N, Auberger P. When autophagy meets cancer through p62/SQSTM1. Am J Cancer Res. 2012;2(4):397-413.

61.   Frake RA, Ricketts T, Menzies FM, Rubinsztein DC. Autophagy and neurodegeneration. The Journal of clinical investigation. 2015;125(1):65-74.

62.   Bortnik S, Gorski SM. Clinical Applications of Autophagy Proteins in Cancer: From Potential Targets to Biomarkers. International Journal of Molecular Sciences. 2017;18(7):1496. doi: 10.3390/ijms18071496. PubMed PMID: PMC5535986.

63.   He Y, Zhao X, Subahan NR, Fan L, Gao J, Chen H. The prognostic value of autophagy-related markers beclin-1 and microtubule-associated protein light chain 3B in cancers: a systematic review and meta-analysis. Tumor Biology. 2014;35(8):7317-26. doi: 10.1007/s13277-014-2060-4.

64.   Zhang J, Ney PA. Role of BNIP3 and NIX in cell death, autophagy, and mitophagy. Cell Death And Differentiation. 2009;16:939. doi: 10.1038/cdd.2009.16.

65.   Birgisdottir ÅB, Lamark T, Johansen T. The LIR motif – crucial for selective autophagy. Journal of Cell Science. 2013;126(15):3237-47. doi: 10.1242/jcs.126128.

66.   Seillier M, Peuget S, Gayet O, Gauthier C, N'Guessan P, Monte M, Carrier A, Iovanna JL, Dusetti NJ. TP53INP1, a tumor suppressor, interacts with LC3 and ATG8-family proteins through the LC3-interacting region (LIR) and promotes autophagy-dependent cell death. Cell Death And Differentiation. 2012;19:1525. doi: 10.1038/cdd.2012.30
https://www.nature.com/articles/cdd201230#supplementary-information.

67.   Wooten MW, Hu X, Babu JR, Seibenhener ML, Geetha T, Paine MG, Wooten MC. Signaling, polyubiquitination, trafficking, and inclusions: sequestosome 1/p62's role in neurodegenerative disease. BioMed Research International. 2006;2006.

68.   Society. AC. Facts for myeloma. https://www.cancer.org/cancer/multiple-myeloma/about/key-statistics.html. Accessed by Nov 20202020.

69.   (NCI) CfDCaPCatNCI. United States Cancer Statistics: Data Visualizations. https://gis.cdc.gov/Cancer/USCS/DataViz.html. Accessed by Nov 20202020.

70.   Gerecke C, Fuhrmann S, Strifler S, Schmidt-Hieber M, Einsele H, Knop S. The Diagnosis and Treatment of Multiple Myeloma. Deutsches Arzteblatt international. 2016;113(27-28):470-6. Epub 2016/08/02. doi: 10.3238/arztebl.2016.0470. PubMed PMID: 27476706;

PMCID: PMC4973001.

71. Society AC. Drug Therapy for Multiple Myeloma. https://www.cancer.org/cancer/multiple-myeloma/treating/chemotherapy.html. Accessed by March 2021.

72. Robak P, Drozdz I, Szemraj J, Robak T. Drug resistance in multiple myeloma. Cancer treatment reviews. 2018;70:199-208. Epub 2018/09/25. doi: 10.1016/j.ctrv.2018.09.001. PubMed PMID: 30245231.

73. Burwick N, Sharma S. Glucocorticoids in multiple myeloma: past, present, and future. Annals of hematology. 2019;98(1):19-28. Epub 2018/08/04. doi: 10.1007/s00277-018-3465-8. PubMed PMID: 30073393.

74. Alanazi F, Kwa FAA, Burchall G, Jackson DE. New generation drugs for treatment of multiple myeloma. Drug discovery today. 2020;25(2):367-79. Epub 2019/11/26. doi: 10.1016/j.drudis.2019.11.008. PubMed PMID: 31765717.

75. Dingli D, Ailawadhi S, Bergsagel PL, Buadi FK, Dispenzieri A, Fonseca R, Gertz MA, Gonsalves WI, Hayman SR, Kapoor P, Kourelis T, Kumar SK, Kyle RA, Lacy MQ, Leung N, Lin Y, Lust JA, Mikhael JR, Reeder CB, Roy V, Russell SJ, Sher T, Stewart AK, Warsame R, Zeldenrust SR, Rajkumar SV, Chanan Khan AA. Therapy for Relapsed Multiple Myeloma: Guidelines From the Mayo Stratification for Myeloma and Risk-Adapted Therapy. Mayo Clinic proceedings. 2017;92(4):578-98. Epub 2017/03/16. doi: 10.1016/j.mayocp.2017.01.003. PubMed PMID: 28291589; PMCID: PMC5554888.

76. Li J-L, Han S-L, Fan X. Modulating autophagy: a strategy for cancer therapy. Chinese journal of cancer. 2011;30(10):655.

77. Kenific CM, Debnath J. Cellular and metabolic functions for autophagy in cancer cells. Trends in Cell Biology. 2015;25(1):37-45. doi: https://doi.org/10.1016/j.tcb.2014.09.001.

78. Kenific CM, Thorburn A, Debnath J. Autophagy and metastasis: another double-edged sword. Current Opinion in Cell Biology. 2010;22(2):241-5. doi: https://doi.org/10.1016/j.ceb.2009.10.008.

79. Moscat J, Karin M, Diaz-Meco MT. p62 in Cancer: Signaling Adaptor Beyond Autophagy. Cell. 2016;167(3):606-9. doi: https://doi.org/10.1016/j.cell.2016.09.030.

80. Kim YS, Shin JH, Bae MK, Lee CY, Kim DJ, Chung KY, Lee JG. Autophagy Activity in Pulmonary Metastatic Tumor Tissues from Colorectal Cancer: A Pilot Study. Yonsei Med J. 2014;55(6):1484-8.

81. Yun Z, Zhichao J, Hao Y, Ou J, Ran Y, Wen D, Qun S. Targeting autophagy in multiple myeloma. Leukemia research. 2017;59:97-104. Epub 2017/06/10. doi: 10.1016/j.leukres.2017.06.002. PubMed PMID: 28599191.

82. Milan E, Fabbri M, Cenci S. Autophagy in Plasma Cell Ontogeny and Malignancy. Journal of Clinical Immunology. 2016;36(1):18-24. doi: 10.1007/s10875-016-0254-9.

83. Jung G, Roh J, Lee H, Gil M, Yoon DH, Suh C, Jang S, Park CJ, Huh J, Park CS. Autophagic Markers BECLIN 1 and LC3 Are Associated with Prognosis of Multiple Myeloma. Acta Haematologica. 2015;134(1):17-24. doi: 10.1159/000368848.

84. Zhang J, Yang Z, Dong J. P62: An emerging oncotarget for osteolytic metastasis. Journal of bone oncology. 2016;5(1):30-7. Epub 2016/03/22. doi: 10.1016/j.jbo.2016.01.003. PubMed PMID: 26998424; PMCID: PMC4782024.

85. Duran A, Linares JF, Galvez AS, Wikenheiser K, Flores JM, Diaz-Meco MT, Moscat J. The Signaling Adaptor p62 Is an Important NF-κB Mediator in Tumorigenesis. Cancer Cell. 2008;13(4):343-54. doi: https://doi.org/10.1016/j.ccr.2008.02.001.

86. Ling J, Kang Ya, Zhao R, Xia Q, Lee D-F, Chang Z, Li J, Peng B, Fleming Jason B, Wang H, Liu J, Lemischka Ihor R, Hung M-C, Chiao Paul J. KrasG12D-Induced IKK2/β/NF-κB Activation by IL-1α and p62 Feedforward Loops Is Required for Development of Pancreatic Ductal Adenocarcinoma. Cancer Cell. 2012;21(1):105-20. doi: https://doi.org/10.1016/j.ccr.2011.12.006.

87. Chude CI, Amaravadi RK. Targeting Autophagy in Cancer: Update on Clinical Trials and Novel Inhibitors2017;18(6):1279. PubMed PMID: doi:10.3390/ijms18061279.

88. Pérez-Hernández M, Arias A, Martínez-García D, Pérez-Tomás R, Quesada R, Soto-Cerrato V. Targeting Autophagy for Cancer Treatment and Tumor Chemosensitization. Cancers (Basel). 2019;11(10):1599. doi: 10.3390/cancers11101599. PubMed PMID: 31635099.

89. Kumar SK, Rajkumar V, Kyle RA, van Duin M, Sonneveld P, Mateos M-V, Gay F, Anderson KC. Multiple myeloma. Nature Reviews Disease Primers. 2017;3:17046. doi: 10.1038/nrdp.2017.46.

90. Zannettino AC, Farrugia AN, Kortesidis A, Manavis J, To LB, Martin SK, Diamond P, Tamamura H, Lapidot T, Fujii N, Gronthos S. Elevated serum levels of stromal-derived factor-1alpha are associated with increased osteoclast activity and osteolytic bone disease in multiple myeloma patients. Cancer research. 2005;65(5):1700-9. Epub 2005/03/09. doi: 10.1158/0008-5472.can-04-1687. PubMed PMID: 15753365.

91. Zhu D, Wang Z, Zhao JJ, Calimeri T, Meng J, Hideshima T, Fulciniti M, Kang Y, Ficarro SB, Tai YT, Hunter Z, McMilin D, Tong H, Mitsiades CS, Wu CJ, Treon SP, Dorfman DM, Pinkus G, Munshi NC, Tassone P, Marto JA, Anderson KC, Carrasco RD. The Cyclophilin A-CD147 complex promotes the proliferation and homing of multiple myeloma cells. Nat Med. 2015;21(6):572-80. Epub 2015/05/26. doi: 10.1038/nm.3867. PubMed PMID: 26005854; PMCID: PMC4567046.

92. Roodman GD. Mechanisms of bone lesions in multiple myeloma and lymphoma. Cancer. 1997;80(8 Suppl):1557-63. Epub 1997/11/15. PubMed PMID: 9362422.

93. Roodman GD. Pathogenesis of myeloma bone disease. Leukemia. 2009;23(3):435-41. Epub 2008/11/29. doi: 10.1038/leu.2008.336. PubMed PMID: 19039321.

94. Ghobrial IM. Myeloma as a model for the process of metastasis: implications for therapy. Blood. 2012;120(1):20-30. Epub 2012/04/27. doi: 10.1182/blood-2012-01-379024. PubMed PMID: 22535658; PMCID: PMC3390959.

95. Hope C, Ollar SJ, Heninger E, Hebron E, Jensen JL, Kim J, Maroulakou I, Miyamoto S, Leith C, Yang DT, Callander N, Hematti P, Chesi M, Bergsagel PL, Asimakopoulos F. TPL2 kinase regulates the inflammatory milieu of the myeloma niche. Blood. 2014;123(21):3305-15. Epub 2014/04/12. doi: 10.1182/blood-2014-02-554071. PubMed PMID: 24723682; PMCID: PMC4046426.

96. Guillerey C, Nakamura K, Vuckovic S, Hill GR, Smyth MJ. Immune responses in multiple myeloma: role of the natural immune surveillance and potential of immunotherapies. Cellular and molecular life sciences : CMLS. 2016;73(8):1569-89. Epub 2016/01/24. doi: 10.1007/s00018-016-2135-z. PubMed PMID: 26801219.

97. Ilcus C, Bagacean C, Tempescul A, Popescu C, Parvu A, Cenariu M, Bocsan C, Zdrenghea M. Immune checkpoint blockade: the role of PD-1-PD-L axis in lymphoid malignancies. OncoTargets and therapy. 2017;10:2349-63. Epub 2017/05/13. doi: 10.2147/ott.s133385. PubMed PMID: 28496333; PMCID: PMC5417656.

98. Xu J, Wu HF, Ang ESM, Yip K, Woloszyn M, Zheng MH, Tan RX. NF-κB modulators in

osteolytic bone diseases. Cytokine & Growth Factor Reviews. 2009;20(1):7-17. doi: https://doi.org/10.1016/j.cytogfr.2008.11.007.

99. Durán A, Serrano M, Leitges M, Flores JM, Picard S, Brown JP, Moscat J, Diaz-Meco MT. The atypical PKC-interacting protein p62 is an important mediator of RANK-activated osteoclastogenesis. Developmental cell. 2004;6(2):303-9.

100. Pickford F, Masliah E, Britschgi M, Lucin K, Narasimhan R, Jaeger PA, Small S, Spencer B, Rockenstein E, Levine B. The autophagy-related protein beclin 1 shows reduced expression in early Alzheimer disease and regulates amyloid β accumulation in mice. The Journal of clinical investigation. 2008;118(6):2190-9.

101. Manley S, Williams JA, Ding W-X. Role of p62/SQSTM1 in liver physiology and pathogenesis. Experimental biology and medicine. 2013;238(5):525-38.

102. Bjørkøy G, Lamark T, Brech A, Outzen H, Perander M, Øvervatn A, Stenmark H, Johansen T. p62/SQSTM1 forms protein aggregates degraded by autophagy and has a protective effect on huntingtin-induced cell death. The Journal of cell biology. 2005;171(4):603-14.

103. Mathew R, Karp CM, Beaudoin B, Vuong N, Chen G, Chen H-Y, Bray K, Reddy A, Bhanot G, Gelinas C. Autophagy suppresses tumorigenesis through elimination of p62. Cell. 2009;137(6):1062-75.

104. Moscat J, Diaz-Meco MT. p62: a versatile multitasker takes on cancer. Trends in biochemical sciences. 2012;37(6):230-6.

105. Zheng Q, Li J, Wang X. Interplay between the ubiquitin-proteasome system and autophagy in proteinopathies. International journal of physiology, pathophysiology and pharmacology. 2009;1(2):127.

106. Ma S, Attarwala IY, Xie X-Q. SQSTM1/p62: A Potential Target for Neurodegenerative Disease. ACS Chemical Neuroscience. 2019;10(5):2094-114. doi: 10.1021/acschemneuro.8b00516.

107. Hetz C, Thielen P, Matus S, Nassif M, Kiffin R, Martinez G, Cuervo AM, Brown RH, Glimcher LH. XBP-1 deficiency in the nervous system protects against amyotrophic lateral sclerosis by increasing autophagy. Genes & development. 2009;23(19):2294-306.

108. Nixon RA. The role of autophagy in neurodegenerative disease. Nature medicine. 2013;19(8):983-97.

109. Nascimento-Ferreira I, Santos-Ferreira T, Sousa-Ferreira L, Auregan G, Onofre I, Alves S, Dufour N, Colomer Gould VF, Koeppen A, Déglon N. Overexpression of the autophagic beclin-1 protein clears mutant ataxin-3 and alleviates Machado–Joseph disease. Brain. 2011;134(5):1400-15.

110. Wills J, Credle J, Oaks AW, Duka V, Lee J-H, Jones J, Sidhu A. Paraquat, but not maneb, induces synucleinopathy and tauopathy in striata of mice through inhibition of proteasomal and autophagic pathways. PloS one. 2012;7(1):e30745.

111. Shibata M, Lu T, Furuya T, Degterev A, Mizushima N, Yoshimori T, MacDonald M, Yankner B, Yuan J. Regulation of intracellular accumulation of mutant Huntingtin by Beclin 1. Journal of Biological Chemistry. 2006;281(20):14474-85.

112. Wu J-c, Qi L, Wang Y, Kegel KB, Yoder J, Difiglia M, Qin Z-h, Lin F. The regulation of N-terminal Huntingtin (Htt552) accumulation by Beclin1. Acta Pharmacologica Sinica. 2012;33(6):743-51.

113. Spencer B, Potkar R, Trejo M, Rockenstein E, Patrick C, Gindi R, Adame A, Wyss-Coray T, Masliah E. Beclin 1 gene transfer activates autophagy and ameliorates the

neurodegenerative pathology in α-synuclein models of Parkinson's and Lewy body diseases. Journal of Neuroscience. 2009;29(43):13578-88.

114. Nassif M, Valenzuela V, Rojas-Rivera D, Vidal R, Matus S, Castillo K, Fuentealba Y, Kroemer G, Levine B, Hetz C. Pathogenic role of BECN1/Beclin 1 in the development of amyotrophic lateral sclerosis. Autophagy. 2014;10(7):1256-71.

115. Mealer RG, Murray AJ, Shahani N, Subramaniam S, Snyder SH. Rhes, a striatal-selective protein implicated in Huntington disease, binds beclin-1 and activates autophagy. Journal of Biological Chemistry. 2014;289(6):3547-54.

116. Lonskaya I, Hebron ML, Desforges NM, Franjie A, Moussa CEH. Tyrosine kinase inhibition increases functional parkin‐Beclin‐1 interaction and enhances amyloid clearance and cognitive performance. EMBO molecular medicine. 2013;5(8):1247-62.

117. Arena G, Gelmetti V, Torosantucci L, Vignone D, Lamorte G, De Rosa P, Cilia E, Jonas E, Valente EM. PINK1 protects against cell death induced by mitochondrial depolarization, by phosphorylating Bcl-xL and impairing its pro-apoptotic cleavage. Cell Death & Differentiation. 2013;20(7):920-30.

118. Zavodszky E, Seaman MN, Moreau K, Jimenez-Sanchez M, Breusegem SY, Harbour ME, Rubinsztein DC. Mutation in VPS35 associated with Parkinson's disease impairs WASH complex association and inhibits autophagy. Nature communications. 2014;5.

119. Ramesh Babu J, Lamar Seibenhener M, Peng J, Strom AL, Kemppainen R, Cox N, Zhu H, Wooten MC, Diaz‐Meco MT, Moscat J. Genetic inactivation of p62 leads to accumulation of hyperphosphorylated tau and neurodegeneration. Journal of neurochemistry. 2008;106(1):107-20.

120. Winslow AR, Chen C-W, Corrochano S, Acevedo-Arozena A, Gordon DE, Peden AA, Lichtenberg M, Menzies FM, Ravikumar B, Imarisio S. α-Synuclein impairs macroautophagy: implications for Parkinson's disease. The Journal of cell biology. 2010;190(6):1023-37.

121. Komatsu M, Waguri S, Chiba T, Murata S, Iwata J-i, Tanida I, Ueno T, Koike M, Uchiyama Y, Kominami E, Tanaka K. Loss of autophagy in the central nervous system causes neurodegeneration in mice. Nature. 2006;441(7095):880-4. doi: http://www.nature.com/nature/journal/v441/n7095/suppinfo/nature04723_S1.html.

122. Hara T, Nakamura K, Matsui M, Yamamoto A, Nakahara Y, Suzuki-Migishima R, Yokoyama M, Mishima K, Saito I, Okano H, Mizushima N. Suppression of basal autophagy in neural cells causes neurodegenerative disease in mice. Nature. 2006;441(7095):885-9. doi: http://www.nature.com/nature/journal/v441/n7095/suppinfo/nature04724_S1.html.

123. Metzger S, Saukko M, Van Che H, Tong L, Puder Y, Riess O, Nguyen HP. Age at onset in Huntington's disease is modified by the autophagy pathway: implication of the V471A polymorphism in Atg7. Human Genetics. 2010;128(4):453-9. doi: 10.1007/s00439-010-0873-9.

124. Lee J-H, Yu WH, Kumar A, Lee S, Mohan PS, Peterhoff CM, Wolfe DM, Martinez-Vicente M, Massey AC, Sovak G. Lysosomal proteolysis and autophagy require presenilin 1 and are disrupted by Alzheimer-related PS1 mutations. Cell. 2010;141(7):1146-58.

125. Yang D-S, Stavrides P, Mohan PS, Kaushik S, Kumar A, Ohno M, Schmidt SD, Wesson D, Bandyopadhyay U, Jiang Y. Reversal of autophagy dysfunction in the TgCRND8 mouse model of Alzheimer's disease ameliorates amyloid pathologies and memory deficits. Brain. 2011;134(1):258-77.

126. Dehay B, Ramirez A, Martinez-Vicente M, Perier C, Canron M-H, Doudnikoff E, Vital A, Vila M, Klein C, Bezard E. Loss of P-type ATPase ATP13A2/PARK9 function induces general lysosomal deficiency and leads to Parkinson disease neurodegeneration. Proceedings of the National Academy of Sciences. 2012;109(24):9611-6.

127. Dehay B, Bové J, Rodríguez-Muela N, Perier C, Recasens A, Boya P, Vila M. Pathogenic lysosomal depletion in Parkinson's disease. Journal of Neuroscience. 2010;30(37):12535-44.

128. Caccamo A, Majumder S, Richardson A, Strong R, Oddo S. Molecular interplay between mammalian target of rapamycin (mTOR), amyloid-β, and tau effects on cognitive impairments. Journal of Biological Chemistry. 2010;285(17):13107-20.

129. Majumder S, Richardson A, Strong R, Oddo S. Inducing autophagy by rapamycin before, but not after, the formation of plaques and tangles ameliorates cognitive deficits. PloS one. 2011;6(9):e25416.

130. Spilman P, Podlutskaya N, Hart MJ, Debnath J, Gorostiza O, Bredesen D, Richardson A, Strong R, Galvan V. Inhibition of mTOR by rapamycin abolishes cognitive deficits and reduces amyloid-β levels in a mouse model of Alzheimer's disease. PloS one. 2010;5(4):e9979.

131. Pavel M, Imarisio S, Menzies FM, Jimenez-Sanchez M, Siddiqi FH, Wu X, Renna M, O'Kane CJ, Crowther DC, Rubinsztein DC. CCT complex restricts neuropathogenic protein aggregation via autophagy. Nature Communications. 2016;7:13821. doi: 10.1038/ncomms13821
https://www.nature.com/articles/ncomms13821#supplementary-information.

132. Ravikumar B, Vacher C, Berger Z, Davies JE, Luo S, Oroz LG, Scaravilli F, Easton DF, Duden R, O'Kane CJ. Inhibition of mTOR induces autophagy and reduces toxicity of polyglutamine expansions in fly and mouse models of Huntington disease. Nature genetics. 2004;36(6):585-95.

133. Malagelada C, Jin ZH, Jackson-Lewis V, Przedborski S, Greene LA. Rapamycin Protects against Neuron Death in In Vitro andIn Vivo Models of Parkinson's Disease. Journal of Neuroscience. 2010;30(3):1166-75.

134. Wang IF, Guo B-S, Liu Y-C, Wu C-C, Yang C-H, Tsai K-J, Shen C-KJ. Autophagy activators rescue and alleviate pathogenesis of a mouse model with proteinopathies of the TAR DNA-binding protein 43. Proceedings of the National Academy of Sciences. 2012;109(37):15024-9.

135. Zhang X, Li L, Chen S, Yang D, Wang Y, Zhang X, Wang Z, Le W. Rapamycin treatment augments motor neuron degeneration in SOD1G93A mouse model of amyotrophic lateral sclerosis. Autophagy. 2011;7(4):412-25. doi: 10.4161/auto.7.4.14541.

136. Zhang Y, Mun SR, Linares JF, Ahn J, Towers CG, Ji CH, Fitzwalter BE, Holden MR, Mi W, Shi X, Moscat J, Thorburn A, Diaz-Meco MT, Kwon YT, Kutateladze TG. ZZ-dependent regulation of p62/SQSTM1 in autophagy. Nature Communications. 2018;9(1):4373. doi: 10.1038/s41467-018-06878-8.

137. Aki T, Unuma K, Noritake K, Hirayama N, Funakoshi T, Uemura K. Formation of high molecular weight p62 by CORM-3. PLoS One. 2019;14(1):e0210474. Epub 2019/01/09. doi: 10.1371/journal.pone.0210474. PubMed PMID: 30620762; PMCID: PMC6324786.

138. Lee Y-S, Kalimuthu K, Seok Park Y, Makala H, Watkins SC, Choudry MHA, Bartlett DL, Tae Kwon Y, Lee YJ. Ferroptotic agent-induced endoplasmic reticulum stress response plays a pivotal role in the autophagic process outcome2020;n/a(n/a). doi:

10.1002/jcp.29571.

139. Kirkin V. History of the Selective Autophagy Research: How Did It Begin and Where Does It Stand Today? Journal of Molecular Biology. 2020;432(1):3-27. doi: https://doi.org/10.1016/j.jmb.2019.05.010.

140. Teramachi J, Silbermann R, Yang P, Zhao W, Mohammad KS, Guo J, Anderson JL, Zhou D, Feng R, Myint KZ, Maertz N, Beumer JH, Eiseman JL, Windle JJ, Xie XQ, Roodman GD, Kurihara N. Blocking the ZZ domain of sequestosome1/p62 suppresses myeloma growth and osteoclast formation in vitro and induces dramatic bone formation in myeloma-bearing bones in vivo. Leukemia. 2016;30(2):390-8. doi: 10.1038/leu.2015.229.

141. Adamik J, Silbermann R, Marino S, Sun Q, Anderson JL, Zhou D, Xie XQ, Roodman GD, Galson DL. XRK3F2 Inhibition of p62-ZZ Domain Signaling Rescues Myeloma-Induced GFI1-Driven Epigenetic Repression of the Runx2 Gene in Pre-osteoblasts to Overcome Differentiation Suppression. Front Endocrinol (Lausanne). 2018;9:344. Epub 2018/07/17. doi: 10.3389/fendo.2018.00344. PubMed PMID: 30008697; PMCID: PMC6033965.

142. Chen J-Z, Wang J, Xie X-Q. GPCR Structure-Based Virtual Screening Approach for CB2 Antagonist Search. Journal of Chemical Information and Modeling. 2007;47(4):1626-37. doi: 10.1021/ci7000814. PubMed PMID: 2007:661823.

143. Yang P, Myint KZ, Tong Q, Feng R, Cao H, Almehizia AA, Alqarni MH, Wang L, Bartlow P, Gao Y, Gertsch J, Teramachi J, Kurihara N, Roodman GD, Cheng T, Xie XQ. Lead discovery, chemistry optimization, and biological evaluation studies of novel biamide derivatives as CB2 receptor inverse agonists and osteoclast inhibitors. J Med Chem. 2012;55(22):9973-87. Epub 2012/10/18. doi: 10.1021/jm301212u. PubMed PMID: 23072339; PMCID: PMC3967745.

144. Yang P, Wang L, Feng R, Almehizia AA, Tong Q, Myint KZ, Ouyang Q, Alqarni MH, Xie XQ. Novel triaryl sulfonamide derivatives as selective cannabinoid receptor 2 inverse agonists and osteoclast inhibitors: discovery, optimization, and biological evaluation. J Med Chem. 2013;56(5):2045-58. Epub 2013/02/15. doi: 10.1021/jm3017464. PubMed PMID: 23406429.

145. Jia-Lin Guo Y-YL, Ya-Zhong Pei. Synthesis and biological evaluation of 3-(piperidin-4-yl)isoxazolo[4,5-d]pyrimidine derivatives as novel PI3Kδ inhibitors[J]. Chin Chem Lett. 2015;26(10):1283-8

146. Kischkel FC, Hellbardt S, Behrmann I, Germer M, Pawlita M, Krammer PH, Peter ME. Cytotoxicity-dependent APO-1 (Fas/CD95)-associated proteins form a death-inducing signaling complex (DISC) with the receptor. The EMBO Journal. 1995;14(22):5579-88. doi: https://doi.org/10.1002/j.1460-2075.1995.tb00245.x.

147. Su M, Mei Y, Sinha S. Role of the Crosstalk between Autophagy and Apoptosis in Cancer. Journal of Oncology. 2013;2013:102735. doi: 10.1155/2013/102735.

148. Muñoz-Escobar J, Matta-Camacho E, Cho C, Kozlov G, Gehring K. Bound waters mediate binding of diverse substrates to a ubiquitin ligase. Structure. 2017;25(5):719-29. e3.

149. Moscat J, Diaz-Meco MT. p62 at the crossroads of autophagy, apoptosis, and cancer. Cell. 2009;137(6):1001-4. doi: 10.1016/j.cell.2009.05.023. PubMed PMID: 19524504; PMCID: 3971861.

150. Cha-Molstad H, Sung KS, Hwang J, Kim KA, Yu JE, Yoo YD, Jang JM, Han DH, Molstad M, Kim JG. Amino-terminal arginylation targets endoplasmic reticulum chaperone BiP for autophagy through p62 binding. Nature cell biology. 2015;17(7):917-29.

151. 2018 Alzheimer's disease facts and figures. Alzheimer's & Dementia: The Journal of the Alzheimer's Association. 2018;14(3):367-429. doi: 10.1016/j.jalz.2018.02.001.

152. 2020 Alzheimer's disease facts and figures. Alzheimer's & Dementia: The Journal of the Alzheimer's Association. 2020;16(3):391-460. doi: 10.1002/alz.12068.

153. Organization. WH. Dementia: Key facts. https://www.who.int/news-room/fact-sheets/detail/dementia. Accessed Jan 20212021.

154. Hebert LE, Weuve J, Scherr PA, Evans DA. Alzheimer disease in the United States (2010-2050) estimated using the 2010 census. Neurology. 2013;80(19):1778-83. Epub 2013/02/06. doi: 10.1212/WNL.0b013e31828726f5. PubMed PMID: 23390181.

155. Taylor CA GS, McGuire LC, Lu H, Croft JB. . Deaths from Alzheimer's Disease — United States, 1999–2014. MMWR Morb Mortal Wkly Rep 2017;66:521–526. DOI: http://dx.doi.org/10.15585/mmwr.mm6620a1external 2017.

156. B. T-V. Mortality from Alzheimer's disease in the United States: Data for 2000 and 2010. National Center for Health Statistics Data Brief, No. 116. National Center for Health Statistics, Hyattsville, MD; 2013.2013.

157. Kocienski P. Synthesis of AZD1656. Synfacts. 2018;14(10):1003.

158. McDonald's Corporation Report 2018. Available at: https://corporate.mcdonalds.com/content/dam/gwscorp/nfl/investor-relations-content/annual-reports/McDonalds_2018_Annual_Report.pdf. Accessed December 4, 2019.2018.

159. Organization. WH. International Statistical Classification of Diseases and Related Health Problems. 10th revision. 2nd edition. WHO Press: Geneva, Switzerland; 2004.2021.

160. Jutkowitz E KR, Gaugler JE, MacLehose RF, Dowd B, Kuntz KM. Societal and family lifetime cost of dementia: Implications for policy. J Am Geriatr Soc 2017;65(10):2169-75.2017.

161. (NIA). NIoA. Treatment of Alzheimer's disease--How Alzheimer's disease is treated? https://www.nia.nih.gov/health/how-alzheimers-disease-treated Accessed Jan 20212021.

162. Jin Y, Wang H. Naringenin Inhibit the Hydrogen Peroxide-Induced SH-SY5Y Cells Injury Through Nrf2/HO-1 Pathway. Neurotoxicity research. 2019;36(4):796-805. Epub 2019/05/12. doi: 10.1007/s12640-019-00046-6. PubMed PMID: 31076999.

163. Huang S-l, He H-b, Zou K, Bai C-h, Xue Y-h, Wang J-z, Chen J-f. Protective effect of tomatine against hydrogen peroxide-induced neurotoxicity in neuroblastoma (SH-SY5Y) cells. Journal of Pharmacy and Pharmacology. 2014;66(6):844-54. doi: https://doi.org/10.1111/jphp.12205.

164. Shipley MM, Mangold CA, Szpara ML. Differentiation of the SH-SY5Y Human Neuroblastoma Cell Line. J Vis Exp. 2016(108):53193-. doi: 10.3791/53193. PubMed PMID: 26967710.

165. Encinas M, Iglesias M, Liu Y, Wang H, Muhaisen A, Cena V, Gallego C, Comella JXJJon. Sequential treatment of SH‐SY5Y cells with retinoic acid and brain‐derived neurotrophic factor gives rise to fully differentiated, neurotrophic factor‐dependent, human neuron‐like cells2000;75(3):991-1003.

166. Christensen J, Steain M, Slobedman B, Abendroth AJJov. Differentiated neuroblastoma cells provide a highly efficient model for studies of productive varicella-zoster virus infection of neuronal cells2011;85(16):8436-42.

167. Milton NGN. Role of Hydrogen Peroxide in the Aetiology of Alzheimer's Disease. Drugs & Aging. 2004;21(2):81-100. doi: 10.2165/00002512-200421020-00002.

168. Shah SZA, Zhao D, Hussain T, Sabir N, Mangi MH, Yang L. p62-Keap1-NRF2-ARE Pathway: A Contentious Player for Selective Targeting of Autophagy, Oxidative Stress and Mitochondrial Dysfunction in Prion Diseases. Front Mol Neurosci. 2018;11:310. Epub 2018/10/20. doi: 10.3389/fnmol.2018.00310. PubMed PMID: 30337853; PMCID: PMC6180192.

169. Kumar KH, Khanum F. Hydroalcoholic extract of cyperus rotundus ameliorates H2O2-induced human neuronal cell damage via its anti-oxidative and anti-apoptotic machinery. Cellular and molecular neurobiology. 2013;33(1):5-17. Epub 2012/08/08. doi: 10.1007/s10571-012-9865-8. PubMed PMID: 22869350.

170. Luo H, Hu J, Wang Y, Chen Y, Zhu D, Jiang R, Qiu Z. In vivo and in vitro neuroprotective effects of Panax ginseng glycoproteins. International journal of biological macromolecules. 2018;113:607-15. Epub 2018/02/07. doi: 10.1016/j.ijbiomac.2018.02.015. PubMed PMID: 29408615.

171. Pisani L, Farina R, Catto M, Iacobazzi RM, Nicolotti O, Cellamare S, Mangiatordi GF, Denora N, Soto-Otero R, Siragusa L, Altomare CD, Carotti A. Exploring Basic Tail Modifications of Coumarin-Based Dual Acetylcholinesterase-Monoamine Oxidase B Inhibitors: Identification of Water-Soluble, Brain-Permeant Neuroprotective Multitarget Agents. J Med Chem. 2016;59(14):6791-806. Epub 2016/06/28. doi: 10.1021/acs.jmedchem.6b00562. PubMed PMID: 27347731.

172. Jang M, Cho EJ, Piao XL. Protective effects of resveratrol oligomers from Vitis amurensis against sodium nitroprusside-induced neurotoxicity in human neuroblastoma SH-SY5Y cells. Archives of pharmacal research. 2015;38(6):1263-9. Epub 2014/10/29. doi: 10.1007/s12272-014-0505-3. PubMed PMID: 25348868.

173. Evangelou E, Ioannidis JPA. Meta-analysis methods for genome-wide association studies and beyond. Nature Reviews Genetics. 2013;14:379. doi: 10.1038/nrg3472.

174. Witte JS. Genome-wide association studies and beyond. Annual review of public health. 2010;31:9-20. doi: 10.1146/annurev.publhealth.012809.103723. PubMed PMID: 20235850.

175. Higaki S, Muramatsu M, Matsuda A, Matsumoto K, Satoh J-i, Michikawa M, Niida S. Defensive effect of microRNA-200b/c against amyloid-beta peptide-induced toxicity in Alzheimer's disease models. PLOS ONE. 2018;13(5):e0196929. doi: 10.1371/journal.pone.0196929.

176. Zhang S-f, Chen J-c, Zhang J, Xu J-g. miR-181a involves in the hippocampus-dependent memory formation via targeting PRKAA1. Scientific Reports. 2017;7(1):8480. doi: 10.1038/s41598-017-09095-3.

177. Schonrock N, Humphreys DT, Preiss T, Gotz J. Target gene repression mediated by miRNAs miR-181c and miR-9 both of which are down-regulated by amyloid-beta. Journal of molecular neuroscience : MN. 2012;46(2):324-35. Epub 2011/07/02. doi: 10.1007/s12031-011-9587-2. PubMed PMID: 21720722.

178. Hébert SS, Horré K, Nicolaï L, Papadopoulou AS, Mandemakers W, Silahtaroglu AN, Kauppinen S, Delacourte A, De Strooper B. Loss of microRNA cluster miR-29a/b-1 in sporadic Alzheimer's disease correlates with increased BACE1/beta-secretase expression. Proceedings of the National Academy of Sciences of the United States of America. 2008;105(17):6415-20. Epub 04/23. doi: 10.1073/pnas.0710263105. PubMed PMID: 18434550.

179. Schipper HM, Maes OC, Chertkow HM, Wang E. MicroRNA expression in Alzheimer

blood mononuclear cells. Gene regulation and systems biology. 2007;1:263-74. Epub 2007/01/01. PubMed PMID: 19936094; PMCID: PMC2759133.

180. Beveridge NJ, Tooney PA, Carroll AP, Gardiner E, Bowden N, Scott RJ, Tran N, Dedova I, Cairns MJ. Dysregulation of miRNA 181b in the temporal cortex in schizophrenia. Human molecular genetics. 2008;17(8):1156-68. Epub 2008/01/11. doi: 10.1093/hmg/ddn005. PubMed PMID: 18184693.

181. Cogswell JP, Ward J, Taylor IA, Waters M, Shi Y, Cannon B, Kelnar K, Kemppainen J, Brown D, Chen C, Prinjha RK, Richardson JC, Saunders AM, Roses AD, Richards CA. Identification of miRNA changes in Alzheimer's disease brain and CSF yields putative biomarkers and insights into disease pathways. Journal of Alzheimer's disease : JAD. 2008;14(1):27-41. Epub 2008/06/06. PubMed PMID: 18525125.

182. Schonrock N, Matamales M, Ittner LM, Gotz J. MicroRNA networks surrounding APP and amyloid-beta metabolism--implications for Alzheimer's disease. Experimental neurology. 2012;235(2):447-54. Epub 2011/11/29. doi: 10.1016/j.expneurol.2011.11.013. PubMed PMID: 22119426.

183. Moradifard S, Hoseinbeyki M, Ganji SM, Minuchehr Z. Analysis of microRNA and Gene Expression Profiles in Alzheimer's Disease: A Meta-Analysis Approach. Scientific Reports. 2018;8(1):4767. doi: 10.1038/s41598-018-20959-0.

184. Mellios N, Huang H-S, Grigorenko A, Rogaev E, Akbarian S. A set of differentially expressed miRNAs, including miR-30a-5p, act as post-transcriptional inhibitors of BDNF in prefrontal cortex. Human molecular genetics. 2008;17(19):3030-42. Epub 07/15. doi: 10.1093/hmg/ddn201. PubMed PMID: 18632683.

185. Packer AN, Xing Y, Harper SQ, Jones L, Davidson BL. The bifunctional microRNA miR-9/miR-9* regulates REST and CoREST and is downregulated in Huntington's disease. The Journal of neuroscience : the official journal of the Society for Neuroscience. 2008;28(53):14341-6. Epub 2009/01/02. doi: 10.1523/jneurosci.2390-08.2008. PubMed PMID: 19118166; PMCID: PMC3124002.

186. Hoye ML, Koval ED, Wegener AJ, Hyman TS, Yang C, O'Brien DR, Miller RL, Cole T, Schoch KM, Shen T. microRNA profiling reveals marker of motor neuron disease in ALS models. Journal of Neuroscience. 2017:3582-16.

187. Nunez-Iglesias J, Liu C-C, Morgan TE, Finch CE, Zhou XJ. Joint Genome-Wide Profiling of miRNA and mRNA Expression in Alzheimer's Disease Cortex Reveals Altered miRNA Regulation. PLOS ONE. 2010;5(2):e8898. doi: 10.1371/journal.pone.0008898.

188. Kupershmidt I, Su QJ, Grewal A, Sundaresh S, Halperin I, Flynn J, Shekar M, Wang H, Park J, Cui W, Wall GD, Wisotzkey R, Alag S, Akhtari S, Ronaghi M. Ontology-Based Meta-Analysis of Global Collections of High-Throughput Public Data. PLOS ONE. 2010;5(9):e13066. doi: 10.1371/journal.pone.0013066.

189. Lamb J, Crawford ED, Peck D, Modell JW, Blat IC, Wrobel MJ, Lerner J, Brunet JP, Subramanian A, Ross KN, Reich M, Hieronymus H, Wei G, Armstrong SA, Haggarty SJ, Clemons PA, Wei R, Carr SA, Lander ES, Golub TR. The Connectivity Map: using gene-expression signatures to connect small molecules, genes, and disease. Science. 2006;313(5795):1929-35. doi: 10.1126/science.1132939. PubMed PMID: 17008526.

190. Lamb J. The Connectivity Map: a new tool for biomedical research. Nature reviews Cancer. 2007;7(1):54-60. doi: 10.1038/nrc2044. PubMed PMID: 17186018.

191. Liberzon A, Subramanian A, Pinchback R, Thorvaldsdóttir H, Tamayo P, Mesirov JP. Molecular signatures database (MSigDB) 3.0. Bioinformatics. 2011;27(12):1739-40.

192. Consortium GO. The Gene Ontology (GO) database and informatics resource. Nucleic acids research. 2004;32(suppl 1):D258-D61.

193. Szklarczyk D, Franceschini A, Wyder S, Forslund K, Heller D, Huerta-Cepas J, Simonovic M, Roth A, Santos A, Tsafou KP. STRING v10: protein–protein interaction networks, integrated over the tree of life. Nucleic acids research. 2014;43(D1):D447-D52.

194. Negron AE, Reichman WE. Risperidone in the treatment of patients with Alzheimer's disease with negative symptoms. International psychogeriatrics. 2000;12(4):527-36. Epub 2001/03/27. PubMed PMID: 11263718.

195. Brodaty H, Ames D, Snowdon J, Woodward M, Kirwan J, Clarnette R, Lee E, Greenspan A. Risperidone for psychosis of Alzheimer's disease and mixed dementia: results of a double-blind, placebo-controlled trial. International journal of geriatric psychiatry. 2005;20(12):1153-7. Epub 2005/11/30. doi: 10.1002/gps.1409. PubMed PMID: 16315159.

196. Tariot PN, Schneider LS, Cummings J, Thomas RG, Raman R, Jakimovich LJ, Loy R, Bartocci B, Fleisher A, Ismail MS, Porsteinsson A, Weiner M, Jack CR, Jr., Thal L, Aisen PS. Chronic divalproex sodium to attenuate agitation and clinical progression of Alzheimer disease. Archives of general psychiatry. 2011;68(8):853-61. Epub 2011/08/04. doi: 10.1001/archgenpsychiatry.2011.72. PubMed PMID: 21810649.

197. Jones RW, Kivipelto M, Feldman H, Sparks L, Doody R, Waters DD, Hey-Hadavi J, Breazna A, Schindler RJ, Ramos H. The Atorvastatin/Donepezil in Alzheimer's Disease Study (LEADe): design and baseline characteristics. Alzheimer's & dementia : the journal of the Alzheimer's Association. 2008;4(2):145-53. Epub 2008/07/18. doi: 10.1016/j.jalz.2008.02.001. PubMed PMID: 18631958.

198. Sparks DL, Sabbagh MN, Connor DJ, Lopez J, Launer LJ, Browne P, Wasser D, Johnson-Traver S, Lochhead J, Ziolwolski C. Atorvastatin for the treatment of mild to moderate Alzheimer disease: preliminary results. Archives of neurology. 2005;62(5):753-7. Epub 2005/05/11. doi: 10.1001/archneur.62.5.753. PubMed PMID: 15883262.

199. Peleg S, Sananbenesi F, Zovoilis A, Burkhardt S, Bahari-Javan S, Agis-Balboa RC, Cota P, Wittnam JL, Gogol-Doering A, Opitz L. Altered histone acetylation is associated with age-dependent memory impairment in mice. Science. 2010;328(5979):753-6.

200. Guan J-S, Haggarty SJ, Giacometti E, Dannenberg J-H, Joseph N, Gao J, Nieland TJ, Zhou Y, Wang X, Mazitschek R. HDAC2 negatively regulates memory formation and synaptic plasticity. Nature. 2009;459(7243):55.

201. Xu K, Dai X-L, Huang H-C, Jiang Z-F. Targeting HDACs: A Promising Therapy for Alzheimer's Disease. Oxidative Medicine and Cellular Longevity. 2011;2011:5. doi: 10.1155/2011/143269.

202. Simpkins JW, Singh M. More than a decade of estrogen neuroprotection. Alzheimer's & dementia : the journal of the Alzheimer's Association. 2008;4(1 Suppl 1):S131-6. Epub 2008/07/22. doi: 10.1016/j.jalz.2007.10.009. PubMed PMID: 18631989.

203. Belanoff JK, Jurik J, Schatzberg LD, DeBattista C, Schatzberg AF. Slowing the progression of cognitive decline in Alzheimer's disease using mifepristone. Journal of molecular neuroscience : MN. 2002;19(1-2):201-6. Epub 2002/09/06. doi: 10.1007/s12031-002-0033-3. PubMed PMID: 12212781.

204. Yulug B, Hanoglu L, Ozansoy M, Isık D, Kilic U, Kilic E, Schabitz WR. Therapeutic role of rifampicin in Alzheimer's disease. Psychiatry and Clinical Neurosciences. 2018;72(3):152-9. doi: 10.1111/pcn.12637.

205. Umeda T, Tanaka A, Sakai A, Yamamoto A, Sakane T, Tomiyama T. Intranasal rifampicin

for Alzheimer's disease prevention. Alzheimer's & dementia (New York, N Y). 2018;4:304-13. doi: 10.1016/j.trci.2018.06.012. PubMed PMID: 30094330.

206. Iizuka T, Morimoto K, Sasaki Y, Kameyama M, Kurashima A, Hayasaka K, Ogata H, Goto H. Preventive Effect of Rifampicin on Alzheimer Disease Needs at Least 450 mg Daily for 1 Year: An FDG-PET Follow-Up Study. Dementia and geriatric cognitive disorders extra. 2017;7(2):204-14. doi: 10.1159/000477343. PubMed PMID: 28690634.

207. Shintani EY, Uchida KM. Donepezil: an anticholinesterase inhibitor for Alzheimer's disease. American journal of health-system pharmacy : AJHP : official journal of the American Society of Health-System Pharmacists. 1997;54(24):2805-10. Epub 1998/01/16. PubMed PMID: 9428950.

208. Korabecny J, Soukup O, Musilek K, Jun D, Kuca K. Amantadine and AChE inhibitor hybrids as candidates for Alzheimer's disease treatment. Alzheimer's & Dementia: The Journal of the Alzheimer's Association. 2013;9(4):P805. doi: 10.1016/j.jalz.2013.05.1668.

209. Lu X, He SY, Li Q, Yang H, Jiang X, Lin H, Chen Y, Qu W, Feng F, Bian Y, Zhou Y, Sun H. Investigation of multi-target-directed ligands (MTDLs) with butyrylcholinesterase (BuChE) and indoleamine 2,3-dioxygenase 1 (IDO1) inhibition: The design, synthesis of miconazole analogues targeting Alzheimer's disease. Bioorganic & medicinal chemistry. 2018;26(8):1665-74. Epub 2018/02/25. doi: 10.1016/j.bmc.2018.02.014. PubMed PMID: 29475581.

210. Ellul J, Archer N, Foy CML, Poppe M, Boothby H, Nicholas H, Brown RG, Lovestone S. The effects of commonly prescribed drugs in patients with Alzheimer's disease on the rate of deterioration. Journal of neurology, neurosurgery, and psychiatry. 2007;78(3):233-9. Epub 09/29. doi: 10.1136/jnnp.2006.104034. PubMed PMID: 17012333.

211. Ames D. Antipsychotics, cognitive decline and death in Alzheimer's disease: the London and South-East Region Alzheimer's Disease longitudinal study. Journal of neurology, neurosurgery, and psychiatry. 2007;78(1):2-. doi: 10.1136/jnnp.2006.100586. PubMed PMID: 17172562.

212. Honjo H, Iwasa K, Kawata M, Fushiki S, Hosoda T, Tatsumi H, Oida N, Mihara M, Hirasugi Y, Yamamoto H, Kikuchi N, Kitawaki J. Progestins and estrogens and Alzheimer's disease. The Journal of steroid biochemistry and molecular biology. 2005;93(2-5):305-8. Epub 2005/04/30. doi: 10.1016/j.jsbmb.2004.12.001. PubMed PMID: 15860274.

213. Valen-Sendstad A, Engedal K, Stray-Pedersen B, Strobel C, Barnett L, Meyer N, Nurminemi M. Effects of hormone therapy on depressive symptoms and cognitive functions in women with Alzheimer disease: a 12 month randomized, double-blind, placebo-controlled study of low-dose estradiol and norethisterone. The American journal of geriatric psychiatry : official journal of the American Association for Geriatric Psychiatry. 2010;18(1):11-20. Epub 2010/01/23. doi: 10.1097/JGP.0b013e3181beaaf4. PubMed PMID: 20094015.

214. Dumont M, Stack C, Elipenahli C, Jainuddin S, Gerges M, Starkova N, Calingasan NY, Yang L, Tampellini D, Starkov AA, Chan RB, Di Paolo G, Pujol A, Beal MF. Bezafibrate administration improves behavioral deficits and tau pathology in P301S mice. Human molecular genetics. 2012;21(23):5091-105. Epub 2012/08/28. doi: 10.1093/hmg/dds355. PubMed PMID: 22922230; PMCID: PMC3490516.

215. Fakhraei N JR, Nikoui V, Bakhtiarian A, Pournaghash Tehrani SS. Effect of Clofibrate, A PPAR-A Receptors Agonist, On Behavioral Despair Associated With Exposure to Forced

Swim in Rats. . Adv J Toxicol Curr Res. 2017;1(2):107-15.

216. Heneka MT, Reyes-Irisarri E, Hüll M, Kummer MP. Impact and Therapeutic Potential of PPARs in Alzheimer's Disease. Current neuropharmacology. 2011;9(4):643-50. doi: 10.2174/157015911798376325. PubMed PMID: 22654722.

217. Owona BA, Zug C, Schluesener HJ, Zhang ZY. Protective Effects of Forskolin on Behavioral Deficits and Neuropathological Changes in a Mouse Model of Cerebral Amyloidosis. Journal of neuropathology and experimental neurology. 2016;75(7):618-27. Epub 2016/06/03. doi: 10.1093/jnen/nlw043. PubMed PMID: 27251043; PMCID: PMC4913438.

218. Yan F, Liang H, Song J, Cui J, Liu Q, Liu S, Wang P, Dong Y, Liu H. Palladium-Catalyzed Cyclization-Heck Reaction of Allenamides: An Approach to 3-Methylene-5-phenyl-1,2,3,4-tetrahydropyridine Derivatives. Organic Letters. 2017;19(1):86-9. doi: 10.1021/acs.orglett.6b03364.

219. Wu Y-T, Tan H-L, Shui G, Bauvy C, Huang Q, Wenk MR, Ong C-N, Codogno P, Shen H-M. Dual Role of 3-Methyladenine in Modulation of Autophagy via Different Temporal Patterns of Inhibition on Class I and III Phosphoinositide 3-Kinase *. Journal of Biological Chemistry. 2010;285(14):10850-61. doi: 10.1074/jbc.M109.080796.

220. Gao L, Lv G, Li R, Liu WT, Zong C, Ye F, Li XY, Yang X, Jiang JH, Hou XJ, Jing YY, Han ZP, Wei LX. Glycochenodeoxycholate promotes hepatocellular carcinoma invasion and migration by AMPK/mTOR dependent autophagy activation. Cancer letters. 2019;454:215-23. Epub 2019/04/14. doi: 10.1016/j.canlet.2019.04.009. PubMed PMID: 30980867.

221. Shao S, Li S, Qin Y, Wang X, Yang Y, Bai H, Zhou L, Zhao C, Wang C. Spautin-1, a novel autophagy inhibitor, enhances imatinib-induced apoptosis in chronic myeloid leukemia. International journal of oncology. 2014;44(5):1661-8. Epub 2014/03/04. doi: 10.3892/ijo.2014.2313. PubMed PMID: 24585095; PMCID: PMC6904104.

222. So KY, Lee BH, Oh SH. The critical role of autophagy in cadmium-induced immunosuppression regulated by endoplasmic reticulum stress-mediated calpain activation in RAW264.7 mouse monocytes. Toxicology. 2018;393:15-25. Epub 2017/11/08. doi: 10.1016/j.tox.2017.10.016. PubMed PMID: 29111403.

223. Kim KY, Park KI, Kim SH, Yu SN, Park SG, Kim YW, Seo YK, Ma JY, Ahn SC. Inhibition of Autophagy Promotes Salinomycin-Induced Apoptosis via Reactive Oxygen Species-Mediated PI3K/AKT/mTOR and ERK/p38 MAPK-Dependent Signaling in Human Prostate Cancer Cells. Int J Mol Sci. 2017;18(5). Epub 2017/05/20. doi: 10.3390/ijms18051088. PubMed PMID: 28524116; PMCID: PMC5454997.

224. Fabrizi C, Somma F, Pompili E, Biagioni F, Lenzi P, Fornai F, Fumagalli L. Role of autophagy inhibitors and inducers in modulating the toxicity of trimethyltin in neuronal cell cultures. Journal of neural transmission (Vienna, Austria : 1996). 2012;119(11):1295-305. Epub 2012/03/15. doi: 10.1007/s00702-012-0785-z. PubMed PMID: 22415064.

225. Torres A, Luke JD, Kullas AL, Kapilashrami K, Botbol Y, Koller A, Tonge PJ, Chen EI, Macian F, van der Velden AW. Asparagine deprivation mediated by Salmonella asparaginase causes suppression of activation-induced T cell metabolic reprogramming. Journal of leukocyte biology. 2016;99(2):387-98. Epub 2015/10/27. doi: 10.1189/jlb.4A0615-252R. PubMed PMID: 26497246; PMCID: PMC4718193.

226. Cook KL, Wärri A, Soto-Pantoja DR, Clarke PA, Cruz MI, Zwart A, Clarke R. Hydroxychloroquine inhibits autophagy to potentiate antiestrogen responsiveness in ER+

breast cancer. Clinical cancer research : an official journal of the American Association for Cancer Research. 2014;20(12):3222-32. Epub 2014/06/15. doi: 10.1158/1078-0432.Ccr-13-3227. PubMed PMID: 24928945; PMCID: PMC4073207.

227. Wang Y, Peng RQ, Li DD, Ding Y, Wu XQ, Zeng YX, Zhu XF, Zhang XS. Chloroquine enhances the cytotoxicity of topotecan by inhibiting autophagy in lung cancer cells. Chin J Cancer. 2011;30(10):690-700. Epub 2011/10/01. doi: 10.5732/cjc.011.10056. PubMed PMID: 21959046; PMCID: PMC4012269.

228. Watson M, Roulston A, Bélec L, Billot X, Marcellus R, Bédard D, Bernier C, Branchaud S, Chan H, Dairi K, Gilbert K, Goulet D, Gratton MO, Isakau H, Jang A, Khadir A, Koch E, Lavoie M, Lawless M, Nguyen M, Paquette D, Turcotte E, Berger A, Mitchell M, Shore GC, Beauparlant P. The small molecule GMX1778 is a potent inhibitor of NAD+ biosynthesis: strategy for enhanced therapy in nicotinic acid phosphoribosyltransferase 1-deficient tumors. Mol Cell Biol. 2009;29(21):5872-88. Epub 2009/08/26. doi: 10.1128/mcb.00112-09. PubMed PMID: 19703994; PMCID: PMC2772749.

229. Avni D, Glucksam Y, Zor T. The phosphatidylinositol 3-kinase (PI3K) inhibitor LY294002 modulates cytokine expression in macrophages via p50 nuclear factor κB inhibition, in a PI3K-independent mechanism. Biochemical pharmacology. 2012;83(1):106-14. Epub 2011/10/19. doi: 10.1016/j.bcp.2011.09.025. PubMed PMID: 22005520.

230. Egan DF, Chun MG, Vamos M, Zou H, Rong J, Miller CJ, Lou HJ, Raveendra-Panickar D, Yang CC, Sheffler DJ, Teriete P, Asara JM, Turk BE, Cosford ND, Shaw RJ. Small Molecule Inhibition of the Autophagy Kinase ULK1 and Identification of ULK1 Substrates. Mol Cell. 2015;59(2):285-97. Epub 2015/06/30. doi: 10.1016/j.molcel.2015.05.031. PubMed PMID: 26118643; PMCID: PMC4530630.

231. Liu J, Xia H, Kim M, Xu L, Li Y, Zhang L, Cai Y, Norberg HV, Zhang T, Furuya T, Jin M, Zhu Z, Wang H, Yu J, Li Y, Hao Y, Choi A, Ke H, Ma D, Yuan J. Beclin1 controls the levels of p53 by regulating the deubiquitination activity of USP10 and USP13. Cell. 2011;147(1):223-34. Epub 2011/10/04. doi: 10.1016/j.cell.2011.08.037. PubMed PMID: 21962518; PMCID: PMC3441147.

232. Hansen SH, Olsson A, Casanova JE. Wortmannin, an inhibitor of phosphoinositide 3-kinase, inhibits transcytosis in polarized epithelial cells. J Biol Chem. 1995;270(47):28425-32. Epub 1995/11/24. doi: 10.1074/jbc.270.47.28425. PubMed PMID: 7499348.

233. Ronan B, Flamand O, Vescovi L, Dureuil C, Durand L, Fassy F, Bachelot MF, Lamberton A, Mathieu M, Bertrand T, Marquette JP, El-Ahmad Y, Filoche-Romme B, Schio L, Garcia-Echeverria C, Goulaouic H, Pasquier B. A highly potent and selective Vps34 inhibitor alters vesicle trafficking and autophagy. Nature chemical biology. 2014;10(12):1013-9. Epub 2014/10/20. doi: 10.1038/nchembio.1681. PubMed PMID: 25326666.

234. Akin D, Wang SK, Habibzadegah-Tari P, Law B, Ostrov D, Li M, Yin XM, Kim JS, Horenstein N, Dunn WA, Jr. A novel ATG4B antagonist inhibits autophagy and has a negative impact on osteosarcoma tumors. Autophagy. 2014;10(11):2021-35. Epub 2014/12/09. doi: 10.4161/auto.32229. PubMed PMID: 25483883; PMCID: PMC4502682.

235. Carew JS, Espitia CM, Zhao W, Han Y, Visconte V, Phillips J, Nawrocki ST. Disruption of Autophagic Degradation with ROC-325 Antagonizes Renal Cell Carcinoma Pathogenesis. Clinical cancer research : an official journal of the American Association for Cancer Research. 2017;23(11):2869-79. Epub 2016/11/25. doi: 10.1158/1078-

0432.Ccr-16-1742. PubMed PMID: 27881580; PMCID: PMC5593077.

236. Carew JS, Nawrocki ST. Drain the lysosome: Development of the novel orally available autophagy inhibitor ROC-325. Autophagy. 2017;13(4):765-6. Epub 2017/01/25. doi: 10.1080/15548627.2017.1280222. PubMed PMID: 28118053; PMCID: PMC5388230.

237. Wang L, Ma C, Wipf P, Liu H, Su W, Xie X-Q. TargetHunter: an in silico target identification tool for predicting therapeutic potential of small organic molecules based on chemogenomic database. The AAPS journal. 2013;15(2):395-406. doi: 10.1208/s12248-012-9449-z.

238. O'Boyle NM, Banck M, James CA, Morley C, Vandermeersch T, Hutchison GR. Open Babel: An open chemical toolbox. Journal of Cheminformatics. 2011;3(1):1-14. doi: 10.1186/1758-2946-3-33.

239. Ertl P. Molecular structure input on the web. Journal of cheminformatics. 2009;2(1):1-9. doi: 10.1186/1758-2946-2-1.

240. Wishart DS, Knox C, Guo AC, Cheng D, Shrivastava S, Tzur D, Gautam B, Hassanali M. DrugBank: a knowledgebase for drugs, drug actions and drug targets. Nucleic acids research. 2008;36(suppl_1):D901-D6. doi: 10.1093/nar/gkm958.

241. Rédei GP. PubChem. New York: Springer; 2008. p. 1599.

242. National Cancer I. Navigate the National Cancer Institute: cancer.gov. Bethesda, Md. U6 - ctx_ver=Z39.88-2004&ctx_enc=info%3Aofi%2Fenc%3AUTF-8&rfr_id=info:sid/summon.serialssolutions.com&rft_val_fmt=info:ofi/fmt:kev:mtx:book&rft.genre=book&rft.title=Navigate+the+National+Cancer+Institute&rft.series=NIH+publication&rft.date=2002-01-01&rft.pub=U.S.+Dept.+of+Health+and+Human+Services%2C+National+Institutes+of+Health%2C+National+Cancer+Institute&rft.volume=no.+03-5008.&rft.externalDocID=5753691&paramdict=en-US U7 - eBook: U.S. Dept. of Health and Human Services, National Institutes of Health, National Cancer Institute; 2002.

243. Bento AP, Gaulton A, Hersey A, Bellis LJ, Chambers J, Davies M, Kruger FA, Light Y, Mak L, McGlinchey S, Nowotka M, Papadatos G, Santos R, Overington JP. The ChEMBL bioactivity database: an update. Nucleic acids research. 2013;42(D1):D1083-D90. doi: 10.1093/nar/gkt1031.

244. Buolamwini JK, Adjei AA. Novel anticancer drug protocols. Totowa, NJ: Humana Press; 2003.

245. Sandeep G, Nagasree KP, Hanisha M, Kumar MMK. AUDocker LE: A GUI for virtual screening with AUTODOCK Vina. BMC research notes. 2011;4(1):445-. doi: 10.1186/1756-0500-4-445.

246. Liu H, Wang L, Lv M, Pei R, Li P, Pei Z, Wang Y, Su W, Xie XQ. AlzPlatform: an Alzheimer's disease domain-specific chemogenomics knowledgebase for polypharmacology and target identification research. J Chem Inf Model. 2014;54(4):1050-60. Epub 2014/03/07. doi: 10.1021/ci500004h. PubMed PMID: 24597646; PMCID: Pmc4010297.

247. Wang L, Ma C, Wipf P, Liu H, Su W, Xie XQ. TargetHunter: an in silico target identification tool for predicting therapeutic potential of small organic molecules based on chemogenomic database. Aaps j. 2013;15(2):395-406. Epub 2013/01/08. doi: 10.1208/s12248-012-9449-z. PubMed PMID: 23292636; PMCID: Pmc3675739.

248. Kogej T, Engkvist O, Blomberg N, Muresan S. Multifingerprint based similarity searches for targeted class compound selection. J Chem Inf Model. 2006;46(3):1201-13. Epub